CRUSTAL SUBDUCTION AND THE EXHUMATION OF (ULTRA)HIGH-PRESSURE TERRANES: CONTRASTING MODES WITH EXAMPLES FROM THE ALPS AND CALEDONIDES

by

Jared P. Butler

Submitted in partial fulfilment of the requirements
for the degree of Doctor of Philosophy

at

Dalhousie University
Halifax, Nova Scotia
June 2013

DALHOUSIE UNIVERSITY

DEPARTMENT OF EARTH SCIENCES

The undersigned hereby certify that they have read and recommend to the Faculty of Graduate Studies for acceptance a thesis entitled "CRUSTAL SUBDUCTION AND THE EXHUMATION OF (ULTRA)HIGH-PRESSURE TERRANES: CONTRASTING MODES WITH EXAMPLES FROM THE ALPS AND CALEDONIDES" by Jared P. Butler in partial fulfilment of the requirements for the degree of Doctor of Philosophy.

Dated: June 3, 2013

External Examiner: _____

Research Co-supervisors _____

_____

Examining Commitee: _____

_____

Departmental Representative: _____

DALHOUSIE UNIVERSITY

DATE: June 3, 2013

AUTHOR: Jared P. Butler

TITLE: CRUSTAL SUBDUCTION AND THE EXHUMATION OF (ULTRA)HIGH-PRESSURE TERRANES: CONTRASTING MODES WITH EXAMPLES FROM THE ALPS AND CALEDONIDES

DEPARTMENT OR SCHOOL: Department of Earth Sciences

DEGREE: PhD CONVOCATION: October YEAR: 2013

Signature of Author

Table of Contents

List of Tables

List of Figures

Abstract

The widespread recognition of (ultra)high-pressure ((U)HP) metamorphic rocks in orogens worldwide suggests that subduction and exhumation of crustal rocks from mantle depths are normal processes at convergent plate margins. However, the dynamics of these processes, in particular the comparative roles of erosion and crustal extension, and the driving forces of extension during (U)HP rock exhumation, remain controversial.

This thesis presents numerical modeling and field/analytical studies that address the geodynamics of crustal subduction and exhumation in two intensely studied orogens, the Alps and the Caledonides. The 2D numerical models show how different scales and durations of orogeny and plate motions can lead to marked contrasts in the style of orogenic growth, crustal subduction, and (U)HP exhumation. In the Western Alps, rapid exhumation ($\sim$1–3 cm a^{-1}) can be explained by local, syn-orogenic extension driven by the buoyant ascent of deforming (U)HP crust from the subduction channel. Later trans-crustal exhumation probably resulted from the combined effects of syn-convergent thrusting, local extension, and erosion. The low temperatures (500–700°C) of Alpine (U)HP metamorphism are attributable to the small size of the orogen and short duration of subduction/exhumation. Contrary to recent suggestions, neither erosion nor absolute extension is required to explain (U)HP exhumation in the Alps.

The Western Gneiss Region (WGR) (Norwegian Caledonides), in contrast, can be explained by subduction to (U)HP conditions followed by plate divergence. Gravitational spreading of a thick, hot orogenic wedge leads to a short period of coeval thrusting and extension. Exhumation of (U)HP crust from the subduction channel is achieved by normal-sense shearing along the top of the (U)HP terrane, with minor associated shortening. Trans-crustal exhumation by vertical thinning of the orogenic wedge results from continued absolute extension and erosion. The comparatively high temperatures (700–800°C) achieved by Caledonian (U)HP rocks reflect the orogen's greater size, slower exhumation rates, and possible stalling of the (U)HP terrane at depth.

These contrasting models underscore the variety of possible mechanisms responsible for (U)HP exhumation, and represent new benchmarks in the understanding of Alpine and Caledonian tectonics and (U)HP rock exhumation in general.

List of Abbreviations and Symbols Used

General Abbreviations	
Abbreviation	Description
ALE	Arbitrary Lagrangian Eulerian
avPT	THERMOCALC Average PT Mode
BS	Blueschist (Metamorphic Facies)
CL	Cathodoluminescence (Imaging)
CLM	Continental Lithospheric Mantle
Cont.	Continental
DM	Dora Maira
DMD	Dry Maryland Diabase
ECM	External Crystalline Massif(s)
GP	Gran Paradiso
GS	Greenschist (Metamorphic Facies)
GSZ	Gressoney Shear Zone
HP	High Pressure (Metamorphism)
HREE	Heavy Rare Earth Elements
ICM	Internal Crystalline Massif(s)
ID-TIMS	Isotope Dilution-Thermal Ionization Mass Spectrometry
IL	Insubric Line
IMC	Inner Microcontinent
IRB	Inner Rift Basin
LC	Lower Crust
LGFZ	Lærdal-Gjende Fault Zone
LP	Low pressure (Metamorphism)
LREE	Light Rare Earth Elements

Continued on next page...

Abbreviation	Description
LS	Large-Scale (Computational Grid)
Ma	Megaannum 'Million Years Ago'
MC	Microcontinent
Mo	Modereck Nappes
MR	Monte Rosa
MU	Money Unit
Myr	Millions of Years
Myr-pb	Millions of Years Post-Breakoff
Myr-pc	Millions of Years Post-Collision
NSDZ	Nordfjord-Sogn Detachment Zone
OC	Oceanic Crust
OLM	Oceanic Lithospheric Mantle
OMC	Outer Microcontinent
ORB	Outer Rift Basin
PC	Procontinent
PFT	Penninic Frontal Thrust
P–T	Pressure–Temperature
P–T–t	Pressure–Temperature–time
PURC	Prowedge-Uplifted Plug-Retrowedge-Conduit
Qtz-Ecl	Quartz-Eclogite (Metamorphic Facies)
RC	Retrocontinent
REE	Rare Earth Elements
Sed.	Sediment
SHRIMP	Sensitive High-Resolution Ion Microprobe
SLM	Sublithospheric Mantle
SS	Small-Scale 'Nested' (Computational Grid)
TC	THERMOCALC
TW	Tauern Window
UHP	Ultra-High Pressure (Metamorphism)
(U)HP	(Ultra)-High Pressure (Metamorphism)

Continued on next page...

Abbreviation	Description
WDS	Wavelength Dispersive Spectroscopy
WGC	Western Gneiss Complex
WGR	Western Gneiss Region (of Norway)
WOL	Wet Olivine
WQ	Wet Quartzite
ZS	Zermatt-Saas

Mineral and End-member Abbreviations	
Abbreviation	Description
Ae	Aegirine
Alm	Almandine
Am	Amphibole
Bt	Biotite
Cel	Celadonite
Coe	Coesite
Cpx	Clinopyroxene
Di	Diopside
En	Enstatite
Fs	Ferrosilite
Grs	Grossular
Grt	Garnet
Hbl	Hornblende
Hed	Hedenbergite
Jd	Jadeite
Kfs	K-Feldspar
Ky	Kyanite
Ms	Muscovite
Omph	Omphacite

Continued on next page...

Abbreviation	Description
Opx	Orthopyroxene
Parg	Pargasite
Phn	Phengite
Pl	Plagioclase
Pyr	Pyrope
Qtz	Quartz
Rt	Rutile
Scp	Scapolite
Spss	Spessartine

Roman Symbols		
Symbol	Description	Units
a	Annum (year)	-
A_R	Volumetric Radioactive Heat Production	μWm^{-3}
A_{SH}	Shear Heating	Wm^{-3}
A	Pre-exponential Factor for Power-Law Flow	MPa^{-n} s^{-1}
c_p	Specific heat	J g^{-1} K^{-1}
C	Cohesion	Pa
D_0	Initial Amount of Daughter Nuclide in Decay Equation	-
D	Amount of Daughter Nuclide in Decay Equation	-
E_S	Surface Erosion Rate	cm a^{-1}
E	Exhumation number	-
f	Viscosity Scaling Factor	-
g	Gravitational acceleration	m s^{-2}
h	Channel thickness	m
$\dot{I}_2'$	Second Invariant of Deviatoric Strain Rate	-
J_2'	Second Invariant of Deviatoric Stress	Pa

Continued on next page...

Symbol	Description	Units
K	Thermal Conductivity	$Wm^{-1}K^{-1}$
n	Number of Atoms in Decay Equation	-
n	Stress Exponent for Power-Law Flow	-
P	Pressure	Pa
$P_{\text{eff}}\partial x$	Effective along-channel pressure gradient	Pa m^{-1}
P_f	Pore Fluid Pressure	Pa
P_{max}	Maximum Recorded Pressure	GPa
Q	Activation Energy for Power-Law Flow	kJ mol^{-1}
R	Gas Constant	J mol^{-1} K^{-1}
T_K	Absolute Temperature	K
T	Pressure	°C or K
t	Time	s
U	Subduction velocity	m s^{-1}
u	Velocity	m s^{-1}
V_p	(Pro-) Convergence Velocity	cm a^{-1}
$V*$	Activation Volume for Power-Law Flow	m^{-3} mol^{-1}
v	Velocity	m s^{-1}
W_s	Viscosity Strain-Weakening Factor	-
x	Spatial coordinate	-
Δx	Amount of Convergence	km
y	Vertical Position Normal to Channel Wall	m

Greek Symbols		
Symbol	Description	Units
α	Thermal Expansivity	K^{-1}
β	Viscous Bulk Modulus	Pa s
ϵ	Strain	-
$\dot{\epsilon}$	Strain Rate	s^{-1}
η	Viscosity	Pa s
η^{v}_{eff}	Effective Viscosity	Pa s
λ	Decay Constant	s^{-1}
ρ	Density	kg m^{-3}
σ_{ij}	Deviatoric Stress Tensor	Pa
σ_y	Yield Stress	Pa
ϕ	Angle of Internal Friction	$^{\circ}$

Acknowledgements

I would like to thank my family, including but not limited to Sonja, Mia, Zoe, Danny, and my Ma, for their patience and support throughout the duration of my work.

I am indebted to my supervisors, Becky Jamieson and Chris Beaumont, for their guidance, patience, and generous financial support. For more than half a decade they and my committee members, Nick Culshaw and Clare Warren, have fostered my interest in convergent margin tectonics through field trips and insightful discussions. The topic of this thesis stemmed directly from Clare's work at Dalhousie.

Many others contributed greatly to the present work. My numerical modeling studies could not have been completed without Douglas Guptill, who in my time as a graduate student has dramatically improved life for SOPALE users. In the field, Peter Robinson introduced me to the complex geology of the northern Western Gneiss Region. Without Peter, our work there would not have been possible. Greg Dunning taught me the painstaking methods of U–Pb dating, for which I am extremely grateful. My field partner and friend, Holly Steenkamp, was pivotal in making our work in Norway a success.

I would also like to thank the following people for their contributions during various stages of my work: Mike Terry, Jorunn Skjelten, Dan MacDonald, Kevin Hewitt, Luke Hilchie, Pam King, Sherri Furey, John Hanchar, Chris Fisher, Dave Grant, Michael Shaffer, Jiggs Diegor, and Mike Tubrett. Also Anne-Marie Ryan, for preventing me from majoring in the Arts.

Finally I would like to thank the excellent graduate students in the department for their company, and for introducing me and my family to many great traditions.

Chapter 1

Introduction

1.1 A New View of Convergent Margin Geodynamics

In 1984, D.C. Smith and C. Chopin independently reported the separate discoveries of coesite, the high-pressure polymorph of quartz (SiO_2), in crustal rocks exposed in the Norwegian Caledonides and the Western Alps, respectively, demonstrating unequivocally the metamorphism of continental crust at pressures $\gtrsim$2.5 GPa (*Chopin*, 1984; *Smith*, 1984). These discoveries led to the recognition of a new category of 'ultrahigh-pressure' (UHP) metamorphism, and began a revolution in the understanding of convergent margin geodynamics (*Ernst and Liou*, 1999; *Chopin*, 2003). Assuming that the metamorphic pressure recorded by these rocks represented lithostatic pressure, i.e., that generated by the weight of overburden, the presence of coesite required the burial of continental crust to depths of $\gtrsim$90 km; far beyond the depths required by most prior studies of blueschist and eclogite facies high-pressure (HP) metamorphic rocks. The profound geodynamic implication of these discoveries was immediately recognized by both authors, i.e., that during the Caledonian and Alpine orogenies, continental crust had been subducted to mantle depths and subsequently exhumed to the surface (*Chopin*, 1984; *Smith*, 1984). However, the notion of such deep continental subduction was not immediately accepted among the geological community. The prevailing view was that only oceanic lithosphere could subduct into the mantle, while continental lithosphere was inherently too buoyant to enjoy the same fate, despite theoretical models demonstrating the latter possibility (e.g., *Molnar and Gray*, 1979). Even more puzzling, however, was how such deeply

subducted continental crust could be transported back to the surface.

The last two decades have seen the number of documented UHP terranes grow to over 20 (*Ernst and Liou*, 1999; *Liou et al.*, 2004), leading to a general, although not universal, consensus that deep continental subduction and subsequent exhumation were 'normal' processes at convergent plate margins throughout the Phanerozoic, which may have fundamentally shaped the evolution of orogens including the Caledonides, the Western Alps, and the Himalaya, among others (*Epard and Steck*, 2008; *Beltrando et al.*, 2010a; *Hacker et al.*, 2010). The recognition that once deeply subducted rocks are now exposed at Earth's surface has sparked a multitude of interdisciplinary studies broadly related to subduction zone processes, from chemical cycling within Earth's lithosphere and mantle (*Behn et al.*, 2011), to the dynamics of subduction and continental collision (*Warren et al.*, 2008; *Gerya et al.*, 2008; *Yamato et al.*, 2008; *Beaumont et al.*, 2009).

The present work uses numerical geodynamic modeling and field-based approaches to address the fundamental geodynamic question posed by UHP continental crust, *How are UHP continental crustal rocks formed and exhumed?* This chapter introduces the definition of UHP metamorphism, and follows with summaries of some of the common features of global UHP terranes, the current understanding of continental subduction and exhumation collated from previous modeling studies, and concludes with an overview of the objectives and content of the thesis.

1.2 Geological Aspects of UHP Metamorphism

1.2.1 Definition and Recognition of UHP Metamorphism

Ultrahigh-pressure (UHP) metamorphism is defined as metamorphism within the stability field of coesite (Fig. 1.1), the latter determined experimentally to require minimum pressures of ~2.5–3 GPa (*Boyd and England*, 1960; *Bose and Ganguly*, 1995; *Ernst and Liou*, 1999). This definition excludes rocks that obviously formed by other 'special' mechanisms, for example, coesite-bearing rocks in impact structures (e.g., *Grieve et al.*, 2012). The elegance of using coesite as an index mineral for defining UHP conditions stems from its chemical simplicity, in that it forms by a simple polymorphic transformation from quartz (or breakdown of a mineral

to release SiO_2) at UHP conditions (e.g., *Ogasawara et al.*, 2002), and that its stability is largely pressure-dependent (*Bose and Ganguly*, 1995). There is, however, one major caveat. The kinetics of quartz/coesite transformation are sufficiently rapid that upon decompression coesite will almost always immediately (on geological timescales) revert to quartz (*Gillet et al.*, 1984; *van der Molen and van Roermund*, 1986; *Mosenfelder and Bohlen*, 1997; *Perrillat et al.*, 2003; *Lenze et al.*, 2005). Consequently, documented coesite is almost exclusively (with rare exceptions, e.g., *Zhang*, 1996) found as inclusions within minerals such as garnet, pyroxene, and zircon, whose high elastic strengths allow them to act as 'pressure vessels', preserving ultrahigh-pressures, and therefore coesite, internally (*Gillet et al.*, 1984; *Parkinson and Katayama*, 1999). These container minerals may later fracture, leading to incipient or complete transformation of the included coesite to quartz, but if fracturing occurs at sufficiently low temperatures, some of the coesite will be preserved (*Perrillat et al.*, 2003). The rare preservation of coesite as inclusions in these minerals makes locating it much like finding a needle in a haystack, yet its presence has dramatic implications for the metamorphic history of the host rock, and by extension its geodynamic evolution.

Fortunately, there are now several other recognized indicators of UHP metamorphism, whose possible presence depends mainly on the composition of the protolith (cf., *Chopin and Sobolev*, 1995; *Ernst and Liou*, 1999; *Chopin*, 2003). Metamorphic (micro)diamond has been documented in several UHP terranes, in most cases in peridotites (e.g., *Vrijmoed et al.*, 2008), but also in some crustal rocks (e.g., pelites; *Dobrzhinetskaya et al.*, 1995), and like coesite its stability is strongly pressure-dependent. However, similar to coesite the presence of microdiamond provides only a lower bound, not an absolute constraint on the pressure of metamorphism. Other mineralogical indicators of UHP metamorphism include majoritic (or supersilicic) garnet (*van Roermund et al.*, 2001), supersilicic titanite (*Ogasawara et al.*, 2002), and K-bearing clinopyroxene (*Ye et al.*, 2000), among others (*Chopin*, 2003), although their interpretation is typically more complicated owing to textural complexities or a lack of experimental constraints. Traditional thermobarometry has also improved considerably, by way of refined thermodynamic datasets (*Holland and Powell*,

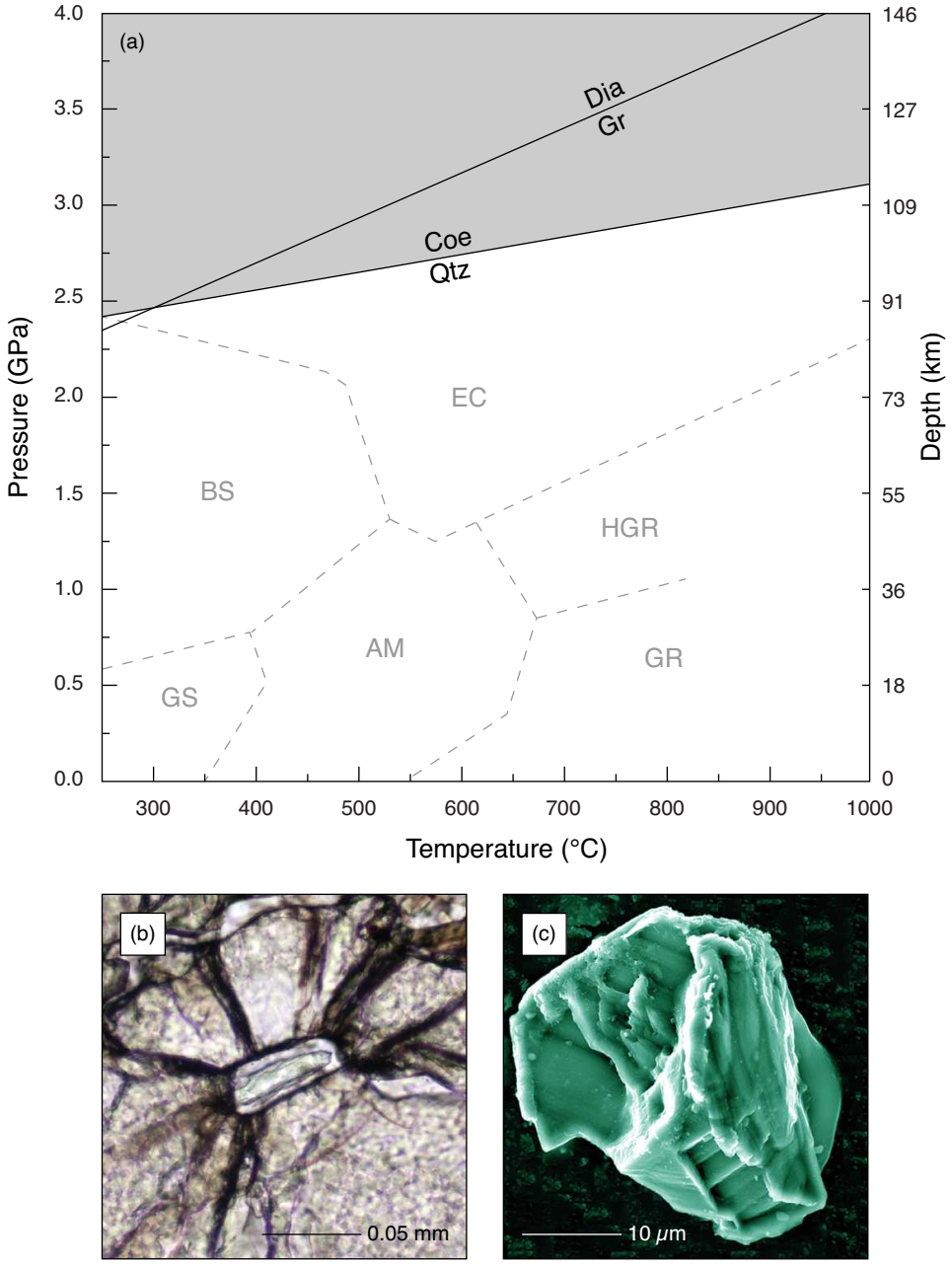

Figure 1.1: Principal indicators of UHP metamorphism. (a) Metamorphic facies diagram showing stability of coesite and diamond, modified from *Liou et al.* (2004). Depth scale calculated assuming lithostatic pressure and a crustal density of 2800 kg m^{-3}. Lower-pressure metamorphic facies are also shown in simplified form. AM=amphibolite facies, BS=blueschist facies, EC=eclogite facies, GR=granulite facies, GS=greenschist facies, HGR=high-pressure granulite facies. (b) Coesite included in garnet showing characteristic radial fracture pattern related to fracturing of host mineral (garnet) during decompression, from *Butler et al.* (2012). The coesite core of the inclusion is surrounded by a thin film of quartz. (c) Secondary electron image (SEM) of metamorphic diamond extracted from gneiss from the Erzgebirge Massif, Germany, from *Dobrzhinetskaya et al.* (2006).

1998; *Powell and Holland*, 2007), such that given the appropriate mineral assemblage it is one of the more reliable approaches to quantifying the absolute pressure-temperature (P–T) conditions of UHP metamorphism, provided the effects of diffusional resetting of mineral compositions can be avoided (*Ravna and Paquin*, 2003). In summary, given some of the additional complexities involved in these other methods, it is generally accepted that coesite and microdiamond provide the most convincing evidence of UHP metamorphic conditions, although they provide only lower bounds on the pressure of metamorphism.

1.2.2 Common Aspects among Global UHP Terranes

Since the initial discoveries by Smith and Chopin, the number of documented UHP terranes has grown considerably (Fig. 1.2; *Ernst and Liou*, 1999; *Liou et al.*, 2004). Among the most studied examples are those exposed in the Western Alps (*Beltrando et al.*, 2010a), the Greenland-Norwegian Caledonides (*Gilotti and McClelland*, 2007; *Hacker et al.*, 2010), the Dabie-Sulu terrane of east-central China (*Zhang et al.*, 2009), the Kokchetav massif of northern Kazakhstan (*Zhang et al.*, 1997), and the Bohemian massif of Germany (*Massonne*, 2011). Many others exist, including more recent discoveries in the Himalaya of India (*Mukherjee et al.*, 2003) and Pakistan (*O'Brien et al.*, 2001), and the most recent discovery of the youngest known UHP rocks in Papua New Guinea (*Baldwin et al.*, 2008). In some, but not all, of these cases evidence of UHP metamorphism was found within known high-pressure terranes. Critically, all known UHP terranes are found at present or former convergent plate margins, typically, but not always within units derived from the lower (subducted) continental plate.

The term 'UHP terrane' is defined here as an area within which UHP rocks are exposed, and does not connote a certain crustal structure, although many exhibit broadly similar architecture (see below) (*Beaumont et al.*, 2009). The area affected by UHP metamorphism may be clearly delineated, with geological structures separating it from 'normal' pressure metamorphic rocks; however, in many examples the areal extent of UHP metamorphism is poorly defined, perhaps owing to the difficulty of establishing UHP metamorphic conditions. New discoveries can change the accepted boundaries of these terranes, and consequently the tectonic models for their formation.

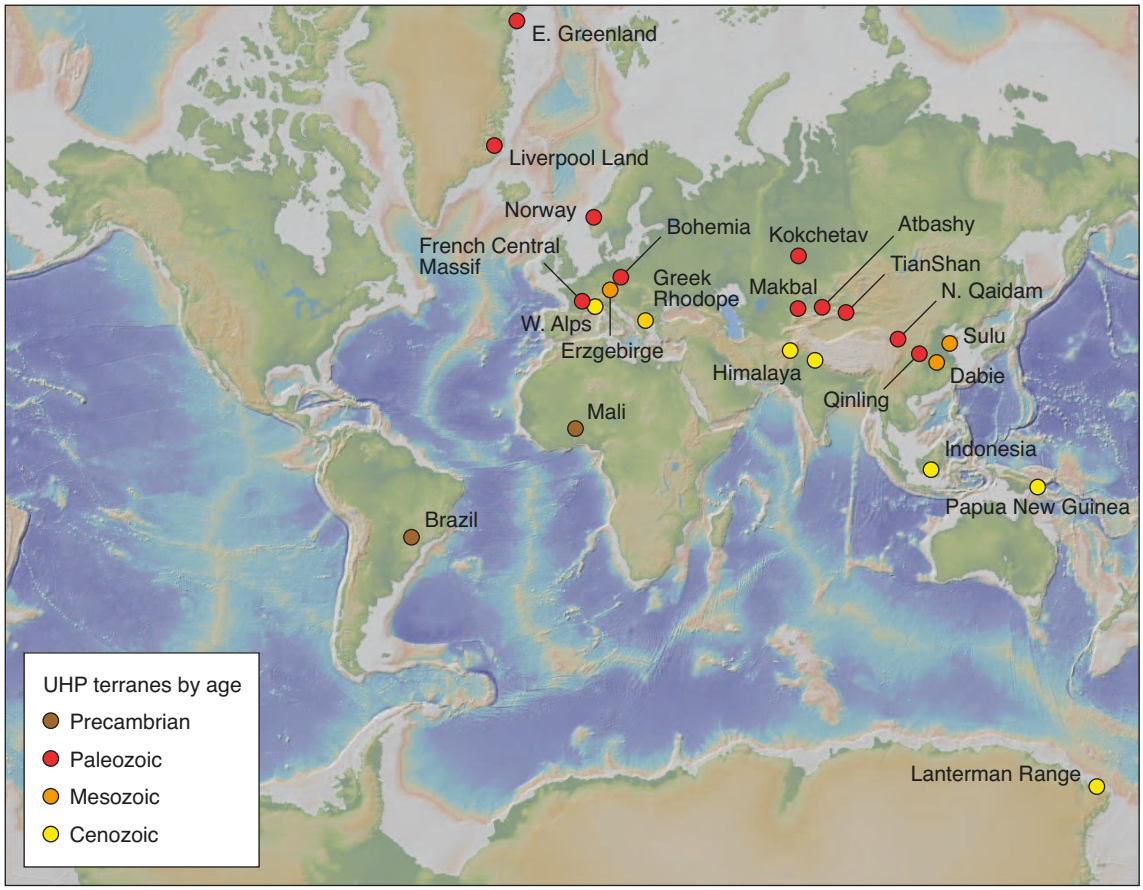

Figure 1.2: Global distribution of UHP terranes. Map shows global distribution of UHP terranes coloured by age, simplified from *Liou et al.* (2004), with global elevation model (Mercator projection) from *Ryan et al.* (2009). UHP terranes are based on well-documented discoveries of coesite and/or microdiamond, which for simplicity have been grouped together. Note that the majority of terranes are Phanerozoic in age.

Characterizing the evolution of UHP terranes requires the integration of petrological, geochronological, structural, and geophysical data, each of which faces unique difficulties. As noted above, defining the extent of UHP metamorphism in a terrane is challenging, owing to the rare preservation of UHP indicator minerals. Geochronology of UHP rocks also faces unique problems, in particular in obtaining the necessary accuracy and precision, and in relating the measured ages (typically U–Pb ages) to metamorphic conditions (e.g., *Rubatto and Hermann*, 2007). Interpreting structural geology in UHP terranes remains difficult as well, largely owing to reworking of UHP terranes at crustal depths, which typically obliterates earlier structures formed at (U)HP conditions (e.g., *Hacker et al.*, 2010). That said, in the last two decades considerable gains have been made in characterizing the tectonometamorphic histories of UHP terranes. The following list summarizes what are now considered to be the main petrological and other characteristics common to the tectonometamorphic evolutions of global UHP terranes (Fig. 1.3).

1. Metamorphic P–T conditions for UHP rocks typically reached from ∼2.5–4.0 GPa and ∼600–800°C (*Hacker*, 1996; *Chopin*, 2003), although higher pressures and temperatures (up to ∼6 GPa and ∼1000°) have been reported from some terranes (*Massonne*, 2003; *Faure et al.*, 2003).

2. UHP metamorphism was, almost always, followed by overprinting metamorphism at 'normal' crustal pressures, with many examples implying nearly isothermal decompression, i.e., decreasing pressure while maintaining nearly constant temperature (*Ernst and Liou*, 1999; *Beltrando et al.*, 2010a; *Hacker et al.*, 2010).

3. Exhumation rates estimated for (U)HP terranes are quite high, commonly ∼1–5 cm a^{-1} (*Rubatto and Hermann*, 2001; *Baldwin et al.*, 2004; *Parrish et al.*, 2006), in many cases approaching or even exceeding local horizontal plate velocities, although slower examples exist (*Carswell et al.*, 2003b).

4. In the case of UHP continental crust, the protoliths of demonstrably UHP rocks, i.e., those that preserve UHP indicators, were typically, but not always, (ultra)mafic lithologies, now exposed as eclogite or peridotite pods enclosed

within migmatitic granitoid gneisses, the latter rarely preserving evidence of UHP metamorphism (*Ernst and Liou*, 1999; *Hacker et al.*, 2010).

In addition to these aspects, many UHP terranes share similar late-stage upper-crustal structural features, which when combined with the above data can provide important clues to the mechanisms of their exhumation (Fig. 1.4; *Beaumont et al.*, 2009).

5. Many UHP terranes occupy the cores of structural domes, ranging in size from <5 km to >50 km wide (*Milnes et al.*, 1997; *Schmid et al.*, 2004; *Xu et al.*, 2006; *Epard and Steck*, 2008), in some cases defined by antiformal folding of previously formed nappe stacks (*Schmid et al.*, 2004).

6. The UHP units are typically juxtaposed with structurally higher 'normal' pressure metamorphic rocks, in some cases comprising low-grade, accretionary wedge and/or upper-crustal sedimentary rocks, and in other examples amphibolite facies rocks formed at deeper crustal levels (*Andersen*, 1998; *Reddy et al.*, 1999; *Xu et al.*, 2006; *Epard and Steck*, 2008).

7. The upper boundary 'pressure-gaps' between the UHP and overlying 'normal' pressure rocks are typically marked by ductile shear zones with normal-sense kinematics, commonly transected by later normal faults, implying crustal extension during and after UHP rock exhumation (e.g., *Andersen*, 1998; *Reddy et al.*, 1999; *Avigad et al.*, 2003).

8. The UHP domes are typically spatially associated with, and may directly underlie, ophiolitic rocks that mark the collisional suture zone between the orogenic lower and upper plates (*Platt*, 1993; *Schmid et al.*, 2004; *Epard and Steck*, 2008). The oceanic parts of sutures, in some cases, also contain evidence of UHP metamorphism.

1.2.3 Some Important Differences among UHP Terranes

The common presence of the above features could be taken as evidence that many UHP terranes originated by similar underlying mechanisms. However, there are some important differences among UHP terranes, listed below, that are difficult to reconcile with a single model.

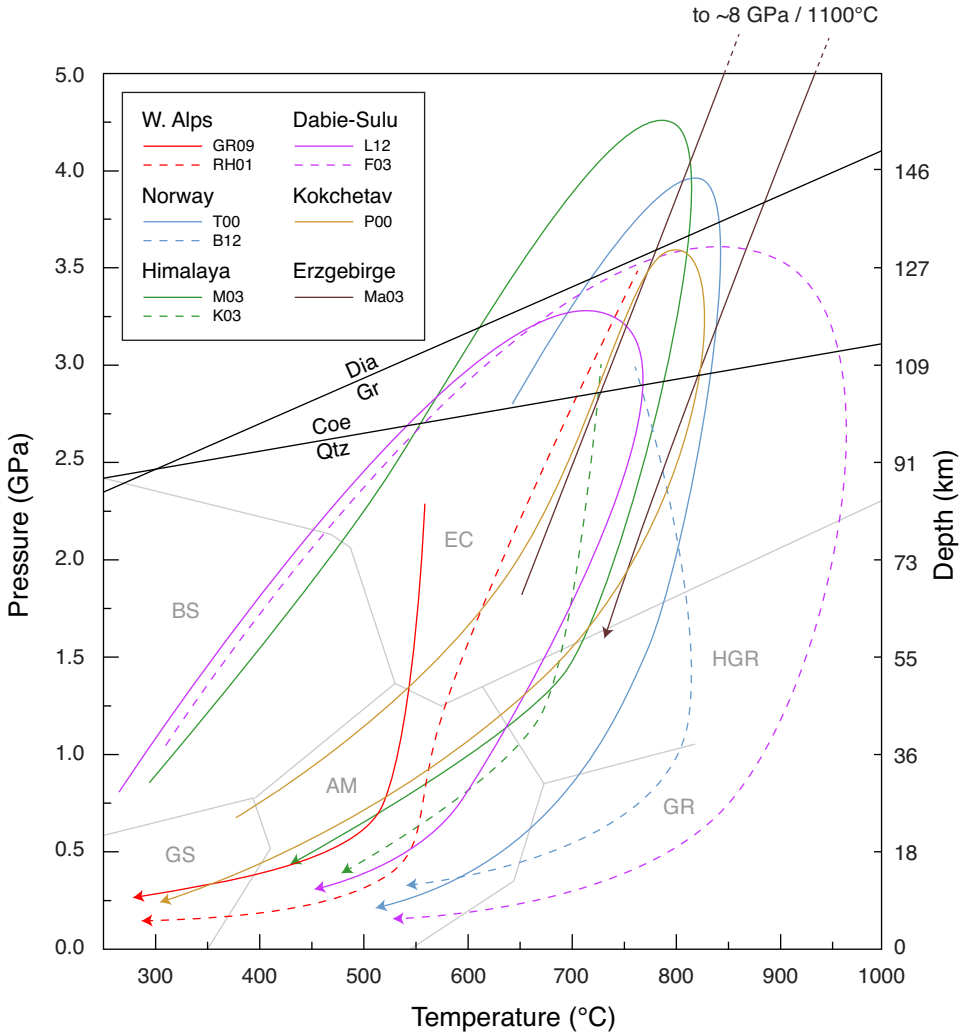

Figure 1.3: Representative P–T paths from global UHP terranes. For clarity the paths are simplified and uncertainties ignored, the latter typically on the order of ±0.25 GPa and 50°C, at a minimum. Most paths lack prograde (increasing pressure and temperature) information owing to obliteration of early assemblages at higher temperatures. Data from *Parkinson* (2000, 'P00'), *Terry et al.* (2000, 'T00'), *Rubatto and Hermann* (2001, 'RH01'), *Faure et al.* (2003, 'F03'), *Kaneko et al.* (2003, 'K03'), *Massonne* (2003, 'Ma03'), *Mukherjee et al.* (2003, 'M03'), *Radulescu et al.* (2009, 'GR09'), *Butler et al.* (2012, B12), *Liou et al.* (2012, 'L12').

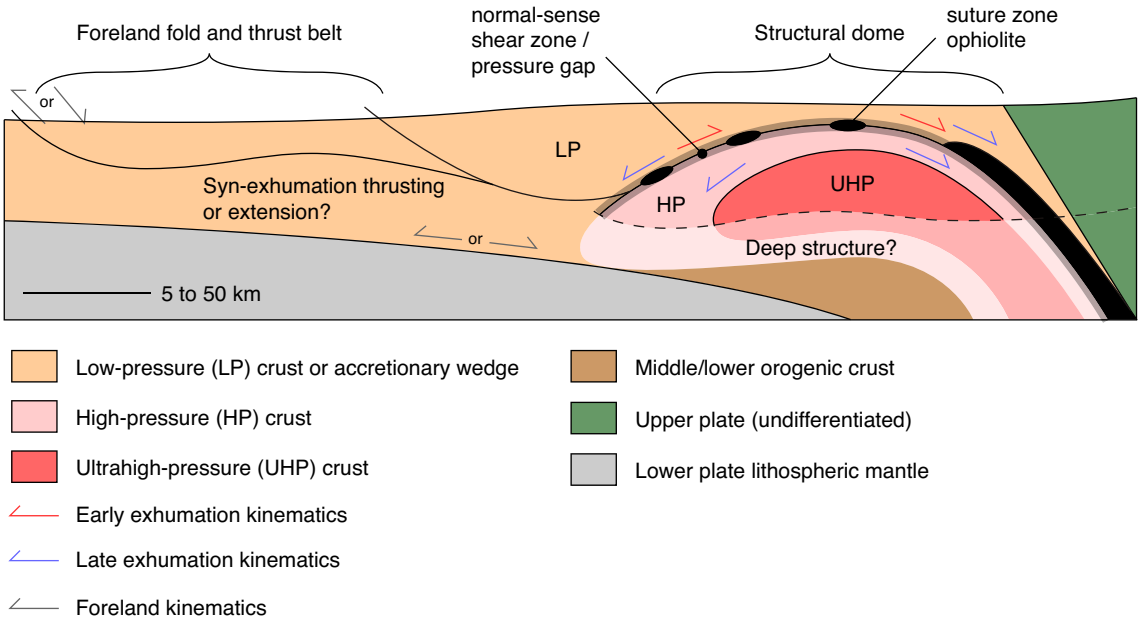

Figure 1.4: Structural elements common to UHP terranes. Modified from *Beaumont et al.* (2009). The schematic (U)HP terrane is shown as a domal structure formed by a folded nappe stack comprising tectonically juxtaposed high-pressure (HP) and ultrahigh-pressure (UHP) units, separated from overlying low-pressure (LP) rocks by a normal-sense shear zone. Vestiges of ophiolite, marking the suture zone, are scattered along this shear zone. In the illustrated example the deep structure indicates thrusting of the exhumed (U)HP units over LP units, implying syn-orogenic exhumation (see text); however, in some orogens the base of the (U)HP terrane is not exposed. Red kinematic indicators show normal-sense shearing formed by initial emplacement of (U)HP units against LP crust. Blue kinematic indicators show extensional reworking of (U)HP units during later doming (e.g., *Avigad et al.*, 2003). Grey kinematic indicators refer to deformation in the foreland of the orogen during (U)HP rock exhumation, and may indicate either continued thrusting, or extensional reactivation of earlier thrusts. The latter feature has been cited in some orogens as evidence of orogen-scale extension resulting from a switch from convergent to divergent plate motions (e.g., *Fossen*, 2010) (see text for details).

1. While many UHP terranes outcrop over relatively small areas, typically ∼2,000–8,000 km^2, some appear to be much larger, covering areas up to ∼20,000 km^2 (*Kylander-Clark et al.*, 2012).

2. While many UHP terranes formed in the early stages of continental collision (so-called 'syn-collisional' UHP terranes, e.g., *Rubatto and Hermann*, 2001; *Parrish et al.*, 2006), some appear to have formed following protracted convergence and crustal thickening ('late-orogenic' UHP terranes; *Butler et al.*, 2008; *Krogh et al.*, 2011; *Kylander-Clark et al.*, 2012).

3. Although in some orogens the (ultra)high-pressure (U)HP domes comprise distinct, often thin, nappes that record varying peak metamorphic pressures (*Avigad et al.*, 2003; *Beltrando et al.*, 2010a), other larger terranes appear to comprise relatively coherent tracts of crust within which peak metamorphic conditions vary gradually over large distances (*Cuthbert et al.*, 2000; *Hacker et al.*, 2010).

4. Similarly, descriptions of deformation of (U)HP units vary among and within single orogens from strongly deformed, mélange-like units (*Federico et al.*, 2007), to relatively undeformed units bounded by weak shear zones (*Lenze and Stöckhert*, 2007).

5. While in most orogens UHP rocks appear in units ascribed to the lower, subducting continental plate (*Beltrando et al.*, 2010a), in others UHP rocks are exposed in both the lower and upper plates (*Gilotti and McClelland*, 2007).

6. While in some orogens UHP rock exhumation can be shown to have coincided temporally with continued shortening, manifested, for example, as thrusting in the foreland (*Wheeler et al.*, 2001) or the thrusting of UHP over lower-pressure rocks (*Le Bayon and Ballèvre*, 2006), implying exhumation during convergence ('syn-convergent' exhumation), in others the evidence points to exhumation following the cessation of plate convergence and subduction ('post-convergent' exhumation) (*Fossen*, 2010; *Little et al.*, 2011).

7. Although in some orogens the transport directions of the UHP units during exhumation were broadly orogen-normal (*Reddy et al.*, 1999), in others exhumation appears to have involved substantial strike-slip deformation (*Krabbendam and Dewey*, 1998).

These differences have led to markedly different models for the formation and exhumation of UHP rocks, as summarized below.

1.3 Geodynamics of UHP Metamorphism and Exhumation

Before reviewing in detail the main types of exhumation models there is a need to address some of the critical questions concerning the origin and subsequent exhumation of UHP rocks, namely where and how on Earth are they formed, and, in a general sense, how are they exhumed?

1.3.1 Deep Continental Subduction or Overpressure?

Although there is now a general consensus that UHP metamorphic rocks formed by the burial of crust to depths $\gtrsim$90 km, given that the concept is integral to the present work, it is worth reiterating the observations underlying this conclusion. That UHP crustal rocks formed by continental subduction is supported by:

1. the high-pressure but relatively low-temperature metamorphic conditions of most UHP rocks (*Ernst and Liou*, 1999), consistent with a perturbed geothermal gradient resulting from the subduction of cool lithosphere into the underlying mantle (*Peacock*, 1996);

2. the rapid burial of rocks to UHP conditions at rates similar to plate horizontal velocities, supported by geochronology (*Lapen et al.*, 2003); and,

3. the typically close association of UHP crustal rocks with ophiolites, denoting former locations of oceanic subduction, consistent with a similar origin (*Lapen et al.*, 2007; *Epard and Steck*, 2008).

These arguments aside, the notion of deep continental subduction has, since its inception, remained the focus of skepticism among some geologists (cf., *Green*, 2005). The fundamental concern is that the thermodynamic pressures recorded by UHP

rocks, which probably correspond mainly to the mean normal stress (*Mancktelow*, 2008), may not, even approximately, correspond to lithostatic pressures resulting from deep burial, but instead to an 'overpressure' which deviates substantially from the lithostatic pressure. The implication is that UHP rocks may not require burial to such extreme depths, negating the need for subduction to explain their origin. Several types of overpressure may exist, ranging from classic 'tectonic' overpressure, to more recent concepts of 'reaction' (*Hartz et al.*, 2007) and 'melting induced' overpressure (*Vrijmoed et al.*, 2009a).

Tectonic overpressure has bearing on many geological processes aside from UHP exhumation, and consequently has received considerable attention in the literature (cf., *Green*, 2005). Interested readers are referred to *Mancktelow* (2008) for a detailed discussion of several geological situations in which tectonic overpressures can arise. There is no question that tectonic overpressures can and do occur. In the most basic form tectonic overpressure is an expected consequence of crustal shortening resulting from horizontal plate motions. The question is of the magnitude of tectonic overpressure in different geological situations, and for the present work, whether tectonic overpressure at convergent plate margins, or in subduction zones, could explain the formation of UHP rocks without the requirement for subduction of continental crust to extreme depths.

The most common argument against UHP rocks forming by tectonic overpressure is that continental crust at temperatures typical of UHP rocks (i.e., ∼600–800°C) is probably too weak to support significant sustained overpressures, and will instead undergo ductile deformation. However, this argument depends strongly on the assumed flow law (or rheology) of the crust (*Mancktelow*, 2008). Moreover, even very weak rocks can experience substantial overpressures under special conditions of confinement, for example in a subduction zone (Fig. 1.5; *Mancktelow*, 1995, 2008). Using analytical and numerical models for the flow of material in a tapered channel with rigid confining walls, *Mancktelow* (1995, 2008) showed that the magnitude of overpressure depends primarily on the distance along the channel and on the ratio of the viscosity of the material in the channel to that defining the channel walls. For a viscosity contrast of 10^4, calculated overpressures in the channel are as high

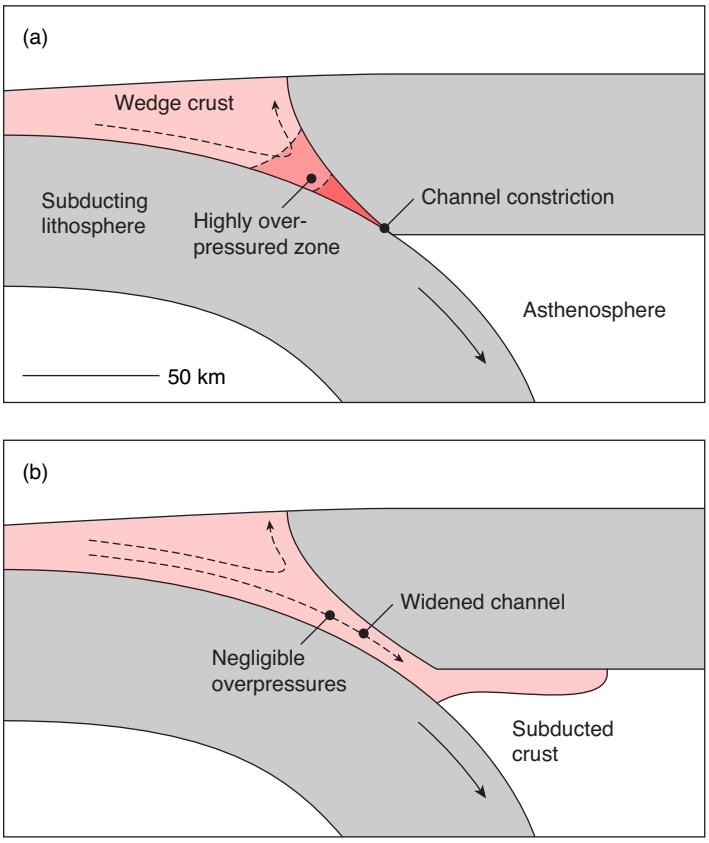

Figure 1.5: Overview of tectonic overpressures in subduction zones. The conceptual model, based on results of analytical and numerical modeling experiments (*Mancktelow*, 1995, 2008; *Li et al.*, 2010b), shows relatively weak crust (pink) flowing into a subduction channel defined by much higher viscosity lithospheric mantle, such that the latter is effectively rigid (i.e., the viscosity, $\eta_{mantle} >> \eta_{crust}$). In (a) material dragged into the base of wedge by the subducting slab reaches maximum overpressures at the 'channel constriction', i.e., the point at which the channel reaches its minimum cross-sectional area. (b) Widening of the channel leads to a decrease in overpressure.

as ∼2 GPa (*Mancktelow*, 2008). However, the assumption of rigid subduction channel walls represents an extreme end-member, and in nature it is possible not only that the mantle 'walls' of the channel may deform, diminishing overpressures, but also that the subduction channel may widen or undergo changes in geometry. More recently, 2D numerical models of continental subduction and UHP rock exhumation designed to address this issue documented typical pressure deviations (over- and underpressures) of ∼0.3 GPa (*Li et al.*, 2010b). There are several advantages to these dynamic models, and numerical models in general, in that they allow for the direct monitoring of dynamical pressures in an evolving system. Similar to the earlier analytical results, overpressures in these models are greatest in channels with wedge-like geometries, and with the strongest confining walls, with an extreme example resulting in overpressures of up to ∼1 GPa. In all of the models, the highest overpressures are achieved at the deepest level of the tapered part of the subduction channel. As the models evolve the channel typically widens and becomes more planar, and consequently the magnitudes of overpressures diminish (Fig. 1.5). Based on these models, the tectonic overpressures at depths considered typical of UHP rocks (∼100 km) are ∼10%, meaning that burial depths calculated assuming lithostatic pressure could be in error by up to 10 km, a minor difference relative to the total depth of burial implied by most (U)HP rocks.

Theoretical arguments aside, it is worth noting that no geological evidence for UHP rocks having formed by tectonic overpressures has ever been documented. An expected consequence of tectonic overpressure in a subduction channel would be that lithologies of varying strength (viscosity) would record pronounced differences in peak metamorphic pressure for the same metamorphic 'event', i.e., the same timespan. Although most (U)HP terranes are in fact characterized by relatively scattered eclogites that preserve evidence of UHP metamorphism enclosed within granitoid gneisses that record lower peak pressures, at present the geochronology suggests that the latter metamorphism occurred after (U)HP metamorphism, not coeval with it. Therefore, although some deviation from lithostatic pressure undoubtedly occurs in subduction zones, until the expected gradients in coeval peak metamorphic pressure can be demonstrated in nature, the assumption that (U)HP rocks were formed by deep subduction has not been refuted. In the author's view demonstrating the case

for an overpressure origin using such evidence will be difficult, owing in part to the susceptibility of the more felsic lithologies that typically surround (U)HP eclogites to metamorphic overprinting, and also in that it may be beyond the current limits of geochronological precision achievable in the dating of minerals grown during metamorphism.

1.3.2 Exhumation by Extension or Erosion?

The primary focus of the present work is to understand how UHP rocks are transported from mantle depths back to the near surface. The generic term for this process is exhumation, which in the case of an (U)HP terrane may be documented by its final unroofing and exposure at the surface, perhaps reinforced by the deposition of UHP detrital minerals in adjacent sedimentary basins (e.g., *Canil et al.*, 2006), or (and more commonly) in decreasing metamorphic pressures documented by petrological studies of UHP rocks (e.g., *Rubatto and Hermann*, 2001). Exhumation fundamentally requires the removal of overburden, and this can only be achieved by extension (resulting in excision of crustal section) and/or thrusting and erosion. For the present work, extension within orogens will be discussed in terms of two broad end-member regimes. The term 'absolute extension' will be used to describe extension at the scale of the entire orogen and underlying lithospheric mantle, owing for example to a switch from convergent to divergent plate motions. The term 'relative extension' in contrast, will be used to describe extension in a limited region of an orogen that is undergoing overall shortening, likely owing to continued convergence. Both types of extension involve the relative separation of rock units with respect to Earth's surface, for example by processes including normal-faulting, ductile normal-sense (simple) shear, and ductile pure-shear vertical thinning, among others. However, these two forms of extension have fundamentally different implications for plate motions in that exhumation by localized extension as described above can take place in an actively shortening orogen during plate convergence, whereas the absence of shortening in any part of an orogen during exhumation may imply absolute extension (*Fossen*, 2010).

In contrast to extension, erosion is generally regarded as playing a subordinate role UHP rock exhumation. This interpretation is supported by:

1. the rapid exhumation rates calculated for UHP terranes, many as high as ∼1–5

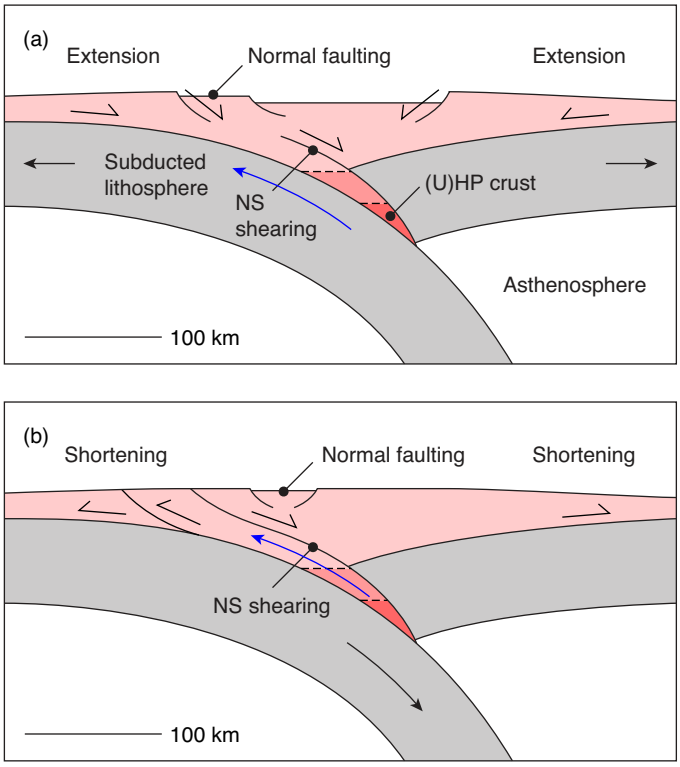

Figure 1.6: End-member modes of crustal extension during (U)HP rock exhumation. (a) Absolute extension case showing exhumation of a partially subducted slab in a bivergent orogen owing to a switch to divergent plate motions. For simplicity, this model ignores the effects of gravitational spreading. Exhumation of the subducted slice of (U)HP crust is accommodated by a normal-sense shear zone, but the slice remains coupled to the slab. In the foreland(s), thrusting has switched to top-hinterland extension. Blue arrow shows trajectory of slab and still attached (U)HP crust. NS=normal-sense. (b) Relative extension case. Here exhumation of the (U)HP slice by normal-sense shearing is accompanied by detachment and thrust-sense motion of the slab over the subducting plate, toward the foreland. Exhumation may still be accompanied by vertical thinning of the overlying wedge, but it occurs while thrust-sense deformation persists in the foreland(s) owing to continued shortening driven by subduction of the lower plate. Blue arrow shows trajectory of detached (U)HP slice over subducting slab.

cm a^{-1} (*Rubatto and Hermann*, 2001; *Parrish et al.*, 2006), which are too high to be explained by erosion, unless extremely rapid erosion was sustained for a considerable length of time (several Myr); and,

2. the common presence in (U)HP terranes of extensional shear zones separating exhumed (U)HP rocks from overlying lower-pressure units, which implies the removal of crustal section by extension, rather than erosion (*Platt*, 1993).

In many cases whether the observed extension represents localized or regional extension remains unclear, owing to incomplete geochronological or structural data. The answer again depends on the sum of the geological evidence from the orogen in question, and it is possible that both forms of extension have contributed to UHP exhumation in different orogens (see below), or at different times in the same orogen.

1.3.3 Geodynamic Models of UHP Rock Exhumation

Understanding the mechanisms of UHP rock exhumation is an interdisciplinary endeavour, requiring insights from petrology, geochronology, and structural geology, among others. However, like many geological phenomena, the process of UHP exhumation involves depths and timescales that are largely beyond the reach of these traditional observational methods. Considerable insight into the mechanics of (U)HP rock exhumation has been gained in the past few decades using geodynamic modeling, from basic conceptual and analytical models (*England and Holland*, 1979; *Platt*, 1986, 1993; *Raimbourg et al.*, 2007), to analogue physical models (*Chemenda et al.*, 1995), and more recently, numerical models (typically 2D finite-element or finite-difference geodynamic models) (e.g., *Burov et al.*, 2001; *Gerya et al.*, 2008; *Warren et al.*, 2008a; *Yamato et al.*, 2008; *Beaumont et al.*, 2009; *Butler et al.*, 2011; *Duretz et al.*, 2012; *Sizova et al.*, 2012).

Numerous analytical and conceptual models have been proposed to explain the exhumation of (U)HP rocks. These models can be broadly subdivided into those in which exhumation is driven primarily by 'internal' or 'external' forces. Models attributing exhumation to internal forces include exhumation by the buoyancy-driven transport of rocks from deep within subduction zones (*England and Holland*, 1979; *Ernst*, 1988; *Raimbourg et al.*, 2007), and exhumation resulting from relative extension within a critical wedge owing to underplating of (U)HP material (*Platt*, 1986).

Models attributing exhumation to external forces, meanwhile, include exhumation by relative extension owing to corner flow of low-viscosity material within an accretionary or orogenic wedge driven by subduction, exhumation by relative extension owing to rollback of the subducting slab during convergence (*Brun and Faccenna*, 2008), and exhumation by absolute extension resulting from divergent plate motions (*Platt*, 1986). The main limitation of conceptual and simple analytical models, however, is that many of the implied underlying forces and processes are not mutually exclusive. For example, deeply subducted UHP crust may be transported upward by buoyancy-driven flow within a subduction channel, but subsequent exhumation to shallower depths may be explained by relative extension of the orogenic wedge by consequent underplating (a process shown by many recent numerical models) (e.g., *Beaumont et al.*, 2009). Similarly, absolute extension may be enhanced by buoyancy-driven diapirism of UHP rocks through the lithosphere (*Ellis et al.*, 2011). For this reason, numerical geodynamic models can offer greater insight because they define only the underlying physics of the system, and allow the processes and related feedbacks to operate and evolve dynamically, subject to the imposed boundary conditions. Moreover, numerical models allow one to test whether or not, and under what conditions a particular model is physically feasible. Some of the more popular and recently explored styles of exhumation models from numerical modeling studies are summarized below.

1.3.4 Syn-convergent Exhumation of UHP Terranes

One of the fundamental distinctions between models of UHP rock exhumation, and in the author's opinion the most important, is whether exhumation takes place during convergence, or after convergence has ceased, here termed syn-convergent and post-convergent exhumation, respectively.

Syn-convergent exhumation of UHP rocks is generally attributed to buoyancy-driven flow of UHP rocks from within the subduction channel, i.e., the conduit comprising subducted crust situated between the lower and upper continental lithospheres. This situation has been explored by several authors using analytical models derived from lubrication theory for the flow of crust within an inclined channel bounded by two relatively rigid plates (Fig. 1.7; e.g., *England and Holland*, 1979; *Raimbourg et al.*, 2007; *Warren et al.*, 2008a). Although simplified, this analytical

model provides a good starting point for understanding the behaviour of many numerical geodynamic models of syn-convergent exhumation. In this model, flow within the channel is governed by two competing forces: the downward shear stress exerted by the subducting lithosphere, which defines the base of the channel, and the upward buoyancy force acting on the crust. The latter is an inherent result of the low density of typical continental crust (the crust in the channel), compared with that of the surrounding mantle peridotite below the base of the crust. The velocity of the crust in the channel is given by:

$$u(x,y) = -(1/2\eta)(yh - y^2)\partial P_{\text{eff}}/\partial x + U(1 - y/h) \tag{1.1}$$

where η is the assumed uniform viscosity, $\partial P_{\text{eff}}/\partial x$ is the effective down-channel pressure gradient (x measured in down-dip direction), y is the position in the channel measured normal to the base, h is the channel thickness, and U is the subduction velocity of the underlying lithosphere (*Warren et al.*, 2008a). The overlying lithosphere (upper boundary of the channel) is assumed to be stationary. Following *Raimbourg et al.* (2007), using non-dimensional variables $u' = u/U$, $h' = h/h^*$, $y' = y/h$, and $x' = x/h$, Eq. 1.2 reduces to:

$$u' = -Eh'^2(y - y'^2)/2 + (1 - y') \tag{1.2}$$

where:

$$E = h^{*2}(\partial P_{\text{eff}}/\partial x)/\eta_{\text{eff}}U \tag{1.3}$$

and:

$$h^* = (2[\eta_{\text{eff}}]U/[\partial P_{\text{eff}}/\partial x])^{1/2} \tag{1.4}$$

where $[\eta_{\text{eff}}]$ and $[\partial P_{\text{eff}}/\partial x]$ are scaled values used to estimate h^*. The term E is referred to as the 'exhumation number', and describes the competition between the upward Poiseuille flow, driven by the pressure gradient, and the downward Couette flow, driven by the shear stress at the base of the channel (Fig. 1.7a). Assuming tectonic overpressures are negligible, the effective pressure depends only on the density contrast between the crust in the channel and the surrounding mantle

(*Raimbourg et al.*, 2007):

$$\partial P_{\text{eff}}/\partial x = (\rho_{mantle} - \rho_{crust})gSin\gamma \tag{1.5}$$

where γ is the dip of the channel. The exhumation number (E) describes the propensity for upward flow of material at a given point in the channel, which will lead to exhumation. Upward flow occurs when $E > 1$, which requires that $\rho_{crust} < \rho_{mantle}$, and is favoured by low traction, which in turn is favoured by low U, low η_{eff}, and large h. Upward flow may occur with a uniform velocity profile along the length of the channel, but more likely will involve variations in E resulting from, among other factors, along-channel variations in the viscosity of the crust (Fig. 1.7b). When $E < 1$, the downward flow dominates, leading to subduction, and when $E \approx 1$ the two flows are approximately balanced, leading to possible detachment and 'stagnation' of crust in the channel, which will in turn give rise to variations in the key parameters. In numerical models, whether material exhumes from the channel depends on the integrated value of E for the entire channel length. For example, thermal weakening at depth may lead to the detachment and stagnation of material, and consequently to thickening in the base of the channel, both of which will tend to drive $E > 1$. However, the overlying crust in shallower portions of the channel may be cooler and/or stronger, leading to an integrated $E < 1$. Therefore, upward flow through the channel, and hence exhumation of UHP crust from the base, can only occur when the integrated channel $E > 1$. Later subduction of stronger continental crust will also affect the integrated E along the channel. In this case the stronger crust may limit the effective thickness of the channel, leading to exhumation by a combination of buoyancy and forced flow resulting from the constriction formed by the stronger crust (Fig. 1.7b), similar to the 'plunger expulsion' mechanism of *Warren et al.* (2008). Applications of the exhumation number concept to interpreting numerical model results are given in *Warren et al.* (2008a) and *Beaumont et al.* (2009).

Several analogue and numerical modeling studies show that buoyancy-driven exhumation of UHP rocks is a physically viable explanation. These models provide additional confirmation of, and elaborate on, the analytical solution, in part because they incorporate the behaviour of the lithosphere and overlying orogen in response

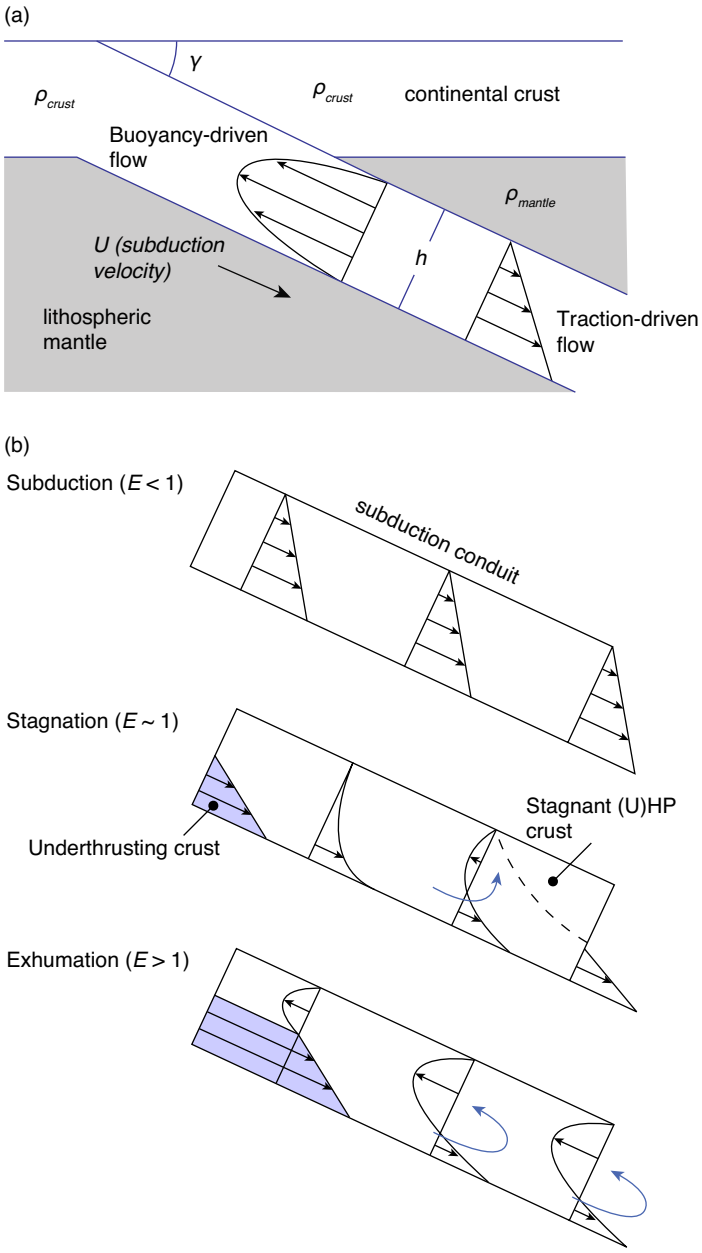

Figure 1.7: Analytical exhumation number model. (a) Illustration of the exhumation number model for UHP rock exhumation within an inclined channel, modified from *Warren et al.* (2008a). ρ_{crust}=density of crust in channel, ρ_{mantle}=density of lithospheric mantle, γ=dip of channel, h=channel thickness, U=subduction velocity. The separate velocity profiles of the buoyancy-driven and traction-driven components of the flow are also shown. (b) E values and associated flow regimes. $E < 1$ results in subduction. $E \sim 1$ occurs when the two flows are balanced, and results in detachment and stagnation of crust in the channel. $E > 1$ leads to exhumation (see text for details).

to the upward flow in the channel. Many of these studies focused on the role of buoyancy and weakening in the subduction channel, for example by strain-weakening and melt-weakening (*Burlini and Bruhn*, 2005; *Warren et al.*, 2008a; *Gerya et al.*, 2008) mechanisms. However, although these models produce P–T–t paths consistent with natural examples, only a few of the most recent studies have explicitly focused on style of deformation during UHP exhumation and the consequent crustal structure of the exhumed UHP terrane (*Beaumont et al.*, 2009). The results of these studies are generally quite similar with regards to the causes and tectonic style of exhumation (Fig. 1.8). Upward flow of material from within the subduction channel leads to underplating of the overlying orogenic wedge, which in turn leads to extension at its rear coupled with coeval foreland-directed thrusting at its toe. The extension at the rear of the wedge leads to the attenuation of the overlying crust, resulting in a dome of mixed (U)HP crust flanked by, and separated from, lower grade metamorphic rocks by extensional shear zones. The key aspect of this type of model is that the observed extension is only relative, and occurs during convergence. The normal-sense shearing (extension) above the exhuming UHP crust is accommodated at depth and in the foreland by thrusting.

The model described above is only one example of a syn-convergent exhumation model, but the underlying mechanism of buoyancy-driven exhumation along the subduction channel has been illustrated by several numerical modeling studies in the last decade. Other proposed mechanisms described in the modeling literature include relative extension resulting from hinge retreat, driven by rollback of the subducting slab (e.g., *Butler et al.*, 2008; *Sizova et al.*, 2012), and diapirism of (U)HP crust through the overlying lithospheric mantle, in cases where the overlying lithosphere is especially weak (*Sizova et al.*, 2012). However, whether or not these mechanisms offer a better explanation for observations from natural (U)HP terranes than the 'channel flow' type of model remains to be shown.

1.3.5 Post-convergent Exhumation of UHP Terranes

Post-convergent exhumation of UHP rocks has been proposed for some UHP terranes, including the examples in the Caledonides (*Fossen*, 2010) and Papua New Guinea (*Little et al.*, 2011). However, these concepts have not been as fully explored by numerical modeling studies as has syn-convergent exhumation.

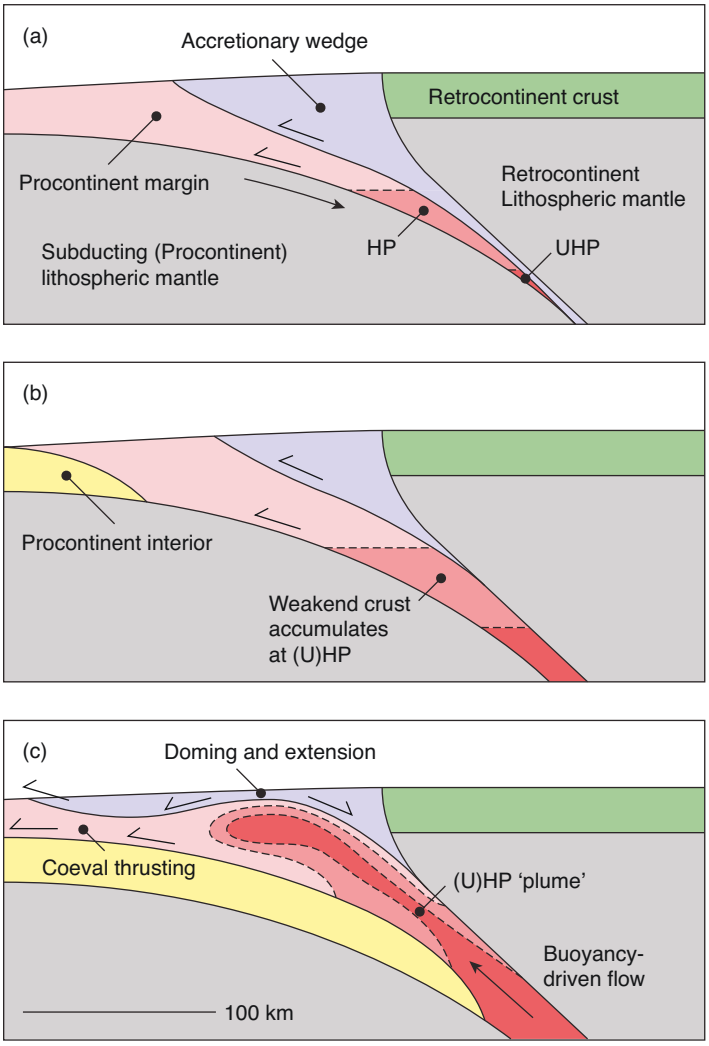

Figure 1.8: Syn-convergent channel flow exhumation model. Modified from (*Beaumont et al.*, 2009). (a) continental margin crust (pink) is subducted to HP and UHP conditions beneath an upper plate (retrocontinent). (b) Continued subduction leads to detachment and accumulation of (U)HP margin crust in the channel. The relatively rigid procontinent interior crust, representing a stronger inboard terrane, begins to underthrust the accreted margin. (c) Buoyancy propels the weakened (U)HP crust upwards along the channel as a plume. The plume tunnels into the shallower orogenic crust, causing uplift and extension of the rear of the accretionary wedge coupled with thrusting at depth and in the foreland.

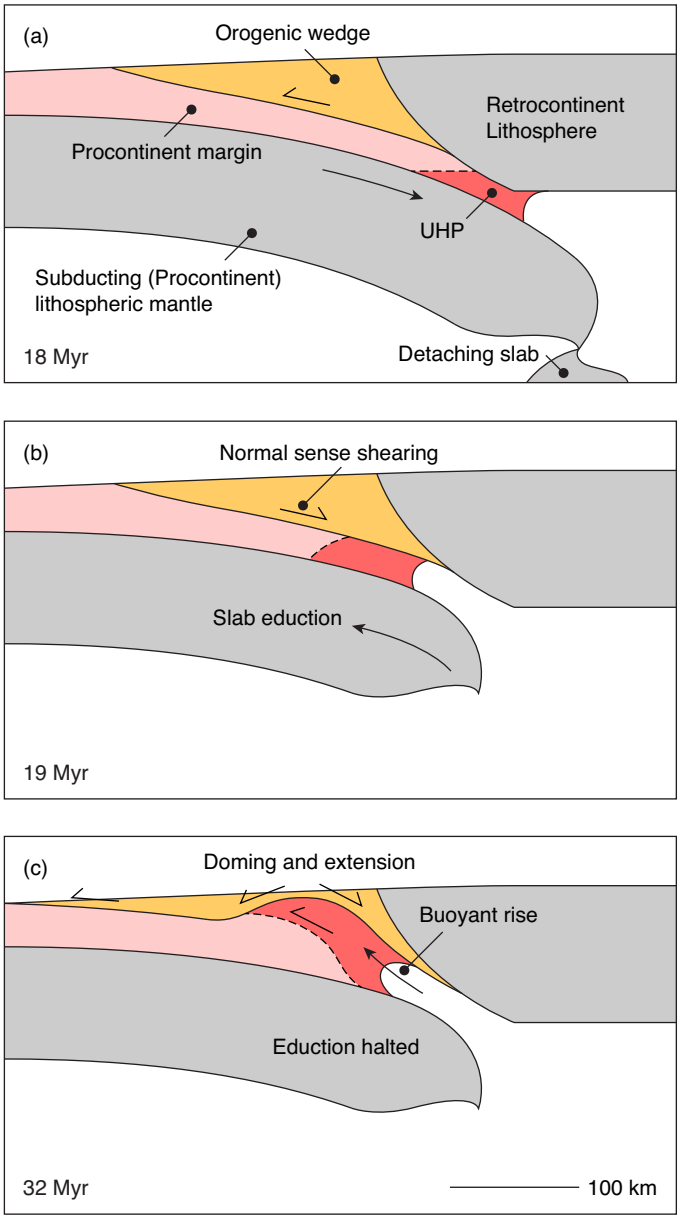

Figure 1.9: Post-convergent slab eduction exhumation model. Based on *Duretz et al.* (2012). (a) Continental lithosphere and overlying crust are subducted to UHP conditions beneath the upper plate, driven by the pull of the oceanic slab, which then undergoes slab breakoff. (b) In response to the breakoff, the subducted slab 'educts', carrying the still attached UHP crust upwards along the subduction channel. (c) Subsequent buoyant rise of material in the subduction channel at depth drives doming and extension of the overlying crust. Note that the exact position of the UHP material and the late thrusting during this stage of the model were not noted by *Duretz et al.* (2012) but have been inferred from their results by the present author. The orogenic wedge (orange) has been exaggerated for effect, and in the original models comprises mainly upper-plate continental crust, rather than material accreted from the lower plate.

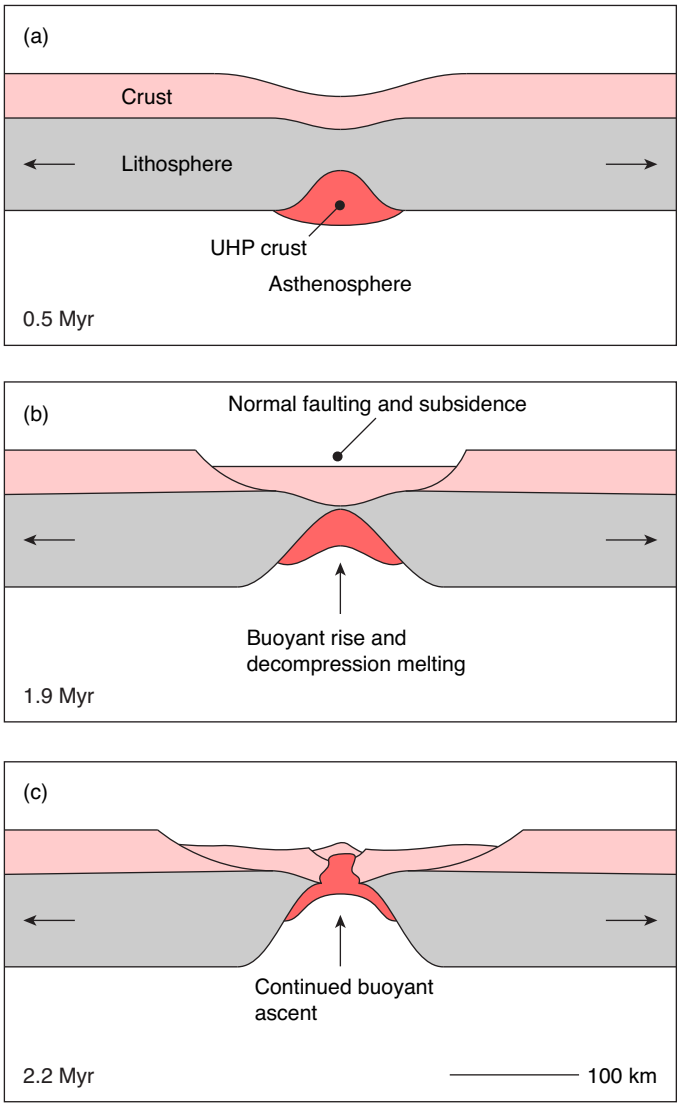

Figure 1.10: Post-convergent active rifting exhumation model. Based on *Ellis et al.* (2011). In this model, the UHP crust begins at the base of the lithospheric mantle, having presumably been transported there during an earlier phase of continental subduction which is not addressed by the model. (a) Rifting (at $\sim$ 1 cm a^{-1}) leads to necking and extension of the crust and lithospheric mantle, and to the incipient ascent of the UHP crust through the latter. (b). Ascent of the UHP crust leads to decompression melting, decreasing its viscosity and increasing its buoyancy (by melting), which in turn assist in localizing deformation of the overlying lithospheric mantle. (c) With further extension the rising UHP diapir reaches the surface.

Exhumation after the cessation of convergence can involve either localized or absolute extension. For example, in the subduction channel (exhumation number) model described above, the cessation of subduction equates to $U = 0$. Consequently, the downward traction disappears (*England and Holland*, 1979) and the UHP crust in the channel may exhume in a fashion broadly similar to that in the channel flow model described above.

Other models appeal to absolute extension of the lithosphere resulting either from changing relative plate motions, or to subduction dynamics, e.g., breakoff of the subducting slab. In the simplest case, exhumation of (U)HP rocks may be achieved by a switch from convergent to divergent plate motions. This mechanism has been proposed to explain the exhumation of (U)HP rocks in the Western Gneiss Region of Norway (*Krabbendam and Dewey*, 1998; *Fossen*, 2010), although this mechanism has not been quantified by numerical modeling. The concept is similar to 'absolute extension' of a convergent margin described above, in which a switch from convergent to divergent plate motions results in 'pullout' of the subducted slab, together with its overlying crust. Exhumation in this case could then be achieved by a combination of normal-sense shear zones formed above the exhuming (U)HP crust and vertical thinning of the overlying orogenic wedge by normal faulting or ductile flow. Although this type of model has not yet been produced by numerical modeling studies, a prototype designed based on (U)HP rock exhumation in Western Norway is explored in Chapter 7.

The numerical models of post-convergent exhumation available in the literature do appeal to absolute extension resulting from divergent plate motions, but in a somewhat different manner than proposed above. In the first example, UHP metamorphism is achieved by deep continental subduction, after which plate convergence ceases owing to breakoff of the subducting slab (Fig. 1.9; *Duretz et al.*, 2012). The breakoff leads to buoyant rebound and 'eduction' (pulling out) of the partially subducted continental lithosphere, and exhumation of UHP rocks to lower crustal depths (*Duretz et al.*, 2012). Subsequent exhumation is achieved by the buoyant rise of crust with respect to the mantle, similar to the syn-convergent numerical models described above. An interesting aspect of this model is that the late-stage structural evolution is quite similar to the channel-flow type model of *Beaumont et al.* (2009),

in that it involves doming at the rear of the orogenic wedge coupled with shortening at depth. Consequently, distinguishing between these two models in nature may be difficult, and it remains to be shown what predictions of the 'eduction' type model could be used to distinguish it from alternatives.

UHP rocks formed by subduction may reside at depth and later exhume by diapirism through the overriding plate (Fig. 1.10 *Ellis et al.*, 2011). These models point to a feedback between diapirism and rifting, in which exhumation leads to decompression melting of the UHP diapir, leading to decreasing viscosity and to a lesser extent density, which localizes rifting and enhances exhumation. Note that 'passive' diapirism, i.e., in the absence of absolute, lithosphere-scale extension, is unlikely to explain UHP rock exhumation, owing to the high strength of the lithospheric mantle. This tends to favour underplating of UHP crust rather than diapirism (e.g., *Warren et al.*, 2008a), unless the overlying lithospheric mantle is especially hot/weak (*Sizova et al.*, 2012), owing for example to arc magmatism. However, in regions undergoing active plate divergence, such as in the Woodlark Basin (Papua New Guinea), diapirism provides a possible explanation for UHP rock exhumation (*Little et al.*, 2011).

1.4 Objectives and Summary of Thesis Content

Despite considerable progress, reconciling the predictions of numerical models with observations from real UHP terranes remains problematic, either because existing numerical models are too generic, or because the data required to constrain the models lack accuracy and/or precision, or simply do not exist. Thus, although several types of models have been proposed, which, if any, of these can explain a given orogen in most cases remains controversial. Consequently, there is a need for both more detailed modeling and field studies, in order to assess the underlying controls on, and geological consequences of UHP rock exhumation in a given orogen.

The present work contributes to understanding the process of UHP rock exhumation by presenting numerical geodynamic models and field constraints. The thesis is divided into two parts. The first part, from Chapters 2 to 4, presents new numerical models designed to explore the geodynamics of UHP rock exhumation, first in a generic sense, and then with applications to the Western Alps.

Chapter 2 presents a simple conceptual framework together with generic numerical models of syn-convergent UHP rock exhumation in order to explore two end-member exhumation styles that can arise in simple 2D orogens. The results offer a simple explanation for why some bivergent (i.e., two-sided) orogens like the Greenland-Norwegian Caledonides may contain UHP rocks both in the subducting and overriding plates.

Chapter 3 presents a more detailed model based on similar principles, but specifically designed to address the syn-convergent exhumation of UHP rocks in Alpine-type orogens, focusing on constraints from the Western Alps. The Western Alpine orogen is among the most studied on Earth, and consequently provides an ideal opportunity to constrain the input as well as to test the predictions of numerical geodynamic models. The model results reproduce many of the key tectonic features of the Western Alps, and can be used to interpret the main stages of the Alpine collision in terms of the basic conceptual framework presented in Chapter 2.

Chapter 4 expands on the model presented in Chapter 3, by systematically exploring the sensitivity of the model to key input parameters, for example the plate convergence velocity and the rheology of the crust. The tests are designed to highlight the main controls on UHP rock exhumation within Alpine-type orogens. The results also provide possible explanations for some of the along-strike variations in the style of tectonism in the Western Alps.

The second part, from Chapters 5 to 7, presents new field constraints and numerical models designed to constrain the mechanics of (U)HP exhumation of the Western Gneiss Region (WGR) of Norway, one of Earth's largest UHP terranes.

Chapter 5 presents the results of a field study on the island of Harøya, in the northwestern WGR, that demonstrates the existence of UHP rocks there and quantifies their metamorphic history. The results provide new constraints on the overall distribution and P–T history of UHP rocks in the northwestern WGR that can be tested against the predictions of numerical geodynamic models.

Chapter 6 presents the results of a geochronology study of the UHP rocks underlying Harøya designed to assess the timing of UHP metamorphism, partial melting, and deformation that accompanied exhumation.

Chapter 7 explores the possible mechanisms of exhumation of late- to post-orogenic

(U)HP terranes, focusing on the WGR. The key characteristics of the WGR are established using data presented in Chapters 5 and 6, combined with existing observational constraints on the evolution of the Caledonides. Various modes of (U)HP terrane exhumation during late- to post-orogenic stages are then explored using numerical geodynamic models designed to capture the general aspects of the orogen.

Chapter 8 comments on the general applicability of numerical geodynamic models to geological problems, contrasts the two modes of orogenesis and (U)HP rock exhumation in the Alps and Caledonides deduced from the present models, and concludes with a list of the key scientific findings of the thesis.

Chapter 2

End-member Modes of Syn-convergent UHP Rock Exhumation in Simple 2D Orogens: Concepts and Numerical Models

2.1 Preface

This chapter is based on the article 'Crustal emplacement of exhuming (ultra)high-pressure rocks: Will that be Pro- or Retro-side?' by J. P. Butler, C. Beaumont, and R. A. Jamieson, published in the journal *Geology* (*Butler et al.*, 2011). The text has been supplemented with a more thorough explanation of the numerical modeling approach used here, and in subsequent chapters, derived from the supplemental material in the original publication. The copyright agreement forms for this and subsequent chapters derived from published manuscripts are presented in Appendix E.

2.2 Abstract

(Ultra)high-pressure ((U)HP) rocks form and exhume from deep within subduction channels, but subsequent horizontal transport in the shallower orogenic crust makes it difficult to reconstruct their tectonic histories. We use a conceptual framework and numerical models to show that buoyant exhumation from within a subduction

conduit formed during one-sided subduction may lead to emplacement of (U)HP rocks into either the lower plate (prowedge) or upper plate (retrowedge) of an orogen, depending on whether the upper plate crust deforms or acts as a backstop during exhumation. Both modes may operate at different positions or different times within an orogen, leading to emplacement of (U)HP rocks into both plates without changing subduction geometry. We propose that retrotransport during exhumation may explain some (U)HP rocks (e.g., Liverpool Land) situated in the upper plate of the Greenland-Norwegian Caledonides.

2.3 Introduction

While there is general agreement that (ultra)high-pressure ((U)HP) metamorphic rocks form during subduction, their exhumation from the subduction zone and subsequent reworking in the crust may obliterate evidence of subduction polarity, the geometry of early fabrics, and other features essential to reconstructing their tectonic histories (e.g., *Hacker et al.*, 2010). Under these circumstances, theoretical (*Raimbourg et al.*, 2007) and numerical (e.g., *Gerya et al.*, 2008; *Warren et al.*, 2008a; *Beaumont et al.*, 2009) models offer complementary insight into how and where (U)HP rocks are exhumed and emplaced into the crust. Here we use a simple conceptual template for collisional orogens to explain how contrasting styles of flow and material transport accompanying exhumation of (U)HP rocks may lead to their emplacement into either the lower or upper plate of a subduction zone. We then demonstrate this behaviour quantitatively using forward numerical models. We discuss implications for (U)HP exhumation in bivergent orogens and conclude with a potential example from the Greenland Caledonides.

2.4 Conceptual PURC Framework

Simple bivergent orogens (*Willett et al.*, 1993) with convergence normal to strike and insignificant orogen-parallel transport, can be considered conceptually to comprise four integral components (PURC; *Beaumont et al.*, 1999) (Figs 2.1, 2.2): two bounding back-to-back thrust-sense critical wedges (P, prowedge; R, retrowedge), a core region that forms an uplifted plug (U) in small cold orogens but may evolve into a plateau in large hot orogens, and an underlying subduction conduit (C) comprising

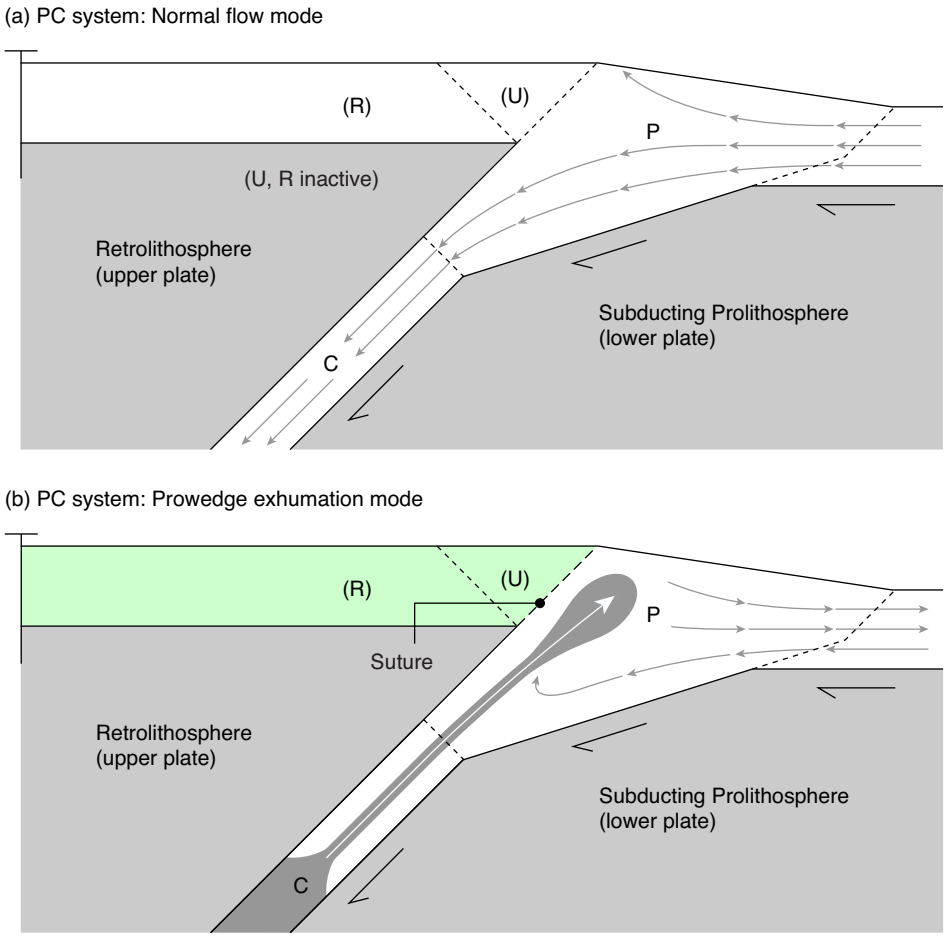

Figure 2.1: Conceptual PURC systematics for PC type orogens. (a) Tectonic style and material flow lines during 'normal' orogenesis, and (b) the prowedge (U)HP exhumation mode, which leads to exhumation and transport of (U)HP rocks toward the lower plate of the orogen. P=prowedge, U=uplifted plug, R=retrowedge, C=conduit. In (c), the green crust represents crust derived from the retrocontinent, separated from procontinent derived crust by the orogenic suture.

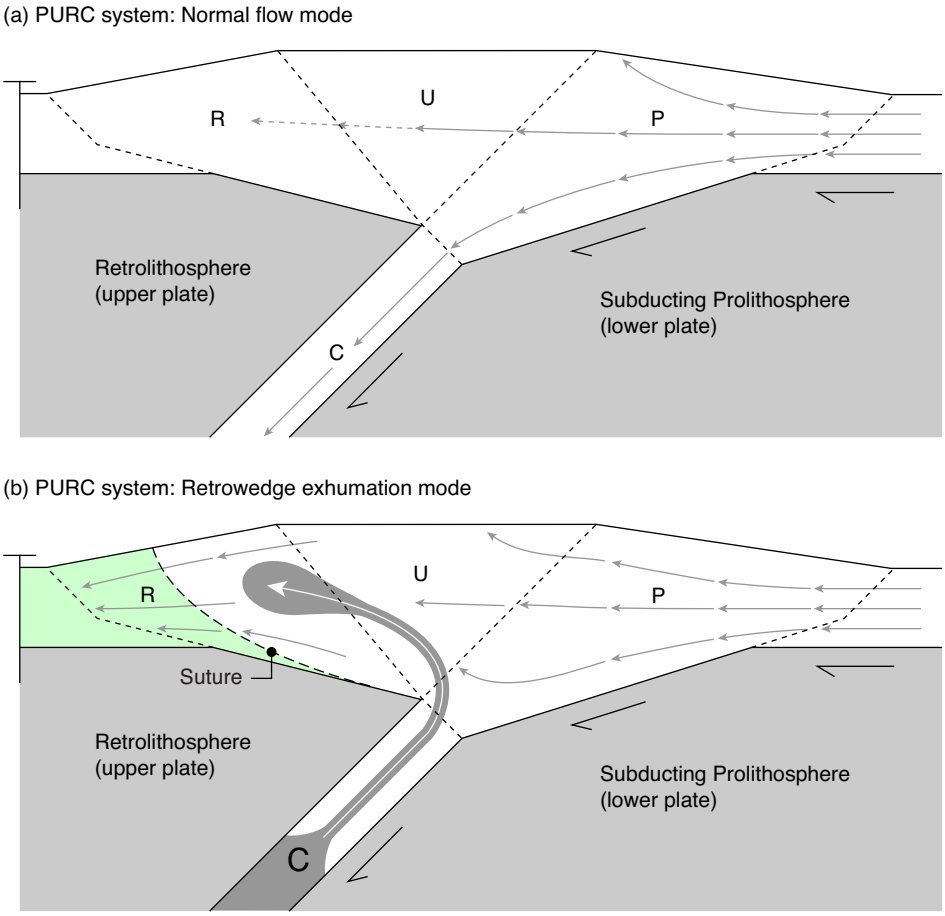

Figure 2.2: Conceptual PURC systematics for PURC type orogens. (a) Tectonic style and material flow lines during 'normal' orogenesis, and (b) the retrowedge (U)HP exhumation mode, which leads to exhumation and transport of (U)HP rocks toward the upper plate of the orogen. P=prowedge, U=uplifted plug, R=retrowedge, C=conduit. In (c), the green crust represents crust derived from the retrocontinent, separated from procontinent derived crust by the orogenic suture.

the subduction channel through which material is transported into the mantle and a storage region for subducted crust. These components have distinctive geometries and mechanics, leading to characteristic flow regimes and transport paths within each zone, and unified behaviour as a system (*Beaumont et al.*, 1999). For example, the Alps is a bivergent orogen with these characteristics and additional transcurrent deformation (*Schmid et al.*, 2004).

In simple orogenic systems, material accreted to P is normally either transferred to C and finally subducted (U and R inactive) (Fig. 2.1a), or transferred to U and possibly to R (Fig. 2.2a). During (U)HP exhumation, however, material deep in C is weakened at high temperature and pressure (*Jolivet et al.*, 2005; *Warren et al.*, 2008a), detaches, and rises as a buoyant plume that can dramatically change the system dynamics. Not only is C dominated by the return flow, but flows in P, U, and R can also be disrupted.

In the prowedge (U)HP exhumation mode (Fig. 2.1b) material flows from C into P forcing uplift, extension and normal faulting, and finally exposure of (U)HP rocks at the surface of P, commonly in the suture footwall. Both the (U)HP rocks and their hosts are derived from the procontinent, but may also contain (U)HP mantle material accreted to C from the retromantle hangingwall. In contrast, a bivergent PURC system may also exhibit retrowedge exhumation (Fig. 2.2b) in which exhuming (U)HP material flows from C into U, where it may be stored or transported into R, along with the orogenic suture. The provenance of (U)HP material remains the procontinent ($\pm$ retromantle), but it will be hosted by retrocrust if the exhuming plume disrupts and crosses the suture.

In the prowedge mode the trajectory of exhuming (U)HP rocks is up and into P, whereas in retrowedge mode it is up and into U with later transport into R. This explains how (U)HP material can be found in either the lower (P) or upper (R) plate of an orogen without requiring different subduction geometries. Below we use numerical models to demonstrate how these modes operate and to examine their basic controls.

2.5 Numerical Modeling Approach

The PURC terminology provides a convenient framework for describing two thermal-mechanical numerical models that illustrate end-member prowedge and retrowedge exhumation modes, termed Model P and Model R, respectively. The basics of the 2D finite-element modeling approach used here are described below, following (*Beaumont et al.*, 2009) and (*Butler et al.*, 2011). The same underlying approach applies to the modeling presented in subsequent chapters.

2.5.1 Explanation of SOPALE-NESTED *Software*

The models were computed using SOPALE-NESTED, a version of the plane strain, arbitrary Lagrangian Eulerian (ALE) software SOPALE (*Fullsack*, 1995) that solves thermal-mechanical creeping flows in a large-scale (LS) domain that contains a second, higher-resolution (small-scale or SS) sub-domain (Fig. 2.3, A.1). In the models presented in this chapter, the LS grid has a maximum resolution (in the lithosphere) of 10×2 km (10×10 km in the sublithosphere region), while the SS grid, positioned in the vicinity of the subduction zone (from 400 to 1400 km, and 190 km deep) has a resolution of 2×2 km. The objective of this approach is to achieve a high-resolution solution in the region of interest (the subduction zone), while minimizing computation time. The two domains share a single cloud of Lagrangian tracking particles that has a sufficiently high density throughout the model domain that the model geometry and properties can be advected through both the LS and SS domains without loss of fidelity. The initial conditions are defined for the entire model and then transferred to the LS and SS domains. For each timestep the nonlinear problem is solved iteratively for the LS domain using the LS boundary conditions. The velocity and temperature from the LS solution at nodes corresponding to the boundaries of the SS domain are then interpolated onto the boundary nodes of the SS domain, and the problem is solved iteratively for the SS domain at the higher resolution. Finally, the Lagrangian particle positions and properties are updated using the LS and SS solutions for their respective domains. Coupling between the LS and SS domains is achieved by the replacement of the LS (velocity) solution by the SS solution within the SS domain. The solutions remain coupled because the Lagrangian cloud, which defines the material properties, is shared between the two grids. This means that particles used to track material properties (e.g., pressure,

temperature, etc.) record the LS solution when they are outside of the SS domain, and the SS solution when they are inside.

2.5.2 Governing Equations

For each timestep, and in each domain (LS and SS) the models solve the equations for incompressible creeping (Stokes) flow subject to mass conservation, and energy balance:

$$\frac{\partial \sigma_{ij}}{\partial x_i} - \frac{\partial P}{\partial x_j} + \rho g_i = 0 \quad i,j = 1,2 \tag{2.1}$$

$$\frac{\partial v_i}{\partial x_i} = 0 \quad i = 1,2 \tag{2.2}$$

$$\rho c_p \left(\frac{\partial T}{\partial t} + v_i \frac{\partial T}{\partial x_i} \right) = K \frac{\partial}{\partial x_i} \frac{\partial T}{\partial x_i} + A_R + A_{SH} + v_2 \alpha g T \rho \quad i = 1,2 \tag{2.3}$$

where σ_{ij} is the deviatoric stress tensor, x_i are the spatial coordinates, P dynamical pressure, ρ density, g gravitational acceleration, v_i a component of velocity, c_p specific heat, T temperature, t time, K thermal conductivity, A_R radioactive heat production per unit volume, A_{SH} shear heating, and α volumetric expansivity. Most of the parameter values vary according to the type of 'geological' material. The last term in the heat balance equation is the temperature correction for adiabatic heating when material moves vertically at velocity v_2. During phase transitions, incompressibility (Eq. 2.2) is replaced by mass conservation (see below).

2.5.3 Model Geometry

The initial model geometry (Figs 2.3, A.1) consists of two continental lithospheres (120 km deep), each comprising 24 km of upper/middle crust overlying 12 km of lower crust, separated by oceanic lithosphere (90 km deep) capped by 8 km of oceanic crust. The upper/middle crust of the continental lithospheres includes a 6 km 'sediment' layer. A small weak zone ('weak seed'), used to facilitate the initiation of subduction, is embedded within the lithospheric mantle at the transition between the ocean and retrocontinent. Each continent's upper/middle crust is divided horizontally into a stronger 'interior', and a weaker 'margin', on the basis that continental margins

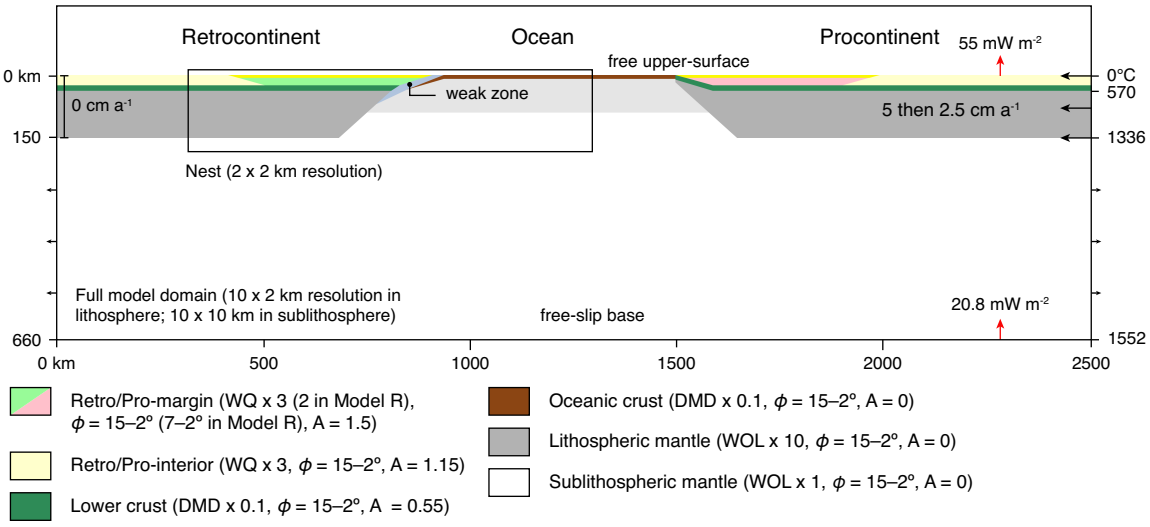

Figure 2.3: Model design. Design of 2D upper-mantle-scale model (see text and figure A.1 for details). Continent crust comprises: 24 km thick upper crust, 12 km lower crust, margins have 6 km weak sediment. Oceanic crust, 8 km. WQ $\times f$, DMD $\times f$, WOL $\times f$ are respectively wet quartzite, dry Maryland diabase and wet olivine flow laws scaled by f; ϕ gives range of frictional-plastic strain-softening; A here is radioactive heat production in μWm^3), referred to as A_R in text (*Beaumont et al.*, 2009). W_s for all crustal materials is 10, over the range of strain $\epsilon = 5$–10. Red arrows represent basal heat flux and surface heat flux.

may consist of younger, more recently accreted terranes, assembled against more metamorphosed, refractory interiors.

	Units	RC interior crust	RC margin crust	PC margin crust	PC interior crust	Lower crust	Oceanic crust	Continental mantle lithosphere	Oceanic mantle lithosphere	Sublithospheric mantle
Mechanical Parameters										
Thickness (max.)	km	24	24	24	24	12	8	114	82	to 660 km
Reference density	kg m^{-3}	2800	2800	2800	2800	2950	2900	3250	3250	3250
Reference density T	K	473	473	473	473	773	273	1609	1609	1609
Reference density HP[a]	kg m^{-3}	2850	2850	2850	2850	3100	3350	-	-	-
Reference density UHP[a]	kg m^{-3}	2900	2900	2900	2900	3100	3350	-	-	-
Effective angle of internal friction (ϕ_{eff})	deg	15–2	15–2, 7–2[c]	15–2	15–2	15–2	15–2	15–2	15–2	15–2
Cohesion	MPa	2	2	2	2	0	0	0	0	0
Flow law	-	WQ	WQ	WQ	WQ	DMD	DMD	WOL	WOL	WOL
Viscosity scaling factor (f)	-	5	3, 2[d]	3	5	0.1	0.1	10	10	1
strain-weakening factor (W)	-	10	10	10	10	10	10	1	1	1
n		4	4	4	4	4.7	4.7	3	3	3
A[b]	Pa^{-n} s^{-1}	8.57×10^{-28}	8.57×10^{-28}	8.57×10^{-28}	8.57×10^{-28}	5.78×10^{-27}	5.78×10^{-27}	1.76×10^{-14}	1.76×10^{-14}	1.76×10^{-14}
Q	kJ mol^{-1}	223	223	223	223	485	485	430	430	430
V^*	m^3 mol^{-1}	0	0	0	0	0	0	1×10^{-5}	1×10^{-5}	1×10^{-5}
Thermal Parameters										
Heat capacity	m^2 s^{-2} K^{-1}	750	750	750	750	750	750	1250	1250	1250
Thermal Conductivity	W m^{-1} K^{-1}	2.25	2.25	2.25	2.25	2.25	2.25	3	2.25	52
Thermal diffusivity	m^2 s^{-1}	1×10^{-6}	1×10^{-6}	1×10^{-6}	1×10^{-6}	1×10^{-6}	1×10^{-6}	0.7×10^{-6}	0.6×10^{-6}	1.4×10^{-5}
Thermal expansion	K^{-1}	3×10^{-5}	3×10^{-5}	3×10^{-5}	3×10^{-5}	3×10^{-5}	3×10^{-5}	3×10^{-5}	3×10^{-5}	3×10^{-5}
Heat production (A_R)	μWm^{-3}	1.15	1.5	1.5	1.15	0.55	0	0	0	0

[a] HP and UHP densities estimated from (*Hacker*, 1996) and *Walsh and Hacker* (2004).

[b] Uniaxial pre-exponential factor converted to tensor invariant form.

[c] Retrocontinental margin crust angle of internal friction is 15–2° and 7–2° in models P and R, respectively.

[d] Retrocontinental margin crust viscosity scaling factor, f, is 3 and 2 in models P and R, respectively.

Table 2.1: Model mechanical and thermal parameters.

2.5.4 Material Mechanical and Thermal Properties

The model materials have both plastic (brittle) and viscous (power-law creep) properties. Drucker-Prager frictional-plastic yielding occurs when:

$$(J_2')^{1/2} = P\sin\phi_{\text{eff}} + C\cos\phi_{\text{eff}} \tag{2.4}$$

where J_2' is the second invariant of the deviatoric stress, P the dynamical pressure (mean stress), and C the cohesion. The effective angle of internal friction, ϕ_{eff}, is defined to include the effects of pore fluid pressures through the approximate relation:

$$P sin\phi_{\text{eff}} = (P - P_f) sin\phi \tag{2.5}$$

where $\phi = 30°$ is the angle of internal of friction for dry conditions ($P_f = 0$). ϕ_{eff} is an apparent angle of internal friction of the material owing to pore fluid pressure and/or strain-softening (see below). For all normal model materials except the weak zone (Fig. 2.3), $\phi_{\text{eff}} = 15°$, approximating hydrostatic fluid pressures. The weak seed material used to initiate subduction has $\phi_{\text{eff}} = 5°$. The ϕ_{eff} of the retrocontinent margin crust is reduced from 15° to 7° in Model R in order to represent pre-existing weakness.

Ductile deformation is modeled as incompressible power-law flow, for which the effective viscosity is:

$$\eta^v_{\text{eff}} = \frac{f}{W_s} A^{-1/n} \dot{I}_2'^{(1-n)/2n} exp\left(\frac{Q + PV^*}{nRT_K}\right) \tag{2.6}$$

where f is a viscosity scaling factor, W_s is a strain-weakening factor (see below), A is the pre-exponential factor, converted to the tensor invariant form (Table 2.1), $\dot{I}'_2$ is the second invariant of the deviatoric strain rate, n is the stress exponent, Q is the activation energy, P is the pressure, V^* is the activation volume for power-law creep, T_K is the absolute temperature and R is the universal gas constant.

The viscous flow laws for the model materials are based on a small set of reliable laboratory-determined flow laws, in order to keep the models as simple as possible and facilitate interpretation. These include wet quartzite for the upper/middle crust (WQ; melt-absent Black Hills quartzite; *Gleason and Tullis*, 1995), dry Maryland

diabase for the lower crust (DMD; *Mackwell et al.*, 1998), and wet olivine for the mantle lithosphere and asthenosphere (WOL; *Karato and Wu*, 1993). The values of the pre-exponetial factor A from these flow laws are scaled linearly by the factor f to represent materials that are either stronger or weaker than the base flow law, dry vs. wet conditions, or moderate changes in composition (*Beaumont et al.*, 2006; *Warren et al.*, 2008a,b). This scaling helps to minimize the number of sources of error while allowing some variation in the flow properties, simplifies the interpretation of model results, and acknowledges uncertainties in the composition and rheological properties of Earth. The choice of reference flow law does not imply that the corresponding Earth material has the composition of the reference material.

In the present models the procontinent and retrocontinent margins each have a WQ flow law, with $f = 3$ (2 in Model R), representing a quartz-dominated crust somewhat stronger than the base WQ flow law, while the overlying sediments have a WQ, $f = 1$ flow law. The continental interiors each have a WQ, $f = 5$ flow law, representing refractory/depleted continental crust. The lower and oceanic crust both have a DMD, $f = 0.1$ flow law, corresponding to the rheology of intermediate granulite (*Mackwell et al.*, 1998). The mantle lithospheres have a depleted WOL flow law with $f = 10$, and the sublithospheric mantle has a WOL flow law with $f = 1$.

The crustal materials undergo a parametric weakening in both the frictional-plastic and ductile regimes (*Huismans and Beaumont*, 2003; *Sobolev and Babeyko*, 2005; *Warren et al.*, 2008a,b), termed 'softening' and 'weakening', respectively. Frictional-plastic materials strain-soften through a linear decrease in the effective angle of internal friction, ϕ_{eff}, with accumulated strain: $\phi_{\text{eff}} = \phi_{\text{eff}}(I_2'^{1/2})$ with ϵ ('strain') used for simplicity. This approach approximates deformation induced mechanical or pore-fluid pressure softening of faults and brittle shear zones. In the following models, for all model materials apart from the weak zone and sediments, ϕ_{eff} is reduced from 15°–2° (or 7°–2° for the retrocontinent margin crust in model R) over $0.5 \leq \epsilon \leq 1.5$ (*Huismans and Beaumont*, 2003). The weak zone is modeled as an initially weak region, $\phi_{\text{eff}} = 5°$, inherited from earlier deformation. The sediments have $\phi_{\text{eff}} = 5°$–2°.

Viscous strain-weakening, representing the combined effects of reaction and strain-weakening mechanisms during ductile deformation, proceeds through a linear decrease in effective viscosity by the factor $W_s = 10$ over the range $5 \leq \epsilon \leq 10$ for all crustal materials in the current models. The mantle lithosphere and sublithospheric mantle materials do not undergo strain-weakening in the models. Previous work has tested the sensitivity of similar models to variations in the strain-weakening factor from $W_s = 1$ to $W_s = 100$ over the range $5 \leq \epsilon \leq 10$ (*Warren et al.*, 2008a), and in the strain-weakening range, from $0.5 \leq \epsilon \leq 1$, and $2 \leq \epsilon \leq 5$ at $W_s = 10$ (Warren et al., 2008b).

The continental upper crusts have radiogenic heat production (A_R) values of 1.5 μWm^{-3} and 1.15 μWm^{-3} for the margins and interiors respectively. Lower crust has $A_R = 0.55$ μWm^{-3}. The resulting heat flow on the continental interiors is 55 mWm^{-2}, consistent with measurements from non-cratonic Phanerozoic continental lithosphere (*Vitorello and Pollack*, 1980). The Moho temperature beneath the continental interiors is ~570°C.

2.5.5 Boundary and Initial Conditions

The initial steady-state temperature field is calculated for the entire model, with 0°C surface temperature, insulated (no flux) side boundaries, radioactive heating (see below; Figs 2.3; Table 2.1), and a basal heat flux of 20.8 mWm^{-2}. For the continental interiors this gives a Moho temperature of 570°C, a basal lithosphere temperature of 1336°C, and corresponding surface heat flow (55 mWm^{-2}) typical of Phanerozoic or older continental lithosphere. The sublithospheric mantle has a high thermal conductivity to maintain a heat flux and temperature gradient of ~0.4 K km^{-1}, corresponding in nature to the mantle adiabatic gradient resulting from mantle convection.

The model has a stress-free upper surface, and no-slip and free-slip sides and base, respectively. Procontinent material enters the model domain at a velocity (V_p) of 2.5 cm a^{-1} (5 cm a^{-1} during oceanic subduction) along the right side of the model domain, and is balanced by a small outward flow of material below the lithosphere on both sides of the model. This outward flow is modulated by a 'pressure-pump' designed to keep the model in constant isostatic equilibrium and to ensure the surface remains balanced with the upper mantle outside the domain by maintaining

an average pressure at the base of the model.

Subduction in the models is initiated dynamically along a weak zone that minimizes the mechanical coupling between the two plates during the subduction initiation stage. However, on the longer term the style of subduction in the models (e.g., slab dip, degree of retromantle deformation, etc.) is dynamic, apart from the velocity boundary conditions. The models presented here were purposely designed to involve a one-sided style of subduction (similar to the weakly coupled models of *Faccenda et al.* (2008)).

2.5.6 Mass, Volume and Density Changes During Phase Transformations

The model crustal materials increase and decrease in density and volume at pressure and temperature conditions corresponding to natural metamorphic phase changes (Table 2.1) (*Warren et al.*, 2008a). The densities of lower continental and oceanic crust change across the eclogite field boundary from 2950 to 3100 kg m^{-3} and from 2900 to 3300 kg m^{-3} respectively, on the assumption that the oceanic crust is more mafic than the assumed intermediate composition lower continental crust. The density of the upper crust changes from 2800 to 2850 (HP) to 2900 kg m^{-3} (UHP), on the assumption that it consists of 10% mafic and 90% felsic material by volume and that all quartz transforms to coesite at UHP conditions (*Warren et al.*, 2008a). These density changes reverse during exhumation.

During these phase changes the incompressibility equation is modified to that of mass conservation: $\partial\rho/\partial t = -\partial\rho v_i/\partial x_i$. This accounts for the associated volume change and its effect on the buoyancy and velocity field. This volume change is calculated numerically by applying additional normal, compressive/dilative forces to finite elements at the time they are subjected to phase-related density changes. The value of the excess pressure is $\Delta P = \Delta\rho/\beta_v\rho$, where β_v is the viscous bulk modulus of the material, and $\Delta\rho/\rho$ is the fractional change in density corresponding to the phase change. The excess pressure compresses material locally and only during the model time steps when the phase changes occur, thereby ensuring mass conservation. The fractional volume change accompanying a phase change is small in these models and its effect on the velocity field is minor because it only applies at the time of the phase change. However, failure to ensure mass conservation has a long-term effect

on the model because the buoyancy forces will be over- or underestimated by the fractional error in the material volume.

2.6 Model Results

2.6.1 Prowedge Exhumation Mode

The prowedge mode (Model P; Figs 2.4, A.2) arises where retrocontinent crust is initially as strong as procontinent crust. During the early stages of collision (Fig. 2.4a), most of the sediment on top of the procontinent margin detaches, accreting to the front or base of P. The stronger margin crust remains coupled to the lower plate and subducts to (U)HP conditions (∼5 GPa/800°C). Margin crust that reaches the base of C detaches from the slab and accumulates as subduction continues. With increasing volume, strain, and temperature, this (U)HP material stored in C becomes sufficiently weak and buoyant that it is exhumed in a rapid pulse (up to ∼5 cm a^{-1}) to the base of P (Fig. 2.4c). In this model the strong retrocontinent crust acts as a backstop, restricting the flow of exhuming crust to P. Rapid prowedge growth results from flow of (U)HP material from C into P, which drives material upwards and outwards by a combination of vertical thinning and extension at the rear of the wedge and thrusting over the procontinent (Fig. 2.4). The final geometry is a prowedge, P, with a structural dome at its rear containing (U)HP procontinent crust, flanked toward its toe by an allochthonous stack of procontinent margin sediment, oceanic suture zone material, and retrocontinent margin crust.

2.6.2 Retrowedge Exhumation Mode

The retrowedge mode (Model R, Figs 2.5, A.3) arises in models of this type when the retrocontinent margin crust is initially somewhat weaker than the procontinent ($\phi_{\text{eff}} = 7°$ vs. $15°$, $f = 2$ vs. 3; Table 2.1). Most of the early material transport is from P into C, with minor flow into U and R leading to limited retrothrusting (Fig. 2.5a). Exhumation of (U)HP material from C into P leads to a brief period of prowedge growth (Fig. 2.5b). However, as the exhuming (U)HP material pierces the orogenic crust the retrocrust fails, leading to a dramatic flow of material from P, through U and into R (Fig. 2.5c). The flow of (U)HP material through R drives vertical thinning in U and at the rear of R, coupled with outward thrusting of R over the retrocontinent, contributing to further growth of R by frontal accretion. The

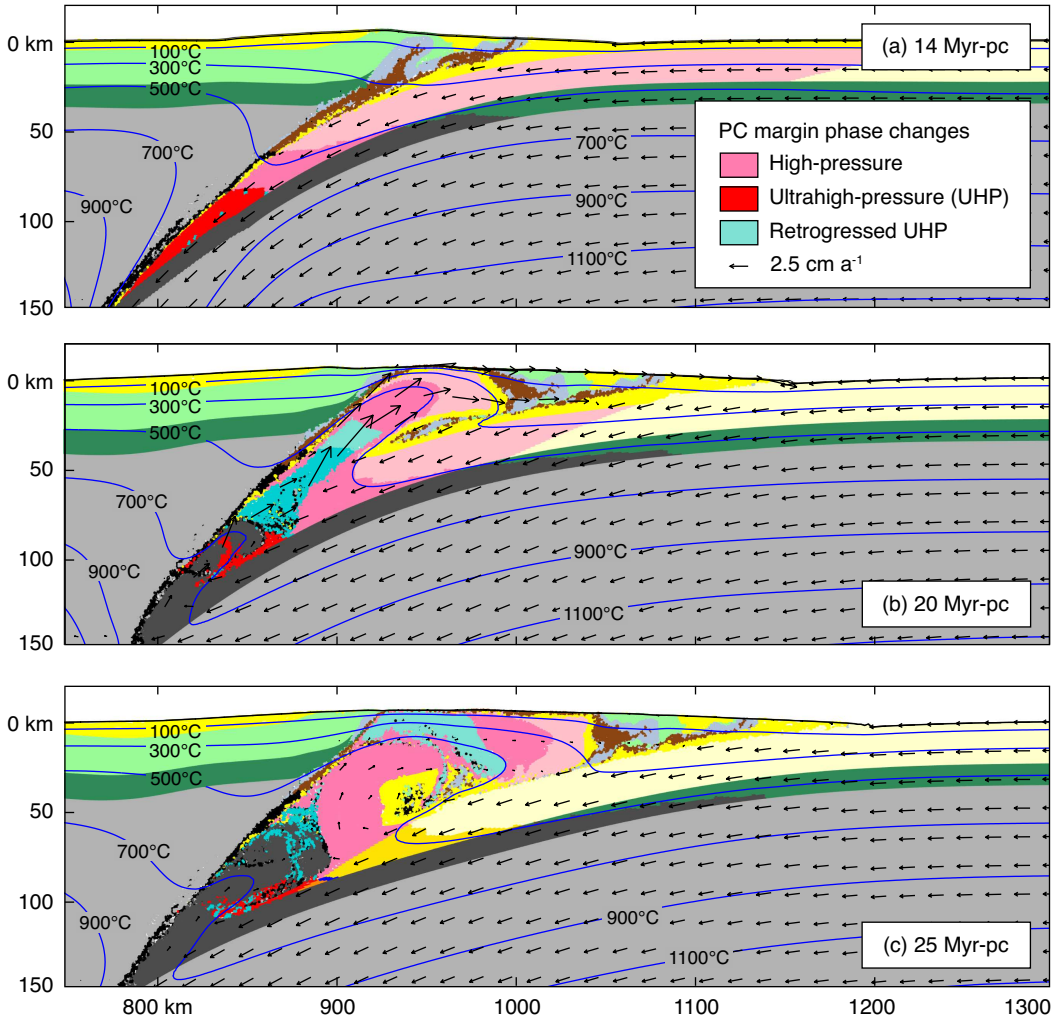

Figure 2.4: Model P results. Time is time elapsed since collision defined as the time of contact of procontinent with accretionary wedge (Myr-pc). Models of this type have weak coupling between the upper and lower plates. (a) PC accretion mode. (b) Early prowedge (U)HP exhumation mode. (c) PC mode following (U)HP emplacement in prowedge.

resulting bivergent orogen comprises a prowedge containing an allochthonous nappe stack, an uplifted and stretched plug, and a retrowedge containing procontinent (U)HP crust overlying normal retrocontinent crust. Similar retrotransport was noted by *Gerya et al.* (2008).

The transport direction of the exhuming (U)HP plume depends on the mechanical response of the orogenic crust to the influx of material from C. For these models this is determined by the strength of the retrocrust. Sensitivity analysis demonstrates that when initial $\phi_{\text{eff}}(\text{Pro}) = 15^\circ$ and $f(\text{Pro}) = 3$, retrocrust with the same properties is strong and acts as a backstop. In contrast, when $\phi_{\text{eff}}(\text{Retro}) \leq 7^\circ$ and $f(\text{Retro}) \leq 2$, the retrocrust is sufficiently weak that it fails, thereby flipping the dominant transport direction from P to R during exhumation. In natural orogens, such upper plate weakening can result from formation of weak faults, earlier accretion of weak terranes, and/or high thermal gradients reflecting arc magmatism. Similarly, in natural systems the onset of retrothrusting may pre- or postdate (U)HP exhumation or coincide with it. The model exhibits an early phase of weak retrothrusting (Fig. 2.5a) but most coincides with (U)HP exhumation.

2.7 Retrowedge Exhumation in the Greenland Caledonides?

The discovery that Devonian (U)HP exhumation took place on both sides of the Greenland-Norwegian Caledonides requires rethinking of models for (U)HP exhumation in bivergent orogens. Silurian to Devonian subduction of Baltica beneath Laurentia is widely accepted (e.g., *Roberts and Gee*, 1985), based in part on widespread (U)HP metamorphism in the Western Gneiss Region (WGR) of Norway (*Cuthbert et al.*, 2000; *Hacker et al.*, 2010). Devonian (U)HP rocks in the Liverpool Land Eclogite Terrane (LLET), east Greenland Caledonides (*Hartz et al.*, 2005; *Augland et al.*, 2010), thus lie in what was then the orogenic upper plate (Fig. 2.6a,b). The weight of evidence, protolith ages and metamorphic history (*Augland et al.*, 2010; *Johnston et al.*, 2010), indicates that the LLET derives from Baltica. If so, there is no need to invoke double subduction (*Faccenda et al.*, 2008) or a polarity flip. Instead, based on our models, we propose that the LLET formed in the Baltican

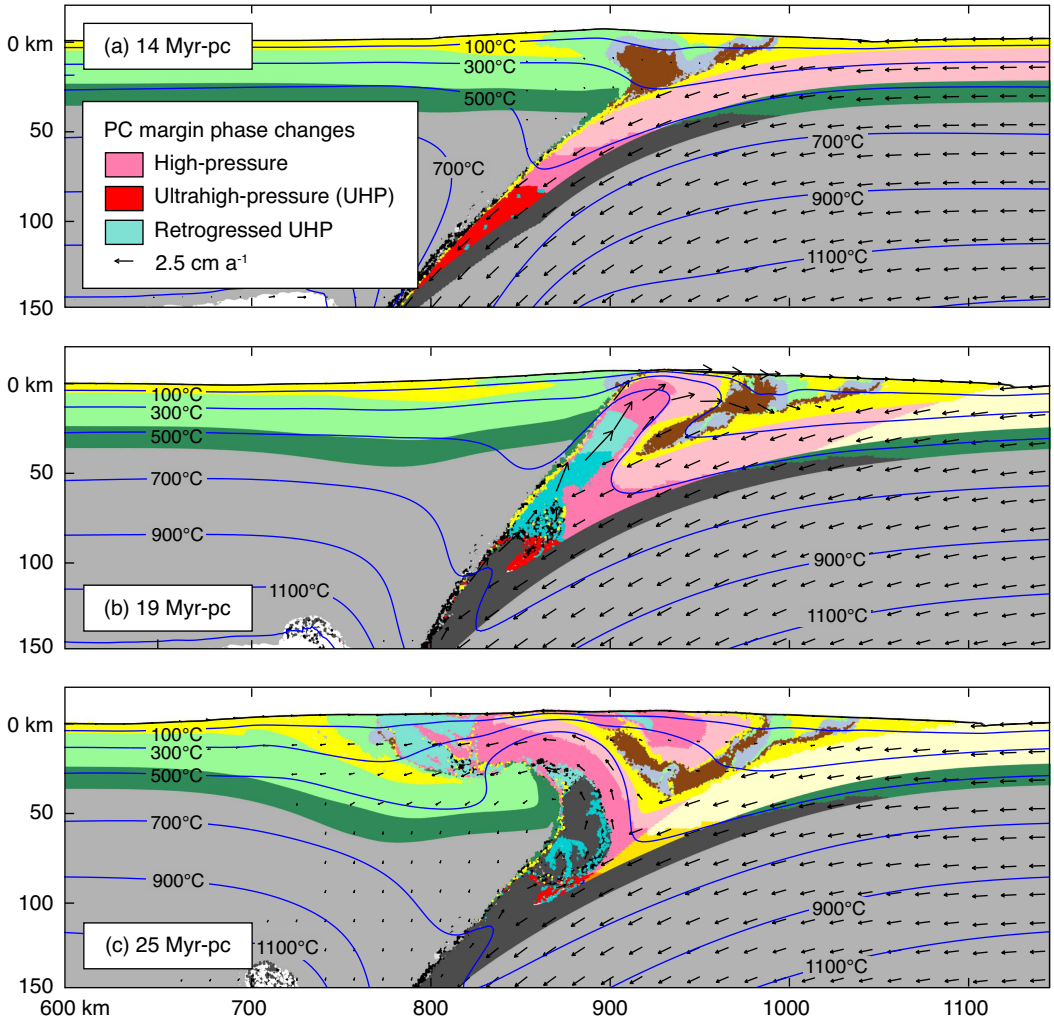

Figure 2.5: Model R results; design as in Fig. 2.3 except for initial ϕ (7° versus 15°) and f (2 versus 3) of retrocontinent margin. (a) PC mode with subsidiary retrothrusting. (b) Early stage of retrowedge (U)HP exhumation mode. (c) PURC geometry following (U)HP emplacement in retrowedge.

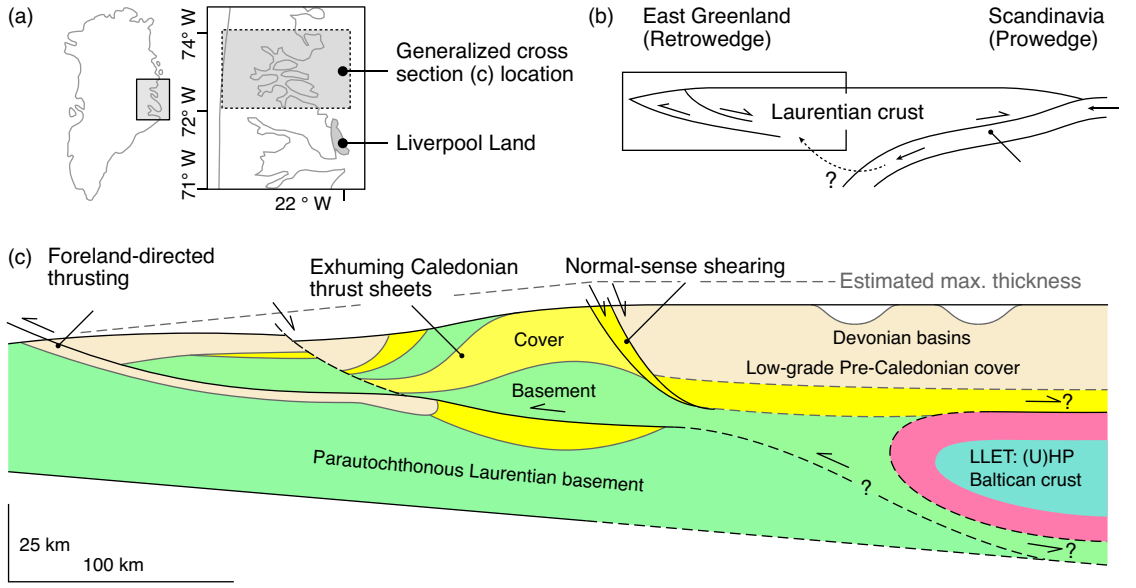

Figure 2.6: Cross-section through east Greenland Caledonides. (a) Location of the east Greenland Caledonides and the Liverpool Land Eclogite Terrane (LLET) (inset). (b) Generalized cross section showing the east Greenland retrowedge in the upper plate of the Caledonian orogen (modified from *White et al.*, 2002), box illustrates interpreted location of cross-section in (c). (c) Reconstruction of east Greenland Caledonides in the Early Devonian (*Hartz et al.*, 2001) modified to show emplacement of the LLET (pink/teal) into the Laurentian retrowedge (green/yellow), while retrothrusting and extension continued closer to the foreland. Solid and dashed lines are documented and speculative aspects, respectively.

lower plate during its subduction, but was then transported to the Laurentian upper plate by retrowedge exhumation, consistent with the accepted subduction polarity, provenance of the LLET, and extensive retrothrusting in east Greenland (e.g., *Higgins and Leslie*, 2008).

Model R shows a case with minor pre-exhumation retrothrusting and with substantial upper plate thickening coeval with (U)HP exhumation. By comparison, Silurian retrothrusting and syn-orogenic extension in the east Greenland Caledonides began before (U)HP exhumation, indicating early onset of the PURC mode, but continued into the Devonian (*Hartz et al.*, 2001; *Higgins and Leslie*, 2008). Emplacement of the LLET into Laurentian crust ∼400 to 380 Ma (*Bowman*, 2008; *Augland et al.*, 2010) was thus broadly coeval with, and possibly linked to, protracted thrusting and exhumation of nappes closer to the foreland along lower, thrust-sense and upper, normal-sense shear zones (*Hartz et al.*, 2001; *White et al.*, 2002) (Fig. 2.6b,c).

Retrowedge mode exhumation in east Greenland was also broadly coeval with prowedge mode exhumation of (U)HP rocks in the WGR, with transport toward Baltica (*Tucker et al.*, 2004). Given that the transport direction may change along strike of the orogen or with time, there is no fundamental incompatibility between opposite styles of exhumation in the WGR and in east Greenland. While we cannot exclude alternative mechanisms, e.g., double subduction or a polarity flip, our proposed explanation is the most parsimonious.

Our 2D generic models cannot explain geological details or out-of-plane flow, or the much younger Carboniferous (U)HP rocks in northeast Greenland (*Gilotti and McClelland*, 2007). They do, however, provide further testable predictions. If correct, our explanation requires that the LLET overlies Laurentian lithosphere. Adjacent Laurentian rocks should not exhibit (U)HP metamorphism, implying juxtaposition after subduction. Finally, the kinematics of structures separating the LLET from adjacent Laurentian rocks should be consistent with retrotransport, and remnants of a suture should exist between them with evidence of deformation coeval with emplacement of the LLET.

2.8 Conclusions

1. The PURC framework is useful for describing flows in orogenic systems, particularly the prowedge and retrowedge (U)HP exhumation modes in which material flows from the conduit (C) into the prowedge (P), or into the uplifted plug (U) and retrowedge (R).

2. The numerical models demonstrate how buoyant exhumation from the subduction conduit drives rapid readjustment of the orogen through syn-orogenic extension and thrusting. Exhuming (U)HP material is transported into the prowedge or retrowedge depending on whether the upper plate crust is strong and acts as a mechanical backstop, or is weak and fails.

3. Orogenic belts may exhibit both modes of (U)HP exhumation, either offset along strike or in sequence, leading to the widespread dispersal of (U)HP rocks into both plates without requiring double subduction or polarity flips. The actual mechanism at work in natural orogens requires constraining both

the provenance and tectonometamorphic history of (U)HP terranes.

4. Retrowedge exhumation of Baltica crust may explain the origin of the (U)HP Liverpool Land Eclogite Terrane situated in the upper plate of the Caledonian orogen. This recognition that deeply subducted material can be widely dispersed during or after exhumation without changing subduction geometry should encourage the search for (U)HP rocks in other upper plate settings.

2.9 Acknowledgements

JPB acknowledges support from an NSERC Canada Graduate Scholarship. CB and RAJ were funded by NSERC Discovery Grants, and CB by a Canada Research Chair and IBM-SUR grant. Numerical models used the software SOPALE, developed at Dalhousie University by P. Fullsack and augmented by members of the Dalhousie Geodynamics Group. SOPALE NESTED was developed from SOPALE by D. Guptill and B. Lee assisted by CB. Constructive reviews by M. Roda, S. Johnston, and an anonymous referee improved the manuscript.

Chapter 3

The Alps 1: a Working Geodynamic Model for Burial and Exhumation of (Ultra)high-pressure Rocks in Alpine-Type Orogens

3.1 Preface

This chapter reproduces the article 'The Alps 1: a working geodynamic model for burial and exhumation of (ultra)high-pressure rocks in Alpine-type orogens' by J. P. Butler, C. Beaumont, and R. A. Jamieson, accepted for publication in the journal *Earth and Planetary Science Letters* June 26, 2013.

3.2 Abstract

Eocene (ultra)high-pressure (U)HP rocks exposed in the Western Alps are generally interpreted to result from subduction of European continental crust beneath Adria and its subsequent exhumation. However, the roles of extension (absolute and relative) versus erosion during exhumation, remain controversial. Here we use 2D numerical geodynamic models to explain the formation and exhumation of (U)HP rocks in an Alpine-type orogen and interpret the results in the conceptual Prowedge–Uplifted Plug–Retrowedge–Conduit (PURC) framework. (U)HP metamorphism of oceanic and microcontinent crust in the models results from burial and accretion to

a subduction channel/conduit formed beneath an advancing retrocontinent. Rapid exhumation from (U)HP conditions is achieved by the buoyancy-driven transport of a composite plume of stacked (U)HP oceanic and microcontinent crust from the subduction conduit to the overlying orogenic prowedge, accommodated by coeval thrusting and normal-sense shearing. Subsequent trans-crustal exhumation is achieved by a combination of doming/extension and later retrotransport of the (U)HP plume through the uplifted plug, during underthrusting of the thick continental margin crust, coupled with increased erosion. Our proposed mechanism implies that exhumation related normal-sense shearing in the Western Alps, per se, was driven from below by the buoyancy of the ascending plume, and that absolute extension of the orogen is not required to explain (U)HP rock exhumation. The efficiency of the exhumation mechanism depends strongly on the buoyancy and strength of the (U)HP plume, suggesting that in order to exhume rapidly, it must achieve a critical size. By implication, the multiple small Eocene (U)HP complexes within the Internal Crystalline Massifs were exhumed as part of a single composite body comprising diverse units aggregated from different levels of the subduction conduit during burial or ascent, rather than as individual small bodies exhumed in separate pulses.

3.3 Introduction

Crustal rocks metamorphosed at (ultra)high-pressures ((U)HP), interpreted to imply burial to and exhumation from depths exceeding 90 km, are an important characteristic of several Phanerozoic orogens (*Chopin*, 2003; *Liou et al.*, 2004). Yet the mechanisms by which these rocks are buried, subjected to high pressure and temperature, and subsequently exhumed remain enigmatic. The current consensus (*England and Holland*, 1979; *Chemenda et al.*, 1995; *Ernst and Liou*, 1999; *Raimbourg et al.*, 2007; *Gerya et al.*, 2008; *Warren et al.*, 2008a; *Beaumont et al.*, 2009), with some notable exceptions (e.g., *Vrijmoed et al.*, 2009b), is that (U)HP rocks form by burial and metamorphism within a subduction channel. Deeply subducted crust may then flow upwards, driven by buoyancy or tectonically induced stresses, to be exhumed by attendant normal-sense shear, extension, and surface erosion during convergence

(*Gerya et al.*, 2008; *Warren et al.*, 2008a; *Yamato et al.*, 2008). Alternative exhumation mechanisms include lithosphere-scale extension, diapirism (*Little et al.*, 2011), and eduction (reverse subduction) of the subducted slab (*Duretz et al.*, 2012).

Despite nearly 30 years of study, several problems concerning the mechanics of (U)HP rock exhumation remain. These include the following:

1. The style and extent of deformation, and the causes of weakening in the subduction channel (e.g., by fluid, melt, reaction, or strain-weakening mechanisms; *Warren et al.*, 2008a; *Angiboust and Agard*, 2010; *Labrousse et al.*, 2011).

2. Whether (U)HP terranes form and exhume as intact pieces of crust (*Chemenda et al.*, 1995; *Hacker et al.*, 2010), and/or as assemblages of distinct crustal units juxtaposed during subduction or exhumation (*Warren et al.*, 2008a; *Angiboust and Agard*, 2010; *Gasco et al.*, 2012).

3. The range of sizes of exhumed (U)HP terranes and the difference in exhumation mechanisms between small and large (U)HP terranes (*Kylander-Clark et al.*, 2012); and,

4. The relative contribution of erosion versus extension during exhumation, and whether exhumation involves extension at the lithospheric scale (resulting from plate divergence; *Fossen*, 2010; *Malusà et al.*, 2011), or involves extension from within-orogen normal-sense shearing while plate convergence and shortening continue (*Wheeler et al.*, 2001).

Consequently, there remains a need for quantitative models that fully explore the feedbacks between deep subduction and the overlying lithosphere, including the shallow crustal and surface processes that operate during (U)HP rock exhumation. The model results must also be tested against observations. For clarity, we refer to the two types of extension as 'lithosphere-scale extension' and 'internal extension', respectively. In the latter case, enhanced shortening elsewhere must compensate for internal extension while convergence continues at the lithospheric scale.

The western Alpine orogen (Western Alps) (Fig. 3.1) is a top candidate for constraining such models, owing to the widespread distribution of HP and UHP rocks, and the wealth of data available on its evolution (e.g., *Schmid et al.*, 1996, 2004;

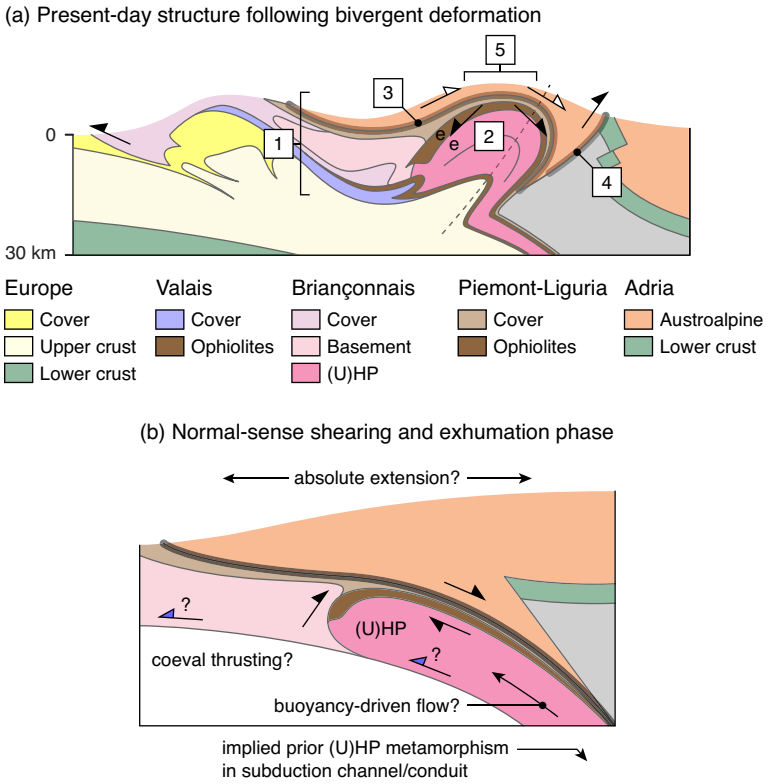

Figure 3.1: Summary of western Alpine tectonics. (a) Generalized cross-section showing key tectonometamorphic features of the Western Alps (modified from (*Schmid et al.*, 2004; *Gasco et al.*, 2009; *Beltrando et al.*, 2010b). The section is based on the ECORS-CROP transect through the Monte Rosa Massif but is intended to capture the main features of the Western Alps, including: (1) the nappe stack comprising (from top to bottom) more external paleogeographic domains; (2) (U)HP metamorphic rocks exposed in the composite (i.e., comprising stacked units) ICMs (coloured (U)HP) and overlying Piemont-Liguria oceanic units; (3) the approximate position of the top-southeast, normal-sense shear zone separating the exhumed (U)HP units from the overlying greenschist facies units; (4) the backthrust (Insubric line); and, (5) late normal-sense shear zones, and the domal structure of the ICMs and associated brittle faults. Contacts have implied early top-northwest kinematics related to initial nappe stacking. White-filled arrows show kinematics of top-southeast normal-sense shearing phase. Solid black arrows show later kinematics, with the normal-sense kinematics flanking the ICM schematically representing greenschist-facies normal-sense shear zones and cross-cutting brittle faults (*Avigad et al.*, 2003; *Lardeaux et al.*, 2006). (b) Schematic representation of normal-sense shearing exhumation phase (modified from *Reddy et al.*, 1999). Grey arrows and text represent contrasting interpretations relating normal-sense shearing alternatively to absolute extension versus synorogenic extension, i.e., during continuing convergence.

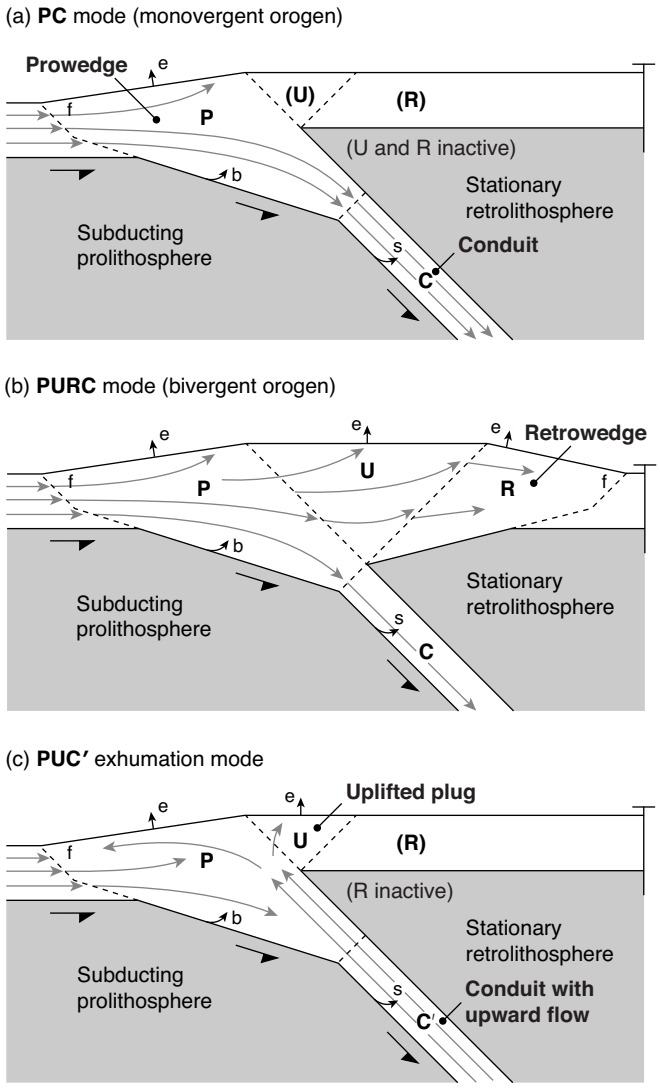

Figure 3.2: Explanation of PURC framework. Conceptual PURC flow modes describing the geometry and material fluxes in three subduction/accretion systems. P: prowedge; U: uplifted plug; R: retrowedge; C: conduit. (a) PC mode. (b) Exhumation of material from C in the PUC′ exhumation mode, where C′ denotes the buoyancy-driven reversal of flow in C. (c) PURC mode. Grey arrows show transfer of material into and through the system. Black arrows/lowercase text refers to fluxes into/out of regions by frontal accretion (f), basal accretion/underplating (b), accretion in the subduction channel (s), and surface erosion (e). The retrocontinent lithosphere is assumed to be stationary

Schmid and Kissling, 2000; *Steck*, 2008). Here, we present results from 2D numerical model experiments designed to explore the geodynamics of (U)HP rock exhumation within an Alpine-type orogen, i.e., one that captures the first-order tectonic characteristics of the Western Alps. Our approach is to develop a general model for Alpine-type orogens, not to simulate any specific Alpine transect, in part because interpretations of Alpine geology are still evolving. In addition, numerical models are inherently simplifications of nature, and so the scale of observations compared with model results must be commensurate with the model resolution. The 1×1 km grid spacing used here can resolve features on the scale of about 3×3 km. Therefore, for comparison with the Western Alps we emphasize the broader tectonics, listed as 'key characteristics' in the next section. Our goal is to understand these basic features.

We interpret the numerical model results, and by implication the Alps, in terms of the 'PURC' geometric/kinematic framework, a generalization of critical wedge mechanics for small orogens (*Willett et al.*, 1993; *Beaumont et al.*, 1999; *Butler et al.*, 2011). The purpose is to represent a complex system in a simple way and to illuminate key features of the model results, and by implication, the Alps. PURC orogens comprise up to four compartments, shown and defined in Figure 3.2: two back-to-back critical wedges (prowedge, P and retrowedge, R), a central uplifted plug (U), and an underlying subduction conduit (C). The conduit includes the active subduction channel and the region in which material from the subduction channel is accreted to the sides of the channel. The conduit therefore acts as a region below which material is subducted into the mantle, within which material detaches and deforms in the subduction channel, and as a repository where accreted material is stored. This simplifies our original terminology (*Beaumont et al.*, 1999) in that the conduit now includes the active channel. Orogenic evolution is described in terms of the formation and transport of crust among these four PURC regions. A PC orogen is one that accretes material to the accretionary/orogenic wedge and subducts material into C (Fig. 3.2a). Bivergent orogens involve retroward transport of material from P or C, into U, and development of R (Fig. 3.2b). In PURC terms, (U)HP rocks are subducted into, and stored in C, prior to being exhumed in the PUC$'$ mode (Fig. 3.2c), where C$'$ denotes reverse (upward) flow in the conduit.

3.4 Key Characteristics of the Western Alps

The Western Alps result from a complex paleogeographic and tectonic evolution that culminated in Cretaceous to Tertiary subduction of the Piemont-Liguria Ocean followed by the rifted European margin, including the Briançonnais microcontinent and the Valais 'Ocean' basin, beneath the Adriatic plate, driven by absolute motion of Adria to the north/northwest (*Stampfli et al.*, 1998; *Schmid et al.*, 2004; *Rosenbaum and Lister*, 2005; *Handy et al.*, 2010). Orogenesis involved an Eocene phase of (north)west-vergent deformation associated with subduction and accretion of oceanic and continental crust beneath the Adriatic plate, and subsequent exhumation of (U)HP rocks to the lower crust. This was followed by an Oligocene phase of bivergent deformation associated with underthrusting of the European margin, local retrotransport (retrocharriage) and exhumation of (U)HP rocks through the crust, and retrothrusting in the southern foreland (*Schmid et al.*, 1996, 2004; *Steck*, 2008).

This evolution involved several key processes (Fig. 3.1) that successful geodynamic models must explain:

1. Progressive accretion of units derived from Piemont-Liguria Ocean and rifted European margin domains beneath the Adriatic plate (*Steck*, 2008);

2. Sequential (U)HP metamorphism of Piemont-Liguria, Brianǫnnais, and Valais domain units from ∼49–35 Ma (review in *Berger and Bousquet*, 2008) at conditions from ∼1.7 GPa/450°C to ≥3.5 GPa/760°C (*Chopin et al.*, 1991; *Rubatto and Hermann*, 2001; *Meffan-Main et al.*, 2004; *Le Bayon and Ballèvre*, 2006; *Radulescu et al.*, 2009; *Gasco et al.*, 2011a,b);

3. Broadly synchronous, rapid exhumation and stacking of (U)HP oceanic and underlying continental (U)HP units at estimated rates of ∼0.5–3.5 cm a^{-1}, followed by lower 'trans-crustal' exhumation at ∼0.5–1.5 cm a^{-1} (*Rubatto and Hermann*, 2001; *Meffan-Main et al.*, 2004; *Le Bayon and Ballèvre*, 2006; *Lapen et al.*, 2007; *Berger and Bousquet*, 2008; *Pleuger et al.*, 2008; *Radulescu et al.*, 2009);

4. Top-southeast, normal-sense shearing during exhumation (∼45–33 Ma) that

emplaced (U)HP rocks against greenschist facies units derived from the Piemont-Liguria Ocean and the overlying Austroalpine orogenic wedge (*Reddy et al.*, 1999, 2003; *Pleuger et al.*, 2008; *Gasco et al.*, 2009, 2012), possibly coeval with top-northwest thrusting at depth (*Avigad et al.*, 2003; *Le Bayon and Ballèvre*, 2006; *Rosenbaum et al.*, 2012), and in the foreland (*Wheeler et al.*, 2001; *Simon-Labric et al.*, 2009); and,

5. Subsequent retrotransport (backthrusting/backfolding) within the orogenic wedge and locally along the Insubric Line, marking the onset of major bivergent deformation (*Schmid et al.*, 1996; *Pleuger et al.*, 2008); and late doming and extension of the composite (U)HP nappe stack at shallow crustal levels (*Avigad et al.*, 2003; *Sue and Tricart*, 2003; *Schwartz et al.*, 2009)

We focus on the Eocene (∼45–35 Ma) (U)HP metamorphism and subsequent exhumation and formation of the composite Internal Crystalline Massifs (ICMs; Monte Rosa, Gran Paradiso, and Dora Maira Massifs), interpreted to comprise deeply subducted remnants of the Briançonnais microcontinent, capped by (U)HP oceanic crust derived from the Piemont-Liguria Ocean (*Schmid et al.*, 2004; *Berger and Bousquet*, 2008; *Lapen et al.*, 2007). Exhumation, imbrication, and stacking within the ICMs was broadly synchronous with Eocene (∼45–33 Ma) crustal-scale, top-southeast (and locally top-northwest) normal-sense shearing that emplaced the ICMs and (U)HP oceanic rocks against mainly greenschist facies rocks (Fig. 3.1b). Although evidence of this 'extension' in the Western Alps is widely recognized (*Ballèvre and Merle*, 1993; *Reddy et al.*, 1999, 2003; *Wheeler et al.*, 2001; *Ganne et al.*, 2006; *Gasco et al.*, 2009; *Rosenbaum et al.*, 2012) its cause remains unclear. Some have interpreted the normal-sense shearing to reflect local, syn-convergent extension during overall shortening (internal extension), driven by forces internal to the orogen (e.g., buoyancy; *Platt*, 1986; *Wheeler et al.*, 2001). Others have suggested these structures formed during lithosphere-scale extension (*Rosenbaum and Lister*, 2005; *Beltrando et al.*, 2010b; *Malusà et al.*, 2011).

The extent to which (U)HP rocks in the Western Alps were exhumed by erosion versus extension is also debated (*Handy et al.*, 2010; *Malusà et al.*, 2011). Some have argued that the highest estimated exhumation rates of ∼3.5 cm a^{-1} (*Rubatto and Hermann*, 2001) are based on unrealistically young ages for peak pressure metamorphism, and

that lower rates of $\lesssim$1 cm a^{-1} (see discussion in *Handy et al.*, 2010) can be explained by erosion. However, substantial pressure gaps between exhumed (U)HP rocks and overlying greenschist-facies units (*Platt*, 1986), and the observation that Alpine basins received only limited sediment until the Oligocene, after the (U)HP units were exhumed to the base of the crust (*Sinclair and Allen*, 1992; *Malusà et al.*, 2011), appear to preclude erosion as the primary exhumation mechanism. Others (e.g., *Malusà et al.*, 2011) have assumed (incorrectly, as we shall show) that syn-convergent exhumation requires extremely rapid erosion, particularly during the rapid exhumation phase. Because this would require more sediment than is observed in Alpine basins, the authors rejected syn-convergent exhumation and proposed that the necessary accommodation space was instead created by lithosphere-scale extension owing to transient plate divergence.

The objective of our numerical modeling is to shed light on these and other questions concerning the geodynamics of (U)HP exhumation in 'Alpine-type' orogens. The models explore the mechanics of (U)HP rock exhumation within a system that reproduces the key characteristics, but not the geological details, of the Western Alps.

3.5 Methods

Here we provide an outline of the methods following *Beaumont et al.* (2009); details are in Appendix B. We use the nested version of the finite element software SOPALE to solve thermal-mechanical creeping (Stokes) flows at the upper-mantle scale. The starting geometry and material properties (Fig. 3.3; Table 3.1) correspond to Mesozoic to Cenozoic Alpine reconstructions (e.g., *Handy et al.*, 2010), and include a retrocontinent with a preexisting orogenic wedge, an oceanic plate, and a procontinent comprising a microcontinent, a rift basin, and a continental margin. The continents and microcontinent each have relatively weaker upper/middle and stronger lower crusts with maximum total thicknesses of 32 km and 22 km, respectively. Crustal units are capped by a thin, weak sediment cover.

Model materials deform by either frictional-plastic (brittle) or power-law viscous (ductile) flow that includes additional respective strain-softening/strain-weakening mechanisms. Frictional-plastic deformation depends on the dynamical pressure and

effective angle of internal friction (ϕ_{eff}; hereafter simply ϕ). For most model materials $\phi = 15$–$4°$, where 15° includes the effect of hydrostatic pore fluid pressure and 4° is the lower limit of ϕ after reduction owing to strain-softening (Appendix B). Viscous flow laws are derived from a small set of reliable laboratory flow laws scaled by the factor f. For viscous strain-weakening, the factor f is linearly scaled between 1 and $1/W_s$ over the range of strain $\epsilon = 5$–10 (Appendix B).

Upper/middle crusts have a scaled wet quartzite (WQ $\times f$, where f varies among crustal units; *Gleason and Tullis*, 1995), whereas the lower and oceanic crusts use a scaled dry Maryland diabase flow law (DMD×0.5 and 0.1 respectively; *Mackwell et al.*, 1998). The mantle materials have a wet olivine flow law (WOL; *Karato and Wu*, 1993) scaled to represent either sublithospheric mantle or dehydrated lithospheric mantle.

The model domain has a stress-free upper surface, and no-slip and free-slip sides and base, respectively. Retrolithosphere convergence (from right of Figure 3.3 at $V_r = -1.5$ cm a^{-1}) drives oceanic subduction while prolithosphere is stationary, (left; Fig. 3.3; $V_p = 0$ cm a^{-1}). V_r is later reduced to -1.0 cm a^{-1} at the onset of microcontinent subduction ('collision'). For simplicity, V_r remains constant during collision, although we acknowledge that in the Alps the convergence rate varied (e.g., *Handy et al.*, 2010).

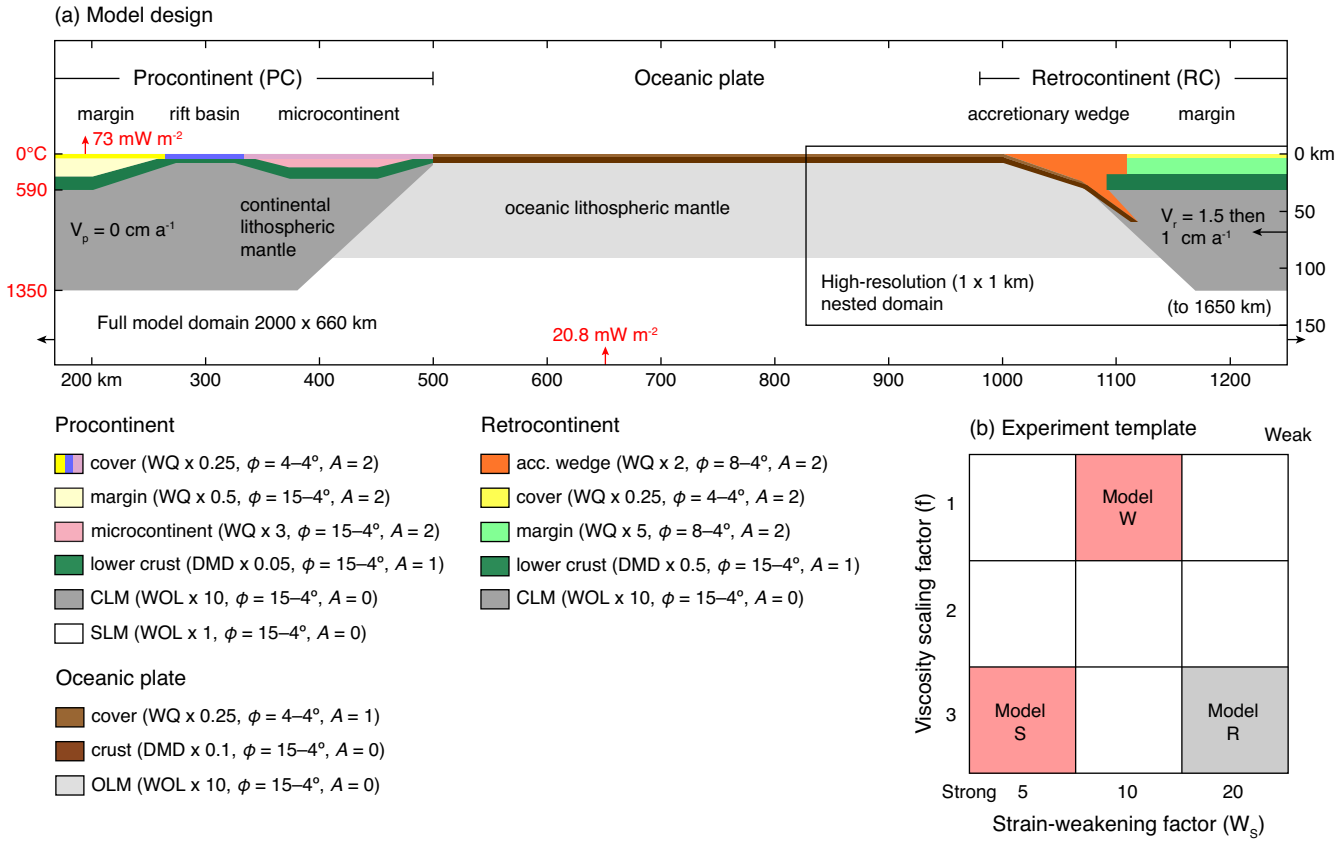

Figure 3.3: Model design. (a) Design of 2D upper-mantle-scale model. WQ=wet quartzite, DMD=dry Maryland diabase, WOL=wet olivine. ϕ=range of effective angle of internal friction (ϕ_{eff}) owing to strain-softening; A=radiogenic heat production (μWm^{-3}; A_R in text). Inset box shows location of nested domain. Black arrows show velocity boundary conditions. Red arrows show basal and surface heat flux. acc. wedge=accretionary wedge, CLM=continental lithospheric mantle, OLM=oceanic lithospheric mantle, SLM=sublithospheric mantle. (b) Experiment template showing tested variations in the initial viscous strength, f, and strain-weakening of material, W_s, in subduction channel. The two models presented, termed Model S (strong), and Model W (weak), represent variations on Model R.

Parameter	Units	PC M crust	P-MC crust	Wedge	RC crust	Cont. sed.	Oceanic sed.	LC	OC	CLM	OLM	SLM
Mechanical Parameters												
Max. thickness	km	20	12	20	20	4	2	22–36	8	to 120	90	660
Reference density[a]	kg m^{-3}	2720	2720	2720	2720	2720	2720	2900	2950	3375	3385	3385
HP density	kg m^{-3}	2770	2770	2770	2770	2770	2770	3100	3400	-	-	-
UHP density	kg m^{-3}	2820	2820	2820	2820	2820	2820	3100	3400	-	-	-
ϕ_{eff}	deg	15–4	15–4	8–4	15–4	4–4	4–4	15–4	15–4	15–4	15–4	15–4
Flow law	-	WQ	WQ	WQ	WQ	WQ	WQ	DMD	DMD	WOL	WOL	WOL
Flow law reference	-	GT95	GT95	GT95	GT95	GT95	GT95	M98	M98	KW93	KW93	KW93
f	-	0.5	1,2,3[b]	2	5	0.25	0.25	0.05	0.1	10	10	1
W_s	-	20	5,10,20[c]	20	20	20	5,10,20[c]	20	20	2	2	1
n	-	4	4	4	4	4	4.7	4.7	4.7	3	3	3
A[d]	Pa^{-n} s^{-1}	8.57×10^{-28}	8.57×10^{-28}	8.57×10^{-28}	8.57×10^{-28}	8.57×10^{-28}	8.57×10^{-28}	5.78×10^{-27}	5.78×10^{-27}	1.76×10^{-14}	1.76×10^{-14}	1.76×10^{-14}
Q	kJ mol^{-1}	223	223	223	223	223	223	485	485	430	430	430
V^*	m^3 mol^{-1}	0	0	0	0	0	0	0	0	1×10^{-5}	1×10^{-5}	1×10^{-5}
Thermal Parameters												
Heat capacity	m^2 s^{-2} K^{-1}	750	750	750	750	750	750	750	750	1250	1250	1250
Thermal conductivity	W m^{-1} K^{-1}	2.25	2.25	2.25	2.25	2.25	2.25	2.25	2.25	2.25	2.25	52[e]
Thermal diffusivity	m^2 s^{-1}	1×10^{-6}	1×10^{-6}	1×10^{-6}	1×10^{-6}	1×10^{-6}	1×10^{-6}	1×10^{-6}	1×10^{-6}	0.6×10^{-6}	0.6×10^{-6}	1.4×10^{-5}
Thermal expansion	K^{-1}	3×10^{-5}	3×10^{-5}	3×10^{-5}	3×10^{-5}	3×10^{-5}	3×10^{-5}	3×10^{-5}	3×10^{-5}	3×10^{-5}	3×10^{-5}	3×10^{-5}
Heat production (A_R)	μWm^{-3}	2	2	2	2	1.75	1.15	1	0	0	0	0

[a] Densities calculated at 273 K using listed coefficient of thermal expansion.

[b] Viscosity scaling factor f varies among experiments (Fig. 3.3). Model S uses $f = 3$ for the P-MC crust.

[c] Strain-weakening factor W_s varies among experiments (Fig. 3.3). Model S uses $W_s = 5$ for the P-MC and Oceanic sed.

[d] Uniaxial pre-exponential factor converted to tensor invariant form.

[e] Note linear increase in thermal conductivity within asthenosphere.

Table 3.1: Material parameters used in model experiments. PC M=procontinent margin, P-MC=pro-microcontinent, Wedge=accretionary wedge, RC=retrocontinent, Cont. sed=continental sediment cover, Oceanic sed.=oceanic sediment cover, LC=lower crust, OC=oceanic crust, CLM=continental lithospheric mantle, OLM=oceanic lithospheric mantle, SLM=sublithospheric mantle. Flow law references are *Gleason and Tullis* (1995)(GT95), *Mackwell et al.* (1998)(M98), and *Karato and Wu* (1993)(KW93).

Thermal boundary conditions include basal heat flux 20.8 mWm^{-2}, 0°C surface temperature, and insulated side boundaries. Radioactive heat production (A_R) is respectively 2.0 and 1.0 μWm^{-3} for the upper/middle and lower crust, resulting in an initial steady-state Moho temperature of 590°C, and surface heat flow 73 mW m^{-2} on the continents. Crustal materials undergo pressure- and temperature-dependent density changes at the eclogite and coesite-eclogite phase transitions (*Warren et al.*, 2008a).(Appendix B). Density reversal implies retrogression, not necessarily to the protolith, but to a material with the original density, e.g., from eclogite to amphibolite.

The dynamically consistent model topography is a product of the model calculation without any imposed constraints except for water loading where the surface is below sea level. Slope-dependent surface erosion acts on the local subaerial topography. It varies spatially according to local slope of the model surface, and is defined by a maximum erosion rate (E_s) that operates on a slope of 45° and is scaled down linearly to the local slope of the surface. In Model S, E_s = 1.5 cm a^{-1}, resulting in typical erosion rates of ∼0.2–1.8 mm a^{-1}.

We started with a reference model (Model R) with $f = 3$ and $W_s = 20$ for the microcontinent crust (Fig. 3.3b), which we know exhumes UHP material. This crust was designed to be initially strong but to undergo substantial strain-weakening. We then tested the sensitivity of Model R to variations in both the initial strength (WQ× f, f = 1,2,3) and amount of strain-weakening (W_s = 5,10,15) to produce a template of models (Fig. 3.3b) while holding other parameters constant. This sensitivity analysis was designed to determine the effect on model results, and whether models with lower values of f and W_s, and therefore closer to standard values, are also successful.

3.6 Model Results

We present selected results from the template of 9 models (Fig. 3.3b). The reference model (R, $f = 3$, $W_s = 20$) and Model W (Weak; $f = 1$, $Ws = 10$) are shown in Figures B.1–B.2 and B.4–B.5 respectively. Here we focus on Model S (Strong; $f = 3$, $W_s = 5$), which we judge to be the best 'upper bound' model, in that it produces and exhumes significant amount of UHP material, whereas Model W, a

'lower bound' model, primarily exhumes HP material. Model S only differs from Model R in that $W_s = 5$ instead of 20. Later, we compare Model S and Model W with Model R. We define the 'onset of collision' to be when the microcontinent first contacts the accretionary wedge, and measure model evolution with respect to this time, 0 Myr-pc.

3.6.1 Model S Description

Model S ($f = 3$, $W_s = 5$) evolves through three main tectonic phases: (1) oceanic and microcontinent subduction; (2) exhumation of microcontinent and oceanic crust; and, (3) bivergent deformation accompanying underthrusting of the procontinent margin (Fig. 3.4), which we interpret using PURC terminology (Fig. 3.2). For consistency with the terminology normally used to describe Alps tectonic evolution velocities are shown (Fig. 3.4e–g) in the stationary retrolithosphere reference frame.

3.6.1.1 Phase 1: PC Mode Oceanic and Microcontinent Subduction

The model begins with 20 Myr of (pre-collision) subduction of oceanic lithosphere beneath the accretionary wedge and retrocontinent, driven by advance of the retrolithosphere over the prolithosphere, ending at 0 Myr-pc (see supplementary appendix for animations). During oceanic subduction, sediment and some oceanic crust are accreted and underplated to the prowedge, with some transported further into the conduit. This material gradually accumulates, forming a small repository of highly strained (U)HP oceanic material near the base of the conduit.

Following closure of the ocean and collision, the microcontinent subducts beneath the prowedge. Weak sediment from the microcontinent is accreted and underplated, resulting in minor growth of the prowedge. The stronger microcontinent upper/middle crust, meanwhile, follows the oceanic crust and sediment into the conduit, where it undergoes HP and then UHP metamorphism by ∼19 Myr-pc (Fig. 3.4a).

Phase 1 deformation mainly involves top-proward shearing between the top of the subducting slab and the overlying prowedge and retrocontinent mantle lithosphere (Fig. 3.4e). Accretion and underplating during oceanic subduction leads to minor uplift of the prowedge and formation of a nascent uplifted plug, bounded at the rear by an incipient retroward shear zone (Fig. 3.4e). Subduction of the microcontinent is accompanied by a transient phase of burial/shortening at the front of the prowedge,

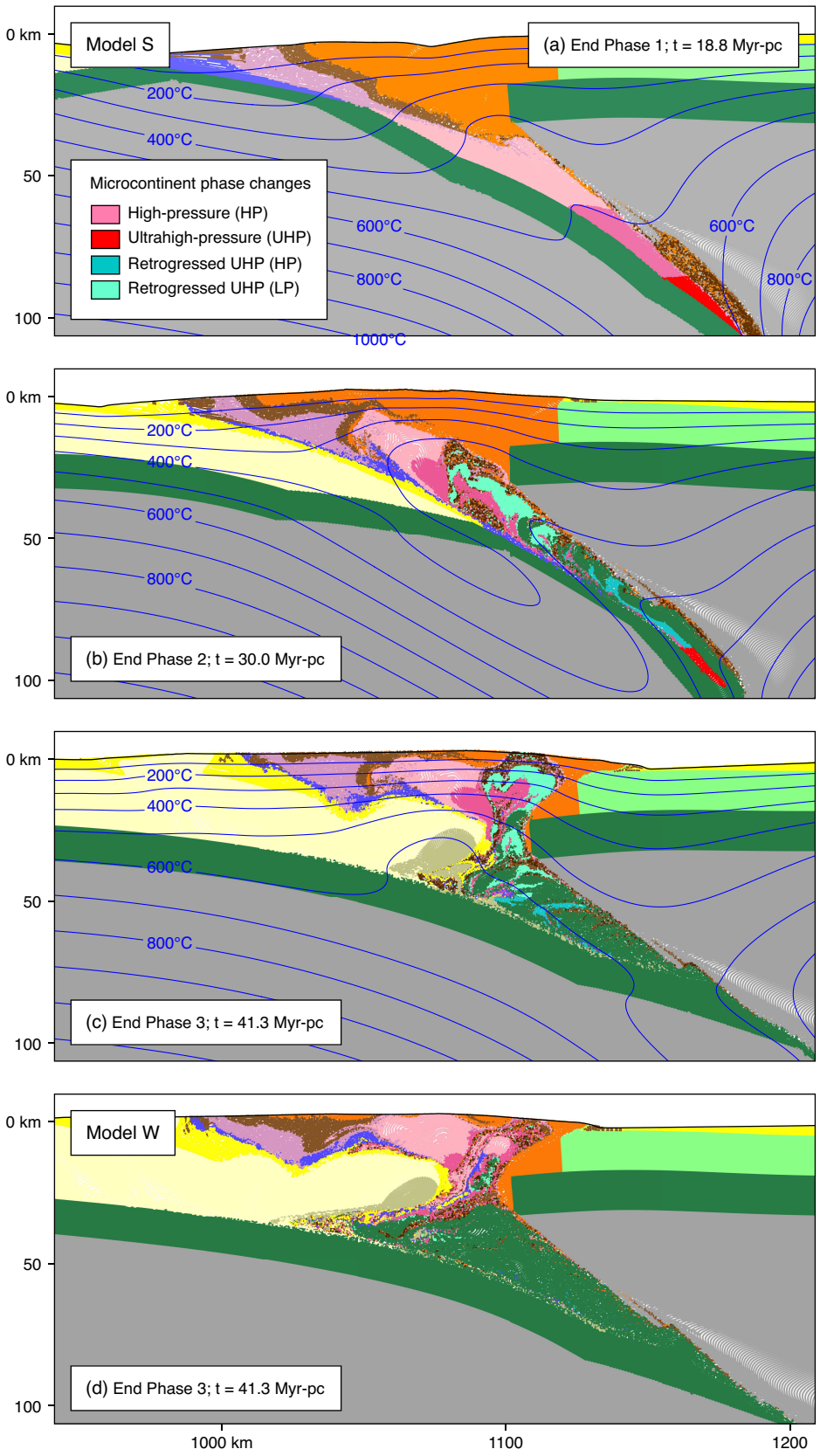

Figure 3.4: Results of Model S and Model W (*Caption on following page*).

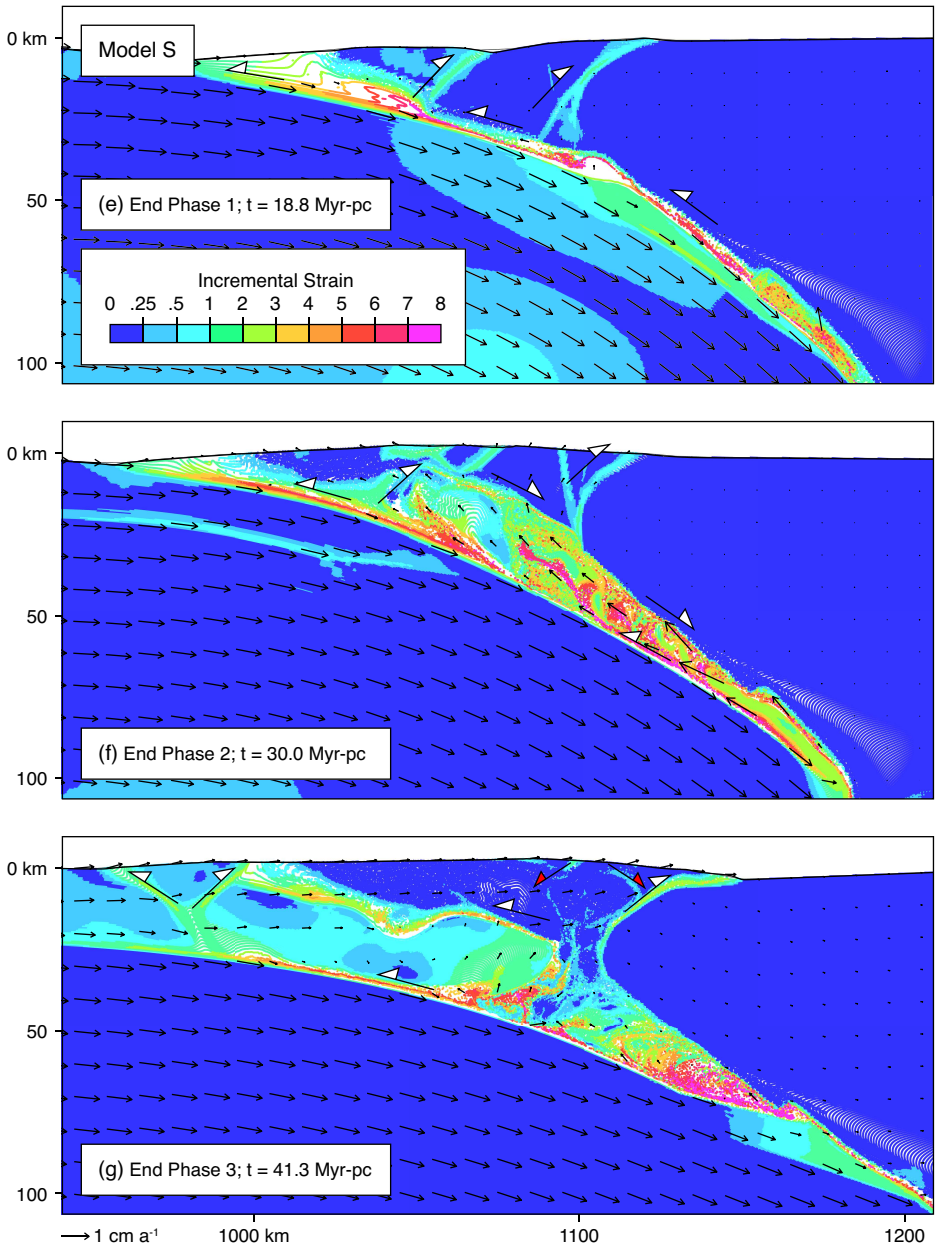

Figure 3.4: Results of Model S and Model W. Model S shown in panels a–c (previous page) and e–f (this page). Final frame of Model W shown in d (previous page). (a–d; previous page) Material colors and isotherms (blue lines) for model times corresponding to the end of each phase of Model S (see section 4 for details). (d) Final frame of Model W (Figs B.4–B.5) contrasting orogenic structure and proportion of exhumed (U)HP crust with that in Model S (c). (e–g; this page) Corresponding incremental strain plots for Model S, representing strain (square root of second invariant) accumulated during each phase, overlain by velocity vectors (shown in stationary retrolithosphere reference frame) for the actual time shown in (a–c). White-filled arrows (e–g) show interpreted kinematics of deformation along dominant shear zones. Red-filled arrows (g) show kinematics of transient normal-sense shear zones flanking the model ICM prior to retrotransport during Phase 3. More complete results from Models R and W are shown in Figures B.1–B.2 and B.4–B.5, respectively

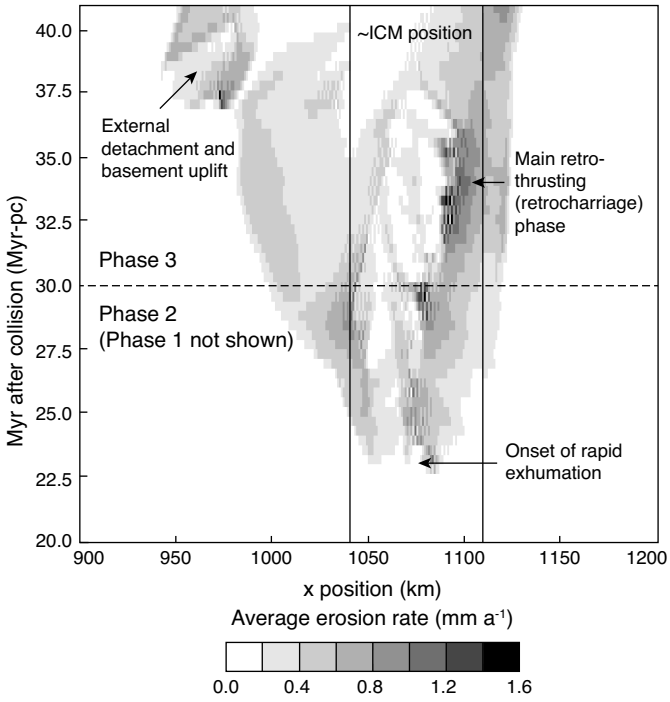

Figure 3.5: Model S erosion rates. Average erosion rates (mm a^{-1}) for the model surface through time (Myr-pc), for Model S. Each grey shade increment corresponds to 0.2 mm a^{-1}. Erosion rates for each location are averaged over 100 timesteps. Phase 1 (oceanic and microcontinent subduction) involves no substantial erosion and is excluded here. Vertical black lines show the approximate position of the exhuming plume or 'ICM' (at depth or the surface), based on the position shown in Figure 3.4. The base of the plot, ∼20 Myr-pc, roughly corresponds to the onset of Phase 2 ((U)HP rock exhumation). Labels indicate where erosion corresponds to identifiable tectonic stages of the model. Erosion rates are on average <0.8 mm a^{-1} during the (U)HP exhumation phase, Phase 2.

manifested in minor subsidence of the wedge and formation of a small retroward shear zone within it (Fig. 3.4e). Throughout Phase 1 the surface of the orogenic wedge remains relatively stable and submarine, and consequently subaerial erosion plays no role at this stage (Fig. 3.5). The model operates in the PC mode (Fig. 3.2a) with very minor uplift of U.

3.6.1.2 Phase 2: PUC′ Mode (U)HP Rock Exhumation with Localized Synorogenic Extension

Exhumation of (U)HP crust from the conduit begins soon after the tip of the microcontinent reaches UHP conditions at ∼20 Myr-pc. There it strain weakens and detaches from the subducting slab beneath the repository of UHP oceanic crust. No

longer contained by strong lithospheric mantle, the UHP oceanic material flows upward, followed by the detached UHP microcontinent crust, reaching the base of the prowedge by ∼30 Myr-pc (Fig. 3.4b). Exhumation of the plume drives the overlying lower-pressure microcontinent crust upward and proward relative to the overlying orogenic wedge. The 'plume' is an assemblage of (U)HP microcontinent crust enveloped by UHP oceanic material. Its ascent is accompanied by internal deformation and stacking resulting in thrusting of UHP over HP microcontinent crust. Beneath the plume, microcontinent lower crust also detaches and begins to exhume, adding to the net buoyancy.

Deformation during Phase 2 is dominated by top-retroward normal-sense shearing at the top of the exhuming plume and top-proward thrusting at its base (Fig. 3.4f). Buoyant insertion of the exhuming material into the prowedge (Fig. 3.4f) causes the wedge to extend. The front of the wedge is forced outward toward the foreland whereas motion of the rear is accommodated by minor uplift and retroward transport in the plug. At the front of the prowedge incoming crust is deflected up and over the exhuming plume. The internal prowedge 'extension' required to make room for the exhuming plume occurs during overall plate convergence, i.e., it is 'internal extension' by our terminology.

Uplift of the prowedge during this pulse of exhumation leads to subaerial exposure, with local erosion rates up to ∼0.8 mm a^{-1} (Fig. 3.5). However, a considerable portion of the prowedge remains submarine, and overall surface erosion remains minor. During Phase 2, the model operates in the PUC′ mode (Fig. 3.2).

3.6.1.3 Phase 3: PUR Mode Retrotransport of (U)HP Plume and Bivergent Deformation

The final model phase starts at ∼30 Myr-pc, as the underthrust procontinent margin reaches the top of the conduit. Growth of the continues by accretion and underplating of rift basin and procontinent margin sediment. Underthrusting of the still-attached thick procontinent margin leads to dramatic uplift of the prowedge and plug (see animations). The mode of deformation now changes to PUR (Fig. 3.2b), because strong (U)HP microcontinent lower crust inhibits entry of margin crust into the conduit. This results in thickening of the margin crust leading to a transient phase of uplift and doming of the (U)HP material, followed by transport toward the retrocontinent (retrocharriage), producing a retro-facing 'backfold' within the

plug. Further convergence leads to detachment and accretion of procontinent upper/middle crust to the base of the orogen, forming a thick thrust sheet. Detachment forces deformation in the still-converging crust in front of the prowedge, culminating in a pulse of basement uplift in the foreland, thereby forming an external basement massif (Fig. 3.4c).

Deformation during this phase is concentrated within thrust-sense shear zones along the base of the prowedge and plug (Fig. 3.4g). The conduit, meanwhile, is effectively inactive owing to clogging by microcontinent lower crust. Early Phase 3 uplift of the rear of the prowedge/plug leads to vertical exhumation and doming accomplished by normal-sense shearing on both sides of the (U)HP nappe. During subsequent retrotransport, the previously normal-sense shear zone overlying the (U)HP nappe is reoriented into a top-retroward, thrust-sense shear zone at the rear of the plug. Detachment of the procontinent crust leads to a jump of the base of the prowedge to the base of the middle crust.

Underthrusting of thick procontinent margin crust uplifts the surface and the entire orogen becomes subaerial. Slope-dependent erosion is concentrated within regions of most active relative uplift, initially the shear zone at the rear of the plug (erosion rates ∼1.2–1.6 mm a^{-1}), and later above the external basement massif (average erosion rates ∼0.2–1 mm a^{-1})(Fig. 3.5).

Phase 3 ends with breakoff of the subducting slab (Fig. B.7) at a depth of 300 km, long after (U)HP exhumation (Phase 2); slab breakoff cannot be responsible for model UHP exhumation.

Transitions from Phases 1 to 3 develop without changes to the model boundary conditions. We therefore interpret these transitions to be emergent properties of the models that develop dynamically.

3.6.2 Sensitivity to Crustal Strength and Strain-Weakening

The amount of exhumed (U)HP crust, the timing and rate of exhumation, and to some extent the style of exhumation in the models depend strongly on the strength evolution of the subducted crust. The sensitivity of the models to the initial viscous strength (f) of the microcontinent crust is illustrated by Model W (Figs 3.4d, B.4–B.6), in which the microcontinent upper/middle crust has a WQ × 1 ($f = 1$) flow law, and $W_s = 10$. During Phase 1 subduction in Model W, the initially weaker

microcontinent crust facilitates shallower detachment, so that only a small amount of crust reaches UHP conditions. The subsequent evolution of the model is very similar to that of Model S. However, whereas in Model S the plume is dominated by coesite-eclogite facies crust, in Model W it comprises mainly blueschist to eclogite facies crust, with minor fragments of coesite-eclogite grade material.

Comparison of Models S and W, and others in the model template, shows that the shift from predominantly HP to UHP exhumation can be achieved by a small variation (WQ $\times$ f = 1 to 3) in the initial strength of the crust. This change does not fundamentally alter the overall tectonic evolution of the model orogen.

In Model R (Figs B.1–B.3), the microcontinent crust and oceanic sediment undergo greater weakening than in Model S ($W_s = 20$ compared with 5), but otherwise these are identical models. The initial (Phase 1) evolution of Model R is similar to Model S, with a considerable amount of microcontinent crust reaching UHP conditions, followed by exhumation at ∼20 Myr-pc. The lower viscosity of the plume results in more rapid exhumation (up to ∼2 cm a^{-1}), and intense deformation, resulting in greater internal 'mixing' of UHP and HP microcontinent crust and the overlying UHP oceanic material. These sensitivity tests show that the general tectonic evolution of Model S can easily be adapted using relatively small changes to f and W_s to explain a range of peak P–T conditions and exhumation rates.

3.7 Comparison of Model S with the Western Alps

3.7.1 Deformation and Orogenic Structure

Model S and Model W replicate many of the tectonometamorphic features of the Western Alps, as shown by a comparison with cross-sections through the three ICMs (Figs 3.6 and 3.7). We focus on a comparison with Model S knowing that in cases where only HP exhumation occurs, Model W is a suitable alternative. Because the model uses a constant V_r, and convergence in the Western Alps was not constant, the model time chosen for comparison is based on consistency of model crustal structure with the Western Alps. This corresponds to ∼190 km of convergence following initial underthrusting of the procontinent margin beneath the prowedge. Corresponding estimates from the Western Alps range from 200 to 100 km (*Schmid and Kissling*, 2000; *Handy et al.*, 2010), and decrease southward, making our choice for comparison

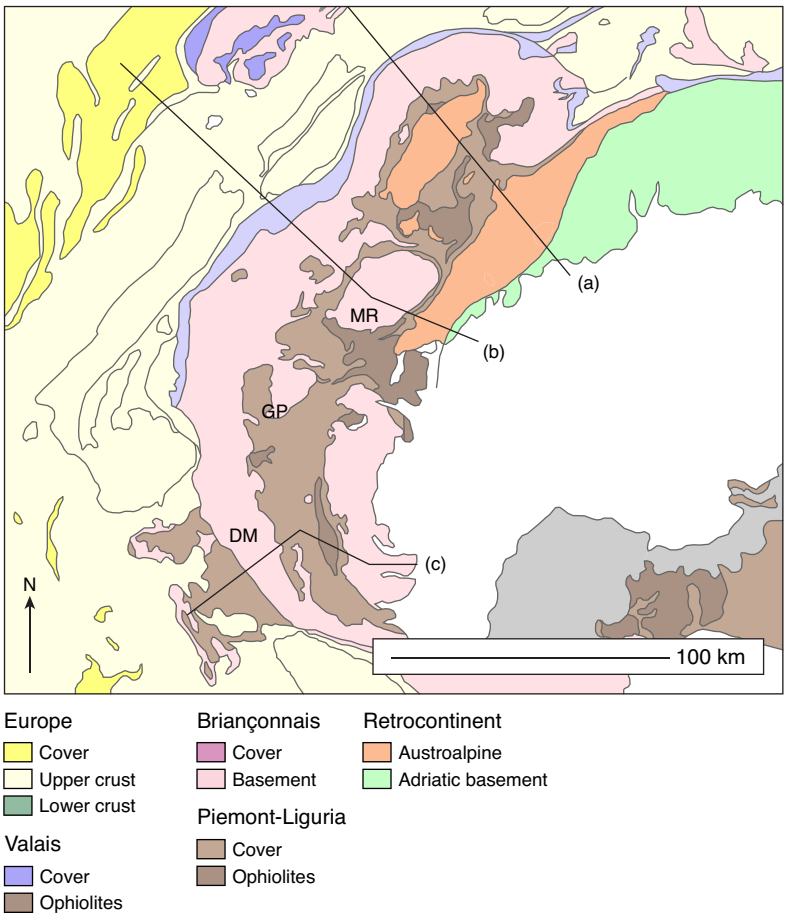

Figure 3.6: Geological map of the Western Alps. Modified from *Schmid et al.* (2004). Lines correspond to geological cross-sections shown in Figure 3.7

an upper limit.

Model S reproduces the following key characteristics of Alpine-type orogens (numbers in Fig. 3.7d):

1. Accretion in the model produces the general provenance and stacking order of the prowedge nappe sequence, with progressively more external domains (from top to bottom) separated by early top-proward (thrust-sense) shear zones.

2. The backfolded nappe comprising (U)HP microcontinent crust enveloped by (U)HP oceanic crust resembles the ICMs and overlying Piemont-Liguria units (e.g., Zermatt-Saas). In both the model and nature, the ICMs are separated from overlying lower-pressure units by a top-retroward normal-sense shear zone (*Reddy et al.*, 1999; *Gasco et al.*, 2012).

3. The structurally composite nature of the exhumed plume resembles the ICMs, with units of varying peak metamorphic grade separated by internal shear zones and thrusting of higher- over lower-pressure rocks, modified by later extensional reworking at shallower depths (*Avigad et al.*, 2003; *Le Bayon and Ballèvre*, 2006; *Pleuger et al.*, 2008; *Gasco et al.*, 2012). For example, the left flank of the (U)HP part of the exhumed plume resembles the Dora Maira structure, with west-dipping units of varying peak pressure separated by later top-NW shear zones. The same kinematics are produced within this part of the model during the transient phase of doming/uplift prior to the onset of major retrotransport.

4. The minor retroward folds within the underplated crust in the prowedge resemble southeast-vergent folds that define the Briançonnais 'fan structure' (*Bucher et al.*, 2003).

5. The exhumed HP 'rift basin' crust situated beneath the (U)HP microcontinent plume is analogous to the 'second' HP oceanic suture in the Western Alps represented by the Valais domain (*Bousquet et al.*, 2002).

6. The zone of retrotransport along the rear of the plug is similar to the Insubric Line, exposed near the Gran Paradiso and Monte Rosa massifs with the originally normal-sense (top-SE in the Western Alps) shear zone reoriented into a top-retroward (top-NW) thrust (*Schmid et al.*, 1996; *Pleuger et al.*, 2008).

7. Detachment of the procontinent middle crust and related zone of external uplift produce features similar to the External Crystalline Massifs exposed proward of the Monte Rosa and Gran Paradiso massifs (*Schmid and Kissling*, 2000).

8. The wedge of lower crust within the upper part of the conduit may correspond to the lower crustal wedge beneath the orogen inferred from seismic data (*Schmid et al.*, 1996; *Schmid and Kissling*, 2000).

There are, however, some limitations to Model S with respect to the cross-sections and inferred structural evolution of the Alps.

1. Although the exhumed 'sheet' of UHP crust is only ∼5 km thick, it is larger than currently recognized UHP units in the Western Alps. However, the amount of exhumed UHP material depends strongly on its strength evolution; Model W reproduces the small amount of exhumed (U)HP crust more accurately.

2. Although the models capture the structurally composite nature of the ICMs, the magnitude of deformation in the model plume is probably greater than in the ICMs. Higher resolution models would permit the development of narrower shear zones and consequently less distributed strain.

Figure 3.7 *(following page)*: Comparison of Model S with key structural features of the Western Alps. All cross-sections at 1:1 scale. (a) Crustal-scale cross-section through the Monte Rosa Massif, after *Schmid et al.* (2004), with location of the top-SE normal-sense Gressoney Shear Zone (GSZ) after *Reddy et al.* (1999, 2003). PFT=Penninic Frontal Thrust; IL=Insubric Line. White-filled arrows show kinematics of extensional shear zone. Black arrows show kinematics of thrusting in the foreland and backthrusting along the Insubric Line. (b) Crustal-scale cross-section through the Gran Paradiso Massif, after *Schmid et al.* (2004), with location of the top-SE Orco Shear Zone (OCS) after *Gasco et al.* (2009). (c) cross-sections through the Dora Maira Massif after (left) *Lardeaux et al.* (2006) and (right) *Avigad et al.* (2003)illustrating top-SW normal-sense shear zones formed at greenschist facies, superimposed on a stack of units of varying peak pressure. The basal contact between the UHP and underlying greenschist (GS) to blueschist (BS) facies rocks is an extensional shear zone that cuts an earlier contact interpreted as a thrust related to emplacement of UHP over lower pressure units (*Avigad et al.*, 2003). Black- and red-filled arrows show kinematics of late, primarily top-SW shear zones and later normal faults, respectively. (d) Simplified geological map of the Western Alps after *Schmid et al.* (2004) showing locations of cross-sections in a–c. (d) Model S result showing key structural elements. Numbers in (a–c) and (d) correspond to general features of Western Alps referred to in text. Red-filled arrows in (d) show normal-sense shear above plume during the transient period of uplift and prior to retrotransport early in Phase 3. Note that in (a), 3 refers to the juxtaposition of coesite-eclogite facies Piemont-Liguria units with the underlying HP Monte Rosa Massif, and to internal stacking within the nappe (e.g., along Stellihorn Shear Zone; *Pleuger et al.*, 2008). In (b), 3 refers to the thrusting and juxtaposition of the upper Gran Paradiso Unit over the lower pressure Money Unit (MU) during exhumation (*Le Bayon and Ballèvre*, 2006). In (c), at right, 3 refers to juxtaposition of units of varying peak pressure during and after exhumation from (U)HP conditions, as indicated by late, greenschist facies normal-sense shear zones (*Avigad et al.*, 2003).

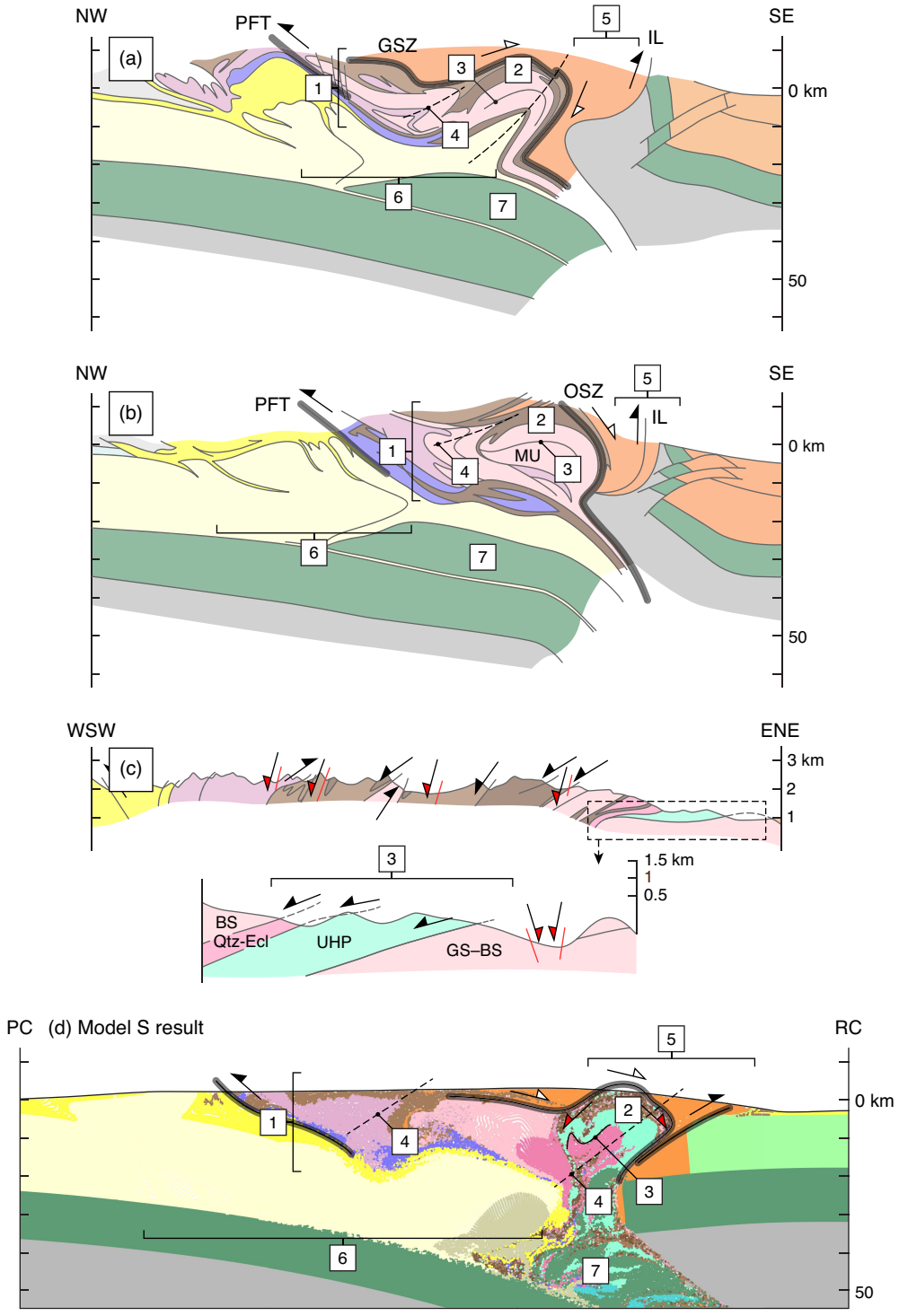
NW
SE
(a)
PFT
GSZ
IL
0 km
50
(b)
OSZ
MU
WSW
ENE
(c)
3 km
2
1
1.5 km
0.5
BS
Qtz-Ecl
UHP
GS–BS
PC
(d) Model S result
RC

3. Although the model reproduces HP metamorphism and exhumation of the Valais Ocean-equivalent 'rift basin' (*Bousquet et al.*, 2002) in the context of a single subduction zone, it does not explain the present-day juxtaposition of the HP Valais units with the very low-grade overlying Zone Houillère (*Bucher and Bousquet*, 2007).

4. The strong backfolding of the (U)HP nappe most closely resembling the Monte Rosa ICM. The amount of retrotransport in the models is directly related to the total Phase 3 convergence and therefore to the choice of model time to compare with the cross-sections. Less (post-)Oligocene convergence in the more southwestern Alps (*Schmid and Kissling*, 2000) may explained the more limited backfolding of the Gran Paradiso and Dora Maira massifs versus the Monte Rosa.

5. The tip of the lower crustal wedge has not advanced as far proward as inferred from the seismic velocity data (*Schmid and Kissling*, 2000).

6. Total retrotransport is less than observed on some transects, with the model lacking a true retrowedge comprising shortened retrocontinent crust. The retrowedge lacks exhumed mantle lithosphere (Ivrea body). Both result from our choice of simplified initial retrocontinent geometry.

3.7.2 P–T *History of Model (U)HP Rocks*

Peak P–T conditions for most of the natural ICMs cluster around ∼1.5–2.5 GPa/450–625°C, followed by broadly isothermal exhumation and overprinting at conditions of ∼1.0 GPa/450–600°C (Fig. 3.8a). An exception is the southern Dora Maira Massif, which reached ∼3.5 GPa/750°C (Fig. 3.8a), with considerable cooling during exhumation.

Selected P–T paths from particles in Model S are similar, although generally cooler than observed (Fig. 3.8b). A wide range of peak pressures (P_{max}) is obtained depending on the position of the particle within the plume. For some earlier buried particles, P_{max} slightly precedes T_{max}, whereas for others P_{max} and T_{max} are essentially synchronous. Some model particles reach ∼3.4 GPa/700°C, similar to the southern Dora Maira Massif, but cooler by ∼50°C. Others reach P_{max}–T_{max} conditions of ∼2.0–2.5 GPa/500–600°C, within uncertainty of estimates for the northern

Dora Maira and the other massifs. During exhumation, model particles undergo minor cooling to ∼1.0 GPa/500°C, followed by broadly isothermal exhumation to ∼0.5 GPa accompanied, for some particles, by minor heating. Lower P_{max} particles undergo near-isothermal decompression, while higher P_{max}–T_{max} particles undergo more cooling during this stage. Maximum tectonic over/under pressures reach ±0.15 GPa. Oceanic particles overlying the model ICM record peak conditions up to ∼3.6 GPa/700°C, consistent with *P*–*T* estimates and the presence of coesite and diamond in the exhumed (U)HP Piemont-Liguria units (*Reinecke*, 1991; *Amato et al.*, 1999; *Groppo et al.*, 2009; *Frezzotti et al.*, 2011).

Although ICM exhumation rates are debated (*Berger and Bousquet*, 2008; *Handy et al.*, 2010), with estimates ranging from ∼0.5–3.5 cm a^{-1} (*Rubatto and Hermann*, 2001; *Meffan-Main et al.*, 2004), there is general agreement that the ICMs underwent an initial phase of rapid exhumation followed by slower trans-crustal exhumation (Fig. 3.8d). In Model S, early exhumation from (U)HP conditions to crustal levels reaches rates of ∼0.7–1.0 cm a^{-1} (Fig. 3.8e), within range of the data, but lower than the highest estimate of ∼3.5 cm a^{-1} from the southern Dora Maira Massif

---

Figure 3.8 *(following page)*: Comparison of model *P*–*T* paths with observations. (a) Published *P*–*T* paths for the ICMs and overlying UHP Piemont-Liguria rocks. DM=Dora Maira; GP=Gran Paradiso; MR=Monte Rosa. Estimates from *Amato et al.* (1999) (A99); *Rubatto and Hermann* (2001) (RH01); *Meffan-Main et al.* (2004) (M04); *Le Bayon and Ballèvre* (2006) (LB06); *Radulescu et al.* (2009) (GR09); *Gasco et al.* (2011b) (G11b; northern DM); and, *Gasco et al.* (2011a) (G11a), and references therein. (b) Selected *P*–*T* particle paths from Model S, with grey boxes showing positions of published *P*–*T* estimates from (a). DM peak=Dora Maira peak conditions. ZS data and ICM data refer to grey boxes representing Zermatt-Saas and ICM peak conditions, respectively. (c) Model particle starting locations. (d) Pressure–time (*P*–*t*) paths for the ICMs (sources as in (a)) except for LB06 which is a composite path based on the *P*–*T* path of *Le Bayon and Ballèvre* (2006) combined age of HP metamorphism and subsequent retrogression from *Engi et al.* (2001); *Lapen et al.* (2007). Coloured bars correspond to approximate age ranges of main tectonic stages of the Western Alps, modified from *Steck* (2008). 'Extension' refers to age range of top-southeast and locally top-northwest normal-sense structures overlying exhumed (U)HP rocks, from *Reddy et al.* (2003) and *Rosenbaum et al.* (2012). (e) *P*–*t* data for Model S particles shown in (b), superimposed on coloured bars representing main 'Alpine-type' tectonic stages in Model S, corresponding the equivalent stages in (d) modified from *Steck* (2008). (f) Model particle final positions.

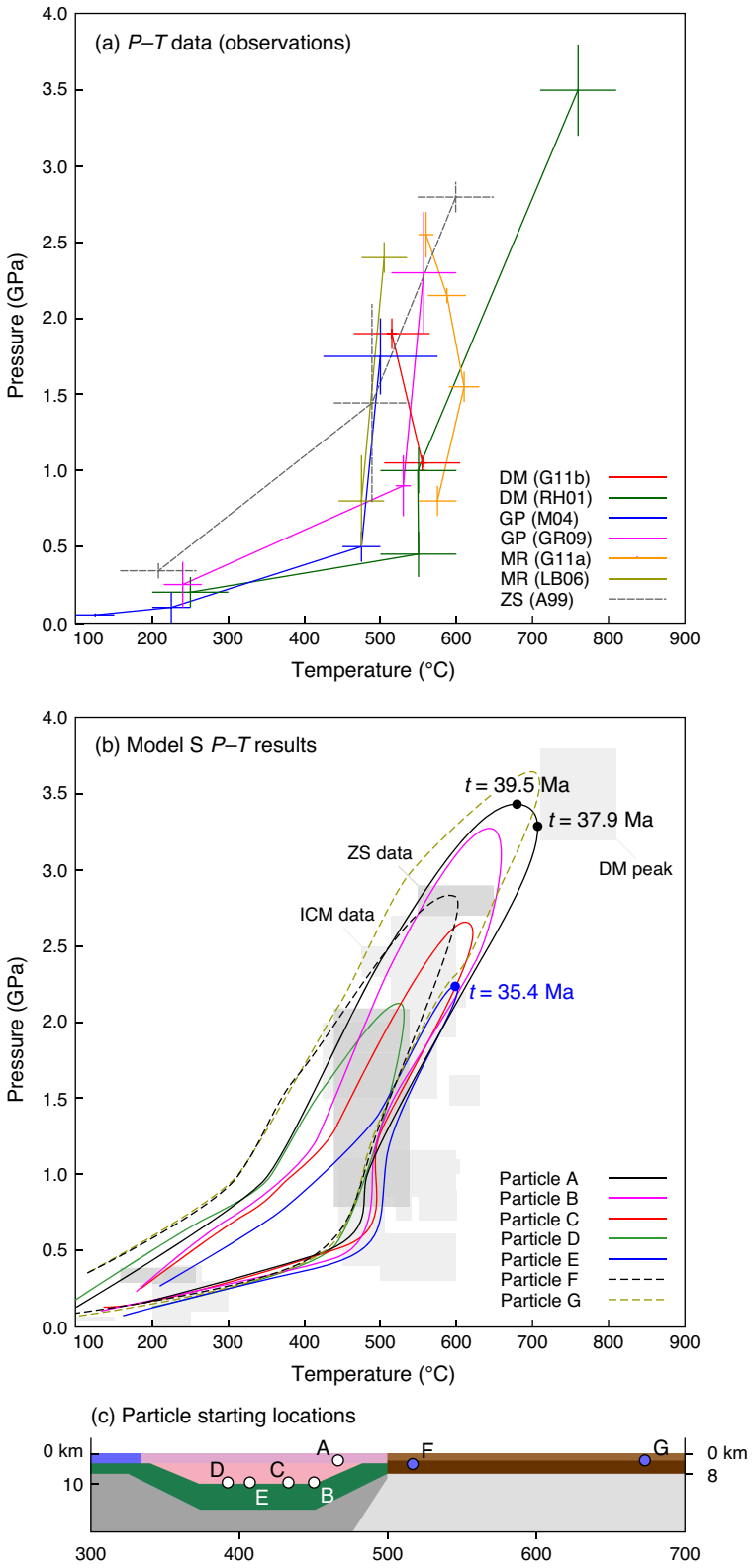
(a) P–T data (observations)
Pressure (GPa)
Temperature (°C)
DM (G11b)
DM (RH01)
GP (M04)
GP (GR09)
MR (G11a)
MR (LB06)
ZS (A99)
(b) Model S P–T results
t = 39.5 Ma
t = 37.9 Ma
ZS data
DM peak
ICM data
t = 35.4 Ma
Particle A
Particle B
Particle C
Particle D
Particle E
Particle F
Particle G
(c) Particle starting locations
0 km
10
A
B
C
D
E
F
G
0 km
8

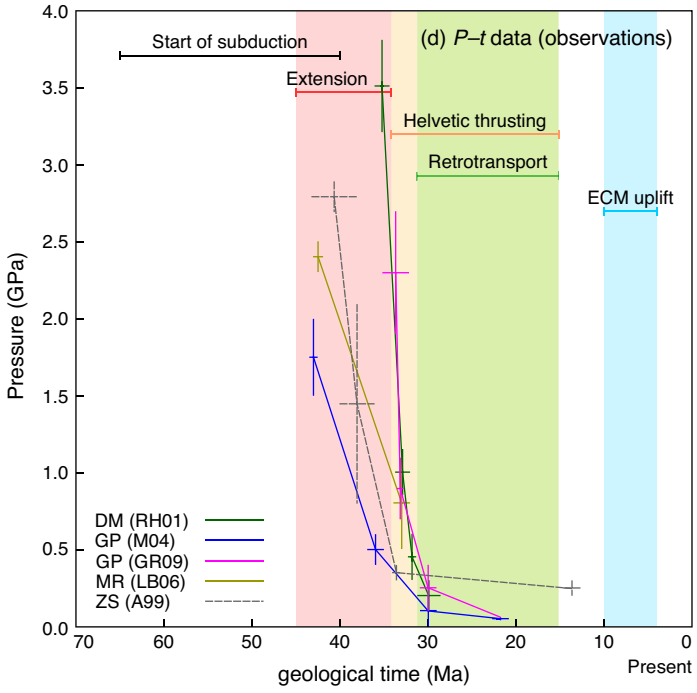
(d) P–t data (observations)
Start of subduction
Extension
Helvetic thrusting
Retrotransport
ECM uplift
DM (RH01)
GP (M04)
GP (GR09)
MR (LB06)
ZS (A99)
Pressure (GPa)
geological time (Ma)
Present

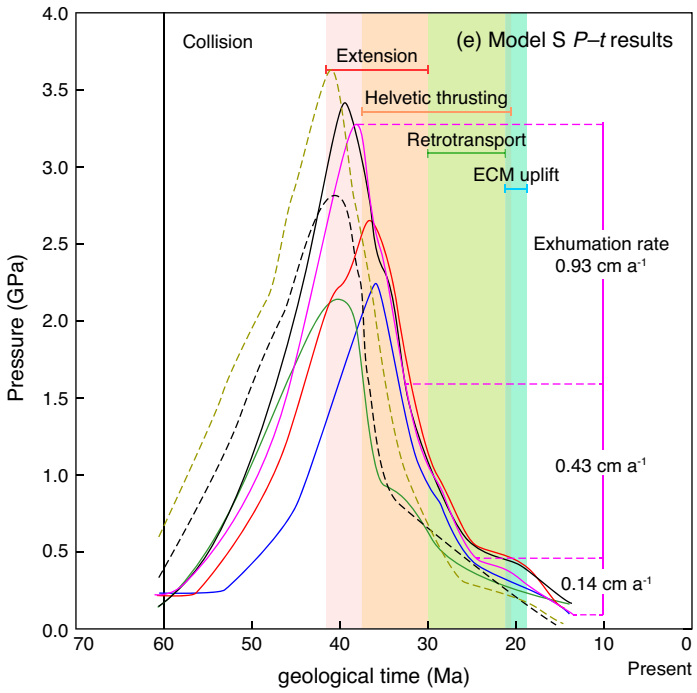
(e) Model S P–t results
Collision
Extension
Helvetic thrusting
Retrotransport
ECM uplift
Exhumation rate
0.93 cm a-1
0.43 cm a-1
0.14 cm a-1
Pressure (GPa)
geological time (Ma)
Present

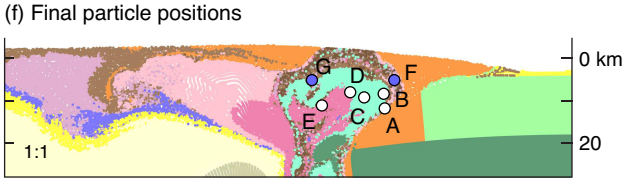
(f) Final particle positions
G
D
F
B
E
C
A
0 km
20
1:1

(*Rubatto and Hermann*, 2001). Model exhumation rates are sensitive to the viscosity of the plume; lower viscosity Model R achieves rates of up to ∼2 cm a^{-1} (Fig. B.3), whereas oceanic particles in Model S achieve rates of ∼1 cm a^{-1}. Given that Models S, R, and W produce higher/lower maximum metamorphic pressures and exhumation rates while retaining the same basic evolution, we suggest that corresponding variations along the Western Alps may also result from equivalent variations (i.e., properties/processes that affect f and W_s) rather than fundamental differences in burial/exhumation mechanisms.

For most particles in Model S, exhumation slows to ∼0.4 cm a^{-1} between ∼1.5–0.5 GPa; particles then stall briefly before continuing to exhume at rates of ∼0.14 cm a^{-1}. We interpret the minor heating evident in some Model S paths to be the result of this slowing and stalling, during which the plume undergoes heating from thermal relaxation of the orogenic wedge at reduced thermal Péclet number. Model S shows a broad range of P–T paths in the exhumed ICM (Fig. 3.8b), indicating that material in the model ICM detached over a range of depths in the subduction conduit, which is likely similar to the natural case.

Model P–T paths are generally similar to the observations; for example 'Particle A' (Fig. 3.8b) compares favourably with the southern Dora Maira massif, and the temperature discrepancies may simply be the result of the models being somewhat too cool. Sensitivity tests, investigated in Part 2 (Jared Butler, pers. comm) demonstrate that a small increase in upper crustal heat production from 2.0 to 2.25 μWm^{-3} removes most of this discrepancy.

3.7.3 Predicted Erosion Rates

The patterns and magnitude of surface erosion in Model S are broadly consistent with stratigraphic and cooling-rate studies in the Western Alps that indicate an inverse correlation between rapid (U)HP exhumation and erosion rates (*Sinclair and Allen*, 1992; *Sinclair*, 1997; *Schlunegger and Willett*, 1999; *Bernet et al.*, 2009; *Malusà et al.*, 2011; *Beucher et al.*, 2012).

During Phase 1 in Model S, erosion is negligible because the prowedge is submarine (Fig. 3.5), consistent with the relatively slow flysch deposition in western Alpine basins during the Eocene, corresponding to burial of the ICMs (*Sinclair and Allen*, 1992; *Sinclair*, 1997; *Kuhlemann et al.*, 2002; *Ford et al.*, 2006).

Erosion rates increase during Phase 2 owing to uplift of the prowedge in response to the intrusion of (U)HP plume, but on average remain relatively low (<0.8 mm a^{-1}; Fig. 3.5), because exhumation is accommodated by internal extension within the prowedge. This is broadly consistent with the Western Alps, where the ∼45–33 Ma period of normal-sense shearing associated with exhumation of the Monte Rosa Massif overlapped in time with continued flysch deposition in the northern Alpine foreland basin (*Sinclair*, 1997). Exhumation of the Dora Maira Massif following ∼35 Ma (U)HP metamorphism (*Rubatto and Hermann*, 2001) broadly coincided with rapid cooling and deposition of HP detritus in the southwestern foreland basin (*Morag et al.*, 2008) and increased erosion during the Oligocene (see below).

Surface erosion plays a greater role in exhumation during Phase 3, owing to the substantial increase in topography, in particular at the rear of the plug (Fig. 3.5). Buoyancy-driven exhumation has ceased, and the now slower exhumation of the model ICM is a result of retrothrust-related uplift and erosion of the plug. The model results are consistent with increased erosion and sediment discharge rates, and with the onset of molasse-type sedimentation in the Western Alps during the Oligocene, observations generally attributed to uplift and greater subaerial exposure of the Western Alps (*Sinclair and Allen*, 1992; *Sinclair*, 1997; *Schlunegger and Willett*, 1999; *Kuhlemann et al.*, 2002; *Bernet et al.*, 2009; *Malusà et al.*, 2011).

Based on comparison with model Phases 1 and 2 with the observations, we conclude that fast erosion is not required to explain the initial stages of rapid (U)HP rock exhumation in the Western Alps.

3.7.4 Comparison of Absolute Timing

We converted Model S to geological time by assuming that microcontinent subduction began at 60 Ma (Fig. 3.8d,e). Doing so results in the onset of (U)HP metamorphism at ∼46 Ma, and peak metamorphism from ∼38–35 Ma. The latter is generally consistent with (U)HP metamorphic ages of the ICMs (but somewhat younger than the Monte Rosa), which range from ∼43–35 Ma (*Berger and Bousquet*, 2008).

Exhumation-related normal-sense shearing begins only a few Myr later in the model (∼42 versus 46 Ma) than in the Western Alps (*Reddy et al.*, 2003; *Rosenbaum et al.*, 2012). Comparison among P–t paths shows that some model particles begin exhumation up to ∼5 Ma earlier than others, again showing that even within an ICM

rocks may record disparate P–t paths related to differential burial and stacking during exhumation. In both the Western Alps and Model S, the onset of normal-sense shearing appears to predate the youngest P_{max} metamorphism (∼35 Ma; *Rubatto and Hermann*, 2001). In Model S, this is explained by continued subduction of microcontinent crust during the earliest stages of exhumation. Furthermore, exhumation of crust from the conduit requires that the overlying material exhumes ahead of it; normal-sense shearing at crustal depths starts with the exhumation of the shallowest material in the channel, and remains active until the deepest material is exhumed. This may explain why some (U)HP rocks in the Western Alps were undergoing (U)HP metamorphism as recently as ∼35 Ma, while normal-sense shearing at crustal levels had been active since ∼46 Ma.

Later exhumation in the model results from a combination of thrusting/backthrusting and erosion, with model times (starting at ∼30 Ma) broadly consistent with the observations (*Steck*, 2008). The exception is the earlier detachment of the continental margin in Model S during Phase 3, which we interpret to be equivalent to detachment and uplift of the External Crystalline Massifs. This discrepancy can be explained by our choice of constant $V_r = -1$ cm a^{-1}, whereas in the Western Alps convergence slowed considerably at ∼20 Ma, to ∼0.2 cm a^{-1} (*Handy et al.*, 2010). An equivalent slowing in the models would stretch a 2 Myr model time increment to 10 Myr.

3.8 A Simple Framework for the Tectonic Evolution of the Western Alps

The evolution of the Western Alps can be described in terms of three main geometrical/kinematic phases each comprising a PURC flow mode inferred from the model results. We briefly restate the Model S PURC flow modes and interpret that the Alps evolved in the same way. The first-order geometry of the Western Alps can be explained by the superposition of these flow modes.

3.8.1 Phase 1: PC Mode Oceanic and Microcontinent Subduction

During Phase 1, Model S operates in the PC mode, in which accretion and underplating lead to growth and advance of P over the procontinent, while subduction beneath P leads to the accumulation of (U)HP crust in C (Fig. 3.9a). U and R are largely inactive. Deformation is concentrated at the basal shear zones of P and C,

with top-proward shear throughout the system.

In the Western Alps context, we interpret this phase to correspond to the late Eocene subduction of remnants of the Piemont-Liguria Ocean and Briançonnais microcontinent southeastward beneath the Austroalpine lid and Adria to (U)HP conditions, while shallower/frontal accretion of material from these domains (e.g., the external Briançonnais) led to progressive growth of P (*Sinclair and Allen*, 1992; *Wheeler et al.*, 2001; *Steck*, 2008). P therefore initially consists of the Austroalpine units, and grows by accretion of material from the proside of the system.

3.8.2 Phase 2: PUC′ Mode Buoyancy-Driven Exhumation with syn-orogenic Extension

During Phase 2, Model S operates in the PUC′ exhumation mode (Fig. 3.9b). P grows by accretion and underplating of procontinent crust, but deformation is dominated by buoyancy-driven exhumation from C into P. Accommodation space for insertion of the exhuming plume into the base of P is produced by its internal extension and proward translation, not erosion.

In the context of the Western Alps, PUC′ flow during Phase 2 corresponds to Late Eocene to Oligocene exhumation of (U)HP Piemont-Liguria and Briançonnais units to the base of the crust. HP Valais domain rocks also exhumed during this period (*Bousquet et al.*, 2002) although it is not clear if they were part of the same pulse. Top-southeast normal-sense shearing along the boundary between P and U was coeval with top-northwest shearing at the base of P. Horizontal extension and splitting of P during this phase can be likened to proward translation of the Dente Blanche klippe. At deeper levels of P and particularly U, top-retroward structures (e.g., the backfolded Entrelor Shear Zone; *Bucher et al.*, 2003) formed during this phase, perhaps in a similar manner to those in Model S (*Meffan-Main et al.*, 2004). In the Alps, U is interpreted to be the region of uplift between P and the Insubric line, such that the rear of U, the Insubric line, becomes an active shear zone in the next phase.

If our interpretation is correct, late Eocene normal-sense shearing in the Western Alps was internal extension driven from below, by the buoyant rise of subducted crust, and not by lithosphere-scale extension. For this mechanism to be viable, the cumulative volume of exhuming crust must have had sufficient buoyancy to disrupt

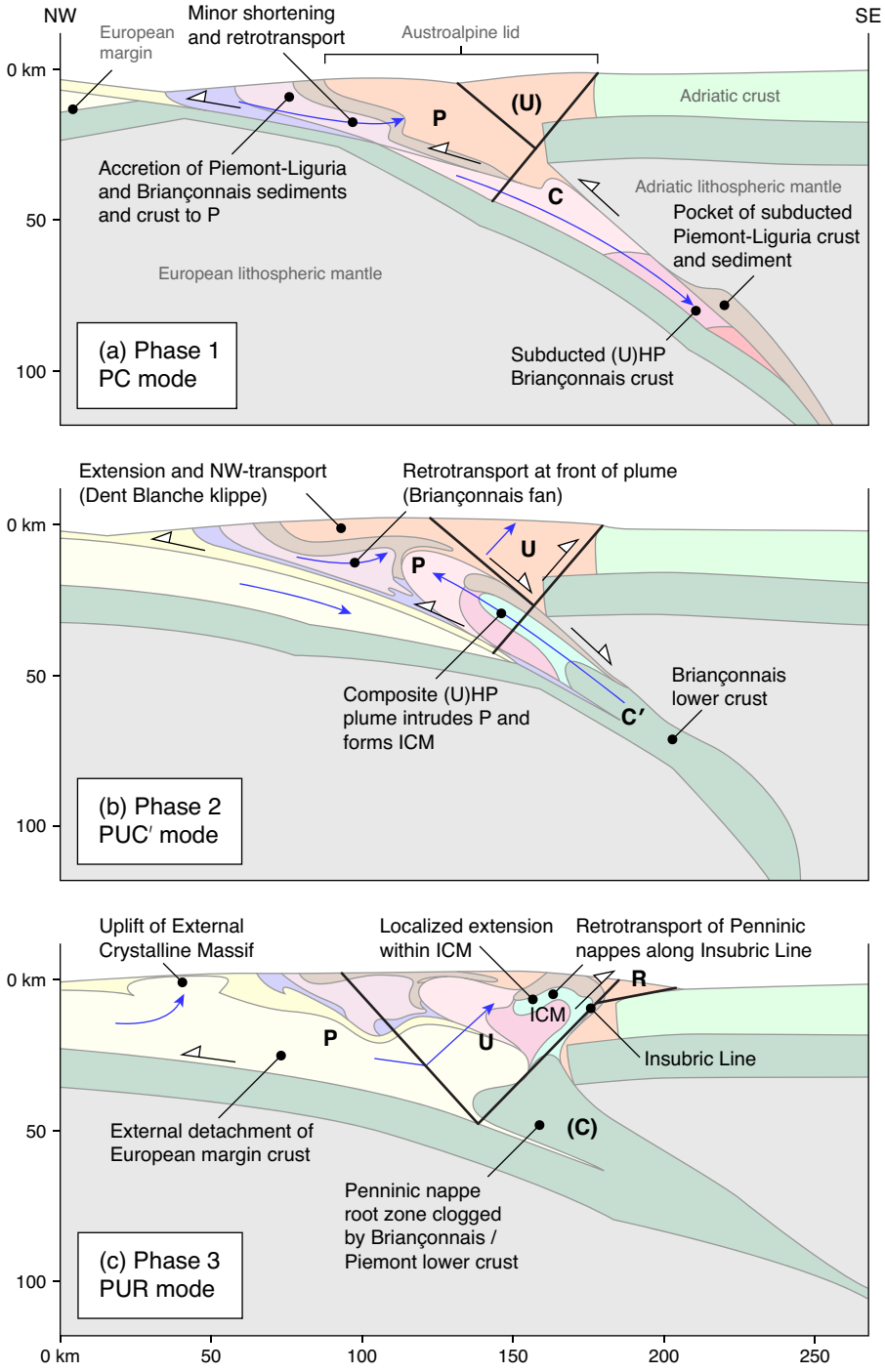

Figure 3.9: PURC interpretation of Model S. P=prowedge, U=uplifted plug, R=retrowedge, C=conduit. Labels refer to corresponding Alps evolution. Blue arrows show flow directions, assuming a stationary retrocontinent and converging procontinent. White-filled arrows show kinematics. (a) PC mode showing accretion to P and (U)HP metamorphism in C. (b) PUC′ mode showing buoyancy-driven transport of (U)HP crust from C to P, resulting in coeval normal-sense shearing and thrusting. (c) PUR phase showing uplift and retrotransport of exhumed (U)HP plume followed by external detachment of procontinent margin crust.

the prowedge. Evidence that parts of the ICMs and overlying oceanic crust comprise aggregates of slices of varying P_{max} (e.g., *Avigad et al.*, 2003; *Le Bayon and Ballèvre*, 2006) implies that the necessary buoyancy was achieved by aggregation and stacking of rocks of varying provenance from different depths of the conduit during their ascent, forming a larger, composite plume.

3.8.3 Phase 3: PUR Mode Bivergent Deformation and Retrothrusting

During Phase 3, Model S operates in the PUR mode (Fig. 3.9c). Subduction ceases and C is inactive because it is clogged by exhumed procontinent lower crust. Underthrusting and detachment of the procontinent leads to significant uplift of P, followed by translation of the accreted procontinent into U. Uplift and exhumation at the rear of P and in U are accommodated by normal-sense shearing along the flanks of the (U)HP dome, followed by retroward transport of the plume (incipient activation of R). The zone of retrotransport is bounded by the steep, top-retroward, thrust-sense shear zone at the rear of U.

In the Western Alps context, the PUR Phase 3 in Model S corresponds to Oligocene and later bivergent deformation in the Western Alps. Underthrusting of the European margin during this period was accompanied by uplift of P and retrothrusting along the Insubric Line (rear of U), leading to backfolding of the exhumed (U)HP nappes (e.g., the Vanzone antiform; *Steck*, 2008) and reorientation of previous normal-sense structures (*Pleuger et al.*, 2008). Further convergence led to the detachment and accretion of the European crust to P, followed by uplift of the External Crystalline Massifs, and continued growth of P toward the foreland (*Schmid et al.*, 1996). In summary, Phase 3 bivergent development of U and R probably resulted from blocking of the Western Alps subduction conduit, C.

3.9 Conclusions

We have used numerical models to investigate the tectonic evolution of Alpine-type orogens, focusing on the mechanism of (U)HP rock exhumation. Based on a comparison of the models with observations, we draw the following conclusions concerning the exhumation of (U)HP rocks in the Western Alps.

1. Rapid exhumation of (U)HP rocks to crustal depths in the models is explained

by upward, buoyancy-driven flow of (U)HP crust from within the subduction conduit, causing localized internal extension of the overlying prowedge and plug. Normal-sense shearing and (U)HP rock exhumation in the Western Alps are consistent with this PUC′ mode.

2. Contrary to previous suggestions, rapid exhumation of (U)HP crust within an Alpine-type orogen, and the Alps *per se*, requires neither lithosphere-scale absolute extension, nor extremely rapid erosion.

3. Subsequent trans-crustal exhumation of (U)HP rocks in the Western Alps during backthrusting is explained by a bivergent orogenic (PUR) style, combined with minor extension within the prowedge and plug, caused by underthrusting of the European margin. This phase does require enhanced erosion.

4. In the models, neither (U)HP rock exhumation nor the transition to bivergent deformation requires breakoff of the subducting slab. We therefore question whether slab breakoff beneath the Alps strongly influenced (U)HP exhumation.

5. Comparisons between Model S and models W and R show that pronounced differences in the volume and peak P–T conditions of exhumed (U)HP material can be caused by minor differences in the initial strength of the subducting crust. The magnitude of crustal strain-weakening (a proxy for all types of weakening) in the subduction conduit strongly influences the rate of exhumation and extent of deformation in the exhuming plume. In nature, equivalent ranges in initial strength (by amounts of 1–3) and subsequent weakening (by factors of 1–5) can arise from a range of factors including variations in lithology, prior degree of metamorphism and inherited structure of the protolith, and the presence of fluid or melt. We suspect that these variations could account for observed along-strike differences in peak pressure conditions and style of stacking and deformation in the Alps Internal Crystalline Massifs.

3.10 Acknowledgements

JPB acknowledges support from an NSERC Canada Graduate Scholarship. CB and RAJ were funded by NSERC Discovery Grants, and CB by the Canada Research

Chair in Geodynamics. Numerical models used the software SOPALE-NESTED, developed from SOPALE by D. Guptill and B. Lee. SOPALE was originally developed at Dalhousie University by P. Fullsack. N. Culshaw and C. Warren are thanked for constructive feedback on an early version of the manuscript. R. Bousquet, T. Gerya, and M. Brandon are thanked for their constructive reviews.

Chapter 4

The Alps 2: Variations on the Basic Model with Comments on the Evolution of the Central and Eastern Alps

4.1 Preface

This chapter elaborates on the geodynamics of (U)HP rock exhumation in Alpine-type orogens by presenting variations on the numerical models described in Chapter 3. The models shown here will form the foundation of a future companion paper, designed to address along-strike variations in the style of (U)HP rock exhumation within the Alpine Orogen, including the Central (Swiss) Alps, and the Eastern Alps. Owing to time constraints some models presented here are considered prototypes, in particular those that attempt to reproduce the key geological aspects of the Alps.

4.2 Introduction

This chapter presents a preliminary version of Part 2 of our study designed to investigate the geodynamics of continental subduction and (ultra)high-pressure ((U)HP) rock exhumation in Alpine-type orogens using 2D upper-mantle-scale numerical model experiments. Part 1 presented a working geodynamic model, Model S, and compared the results with observational constraints on the tectonometamorphic

evolution of the Western Alps. The objective was to present and interpret a self-consistent model that explains the main tectonic characteristics of the Western Alps, focusing on the Eocene and later evolution of the (U)HP Internal Crystalline Massifs (ICMs), generally considered to have formed by the deep subduction and exhumation of the Briançonnais microcontinent.

Part 1 showed that (U)HP exhumation in the Western Alps can be explained by a model involving exhumation of a composite (U)HP 'plume', driven from below by the buoyancy of weakened (U)HP crust. Neither rapid erosion nor absolute extension are required to explain (U)HP exhumation. Instead, the normal-sense shearing ('within-orogen' extension) documented throughout the Western Alps can be explained by the initial, rapid emplacement of the buoyant (U)HP plume beneath the relatively stationary (Austroalpine) orogenic wedge, coupled with thrusting at depth and in the foreland. Subsequent 'trans-crustal' exhumation, in contrast, is the result of a combination of orogen-scale bivergent thrusting and accompanying erosion.

Part 2 of this study presents an expanded set of model experiments designed to elucidate the main controls on the behaviour of Model S, and by extension the geodynamic evolution of Alpine-type orogens. The objectives are to identify geologically significant input parameters; to assess to what extent variations in these parameters affect the style of (U)HP rock exhumation and orogenic evolution shown in Model S; and, to discuss how consequent variations in tectonic style can be used to explain some of the along-strike variations in the evolution of the Alpine Orogen. The modeling approach and design are presented in Part 1 of this study. Definitions of the input parameters explored here are restated where necessary.

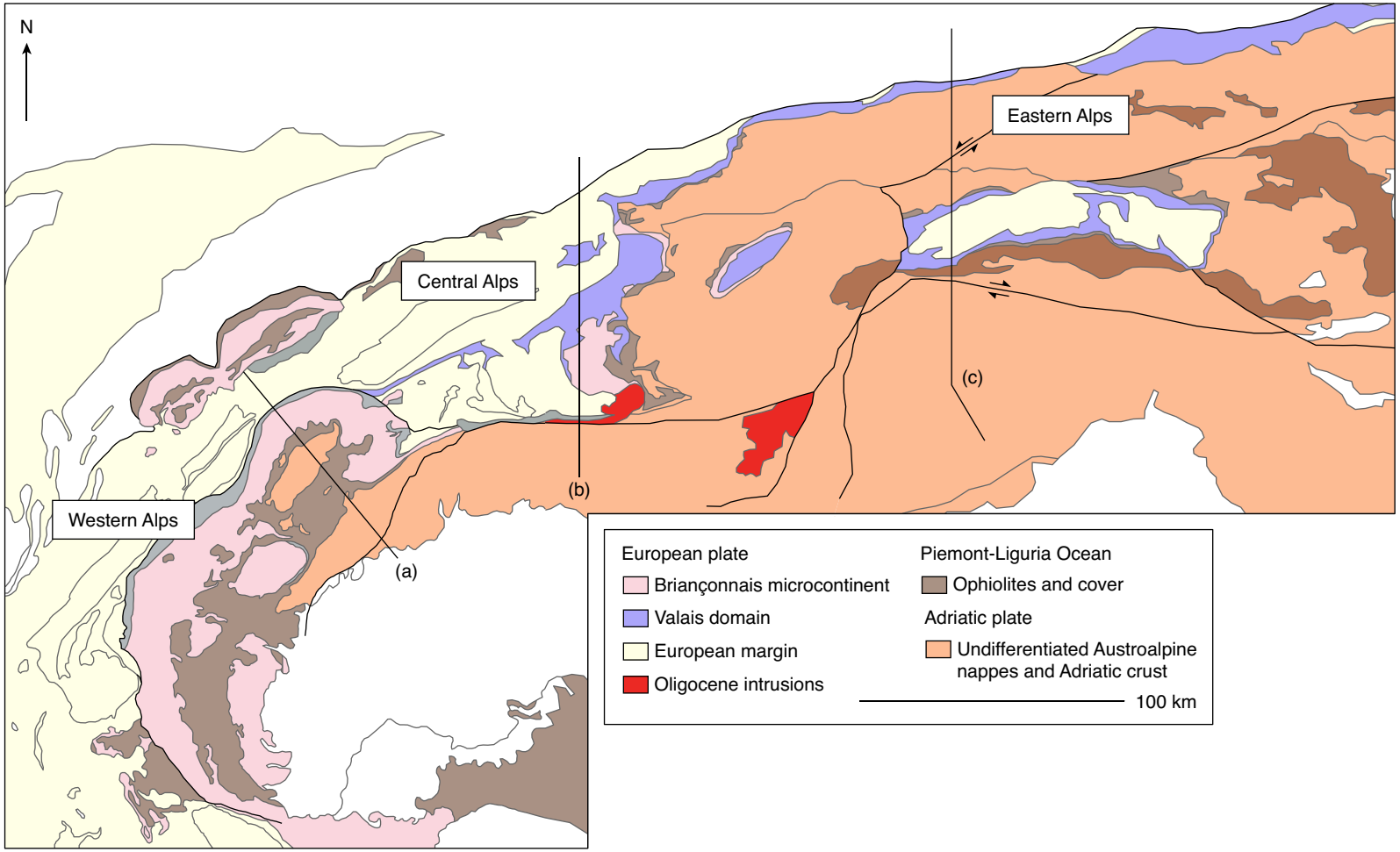

Figure 4.1: Geological map of the Alpine Orogen (simplified from *Schmid et al.* 2004). Tectonic units derived from the Austroalpine terrane and Adriatic plate have been grouped for simplicity. Lines (a–c) show positions of cross-sections in Figure 4.3.

4.3 Contrasts in Tectonic Features along the Alpine Orogen

The Alpine Orogen comprises the Western, Central (Swiss), and Eastern Alps (*Schmid et al.*, 2004) (Fig. 4.1). The orogen is highly arcuate, trending northward through the Western Alps from France/Italy to Switzerland, and then eastward to Austria through the Central and Eastern Alps. The overall structure of the orogen consists of an allochthonous nappe stack, situated above the European plate, comprising elements derived from the extended European margin and adjacent ocean basins, and accreted to the upper-plate (Adria and Austroalpine terrane) during Paleocene–Oligocene subduction (*Schmid et al.*, 2004; *Steck*, 2008; *Schmid et al.*, 2011). (U)HP metamorphism during subduction of the European plate is recorded locally in all three sections (*Berger and Bousquet*, 2008). However, in detail there are important tectonometamorphic differences along the orogen that are impossible to address with a single geodynamic model. These features are summarized below.

4.3.1 Provenance of (U)HP Units

The provenance of the principal (U)HP units varies along the orogen. The (U)HP ICMs of the Western Alps comprise Variscan crystalline (granitoid) basement, and metasedimentary units, both containing eclogites or (U)HP parageneses, that are generally ascribed to the Briançonnais microcontinent (*Schmid et al.*, 2004). These are draped by units derived from the Piemont-Liguria Ocean that record somewhat earlier (U)HP metamorphism (*Berger and Bousquet*, 2008). The principal (U)HP units in the Central and Eastern Alps, in contrast, were derived from the outermost European margin, not the Briançonnais microcontinent (*Schmid et al.*, 2004). The Adula nappe of the Central Alps is a large (∼40 km wide) composite nappe comprising diverse granitoid and metasedimentary units, all containing eclogites (*Nagel*, 2008), aggregated during subduction and exhumation. The overlying Tambo and Suretta nappes, of the Briançonnais domain, are volumetrically minor, and did not reach (U)HP conditions. In the Eastern Alps, the thin (U)HP Eclogite Zone of the Tauern window comprises metasedimentary rocks containing eclogites (both lithologies record (U)HP metamorphism), interpreted as sediments and mafic rocks deposited on/intruded into the European margin; no remnant of the Briançonnais

microcontinent has been recognized there (*Schmid et al.*, 2011). The overlying Modereck nappes, ascribed to the distal European margin, and overlying Valasian units also locally record (U)HP metamorphism. The absence of the Briançonnais domain in the Eastern Alps has led to the view that the former was a northeastward tapering promontory of the Iberian microcontinent (*Stampfli et al.*, 1998; *Handy et al.*, 2010).

4.3.2 P–T Conditions and Timing of Metamorphism

The maximum *P–T* conditions of (U)HP metamorphism vary somewhat along the length of the orogen (Fig. 4.2), likely reflecting different depths and/or timescales of burial. In the Western Alpine ICMs, peak (pressure) *P–T* conditions reached ∼3.5 GPa/750°C, but were locally as low as ∼2 GPa/550°C (*Rubatto and Hermann*, 2001; *Le Bayon and Ballèvre*, 2006). Peak conditions in the Adula nappe are ∼2.5–3 GPa/750–850° in the southeast, and decrease systematically northward (see references in *Nagel*, 2008). In the Eastern Alps, meanwhile, peak metamorphism of the Eclogite Zone reached considerably lower pressures, ∼2–2.5 GPa/550–600°C (see references in *Smye et al.*, 2011).

The timing of (U)HP metamorphism of the principal (U)HP units along the orogen is broadly similar. Ages of ∼45–35 Ma in the Western Alps are typically attributed to (U)HP metamorphism of the ICMs (*Rubatto and Hermann*, 2001; *Berger and Bousquet*, 2008). A similar range of ages, ∼46–35 Ma, has been reported for (U)HP metamorphism of the Adula nappe (see references in *Nagel*, 2008). The age of (U)HP metamorphism of the Eastern Alps Eclogite Zone is controversial, with data indicating metamorphism between ∼45–35 Ma (see references in *Kurz et al.*, 2009), or alternatively as recently as ∼31 Ma (*Glodny et al.*, 2005; *Nagel, T.J. and Herwartz, D. and Rexroth, S. and Münker, C. and Froitzheim, N. and Kurz, W.*, 2013). When combined with age constraints on subsequent (typically greenschist facies) deformation and metamorphism, these ages point to exhumation rates of up to ∼1–3 cm a^{-1} along the orogen (*Rubatto and Hermann*, 2001; *Glodny et al.*, 2005; *Berger and Bousquet*, 2008; *Radulescu et al.*, 2009).

The magnitude of subsequent thermal overprinting was greatest in the Central

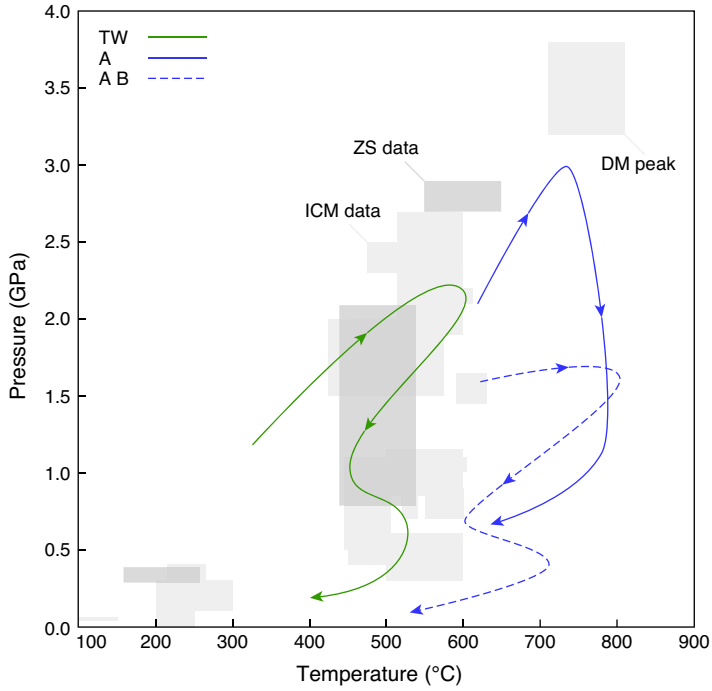

Figure 4.2: Selected P–T Paths from the Alps. Blue and green lines show simplified P–T paths from the Central Alps and Eastern Alps, respectively. TW=generalized path for Tauern Window after *Warren et al.* (2012a). A=general path for the Adula nappe in the vicinity of the Southern Steep Belt, from *Nagel* (2008). A B=generalized path for Adula nappe from *Beltrando et al.* (2010b). Grey boxes show constraints from the Western Alps, as in Figure 3.8. DM=Dora Maira, ICM=Internal Crystalline Massif, ZS=Zermatt Saas. See Figure 3.8 for data sources. Note varying degrees of late thermal overprinting, with highest temperatures achieved in the Central Alps.

Alps. *P–T* paths from the Western and Eastern Alps show isothermal decompression (in some cases minor cooling), locally followed by minor thermal overprinting at ∼500–600°C (*Rubatto and Hermann*, 2001; *Meffan-Main et al.*, 2004; *Le Bayon and Ballèvre*, 2006; *Kurz et al.*, 2009). The Adula nappe (Central Alps), in contrast, records hotter overprinting at ∼0.75 GPa/700°C (*Engi et al.*, 2004; *Rubatto et al.*, 2009), coupled with partial melting(*Rubatto et al.*, 2009) and local magmatism. Why such high temperatures were achieved in the Central Alps until ∼20 Ma (*Janots et al.*, 2009), almost 10 Myr after the ICMs of the Western Alps had cooled through ∼250°C (*Berger and Bousquet*, 2008), remains unclear.

4.3.3 Structure and Tectonic Evolution

Tectonic reconstructions indicate that the Western, Central, and Eastern Alps underwent broadly similar evolutions involving eastward to southward subduction of European (and oceanic) units beneath the Adriatic plate, followed by exhumation and subsequent bivergent deformation. There are, nonetheless, noteworthy contrasts in the crustal structure and apparent style of deformation between these regions. The main differences between the Western, Central, and Eastern Alps can be summarized as follows (see numbers in Figure 4.3).

1. The size and aspect ratios of the principal (U)HP units vary along the orogen. The (U)HP ICMs range in maximum thickness from ∼10 km (for the Monte

Figure 4.3 *(following page)*: Cross-sections through the Alpine Orogen. All cross-sections at 1:1 scale. (a–c) Interpreted crustal-scale cross-sections through (a) the Monte Rosa Massif (Western Alps), (b) the Central (Swiss) Alps, and (c) the Eastern Alps (TRANSALP) profile, modified from *Schmid et al.* (2004). (d) Alternative interpretation of the TRANSALP profile, after *Castellarin et al.* (2006). IL/PL=Insubric Line/Peri-Adriatic Line. Numbers refer to contrasting structural features listed in text. Black arrows show kinematics of Alpine deformation along certain shear zones. White arrows (a) show kinematics of normal-sense shear related to (U)HP exhumation. Colours as in Figure 4.1. In (d) the Penninic nappes are grouped into a single unit coloured blue. MR=Monte Rosa Nappe, T=Tambo/Suretta nappes (grouped here), A=Adula Nappe, TW=Tauern Window, Mo=Modereck Nappe. The Mo is a European-margin derived unit that drapes the lower-pressure European basement exposed in the TW, and locally records HP metamorphism. The Eclogite Zone is not shown on either (c) or (d), but is exposed on the southern flank of the TW structurally beneath the Mo.

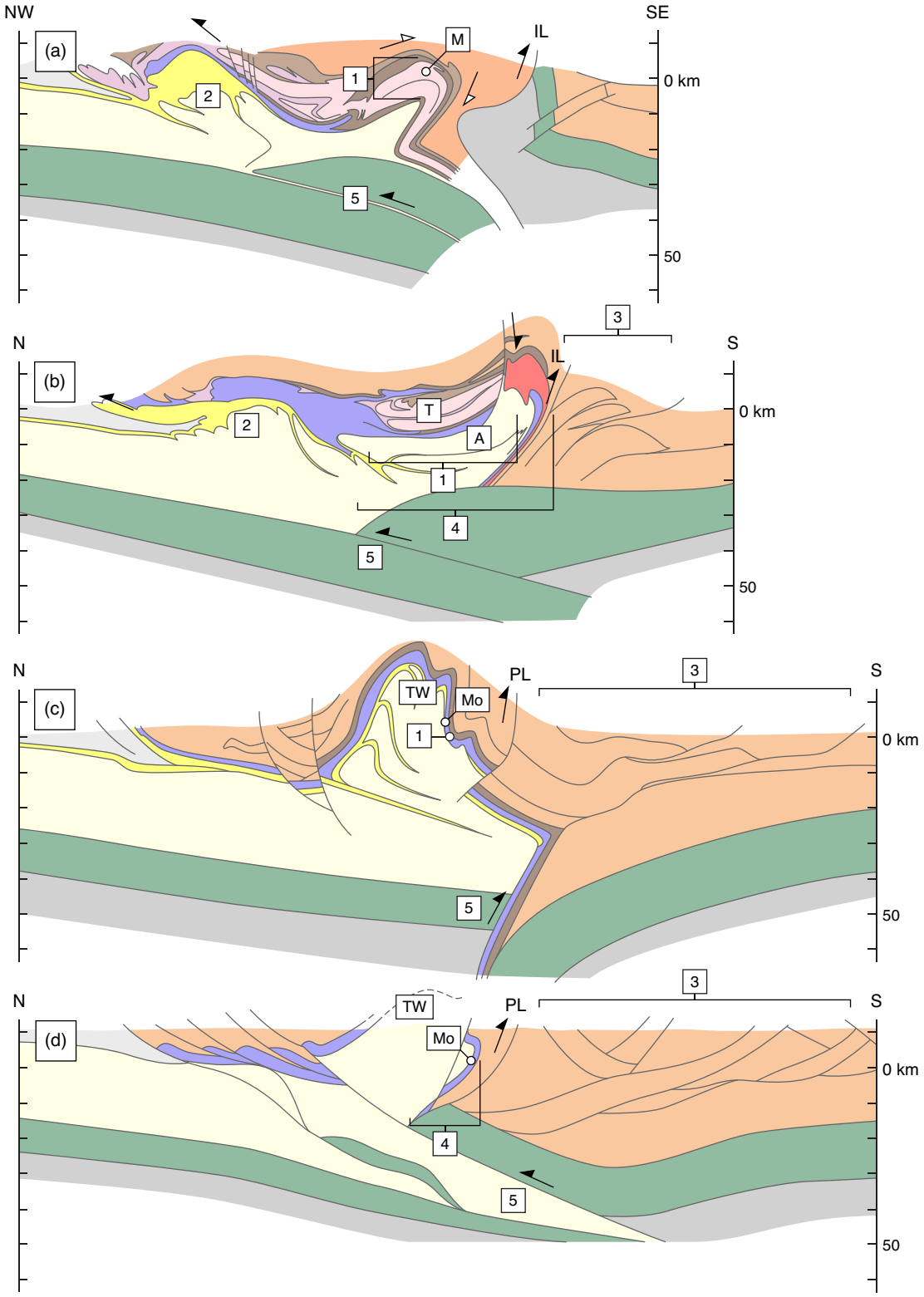
NW
SE
(a)
M
IL
1
2
5
0 km
50
N
S
(b)
3
IL
T
2
A
1
4
5
0 km
50
N
S
(c)
TW
Mo
PL
3
1
5
0 km
50
N
S
(d)
TW
PL
3
Mo
4
5
0 km
50

Rosa Massif) to nearly ∼20 km for the Gran Paradiso Massif. The Adula nappe of the Central Alps has a similar thickness (≲10 km), but a considerably larger aspect ratio (i.e., is longer/thinner). In the Eastern Alps, the Eclogite Zone and associated (U)HP Modereck nappes form extremely thin, (∼1–2 km) slivers exposed at the edges of the Tauern window.

2. Foreland-propagating deformation in the Western and Central Alps resulted in Miocene uplift of the External Crystalline Massifs. No equivalent massifs exist in the Eastern Alps, where uplift/exhumation remained concentrated in the axial region of the orogen.

3. The width of the (upper plate) retrowedge formed by shortening of the Adriatic plate varies from relatively narrow (≲25 km) in the Western Alps, to ∼50 and up to ∼100 km in the Central and Eastern Alps, respectively (*Schmid et al.*, 2004; *Rosenberg and Berger*, 2009). The apparently minor amount of upper plate shortening in the Western Alps may have resulted from the exhumed, and mechanically strong, Ivrea mantle located there acting as an orogenic 'backstop' (e.g., *Schmid et al.*, 2004; *Butler et al.*, 2011).

4. Similarly, the amount of retrotransport of the exhumed lower plate nappes 'onto' the upper plate varies from nil in the Western Alps, to up to ∼25 km in the Eastern Alps. Conversely, retrotransport in the Central Alps appears to have transported the Adula and surrounding nappes ∼50 km over the Adriatic plate. The magnitude of retrotransport of lower plate crust does not necessarily correlate with the apparent amount of upper-plate shortening, as shown in the Eastern Alps.

5. Contrasting styles of lower crustal deformation are apparent beneath the Western and Central Alps (*Rosenberg and Berger*, 2009). In the Western Alps, duplication of the European (and possibly Briançonnais?) lower crust is ascribed to detachment and proward thrusting. The lower crust of the Central Alps, in contrast, dips toward the orogen, and appears to have been separated from the Adriatic upper crust during its underthrusting beneath the Adula and related nappes. In the Eastern Alps, depending on the interpretation, the Adriatic

Moho either dips beneath the orogen (Fig. 4.3c), with no apparent deformation, or dips toward Adria (Fig. 4.3d), and appears to have undergone some ductile deformation.

The lithospheric/upper mantle structure beneath the Eastern Alps remains controversial owing to conflicting geophysical data and interpretations. Some have argued that the polarity of subduction changes from southward beneath the Central Alps to northward beneath the Eastern Alps, i.e., from subduction of European to Adriatic lithosphere (*Lippitsch et al.*, 2003). Others have concluded that the subduction polarity remains northward beneath the Eastern Alps (*Mitterbauer et al.*, 2011). The present models do not incorporate reversals of subduction polarity, although we admit that the process may be important for understanding some of the above differences, in particular the magnitude of late retroshortening in the Eastern Alps.

4.3.4 Contrasts in Plate Convergence Rate

The final difference addressed here, not readily apparent from the above observations, is that the arcuate form of the orogen probably resulted in considerably different orogen-normal convergence rates along the orogen during collision. Maximum north(northwestward) convergence rates reached $\sim$1.3 cm a^{-1} (*Handy et al.*, 2010) during subduction of the Briançonnais terrane and subsequent collision of the European margin. Beginning in the Miocene, motion of Adria became more eastward, and the convergence rate decreased to $\lesssim$0.5 cm a^{-1} (*Handy et al.*, 2010). Depending on the strike, the orogen-normal convergence rates during these periods may have been considerably lower, and some have even suggested that the Western Alps was subject to a transient period of divergent plate motion (*Malusà et al.*, 2011).

4.4 Model Design

Below we present a series of numerical models designed to explore variations on the basic model (Model S) presented in Part 1 of this study. Starting with a model that has been shown to 'work' for the Western Alps, the objective is to test variations on this model in order to gain insight into both the sensitivity of the model to key parameters, and variations in tectonic style along the Alpine Orogen.

Model	Difference from Model S
E1	Erosion rate, $E_s = 1.0$ cm a^{-1} ($E_s = 1.5$ cm a^{-1} in Model S)
E2	Erosion rate, $E_s = 2.0$ cm a^{-1}
V0.5	Convergence velocity, $V_r = 0.5$ cm a^{-1} ($V_r = 1.0$ cm a^{-1} in Model S)
V1.5	Convergence velocity, $V_r = 1.5$ cm a^{-1}
DV0.25	Convergence velocity, V_r = -0.25 cm a^{-1}
DV0.5	Convergence velocity, V_r = -0.5 cm a^{-1}
SMC	Smaller microcontinent/margin geometry
NMC	No microcontinent, different margin geometry
WR1	Retro UC $f = 0.005$
WR2	Retro UC $f = 0.5$, LC $f = 0.0005$

Table 4.1: Summary of sensitivity experiments. The models are listed in order of appearance in text, and described in terms their differences from Model S. See text for details. E_s= max. erosion rate for a slope of 45°, V_r=convergence rate, UC=upper crust, LC=lower crust, f=viscosity scaling factor.

The starting geometry and input parameters of the models are based on Model S, except where noted. The geometry corresponds roughly to the Mesozoic to Cenozoic paleogeography of the Alpine system (*Stampfli et al.*, 1998; *Rosenbaum and Lister*, 2005; *Handy et al.*, 2010), and comprises a retrocontinent (representing Adria) with an adjacent orogenic wedge (Austroalpine), an oceanic plate (Piemont-Liguria; ∼500 km wide), and a procontinent (Eurasia) comprising a microcontinent (Briançonnais; ∼175 km wide), a narrow rift basin (Valais 'Ocean'; ∼75 km wide) and a continental margin (European margin).

These are 'sensitivity' experiments that illustrate variations on Model S achieved by varying certain input parameters, including the model convergence velocity, crustal strength, and model starting geometry, among others (Table 4.1, Fig. 4.16). For some experiments, the models differ from Model S (parameter values in Table 3.1) in only a single parameter value (e.g., retrocontinent convergence velocity, V_R), whereas other experiments involve changes in multiple, but related parameters, in order to illustrate a certain style or behaviour. For most the cases we provide a summary of the results, rather than a detailed examination of individual models, as in Chapter 3.

4.5 Sensitivity Experiments

The complexity of the modeling approach makes testing and/or showing the effects of all possible parameters impractical. We have therefore chosen to present a subset of parameters, selected because they are subject to considerable geological uncertainty in a general sense, or because they provide direct insight into the causes of the differences along the Alpine Orogen noted above. The results of these experiments are presented below.

4.5.1 Erosion Rate

In Part 1 of this study, Model S was used to illustrate that exhumation of (U)HP crust in Alpine-type orogens can be accommodated mainly by relative extension, and does not require extremely fast erosion. However, the extent to which varying erosion rates affect the overall model orogenic evolution was not demonstrated.

To illustrate the effects of surface erosion on the model evolution, two additional experiments, exploring lower and higher reference erosion rates, are presented below. The reference surface erosion rate (E_s) is defined as erosion rate operating on a surface with a slope of 45°. In Model S, $E_s = 1.5$ cm a $^{-1}$, resulting in actual model erosion rates of up to ∼1.6 mm a^{-1}. The experiments shown below, models E1 and E2, have $E_s = 1$ and 2 cm a^{-1}, respectively. All other aspects and input parameters of models E1 and E2 are identical to Model S.

The evolution of models E1 and E2 is similar to Model S (Fig. 4.4). Each model involves an initial phase of microcontinent subduction (Phase 1), followed by exhumation of a buoyant (U)HP plume accommodated by thrusting and shallower extension of the prowedge (Phase 2), and finally a phase of bivergent deformation resulting in retrotransport/backfolding of the exhumed plume, and thrusting in the external procontinent foreland.

The overall patterns of erosion in models S, E1 and E2 are similar, with average erosion rates in equivalent regions (e.g., the top of the prowedge) typically within ±0.2–0.4 mm a^{-1} of those in Model S (Fig. 4.5). In Model E2, the maximum erosion rate only locally exceeds 1.6 mm a^{-1}, and is achieved in the vicinity of the backthrust, similar to Model S (Fig. 4.5b). The rate of erosion systematically affects the total width of the orogen, with lower erosion rates/less erosion resulting in external uplift of the procontinent margin somewhat further (∼25–50 km) into the procontinent

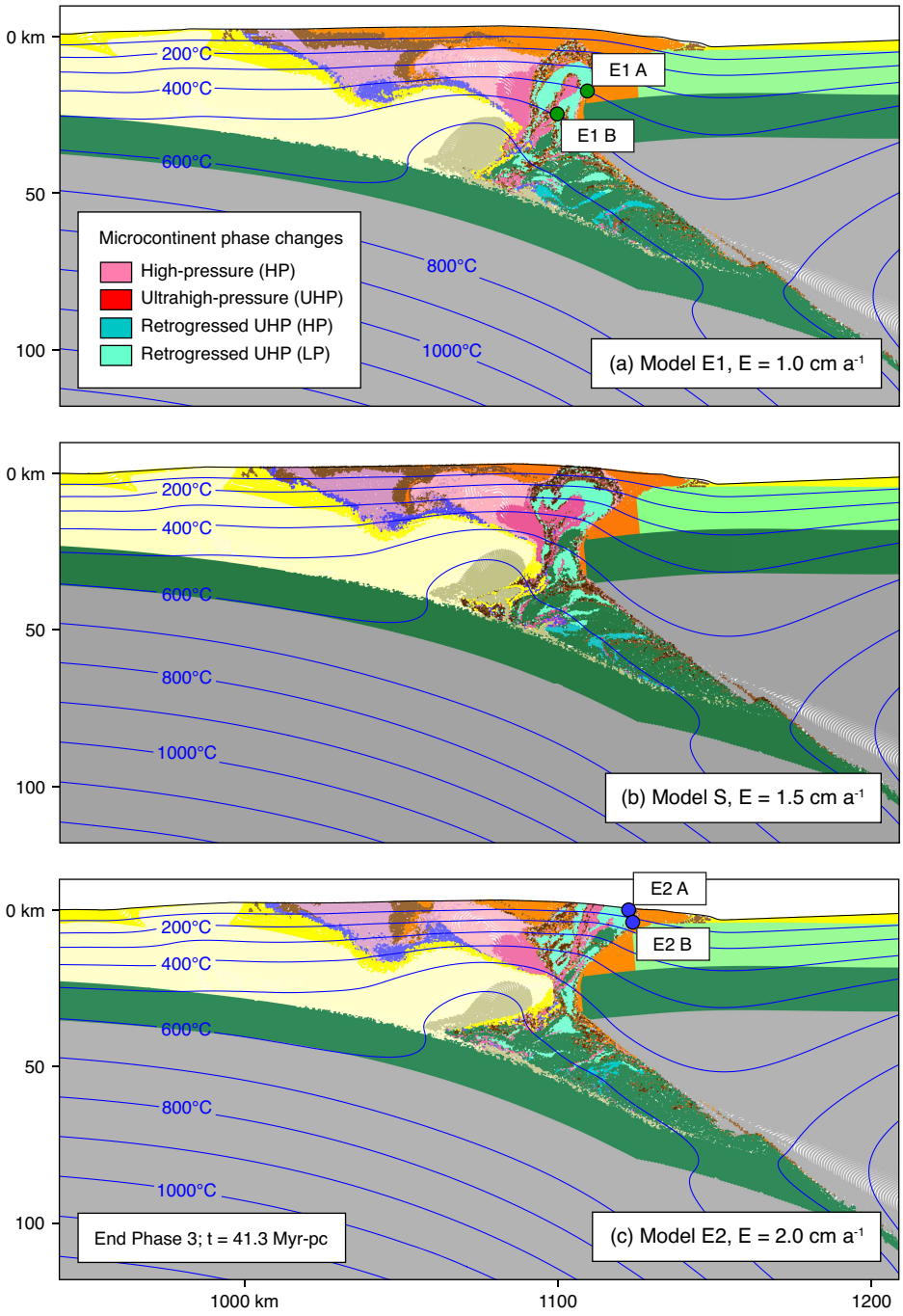

Figure 4.4: Comparison of models E1, E2, and S. All models shown at 41.3 Myr-pc, after the same amount of convergence used for comparison with the Western Alps in Part 1. (a) Model E1, with $E_s = 1.0$ cm a^{-1}. (b) Model S, with $E_s = 1.5$ cm a^{-1}. (c) Model E2, with $E_s = 2.0$ cm a^{-1}. E_s is the maximum surface erosion rate that would act on a slope of 45°. Actual model erosion rates are substantially lower (Fig. 4.5) Green and blue circles indicate positions of model P–T–t particles shown in Figures 4.7 and 4.8. To facilitate comparison, the initial particle positions are the same in each model.

foreland (Figs 4.4 and 4.5b,c). The position of the retrothrust and the width of the uplifted region at the rear of the plug, meanwhile, remain relatively unchanged.

Pressure-time (*P–t*) paths from models E1 and E2 (Figs 4.6, 4.7, and 4.8) show that the rate of surface erosion mainly affects the rate of trans-crustal exhumation (Phase 3), and has little impact on the rates of rapid (U)HP exhumation from the subduction channel (Phase 2). In models E1 and E2, as well as Model S, maximum exhumation rates reach ∼1 cm a^{-1} (Fig. 4.8), supporting our conclusion that rapid (U)HP rock exhumation in the models is primarily accommodated by localized extension and coeval thrusting, and not erosion. In general, higher erosion rates obviously contribute to faster exhumation; however, given that exhumation rates in the Alps averaged ∼0.2–0.5 mm a^{-1}, and perhaps locally approached ∼1.0 mm a^{-1} (*Schlunegger and Willett*, 1999; *Bernet et al.*, 2009), erosion on its own cannot account for rapid exhumation. Trans-crustal exhumation occurs at rates ranging from ∼0.3–$\lesssim$0.05 cm a^{-1}, with particles Model E2 on average exhuming at rates ∼0.1 cm a^{-1} faster than in Model E1 (Figs 4.5 and 4.8).

Individual *P–T–t* tracking particles from models E1 and E2 echo the trends described above (Figs 4.7 and 4.8). Equivalent tracking particles, i.e., particles from models E1 and E2 with the same starting positions, show nearly identical *P–T–t* histories prior to decompression to ∼1 GPa, roughly corresponding to the base of the crust (Fig 4.11). At this point the paths diverge, with the Model E1 particles exhuming more slowly than those in E2 (∼0.1 versus 0.3 cm a^{-1}; Figs 4.6 and 4.8b). In both models, the maximum trans-crustal exhumation rates exceed maximum erosion rates (Fig. 4.5), demonstrating some component of localized extension. Comparison of the particle *P–T* paths shows that the faster exhuming particles in Model E2 undergo less heat loss during the early stages of trans-crustal exhumation. The latter observation may result from the more rapid advection of hot (U)HP crust from the subduction channel through the crust in Model E2, and therefore less diffusional heat loss, when compared with Model E1. Although in some models more slowly exhuming particles may be subjected to greater heating owing to thermal relaxation of the orogen (see below), on the timescale of exhumation in Model E1 this effect appears to be minor.

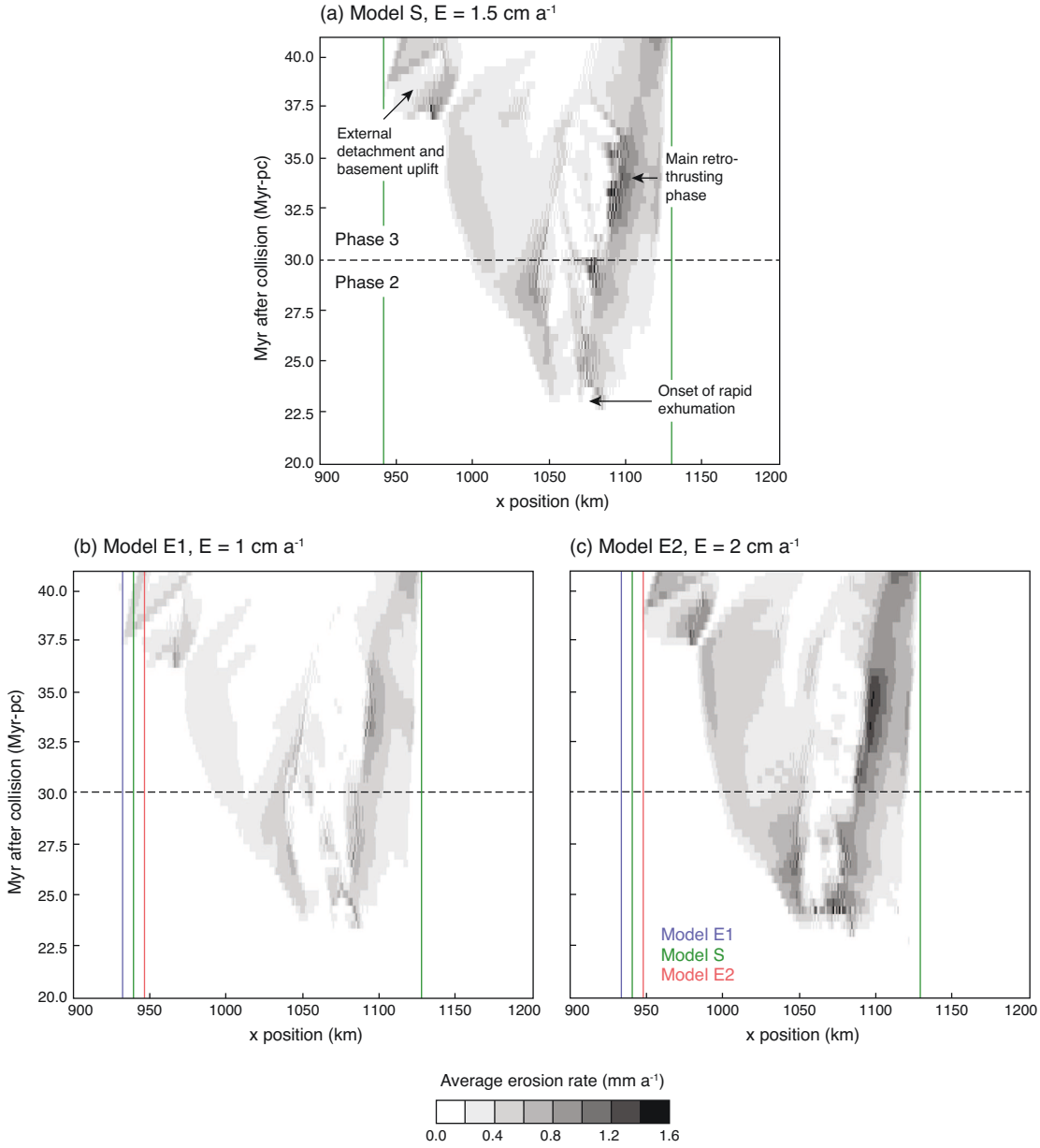

Figure 4.5: Comparison of average model erosion rates versus time, in Myr post-collision (Myr-pc). (a) Model S, with $E_s = 1.5$ cm a^{-1}. Labels illustrate correspondence between erosion rates and key phases of model evolution. Green lines indicate width of orogen. (b) Model E1, with $E_s = 1.0$ cm a^{-1}. Coloured lines represent width of orogen as shown in (c). (c) Model E2, with $E_s = 2.0$ cm a^{-1}.

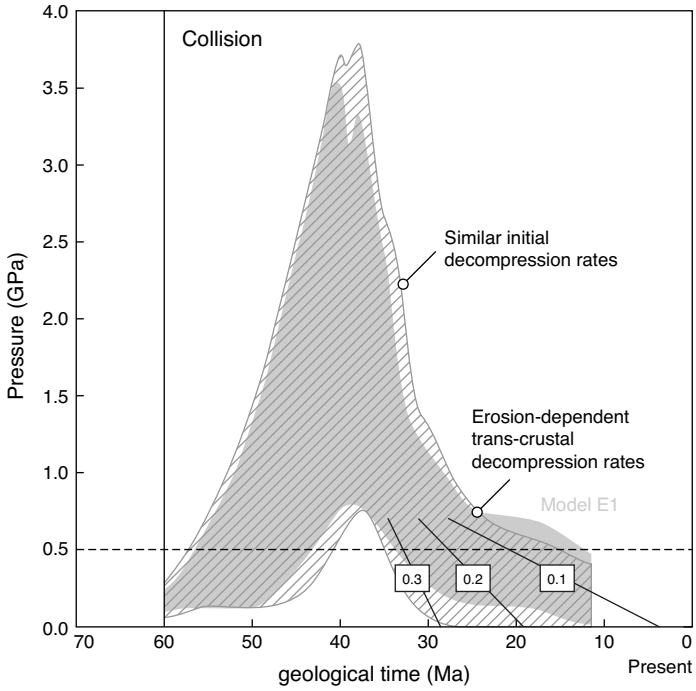

Figure 4.6: Effects of erosion on model P–t paths. The data are shown as envelopes encompassing all paths from particles exhumed to pressures below 0.5 GPa by the end of the model run. Model E1 data are shown in solid grey. Model E2 data are indicated by the diagonal line pattern. All data have been converted to geological time assuming the onset of microcontinent subduction 60 Ma (following the approach in Part 1). Black diagonal lines show slopes for exhumation rates of 0.1, 0.2, and 0.3 cm a^{-1}, calculated assuming an average crustal density of 3000 kg m^{-3}. The latter do not necessarily correspond to the actual model exhumation rates, owing to contrasting dynamical pressure histories for each particle, but provide an approximate illustration of the variations in the rate of trans-crustal exhumation.

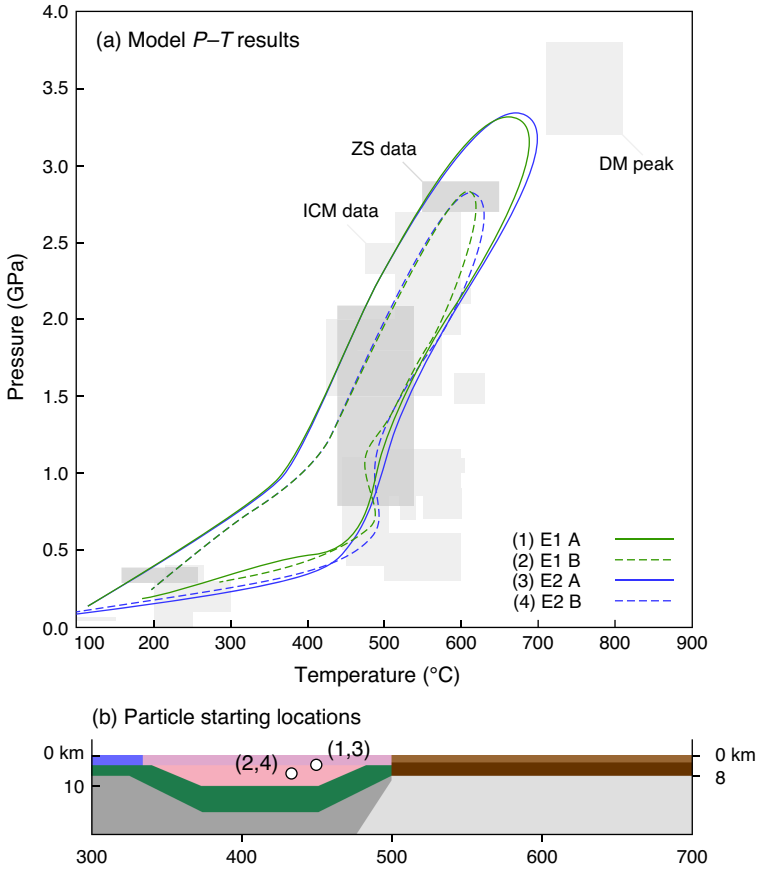

Figure 4.7: Model E1 and E2 P–T paths. (a) Comparison of selected P–T paths from models E1 and E2 with observations from the Western Alps. DM=Dora Maira, ICM=Internal Crystalline Massif, ZS=Zermatt Saas. See Figure 3.8 for data sources. Two sets of particles are shown (A and B) for each model, each representing a single starting position within the microcontinent crust. (b) Starting positions for particles A and B. Numbers correspond to tracking particles shown in (a).

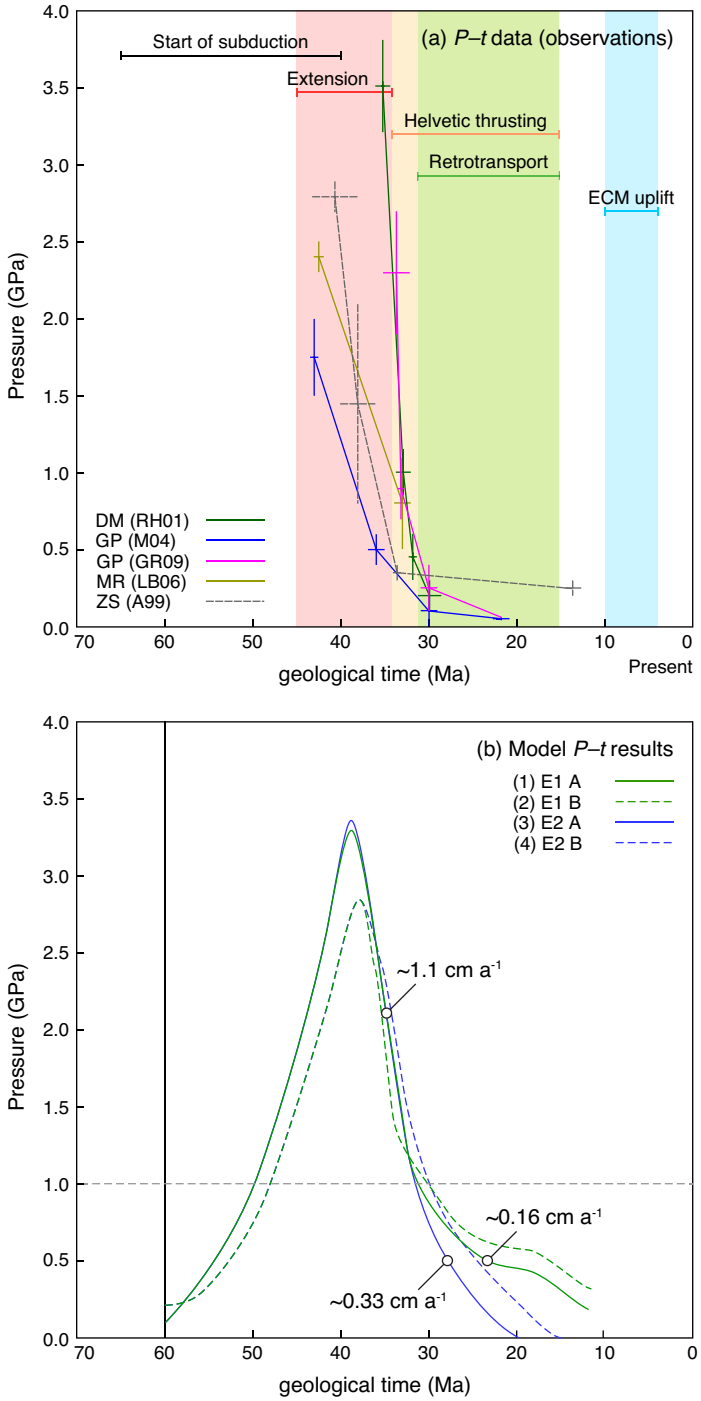

Figure 4.8: Model E1 and E2 P–t paths. (a) Representative P–t paths and tectonic stages from the Western Alps. See Figure 3.8 for data sources. (b) Comparison of selected P–t paths from models E1 and E2. Dashed horizontal line shows approximate pressure (1 GPa) at base of orogenic crust. Quoted rates are exhumation rates for particles E1 A and E2 A, averaged over the interval from peak pressures to 1 GPa, and from 1 GPa to their final depth/pressure. Note the identical initial exhumation rate of ∼1 cm a^{-1} from (U)HP conditions to the base the crust, followed by diverging trans-crustal exhumation corresponding to the model erosion rate.

4.5.2 Convergence Rate

The rate of subduction, driven largely by the plate convergence velocity, strongly affects the rate and style of continental subduction and exhumation (*Warren et al.*, 2008a). Model S (Chapter 3) had a retrocontinent convergence velocity (V_r) of 1 cm a^{-1} during collision (boundary condition velocity of -1 cm a^{-1}; the sign corresponding to the model coordinate system), which was generally successful in reproducing the overall timing of Western Alpine tectonic events. However, as noted above orogen-normal convergence rates likely varied along the Alpine Orogen. Models V0.5 and V1.5 have V_r = 0.5 and 1.5 cm a^{-1}, respectively, during the collision phase of the models, compared with V_r = 1.0 cm a^{-1} in Model S, to illustrate the effect of lower and higher convergence rates.

The experiments show that the rate of convergence exerts a strong control on the amount of microcontinent crust subducted to (U)HP conditions. In Model V0.5 (Fig. 4.9a), the leading edge of the microcontinent nearly reaches UHP conditions before detaching and commencing buoyant exhumation by 34 Myr-pc. The microcontinent crust exhumes in two rapid pulses, the first exhuming the most deeply buried (outermost) microcontinent crust, and the second the trailing edge of the microcontinent, both of which have exhumed to lower crustal depths by 54 Myr-pc. Retrotransport and trans-crustal exhumation of the plume begins at 61 Myr-pc, as the leading edge of the procontinent margin underthrusts the prowedge (Fig. 4.9b). Exposure of the HP crust occurs by 65 Myr-pc . The final geometry of the model (Fig. 4.9c) is reminiscent of Model S, with the exception that the plume comprises primarily HP and lower pressure crust, rather than UHP crust.

In Model V1.5 (Fig. 4.10), the microcontinent crust remains more strongly coupled to the subducting slab, and consequently both the amount of microcontinent crust that reaches UHP conditions, and the maximum depth of subduction, are greater than in models V0.5 and S. The result (Fig. 4.10a) is that exhumation of the (U)HP plume commences after the model has undergone a greater amount of plate convergence than in those models, with the plume reaching the lower crust by 25 Myr-pc, overlapping in time with deep underthrusting of the procontinent margin (Fig. 4.10b). Retrotransport and trans-crustal exhumation of the (U)HP plume commence immediately after, with the plume reaching the shallow crust by

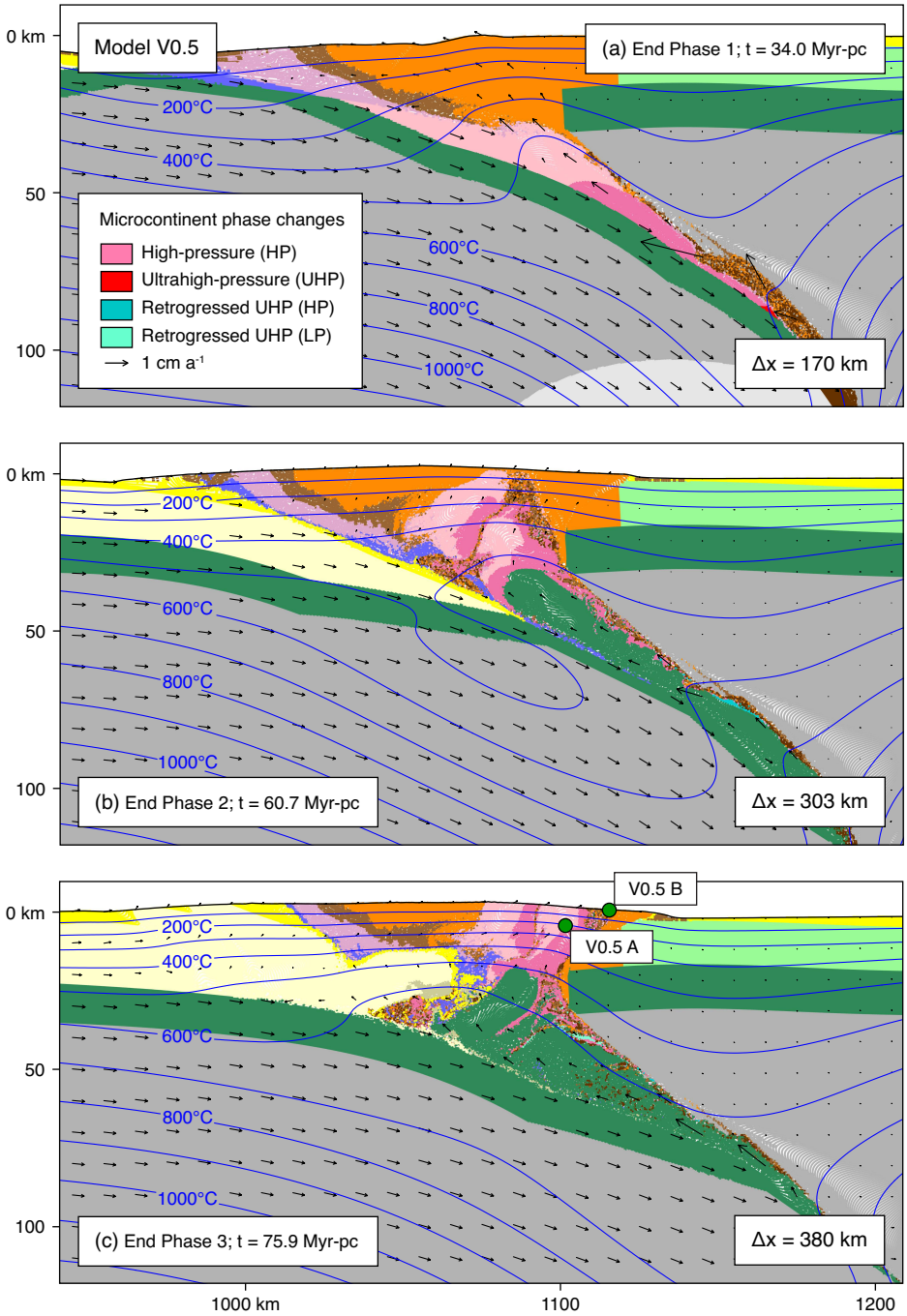

Figure 4.9: Results of Model V0.5. (a–c) Material colours and isotherms (blue lines) for model times corresponding to the end of each phase. Δx refers to amount of convergence following microcontinent collision. Green circles indicate positions of model P–T–t particles shown in Figures 4.11 and 4.12. Velocities shown in stationary retrolithosphere reference frame.

28 Myr-pc (Fig. 4.10c).

Comparison of representative P–T and P–t paths from models V0.5, V1.5, and S (Figs 4.11 and 4.12) reveals systematic variations in both the maximum P–T conditions as well as the degree of heat loss during decompression. Model V1.5 particles achieve the highest P–T conditions ($\sim$3.6 GPa/725°), but experience greater cooling during decompression. Minor late reheating of some particles is the result of their stalling in the crust (Fig 4.11a). Model V0.5 particles, in contrast, achieve lower P–T conditions ($\sim$2.6 GPa/625°), but undergo near isothermal decompression to crustal depths (Fig 4.11a). The observed relationship between convergence rate and the thermal evolution of the (U)HP plume can be explained by thermal relaxation of the thickened orogenic crust, with the slower Model V0.5 achieving higher temperatures than V1.5 after similar amounts of convergence (compare isotherms in Figures 4.9 and 4.10).

P–t paths for the same particles show that despite affecting the rates of burial and trans-crustal exhumation, the rate of initial rapid exhumation is relatively insensitive to the convergence rate (Fig 4.12b). Each model produces initial exhumation rates of $\sim$1 cm a^{-1}, followed by varying rates of trans-crustal exhumation. Models V1.5 and S achieve (U)HP metamorphism from $\sim$45–35 Ma (geological time), within the timespan suggested by observational constraints from the Western Alps. Corresponding trans-crustal exhumation rates for models V1.5 and S are $\sim$0.44 and $\sim$0.23 cm a^{-1}, respectively, the former closer to observational constraints from the Western Alps than Model S. Model V0.5, in contrast, achieves (U)HP metamorphism too late, and subsequent trans-crustal exhumation proceeds so slowly, at $\sim$0.07 cm a^{-1}, that if applied to the Western Alps, the (U)HP rocks there would not exhume for another $\sim$10–20 Myr. That the models produce similar initial exhumation rates indicates that exhumation is driven by buoyancy, rather than tectonic forces. In theory, buoyant exhumation rates should be greater for models with lower convergence rates because the subducting slab exerts less downward traction on the (U)HP plume. However, the models also produce dramatically different amounts of (U)HP crust, and it appears that the larger buoyancy force associated with a larger plume, in particular in Model V1.5, counteracts the effect of increased slab traction in that model.

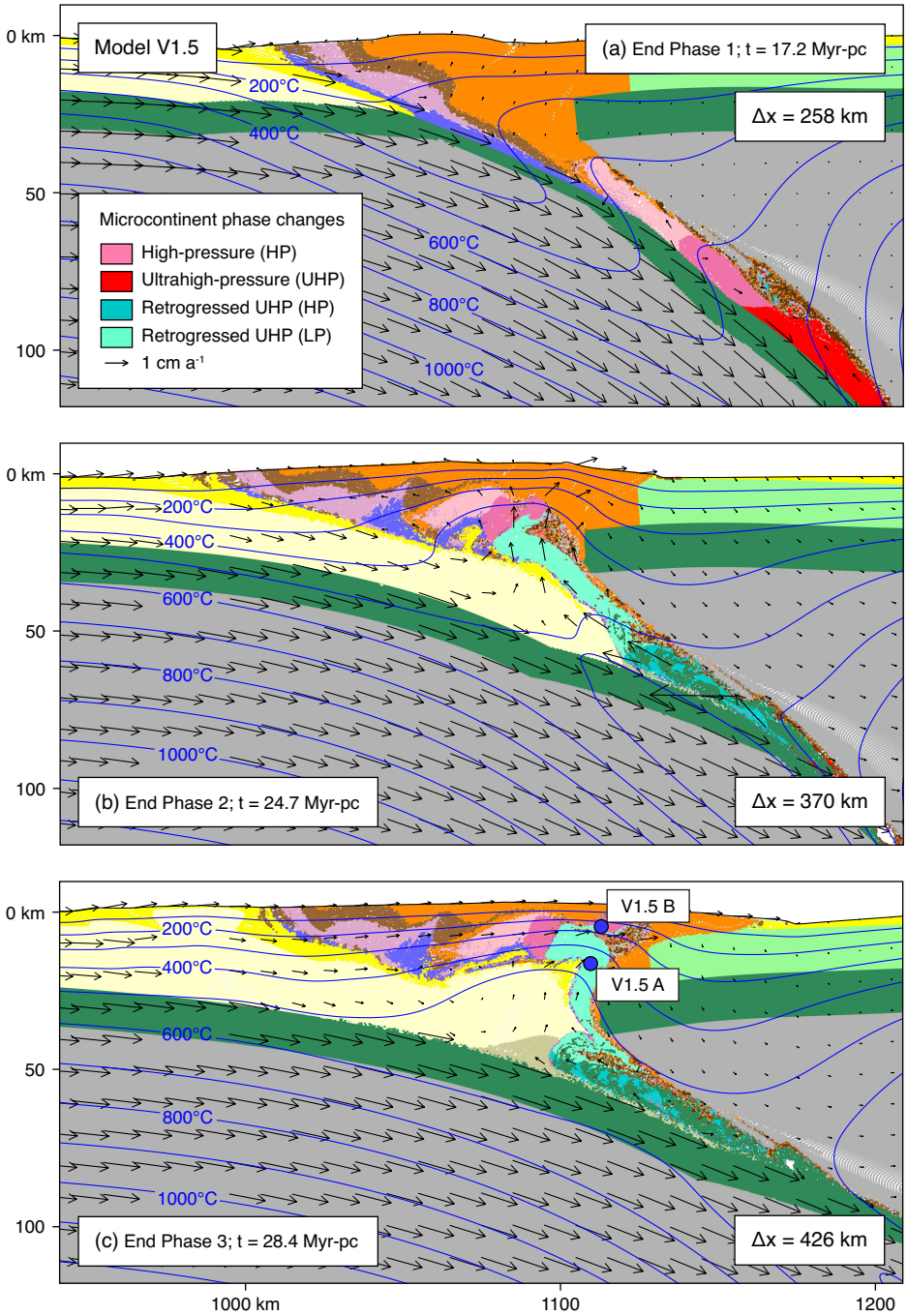

Figure 4.10: Results of Model V1.5. (a–c) Material colours and isotherms (blue lines) for model times corresponding to the end of each phase. Δx refers to amount of convergence following microcontinent collision. Blue circles indicate positions of model P–T–t particles shown in Figures 4.11 and 4.12. Velocities shown in stationary retrolithosphere reference frame.

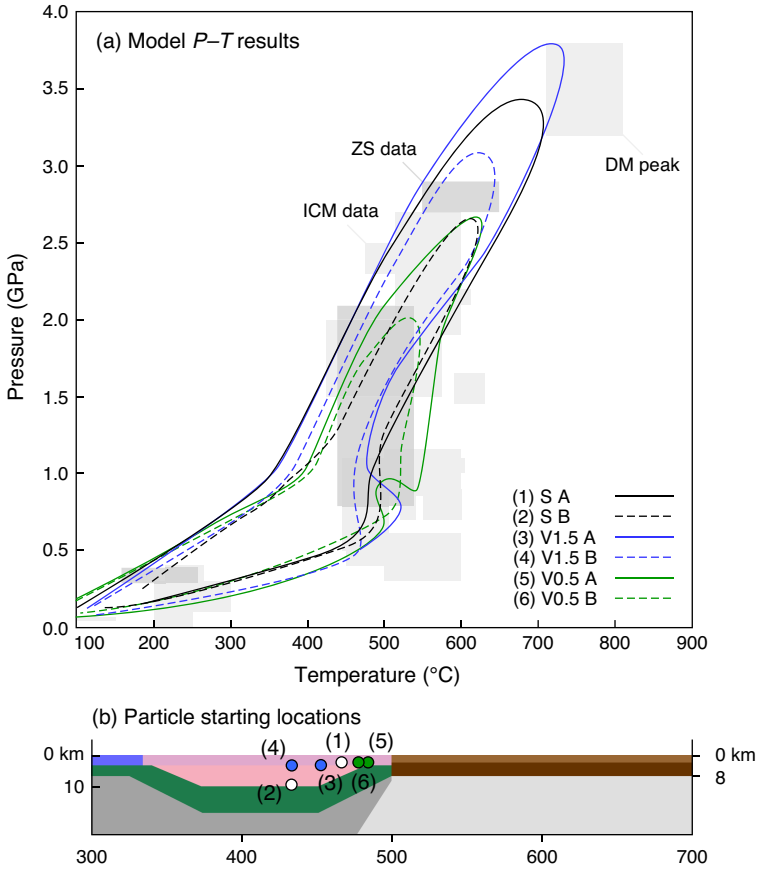

Figure 4.11: Model V0.5 and V1.5 P–T paths. (a) Comparison of selected P–T paths from models V0.5 and V1.5 with observations from the Western Alps. Selected P–T paths from Model S shown for comparison. DM=Dora Maira, ICM=Internal Crystalline Massif, ZS=Zermatt Saas. See Figure 3.8 for data sources. (b) Starting positions for tracked particles. Numbers correspond to P–T paths in (a).

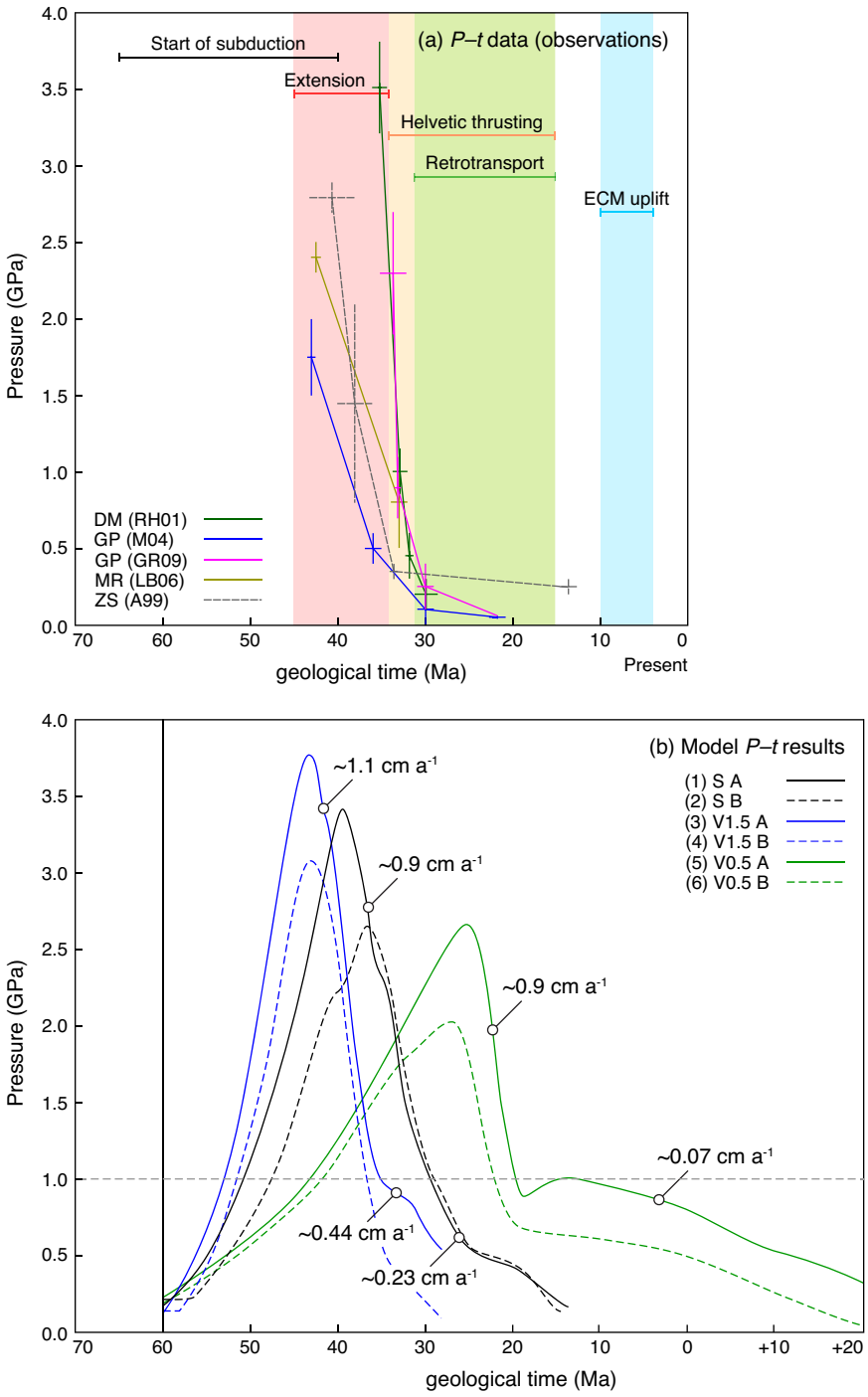

Figure 4.12: Model V0.5 and V1.5 P–t paths. (a) Representative P–t paths and tectonic stages from the Western Alps. See Figure 3.8 for data sources. (b) Comparison of selected P–t paths from models V0.5, V1.5, and S. Note the similar initial exhumation rates despite widely varying rates of burial and trans-crustal exhumation. Dashed horizontal line shows approximate pressure (1 GPa) at base of orogenic crust. Quoted rates are exhumation rates for particles S A, V1.5 A, and V0.5 A, averaged over the interval from peak pressures to 1 GPa, and from 1 GPa to their final depth/pressure.

4.5.3 Plate Divergence

As noted in Part 1, it is generally agreed that (U)HP rocks in the Western Alps were exhumed by extension, manifested in top-E, normal-sense shear zones exposed above the ICMs. The driving force of this extension, however, remains debated. Some have suggested that these shear zones represent localized, syn-orogenic extension during overall shortening (driven by subduction), as illustrated by Model S and variants presented above. Others have suggested that these shear zones formed during absolute (i.e., lithosphere-scale) extension, owing either to rollback of the subducting slab, or to a transient phase of plate divergence. To fully assess the applicability of these concepts to the Alps is beyond the scope of this work. We however feel it is worthwhile exploring the basic consequences of divergent plate motions on the models presented here. Models DV0.25 and DV0.5 (not shown) test the effects of divergent plate motions by switching the convergence velocity V_r from 1 cm a^{-1} to -0.25 cm a^{-1}, and -0.5 cm a^{-1} (negative velocities produce rightward motion in the present reference frame), respectively. The divergent plate velocities were applied to Model S at the time of maximum microcontinent subduction, immediately prior to the onset of rapid exhumation. Because the structural evolution of models DV0.25 and DV0.5 is fundamentally similar we describe the results of Model DV0.25, and note where Model DV0.5 differs.

Model DV0.25 begins at 21 Myr-pc, with microcontinent crust at (U)HP conditions in the subduction channel (Fig. 4.13a). The procontinent margin, meanwhile, has just reached the toe of the prowedge, but has not begun to underthrust. During the initial stages of the model the procontinent and retrocontinent lithospheres remain coupled, resulting in only minor net divergence (Fig. C.1a). Minor exhumation of the (U)HP oceanic and microcontinent crust occurs during this phase, driven by buoyancy, resulting in minor growth of the prowedge. At deeper levels, the oceanic slab undergoes slow necking, but remains attached to the procontinent lithosphere. At 36 Myr-pc the subducted oceanic slab detaches (Fig. C.1b), the two continents decouple, and plate divergence commences. A small amount of (U)HP microcontinent crust exhumes upward along the subduction channel, overtaking the underlying slab, which is also, in this reference frame, ascending 'backward' up the subduction zone (Fig. 4.13b), although exhumation rates are substantially lower than in Model

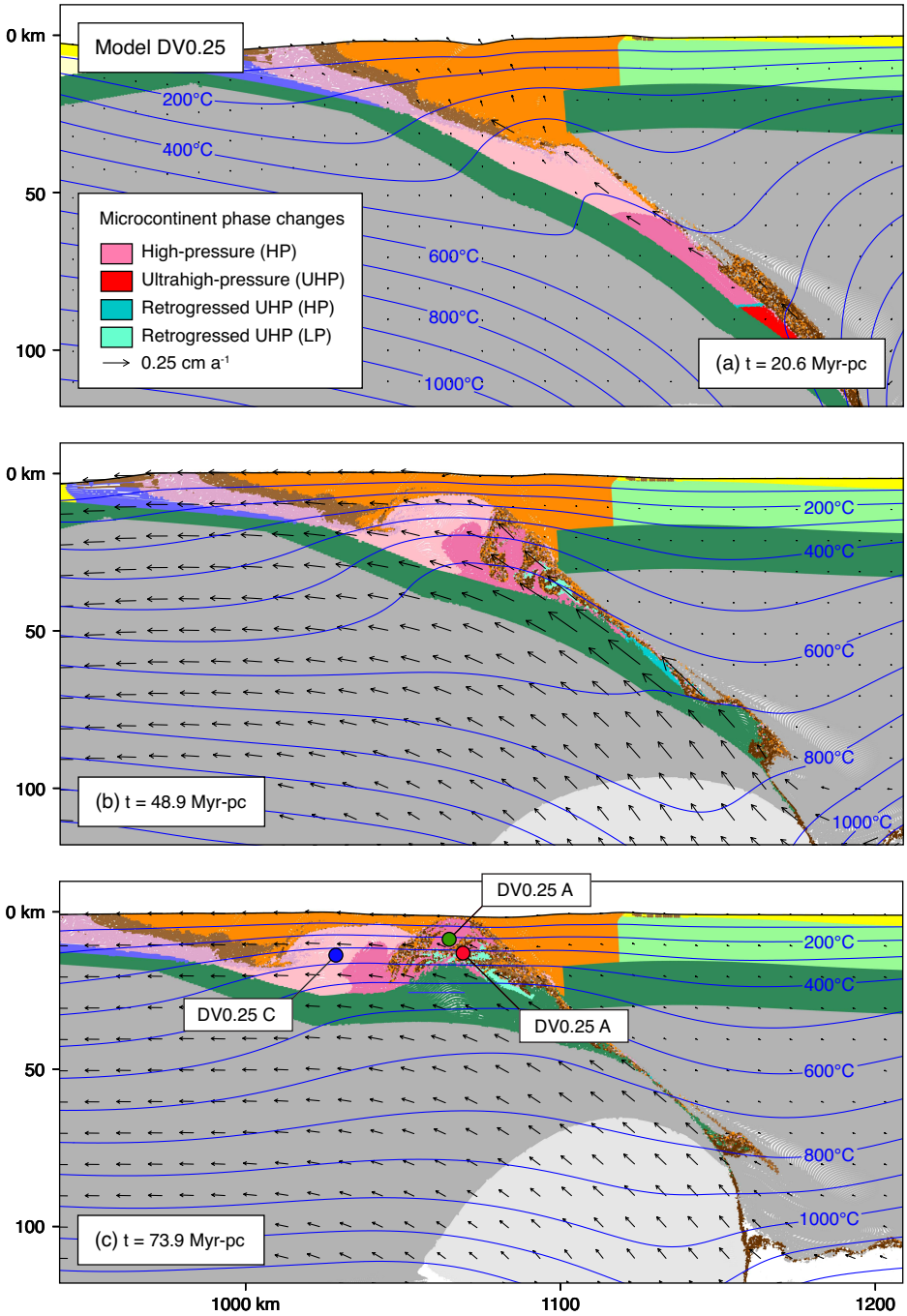

Figure 4.13: Results of Model DV0.25. (a–c) Material colours and isotherms (blue lines) for model times corresponding to phases discussed in text. Divergence at 10.25 cm a^{-1} starts 19 Myr-pc, following convergence at 1 cm a^{-1}. For consistency with other figures, the model is shown in the 'stationary retrocontinent' reference frame. Coloured circles indicate positions of model P–T–t particles shown in Figures 4.14 and 4.15.

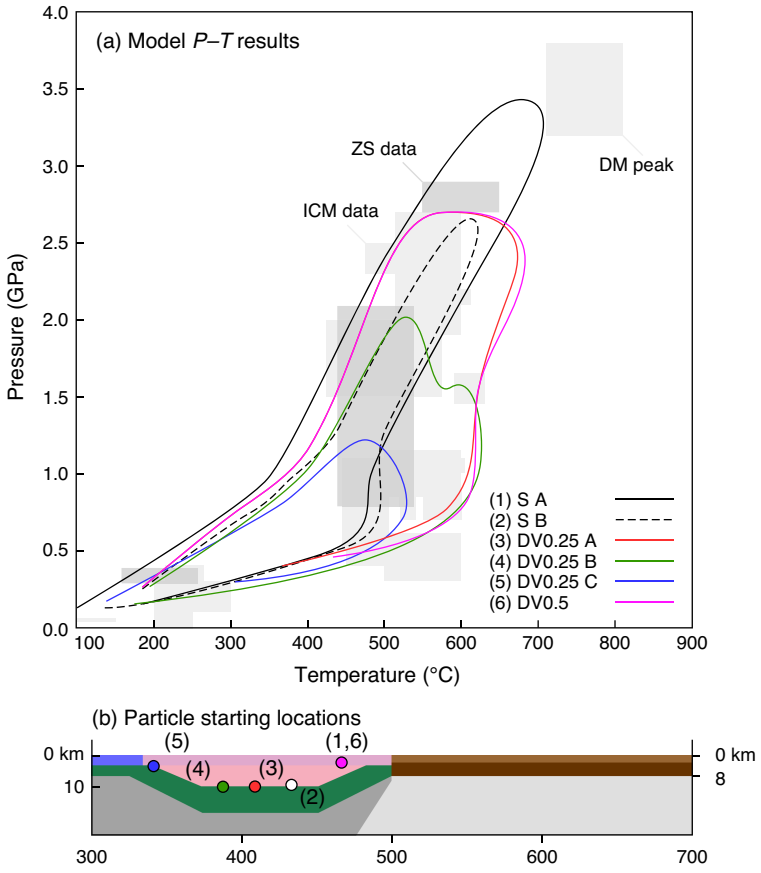

Figure 4.14: Model DV0.25 and DV0.5 P–T paths. Selected P–T paths from Model S shown for comparison. DM=Dora Maira, ICM=Internal Crystalline Massif, ZS=Zermatt Saas. See Figure 3.8 for data sources. (b) Starting positions for tracked particles. Numbers correspond to P–T paths in (a).

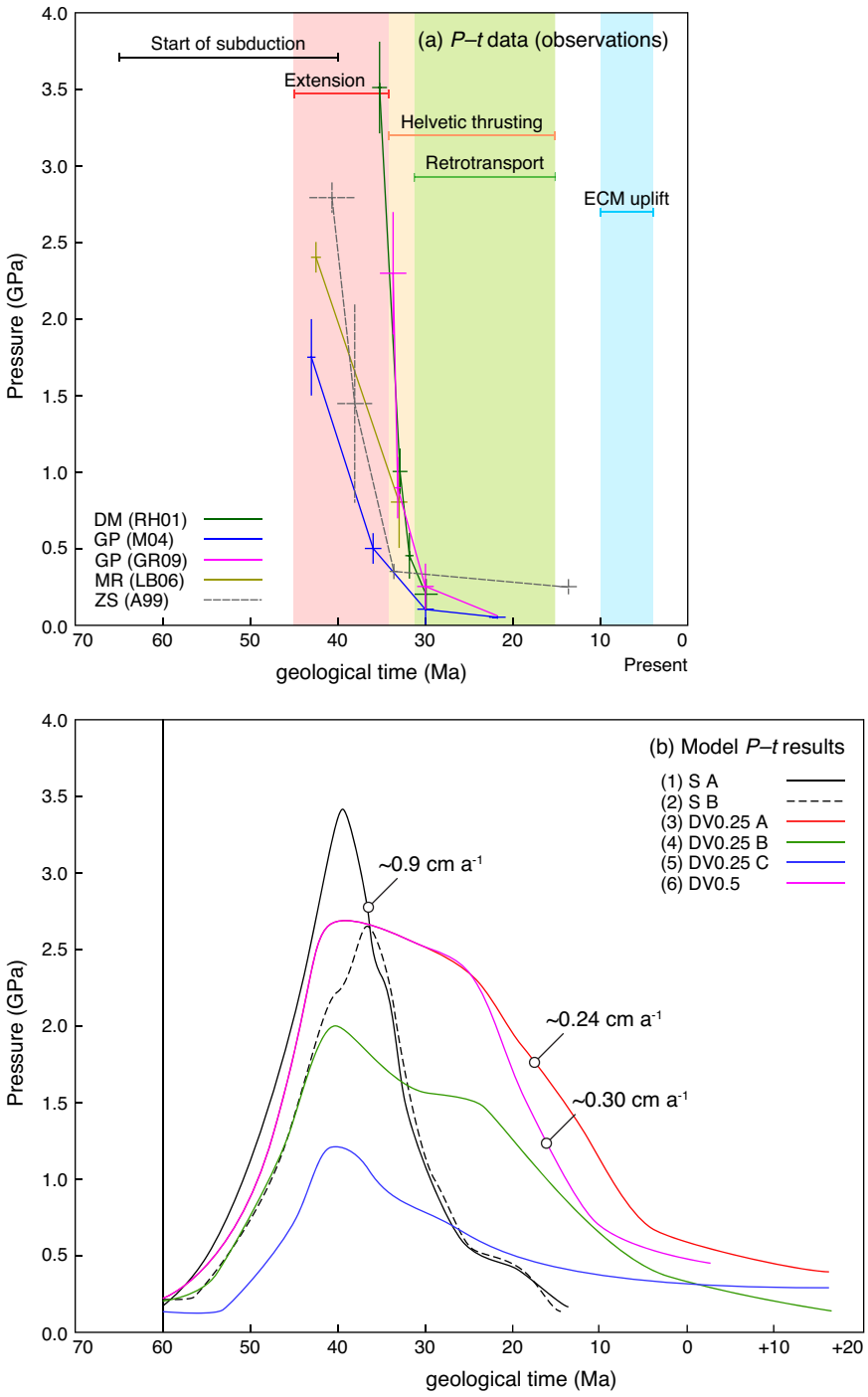

Figure 4.15: Model DV0.25 and DV0.5 P–t paths. (a) Representative P–t paths and tectonic stages from the Western Alps. See Figure 3.8 for data sources. (b) Comparison of selected P–t paths from models DV0.25, DV0.5, and S. Quoted exhumation rate for particle S A is averaged over the interval from peak pressures to 1 GPa. Quoted rates for particles DV0.25 A and DV0.5 are for the maximum rate interval corresponding to the onset of extension (in geological time at ∼23 Ma. Average rates from peak pressure are considerably lower owing to the ∼20 Myr stalling prior to slab detachment and extension.

S (Fig. 4.15b). Similar to Model S, exhumation of the microcontinent is accommodated by normal-sense shear and vertical thinning within the prowedge. However, whereas extension in Model S is accommodated by shortening at the front of the prowedge, in Model DV0.25 the entire prowedge is extended, and the wedge is not thrust over the procontinent margin during exhumation. Further divergence leads to buoyant rebound of procontinent lithosphere and weakened lower crust, which ascend beneath the (U)HP plume, driving it upward to shallow crustal depths, by 74 Myr-pc. By this time the orogen has undergone considerable extension and consequent subsidence, and a large portion of the prowedge is submarine (Fig. 4.13c). Erosion rates during the early stages of Model DV0.25 (not shown) remain low, reaching maximum rates of $\lesssim$0.4 mm a^{-1}. Model DV0.5 is essentially identical to Model DV0.25, but once divergence commences (following breakoff) it evolves twice as fast.

P–T and *P–t* paths for Models DV0.25 and DV0.5 differ considerably from those of Model S (Figs 4.14 and 4.15). Whereas decompression from (U)HP conditions in Model S is accompanied by minor cooling, with some paths nearly isothermal, particles from Model DV0.25 show considerable heating. The delayed onset of exhumation for the most deeply buried microcontinent crust results in isobaric heating of the (U)HP crust from ∼500 to 650°C (Fig. 4.14). Subsequent exhumation is near-isothermal to ∼1 GPa/600°C. Similar heating is experienced by equivalent particles from Model DV0.5. Particles that achieve lower peak pressures, corresponding to less burial, undergo a similar magnitude of heating during decompression. The heating in models DV0.25 and DV0.5 results from the considerably higher geothermal gradient when compared with Model S, and can be interpreted as the result of thermal relaxation and absence of underthrusting of cool procontinent lithosphere.

None of the recorded particles from either divergent model exhume within the timespan required by observational constraints from the Western Alps (Fig. 4.15). *P–t* paths for particles from Model DV0.25 show an initial period of extremely slow decompression, representing the very minor amount of exhumation that precedes net extension. The onset of extension corresponds to an increase in exhumation rates to ∼0.24 cm a^{-1}, whereas the equivalent particle from Model DV0.5 achieves a maximum exhumation rate of ∼0.3 cm a^{-1}. Even though in both divergent models

the (U)HP plume appears to outpace ascent of the underlying slab, the observed exhumation rates are close to what one would expect for exhumation driven purely by extension. The fact that buoyancy plays a comparatively minor role in exhumation in these models, when contrasted with those above, can be attributed to the small amount of crust that reaches (U)HP conditions and hence lower buoyancy of the plume. In all of the prior models, continued subduction of crust to (U)HP conditions following the onset of exhumation effectively 'replenishes' the buoyant push at the base of the plume. In the divergent models, subduction ceases, and no further buoyant push is provided.

4.5.4 Microcontinent Size and Margin Geometry

The propensity for buoyancy-driven flow of (U)HP crust from the subduction conduit/channel depends critically on the volume of subducted crust. Not only must the buoyancy of the crust be sufficient to overcome the downward traction exerted by the slab, the exhuming plume must also have sufficient buoyant push from below to penetrate the overlying crust. The amount of crust that reaches the conduit is in part determined by the thickness and length of the 'detachable' microcontinent crust, which in Model S is derived from the 12 km of upper/middle crust with a scaled wet quartzite flow law (WQ $\times$ 3), but also later includes the 10 km-thick, dry Maryland diabase based lower crust (DMD $\times$ 0.1). The geometry of the model microcontinent and margin in the models presented in Chapter 3 was based on the pre-orogenic paleogeography of the Western Alps, and was intended to produce a volume of exhumed (U)HP microcontinent crust similar to that exposed in the ICMs. However, most paleogeographic reconstructions show that the width of the Briançonnais terrane diminished toward the northwest, eventually disappearing in the vicinity of the Eastern Alps.

To illustrate the impact of along-strike variations in the width of the Briançonnais microcontinent we conducted two additional experiments in which the geometry of the model 'rifted margin' varies from that in Model S (Fig. 4.16). Model SMC (small microcontinent) is like Model S, but has a narrower microcontinent (100 km wide compared with 175 km), and a more tapered continental margin (200 km wide tapered region versus 50 km in Model S). The additional tapering was implemented

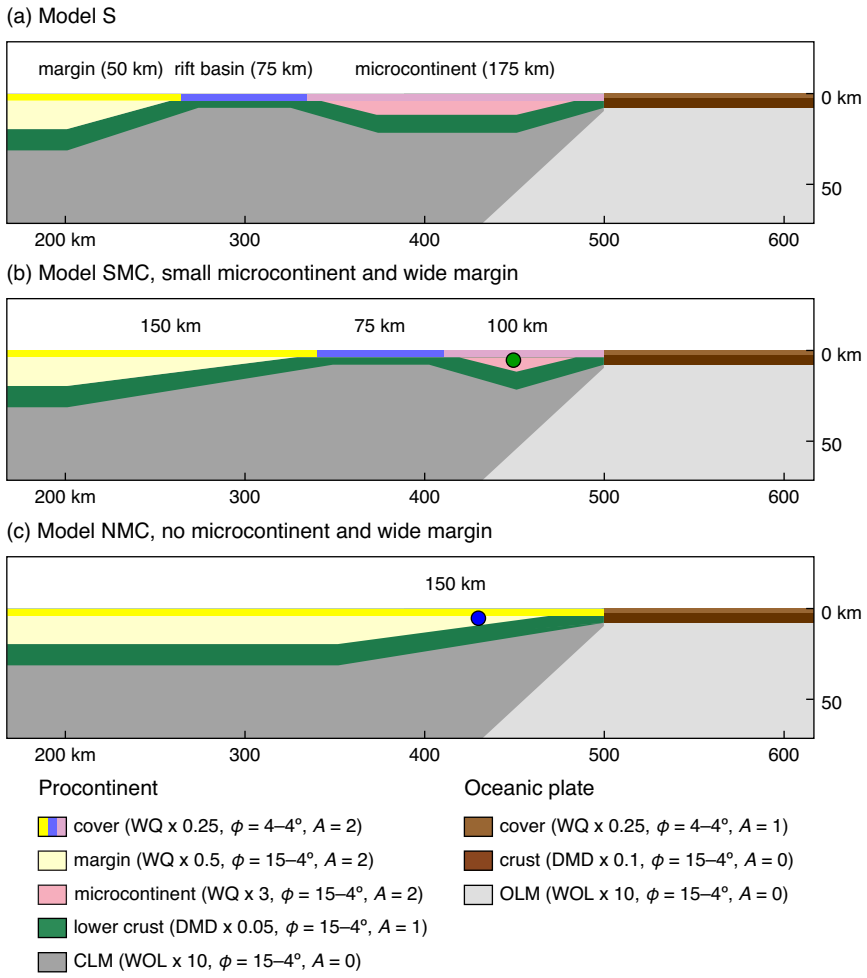

Figure 4.16: Variations on Model S geometry. (a) Model S starting geometry of procontinent margin, rift basin, and micrcontinent. (b) Starting geometry of 'SMC' models with smaller microcontinent and wider procontinent margin. (c). Starting geometry of 'NMC' models with no microcontinent and a wide procontinent margin. The geometry of the retrocontinent does not vary among models. Coloured circles in (b) and (c) show positions of model P–T–t particles shown in Figures 4.19 and 4.20. WQ=wet quartzite, DMD=dry Maryland diabase, WOL=wet olivine. ϕ=range of effective angle of internal friction (ϕ_{eff}) owing to strain-softening; A=radiogenic heat production (μWm^{-3}; A_R in text). CLM=continental lithospheric mantle, OLM=oceanic lithospheric mantle, SLM=sublithospheric mantle. Material properties are same as in Model S. For details see Figure 3.3.

to facilitate subduction, ideally to (U)HP conditions, similar in theory to subduction of the European margin in the Central and Eastern Alps. Model NMC (no microcontinent) is like model SMC, but has no microcontinent. In both variants, the leading edge of the microcontinent/margin occupies the same position, i.e., the oceanic plate remains the same size. To facilitate comparison, the material and thermal parameters are identical to those used in Model S.

The models are the same as Model S up to the point of subduction. Model SMC (Fig. 4.17) begins with subduction of the small microcontinent beneath the accretionary wedge. The relatively thin, and consequently cooler (than Model S), microcontinent remains coupled to the slab until 27 Myr-pc, at which point the entire microcontinent has reached (U)HP conditions at the very bottom of the channel, defined by the depth of the retrocontinent lithospheric mantle. Rapid exhumation begins 29 Myr-pc, with the ascent of a thin (∼5–10 km thick) plume of mixed (U)HP oceanic and microcontinent crust. Similar to Model S, emplacement of the plume into the prowedge at 36 Myr-pc (Fig. 4.17b) is accommodated by localized extension and coeval shortening. However, in contrast to Model S, overall displacement of the prowedge in Model SMC involves only minor uplift, owing to the considerably smaller (U)HP plume. As in Model S, subsequent underthrusting of the procontinent margin crust leads to retrotransport/backfolding of the thin (U)HP plume. The procontinent margin then detaches, forming an uplifted, external massif (Fig. 4.17c).

Model NMC (Fig. 4.18) begins with subduction of the thinned procontinent margin beneath the accretionary wedge. Similar to Model S, a small repository of (U)HP oceanic crust, formed during earlier oceanic subduction, remains stored at the base of the subduction channel, but has not yet exhumed. By 17 Myr-pc, the leading edge of the margin has reached near-UHP blueschist facies metamorphic conditions (Figs 4.18a and 4.19). At 19 Myr-pc, the tip of the margin reaches the repository of (U)HP oceanic crust. The latter ascends rapidly upward, preventing the relatively weak (WQ, $f = 1$) margin crust from subducting further. The margin shortens in response to the clogging of the channel, starting at depth and migrating rapidly proward, resulting in external detachment of the margin in the foreland (Fig. 4.18b). Further convergence leads mainly to continued proward accretion of the weak margin, and to proward tunneling of lower crust, leading to the formation of a broad

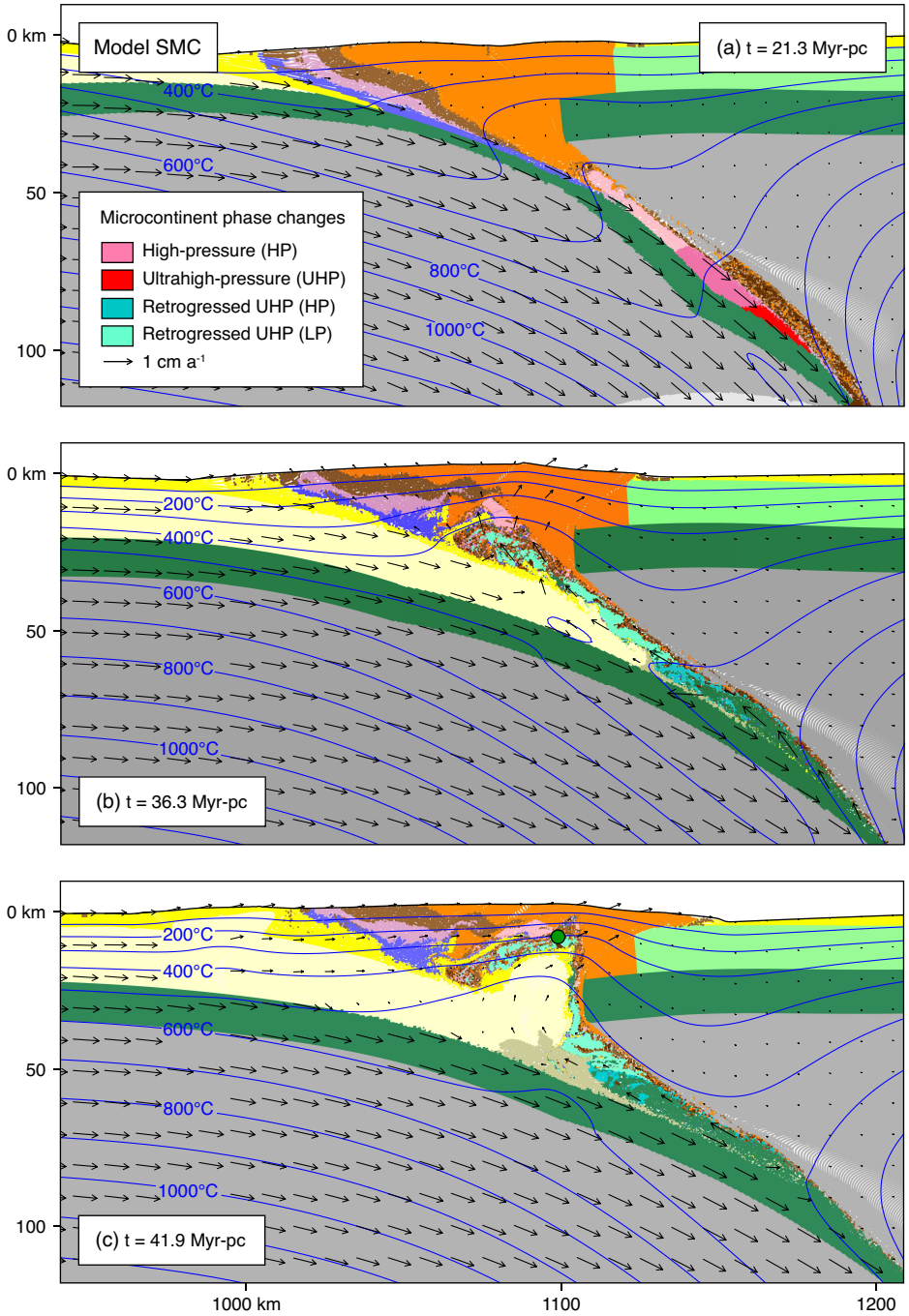

Figure 4.17: Results of Model SMC. (a–c) Material colours and isotherms (blue lines) for model times corresponding to phases discussed in text. For consistency with other figures, the model is shown in the 'stationary retrocontinent' reference frame. Green circle indicates position of model P–T–t particle shown in Figures 4.19 and 4.20.

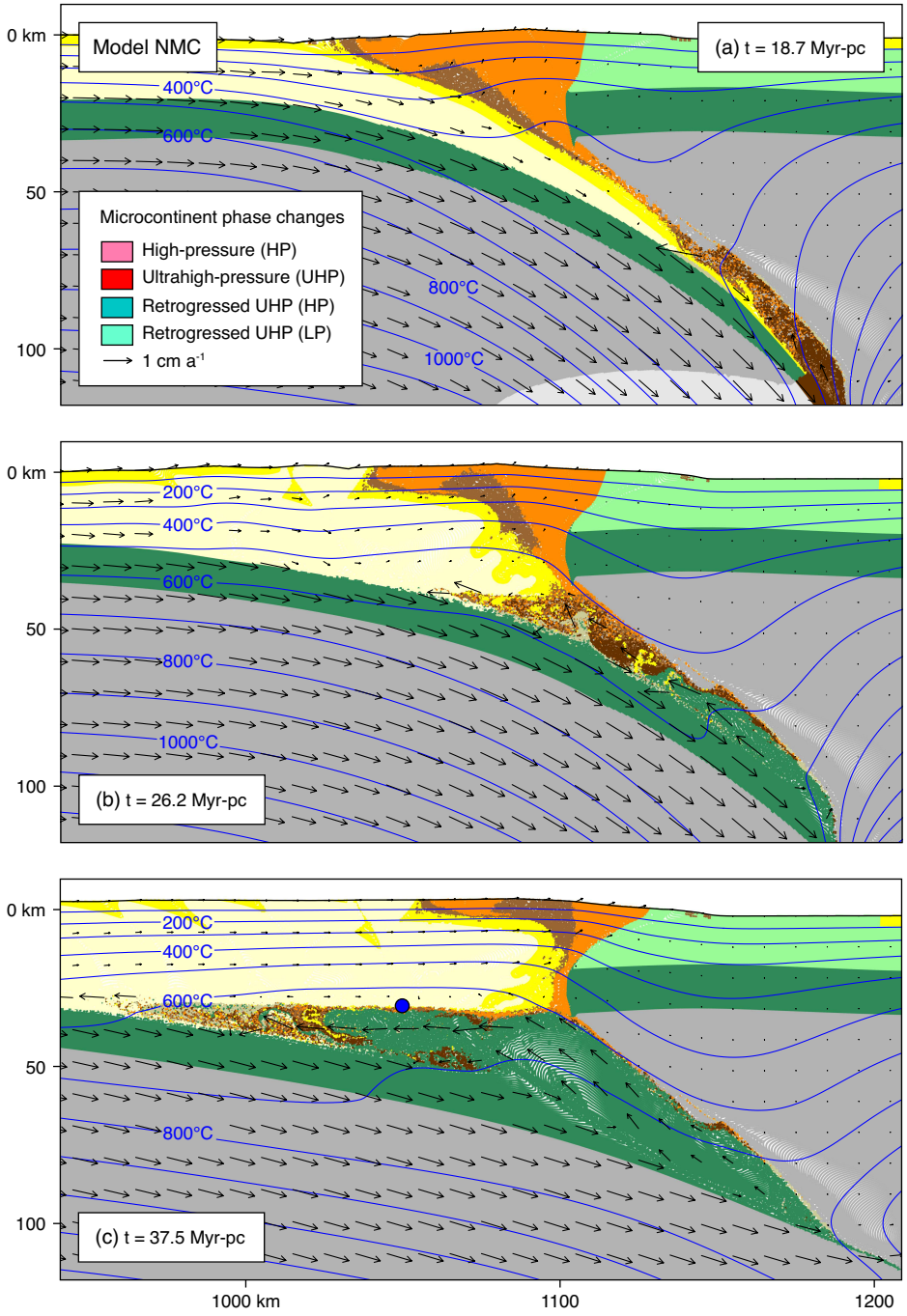

Figure 4.18: Results of Model NMC. (a–c) Material colours and isotherms (blue lines) for model times corresponding to phases discussed in text. For consistency with other figures, the model is shown in the 'stationary retrocontinent' reference frame. Consequently, during extension (b–c) the lower plate appears to be in motion when in fact it is the upper plate that is retreating toward the right. Blue circle in (c) indicates position of model P–T–t particle shown in Figures 4.19 and 4.20.

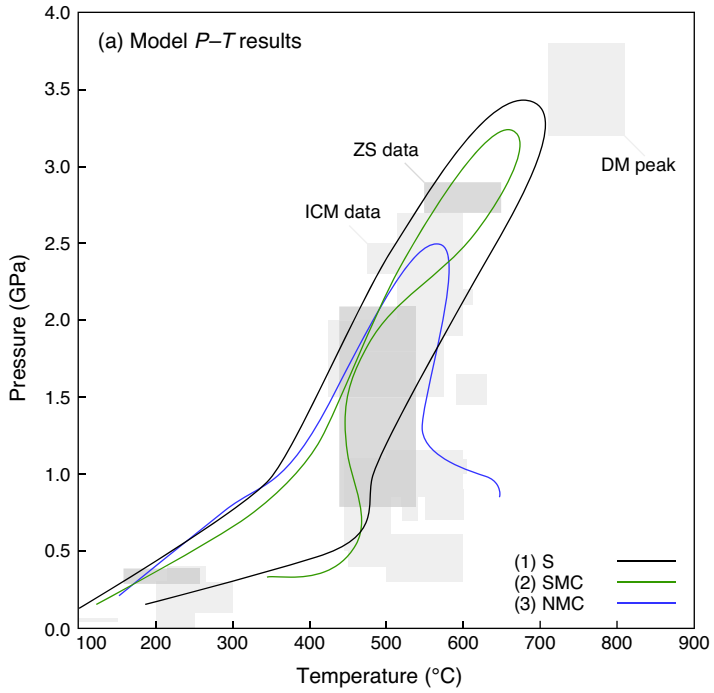

Figure 4.19: Model SMC and NMC P–T paths. Selected P–T path from Model S shown for comparison. DM=Dora Maira, ICM=Internal Crystalline Massif, ZS=Zermatt Saas. See Figure 3.8 for data sources. Starting positions for tracked particles from models SMC and NMC shown in Figure 4.16.

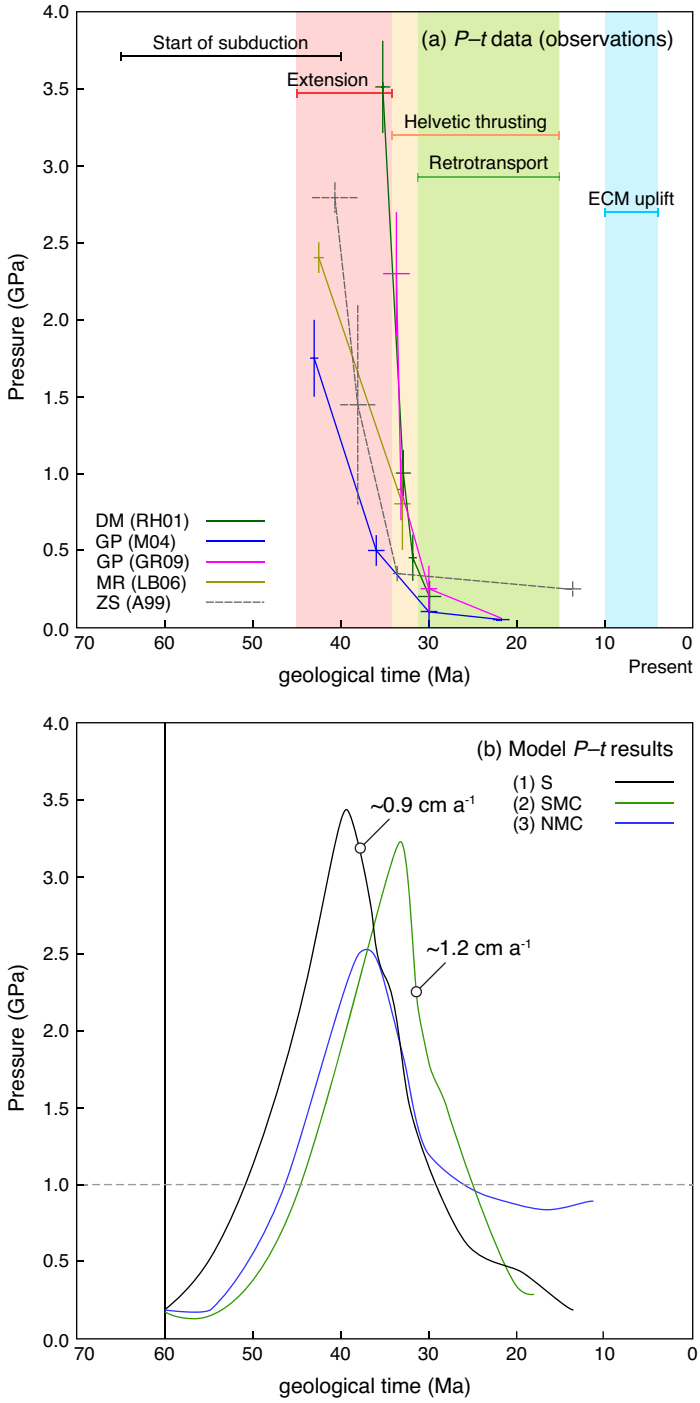

Figure 4.20: Model SMC and NMC P–t paths. (a) Representative P–t paths and tectonic stages from the Western Alps. See Figure 3.8 for data sources. (b) Comparison of selected P–t paths from models SMC, NMC, and S. Quoted exhumation rate for particle S A is averaged over the interval from peak pressures to 1 GPa. Quoted rate for particle from Model SMC is for the maximum rate interval from peak pressure to ∼1.6 GPa.

lower crustal wedge. The retrocrust, which is relatively strong (WQ, $f = 5$), remains mostly undeformed, with retrotransport of the procontinent margin crust limited to the backthrust at the rear of the plug (Fig. 4.18c). The inability of the margin to reach (U)HP conditions and the apparent ease with which it is detached from the procontinent result from its low strength (WQ, $f = 0.5$), which was chosen in Model S (and used here for consistency) in order to facilitate external detachment of the procontinent margin, as in the Western Alps.

P–T–t paths from models SMC and NMC differ considerably from those of Model S. Peak *P–T* conditions achieved by particles exhumed in Model SMC are similar to those of Model S. However, during initial exhumation the (U)HP plume in Model SMC undergoes considerably greater cooling than in Model S, to the extent that by the time the plume has decompressed to 1.5 GPa, its temperature is equivalent to that during burial. Subsequent trans-crustal exhumation leads heating by ∼50°C. The strong cooling during decompression in Model SMC can be explained by the fact that the (U)HP plume is considerably thinner, and therefore less thermally insulated than in Model S, so that despite its high exhumation rate (∼1.2 cm a^{-1} (Fig. 4.20b), it is unable to retain its heat. In Model NMC, the leading edge of the procontinent margin reaches near (U)HP conditions of ∼2.5 GPa/575°C (Figs 4.19 and 4.20), followed by near-isothermal decompression to crustal depths. The (U)HP part of the margin then stalls at the base of the crust where it undergoes thermal overprinting.

4.5.5 Models with Enhanced Retrotransport and/or Retroshortening

As noted above, the magnitude of upper plate (retro)shortening, manifested in the southern Alpine retrowedge, varies considerably along the orogen (*Schmid et al.*, 2004) (Fig. 4.3). In Model S, the retrocontinent crust is relatively strong (WQ×5), and consequently the amount of retroshortening in Model S and variants presented in Part 1 is minor. To assess the effects of retroshortening on the kinematic and thermal evolution of the models, two additional experiments were conducted in which the retrocontinent crust was made substantially weaker, in order to represent preconditioning of the retrocontinent resulting, for example, from deformation during previous rifting. In Model WR1 (weak retrocontinent 1), the initial strength of

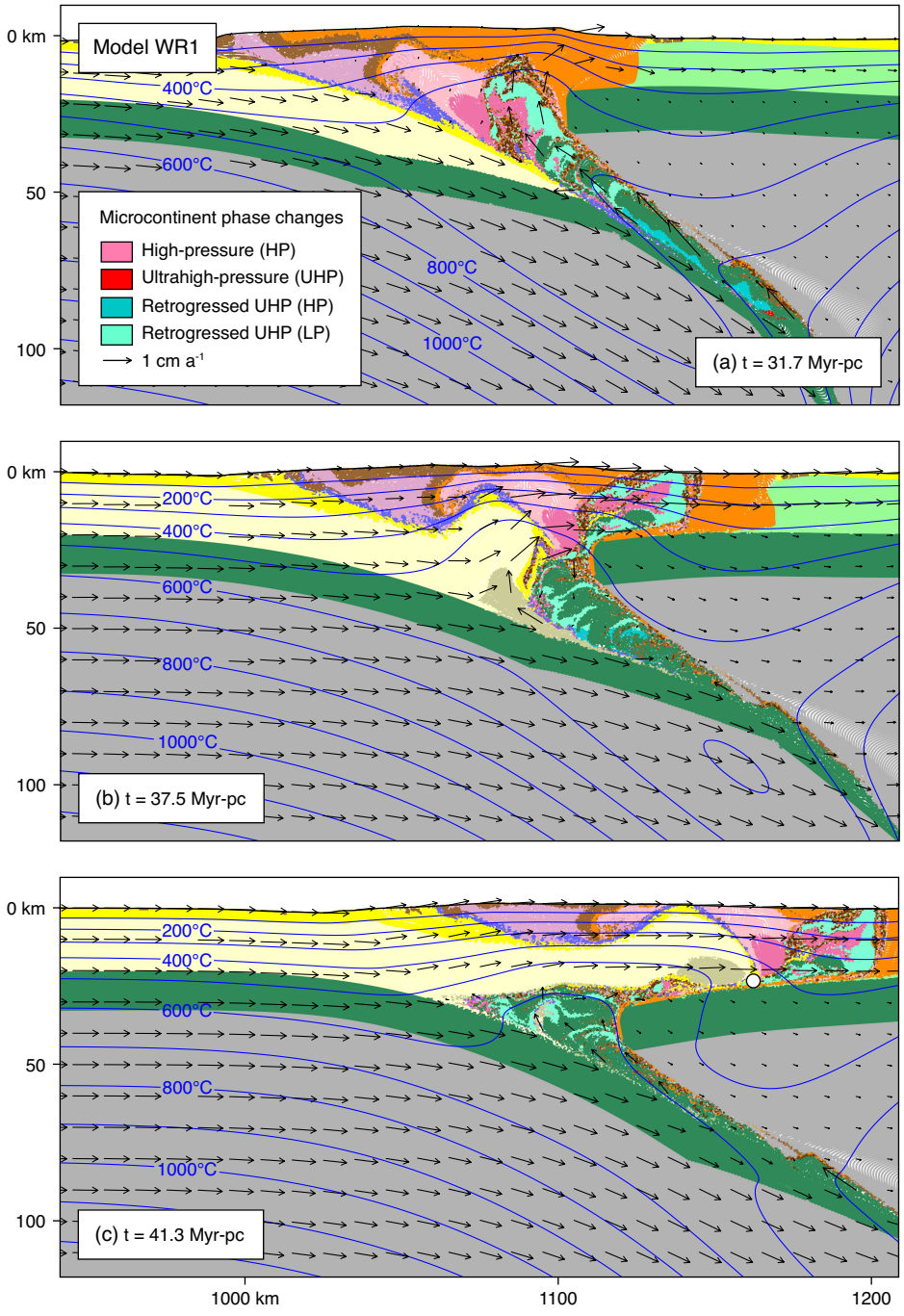

Figure 4.21: Results of Model WR1. (a–c) Material colours and isotherms (blue lines) for model times corresponding to phases discussed in text. White circle shows position of P–T particle shown in Figure 4.25.

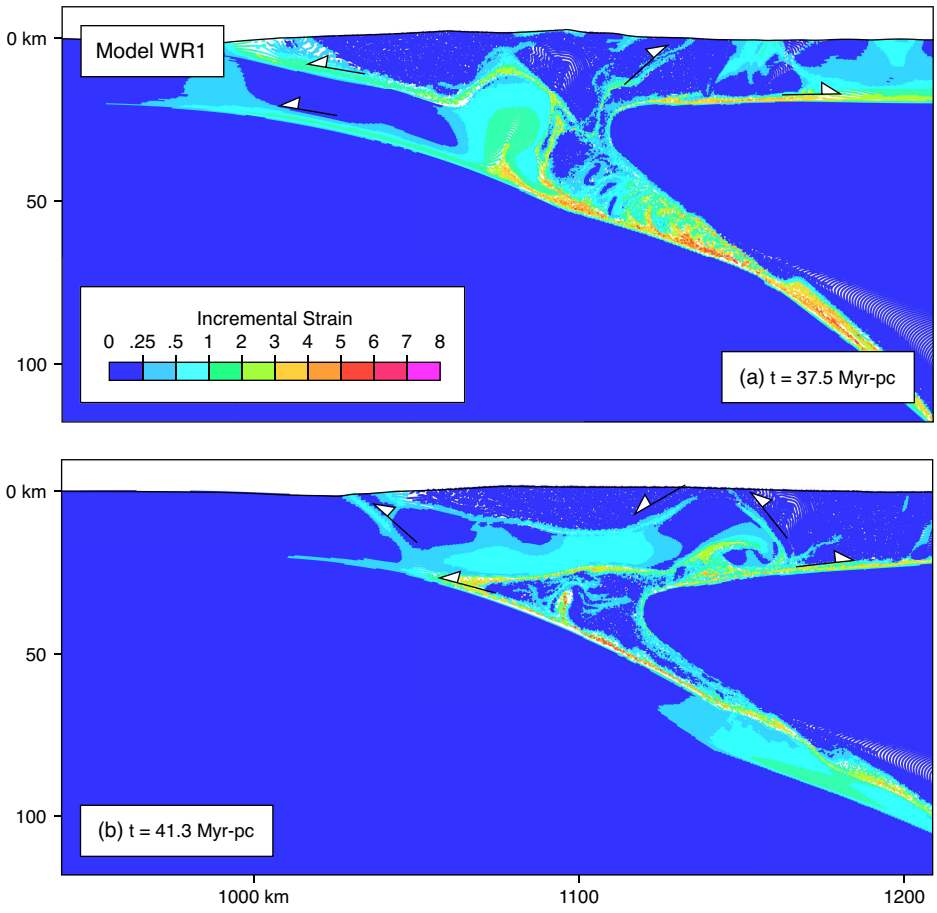

Figure 4.22: Incremental strain plots for Model WR1. Colours represent strain (square root of second invariant) accumulated during phases discussed in text. Times shown correspond to end of interval over which incremental strain was calculated. (a) Incremental strain for the period 31.7–37.5 Myr-pc. (b) Incremental strain for the period 37.5–41.3 Myr-pc. White-filled arrows show interpreted kinematics of deformation along dominant shear zones.

the retrocontinent upper crust was reduced to WQ×0.005, i.e., $f = 0.005$ (compared with WQ×5 in Model S) in order to represent pre-weakened upper crust. In Model WR2, the lower crust strength was reduced to DMD×0.0005 (compared with DMD×0.05 in Model S), while the upper crust was reduced to WQ×0.5 (i.e., has the same strength as the procontinent margin crust). In both models the dramatic strength reductions were implemented in order to ensure the desired retrocontinent shortening was achieved. Similar results may be achieved with stronger crust, but have yet to be tested. The changes to the material properties were applied to Model S at the end of Phase 2, i.e., immediately following exhumation of the (U)HP plume to the prowedge and before the onset of retrotransport. Although models with weak retrocrust may exhibit earlier retroshortening, the purpose of these experiments was to explore the effects of enhanced retroshortening after initial (U)HP rock exhumation, as in the Alps.

Model WR1 commences 30 Myr-pc, immediately following emplacement of the (U)HP plume within the prowedge. Subsequent underthrusting by the procontinent margin leads to uplift and exhumation of the plume at the rear of the plug (Fig. 4.21a), as in Model S. Failure of the retrocontinent upper crust ensues, detaching from the retrocontinent lower crust by 35 Myr-pc (Figs 4.21b and 4.22a). The plume and adjacent accretionary wedge (originally situated on the retrolithosphere) undergo lateral 'shunting' across the retrocontinent lower crust and mantle, driven by continued convergence and 'flow through' of the procontinent margin crust (Figs 4.21c and 4.22b). The resulting bivergent orogen contains a retrowedge comprising laterally transported (U)HP procontinent and retrocontinent crust, situated above a down-flexed wedge of undeformed retrocontinent lower crust and lithospheric mantle. The magnitude of retrotransport of the (U)HP plume across the upper plate by 41 Myr-pc is ∼100 km.

In Model WR2, in contrast, retrotransport of the (U)HP plume is facilitated by detachment of the much weaker lower crust from the upper plate. Initial retrotransport leads to backfolding of the leading edge of the retrocontinent lower crust (Fig. 4.23a,b). Beginning 38 Ma-pc, the lower crust fails along a shear zone at its base, and the plume is shunted retroward, overriding the retrolithosphere (Figs 4.23b and 4.24a). Continued convergence leads to flow through of the procontinent margin

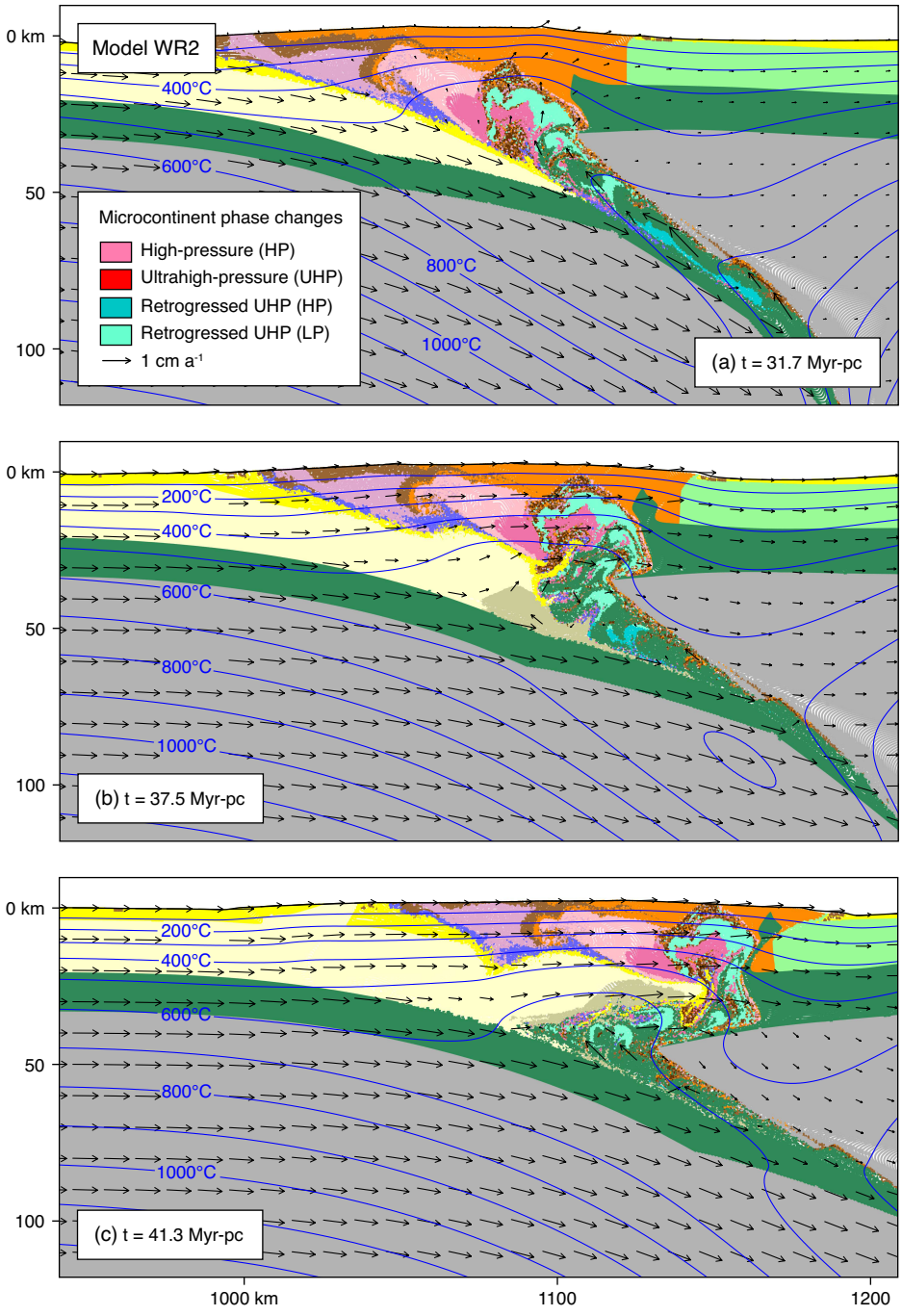

Figure 4.23: Results of Model WR2. (a–c) Material colours and isotherms (blue lines) for model times corresponding to phases discussed in text.

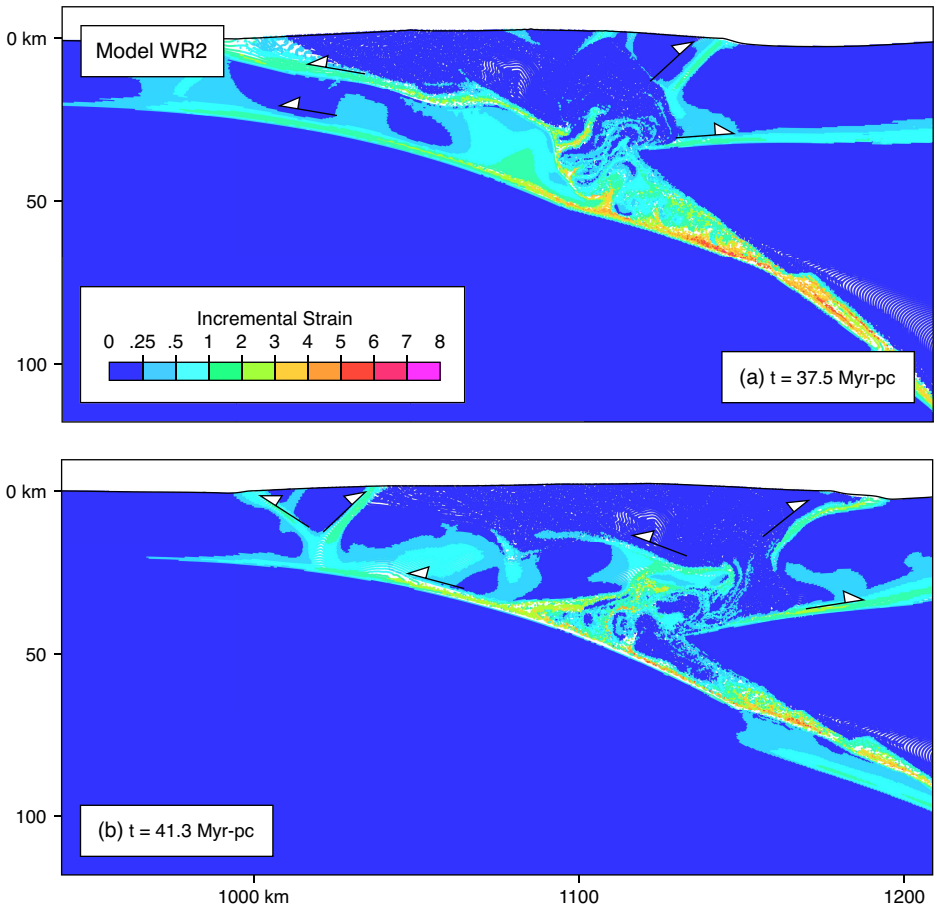

Figure 4.24: Incremental strain plots for Model WR2. Colours represent strain (square root of second invariant) accumulated during phases discussed in text. Times shown correspond to end of interval over which incremental strain was calculated. (a) Incremental strain for the period 31.7–37.5 Myr-pc. (b) Incremental strain for the period 37.5–41.3 Myr-pc. White-filled arrows show interpreted kinematics of deformation along dominant shear zones.

crust onto the retrolithosphere, which drives further shunting, and by 41 Ma-pc the plume has undergone ∼50 km of lateral transport over the retrocontinent (Figs 4.23c and 4.24b). Some retrocontinent lower crust remains smeared beneath the plume, whereas at the retroside of the plume, the lower crust has thickened by ∼2 km. Finally, external detachment of the procontinent margin crust occurs (Figs 4.23c and 4.24b), but in a position much closer to the retrocontinent than in Model S.

4.6 Summary and Implications for (U)HP Rock Exhumation Along the Alpine Orogen

The models presented here provide further insight into the controls on (U)HP exhumation in Alpine-type orogens, as well as potential explanations for some of the variations in the style of (U)HP rock exhumation and tectonics along the Alpine Orogen described above.

4.6.1 Contrasts in Provenance, P–T Conditions, and Exhumation Rates

Differences in the provenance of the principal (U)HP units (Fig. 4.3) in the Alpine orogen can probably be attributed to contrasts in the distribution and size of paleogeographic domains along the orogen. Model S, and most variants based on the same starting geometry, achieve (U)HP metamorphism and exhumation of the microcontinent and adjacent oceanic crust, analogous to the Briançonnais and Piemont-Liguria (U)HP units, respectively, exposed in and above the Western Alps ICMs. Models SMC (Fig. 4.17c) and NMC (Fig. 4.18c) fail to produce the degree of (U)HP metamorphism and exhumation of the procontinent margin (analogous to the European margin) required to explain the (U)HP units in the Central and Eastern Alps, although these models can probably be modified to achieve better results. Factors that would potentially promote subduction of the procontinent margin in models SMC and NMC can be inferred from Model S variants (shown above and in Chapter 3) that produce greater subduction and (U)HP metamorphism of the microcontinent crust.

The depth of microcontinent crust subduction depends critically on its strength. Model W (Chapter 3, Fig. 3.4) showed that initially weaker microcontinent crust

leads to shallower detachment, and hence lower peak P–T conditions. The convergence rate in the models (V0.5 and V1.5; Figs 4.9 and 4.10) exerts similar control on both the amount of crust to reach (U)HP conditions, and the maximum depth of burial. Higher convergence rates (Model V1.5) lead to greater traction exerted on the subducting crust, carrying more of it to greater depths (Fig. 4.10b,c). Lower convergence (V0.5) rates not only provide less slab traction, but slower subduction allows greater time for thermal relaxation and hence weakening of the subducting crust, which further promotes shallow detachment (Fig. 4.9b,c). However, while varying convergence rates could have affected the depth of subduction along the Alpine Orogen, the fact that some of the highest metamorphic pressures are recorded in the Western Alps, where orogen-normal convergence rates were probably lowest, makes this explanation unlikely. Model SMC (Fig. 4.17b,c) subducts a greater proportion of the microcontinent to (U)HP conditions, owing to the thinner, and hence cooler/stronger microcontinent crust. Consequently, it is possible that variations in peak P–T conditions and the sizes of (U)HP units along the Alps arose from combinations of contrasting crustal strengths and thicknesses resulting from along-strike variations in the extent of crustal thinning/weakening produced during previous rifting.

The temperature associated with (U)HP metamorphism in the models is similar over the range of parameters tested here, insofar as all of the models produce a similar subduction zone thermal gradient. In theory, slower subduction (Model V0.5) should produce a hotter subduction zone, owing to the greater time allowed for thermal relaxation to offset the advection of cool lithosphere beneath the retrocontinent. However, heating associated with thermal relaxation in Model V0.5 mainly affects the overlying orogen, probably because shallow detachment of the microcontinent crust prevents any appreciable amount of radiogenic crust from flowing deeper into the subduction channel. Higher overall temperatures will be achieved in models with greater crustal radiogenic heat production (currently in progress).

Exhumation rates in the models are relatively insensitive to the range of convergence rates tested here, with similar maximum rates of initial exhumation, $\sim$1 cm a^{-1}, in models with convergence rates of 0.5, 1, and 2 cm a^{-1} (Fig. 4.12b). The latter can explained by the fact that exhumation in the models is primarily driven by

buoyancy. In theory, buoyancy-driven exhumation should be faster in models with less slab traction (V0.5), or in models with larger, and hence more buoyant plumes (V1.5). However, for the models shown here these factors appear to exert only minor influences. Conversely, trans-crustal exhumation in the models, driven largely by retrothrusting and erosion, is primarily controlled by convergence rate (Fig. 4.12b). Erosion exerts a similar, but more subtle, control on the models, with little effect on initial rapid exhumation, and greater influence during trans-crustal exhumation (Fig. 4.8b).

The thermal evolution of the exhuming (U)HP crust is sensitive to several factors, also related to thermal relaxation of the orogenic crust. Cooling of the plume should depend partly on its ability to remain thermally insulated, and hence retain its heat, as it exhumes. Failure to do this is best illustrated by Model SMC (Figs 4.17 and 4.19), in which the thin plume rapidly cools during initial exhumation. However, in the models shown here, even the largest (U)HP plumes (models S and V1.5; Figs 3.4 and 4.10) quickly equilibrate to ambient crustal temperatures. The hottest decompression paths (not including the divergent models) are instead achieved at slower convergence rates (Model V0.5; Fig. 4.9), which allow more time for thermal relaxation of the orogen (Fig. 4.9b,c), resulting in isothermal decompression P–T paths (Fig. 4.11a). Faster convergence, accompanied by earlier exhumation, results in the ascent of the plume into cooler orogenic crust (Fig. 4.10b,c). However, although the isothermal decompression paths produced by Model V0.5 are closer to P–T paths from the Western Alps, the timing of (U)HP metamorphism and subsequent exhumation are too slow to match the data (Fig. 4.12). Slower convergence is therefore an unlikely explanation for the discrepancy between temperatures achieved by Model S and the (U)HP rocks in the Western Alps during decompression (Chapter 3, Fig. 3.8b). It is possible that the orogen was simply hotter overall, prior to and following (U)HP rock exhumation.

The magnitude of subsequent thermal overprinting depends mainly on the residence time of the (U)HP crust at lower/middle crustal depths. In each model there is a tendency for the deepest part of the (U)HP plume to 'stall' and remain buried within the lower/middle crust. These deepest parts of the plume are subjected to enhanced thermal overprinting as the thickened orogenic crust thermally relaxes.

Stalling is also promoted by retrocontinent deformation (models WR1 and WR2; Figs 4.21 and 4.23), which leads to lateral transport rather than exhumation of the plume. The temperatures achieved by stalled particles in the models (Fig. 4.25) are lower than the highest achieved in the Alps, and occur at somewhat higher pressures (∼1 GPa versus 0.5 GPa). Achieving higher temperatures at lower pressures will probably require greater crustal heat production in addition to time for thermal relaxation to occur. Similar stalling of the (U)HP rocks at crustal depths and subsequent thermal relaxation can probably explain the thermal overprinting in the Alps. In addition, the fact that the lower plate crust in the Central Alps underwent considerable lateral transport across the retrolithosphere, with associated crustal thickening, may explain the greater degree of thermal overprinting there. Recent chronological data (*Rubatto et al.*, 2009) suggest that Barrovian metamorphism in the (north)Western and Central Alps may have lasted considerably longer than previously thought (from ∼32–22 Ma compared to ∼32–29 Ma), suggesting that longer residence of (U)HP crust at middle crustal depths (similar to Model WR1) may be permissible.

4.6.2 Structure and Tectonics

Many of the models produce tectonic elements that are similar to features observed in the Central and Eastern Alps (Fig. 4.3b–d), although clearly no one model reproduces the geology of these areas. For example, the subhorizontal attitude, and positions of the Adula nappe and underlying lower pressure European crust (Fig. 4.3b) are similar to the geometry and position of the (U)HP nappe in models V1.5 (Fig. 4.10c) and WR1 (Fig. 4.21c). Similarly, if the microcontinent in Model SMC (Fig. 4.17c) is interpreted to represent the leading edge of the European margin, then the final geometry of the plume is reminiscent of the Eastern Alps, with extremely thin (few km thick) (U)HP nappes wrapped over the European basement exposed in the Tauern Window (Fig. 4.3c,d). Similar features (i.e., stronger crust, thinner margins) will be incorporated into models with the SMC and NMC geometries, which were intended to address the Central and Eastern Alps.

Each of the models produces external detachment of the procontinent margin, analogous to the External Crystalline Massifs in the Western and Central Alps (Fig. 4.3a,b). The latter can be explained by the relatively low strength of the margin

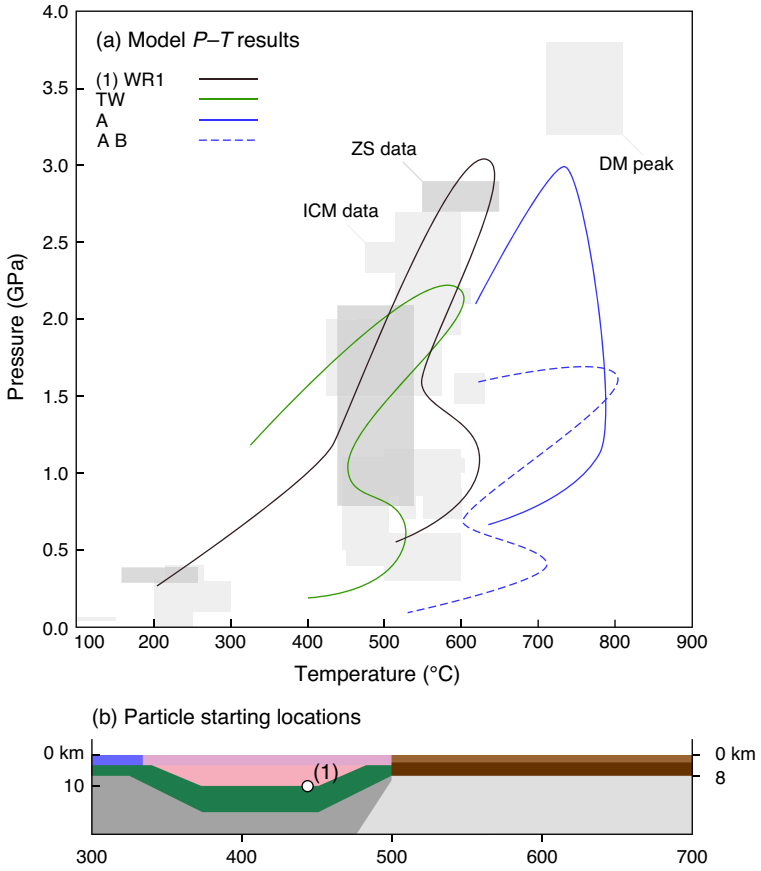

Figure 4.25: *P–T* Path for 'Stalled' Particle from Model WR1 Compared with Observations. See Figure 4.21c for location of particle. TW=generalized path for Tauern Window after *Warren et al.* (2012a). A=general path for the Adula nappe in the vicinity of the Southern Steep Belt, from *Nagel* (2008). A B=generalized path for Adula nappe from *Beltrando et al.* (2010b). Grey boxes show constraints from the Western Alps, as in Figure 3.8. DM=Dora Maira, ICM=Internal Crystalline Massif, ZS=Zermatt Saas. See Figure 3.8 for data sources.

in the models (WQ×0.5), which facilitates detachment and subsequent uplift. None of the models presented here illustrate the style of 'flow through' of the European margin crust exhibited in the Eastern Alps, where exhumation/uplift is strictly limited to the core of the orogen (Fig. 4.3c,d). Sensitivity tests, not presented here, show that this style of centralized uplift can be achieved in models with stronger (WQ×2) margin crust.

Models WR1 and WR2 (Figs 4.21 and 4.23) show that the strength of the retrocrust exerts primary control over the amount of retrotransport and accompanying retrocrust shortening. The contrasts in the amount of retrotransport along the orogen can therefore be attributed to varying degrees of 'buttressing' by the retrocontinent. The obvious example is the Ivrea mantle, already exhumed prior to subduction in the Western Alps (Fig. 4.3a), which probably acted as a backstop because of the relative strength of lithospheric mantle, resulting in the very limited retrotransport observed there.

The style of retroshortening in the models (WR1 and WR2; Figs 4.21 and 4.23) is different from that observed in the Central and Eastern Alps. Whereas both parts of the orogen contain retro(critical)wedges (Fig. 4.3b–d), deformation of the retrocrust in the models involves homogeneous thickening, probably because of its very low ductile strength. Models that favoured brittle deformation over ductile thickening would probably produce more applicable styles of retrodeformation. That said, Model WR1 successfully reproduces the magnitude of retrotransport observed in the Central Alps (Fig. 4.3b), with emplacement of the procontinent (U)HP crust at least ∼50 km over the retrocontinent lower crust and lithospheric mantle. A crucial point is that in all of the models, the amount of retrocrust shortening is proportional to the amount of transport of procontinent crust onto the retrocontinent. The latter appears consistent with the structure of the Western and Central Alps. However, in the Eastern Alps, where the retrowedge is at its greatest width along the orogen, the amount of retrotransport of procontinent (European crust) appears minor (Fig. 4.3c,d). An alternative explanation for the Eastern Alps is that additional shortening not accounted for by 'indentation' of procontinent crust can be attributed to removal of the underlying Adriatic lithosphere resulting from a flip of subduction polarity (*Lippitsch et al.*, 2003).

Finally, some of the models produce contrasting styles of lower crustal deformation similar to those observed beneath the Western and Central Alps (Fig. 4.3a,b). Models S, V0.5, and NMC (Figs 3.4, 4.9 and 4.18), among others, successfully reproduce the procontinent lower crustal wedge situated beneath the European crust in the Western Alps (Fig. 4.3a). The difference is that whereas in the Western Alps duplication of the European lower crust is attributed to large-scale thrusting (*Schmid and Kissling*, 2000), in the models the wedge is produced by ductile flow of highly deformed microcontinent and margin lower crust, a large portion of which reached (U)HP conditions. In contrast, Model WR1 (Fig. 4.21c) reproduces the apparent indentation by the retrocontinent lower crust and lithospheric mantle beneath the exhumed procontinent crust observed in the Central Alps (Fig. 4.3b). The style of retrocontinent lower crustal detachment in Model WR2 (Fig. 4.23c) has not been observed in the Alps.

4.6.3 Plate Divergence as a Mechanism for (U)HP Rock Exhumation in the Alps?

The recent suggestion (*Malusà et al.*, 2011) that (U)HP rock exhumation in the Western Alps resulted from transient plate divergence is not supported by the models shown above. The mechanism proposed by *Malusà et al.* (2011) involves exhumation of (U)HP rocks from the subduction channel into 'free space' created by a brief phase of orogen-normal divergence along the Western Alps resulting from minor changes in the longitudinal component of oblique plate motion (*Dewey et al.*, 1989). The appeal to plate divergence stems from the apparent lack of orogenic detritus deposited in certain Alpine basins during the timespan of (U)HP rock exhumation as evidence for a lack of substantial erosion, which they view a prerequisite of syn-convergent (U)HP rock exhumation. The models presented here not only disprove this assertion concerning erosion, but provide other reasons why plate divergence may not influence (U)HP rock exhumation in the fashion *Malusà et al.* (2011) envision.

Exhumation in models DV0.25 (Fig. 4.13) and DV0.5 initially proceeds by buoyancy-driven flow along the subduction channel, albeit much more slowly than in other models (Fig. 4.15b). It is only when breakoff of the subducted slab occurs that appreciable net divergence occurs, and even then exhumation rates do not exceed $\sim$0.3 cm a^{-1}, far lower than necessary to explain exhumation of (U)HP rocks in the

Western Alps. *Malusà et al.* (2011) suggest that plate divergence produced net extension of ∼30 km and occurred over ∼14 Myr (from 49–35 Ma), with accompanying exhumation rates reaching ∼1–3 cm a^{-1}. However, the models indicate that even if divergence had commenced immediately after the change in plate motion, that exhumation would probably have been too slow to bring (U)HP rocks to crustal depths in such little time. Therefore, although the present models cannot disprove their hypothesis, it remains to be shown that their conceptual model offers a better explanation than the style of syn-convergent exhumation shown by Model S. Finally, it should be noted that (U)HP rocks are exposed along the entire Alpine Orogen, in places where it is unlikely that orogen-normal divergence ever occurred. By implication, divergence cannot be considered necessary for (U)HP exhumation in the Alps in general.

4.7 Conclusions

1. The experiments presented here show that the style of (U)HP rock exhumation in Model S is generally similar over a range of parameter values appropriate for the Alpine Orogen. The robustness of the results across this range of parameters supports the applicability of the models to the Alps.

2. Certain experiments provide insight into variations in tectonometamorphism along the Alpine Orogen that were not addressed in Model S. These include contrasts in peak P–T conditions, the subsequent thermal history of exhumed (U)HP rocks, and the style of orogen-scale deformation, in particular that of retrotransport and retroshortening.

3. Among the most influential factors overall are the convergence rate and the initial strength of crustal units. The latter influences both the depth of burial of subducting units, as well as the distribution of orogen-scale deformation during exhumation. Variations in the strength of model crustal units may be linked geologically to lithological contrasts among (U)HP units, or indirectly to contrasts in the initial thickness and consequent thermal state of the crust resulting from different amounts of thinning during previous rifting.

4. Insights gained from these experiments will be incorporated into future models

for the Central and Eastern Alps, in order to explore the mechanisms of (U)HP rock exhumation for these regions in detail.

5. Models with plate divergence, considered by some to be a viable mechanism for exhuming Alpine (U)HP rocks, are less consistent with the observations than syn-convergent exhumation models (like Model S), in particular with respect to exhumation rates and the overall tectonics of the Western Alps.

Chapter 5

Discovery of Coesite-Eclogite from the Nordøyane UHP Domain, Western Gneiss Region, Norway: Field Relations, Metamorphic History, and Tectonic Significance

5.1 Preface

This chapter is based on the article 'Discovery of coesite-eclogite from the Nordøyane UHP domain, Western Gneiss Region, Norway: field relations, metamorphic history, and tectonic significance' by J. P. Butler, R. A. Jamieson, H. M. Steenkamp, and P. Robinson, published in the *Journal of Metamorphic Geology* (*Butler et al.*, 2012).

5.2 Abstract

Ultrahigh-pressure (UHP) rocks from the Western Gneiss Region (WGR) of Norway record subduction of Baltican continental crust during the Silurian to Devonian Scandian continental collision. Here we report a new coesite locality from the island of Harøya in the Nordøyane UHP domain, the most northerly yet documented in the WGR, and reconstruct the pressure-temperature (P–T) history of the host eclogite. The coesite-eclogite lies within migmatitic orthogneiss, interpreted as Baltica basement, that underwent multiple stages of deformation and partial melting during exhumation. Two stages of metamorphism have been deduced

from petrography and mineral chemistry. The early (M1) assemblage comprises garnet ($Pyr_{38-41}Alm_{35-37}Grs_{23-26}Spss_1$) and omphacite ($Na_{0.35-0.40}Ca_{0.57-0.60}Fe^{2+}_{0.08-0.10}Mg_{0.53}Fe^{3+}_{0.01}Al^{VI}_{0.40-0.42})_2(Al^{IV}_{0.03-0.06}Si_{1.94-1.97})_2O_6$), with subordinate phengite, kyanite, rutile, coesite, and apatite, all present as inclusions in garnet. The later (M2) assemblage comprises retrograde rims on garnet ($Pyr_{38-40}Alm_{40-44}Grs_{16-21}Spss_1$), diopside rims on omphacite ($Na_{0.04-0.06}Ca_{0.88-0.91}Fe^{2+}_{0.09-0.13}Mg_{0.81-83}Fe^{3+}_{0.08}Al^{VI}_{0.03})_2$ ($Al^{IV}_{0.07-0.08}Si_{1.92-1}$ plagioclase, biotite, pargasite, orthopyroxene, and ilmenite. Metamorphic P–T conditions estimated using THERMOCALC are ∼3 GPa/760°C for M1, consistent with the presence of coesite, and ∼1 GPa/813°C for M2, consistent with possible phengite dehydration melting during decompression. Comparison with other WGR eclogites containing the same assemblage shows a broad similarity in peak (M1) P–T conditions, confirming suggestions that large portions of the WGR were buried to depths of ∼100 km during Scandian subduction. Field relations suggest that exhumation, accompanied by widespread partial melting, involved an early phase of top-northwest shearing, followed by subhorizontal sinistral shearing along northwest-dipping foliations, related to regional transtension. The present results add to the growing body of data on the distribution, maximum P–T conditions, and exhumation paths of WGR coesite-eclogites and their host rocks that is required to constrain quantitative models for the formation and exhumation of UHP metamorphic rocks during the Scandian collision.

5.3 Introduction

The Western Gneiss Region (WGR) of Norway exposes reworked Proterozoic Baltica basement gneisses containing abundant eclogites beneath a sequence of Late Silurian to Early Devonian thrust nappes (Fig. 5.1) (*Terry and Robinson*, 2003). Coesite and microdiamond, formed during Early Devonian Scandian ultrahigh-pressure (UHP) metamorphism, are found in eclogites and garnet peridotites within both the Baltica basement and overlying nappes, and also within the host rocks themselves (*Dobrzhinetskaya et al.*, 1995; *Wain et al.*, 2000). However, despite agreement that these rocks formed by subduction of continental crust to depths exceeding ∼100 km, the volume and continuity of subducted crust and the mechanisms responsible for its exhumation remain problematic (*Andersen*, 1998; *Tucker et al.*, 2004; *Hacker*,

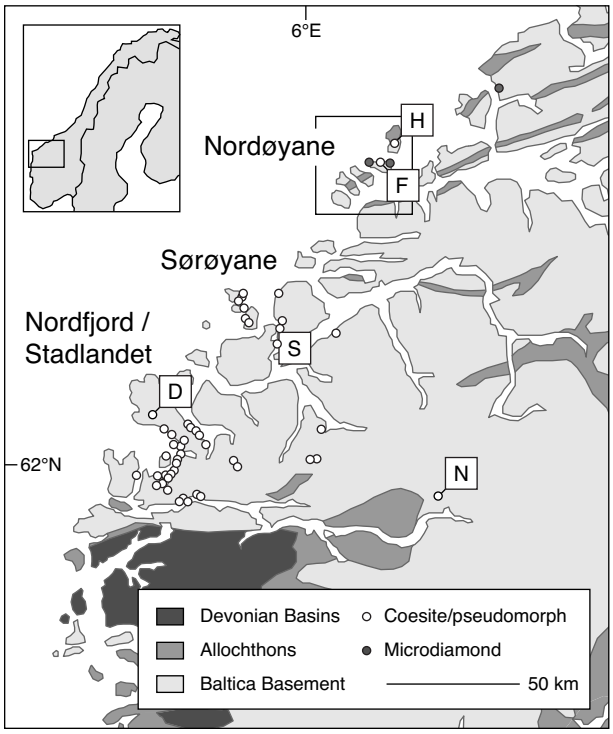

Figure 5.1: Simplified geological map of the Western Gneiss Region. Baltican basement of the WGR is overlain by Caledonian allochthons. Coesite/pseudomorph- and microdiamond-bearing rocks (circles) appear within the Nordfjord/Stadlandet, Sørøyane, and Nordøyane domains. Box shows location of map in Fig. 5.2. Letters indicate (re)calculated P–T estimate samples from *Terry et al.* (2000) (F); *Carswell et al.* (2003b) (S); *Ravna and Terry* (2004) (D); *Young et al.* (2007) (N); and this study (H) (results in Fig. 5.11).

2007; *Hacker et al.*, 2010; *Krogh et al.*, 2011). Three UHP domains are recognized along the west Norwegian coast – Nordfjord/Stadlandet, Sørøyane, and Nordøyane – separated by Baltica basement gneisses that lack evidence of UHP metamorphism (Fig. 5.1) (see *Hacker et al.*, 2010). The earliest discovery of coesite in the WGR was made at Selje (*Smith*, 1984) in the Nordfjord/Stadlandet domain, where coesite is relatively common (*Wain*, 1997; *Cuthbert et al.*, 2000; *Wain et al.*, 2000). Later discoveries of coesite and microdiamond (*Dobrzhinetskaya et al.*, 1995; *Terry et al.*, 2000; *van Roermund et al.*, 2002; *Carswell et al.*, 2003a; *Root et al.*, 2005) extended the area known to have been affected by UHP metamorphism over 100 km to the northeast, making the WGR one of Earth's largest UHP terranes. However, preserved coesite has not, until now, been documented in the Nordøyane UHP domain.

Here we describe the field relations and P–T history of a coesite-eclogite from

the island of Harøya – the first coesite documented in the Nordøyane UHP domain. This new discovery supports previous interpretations (*Dobrzhinetskaya et al.*, 1995; *Terry et al.*, 2000; *van Roermund et al.*, 2002) that the rocks that underlie the northern WGR were subducted to mantle depths during the Scandian continental collision, and that melting and extension contributed to their exhumation (*Terry and Robinson*, 2003; *Labrousse et al.*, 2011).

5.4 The Nordøyane UHP Domain

The Nordøyane UHP domain (Fig. 5.2) extends from the islands of Nordøyane ('the north islands') to the nearby mainland and includes the northernmost UHP rocks exposed in the WGR. The islands are underlain by three contrasting lithotectonic segments comprising granodioritic to dioritic Baltica basement gneisses overlain by, and infolded with, supracrustal rocks of the Sætra and Blåhø nappes (Fig. 5.2) (*Terry et al.*, 2000; *Terry and Robinson*, 2003, 2004). These nappes, remnants of Late Neoproterozoic Baltican margin deposits and a marginal volcanic-sedimentary terrane respectively, are part of a regional tectonostratigraphy that can be traced from Nordøyane to the orogenic foreland (*Gee*, 1975, 1980; *Robinson*, 1995; *Tucker et al.*, 2004; *Hollocher et al.*, 2007). Eclogites appear only within the northern and southern segments.

Direct evidence of UHP metamorphism has so far been documented only in the northern segment. This includes microdiamond in supracrustal garnet-biotite-kyanite gneiss on Fjørtoft (*Dobrzhinetskaya et al.*, 1995), polycrystalline quartz pseudomorphs after coesite in eclogites from Fjørtoft and Flemsøy, supported by thermobarometry (*Cuthbert et al.*, 2000; *Terry et al.*, 2000), thermobarometry of orthopyroxene-bearing eclogites from Fjørtoft (*Carswell et al.*, 2006), and microdiamond and majoritic garnet in peridotites from Fjørtoft and the mainland east of Nordøyane (*van Roermund and Drury*, 1998; *van Roermund et al.*, 2002; *Vrijmoed et al.*, 2006, 2008). The coesite-eclogite described in this work links the basement gneisses of Harøya to northern segment rocks on nearby Fjørtoft.

The (U)HP metamorphism in Nordøyane has been dated at ∼415 to 410 Ma (*Krogh et al.*, 2011) and is locally associated with fabrics indicating top-southeast

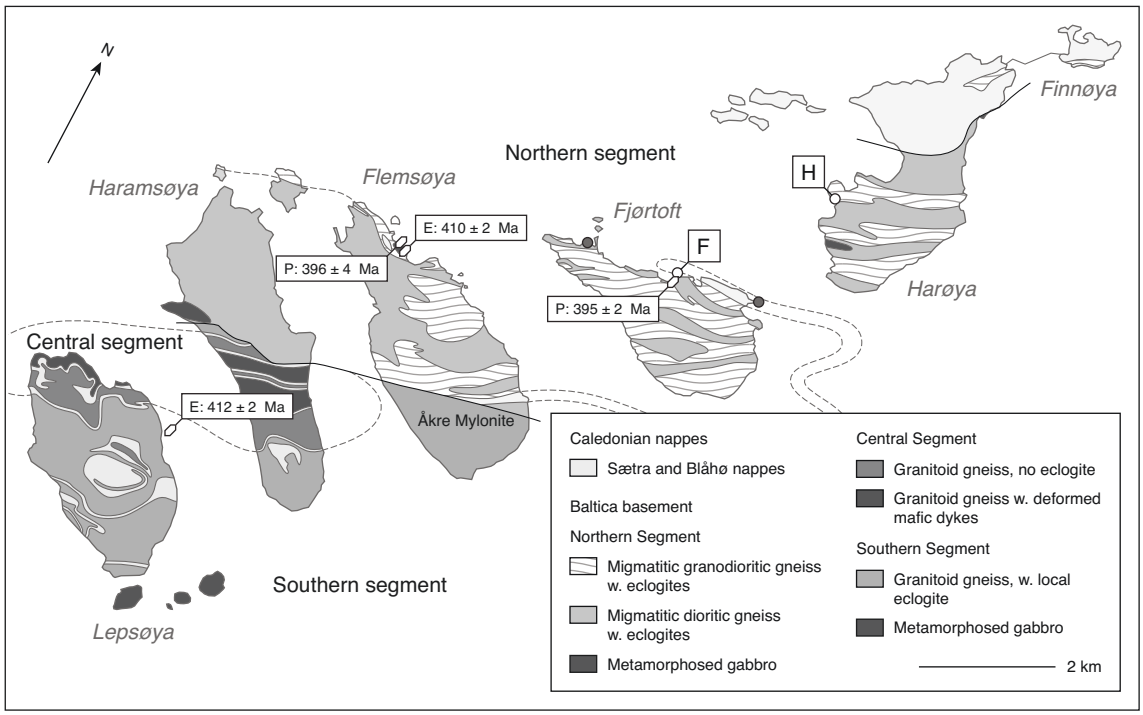

Figure 5.2: Simplified geological map of Nordøyane (*Terry and Robinson*, 2003). Mainland excluded. The Baltica basement on southern Harøya is correlated here with the northern segment of Nordøyane. The garnet-biotite gneiss at the southern end of Harøya (Fig. 5.3a) is too narrow to show here. Letters indicate (re)calculated P–T estimate samples from *Terry et al.* (2000) (F) and this study (H) (results in Fig. 5.11). Circles show coesite/pseudomorph (white) and microdiamond (grey) localities. Selected U–Pb ages from *Krogh et al.* (2011) are shown for eclogites (E) and cross-cutting pegmatites (P).

thrusting (*Terry and Robinson*, 2004), consistent with Scandian northwestward subduction of Baltica beneath Laurentia (*Torsvik*, 1998). Subsequent exhumation led to upper-amphibolite facies overprinting and local partial melting at ∼395 Ma (*Tucker et al.*, 2004; *Krogh et al.*, 2011). The later stages of exhumation were accompanied by amphibolite facies sinistral shearing along northwest-dipping foliations that dominate the northern WGR. This has been linked to regional-scale sinistral transtension that produced well documented E–W stretching and top-west extension near Nordfjord (*Milnes et al.*, 1997; *Andersen*, 1998; *Krabbendam and Dewey*, 1998).

5.5 Geology of Harøya and Finnøya

The study area includes the islands Harøya and Finnøya, situated ∼1 km northeast of Fjørtoft. The geology can be described in terms of a northern domain underlying northern Harøya and Finnøya, and a southern domain underlying southern Harøya (Fig. 5.3a), separated by a poorly exposed, mylonitic shear zone locally cut by scapolite-bearing pegmatites (*Steenkamp*, 2012).

5.5.1 Lithology

The northern domain comprises metamorphosed supracrustal rocks of the Blåhø nappe, including migmatitic garnet-kyanite-biotite gneiss, garnet-amphibolite, and minor marble, underlain by migmatitic granodioritic gneiss with retrogressed eclogites that may represent an infolded or tectonically juxtaposed exposure of Baltica basement rock (*Steenkamp*, 2012). Evidence for eclogite facies metamorphism of the supracrustal belt is rare, but one large eclogite pod was found within interlayered garnet-amphibolite and felsic garnet-gneiss exposed near the causeway between Harøya and Finnøya, near the boundary between the two domains.

The southern domain comprises several belts of migmatitic granodioritic hornblende-biotite gneiss (Fig. 5.4a) and dioritic garnet-clinopyroxene-hornblende-scapolite gneiss (Fig. 5.4b), both containing abundant eclogites and eclogite facies metamorphosed gabbro pods, as well as minor augen gneiss, garnet-biotite gneiss with eclogites, and deformed granitoid rocks. The coesite-eclogite was found within the northern belt of migmatitic granodioritic gneiss. Regional correlation is complicated by high strain and variable degrees of melting (Fig. 5.4). However, migmatitic orthogneisses in

both domains resemble Baltica basement rocks underlying other parts of Nordøyane with respect to both their lithology and association with abundant eclogite and gabbro pods (*Terry and Robinson*, 2003; *Krogh et al.*, 2011; *Røhr et al.*, 2013). Several thin belts of garnet-biotite gneiss on southern Harøya (e.g., in Myklebust; Fig. 5.3a) may represent tectonically juxtaposed exposures of Blåhø nappe, although lacking associated garnet-amphibolite and marble.

Figure 5.3 *(following page)*: (a) Geological map of Harøya and Finnøya. The northern domain comprises supracrustal rocks of the Blåhø nappe, overlying Baltica basement. The southern domain comprises several northwest-dipping belts of deformed migmatitic gneisses with eclogites, with infolds of garnet-biotite gneiss that may or may not represent Blåhø nappe. Repetition of units in the southern domain probably reflects post-(U)HP folding about subhorizontal west-plunging axes. (b) Equal area, lower hemisphere stereographic projections showing fabric orientations (poles to foliations and lineations) for the northern and southern domains.

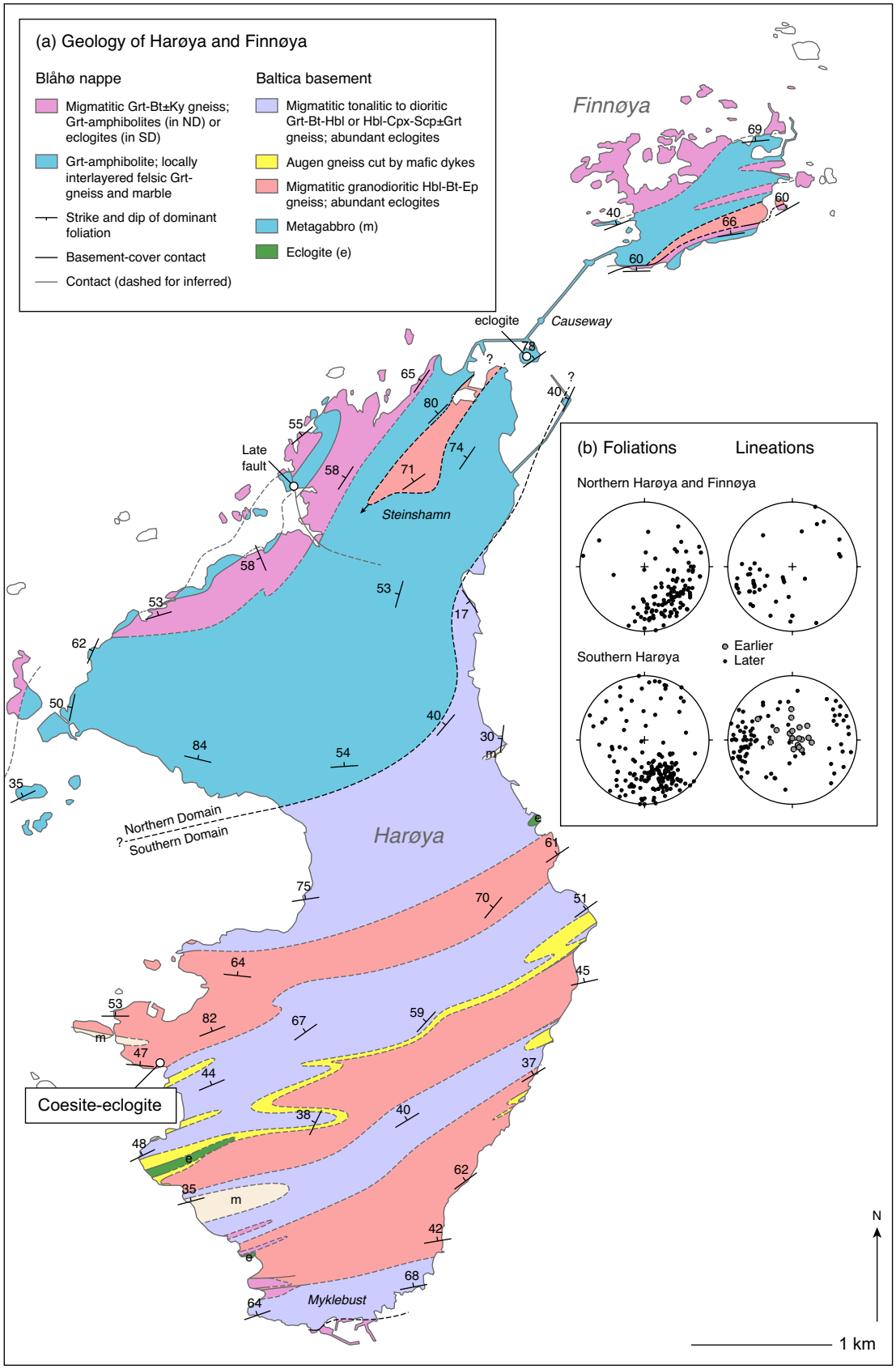
(a) Geology of Harøya and Finnøya
Blåhø nappe
Migmatitic Grt-Bt±Ky gneiss; Grt-amphibolites (in ND) or eclogites (in SD)
Grt-amphibolite; locally interlayered felsic Grt-gneiss and marble
Strike and dip of dominant foliation
Basement-cover contact
Contact (dashed for inferred)
Baltica basement
Migmatitic tonalitic to dioritic Grt-Bt-Hbl or Hbl-Cpx-Scp±Grt gneiss; abundant eclogites
Augen gneiss cut by mafic dykes
Migmatitic granodioritic Hbl-Bt-Ep gneiss; abundant eclogites
Metagabbro (m)
Eclogite (e)
Finnøya
eclogite
Causeway
Late fault
Steinshamn
Northern Domain
Southern Domain
Harøya
Coesite-eclogite
Myklebust
(b) Foliations
Lineations
Northern Harøya and Finnøya
Southern Harøya
Earlier
Later
N
1 km

Figure 5.4: Field photographs of eclogites and migmatitic gneisses on Harøya. (a) Eclogite pod within deformed granodioritic migmatite that hosts the coesite-eclogite. (b) Migmatitic tonalitic gneiss with interconnected leucosomes. (c) Deformed granitic pegmatite collected in 'fish-mouth' of large eclogite pod. (d) Mylonitic fabric developed in granodioritic migmatite with down-dip, top-northwest kinematics (inset) folded by subhorizontal west-plunging folds. Hammer for scale.

5.5.2 Partial Melting

The southern domain gneisses are highly migmatitic (Fig. 5.4a–c). Partial melting appears to have accompanied decompression of the eclogites and host gneisses, although melting at UHP conditions (*Gordon et al.*, 2011; *Labrousse et al.*, 2011) cannot be ruled out. Field relations suggest that two stages of melting affected the southern domain gneisses. The earlier stage formed abundant planar leucosomes that wrap around and form strain shadows against eclogites (Fig. 5.4a). Where spared by later deformation, these leucosomes form interconnected networks suggesting considerable partial melting (Fig. 5.4b) (*Sawyer*, 2008). The timing and *P–T* conditions of early melting are unclear. Some leucosomes contain hornblende (and locally scapolite), implying crystallization at amphibolite facies conditions. However, given the generally high strain, it is possible that earlier leucosomes formed at UHP conditions were completely obscured by the pervasive younger fabric.

Later granitic pegmatites locally cut the earlier leucosomes, and the concentration of pegmatite in eclogite boudin necks (Fig. 5.4c) indicates that some partial melting was synchronous with outcrop-scale extension. Some pegmatitic veins can be traced into retrogressed rims on eclogites that contain hornblende-rich leucosomes, suggesting that they also crystallized at amphibolite facies conditions.

5.5.3 Deformation

Deformation within the southern domain is dominated by fabrics formed during decompression of the eclogites and host gneisses (Figs 5.3b and 5.4a–d). Eclogite facies fabrics are preserved in some eclogite and metamorphosed gabbro pods; however, their plunge directions (broadly N–S) probably reflect the effects of later folding (*Terry and Robinson*, 2004). Subsequent deformation at amphibolite facies was partitioned into the migmatitic gneisses surrounding the eclogites. The earliest deformation features within the gneisses are amphibolite facies mylonite zones in which down-dip lineations associated with top-northwest kinematics trend parallel to the axes of steeply plunging folds (Fig. 5.4d), implying local NW–SE extension. The same fabrics appear at some contacts between Baltica basement and supracrustal rocks, e.g., west of Myklebust. These fabrics deform both retrogressed eclogites and the host migmatites, but are also locally cut by leucosomes. Similar top-northwest fabrics have been recorded on Gossa to the east (*P. Robinson*,

unpublished data). Top-northwest kinematics along present-day northwest-dipping foliations implies normal-sense shearing. If so, the coesite-bearing rocks on southern Harøya should be structurally overlain to the northwest by rocks that experienced lower peak pressures, consistent with preliminary data from supracrustal rocks from northern Harøya (*Steenkamp et al.*, 2011). However, these fabrics have clearly been modified by later deformation, and further work is required to constrain their significance. Subsequent sinistral shearing, also at amphibolite facies, produced pervasive, moderately west-plunging to subhorizontal lineations and folds in both the northern and southern domains (Figs 5.3b and 5.4d). Similar structures throughout the northern WGR, also widely associated with pegmatite in boudin necks (Fig. 5.4c), have been attributed to regional-scale sinistral transtension (*Krabbendam and Dewey*, 1998; *Terry and Robinson*, 2003) and coeval partial melting.

5.6 Description of Coesite-Eclogite

5.6.1 Sample Description and Petrography

The coesite-eclogite was sampled from a ∼1.5 m diameter eclogite pod, situated on the west coast of Harøya within the northern belt of migmatitic granodioritic gneiss (Fig. 5.3a). The sample is a medium-grained, retrogressed eclogite comprising garnet and clinopyroxene, with minor rutile, phengite, kyanite, and coesite, within a matrix of plagioclase, biotite, amphibole, orthopyroxene, quartz, and ilmenite (Fig. 5.5). It has a relict granoblastic texture, defined by omphacite, and a weak foliation defined by the shape-preferred orientation of ovoid garnet porphyroblasts and biotite. The garnet porphyroblasts are 0.25–1 mm in diameter, ovoid, and exhibit embayed grain boundaries surrounded by plagioclase moats (Fig. 5.6a). Most contain only a few inclusions, typically omphacite, rutile, apatite, kyanite, coesite, and phengite. Most inclusion types appear throughout the garnets, except for kyanite, which typically appears in clusters of approximately 10 to 20 ovoid grains in garnet cores. Phengite inclusions in garnet have in many cases undergone partial replacement by biotite.

Coesite inclusions within garnet are 0.025–0.05 mm in diameter, and hexagonal or rectangular (Fig. 5.7a). They are readily identified by outward radiating fractures that typically extend to the edge of the host garnet. Most inclusions consist

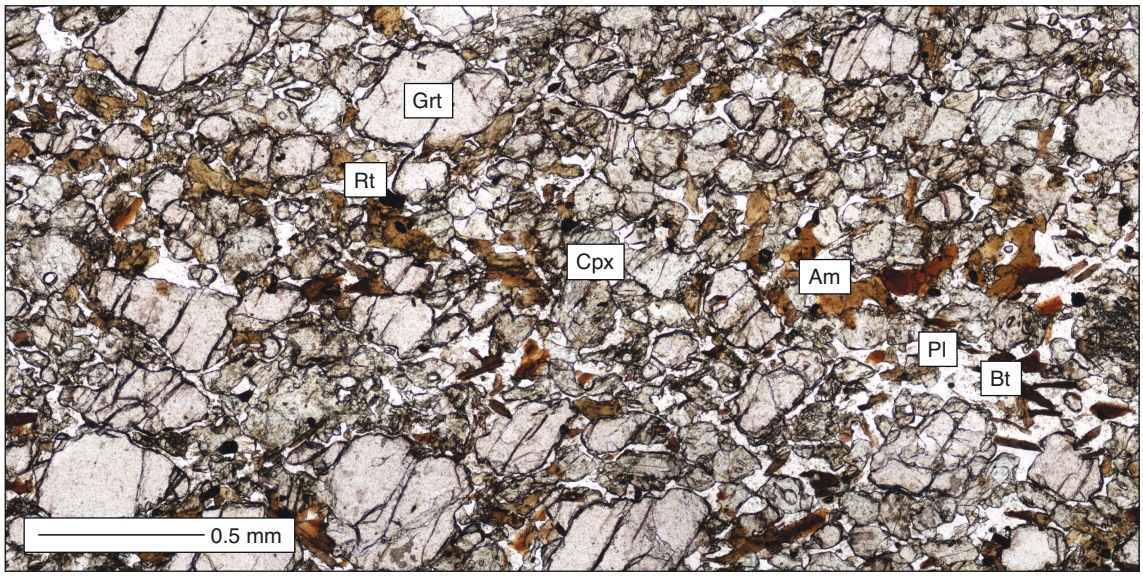

Figure 5.5: Thin section photograph of coesite-eclogite. The sample consists of relict garnet and clinopyroxene, in addition to minor rutile, phengite, kyanite, and coesite, within a matrix of plagioclase, biotite, hornblende, orthopyroxene, quartz, and ilmenite.

of cores of high-relief coesite surrounded by fine-grained, polycrystalline radial textured quartz (Fig. 5.7b) (e.g., *Wain et al.*, 2000). The cores constitute 50–90% of the volume of the inclusions, and in some cases coesite is in direct contact with the host garnet. Other examples consist solely of polycrystalline quartz, owing to more complete retrogression. Coesite inclusions have not been identified in any other phase; however, their inclusion in garnets that also contain clinopyroxene and kyanite suggests that these minerals may have equilibrated together.

Omphacite appears throughout the sample as irregular porphyroblasts from 0.25–0.5 mm in diameter and, more typically, as matrix grains 0.25 mm in diameter (Fig. 5.6a–c). Where in contact with other matrix omphacites it exhibits a relict granoblastic texture. Most grains contain only a few inclusions, typically of rutile and apatite. Contacts between adjacent grains appear to have undergone reaction to a medium-grained clinopyroxene + plagioclase symplectite, resulting in a 'spongy' texture in more retrogressed areas (Fig. 5.6b). Where omphacite adjoins garnet and biotite, the omphacite appears to have undergone reaction to fine-grained orthopyroxene + plagioclase symplectite, in places intergrown with amphibole (Fig. 5.6c). Quartz and amphibole form regularly oriented rods within the cores many of the

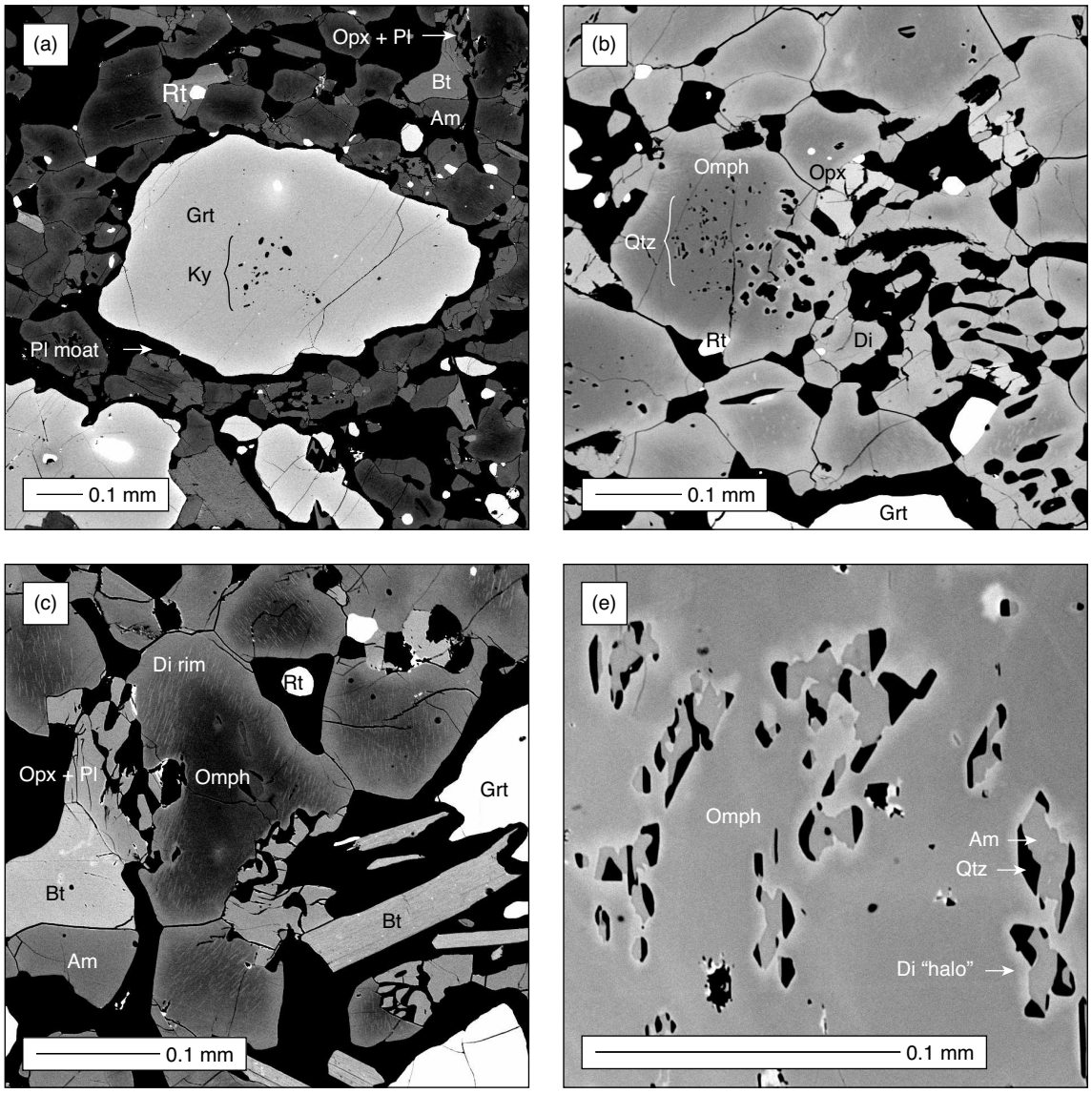

Figure 5.6: Representative textures in the coesite-eclogite. (a) Garnet with inclusions of kyanite surrounded by plagioclase moat. Biotite, hornblende, and orthopyroxene appear within the matrix. (b) Matrix clinopyroxene transformed to diopside + plagioclase symplectite. (c) Matrix clinopyroxene partially transformed to orthopyroxene + plagioclase symplectite. (d) Quartz + amphibole rods within cores of matrix clinopyroxene.

omphacite grains (Fig. 5.6d).

Plagioclase appears in symplectites and throughout the matrix as interconnected moats or rims, commonly as large poikiloblastic grains surrounding garnet and omphacite (Figs 5.5 and 5.6a). Some zones are characterized by optically continuous pools of plagioclase with abundant, randomly oriented biotite, that may represent former partial melt.

Biotite within the matrix forms hypidioblastic reddish-brown laths on average 0.25 mm long (Fig. 5.6c). Except where it has replaced phengite within garnet, biotite appears solely within the matrix, typically adjacent to garnet and within matrix zones dominated by plagioclase. Where biotite adjoins garnet, the two are typically separated by moats of plagioclase, and the biotite grains have cuspate forms that conform to the embayed garnet boundaries.

Amphibole forms irregular brownish-green grains 0.25 mm in diameter, locally with biotite inclusions (Fig. 5.6c). It is confined to the matrix, and is most abundant in zones where omphacite has transformed into clinopyroxene + plagioclase symplectite. In some places amphibole has clearly replaced matrix clinopyroxene while in others the two share straight grain boundaries. Some matrix amphiboles are separated from clinopyroxene by films of plagioclase. Where adjacent to orthopyroxene + plagioclase symplectite, amphibole appears in smooth contact with both minerals. Amphibole also appears in smooth contact with garnet.

Rutile forms xenoblastic to hypidioblastic (prismatic) grains 0.05 mm in diameter, within both garnet and clinopyroxene, and in the matrix where it is partly replaced by ilmenite. Apatite is similarly fine-grained and xenoblastic, and appears throughout the sample. Quartz is present throughout the matrix.

5.6.2 Raman Spectroscopy

Raman spectra of coesite were obtained using a Jobin Yvon T64000 Raman Spectrometer at the Hewitt Raman Spectroscopy Facility at Dalhousie University. The excitation wavelength was produced at 514.5 nm by an Argon ion laser with a power of 5 mW, and a spot size of 5 μm.

Raman spectra for the coesite inclusions (Fig. 5.7c) show the characteristic peaks for coesite at 521, 271, 171, and 117 cm^{-1}, in addition to minor peaks at 427, 356, 326, and 151 cm^{-1}, the latter four typical but not diagnostic of natural coesites

(*Boyer et al.*, 1985). Also present are the characteristic peaks for quartz at 466, 205, and 128 cm^{-1}. Such superposition of coesite and quartz peaks is typical of natural coesites (*Boyer et al.*, 1985; *Wain et al.*, 2000), and may reflect transformation of coesite to quartz at the crystal lattice scale, or overlapping of the coesite cores and quartz rims by the Raman laser.

5.6.3 Mineral Chemistry

Compositions of garnet, clinopyroxene, plagioclase, amphibole, biotite, phengite, and orthopyroxene were determined at Dalhousie University on a JEOL JXA 8200 electron microprobe, using an accelerating voltage of 15 kV, a beam current of 20 nA, and a spot size of 1 to 5 μm. Garnet, matrix clinopyroxene, and plagioclase were further investigated by point traverses and WDS X-ray maps.

The garnet porphyroblasts (Tables 5.1, 5.2, D.1 and D.2) exhibit zoning characterized by flat, high-Ca cores (max. Grs_{26}) followed by a sharp increase in Fe and minor Mn, at the expense of Ca and sometimes Mg, within $\sim$100 μm of the rims (Figs 5.8, D.1a and D.2a). Representative paired core and rim compositions are $Prp_{41}Grs_{23}Alm_{35}Spss_1$ and $Prp_{41}Grs_{16}Alm_{42}Spss_1$ respectively. None of the garnets show increasing Mg from core to rim, as seen in prograde zoned garnet from other WGR eclogites (*Wain et al.*, 2000). The presence of coesite inclusions near both the cores and rims of garnet grains suggests that garnet growth originally took place entirely at UHP conditions.

The matrix omphacite (Tables 5.2, 5.3, D.4 and D.5) exhibits diffuse zoning from omphacite cores (up to Jd_{28}, $Fe^{2+}/(Fe^{2+} + Mg) = 0.178$) to diopside rims (as low as Jd_1, $Fe^{2+}/(Fe^{2+} + Mg) = 0.135$) in contact with plagioclase; symplectites consist of diopside intergrown with plagioclase (Figs 5.9, D.1b and D.2b). The decrease in Jd content from core to rim is accompanied by an increase in Al^{IV} substitution (Fig. 5.10). In some cases this zoning is truncated by orthopyroxene + plagioclase symplectite. The hornblende in the quartz + hornblende rods within the cores of matrix omphacites is alumino-pargasite (*Leake et al.*, 1997), typically with $Fe^{2+}/(Fe^{2+} + Mg) = 0.164$, up to 1.06 Al^{VI} and low Ti (up to 0.03 p.f.u.)(Table S1), surrounded by haloes of lower-Jd omphacite (typically Jd_{15}, $Fe^{2+}/(Fe^{2+} + Mg) = 0.118$)(Table D.6). Similar features have been documented in eclogites from Nordøyane (*Terry and Robinson*, 2001) and from the Eastern Blue Ridge, North Carolina (*Page et al.*, 2005). Most

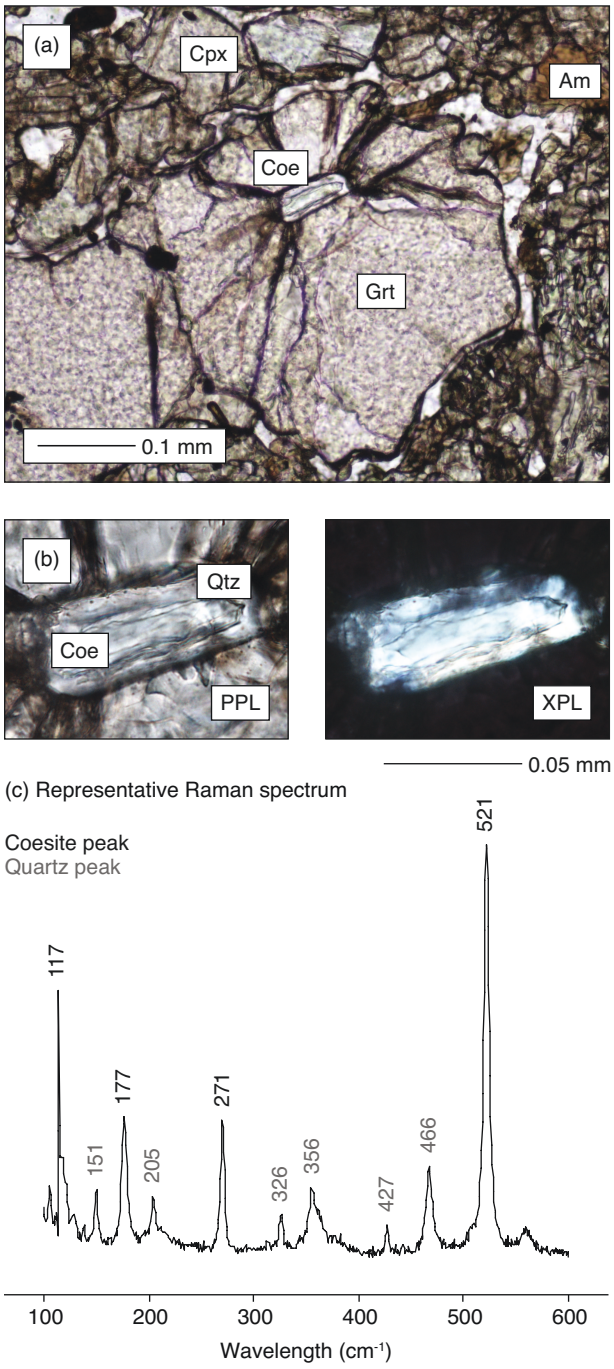

Figure 5.7: Coesite photograph and representative Raman spectrum. (a,b) Coesite inclusion within garnet with outward radiating fractures (a), and internal rim of polycrystalline quartz surrounding core of coesite (b). (c) Raman spectrum showing the characteristic peaks for coesite and quartz.

Mineral	Garnet					
Setting	c1	r1	c2	r2	c3	r3
SiO_2	39.78	39.24	39.67	39.37	39.12	38.98
TiO_2	0.03	0.05	0.00	0.02	0.00	0.00
Al_2O_3	22.07	21.90	22.30	22.01	21.97	21.84
Cr_2O_3	0.02	0.05	0.01	0.00	0.02	0.01
FeO	17.27	20.33	16.83	19.20	17.80	20.57
MnO	0.32	0.57	0.28	0.49	0.37	0.54
MgO	11.09	10.95	10.71	10.49	10.22	10.17
CaO	8.79	6.10	9.81	7.87	9.30	6.28
Total	99.37	99.19	99.61	99.45	98.80	98.39
No. of O	12	12	12	12	12	12
Si	3.00	2.99	2.98	2.99	2.98	3.00
Ti	0.00	0.00	0.00	0.00	0.00	0.00
Al^{IV}	0.00	0.01	0.02	0.01	0.02	0.00
Al^{VI}	1.96	1.95	1.96	1.95	1.95	1.98
Cr	0.00	0.00	0.00	0.00	0.00	0.00
Fe^{2+}	1.09	1.29	1.06	1.22	1.13	1.32
Mn	0.02	0.04	0.02	0.03	0.02	0.04
Mg	1.25	1.24	1.20	1.19	1.16	1.16
Ca	0.71	0.5	0.79	0.64	0.76	0.52
Total	8.03	8.02	8.03	8.03	8.02	8.02
Prp	40.7	40.4	39.1	38.6	37.7	38.3
Grs	23.2	16.2	25.8	20.8	24.7	17
Alm	35.5	42.1	34.5	39.6	36.8	43.5
Spss	0.7	1.2	0.6	1	0.8	1.2
FM	0.466	0.510	0.469	0.506	0.493	0.532

Table 5.1: Representative electron microprobe analyses of garnet core and rim pairs. Analyses normalized to 12 oxygens, with all Fe assumed to be Fe^{2+}. End-members are Prp=pyrope; Grs=grossular; Alm=almandine; Spss=spessartine. FM = $Fe^{2+}/(Fe^{2+} + Mg)$.

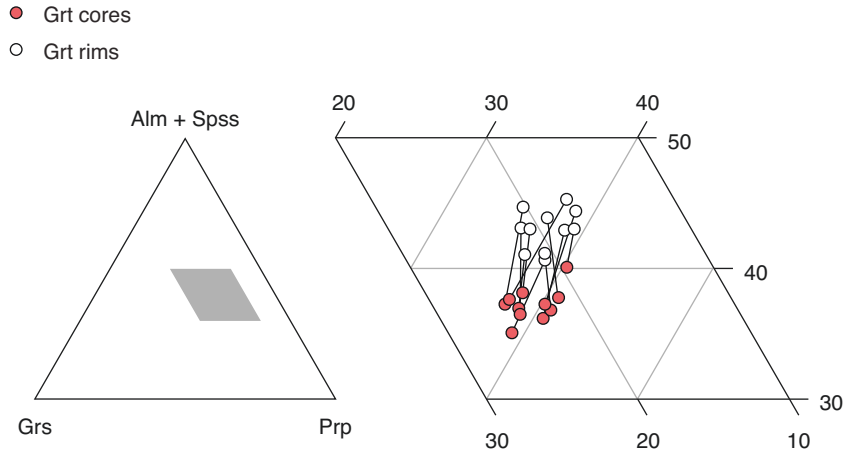

Figure 5.8: Single-grain variations in garnet compositions. Compositions of garnet core and rim pairs expressed as end-members almandine (Alm) + spessartine (Spss), grossular (Grs) and pyrope (Prp). See Figs D.1 and D.2 for details.

Mineral	Setting	Formula
Garnet		
	matrix core	$(Mg_{1.25}Fe^{2+}_{1.09}Ca_{0.71}Mn_{0.02})_{3.07}Al^{VI}_{1.96}Si_{3.00}O_{12}$
	rim	$(Mg_{1.24}Fe^{2+}_{1.29}Ca_{0.50}Mn_{0.04})_{3.07}Al^{VI}_{1.96}Si_{2.99}O_{12}$
	max. Grs	$(Mg_{1.20}Fe^{2+}_{1.06}Ca_{0.79}Mn_{0.02})_{3.07}Al^{VI}_{1.98}Si_{2.98}O_{12}$
Omphacite		
	matrix core	$(Na_{0.28}Ca_{0.65}Fe^{2+}_{0.07})(Fe^{2+}_{0.07}Mg_{0.60}Fe^{3+}_{0.01}Al^{VI}_{0.31})(Al^{IV}_{0.05}Si_{1.95})_2O_6$
	matrix rim	$(Na_{0.04}Ca_{0.88}Fe^{2+}_{0.08}Mg_{0.28})(Fe^{2+}_{0.05}Mg_{0.55}Fe^{3+}_{0.08}Ti_{0.01}Al^{VI}_{0.31})(Al^{IV}_{0.08}Si_{1.92})_2O_6$
	inclusion in Grt	$(Na_{0.40}Ca_{0.57}Fe^{2+}_{0.03})(Fe^{2+}_{0.04}Mg_{0.53}Fe^{3+}_{0.01}Al^{VI}_{0.42})(Al^{IV}_{0.03}Si_{1.97})_2O_6$
Phengite		
	inclusion in Grt	$(K_{0.81})(Ti_{0.03}Fe^{2+}_{0.05}Mg_{0.36}Al^{VI}_{1.61})_{2.05}(Al^{IV}_{0.54}Si_{3.46})_4O_{10}(OH)_2$
Plagioclase		
	matrix core	$(Na_{0.77}K_{0.01}Ca_{0.19})_{0.97}Al_{1.20}Si_{2.81}O_8$
	matrix rim	$(Na_{0.63}K_{0.01}Ca_{0.35})_{0.99}Al_{1.34}Si_{2.65}O_8$
Biotite		
	matrix	$(Na_{0.01}K_{0.91})_{0.92}(Ti_{0.24}Fe^{2+} + 0.64Mg_{1.93}Al^{VI}_{0.08})_{2.89}(Al^{IV}_{1.26}Si_{2.74})_4O_{10}(F_{0.04}Cl_{0.01}OH_{1.95})$
Amphibole		
	matrix	$(Na_{0.45}K_{0.21})_{0.66}(Ca_{1.82}Na_{0.18})_{2.00}(Al^{VI}_{0.46}Ti_{0.22}Fe^{3+}_{0.33}Fe^{2+}_{0.79}Mg_{3.18})_{4.98}$ $(Al^{IV}_{1.72}Si_{6.28})_8O_{22}(F_{0.03}Cl_{0.01}OH_{1.95})$
	rod in omphacite	$(Na_{0.57}K_{0.02})_{0.59}(Ca_{1.81}Na_{0.19})_{2.00}(Al^{VI}_{1.06}Ti_{0.02}Cr_{0.01}Fe^{3+}_{0.30}Fe^{2+}_{0.59}Mg_{3.01})_{4.99}$ $(Al^{IV}_{1.81}Si_{6.19})_8O_{22}(F_{0.05}OH_{1.95})$
Orthopyroxene		
	symplectite	$(Ca_{0.01}Fe^{2+}_{0.49}Mg_{0.49})(Mg_{0.94}Fe^{3+}_{0.05}Al^{VI}_{0.01})(Al^{IV}_{0.06}Si_{1.94})_2O_6$

Table 5.2: Representative mineral formulae of phases referred to in text. Garnet normalized to 12 oxygens, with all Fe assumed to be Fe^{2+}. Pyroxene normalized to 4 cations with Fe^{3+} estimated by charge balance (*Robinson*, 1981). Mica normalized to 11 O. Plagioclase normalized to 8 O. Amphibole normalized to 23 O with Fe^{3+} estimated assuming a sum of 13 cations excluding Ca, Na, and K (*Leake et al.*, 1997).

Mineral	Omphacite					
Setting	c1	r1	c2	r2	i	i
SiO_2	54.23	51.4	52.19	51.95	55.73	54.61
TiO2	0.05	0.22	0.23	0.24	0.03	0.07
Al_2O_3	8.70	2.44	8.75	2.39	10.71	10.92
Cr_2O_3	0.10	0.06	0.07	0.08	0.03	0.04
FeO	4.86	6.80	5.45	5.57	2.77	3.54
MnO	0.02	0.05	0.03	0.04	0.04	0.03
MgO	11.26	14.94	11.03	14.72	10.09	10.08
CaO	17.00	21.89	17.62	22.96	14.95	15.85
Na_2O	4.01	0.60	3.55	0.80	5.81	5.11
Total	100.23	98.40	98.92	98.75	100.16	100.25
No. of Cations.	4	4	4	4	4	4
Si	1.95	1.92	1.91	1.93	1.97	1.94
Ti	0.00	0.01	0.01	0.01	0.00	0.00
Al^{IV}	0.05	0.08	0.09	0.07	0.03	0.06
Al^{VI}	0.31	0.03	0.28	0.03	0.42	0.40
Cr	0.00	0.00	0.00	0.00	0.00	0.00
Fe^{2+}	0.13	0.13	0.12	0.09	0.08	0.1
Fe^{3+}	0.01	0.08	0.05	0.08	0.01	0.01
Mn	0.00	0.00	0.00	0.00	0.00	0.00
Mg	0.60	0.83	0.6	0.81	0.53	0.53
Ca	0.65	0.88	0.69	0.91	0.57	0.60
Na	0.28	0.04	0.25	0.06	0.40	0.35
Total	3.98	4.00	4	3.99	4.01	3.99
Q	71.4	95.5	73.7	94.00	59.6	63.7
Jd	27.5	1.1	22.5	1.7	39.8	35.8
Ae	1.1	3.4	3.8	4.3	0.6	0.5
FM	0.178	0.135	0.167	0.101	0.131	0.159

Table 5.3: Representative electron microprobe analyses of omphacite. Includes analyses of matrix omphacite core and rim pairs, and omphacite included in garnet. Analyses normalized to 4 cations, with Fe^{3+} estimated using charge balance constraints. Na-clinopyroxene end-members (*Morimoto et al.*, 1988) are: Q=quadrilateral; Jd=jadeite; Ae=aegirine. FM = $Fe^{2+}/(Fe^{2+} + Mg)$.

Stage	M1			M2					
Mineral	Grt	Omph	Phn	Grt	Cpx	Pl	Bt	Hbl	Opx
Setting	c	i	i	r	r	r			
SiO_2	39.67	55.73	52.23	39.24	51.40	59.35	36.94	42.92	53.13
TiO_2	0.00	0.03	0.53	0.05	0.22	0.01	4.24	2.01	0.04
Al_2O_3	22.30	10.71	27.53	21.90	2.44	25.49	15.23	12.67	1.72
Cr_2O_3	0.01	0.03	0.06	0.05	0.06	0.00	0.08	0.04	0.05
FeO	16.83	2.77	0.90	20.33	6.80	0.39	10.23	9.21	17.57
MnO	0.28	0.04	0.00	0.57	0.05	0.00	0.00	0.02	0.16
MgO	10.71	10.09	3.61	10.95	14.94	0.01	17.43	14.60	26.26
CaO	9.81	14.95	0.02	6.10	21.89	7.38	0.06	11.61	0.38
Na_2O		5.81	0.02		0.60	7.27	0.00	2.23	0.01
K_2O			9.54			0.19	9.66	1.14	
F							0.18	0.07	
Cl							0.07	0.06	
Total	99.61	100.16	94.44	99.19	98.40	100.09	94.12	96.58	99.18
No. of O	12	4 Cat.	11	12	4 Cat.	8	11	23	4 Cat.
Si	2.98	1.97	3.46	2.99	1.92	2.65	2.74	6.28	1.94
Ti	0.00	0.00	0.03	0.00	0.01	0.00	0.24	0.22	0.00
Al	1.98	0.45	2.15	1.96	0.11	1.34	1.33	2.18	0.07
Cr	0.00	0.00	0.00	0.00	0.00	0.00	0.00	0.00	0.00
$Fe_{tot.}$	1.06	0.08	0.05	1.29	0.21	0.00	0.64	1.12	0.51
Mn	0.02	0.00	0.00	0.04	0.00	0.00	0.00	0.00	0.00
Mg	1.20	0.53	0.36	1.24	0.83	0.00	1.93	3.18	1.44
Ca	0.79	0.57	0.00	0.50	0.88	0.35	0.00	1.82	0.01
Na		0.40	0.00		0.04	0.63	0.01	0.63	0.00
K			0.81			0.01	0.91	0.21	
F							0.04	0.03	
Cl							0.01	0.01	
Total	8.03	4.00	6.86	8.02	4.00	4.98	7.85	15.68	3.97

Table 5.4: Electron microprobe analyses of minerals used in P–T calculations. Analyses normalized to specified number of oxygens, with exception of pyroxenes which are normalized to 4 cations. c=core; r=rim; i=inclusion.

matrix omphacites exhibit submicroscopic lamellae (Fig. 5.6c) too small to analyze with EMP, although semi-quantitative analyses suggest they may be orthopyroxene.

The omphacite included in garnet (Tables 5.2, 5.3, and D.3) has higher maximum Jd contents (up to Jd_{40}, $Fe^{2+}/(Fe^{2+} + Mg) = 0.131$), than that in the matrix. The variation in Na content (from Jd_{10} to Jd_{40}) among analyzed inclusions (Fig. 5.9) probably represents a combination of zoning, and the effects of sectioning. There does not appear to be a correlation between omphacite inclusion composition and position within garnet. Like the matrix grains, the lower-Jd omphacites within garnet show a trend towards increasing Al^{IV} substitution (Fig. 5.10). None of the analyses suggest the residual presence of a Ca-Eskola component (*Page et al.*, 2005). Most phengite inclusions (Tables 5.2, 5.4 and D.8) in garnet exhibit partial replacement by biotite. The best analyses from grains with minimal replacement exhibit a maximum Si content up to 3.46 Si p.f.u., assuming 11 O. The matrix plagioclase (Tables 5.2, 5.4, D.11 and D.12) exhibits zoning characterized by a sharp increase in anorthite content from core to rim, typically within $\sim$5 μm of the grain boundary, from An_{20} to An_{37} (Fig. D.1b). Plagioclase in symplectites exhibits similar zoning. The biotite (Tables 5.2, 5.4 and D.9) is Mg-rich phlogopite, typically with $Fe^{2+}/(Fe^{2+} + Mg) = 0.251$, with minor $Al^{IV}Al^{VI}$ substitution towards eastonite (typically with 1.26 Al^{IV} p.f.u., assuming 11 O), and up to 0.30 Ti p.f.u. The amphibole (Tables 5.2, 5.4 and D.10) is pargasite (*Leake et al.*, 1997), typically with $Fe^{2+}/(Fe^{2+} + Mg) = 0.201$, and up to 0.48 Al^{VI} and 0.22 Ti p.f.u. The orthopyroxene (Tables 5.2, 5.4 and D.7) intergrown with plagioclase is bronzite, typically $En_{75}Fs_{25}$, with minor Al^{IV} substitution (Fig. 5.10).

5.7 Mineral Assemblages and Reaction Textures

The above observations support a two-stage equilibration history involving metamorphism in the coesite-eclogite facies (M1) followed by decompression through the granulite facies (M2).

The M1 mineral assemblage is interpreted to have comprised garnet and omphacite, with minor phengite, kyanite, rutile, coesite, and apatite. The restriction of kyanite to cores of garnet, and lack of its breakdown products in the matrix, makes its inclusion in this assemblage uncertain; however, its low modal abundance

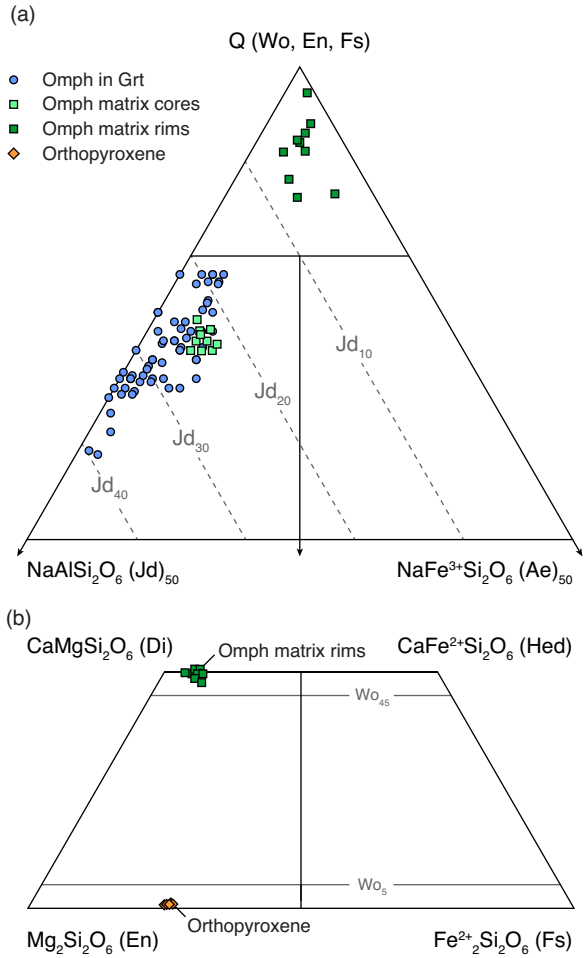

Figure 5.9: Single-grain variations in clinopyroxene compositions. (a) Na-clinopyroxene ternary diagram (*Morimoto et al.*, 1988) showing range of clinopyroxene compositions in the coesite-eclogite. (b) Pyroxene quadrilateral (*Morimoto et al.*, 1988) showing compositions of diopside rims and orthopyroxene. Q=quadrilateral. Jd=jadeite; Ae=aegirine; Di=diopside; Hed=hedenbergite; En=enstatite; Fs=ferrosilite.

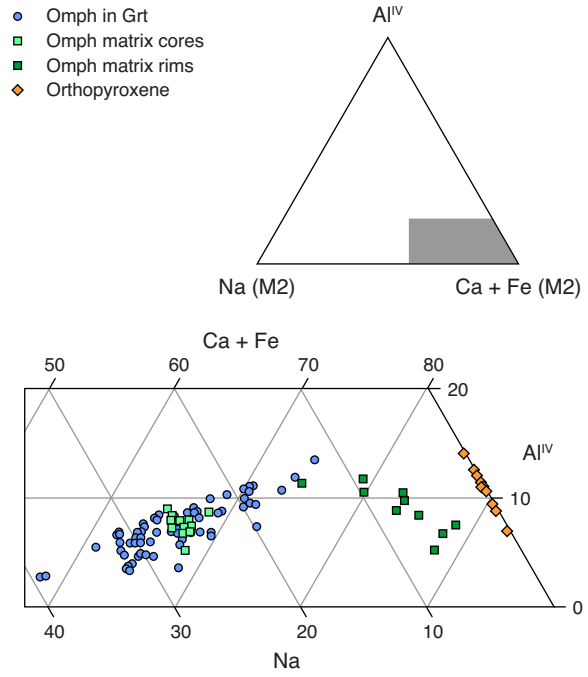

Figure 5.10: Details of non-quadrilateral substitutions in clinopyroxene. Ternary plot of non-quadrilateral substitutions in pyroxene in terms of Na (M2 site), Ca + Fe (M2 site) and Al^{IV}. Omphacites in garnet show a trend from high-Na to lower-Na accompanied by increasing Al^{IV}, related to increasing $Fe^{3+}Al^{IV}$ substitution (not shown). Matrix omphacites show a similar trend from Na-rich cores to Na-poor rims, accompanied by a minor increase in Al^{IV}. Orthopyroxenes show some Al^{IV} substitution.

may simply reflect the bulk composition of the rock.

The M2 mineral assemblage is interpreted to have comprised garnet (rims), diopside, plagioclase, biotite, pargasite, orthopyroxene, and ilmenite. This interpretation is based on the involvement of these phases in symplectic intergrowths and shared grain boundaries, although demonstrating equilibrium is difficult owing to the textural heterogeneity. Textures associated with the M2 assemblage are typical of retrogressed eclogites in which decompression led to breakdown of garnet and omphacite to form sodic plagioclase and other minerals. Diopside rims on omphacite and diopside + plagioclase symplectites, for example, can be explained by a generalized reaction like (*Schmitt*, 1963):

$$\mathrm{Omph} + \mathrm{Qtz} = \mathrm{Di} + \mathrm{Pl} \tag{5.1}$$

Similarly, plagioclase moats surrounding garnet can be explained by a reaction like:

$$\mathrm{Grt} + \mathrm{Omph} = \mathrm{Di} + \mathrm{Pl} \tag{5.2}$$

The presence of biotite throughout the matrix and replacing phengite inclusions in garnet can be explained by a reaction like:

$$\mathrm{Grt} + \mathrm{Phn} = \mathrm{Bt} + \mathrm{Qtz} \tag{5.3}$$

The presence of pargasite and orthopyroxene, the latter found within symplectites after omphacite and adjacent to plagioclase moats on garnet, can be explained by reactions like:

$$\mathrm{Grt} + \mathrm{Omph} + \mathrm{Qtz} + \mathrm{H2O} = \mathrm{Am(Parg)} + \mathrm{Pl} \tag{5.4}$$

and:

$$\mathrm{Grt} + \mathrm{Omph} + \mathrm{Qtz} = \mathrm{Opx} + \mathrm{Pl} \tag{5.5}$$

However, the presence of orthopyroxene + plagioclase symplectite adjacent to omphacite with no nearby (in section) garnet, suggests possible formation by a reaction like:

$$\text{Omph} = \text{Opx} + \text{Pl} \tag{5.6}$$

5.8 Thermobarometry

The Harøya coesite-eclogite provides a new opportunity to place quantitative constraints on the *P*–*T* history of the northern WGR. The *P*–*T* conditions of M1 metamorphism were estimated using two approaches. The first approach ('Fe-excluded') used the intersection of net-transfer reactions among the Mg-end-members of clinopyroxene and garnet, together with kyanite, phengite, and coesite:

$$\begin{aligned} 6\text{CaMgSi}_2\text{O}_6\ (\text{Di}) + 3\text{KAl2Si}_3\text{O}_{10}(\text{OH}_2)\ (\text{Ms}) = \\ \text{Mg}_3\text{Al}_2\text{Si}_3\text{O}_{12}\ (\text{Prp}) + 2\text{Ca}_3\text{Al}_2\text{Si}_3\text{O}_{12}\ (\text{Grs}) + \\ 3\text{KAlSi}_4\text{O}_{10}(\text{OH})_2\ (\text{Cel, i.e., leucophyllite}) \end{aligned} \tag{5.7}$$

$$\begin{aligned} \text{Mg}_3\text{Al}_2\text{Si}_3\text{O}_{12}\ (\text{Prp}) + 2\text{Ca}_3\text{Al}_2\text{Si}_3\text{O}_{12}\ (\text{Grs}) + 2\text{SiO}_2\ (\text{Coe}) = \\ 2\text{Al}_2\text{Si}_{\text{O5}}\ (\text{Ky}) + 3\text{CaMgSi}_2\text{O}_6\ (\text{Di}) \end{aligned} \tag{5.8}$$

This method is probably the best approach to quantifying equilibrium *P*–*T* conditions for eclogites (*Ravna and Terry*, 2004; *Hacker*, 2006) for two reasons: (1) it minimizes the effects of retrograde diffusion owing to the larger length-scale of net-transfer (grain-scale) versus exchange (grain-boundary-scale) reactions (*Hacker*, 2006); and, (2) it avoids the uncertainty inherent in estimating Fe^{3+} in minerals analyzed by EMP. The latter is a widely recognized issue with Fe^{2+}-Mg exchange thermometers and is especially problematic for omphacite because of its potential to deviate from ideal stoichiometry, which makes Fe^{3+} estimation based on charge balance constraints impossible (see *Ravna and Paquin*, 2003)

P–*T* estimates based on these reactions were calculated using THERMOCALC (version 3.33; *Holland and Powell*, 1998) with mineral activities (Table 5.5) calculated using the software AX (http://www.esc.cam.ac.uk/research/research-groups/holland/ax). We also used the spreadsheet of *Ravna and Terry* (2004), which uses expressions derived from the same thermodynamic database but using a different activity model

Stage	M1	M2
End-member	Activity	
Grt		
py	0.124	0.097
gr	0.049	0.0133
alm	0.024	0.061
Cpx		
di	0.5	0.73
hed	0.072	0.12
jd	0.4	0.039
Ms		
mu	0.47	
cel	0.18	
fcel	0.025	
Bi		
phl		0.22
ann		0.0068
east		0.038
Hbl		
tr		0.059
fact		0.000 016
ts		0.0003
parg		0.103
Opx		
en		0.51
fs		0.064
Fsp		
an		0.46
ab		0.64
Other	coe ky	q

Table 5.5: End-member activities and phases used in THERMOCALC calculations. End-members used by THERMOCALC are: py=pyrope; gr=grossular; alm=almandine; di=diopside; hed=hedenbergite; jd=jadeite; mu=muscovite; cel=celadonite; fcel=Fe-celadonite; pa=paragonite; phl=phlogopite; ann=annite; east=eastonite; tr=tremolite; fact=Fe-actinolite; ts=Tschermakite; parg=pargasite; en=enstatite; fs=ferrosilite.

for garnet (*Ganguly et al.*, 1996). The two approaches are similar but only THERMOCALC propagates minimum uncertainties to the calculated pressure and temperature (*Worley and Powell*, 2000; *Powell and Holland*, 2008). The *Ravna and Terry* (2004) expressions assume minimum uncertainties of ± 65°C and ± 0.3 GPa.

Maximum pressure and corresponding temperature for M1 (Table 5.4) were determined using the composition of clinopyroxene with the minimum activity of diopside, (a_{Di}^{Cpx}) (maximum Jd content), garnet with the maximum $(a_{Grs}^{Grt})^2 a_{Prp}^{Grt}$, and phengite with the maximum Si content, a_{Cel}^{Phn} (*Cuthbert et al.*, 2000; *Ravna and Terry*, 2004; *Young et al.*, 2007). Although we cannot demonstrate that these were equilibrium compositions, we argue that this approach is preferable over using texturally associated compositions (e.g., adjacent grains) because of the obvious retrograde diffusion in the sample.

The second approach ('Fe-included') used THERMOCALC's average *P*–*T* mode (avPT) to calculate the equilibrium *P*–*T* conditions based on reactions among all end-members of the M1 assemblage, with Fe^{3+} estimated from stoichiometry (using

the software AX). We also compared the results of the *Ravna and Terry* (2004) expressions with those of the garnet-clinopyroxene Fe^{2+}-Mg exchange thermometer of *Ravna* (2000), with Fe^{3+} in garnet and omphacite calculated as $3 - (Al + Ti + Cr)$ and $Na - (Al + Cr)$ atoms p.f.u., respectively. In each case we applied the Fe^{3+} estimation method used in the source papers; as noted above, all of these schemes are sensitive to uncertainties in Si p.f.u. calculated from EMP analyses and should be treated with caution (*Ravna and Paquin*, 2003). Nevertheless, consistency between the results of the Fe-included calculations and those of the Fe-excluded approach described above suggests that errors in calculating Fe^{3+} are not large enough to invalidate the results.

Each of the methods yields *P–T* estimates consistent with the presence of coesite in the sample (Fig. 5.11a; Table 5.6). The Fe-excluded approach using THERMOCALC yields *P–T* conditions of 2.96 ± 0.35 GPa/757 ± 73°C, while the *Ravna and Terry* (2004) expressions yield similar but somewhat higher conditions of 3.25 GPa/814°C, consistent with previously noted discrepancies (*Hacker*, 2006), and probably owing to the different garnet activity model. The Fe-included approach, using avPT mode, produces similar *P–T* conditions of 2.94 ± 0.33 GPa and 763 ± 73°C, while the garnet-clinopyroxene thermometer (*Ravna*, 2000) yields a temperature of 816°C at a pressure of 3.25 GPa (Fig. 5.11a; cf. results of *Ravna and Terry* (2004) method). The strong similarity between the Fe-excluded and Fe-included results suggests that the Fe^{3+} estimated for omphacite (and garnet) is approximately correct, perhaps owing to the apparently near-ideal stoichiometry of the omphacite (Table 5.3). Excluding kyanite from the peak assemblage (for reasons noted above) using avPT mode, yields 2.96 ± 0.35 GPa/797 ± 159°C, i.e., identical to the above estimates within uncertainty, with larger errors probably reflecting the reliance of the estimate on the inherently more uncertain Fe-end-members. The agreement among these methods supports our choice of equilibrium mineral compositions and suggests that the estimated *P–T* conditions of M1 metamorphism are robust within their uncertainties.

Equilibrium *P–T* conditions for M2 were estimated using avPT mode for the M2 assemblage biotite, clinopyroxene (diopside rims), garnet (rims), pargasite, plagioclase (rims), and orthopyroxene (Tables 5.4 and 5.5). Using reactions among all

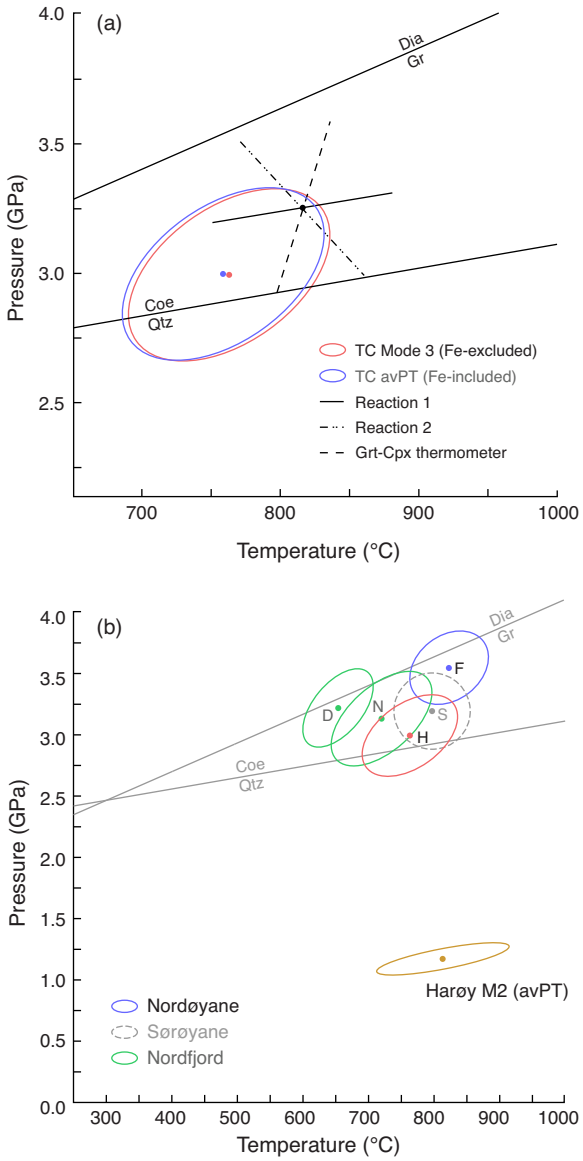

Figure 5.11: P–T results for coesite-eclogite. (a) P–T results for M1 calculated using THERMOCALC (ellipses) and the expressions of *Ravna and Terry* (2004) (lines), using mineral compositions from Table 5.4. THERMOCALC Fe-excluded and Fe-included estimates calculated using mode 3 and mode 2 (avPT) respectively, using end-member activities from Table 5.5. (b) P–T results for M2 calculated using THERMOCALC avPT mode, using data from Table 5.4; and comparison of peak (UHP) P–T conditions, recalculated from the literature, for selected garnet-clinopyroxene-phengite-kyanite-coesite/quartz eclogites from the Nordfjord/Stadlandet, Sørøyane, and Nordøyane UHP domains. Only THERMOCALC (Fe-excluded) results are shown. Nordfjord samples from *Ravna and Terry* (2004) (D; Drage) and *Young et al.* (2007) (N; Y1614B). Sørøyane estimate (S) from *Carswell et al.* (2003b), not recalculated and shown with assumed uncertainties of 0.25 GPa and 50°C. Nordøyane samples from *Terry et al.* (2000) (F; 1066b) and this study (H). See Fig. 5.2 for sample locations.

Stage	M1					M2	
Approach	Fe-excl.	Fe-incl.	Fe-incl.	Fe-excl.	Fe-incl.	All	Some
Method	TC mode 3	TC avPT	TC avPT	RT	RT/R	TC avPT	TC avPT
T (°C)	757	763	797	814	816	813	782
s.d.(T)	73	73	159	65	100	101	106
P (GPa)	2.96	2.94	2.96	3.25	3.25	1.15	1.13
s.d.(P)	0.35	0.33	0.35	0.3	0.3	0.13	0.13
cor.	0.465	0.466	0.391	-	-	0.767	0.766
sigfit	-	0.39	0.5	-	-	0.69	0.74
No. of reactions	4	4	3	-	-	10	8
end-members excluded	alm hed fcel	-	ky	-	-	-	fact ts

Table 5.6: Results of P–T calculations for M1 and M2 for Harøya coesite-eclogite. M1 conditions based on Fe-excluded (Fe-excl.) approach calculated using THERMOCALC (TC mode 3) and expressions of *Ravna and Terry* (2004) (RT). Estimates based on Fe-included (Fe-incl.) approach calculated using THERMOCALC (TC avPT) for assemblages with and without kyanite, and by combining Reaction 1 of *Ravna and Terry* (2004) with the garnet-clinopyroxene Fe^{2+}-Mg exchange thermometer of *Ravna* (2000) (RT/R). Correlation factor (cor.), sigfit, No. of reactions, and end-members excluded are THERMOCALC parameters. Uncertainties for the expressions of *Ravna and Terry* (2004) and *Ravna* (2000) are assumed. M2 conditions calculated using THERMOCALC avPT mode (TC avPT), with all end-members ('All'), and excluding end-members with the most uncertain activities ('Some').

end-members yields 1.15 ± 0.13 GPa/813 ± 101°C (Table 5.6; Fig. 5.11b). Excluding the most uncertain end-members (Fe-actinolite and tschermakite) yields a lower temperature estimate of 1.13 ± 0.13 GPa/782 ± 106°C. Calculating temperature at a fixed pressure of 1.15 GPa yields 798 ± 63°C.

5.9 Comparison with Previous Data

The P–T estimates for M1 metamorphism on Harøya are similar to peak-pressure conditions estimated for eclogites from across the WGR. For comparison, we recalculated the P–T conditions of selected eclogites with the same mineral assemblage from the Nordfjord/Stadlandet and Nordøyane UHP domains (Table D.13). Assuming minor analytical uncertainties, the differences among these estimates should reflect real differences in peak P–T conditions (*Worley and Powell*, 2000). The comparison (Fig. 5.11b) shows that the P–T conditions of M1 metamorphism on Harøyya were somewhat lower pressure, but within uncertainty of those for Nordfjord (3.12 ± 0.38 GPa/717 ± 77°C) and Fjørtoft (3.48 ± 0.29 GPa/822 ± 61°C) recalculated with the Fe-excluded approach using THERMOCALC. The expressions of *Ravna and Terry* (2004) yield somewhat higher conditions for Nordfjord (up to 3.21

GPa/765°C) and Harøya (3.25 GP/814°C), but lower pressures for Fjørtoft (3.16 GPa/849°C). Both sets of estimates are similar to the ∼2.7–3.8 GPa/∼820–850°C estimated for 'external' orthopyroxene eclogites from Nordøyane (*Carswell et al.*, 2006). The pressure of M1 metamorphism on Harøya does not appear to have reached the diamond stability field, apparently at odds with discoveries of microdiamond on Fjørtoft (*Dobrzhinetskaya et al.*, 1995; *van Roermund et al.*, 2002) and the nearby mainland (*Vrijmoed et al.*, 2008), and the higher-pressure estimates from orthopyroxene-bearing eclogites (*Carswell et al.*, 2006). There are several possible explanations for this discrepancy. (1) The retrograde diffusion in our sample could mean that peak mineral compositions were not preserved, making our P–T estimate a minimum. However, given the slopes of the net-transfer reactions used, a higher pressure estimate should result in a lower temperature. The close agreement between the temperatures estimated using the two approaches supports our choices of compositions and suggests that our pressure estimates are robust. (2) The eclogite P–T path could have passed through the diamond stability field, but if it reached peak temperature in the coesite field, mineral compositions would most likely record the higher T, lower P conditions. However, without constraints on the prograde path this possibility cannot be tested. (3) Finally, the eclogite might actually have experienced lower peak pressures than the nearby microdiamond-bearing rocks, implying that these units were juxtaposed during exhumation. The additional pressure of ∼0.5 GPa required to elevate the Harøya estimate to the diamond stability field would imply a difference of ∼15–20 km in burial depth. Specific structures that could have accommodated such offsets have not been documented in the area, but the pervasive post-M1 strain could have accommodated significant displacement and/or overprinted early structures. None of these explanations accounts for the much more dramatic difference between the P–T estimates for these eclogites and the conditions of ∼5.5–6 GPa/800–1000°C calculated for some garnet-peridotites from the northern WGR (e.g., *Vrijmoed et al.*, 2006; *Spengler et al.*, 2009). The latter are interpreted as representing Scandian metamorphism after these bodies were emplaced into Baltican crust, requiring subduction of Baltica to depths at least ∼75 km greater than those suggested by the eclogites. This discrepancy underscores the

need for more geochronological data from examples with well constrained petrological and field relations. The P–T estimates for M2 on Harøyya are consistent with previous estimates from Fjørtoft that indicate retrogression at ∼1.2 GPa/780°C during formation of the dominantly sinistral (top-west) fabrics (*Larsen et al.*, 1998; *Terry and Robinson*, 2003). Both are consistent with, but somewhat higher than estimates for amphibolite facies retrogression from Nordfjord (*Walsh and Hacker*, 2004; *Hacker et al.*, 2010), indicating that the WGR underwent broadly isothermal decompression.

5.10 Tectonic Implications

The discovery of coesite in Nordøyane confirms previous suggestions that the gneisses that underlie the northern WGR were subducted to UHP conditions during the Scandian orogeny. Peak metamorphic conditions reached ∼3 GPa/760°C, and were followed by broadly isothermal decompression to ∼1 GPa/813°C (Fig. 5.12a). The corresponding ages on Harøya are unknown, but are probably similar to the ∼410 Ma and ∼395 Ma ages of eclogite facies metamorphism and subsequent amphibolite facies sinistral extension documented elsewhere in Nordøyane from U–Pb geochronology (*Tucker et al.*, 2004; *Krogh et al.*, 2011).

Whether all three UHP domains in the WGR were exhumed together within a coherent volume of crust or formed discrete tectonic units remains unclear (see *Cuthbert et al.*, 2000; *Terry and Robinson*, 2004; *Root et al.*, 2005; *Hacker et al.*, 2010; *Krogh et al.*, 2011). The similarity in P–T conditions suggests that these widely separated eclogites underwent broadly similar tectonic histories. Regional isothermal decompression from UHP conditions is also consistent with exhumation of a large volume of crust according to thermal modeling (*Root et al.*, 2005). However, the gneisses of Nordøyane clearly underwent pervasive deformation at both eclogite- and amphibolite facies conditions as well as partial melting during exhumation (*Terry and Robinson*, 2003, 2004). If these rocks were exhumed as part of a single coherent body, that body must have been strongly affected by internal deformation and could not have behaved as a rigid slab.

The widespread partial melting apparent in the Baltica basement rocks on Harøya may have promoted exhumation by decreasing the viscosity and/or increasing the

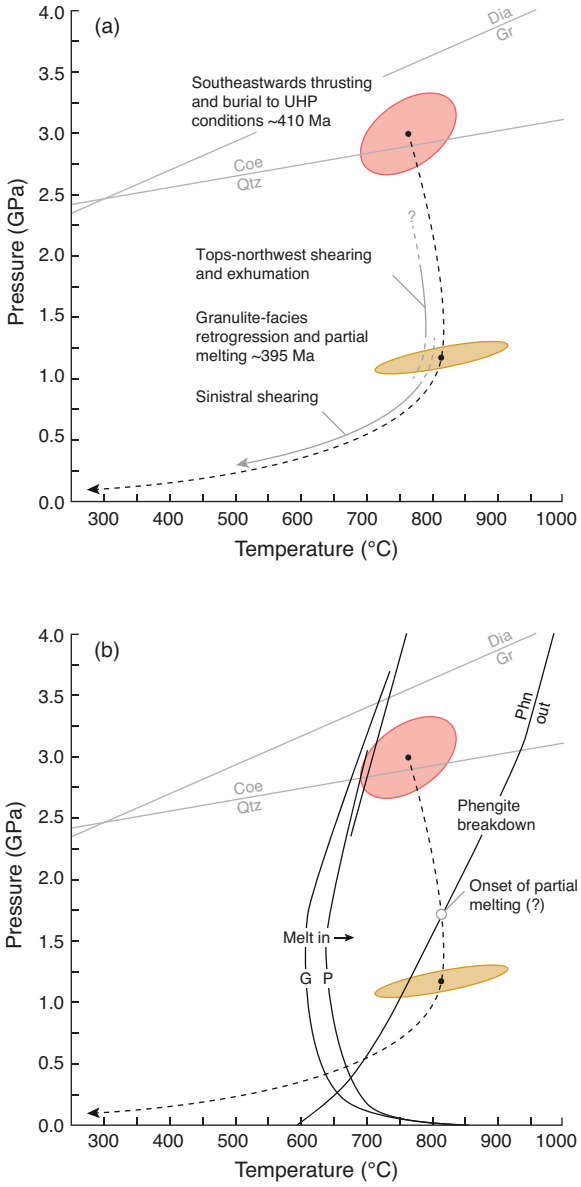

Figure 5.12: (a) Pressure–temperature–deformation history of the coesite-eclogite and surrounding gneiss on Harøya. Time constraints from *Krogh et al.* (2011) for rocks elsewhere on Nordøyane. (b) Comparison of P–T history with experimentally determined wet solidi for granitic (G; *Huang and Wyllie*, 1981) and pelitic rocks (P; *Nichols and Stern*, 1994; *Hermann and Spandler*, 2008), respectively. Phengite breakdown curve from *Hermann* (1997).

buoyancy of the subducted crust (*Raimbourg et al.*, 2007; *Warren et al.*, 2008). Recent work in the northern WGR has suggested that partial melting began at UHP conditions (*Gordon et al.*, 2011; *Labrousse et al.*, 2011), although whether this was the case on Harøya remains to be shown. The P–T conditions of M1 and M2 metamorphism were both above the temperature required for water-saturated partial melting of average crustal rocks (Fig. 5.12b), suggesting that partial melting could have begun during either stage. However, in the absence of an obvious source of fluids partial melting was more likely to have been driven by the breakdown of hydrous minerals like phengite or biotite (*Whitney et al.*, 2004). Comparison of our P–T path with experimental constraints on phengite stability in crustal rocks (Fig. 5.12b) (*Hermann*, 1997) indicates that partial melting resulting from phengite dehydration was more likely to have taken place during decompression than at UHP conditions. Some melting during decompression is strongly supported by our field observations on Harøya. Even a small proportion (7%) of interstitial melt would have dramatically reduced the strength of the subducted crust and therefore facilitated UHP exhumation (*Rosenberg and Handy*, 2005; *Warren et al.*, 2008; *Labrousse et al.*, 2011). A goal of future work in Nordøyane should be to constrain the age and conditions of partial melting and its relationship to UHP metamorphism and deformation.

5.11 Conclusions

1. The discovery of coesite-eclogite on Harøya confirms that the Baltica basement rocks underlying the northern WGR experienced UHP metamorphism during Scandian subduction.

2. The early coesite-eclogite facies (M1) mineral assemblage comprised garnet, omphacite, phengite, kyanite, rutile, coesite, and apatite. The later granulite facies (M2) mineral assemblage comprised garnet (rims), diopside, plagioclase, biotite, pargasite, orthopyroxene, and ilmenite.

3. Peak metamorphic conditions reached ∼3 GPa/760°C (M1), and were followed by isothermal decompression to ∼1 GPa/813°C (M2). Both stages are consistent with previous estimates from UHP eclogites from across the WGR.

4. Basement and supracrustal rocks on Harøya were pervasively deformed at amphibolite facies conditions during exhumation. Deformation involved an early phase of top-northwest shearing, possibly related to exhumation beneath normal-sense (top-northwest) shear zones. The dominant fabrics formed later during sinistral transtension.

5. Exhumation was accompanied by at least two stages of partial melting, the later one synchronous with extension at amphibolite facies. Whether early melting began at UHP conditions or during decompression is not clear, although our P–T estimates support the latter. In either case, melting may have played a critical role in the mechanics of UHP exhumation in the northern WGR.

5.12 Acknowledgements

JPB acknowledges support from a Natural Sciences and Engineering Research Council (NSERC) Canada Graduate Scholarship; HMS was supported by a Dalhousie Graduate Scholarship. Field and analytical work were funded by an NSERC Discovery Grant to RAJ. Field observations and cooperation of PR during this project, and field and petrologic investigations on Harøya and Finnøya, going back to 1992, were supported by the Geological Survey of Norway (NGU). Arne Solli of NGU provided digital topographic base maps. Mike Terry offered advice in the field and information on the use of petrologic programs. Greg Dunning offered advice in the field. Andrew Smye assisted with THERMOCALC calculations. Dan MacDonald assisted with EMP analyses. Clare Warren provided comments on the manuscript. Jorunn Skjelten provided superb accommodation on Harøya. Reviews from E.J.K. Ravna and S.J. Cuthbert, and editorial comments from D. Robinson improved this manuscript.

Chapter 6

Geochronology of Eclogites and Migmatites from Harøya

6.1 Introduction

Knowledge of the absolute age of deformation and metamorphism is fundamental to reconstructing the tectonic histories of exhumed ultrahigh-pressure (UHP) terranes. The discovery of the coesite-eclogite and associated migmatitic orthogneisses on Harøya prompted an attempt to constrain the absolute timing of these features using high-precision U–Pb geochronology of zircon and other accessory phases, coupled with trace element geochemistry of zircon. The objectives of this work were to determine:

1. the age of (ultra)high-pressure (U)HP metamorphism of eclogites from within the migmatitic Baltica basement orthogneisses underlying Harøya;

2. the age of subsequent exhumation to, and cooling of the eclogites and gneisses at crustal depths; and,

3. the timing of partial melting of the migmatitic orthogneisses, by determining the age of crystallization of partial melt, in particular whether melting occurred before, during, or after (U)HP metamorphism.

Of these, the third has the greatest potential for contributing to the understanding of the evolution of the WGR. Several workers have recently proposed that the Baltica basement gneisses underlying the northern WGR underwent Scandian partial melting, either at UHP conditions, or during their exhumation to crustal depths.

In either case, the consequent weakening of the crust would have had a profound effect on the mechanics of exhumation by assisting the flow of the crust from mantle depths or controlling the style of deformation at crustal levels (*Labrousse et al.*, 2011). However, there are no firm geochronological constraints from these rocks demonstrating the timing of partial melting with respect to eclogite facies metamorphism. The results of this investigation so far are, unfortunately, inconclusive, but have been included here for completeness and posterity.

6.2 Overview of U–Pb Geochronology

We begin with a brief overview of radiometric dating, U–Pb geochronology, the ID-TIMS method, and the application of these approaches to the dating of accessory phases in metamorphic rocks. The following is included a primer for non-specialists, and for a more thorough overview of the method and associated uncertainties readers are referred to *Mattinson* (1987), *Parrish and Noble* (2003), *Dickin* (2005), and references therein.

6.2.1 Radiometric Dating

Radiometric dating techniques are based on the law of radioactive decay (*Rutherford and Soddy*, 1902), which states that the rate of decay of a parent nuclide to a stable daughter product is proportional to the number of atoms, n, present at any time, t (*Rutherford and Soddy*, 1902; *Dickin*, 2005):

$$-\frac{dn}{dt} = \lambda n \tag{6.1}$$

where λ is a proportionality constant characteristic of the radionuclide in question, and is referred to as the decay constant. Following the derivation provided by *Dickin* (2005), and many others, the amount of daughter radionuclide after a certain time is given by:

$$D = D_0 + n(e^{-\lambda t} - 1) \tag{6.2}$$

Equation 6.2 states that the amount of daughter nuclide, D, after time, t, equals the initial amount of the daughter nuclide D_0, in addition to the amount produced by decay of the number of parent nuclides over a given time, t. This equation is the basis of most radiometric dating methods. The fundamental assumption underlying

its application is that the decay constant, λ, has not changed during Earth's history. This assumption is supported by several lines of evidence (details in *Dickin*, 2005). Other assumptions inherent in the U–Pb geochronology method are discussed below.

6.2.2 U–Pb Geochronology

Uranium–lead (U–Pb) geochronology is made possible by the radioactive decay of ^{235}U and ^{238}U to ^{207}Pb and ^{206}Pb, respectively. The daughter Pb isotopes are the final products of two complex decay chains (the actinium and uranium series respectively); however, because the half-lives of the intermediate products are relatively short, for timescales of several Myr they can be ignored (*Dickin*, 2005). There are two other stable Pb isotopes, ^{204}Pb, and ^{208}Pb, the latter produced by the decay of ^{232}Th and which forms the basis of U–Th–Pb geochronology. Of these, only ^{204}Pb is not produced by radioactive decay.

Taking the form of Equation 6.2, the concentration of radiogenic ^{206}Pb and ^{207}Pb in a mineral after time, t, can be expressed as (*Dickin*, 2005):

$$^{206}\mathrm{Pb}_f = ^{206}\mathrm{Pb}_i + ^{238}\mathrm{U}(e^{\lambda_{238}t} - 1) \tag{6.3}$$

$$^{207}\mathrm{Pb}_f = ^{207}\mathrm{Pb}_i + ^{235}\mathrm{U}(e^{\lambda_{235}t} - 1) \tag{6.4}$$

where Pb_f and Pb_i are the final and initial concentrations of the Pb isotopes respectively. Assuming that the mineral being dated does not incorporate Pb into its crystal structure at the time of formation, which may not always hold true but for which corrections exist, then these equations simplify to:

$$\frac{^{206}\mathrm{Pb}}{^{238}\mathrm{U}} = (e^{\lambda_{238}t} - 1) \tag{6.5}$$

$$\frac{^{207}\mathrm{Pb}}{^{235}\mathrm{U}} = (e^{\lambda_{235}t} - 1) \tag{6.6}$$

Alternatively, the ^{207}Pb/^{206}Pb ('lead–lead') age can be obtained by dividing the above two equations. Using these equations, the decay constants of ^{238}Pb and ^{235}Pb, and the ratios of the parent and daughter isotopes determined via mass spectrometry, one can calculate the age of a mineral. The most common U–Pb geochronometer is zircon, but baddelyite, monazite, rutile, and titanite are also used (*Parrish and Noble*, 2003). The decay constants of ^{238}U and ^{235}U are 1.55125

x 10^{-10} a^{-1} and 9.8485 x 10^{-10} a^{-1} respectively (*Jaffey et al.*, 1971). The resulting half-life, defined as the time required for half of the parent nuclide to decay to the final daughter product, for ^{238}U is ∼4.5 Gyr (similar to the age of Earth), compared to ∼0.7 Gyr for ^{235}U (*Dickin*, 2005).

6.2.3 Concordance and Discordance

The existence of two separate U decay series makes U–Pb dating among the most robust geochronological methods, because it provides an internal check on the consistency of ages. When the two ages agree (Equations 6.5 and 6.6), they are said to be concordant, and can therefore be interpreted as representing some geological event (e.g., crystallization or cooling of a mineral). When the two ages do not agree, they are termed discordant. The main assumptions inherent in interpreting concordant ages as geologically meaningful are that (*Dickin*, 2005):

1. the mineral being dated contains only radiogenic lead (inherited Pb is referred to as 'common' Pb;
2. there have been no gains or losses of U or Pb since the mineral crystallized;
3. there have been no gains or losses of intermediate daughter products;
4. proper corrections have been made for the initial common Pb and $^{206}Pb/^{207}Pb$ composition (assuming assumption 1 is broken); and,
5. the proper decay constants have been used.

In practice, one or more of these assumptions is usually broken, and much of the development of the method has focused on properly characterizing, and minimizing the resulting uncertainty (*Mattinson*, 1987; *Parrish and Noble*, 2003). For example, it is common for zircon analyses to contain some common Pb beyond that attributable to lab contamination (the 'lab blank'), and this requires correction based on the approximate age of the mineral (*Stacey and Kramers*, 1975).

The principles of concordance and discordance are best illustrated using the concordia diagram (Fig. 6.6; *Wetherill*, 1956), which plots a line of equivalent time in terms of $^{207}Pb/^{235}U$ against $^{206}Pb/^{238}U$. Concordant ages plot on this line, within their uncertainty, and discordant ages do not. Note that the slope of the concordia

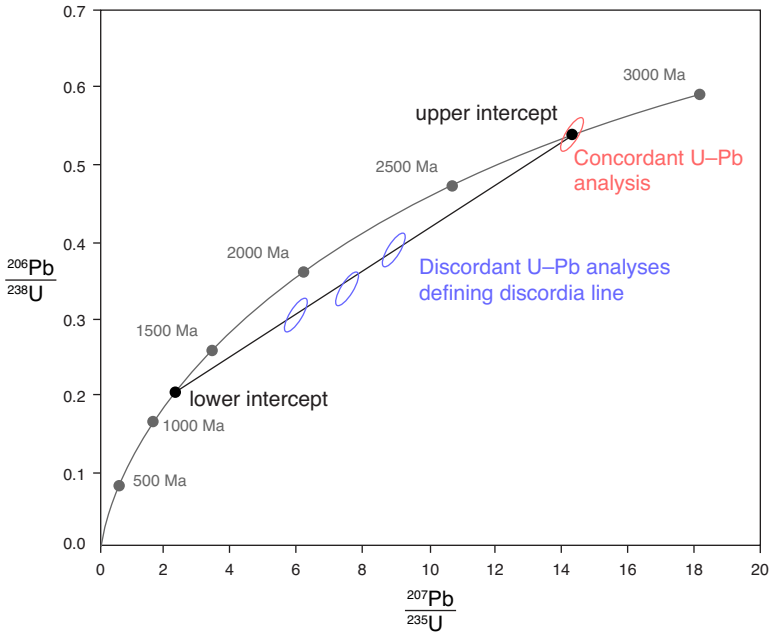

Figure 6.1: Schematic illustration of concordia diagram showing concepts described in text. The concordant analyses in this case corresponds to the upper intercept of the discordia line. This type of data could arise, for example, by dating a suite of igneous zircons with metamorphic overgrowths. The concordant age could be obtained by physically abrading the grains to remove the overgrowths. The lower intercept corresponds to the time of Pb loss or of younger metamorphic zircon growth.

curve increases dramatically toward the present day, which reflects the different half-lives of the two decay series. The differences in decay constants therefore mean that for younger rocks uncertainties in $^{207}Pb/^{235}U$ correspond to greater uncertainties in the calculated age (*Mattinson*, 1987).

The primary causes of discordance are Pb loss and inheritance, which each produce similar effects on the concordia diagram. Pb loss is now generally regarded as the result of radiation damage of zircons at relatively low temperatures (see *Davis et al.*, 2003; *Dickin*, 2005). Inheritance, in contrast, refers to the case in which the mineral being dated contains distinct domains representing two or more generations of growth. Although originally applied mainly to igneous zircons, with cores of grains inherited from the intruded host rock or protolith (*Davis et al.*, 2003), the term can also be applied to metamorphic rocks in which new zircon has overgrown an older, either igneous or metamorphic core. On the concordia diagram, multiple discordant analyses may define a line, whose validity can be checked statistically (e.g., *Davis*, 1982). The upper location at which this line intersects concordia is termed the upper intercept, and is typically taken as the age of original crystallization, whereas the lower intercept represents either the age of Pb loss, or of new mineral growth. The length of the segment from the lower intercept to a discordant analysis along the line corresponds to the magnitude of Pb loss, or in the case of new growth to the proportion of new radiogenic Pb versus old (*Wetherill*, 1956). Although common in the (early) literature, such ages are now considered insufficient for properly constraining the history of most metamorphic rocks.

Because the validity of an age is based on concordance, much of the early development of U–Pb geochronological methods focused on understanding and minimizing discordance, in particular in zircon analyses (*Davis et al.*, 2003). Several novel techniques involving physical or chemical pre-treatment of zircons in order to remove damaged discordant domains were developed, many by renowned Canadian geochronologist Tom Krogh, and applied to ID-TIMS (*Krogh*, 1973, 1982; *Davis et al.*, 2003; *Mattinson*, 2005). The technique employed depends on the geological problem. For example, to date metamorphic overgrowths, the outer rims may be physically separated from inherited cores (*Krogh et al.*, 2011), although this can be difficult. The more recent development of several microbeam techniques

(see *Košler and Sylvester*, 2003; *Müller*, 2003; *Foster*, 2010; *Fisher et al.*, 2010) has allowed geochronologists to side-step this problem by targeting different growth domains (e.g., *Rubatto and Hermann*, 2001), although the resulting analyses are generally less precise.

The crucial point that arises from the dependence of U–Pb geochronology on concordance is that accuracy (in the sense of the 'true' age of the geological event) and precision are inextricably linked. Low precision measurements with large error ellipses on the concordia diagram may appear concordant, despite actually lying along a discordia line. This poses a potential problem for dating rocks from UHP terranes, where the petrological evidence typically points to multiple stages of metamorphism in relatively short timespans (tens of Myr) (*Chopin*, 2003)

6.2.4 The ID-TIMS Method

U–Pb geochronology can be undertaken by two main types of method: Isotope-Dilution Thermal Ionization Mass Spectrometry (ID-TIMS), which involves the dissolution of and chemical separation of U and Pb from the mineral of interest, followed by physical loading into a mass spectrometer (*Parrish and Noble*, 2003; *Dickin*, 2005); and microbeam techniques in which a portion of the sample is ionized using a microbeam (ion beam or laser), followed by automatic transfer to a mass spectrometer. Each method has its advantages and disadvantages. It is generally agreed that ID-TIMS offers the greatest potential precision (typically producing ages with uncertainties of $\sim$0.1% versus 1% for Laser Ablation Inductively Coupled Mass Spectrometry (LA-ICPMS) (*Košler and Sylvester*, 2003), the least precise microbeam method), but that this precision comes at the expense of the sampling control and ability to target specific growth domains offered by microbeam methods. Ion beam techniques (e.g., Sensitive High Resolution Ion Microprobe; SHRIMP) can under certain conditions offer precision comparable to ID-TIMS, but the instruments themselves are expensive and consequently rare. For understanding rapid UHP rock exhumation, the precision afforded by ID-TIMS is ideal, because it can be used to distinguish between closely spaced metamorphic events. However, it must be demonstrated that the dated sample represents a distinct growth domain, which for zoned zircons requires physical separation of the domains. Microbeam techniques, in contrast, can be used to isolate each domain, but as noted above, at

the expense of precision.

The ID-TIMS method involves physical separation of the minerals to be dated from the rock sample, followed by chemical dissolution. An isotopic tracer, or 'spike' is then added to the dissolved sample prior to chemical separation of U and Pb, the concentrations of which are then measured separately using TIMS. The tracer is an isotopic mixture of known proportions, typically of ^{205}Pb (an artificial isotope; *Parrish and Krogh*, 1987)) and ^{235}U. The tracer/isotope ratio of the sample remains constant, counteracting potential fractionation resulting from incomplete recovery during chemical separation, and differences in measured concentrations resulting from different ionization efficiencies during TIMS analysis. The details of the method have changed somewhat but this basic approach has been used for several decades (*Parrish and Noble*, 2003; *Davis et al.*, 2003)

A multitude of studies exists concerning the treatment and propagation of analytical uncertainties in U–Pb geochronology using ID-TIMS, a full review of which is beyond the scope of this chapter. The main contributions to uncertainty, ignoring problems in interpretation arising from geological complexity, can be summarized as (*Mattinson*, 1987; *Parrish and Noble*, 2003):

1. random error arising from uncertainty in the ratio measurement and fractionation correction during mass spectrometry;

2. random error arising from uncertainty in the isotopic composition used in correcting for common Pb, taking into account the contribution from lab contamination (the 'lab blank'); and,

3. systematic error arising from uncertainty in the composition of the isotopic tracer, as well as the decay constants.

Generally speaking, overcoming these uncertainties depends largely on the ability to maintain a low lab blank, so that the correction for common Pb can be made accurately; the ID-TIMS method therefore requires extreme diligence in maintaining clean lab conditions.

6.2.5 U–Pb Geochronometers

Zircon ($ZrSiO_4$), monazite ($(Ce, La, Nd, Th)PO_4$), titanite ($CaTiSiO_5$), and rutile (TiO_2) are among the most commonly used U–Pb geochronometers (*Frost et al.*,

2001; *Hoskin and Schaltegger*, 2003; *Parrish and Noble*, 2003; *Meinhold*, 2010). Their usefulness results from their ubiquity in crustal rocks and tendency to incorporate U in their crystal structure. Of these, zircon is generally considered the most robust, because of its refractory nature and tendency to incorporate U, while virtually excluding Pb during crystallization (*Speer*, 1982; *Parrish and Noble*, 2003). In contrast, titanite and rutile typically incorporate more common Pb, and because of their composition are more likely to have been involved in metamorphic reactions. Consequently, titanite and rutile may provide useful information concerning the conditions of their formation, but are less likely than zircon to record multiple geological events.

The meaning of a U–Pb age depends on the geochronometer being used, and it has long been recognized that such ages do not necessarily record the time at which the mineral crystallized. The reason is that the dated mineral may have remained open to Pb diffusion for some period after its crystallization. *Dodson* (1973) recognized this, and coined the term 'closure temperature', defined as the temperature corresponding to the apparent age of a mineral. The key factors affecting the closure temperature of a species with a given diffusion rate in a mineral are the grain size and cooling rate. The latter poses a special problem for UHP terranes that have undergone rapid exhumation and cooling (*Warren et al.*, 2012b), because for a given grain size, closure temperature varies with the cooling rate. Consequently, for detailed studies of cooling history, an independent assessment of the cooling rate (which can be obtained via forward modeling, e.g., *Warren et al.*, 2012b) is required to interpret the meaning of U–Pb ages.

Closure temperatures for Pb diffusion in zircon, titanite, and rutile have been determined by calculation using experimentally determined diffusion coefficients, as well as by dating of rocks with well constrained metamorphic histories. However, the results of these two approaches are, at times, at odds with one another. The closure temperature of zircon (of a typical size), based on experimental data, is probably $\gtrsim$900°C (*Cherniak and Watson*, 2001). This agrees with a wide body of literature showing the preservation of inherited zircon in rocks that have undergone granulite facies or high-temperature (U)HP metamorphism (e.g., *Bingen et al.*, 2004; *Krogh et al.*, 2011). The closure temperatures for Pb diffusion in titanite and rutile

are not as well constrained. The closure temperature for titanite is lower than that of zircon, probably ∼650–700°C (*Cherniak*, 1993; *Scott and St-Onge*, 1995; *Frost et al.*, 2001). Rutile probably has the lowest closure temperature of the three, ∼550–620°C, although both lower and higher values have been proposed (see references in *Frost et al.*, 2001), and may overlap with that of titanite under certain conditions. The fact that these three minerals have somewhat different closure temperatures can be exploited to reconstruct different stages in the history of a metamorphic rock.

6.3 U–Pb Geochronology

6.3.1 Methods

U–Pb geochronology of samples from Harøya (Fig. 6.2) was performed at the Geochronology Laboratory in the Department of Earth Sciences, Memorial University of Newfoundland, following the methods summarized by *Sánchez-García et al.* (2008).

Following physical separation from the rock sample, zircon, titanite, and rutile grains were selected for analysis on the basis of morphology and optical clarity, following the examples of *Corfu et al.* (2003) and *Krogh et al.* (2011). Zircon grains with obvious cloudy or inclusion filled cores were avoided; however, later imaging using cathodoluminescence (CL) nonetheless revealed considerable internal complexity (see below). A total of 33 fractions were analyzed, comprising 24 zircon fractions from six samples, 4 rutile fractions from two samples, and 3 titanite fractions from one sample.

Zircons selected for analysis were subjected to an initial stage of annealing at 900°C for 36 hours, following the chemical abrasion approach of *Mattinson* (2005). Selected grains were then cleaned, loaded into Krogh-type TEFLON bombs (*Krogh*, 1973) with HF, and chemically etched at 200°C for 4 hours. Final selected zircon fractions were then washed in distilled HNO_3, doubly distilled H_2O, and then distilled acetone, prior to reloading into bombs. A mixed $^{205}Pb/^{235}U$ tracer was added, along with 15 drops of distilled HF, and the bombs were then placed in an oven at 210°C for 5 days to dissolve the zircons. Pb and U were extracted using the ion exchange chemistry procedure of *Krogh* (1973), modified by scaling the columns and reagent volumes to one tenth, in order to minimize the lab blank. The purified Pb and U were then collected in a clean beaker in a single drop of pure H_3PO_4. Titanite

and rutile fractions were treated to the same washing and dissolution procedure, but owing to the larger sample sizes the chemical separation procedure used the larger column sizes (*Krogh*, 1973).

Pb and U were added to silica gel and dilute H_3PO_4 and loaded onto Re filaments. Isotopic concentrations were measured on a multi-collector Finnigan MAT 262 thermal ionization mass spectrometer. The Faraday cups were calibrated using the NBS 981 Pb standard, and the ion counting SEM detector calibrated against a Faraday cup by measuring a known Pb isotopic ratio. Samples with low Pb concentrations (most eclogite zircons) were measured by peak jumping on the ion counter, with measurement times weighted according to the amounts of each mass present. U was measured by static double Faraday collection. A series of sets of data were measured in the temperature range 1400°C to 1550°C for Pb and 1550°C to 1640°C for U, and the best sets combined to produce a mean value for each ratio. The measured ratios are corrected for Pb and U fractionation of 0.1% amu and 0.03% amu respectively as determined from repeat measurements of NBS standards. The ratios were also corrected for laboratory procedure blanks (1–10 pg Pb, 0.3 pg U) and for common Pb above the laboratory blank calculated using the two-stage model of *Stacey and Kramers* (1975). The calculated ages used the decay constants of *Jaffey et al.* (1971).

Selected zircons representative of each fraction were mounted in epoxy and polished to reveal their cores. The mounted grains were then imaged using cathodoluminescence microscopy.

6.3.2 Eclogite Sample JB10-47

Sample JB10-47 was collected from a several-metre-long, tabular and foliated retrogressed eclogite body exposed on the southwestern coast of Harøya (Fig. 6.3a). The eclogite bodies there appear chaotically mixed within deformed migmatitic gneiss (Fig. 6.3b). Granitic pegmatites and leucosomes, locally with hornblende, have pooled in the necks of the boudinaged eclogites. The sample was chosen on the basis of its clear field relations with respect to the surrounding migmatite and cross-cutting pegmatites, as well as the size of the eclogite body–zircon is generally scarce in eclogite and as such a large volume of sample is typically required.

The eclogite consists of medium-grained garnet and omphacite, both with inclusions of rutile, with apatite and minor phengite included in garnet (Fig. 6.4a). Most of the omphacite has been transformed to clinopyroxene + plagioclase symplectite. Plagioclase, quartz, biotite, hornblende, and ilmenite (after rutile) are present within the matrix. Zircon is present within garnet and the matrix, indicating that it formed either prior to, or during eclogite facies metamorphism, although some may have formed later. The presence of rutile in both garnet and omphacite links it with the eclogite facies assemblage.

Physical disaggregation of sample JB10-47 yielded abundant clear, small (∼50–100 μm), multifaceted zircon grains. Their morphology is identical to 'soccerball' zircons typical of eclogites (*Corfu et al.*, 2003; *Krogh et al.*, 2011). Some larger, strongly metamict, prismatic zircons were also recovered, as were abundant, clear rutile grains.

Multiple fractions of the multifaceted zircon were selected for U–Pb geochronology on the basis of their morphology and clarity. The assumption was that these grains, with no optically distinguishable cores, formed entirely at eclogites facies conditions. However, subsequent CL imaging proved this assumption to be false. Unfortunately, the CL imaging of all zircons in this study was conducted after the initial round of analyses. Had it been done initially, alternative measures could have been taken to target specific growth domains.

The internal structure of the multifaceted zircons revealed by CL imaging is remarkably consistent (Fig. 6.5a). Of over a hundred grains imaged, all contain generally homogeneous to mottled cores surrounded by homogeneous rims, the latter typically 10–20 μm wide. In most grains, the cores and rims are separated by a thin, discontinuous bright CL rim. The cores lack any form of oscillatory zoning. Many of the rims contain inclusions of rutile and apatite.

Six zircon fractions, comprising from 1 to 7 small soccerballs, each yielded highly discordant ages (Fig. 6.6). Remarkably, some of the these analyses overlap, reinforcing the consistency of internal structure observed using CL imaging. The discordant ages do not define a statistically valid line, but a line anchored at ∼413 Ma, the approximate age of eclogites on Nordøyane (*Krogh et al.*, 2011), projects toward an upper intercept of ∼960 Ma (Fig. 6.6a).

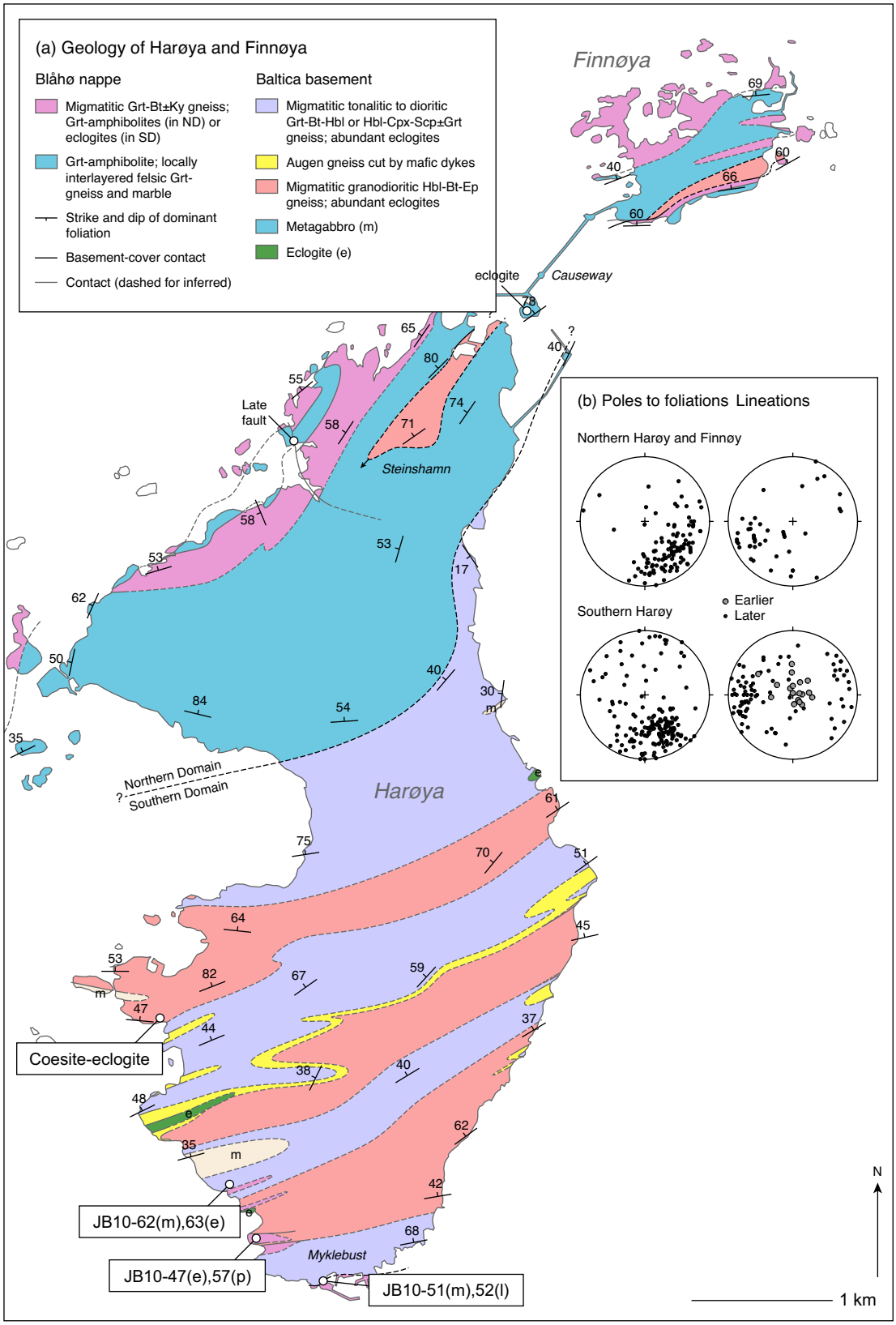

Figure 6.2: (a) Geological map of Harøya with U–Pb sample locations. Labels show location of coesite-eclogite and geochronology sample locations. e=eclogite, l=leucosome, m=migmatite, p=pegmatite. (b) Equal area stereographic plots of structural data.

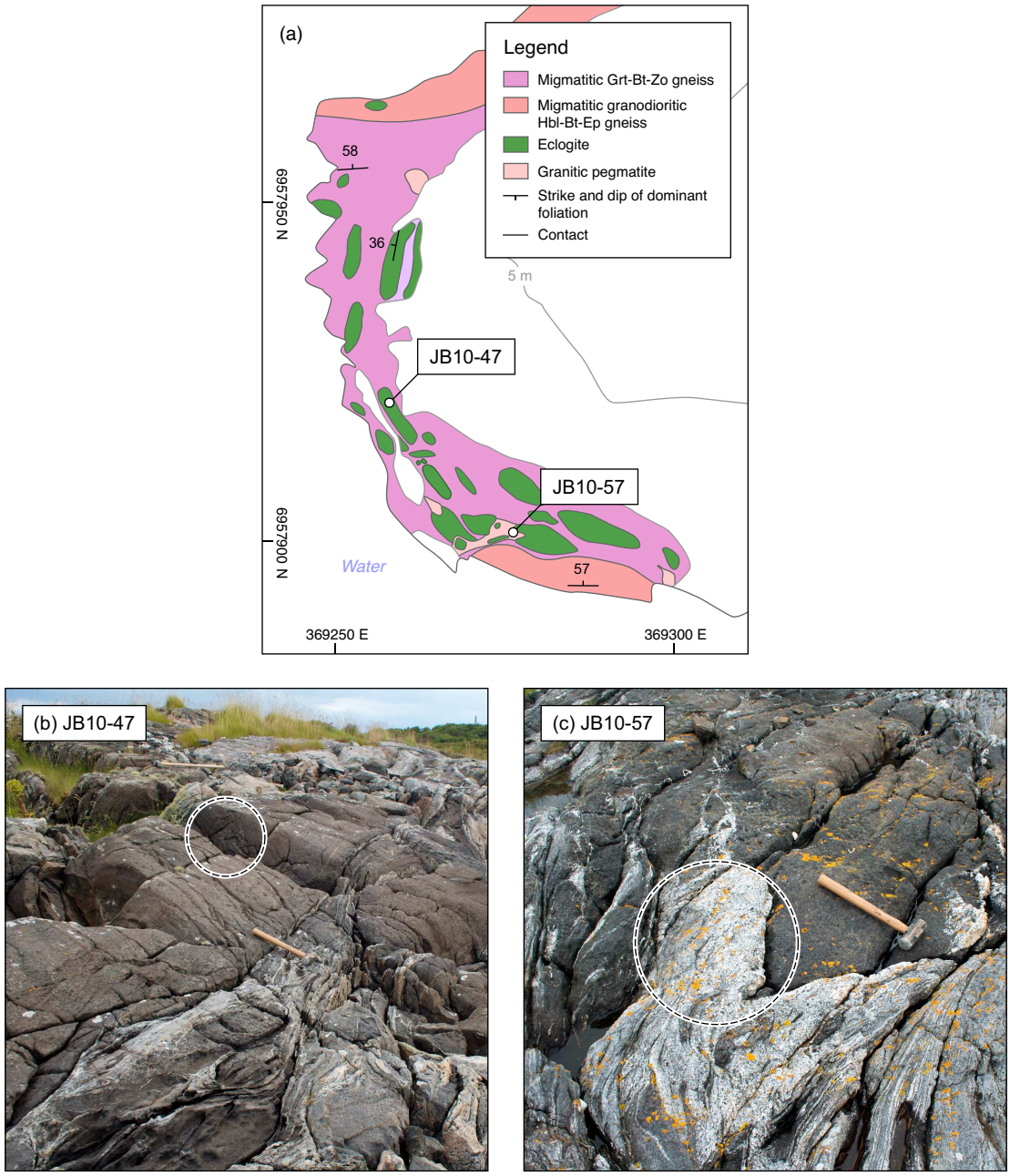

Figure 6.3: (a) Outcrop geological map and photographs showing setting of U–Pb geochronology samples JB10-47 and JB10-57. (b) Sample JB10-47 is from a large, tabular eclogite body hosted by strongly deformed (chaotic textured) migmatitic gneiss. (c) Sample JB10-57 is from a syn-extensional 'fish-mouth' boudin neck pegmatite formed against a large eclogite body. Circles in photographs indicate approximate sample locations.

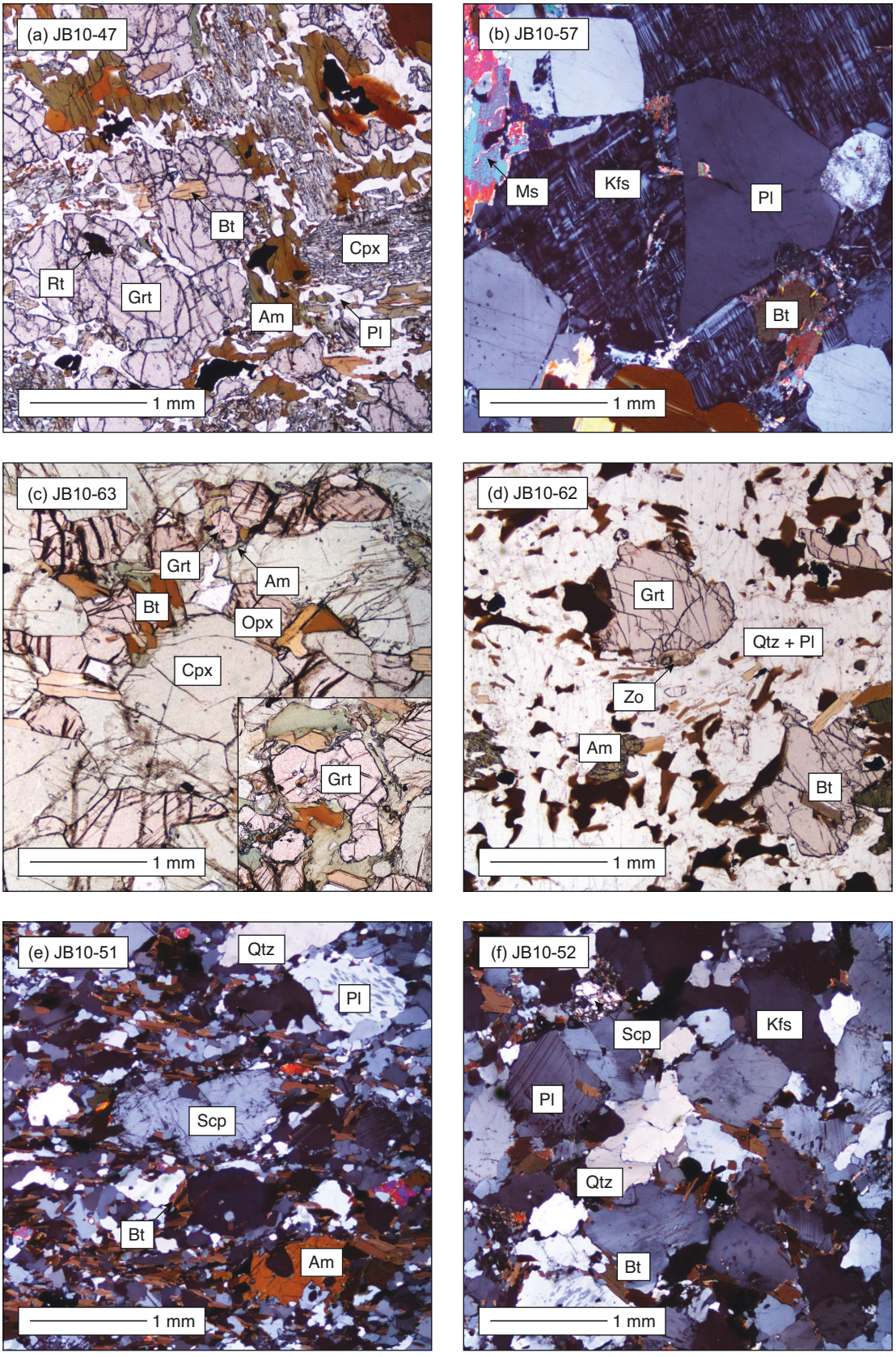

Figure 6.4: Thin section photographs of geochronology samples presented in order of discussion in text.

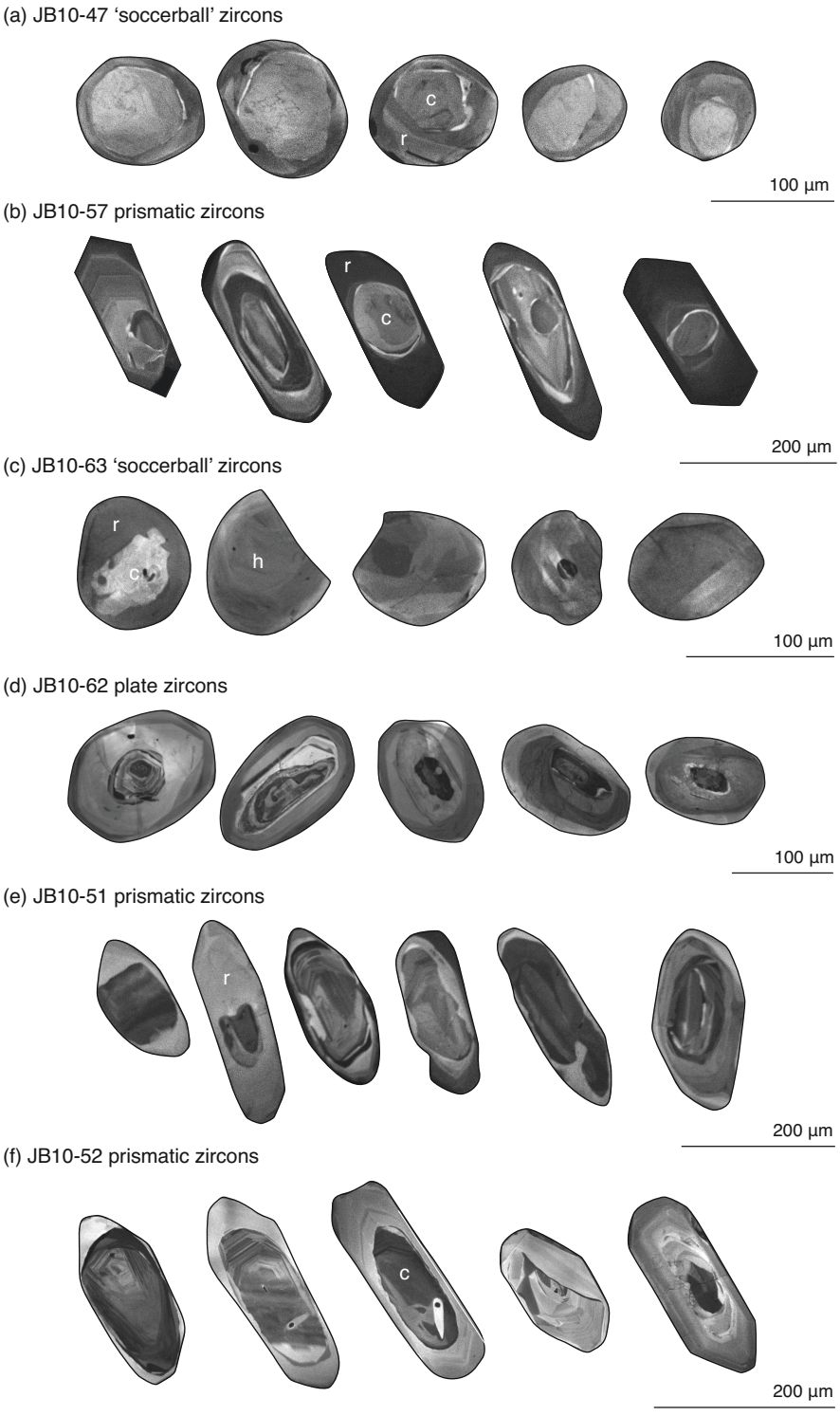

Figure 6.5: Cathodoluminescence images of zircons representative of analyzed fractions from samples. See text for details. c=core; r=rim; ir=inner rim; or=outer rim; h=homogeneous domain.

Sample JB10-47 also yielded abundant clear to variably altered prismatic rutile. Two fractions, comprising 60 and 100 grains, each yielded concordant ages of 377.8 ± 2.2 Ma and 378.4 ± 2.5 Ma. The mean $^{206}Pb/^{238}U$ age of the two analyses is 378 ± 1.6 Ma (Fig. 6.6b).

6.3.3 Note Added In Press

Additional geochronology results were obtained following defence of this thesis. Sample JB10-102 is a relatively fresh eclogite from the eastern coast of Harøya within the central belt of granodioritic migmatite. The sample yielded abundant small clear zircon balls. U–Pb analysis of several multigrain fractions (2–4 grains) following the methods outlined above yielded several discordant ages. The ages define a line extending from the upper intercept at 1645 ± 10 Ma to 403 ± 10 Ma. Based on the zircon morphology and previous results, the lower intercept is tentatively interpreted as the age of eclogite facies metamorphism.

These results are highly interesting for two reasons. First, existing zircon ages from the northern WGR are generally >410 Ma (*Krogh et al.*, 2011), which would make this the youngest eclogite found within the region. Second, the lower intercept for sample JB10-47, also interpreted as the age of eclogite facies metamorphism, is 413 ± 10 Ma. Although more precise data are required to confirm this, it is possible that samples JB10-47 and JB10-102 underwent eclogite facies metamorphism up to 10 Myr apart. If true, this would imply either that eclogites within a single subducted unit underwent transformation to eclogite at very different times, owing for example to the availability of fluids, or alternatively, that these units were buried to (U)HP conditions at different times and juxtaposed during later exhumation.

Table 6.1: U–Pb analytical data for Harøya geochronology samples.

		Concentration (ppm)		Measured	Corrected atomic ratios								Age (Ma)		
Fraction	Weight (mg)	U	Pb^*	Pb_c (pg)	$\frac{^{206}Pb}{^{204}Pb}$	$\frac{^{208}Pb}{^{206}Pb}$	$\frac{^{206}Pb}{^{238}U}$	2σ	$\frac{^{207}Pb}{^{235}U}$	2σ	$\frac{^{207}Pb}{^{206}Pb}$	2σ	$\frac{^{206}Pb}{^{238}U}$	$\frac{^{207}Pb}{^{235}U}$	$\frac{^{207}Pb}{^{206}Pb}$
JB10-47															
Z1 7 sml balls	0.004	1008	84.6	2	11435	0.0387	0.08873	46	0.7597	36	0.06210	16	548	574	677
Z2 7 balls	0.004	594	48.9	2	5029	0.0349	0.08726	56	0.7408	44	0.06157	22	539	563	659
Z3 6 sml balls	0.003	567	47.2	2	4243	0.0418	0.08782	70	0.7462	52	0.06162	26	543	566	661
Z4 4 sml balls	0.001	337	26.7	8	306	0.0344	0.08422	46	0.7068	108	0.06087	82	521	543	635
Z5 4 sml balls	0.001	154	12.0	7	171	0.0321	0.08308	82	0.6867	242	0.05995	190	514	531	602
Z6 1 sml ball	0.000	100	9.1	3	75	0.0452	0.09573	212	0.7852	1114	0.05948	784	589	588	585
R1 100	0.200	162	8.8	95	1307	0.0011	0.06035	36	0.4511	26	0.05421	12	378	378	380
R2 60	0.120	129	7.1	92	656	0.0003	0.06046	40	0.4508	32	0.05408	20	378	378	374
JB10-51															
T1 40 yellow	0.080	403	24.1	2118	77	0.0786	0.06153	22	0.4543	42	0.05355	42	385	380	352
T2 50 yellow	0.100	646	38.9	3548	87	0.1119	0.06008	32	0.4477	48	0.05405	48	376	376	373
T3 60 yellow	0.120	562	40.3	3689	101	0.0913	0.07258	44	0.5794	72	0.05790	56	452	464	526
Z1 2 prism tips	0.002	79	8.1	16	87	0.0242	0.10930	92	1.0541	682	0.06995	414	669	731	927
Z2 2 prism tips	0.002	335	49.8	18	370	0.0441	0.15422	90	1.6188	164	0.07613	64	925	978	1098
Z3 2 prism tips	0.002	93	7.7	11	113	0.0334	0.08795	66	0.8410	308	0.06935	232	543	620	909
JB10-52															
Z1 1 prism tip	0.002	727	165.6	2	7794	0.1649	0.21098	182	2.6032	204	0.08949	34	1234	1302	1415
Z2 2 prism tips	0.002	573	77.3	3	3245	0.0252	0.14315	60	1.3927	52	0.07056	22	862	886	945
Z3 2 prism tips	0.002	303	46.9	2	2622	0.0600	0.15781	90	1.8029	78	0.08286	34	945	1047	1266
JB10-57															
Z1 1 prism	0.002	10662	692.8	4	19417	0.0090	0.07088	50	0.5628	38	0.05758	14	441	453	514
Z2 3 prisms	0.004	3314	334.8	12	7786	0.0795	0.10155	76	1.0799	80	0.07713	6	623	744	1124
Z3 2 prisms	0.003	1543	222.9	4	9397	0.1098	0.14033	74	1.6772	90	0.08668	8	847	1000	1353
Z4 1 prism tip	0.002	2181	123.0	15	858	0.0047	0.06196	32	0.4642	38	0.05434	36	388	387	385
Z5 2 prism tips	0.002	2132	120.2	18	945	0.0043	0.06196	32	0.4632	36	0.05422	34	388	386	380
Z6 2 prism tips	0.002	1748	98.5	133	120	0.0025	0.06206	50	0.4600	96	0.05376	98	388	384	361
JB10-62															
Z1 4 plates	0.004	138	11.1	5	608	0.0481	0.08440	42	0.8009	60	0.06882	44	522	597	893
Z2 6 plates	0.006	139	13.5	7	786	0.0350	0.10193	62	1.0697	80	0.07611	46	626	739	1098
Z3 7 plates	0.007	152	15.0	12	592	0.0457	0.10206	68	1.0763	94	0.07649	50	626	742	1108
TZ1 45	0.090	992	139.0	97	7470	0.1770	0.13874	176	1.6417	208	0.08582	6	838	986	1334
TZ2 40	0.080	1222	189.7	41	22251	0.1375	0.14729	92	1.7780	112	0.08755	4	886	1037	1373

Continued on next page

		Concentration (ppm)		Measured	Corrected atomic ratios								Age (Ma)		
Fraction	Weight (mg)	U	Pb^*	Pb_c (pg)	$\frac{^{206}Pb}{^{204}Pb}$	$\frac{^{208}Pb}{^{206}Pb}$	$\frac{^{206}Pb}{^{238}U}$	2σ	$\frac{^{207}Pb}{^{235}U}$	2σ	$\frac{^{207}Pb}{^{206}Pb}$	2σ	$\frac{^{206}Pb}{^{238}U}$	$\frac{^{207}Pb}{^{235}U}$	$\frac{^{207}Pb}{^{206}Pb}$
R1 40 grains	0.080	20	1.1	55	130	0.0131	0.06012	76	0.4410	152	0.05320	172	376	371	337
R2 60 grains	0.120	46	2.6	72	307	0.0175	0.06030	30	0.4481	32	0.05390	32	377	376	367
JB10-63															
Z1 2 balls	0.002	759	197.5	2	10490	0.2928	0.21780	110	2.8644	136	0.09538	20	1270	1373	1536
Z2 4 balls	0.002	291	55.2	2	2705	0.2294	0.16701	198	2.0756	236	0.09014	46	996	1141	1428
Z3 6 balls	0.003	259	47.4	3	2874	0.2158	0.16287	70	2.0090	88	0.08946	30	973	1119	1414

6.3.4 Granitic Pegmatite Sample JB10-57

Sample JB10-57 was collected from a deformed granitic pegmatite within the neck of a boudinaged eclogite, at the same outcrop as eclogite sample JB10-47 (Fig. 6.3). Where adjacent to eclogites, the pegmatite locally contains Hbl, although it was not found in thin section. The pegmatite is locally strongly deformed, and has been transposed into the foliation at the southern end of the outcrop. The deformation of, and association of the pegmatite, with boudinaged retrogressed eclogites suggests that it crystallized during and prior to the end of the sinistral shearing event that affected the study area (Chapter 5).

The pegmatite consists of coarse-grained quartz, K-feldspar, plagioclase, and biotite (Fig. 6.4b). Biotite is locally replaced by muscovite. Zircon is present throughout the sample, most obviously as inclusions in biotite.

The sample yielded abundant clear, euhedral prismatic zircons. Some of these exhibit optically distinguishable cores marked by inclusions, and the first analytical fractions included only clear, apparently core-free grains. However, CL imaging again revealed that representative, apparently core-free grains show considerable complexity in internal structure, most including inherited cores (Fig. 6.5b). The inherited cores are generally oscillatory zoned, although some exhibit more patchy or sector zoning. Many exhibit embayed boundaries. The surrounding cores are mostly homogeneous and generally, although not always, darker in CL.

Three whole grain fractions, comprising from 1 to 3 euhedral prisms, each yielded discordant analyses. Following this, three additional fractions comprising from 1 to 2 physically separated prism tips were analyzed, each yielding a concordant age, with a mean $^{206}Pb/^{238}U$ age of 388 $\pm$ 1.3 Ma (Fig. 6.6c).

6.3.5 Eclogite Sample JB10-63

Sample JB10-63 was collected from a metre-scale eclogite body lying within strongly deformed migmatitic gneiss on the west coast of Harøya north of samples JB10-47/57 (Fig. 6.7). The eclogites there also form chaotically distributed pods within the migmatite host (Fig. 6.7a,b). Toward the north side of the outcrop, both rock types have been transformed to fine-grained mylonite with a subhorizontal lineation.

The eclogite consists of relatively well preserved garnet, omphacite, orthopyroxene,

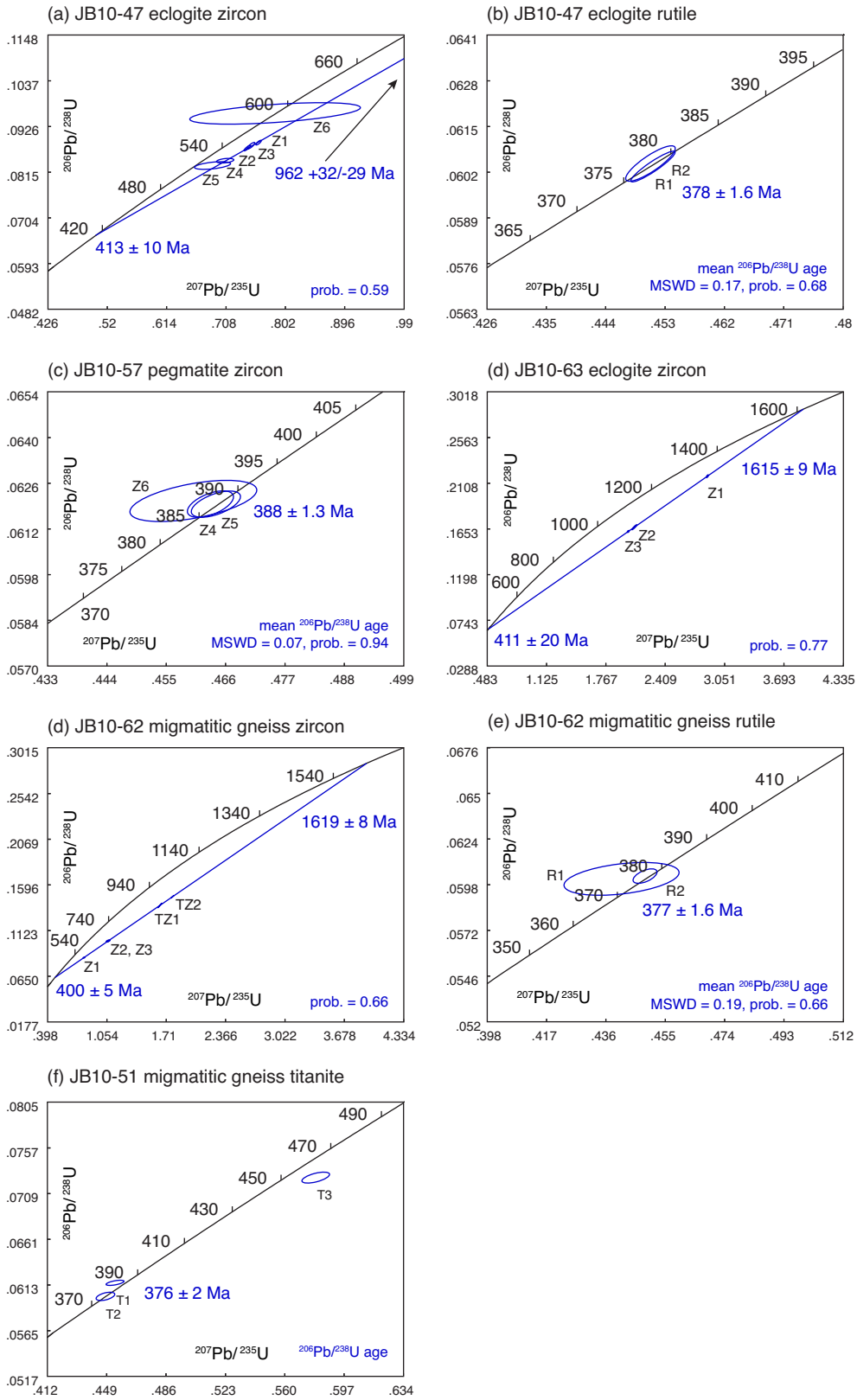

Figure 6.6: Concordia diagrams illustrating results of U–Pb geochronology. Zircon analyses from samples JB10-51 and JB10-52 are omitted. Labels Z1, R1, T1, etc., refer to zircon, rutile, and titanite analytical fractions listed in Table 6.1.

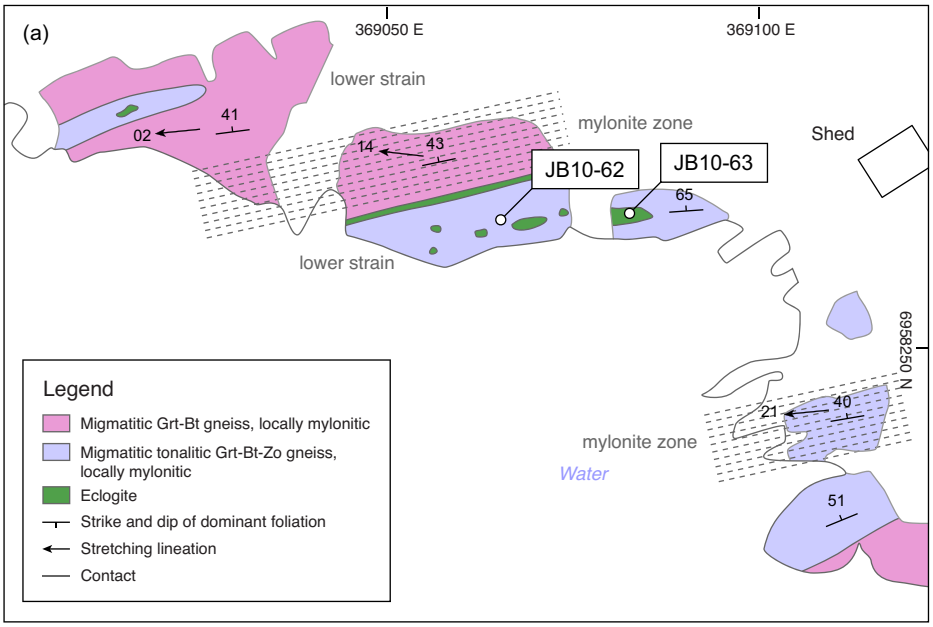

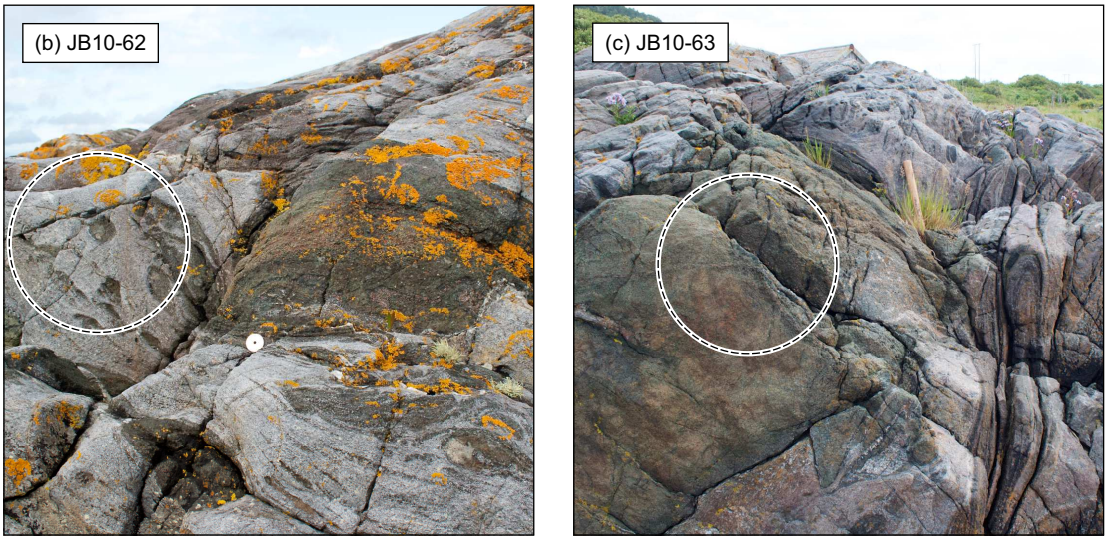

Figure 6.7: (a) Outcrop geological map and photographs showing setting of U–Pb geochronology samples JB10-62 and JB10-63. (b) Sample JB10-62 is from a highly deformed migmatitic gneiss that contains abundant eclogite pods. (c) Sample JB10-63 is from a large eclogite pod within the migmatitic gneiss. Circles in photographs indicate approximate sample locations.

biotite, and rutile (Fig. 6.4c). Some omphacite grains have undergone partial transformation to clinopyroxene + plagioclase symplectite. Garnet is partly replaced by amphibole and plagioclase. Zircon is present within garnet, omphacite, and orthopyroxene, implying crystallization prior to or during eclogite facies metamorphism.

Similar to the other eclogite, the sample yielded both anhedral prismatic zircons and rounded 'soccerball' zircons, although fewer than sample JB10-47. CL imaging of the soccerballs revealed considerable variety in internal texture (Fig. 6.5c). Some grains appear homogeneous in CL. Others contain highly irregular, embayed cores lacking any oscillatory zoning, while others appear sector zoned, but lacking any clear core or rim.

Three whole grain fractions, comprising from 2 to 6 soccerballs, each yielded discordant analyses. The analyses define a discordia line, extending from 411 ± 20 Ma to 1615 ± 9 Ma (77% probability of fit) (Fig. 6.6d).

6.3.6 Migmatitic Grt-Bt Gneiss Sample JB10-62

Sample JB10-62 was collected from the migmatitic gneiss surrounding eclogite sample JB10-63 (Fig. 6.7a). The migmatitic gneiss is medium-grained and strongly deformed, even where not converted to fine-grained mylonite (Fig. 6.7c).

The sample consists of medium-grained porphyroblasts of garnet and zoisite within a quartzo-feldspathic matrix (Fig. 6.4d). Biotite and hornblende are present throughout the matrix, the former defining a moderate schistosity. The quartzo-feldspathic matrix is deformed, exhibiting strongly embayed grain boundaries (indicative of grain boundary migration), and elongate, mosaic-textured deformed quartz grains. Locally preserved quartz/plagioclase films on embayed garnet grains, graphic quartz intergrowths in feldspar, and relict interstitial melt attest to earlier partial melting (Fig. 6.8).

The sample yielded abundant zircons, including clear euhedral prisms and subhedral prismatic 'plates'. Of these, the plates were selected for TIMS analysis on the basis of their clarity and morphology. CL imaging of the plates revealed relatively consistent internal textures characterized by complex inherited cores surrounded by homogeneous to zoned rims (Fig. 6.5d). Some grains exhibit embayed, oscillatory zoned cores surrounded by homogeneous darker CL rims (inner rims), themselves surrounded by brighter CL rims (outer rims), perhaps implying more than two stages

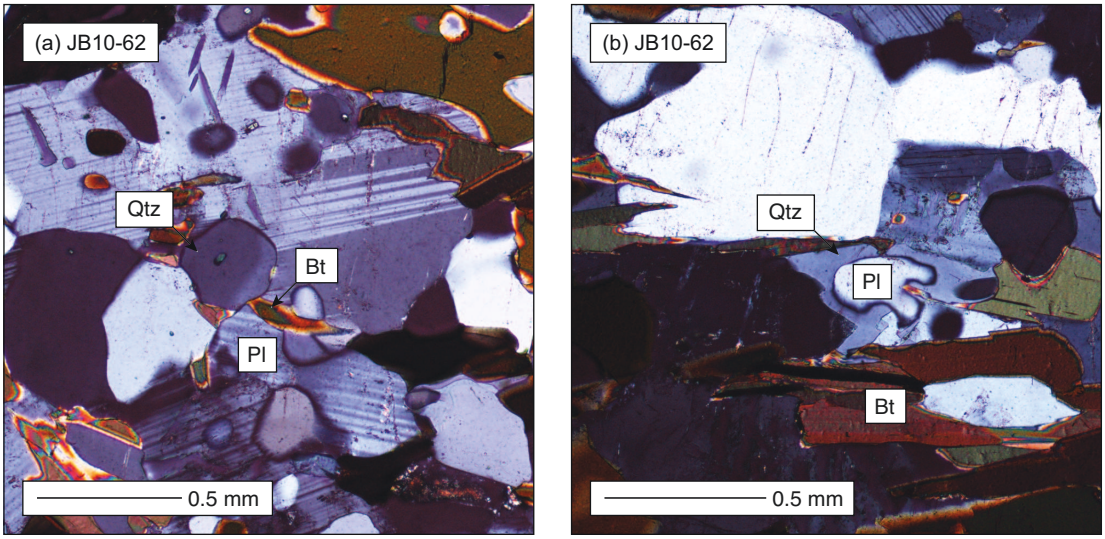

Figure 6.8: Thin section photographs showing partial melt textures in sample JB10-62. (a) Rounded quartz and plagioclase grains defining triple junction, with interstitial biotite, are reminiscent of incipient partial melt features in many migmatites (*Sawyer*, 1999). (b) Interstitial quartz (former melt?) surrounding plagioclase.

of metamorphic zircon growth. For the purposes of interpreting the trace element geochemistry we assumed that the few homogeneous light CL grains represented the same stage of growth as the light CL outer rims on more complex grains (see below).

Three whole grain fractions, comprising from 2 to 6 prismatic plates, each yielded discordant analyses. An additional two fractions comprising 40 and 45 grains were analyzed on the assumption that they were titanites, but instead turned out to be zircon, and gave discordant analyses (fractions 'TZ'). The analyses define a discordia line, extending from 400 ± 5 Ma to 1619 ± 8 Ma (66% probability of fit) (Fig. 6.6d).

Two rutile analyses, comprising 40 to 60 clear prismatic rutiles, yielded discordant and concordant analyses, respectively. The concordant analysis has a $^{206}Pb/^{238}U$ age age of 377 ± 1.6 Ma (Fig. 6.6e).

6.3.7 Migmatitic Tonalitic Gneiss Sample JB10-51

Sample JB10-51 was collected from a deformed migmatitic tonalitic gneiss on the southern tip of Harøya, in Myklebust (Fig. 6.9a). The gneiss (deformed dioritic migmatite) hosts several orthopyroxene-bearing eclogites (Fig. 6.9b). Elsewhere on the island this unit displays abundant interconnected leucosomes suggesting a considerable degree of partial melting. However, in Myklebust the unit is strongly

deformed, with a porphyroclastic texture and a subhorizontal lineation likely related to late, relatively low-temperature shearing. The dioritic migmatite is juxtaposed to the south against a fine-grained, garnet-porphyroclastic mylonite, which may represent a strongly deformed part of the Blåhø nappe. The latter mylonites are locally cut by leucosomes folded about subhorizontal axes (Fig. 6.9c).

The sample consists of coarse-grained porphyroclasts of plagioclase and scapolite within a fine-grained quartzo-feldspathic matrix, with hornblende, biotite and minor zoisite (Fig. 6.4e). Biotite forms a spaced schistosity. K-feldspar is rare. Garnet and clinopyroxene, abundant in less deformed parts of the same unit, are rare to absent. Leucosomes in less deformed parts contain plagioclase, scapolite, and hornblende. Feldspars exhibit graphic quartz intergrowths. Zircon is present throughout the matrix, but whether it is included in earlier phases (e.g., garnet) has not been determined. Titanite is present throughout the matrix.

The sample yielded abundant, clear prismatic zircons. Similar to sample JB10-57, CL imaging revealed these to have a considerable variety of internal textures (Fig. 6.5e). All imaged grains show inherited cores, some oscillatory zoned, others sector zoned. The rims are generally brighter in CL, and either homogeneous or sector zoned.

Three fractions, each comprising 2 physically separated zircon tips, yielded discordant analyses. The results do not define a discordia line.

Three titanite fractions, each comprising 40 to 60 grains, yielded two discordant and one concordant set of ages. The one concordant $^{206}Pb/^{238}U$ age is 376 ± 2 Ma (Fig. 6.6f).

6.3.8 Cross-cutting Leucosome Sample JB10-52

Sample JB10-52 was collected from a thin band of cross-cutting leucosome collected from within the top-northwest shear zone at the southern end of Myklebust, metres across strike from sample JB10-51 (Fig. 6.9). The leucosome cuts the early mylonitic fabric, but is also locally folded into concordance with it, indicating that it formed during or after the top-northwest shearing event that affected this locality (*Butler et al.*, 2012).

The sample, in thin section, consists of granitic leucosome with minor quartzo-feldspathic melanosome. The latter may represent some of the surrounding host rock

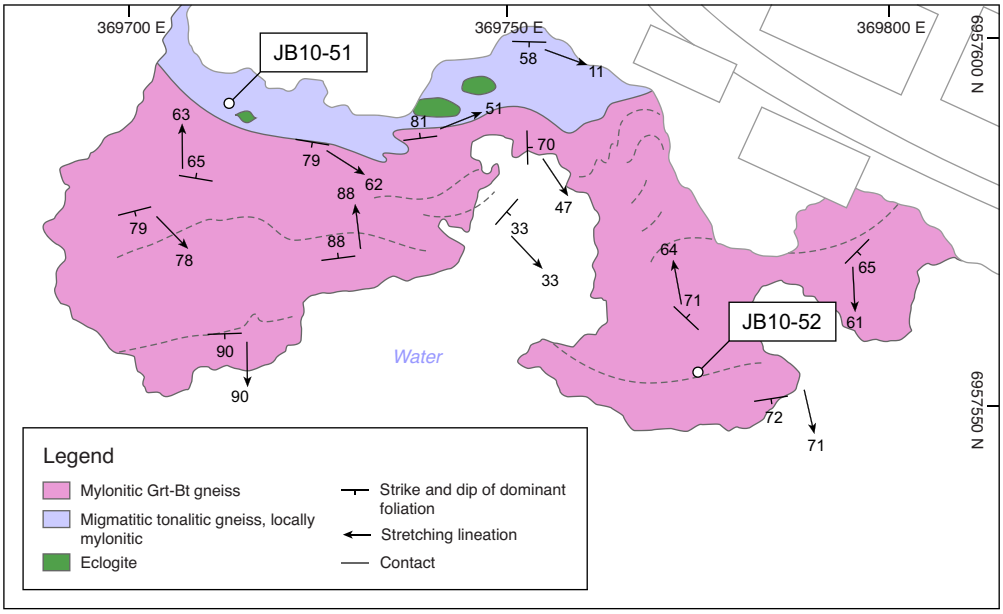

Figure 6.9: (a) Outcrop geological map and photographs showing approximate setting of U–Pb geochronology samples JB10-51 and JB10-52. Both samples were taken 'out of frame'. (b) Mylonitized migmatitic gneiss from which sample JB10-51 was collected. (c) Sample JB10-52 was collected from this thin, folded leucosome. The leucosome cuts a strong L–S mylonitic fabric with tops-NW kinematic indicators.

as the band of leucosome was quite thin. The leucosome consists of medium-grained quartz, K-feldspar, and plagioclase, with biotite, hornblende, minor scapolite, and minor (relict/embayed) garnet and clinopyroxene. The finer-grained melanosome contains abundant hornblende, minor scapolite, and clinopyroxene. Zircon is present throughout the leucosome.

The sample yielded abundant subhedral to euhedral prismatic zircons. CL imaging showed most contain oscillatory zoned cores surrounded by typically homogeneous, brighter CL rims. Three fractions, each comprising 1 to 2 physically separated zircon tips, yielded discordant analyses. The results do not define a discordia line.

6.4 Zircon Trace Element Geochemistry

Because of its refractory nature and tendency to survive multiple geological events, linking a population of zircon to a metamorphic event can be difficult. While some studies have linked zircon growth to specific metamorphic reactions (*Hoskin and Schaltegger*, 2003, and references therein), generally demonstrating what reactions took place, and quantifying their P–T conditions, remains problematic. The most common approach to this problem is to use textural criteria, including the internal zoning and distribution of zircon with respect to other metamorphic phases, combined with its trace and rare earth element (REE) composition, to link zircon growth with a certain metamorphic assemblage. The underlying premise is that the trace element or REE composition of the chemical volume from which zircon grows can be linked to the growth of certain metamorphic phases that preferentially incorporate or exclude certain REE or other trace elements (*Hoskin and Schaltegger*, 2003; *Rubatto*, 2002; *Bingen et al.*, 2004). These data can then be combined with knowledge of metamorphic phase equilibria, or quantitative thermobarometry, to constrain the P–T conditions of zircon growth. Whether a phase includes or excludes an element depends on its crystal structure and the atomic radii of the element in question. For example, Th and the light REE (LREE; e.g., Pr), which have large atomic radii, can substitute for Ca in epidote-group minerals; therefore zircon grown in the presence of a crystallizing epidote-group mineral may be relatively depleted in Th and LREE (*Bingen et al.*, 2004). The opposite is true for garnet, which preferentially

incorporates the HREE, leading to relative HREE depletion in zircon grown coeval with crystallizing garnet (*Rubatto*, 2002).

Several studies have shown that metamorphic zircon commonly exhibits several distinct features, when compared with igneous zircon, observed in chondrite-normalized plots. The features relevant to this study include (see refs. in *Hoskin and Schaltegger*, 2003; *Rubatto*, 2002; *Bingen et al.*, 2004):

1. relatively low Th/U values for metamorphic zircon, and for zircon grown in the presence of partial melt (typically Th/U $\leq$ 0.07), when compared with igneous zircon (Th/U $\geq$ 0.5);

2. relative depletion of light REE (LREE), with respect to heavy REE (HREE) in zircon grown during coeval with precipitation of epidote-group minerals;

3. small to negative Eu anomalies (expressed as Eu/Eu*), in cases where zircon has grown in the absence of plagioclase; and,

4. relative depletion of HREE versus LREE (expressed as high Dy_N/Yb_N) in zircon grown during coeval precipitation of garnet.

The reason for the lower Th/U values of metamorphic zircon when compared with igneous zircon is not fully understood, but is nonetheless supported by a wide body of data (*Hoskin and Schaltegger*, 2003). Th/U values are also typically lower for amphibolite facies than for granulite facies rocks. As noted above, coeval growth of an epidote-group mineral can lead to relative depletion of Th, but is unlikely to explain this trend across all metamorphic rocks.

The absence of the Eu anomaly is of particular importance to high-pressure metamorphic rocks. Eu^{2+} is strongly incorporated into plagioclase during crystallization, such that, depending on the oxidation state of Eu, zircon formed in granitoid rocks at normal crustal depths will typically exhibit a large negative Eu anomaly (Fig. 6.10d). The absence of such anomalies in high-pressure metamorphic rocks, namely eclogites, is therefore commonly interpreted as evidence for the breakdown or absence of plagioclase during zircon growth. The relative depletion of HREE in zircon grown coeval with garnet is equally important to understanding zircon growth in high-pressure rocks, in which garnet is often a key constituent. Garnet,

like zircon, has a strong affinity for HREE (*Rubatto*, 2002). Therefore, zircon grown in the presence of crystallizing garnet will tend to be relatively depleted in HREE (Fig. 6.10d). These features can be used to link zircon growth with specific chemical changes or mineralogical assemblages in the host rock. However, caution must be exercised when interpreting these features, in particular with respect to the reaction volume from which the zircon crystallized, and whether it crystallized from an open or closed system (*Rubatto*, 2002).

6.4.1 Methods

The trace element compositions of zircons representing the analyzed fractions from samples JB10-47, JB10-62, and JB10-63 were measured using a Finnigan ELEMENT XR double-focusing magnetic-sector inductively coupled plasma mass spectrometer (HR-ICPMS), coupled with a GEOLAS 193 nm excimer laser system, at Memorial University of Newfoundland. Analyses were corrected by repeated measurements of the 91500 zircon standard. A spot size of 20 μm was used for all analyses.

The resulting REE concentrations were calculated assuming stoichiometric zircon ($ZrSiO_4$). The actual compositions of the zircon may vary from ideal stoichiometry (e.g., by incorporating Hf; *Hoskin and Schaltegger*, 2003), which if true would affect the absolute, but not relative, abundances of REE, which are the focus here. The resulting REE concentrations of the zircons are illustrated here as chondrite-normalized abundances using the values of *Taylor et al.* (1981) (Fig. 6.10).

6.4.2 Eclogite Sample JB10-47

The trace element and REE compositions of the zircon cores and rims from eclogite sample JB10-47 show remarkable consistency (Fig. 6.10a). The cores are characterized by variable Th/U values (0.06–0.30; although half of the analyzed cores have Th/U $\leq$ 0.1), small Eu anomalies ($Eu/Eu^* = 0.65–0.99$), and minor enrichment of HREE ($Dy_N/Yb_N = 0.09–0.26$). The rims are characterized by similar but overall lower Th/U values (0.06–0.09), very small, mostly positive Eu anomalies ($Eu/Eu^* = 0.94–1.25$), and strong relative depletion of HREE ($Dy_N/Yb_N = 0.58–0.74$). All of the zircons exhibit strong enrichment in Ce, and otherwise variable concentrations of LREE, notably Pr, although there does not appear to be a systematic trend.

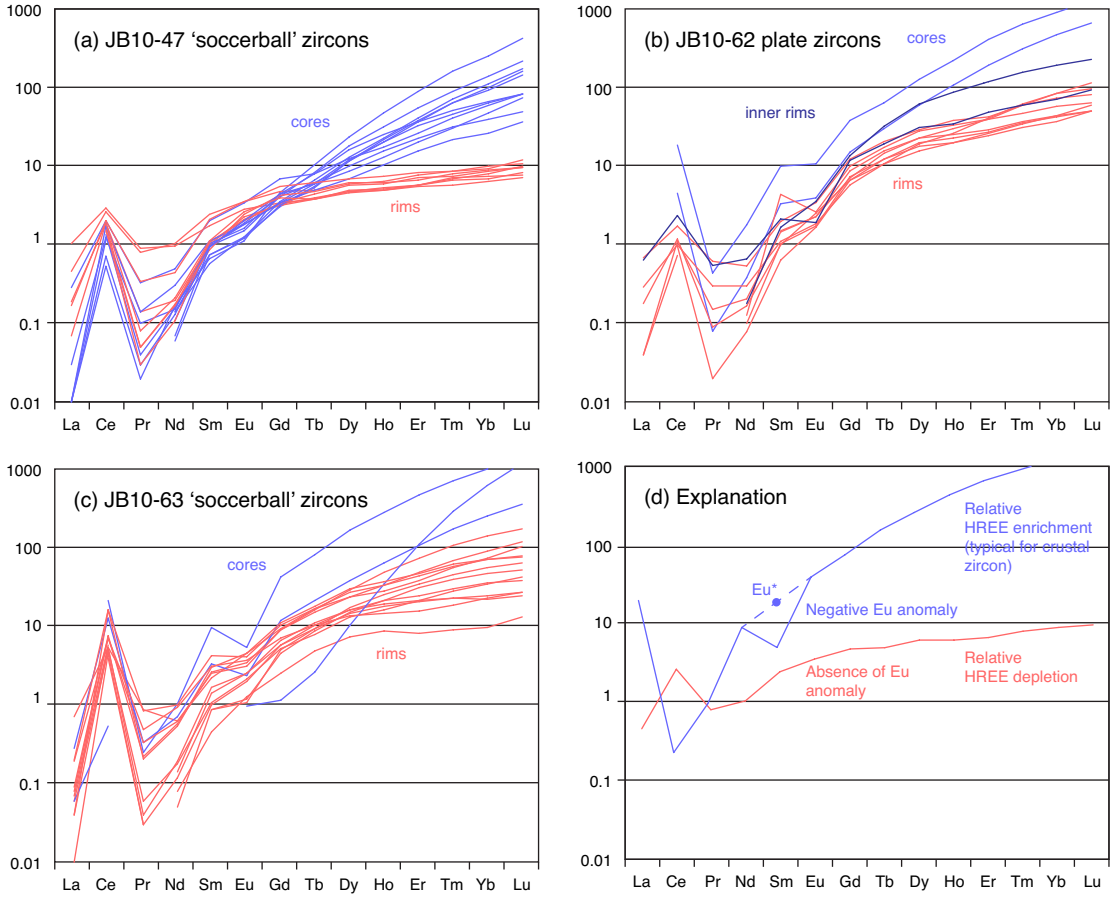

Figure 6.10: chondrite-normalized rare earth element abundances for zircons from samples (a) JB10-47, (b) JB10-62, and (c) JB10-63. See text for details. The 'Explanation' panel illustrates the main features typical of igneous zircons (blue) and eclogite facies metamorphic zircons (pink).

6.4.3 Eclogite Sample JB10-63

Zircons from eclogite sample JB10-63 show somewhat more variable compositions (Fig. 6.10b). The cores are characterized by relatively high Th/U values (0.12–0.79), more pronounced negative Eu anomalies ($Eu/Eu^* = 0.26–0.51$), and relative enrichment of HREE ($Dy_N/Yb_N = 0.02–0.17$). The homogeneous rims, or cores in grains where no obvious inherited core exists, are characterized by lower Th/U values (0.02–0.13; although most have $Th/U \leq 0.08$), relatively small Eu anomalies ($Eu/Eu^* = 0.65–1.17$), and range from somewhat enriched to relatively depleted in HREE ($Dy_N/Yb_N = 0.21–0.76$).

6.4.4 Migmatitic Gneiss Sample JB10-62

Zircons from sample JB10-62 are characterized by contrasting core and rim REE compositions (Fig. 6.10c). The oscillatory zoned cores found in some grains are characterized by relatively high Th/U values (0.39–0.45), negative Eu anomalies ($Eu/Eu^* = 0.55–0.57$), and relative enrichment of HREE ($Dy_N/Yb_N = 0.13–0.14$) (Fig. 6.10). The inner (dark CL rims), where present, are characterized by high Th/U values (0.41), variable negative Eu anomalies ($Eu/Eu^* = 0.39–0.75$), and somewhat lower enrichment of HREE ($Dy_N/Yb_N = 0.33–0.43$). The outer (light CL rims) are characterized by relatively low Th/U (0.01–0.04; with most below 0.30), variable small to negligible negative Eu anomalies ($Eu/Eu^* = 0.40–1.00$), and somewhat lower enrichment of HREE ($Dy_N/Yb_N = 0.18–0.52$).

6.5 Interpretation of U–Pb Geochronology and Zircon Geochemistry

6.5.1 Proterozoic Zircon Cores

The discordia lines defined by zircon analyses from samples JB10-63 (eclogite) and JB10-62 (enclosing migmatitic gneiss) provide approximate constraints on the protolith ages of the Baltica basement rocks that underlie Harøya. The upper intercepts obtained from these samples are 1615 ± 9 Ma and 1619 ± 8 Ma, respectively. These ages are very similar to early Mesoproterozoic protolith ages of ∼1686–1594 Ma from a nearby Haramsøya (*Krogh et al.*, 2011), and throughout the WGR (*Austrheim et al.*, 2003) and southern Norway, related to a prolonged period of calc-alkaline magmatism that affected the southern Baltic shield (*Tucker et al.*, 1987;

Andersen et al., 2004). The upper intercept ages presented here are interpreted as the time of crystallization of the igneous protoliths. This interpretation is supported in each case by the relatively high Th/U ratios of the zircon cores, and in the case of sample JB10-62, by the preservation of oscillatory zoned cores typical of igneous zircon (*Corfu et al.*, 2003). The exact nature of the igneous protoliths of samples JB10-62 and JB10-63 has not been determined, but their mineralogy indicates they may have originated as tonalitic and gabbroic intrusions, respectively.

The youngest inherited age component determined in this study comes from sample JB10-47. Anchoring a discordia line at ∼413 Ma, the probable time of Scandian high pressure metamorphism (see below) yields an upper intercept of ∼960 Ma, similar to Sveconorwegian protolith ages from Baltica basement rocks throughout the WGR. However, the lack of oscillatory zoning and low Th/U values of the zircon cores in sample JB10-47 suggests that they formed during metamorphism, rather than crystallization of an igneous protolith.

6.5.2 Scandian Zircon Overgrowths

The oldest Scandian ages in this study were obtained from the eclogites, and provide approximate constraints on the timing of eclogite facies metamorphism of the Baltica basement rocks that underlie Harøya. Of the two eclogite samples, the lower intercept of the discordia line obtained from sample JB10-63 (411 ± 20 Ma) provides the best estimate for the timing of eclogite facies metamorphism. This age is similar, albeit with much greater uncertainty, to ∼415–410 Ma ages obtained from eclogite zircons throughout Nordøyane and the nearby mainland (*Krogh et al.*, 2011). The relatively good fit of the line pinned at 413 Ma for sample JB10-47 indicates that it is probably close to the correct age of eclogite facies metamorphism for that sample as well.

Several aspects of the textural and trace element compositions of the zircon rims are consistent with crystallization at eclogite facies conditions. The zircons in JB10-47 are remarkably consistent in that all contain an inherited core, suggesting that metamorphic zircon growth may have resulted from the dissolution and reprecipitation of Zr from the inherited Sveconorwegian cores, perhaps driven by reaction with a metamorphic fluid ('secondary crystallization'; *Bingen et al.*, 2001;

Hoskin and Schaltegger, 2003). Alternatively, Scandian zircon growth may have resulted from breakdown of Zr-bearing phases, for example rutile or primary clinopyroxene, during eclogite facies metamorphism (*Bingen et al.*, 2001). The present data are insufficient to distinguish between these interpretations. The trace element compositions of the zircon rims in sample JB10-47 exhibit negligible Eu anomalies, indicative of zircon growth during the breakdown, or in the absence, of plagioclase, as well as strong relative HREE depletion, indicative of coeval growth of (or growth within the stability field of) garnet, two mineralogical changes characteristic of the transformation of a basaltic/gabbroic protolith to eclogite. The zircon rims from sample JB10-63 also have small to negligible Eu anomalies, but interestingly exhibit considerable variation in the extent of relative HREE depletion. Most of the garnet in sample JB10-63 appears to have undergone partial decomposition (surrounded by plagioclase and amphibole). The variable degrees of HREE depletion in these zircons may therefore reflect prolonged crystallization of zircon, perhaps beginning at eclogite facies conditions and lasting through decompression and consequent decomposition of garnet. Alternatively, because garnet is less abundant than in sample JB10-47, zircons locally isolated from garnet may not have had to compete with garnet for HREE. Unfortunately, the current dataset is insufficient to test these possibilities.

Perhaps the most tantalizing of the results is the lower intercept obtained from sample JB10-62 of 400 ± 5 Ma. This age is younger than the age of eclogite facies metamorphism in Nordøyane, but up to 5 Myr older than published ages of ∼395 Ma from amphibolite facies, syn-extensional pegmatites (*Tucker et al.*, 2004; *Krogh et al.*, 2011). The absence of HREE depletion in the zircon outer rims from sample JB10-62 implies crystallization during the decomposition of garnet, consistent with the observed garnet textures. The relative abundance of HREE could have been affected by the presence of zoisite, which may have depleted the host rock in LREE. Coupled with the textural indicators of partial melting noted above, we interpret the zircon rims to have formed during partial melting of the migmatitic gneisses during decompression from eclogite facies conditions. Unfortunately the lower intercept age is relatively imprecise, and testing this hypothesis will require further study, ideally using microbeam analyses.

The youngest Scandian, and only concordant, zircon age of 388 ± 1.3 Ma was obtained from sample JB10-57. This age is interpreted as the time of pegmatite crystallization at amphibolite facies, during extension of the surrounding eclogite blocks. Similar, albeit somewhat older, ages of ∼395 Ma have been reported from titanites and zircons from boudin neck pegmatites from throughout the northern WGR (*Tucker et al.*, 2004; *Krogh et al.*, 2011). The new age presented here demonstrates that the Baltican crust remained sufficiently hot that partial melts persisted until ∼388 Ma.

6.5.3 Scandian Titanite and Rutile Ages

Only one concordant titanite age, 376 ± 2 Ma, was obtained, from sample JB10-51. This age is considerably younger than the widespread ∼395 Ma titanite ages from the northern WGR attributed to cooling after amphibolite facies metamorphism (*Tucker et al.*, 2004), and there are several arguments as to why this age, if valid, represents later deformation rather than cooling. First, it is identical to rutile ages from this study (see below). Although closure temperature depends on several factors including grain size and cooling rate, rutile ages are generally younger than titanite ages from the same samples. Second, the age is identical to the ∼375 Ma age of monazite in mylonitized garnet biotite gneiss exposed in a shear zone on the northern coast of Fjørtoft, just a few hundred metre to the south, interpreted as having formed by hydrothermal equilibration during the latest shearing to affect the study area (*Terry et al.*, 2000). The young titanite age presented here is therefore interpreted as a crystallization age representing late sinistral deformation of the migmatitic tonalitic gneiss on southern Harøya, rather than cooling through titanite closure, which likely took place prior to the rutile ages presented below.

Two samples, JB10-47 and JB10-62, yielded virtually identical concordant rutile analyses of 378 ± 1.6 Ma and 377 ± 1.6 Ma, respectively. These ages are very similar to rutile ages of 377 ± 1 and 374 ± 1 from gabbro on Flemsøya (*Krogh et al.*, 2011). Whether these ages represent cooling through the closure temperature of rutile or later deformation is unclear, nonetheless it can be concluded that the rocks underlying Harøya had cooled through temperatures typical of Pb closure in rutile (∼300–650°C) by ∼375 Ma at the latest.

6.6 Implications for the Tectonic Evolution of UHP Rocks from Harøya

The present results can be used to place approximate time constraints on the *P–T–d* path of *Butler et al.* (2012) for the Harøya coesite-eclogite and enclosing Baltica basement rocks (Fig. 6.11). Peak conditions for the coesite-eclogite reached ∼3 GPa/760°C, and are interpreted as representing the subduction of Baltica basement beneath Laurentia during the late (Scandian) phase of the Caledonian orogeny. The lower intercept age of ∼410 Ma presented here, although from a different sample, is similar to previous ∼415–410 Ma ages for eclogite facies zircons from Nordøyane (*Krogh et al.*, 2011). Whether these ages represent the onset of eclogite facies metamorphism or peak UHP conditions cannot be determined with the present data, but in any case show that (U)HP metamorphism had begun by ∼415 Ma.

Subsequent isothermal decompression of the coesite-eclogite led to upper amphibolite/lower granulite facies overprinting at conditions of ∼1 GPa/800°C, and is interpreted as representing the initial exhumation of the UHP Baltica basement from mantle depths to the middle of the thickened orogenic crust. This metamorphism has not been dated directly, but could correspond to the ∼400 Ma lower intercept obtained from sample JB10-62, interpreted as representing zircon crystallization following partial melting and decomposition of garnet.

In contrast to this interpretation, *Gordon et al.* (2013) suggest that partial melting in the Nordøyane domain took place at (U)HP conditions. The authors documented LA-ICPMS U–Pb ages and REE compositions of zircons sampled from different textural varieties of leucosomes from the WGR, including samples from Finnøya, just north of Harøya. Their data, although lacking in analytical precision, suggest that zircons in partial melts that now form layer-parallel leucosomes on Finnøya formed between ∼410–400 Ma. REE analyses of these zircons show negligible Eu anomalies as well as HREE depletion. The authors interpret these data as indicating that partial melting began at (U)HP conditions, whereas final crystallization of the plagioclase-bearing leucosomes obviously occurred at lower pressures. Although compelling, the data are somewhat scattered. In one sample, the oldest (∼408 Ma) spot analysis curiously shows significantly less HREE depletion than younger analyses, despite being much closer to the generally accepted ∼415–410 Myr

age of (U)HP metamorphism in Nordøyane. Moreover, no attempt to link the observed REE compositions to the petrology of the samples is presented. Many of the granodioritic gneisses from Harøya and Finnøya contain abundant epidote (and allanite), titanite, and zoisite, which are known to incorporate significant amounts of REE, including Eu. Titanite in particular, although having a far greater affinity for LREE, has in some cases been shown to have an ability to incorporate amounts of HREE similar to that of Garnet (*Sassi et al.*, 2000). Failure to account for the presence of these phases, which may constitute a greater modal proportion than garnet in felsic orthogneisses, could lead to erroneous interpretations of the zircon REE compositions, for example if the interpretation of relative HREE enrichment in zircon failed to account for the presence of abundant titanite. A more robust approach would therefore be to assess the actual distribution of REE among all the potential REE-bearing minerals in the dated samples. Similar attempts by the present study to constrain the timing of partial melting were unsuccessful, and the data of *Gordon et al.* (2013) are so far the constraints on the time of partial melting of the northern WGR at (U)HP conditions or during early exhumation. This melting likely exerted a strong control on the mechanics of subduction and exhumation in the WGR.

The concordant zircon age of 388 ± 1.3 Ma for the syn-extensional pegmatite is consistent with, but somewhat younger than, previously published ∼395 Ma ages for similar pegmatites on Nordøyane, and is interpreted as representing the timing of amphibolite-facies sinistral shearing that affected the study area following decompression to granulite facies. This age places a more concrete, but lower, boundary on the time of exhumation to crustal levels.

The concordant rutile age of 378 ± 1.6 Ma is interpreted to represent cooling of the Baltica basement through approximately 550–620°C, although estimates of the closure temperature in rutile reach as low as 300°C. The youngest monazite ages of ∼375 Ma from shear zones on Fjørtoft (*Terry et al.*, 2000), and the one concordant 376 ± 2 Ma titanite age presented here, suggest that sinistral shearing resulting from regional scale transtension continued to affect the study area at least until this time, suggesting that cooling and unroofing were accommodated by a prolonged period of extension. The final stages of cooling are recorded by a well constrained $^{40}Ar/^{39}Ar$

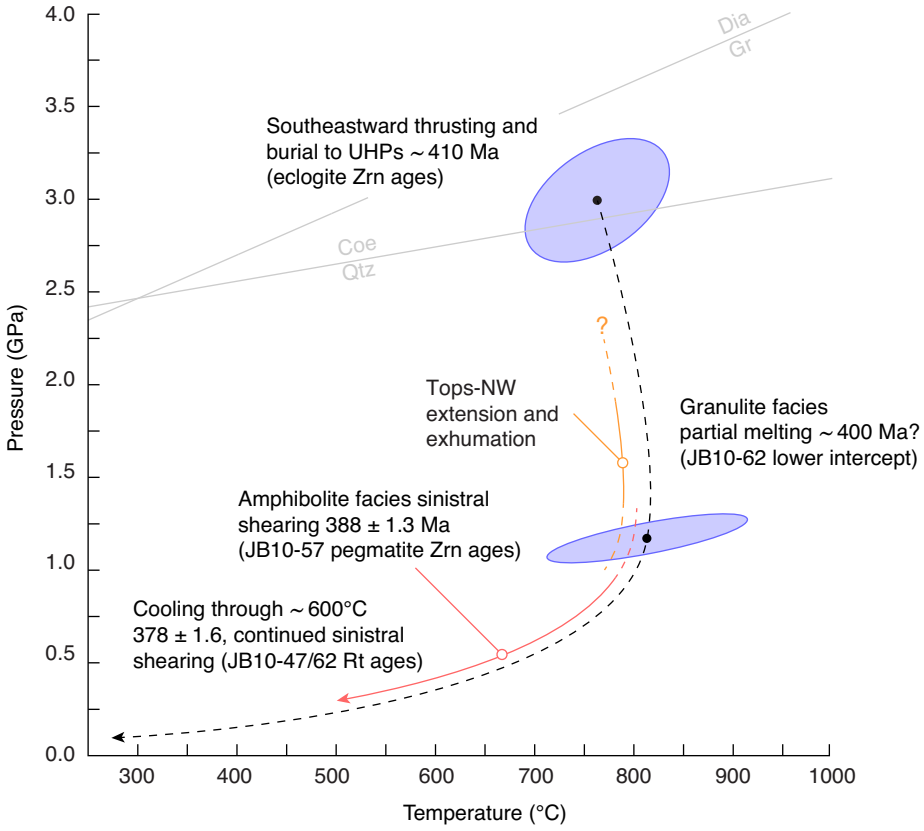

Figure 6.11: Composite pressure–temperature–deformation–time path for UHP Baltica basement rocks on Harøya. P–T conditions for Harøya coesite-eclogite from *Butler et al.* (2012). Zrn=zircon, Rt=rutile. See text for details.

age of 366.5 ± 0.7 Ma, obtained from phengite sampled from a deformed granitic pegmatite within the Baltica basement on southern Harøya (*Steenkamp*, 2012).

The present data allow for a very rough estimate of the rate at which the Baltica basement rocks that underlie Harøya were exhumed from the mantle. The lowest possible exhumation rate, obtained by taking the ∼410 age of UHP metamorphism (assuming the zircon age corresponds to peak P–T), the age of amphibolite facies sinistral extension (as a lower bound on the granulite facies overprint), and assuming an average crustal density of 2800 kg m^{-3}, is ∼0.32 cm a^{-1}. An alternative is to accept the lower intercept of ∼400 Ma from sample JB10-62 as the approximate age of the granulite facies overprint, which doubles the exhumation rate to ∼0.71 cm a^{-1}. Both estimates are within the range of previous estimates from the WGR, although in general the calculated exhumation rates from rocks in the southern UHP domains are higher because the timing of UHP metamorphism there, ∼405–400 Ma, was much later than in Nordøyane. The geodynamic implications of these estimates could be quite different, with one suggesting slow, gradual exhumation, and the other more punctuated exhumation followed by slower cooling at crustal depths.

The data can be summarized as follows:

1. (U)HP metamorphism of the northern WGR occurred ∼415–410 Ma.

2. Subsequent exhumation to middle crustal depths took place by ∼395–389 Ma.

3. Exhumation was accompanied by crystallization of partial melts, which may have been generated at (U)HP conditions, during decompression, or both.

4. Subsequent cooling through titanite and rutile closure was relatively slow, taking place ∼10 Myr after exhumation to middle crustal depths.

5. The estimated rate of exhumation of the northern WGR, although highly assumption-dependent, is relatively low ($\lesssim$1 cm a^{-1}), compared with many other (U)HP terranes, but consistent with previous estimates from the WGR.

The implications of these data for the orogen-scale evolution of the Scandinavian Caledonides/WGR are discussed in Chapter 7.

Chapter 7

Contrasting Modes of Late- to Post-orogenic Exhumation of (Ultra)high-pressure Terranes

7.1 Preface

This chapter presents preliminary results of a numerical modeling study designed to investigate (U)HP rock exhumation in the Western Gneiss Region of Norway. Although the work presented here will form the basis of a future manuscript, many aspects of the models are likely to change prior to submission, and the results should therefore be considered preliminary.

7.2 Introduction

Many Phanerozoic orogens expose (ultra)high-pressure ((U)HP) metamorphic terranes attributed to deep subduction of continental margins during orogenesis (*Ernst and Liou*, 1999; *Chopin*, 2003; *Liou et al.*, 2004; *Kylander-Clark et al.*, 2012). How these terranes are exhumed from depths exceeding ∼100 km remains controversial, but considerable insight has been gained through geodynamic modeling based on observational constraints from natural orogens (*Chemenda et al.*, 1995; *Gerya et al.*, 2008; *Warren et al.*, 2008; *Beaumont et al.*, 2009; *Ellis et al.*, 2011; *Duretz et al.*, 2012). Most of these studies indicate that the exhumation of (U)HP terranes is fundamentally linked to the inherent buoyancy of deeply subducted continental crust and/or lithosphere, although the actual exhumation mechanism, generally upward flow of

(U)HP crust accommodated by either absolute or localized, syn-convergent extension, differs considerably among models. The buoyant crust may detach and exhume as a relatively rigid slab, bounded by coeval normal- and thrust-sense shear zones (*Chemenda et al.*, 1995). Alternatively, the subducted crust may weaken at depth, and flow upward as a buoyant plume, driving coeval shallow crustal extension and thrusting (*Gerya et al.*, 2008; *Warren et al.*, 2008; *Beaumont et al.*, 2009). Breakoff of the subducting slab may lead to reverse subduction (or 'eduction'), in which the (U)HP terrane and underlying lithosphere are exhumed together by absolute extension (*Duretz et al.*, 2012). In certain cases, (U)HP crust may reside at mantle depths for some time, to be exhumed by later diapiric ascent, also the result of lithosphere-scale extension (*Ellis et al.*, 2011). Each of these mechanisms may exist and apply to different natural (U)HP terranes.

The wide variety of exhumation models reflects the growing recognition that globally, (U)HP terranes vary considerably in terms of their size (i.e., thickness and areal extent), their pressure–temperature–time (P–T–t) evolution, and the kinematics/tectonics of their exhumation (cf. *Kylander-Clark et al.*, 2012). These differences are difficult to reconcile within a single 'one size fits all' model. In particular, there appear to be marked differences between (U)HP terranes formed and exhumed during the early stages of orogenesis, beneath relatively small orogens, and those that formed and exhumed following protracted collision, beneath 'mature' large orogens. The former case, 'early-collisional' terranes, typified by those in the Western Alps and Himalaya, are generally small (∼1–5 km thick, ∼500 km^2), underwent short-duration (U)HP metamorphism (a few Myr), and exhumed rapidly (up to ∼5 cm a^{-1}) (*Rubatto and Hermann*, 2001; *Parrish et al.*, 2006; *Epard and Steck*, 2008; *Beltrando et al.*, 2010a). In contrast, 'late-orogenic' (U)HP terranes, like the Western Gneiss Region of Norway and the Dabie-Sulu terrane, tend to be much larger (∼10–15 km thick, ∼30,000 km^2), underwent longer duration (U)HP metamorphism (tens of Myr), and exhumed more slowly (∼0.1–1 cm a^{-1}) (*Hacker et al.*, 2010; *Kylander-Clark et al.*, 2012). Although a causative relationship between orogenic stage and these aspects (e.g., size, timing of formation/exhumation) has not been demonstrated, the data indicate that terranes of these two types may have undergone very different styles of burial and/or exhumation.

Here we define a 'late- to post-orogenic (U)HP terrane' as one formed and/or exhumed during waning orogenesis, where protracted convergence and shortening have already given rise to considerable crustal thickening, heating, and a wide orogen. We define post-orogenic exhumation to be after plate convergence ceased, whereas late-orogenic exhumation occurs during the late stages of plate convergence. In contrast to early-orogenic (U)HP terranes, there are several processes implied by late- to post-orogenic (U)HP terranes that have not been addressed in an integrated manner by previous modeling studies. These include (but are not limited to):

1. how an existing thick orogenic wedge, in particular one that is hot and consequently thermally weakened, affects the burial and exhumation of crust to (U)HP conditions;

2. how changes in plate motions at the end of orogenesis affect (U)HP terrane exhumation, as a result of changes in tectonic forces that may contribute to exhumation; and,

3. whether late- to post-orogenic gravitational spreading of thickened orogenic crust may contribute to exhumation or, alternatively, obscure structures related to exhumation.

4. whether or not erosion contributes substantially to (U)HP rock exhumation.

Here we present 2D numerical geodynamic models designed to explore these and other questions related to the mechanics of late- to post-orogenic exhumation of (U)HP terranes, motivated by observational constraints from the Western Gneiss Region (WGR) of Norway, a large (U)HP terrane formed and exhumed during the late stages of the Caledonian orogeny (*Roberts and Gee*, 1985; *Cuthbert et al.*, 2000; *Hacker et al.*, 2010, e.g.,). The objective is not to reproduce the geology of the Caledonides or WGR precisely. Rather, we use generally accepted aspects of the Caledonidian/WGR evolution to establish key constraints on late-orogenic (U)HP terrane formation, and to highlight some of the outstanding questions concerning how these terranes might have exhumed. We then use numerical model experiments to explore the mechanics of (U)HP terrane exhumation in a generic orogen that meets these basic observational criteria. We conclude with a discussion of the models

with respect to the evolution of the WGR and discuss implications for outstanding questions concerning its formation and exhumation.

7.3 The Western Gneiss Region: a Large, Late-orogenic (U)HP Terrane

The Western Gneiss Region (WGR) of Norway exposes the deep crustal levels of the Greenland-Norwegian Caledonides, a large bivergent orogen formed during the Ordovician–Devonian subduction of the Iapetus Ocean, and later underthrusting of the Baltican continental margin beneath Laurentia during continent–continent collision (*Roberts and Gee*, 1985; *Roberts*, 2003; *Hacker et al.*, 2010) (Figs 7.1 and 7.2). The term WGR strictly refers to the area, whereas the Western Gneiss Complex (WGC) refers to the Proterozoic Baltican gneiss units that dominate the WGR. For simplicity, we use the term WGR to refer to the area and (U)HP terrane in general.

The Scandinavian side of the orogen comprises a stack of allochthonous nappes (Figs 7.1 and 7.2), derived from the rifted Baltican margin (grouped into the Lower and Middle Allochthons), Iapetan ophiolites, and volcanic arcs of both peri-Laurentian and peri-Baltican affinity (Upper Allochthon), and, at the highest structural levels, the Laurentian continental margin (Uppermost Allochthon) (cf. *Roberts and Gee*, 1985; *Gee et al.*, 2012). These nappes are overlain tectonically, and in the case of the Upper Allochthon unconformably, by a series of Devonian–Carboniferous conglomerate/sandstone basins formed during late- to post-orogenic extension (e.g., *Osmundsen and Andersen*, 2001). The provenance and accretion history of some of these nappes remains unclear, and several interpretations exist (*Roberts*, 2003; *Brueckner and van Roermund*, 2004). That said, it is generally agreed that the nappes were emplaced by progressive eastward stacking, whether by subduction beneath the Laurentian margin or intervening arcs in Iapetus, followed by several hundred kilometres of westward underthrusting of the Baltican margin beneath the nappes during the Silurian 'Scandian' orogeny (*Hacker and Gans*, 2005).

Evidence of pre-Silurian/Devonian high-grade and locally (U)HP metamorphism, partial melting, and (at the highest structural levels) arc magmatism prior to terminal collision between Baltica and Laurentia is found throughout the nappe stack (*Roberts*, 2003; *Hacker and Gans*, 2005; *Gee et al.*, 2012). Some of these events took

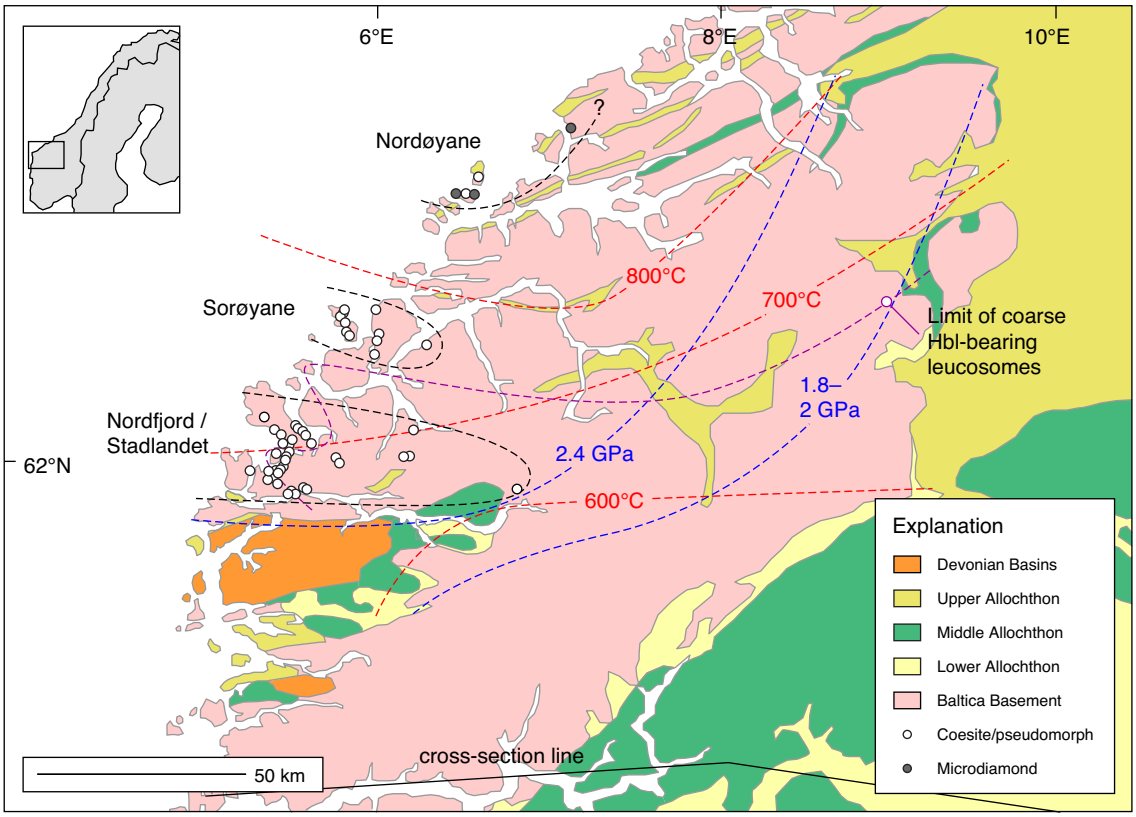

Figure 7.1: Geological map of the Western Gneiss Region. Petrological data summarized from *Hacker et al.* (2010). Circles indicate locations of coesite- and microdiamond-bearing rocks (primarily eclogites). Black dashed lines show approximate boundaries of the three (U)HP domains. Red and blue dashed lines are contours of peak metamorphic temperatures and pressures, respectively, based on P–T calculations. The 1.8–2.0 GPa 'isobar' represents the eastward limit of known eclogite bodies within the WGC, but does not include eclogites within the allochthons located further north. The purple line indicates the eastward limit of coarse-grained, hornblende-bearing leucosomes attributed, based on local geochronological evidence, to partial melting during Scandian orogeny. 'Cross-section line' indicates position of cross-section shown in Figure 7.2. No crustal-scale cross-section for the northernmost WGR exists.

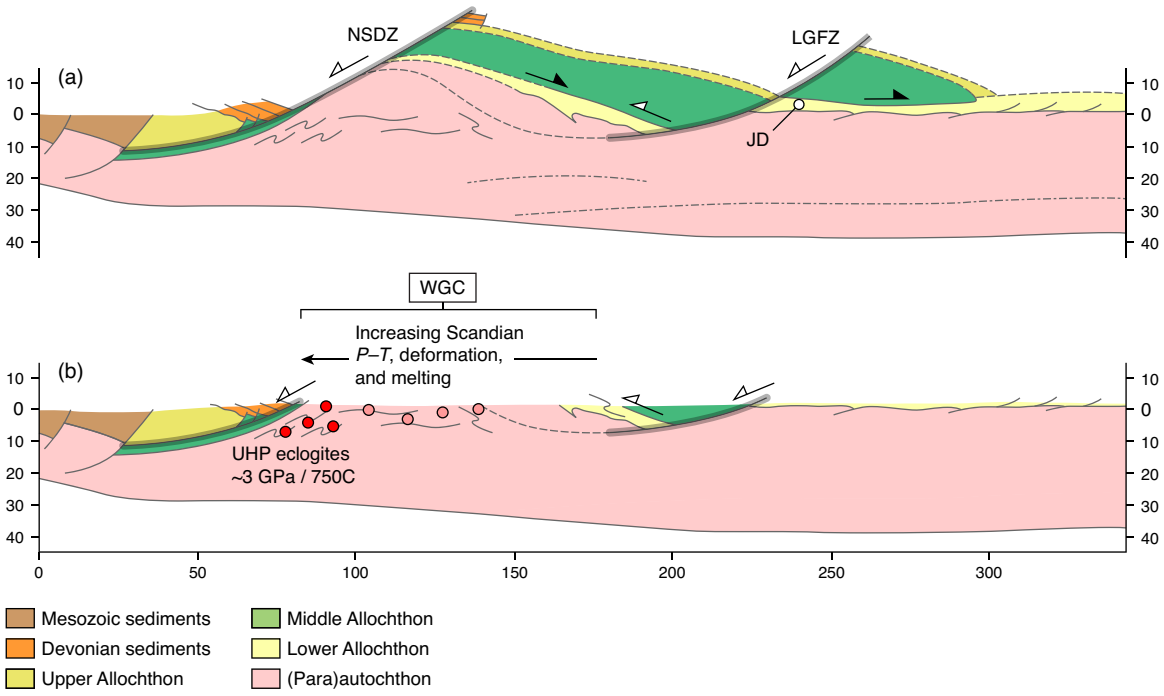

Figure 7.2: Cross-section through the Western Gneiss Region. Modified from *Milnes et al.* (1997). 1:1 scale. (a) Inferred structure following Late Scandian extension. (b) Present-day surface after erosion. WGC=Western Gneiss Complex, NSDZ=Nordfjord-Sogn Detachment Zone, LGFZ=Lærdal-Gjende Fault Zone, JD=Jotun Detachment. Red and pink circles show schematic distribution of UHP and HP eclogites across the WGR. Black-filled arrows show top-E kinematics of early Scandian thrust-sense emplacement of allochthons over Baltica. White-filled arrows show subsequent top-W kinematics related to 'backsliding' along the base of the nappe stack (within the Lower/Middle allochthons). Form lines show regions of WGR with strong Scandian deformation. See Figure 7.1 for location of cross-section.

place far from Baltica, along the margin of Laurentia or within Iapetus (*Roberts*, 2003). Most relevant to the present work are those events that affected nappes of known Baltican affinity now exposed within the Middle Allochthon. Throughout central Sweden/Norway, the Bergen Arc, and the WGR, nappes within the Middle Allochthon record Late-Ordovician–Silurian upper amphibolite to granulite facies metamorphism, and in several places (U)HP metamorphism (*Jamtveit et al.*, 1990; *Bingen et al.*, 2004; *Hacker and Gans*, 2005; *Johnston et al.*, 2007; *Janák et al.*, 2012; *Gee et al.*, 2012; *Root and Corfu*, 2012; *Steenkamp*, 2012). These events probably correspond to the collision of Baltica with peri-Laurentian arcs (*Furnes et al.*, 2012), rather than terminal continent–continent collision, which began somewhat later (Middle Silurian, ∼425 Ma; *Andersen et al.*, 1990; *Torsvik*, 1998). Nonetheless, they indicate that (U)HP metamorphism of the WGR was the final, late-orogenic stage of a ∼50 Myr period of accretion of Iapetean terranes, continental subduction, and crustal thickening of the rifted Baltican margin (*Gee et al.*, 2012).

The leading edge of the Baltican margin now exposed in the WGR therefore underthrust beneath what was already thick (at a minimum ∼35–45 km; *Hacker and Gans*, 2005) and laterally extensive orogenic crust formed by prior accretion. Evidence of deep subduction is recorded in abundant (U)HP eclogite and peridotite bodies enclosed within the Proterozoic Baltican orthogneisses (the WGC) that dominate the WGRm, and locally in deeply infolded remnants of the overlying nappes (*Cuthbert et al.*, 2000).

(U)HP metamorphism of Baltican basement eclogites from ∼415–400 Ma (*Carswell et al.*, 2003a; *Krogh et al.*, 2011) reached maximum P–T conditions of ∼3.5 GPa/800°C (*Wain et al.*, 2000; *Cuthbert et al.*, 2000; *Terry et al.*, 2000; *Ravna and Terry*, 2004; *Young et al.*, 2007; *Butler et al.*, 2012), corresponding to burial to depths of $\gtrsim$120 km. Whether the ∼415–400 Ma ages of eclogite zircons from the WGR necessarily correspond to the peak of (U)HP metamorphism remains unclear; only ∼402 Ma zircons studied by *Carswell et al.* (2003a) contain coesite inclusions and thus demonstrably formed at UHP conditions. Lu–Hf ages of WGR eclogites ranging from ∼414 to 397 Ma are interpreted as representing prolonged (U)HP metamorphism, possibly resulting from slow subduction (*Kylander-Clark et al.*, 2009). The highest pressure coesite-bearing UHP eclogites are exposed within three domains along the coast

(Nordfjord, Sørøyane, and Nordøyane), together covering approximately 5,000 km^2 (*Root et al.*, 2005). East of the UHP domains, HP eclogites lacking evidence of UHP conditions are found up to ∼100 km toward the foreland, covering ∼30,000 km^2 (*Hacker et al.*, 2010). The overall (south)eastward decrease from high-temperature (U)HP conditions, in particular near Nordøyane, to moderate-temperature HP conditions near the eastern edge of the WGR, has been interpreted as a metamorphic gradient reflecting deeper subduction in the west (e.g., *Kylander-Clark et al.*, 2009). However, whether (U)HP metamorphism was precisely coeval across the WGR, i.e., the variations in metamorphic grade represent a true metamorphic gradient rather than either the effects of diachronous metamorphism or subsequent tectonic juxtaposition, remains to be shown. Similarly, the nature of the transitions between regions with UHP and HP eclogites, in particular whether they represent tectonic juxtaposition or metamorphic gradients (or kinetic factors, e.g., fluid availability), remains unclear (cf. *Cuthbert et al.*, 2000), although the metamorphic gradient interpretation is widely assumed (*Hacker et al.*, 2010; *Duretz et al.*, 2012).

Metamorphism at (U)HP conditions may have been accompanied by intense deformation, although fabrics formed during this stage are largely confined to mafic bodies hosted within orthogneiss, and have invariably been reoriented by the dominant amphibolite facies deformation. In the Nordøyane domain, steeply plunging eclogite facies lineations formed during top-SE shearing, consistent with northwestward subduction of Baltica beneath Laurentia (*Torsvik*, 1998; *Terry and Robinson*, 2004). Further south, eclogite facies fabrics are more randomly oriented (*Hacker et al.*, 2010), although locally a progression from steep N–S to shallow E–W lineations has been preserved (*Andersen et al.*, 1994). Whether the bulk of the WGR was strongly deformed at (U)HP conditions may never be known.

Exhumation to the base/middle of the thickened orogenic crust resulted in near-isothermal decompression from eclogite to amphibolite (and locally granulite) facies P–T conditions from ∼0.5 GPa/600°C to ∼1.5 GPa/800°C (*Labrousse et al.*, 2004; *Root et al.*, 2005; *Terry and Robinson*, 2003; *Walsh and Hacker*, 2004; *Butler et al.*, 2012) by ∼395–390 Ma (*Tucker et al.*, 2004; *Kylander-Clark et al.*, 2009; *Krogh et al.*, 2011). Coeval crystallization of leucosomes (inceasingly abundant toward the west) in the WGR gneisses during this phase attests to partial melting either during (U)HP

metamorphism or subsequent decompression (*Tucker et al.*, 2004; *Krogh et al.*, 2011; *Labrousse et al.*, 2011; *Gordon et al.*, 2013). U–Pb ages of titanite and rutile, as well as systematic variations in isotopic resetting of titanite, suggest that cooling took place somewhat earlier in the east, consistent with the overall (north)westward increase in maximum ((U)HP) metamorphic conditions (*Tucker et al.*, 2004; *Kylander-Clark et al.*, 2009; *Hacker et al.*, 2010). Subsequent cooling of the WGR orthogneisses through ∼400°C took place by ∼400 Ma in the east, and by ∼385–360 Ma in the west, with the youngest ages preserved in the (U)HP domains (*Root et al.*, 2005; *Walsh et al.*, 2007; *Steenkamp*, 2012).

Ductile deformation during and/or after decompression was dominated by E–W (constrictional) stretching and subsequent top-W shearing, and in the northernmost WGR, NE–SW sinistral shearing (*Andersen et al.*, 1991; *Milnes et al.*, 1997; *Krabbendam and Dewey*, 1998; *Terry and Robinson*, 2003). Near Nordfjord, Baltican basement gneisses containing (U)HP eclogites were juxtaposed with overlying lower pressure rocks along the top-W (normal-sense) Nordfjord Sogn Detachment Zone (NSDZ) and equivalent structures (*Andersen*, 1998). The NSDZ formed at lower crustal depths (at ∼0.6–1 GPa) from ∼410–400 Ma, before being exhumed, transected by brittle faults, and tectonically overlain by Devonian sediments (*Johnston et al.*, 2007) (Fig. 7.3). Further toward the foreland, the (basal) Jotun detachment was reactivated as a top-W extensional shear zone (*Fossen and Dunlap*, 1998). The existence of a top-W shear zone similar in nature to the NSDZ has been postulated in the northern WGR based primarily on geochronological evidence (*Tucker et al.*, 2004; *Robinson et al.*, 2012). At the surface, late- to post-orogenic extension was accompanied by deposition of a series of deep, Devonian–Carboniferous extensional basins, including the Hornelen, Kvamshesten, and Solund basins, within the hangingwall of, and broadly coeval with, motion along the NSDZ (*Osmundsen and Andersen*, 2001). Fossil ages from these basins indicate that deposition started as early as the Early Devonian (∼415 Ma) and possibly lasted until the Early Carboniferous (∼360 Ma; *Eide et al.*, 2005).

The observational constraints can be distilled into the following minimum criteria that any successful geodynamic model for the evolution of the Caledonides/WGR should reproduce (Figs 7.1, 7.2, and 7.3).

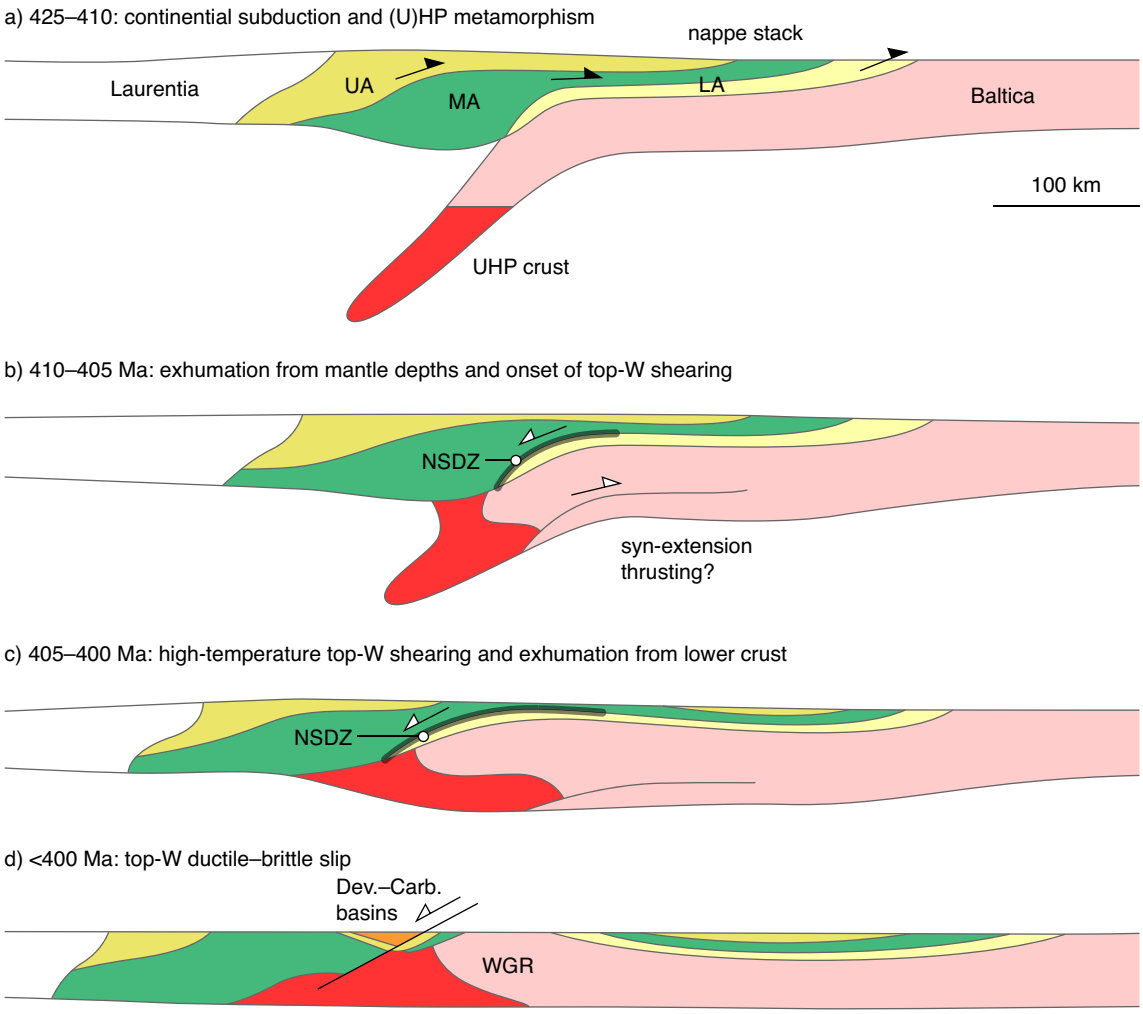

Figure 7.3: Conceptual tectonic model for the WGR, after *Johnston et al.* (2007). UA, MA, and LA are Upper, Middle and Lower allochthons, respectively. WGC=Western Gneiss Complex. (a) Scandian subduction of the WGR to mantle depths resulting in (U)HP metamorphism. (b) Onset of amphibolite facies, top-W shearing along the Nordfjord-Sogn Detachment Zone (NSDZ), concentrated within the Lower and Middle allochthons. Whether this shearing was accompanied by top-E thrusting at depth is debated. (c) Continued top-W deformation along the NSDZ. (d) Late overprinting of the NSDZ by top-W normal faults and juxtaposition of Devonian basins with the exhumed (U)HP WGR. The model does not attempt to explain the driving force of exhumation.

1. Pre-Scandian accretion of progressively more proximal (to Baltica) terranes to the upper orogenic plate (Laurentia or a nearby arc) led to growth of a thick orogenic wedge (∼35–45 km), and to local (U)HP and granulite facies metamorphism.

2. Subsequent Scandian subduction led to (U)HP metamorphism across a wide portion of the Baltican margin at conditions of ∼3.5 GPa/800°C, and somewhat lower P–T conditions (P = 1.8–2 GPa, $T \approx 600$°C) in the eastern WGR. Subduction probably commenced ∼425 Ma, with the WGR reaching peak pressure conditions from ∼415–400 Ma. The combination of high metmorphic temperatures at peak P conditions, and the broad timespan of garnet growth indicated by Lu–Hf ages (*Kylander-Clark et al.*, 2009) suggest that subduction may have been relatively slow ($\lesssim$1 cm a^{-1}).

3. Deformation during subduction involved top-SE shearing of the WGR and parts of the overlying allochthons at (U)HP conditions, coupled with broadly westward underthrusting of Baltica beneath the allochthons.

4. Exhumation of the entire WGR to mid-orogenic crustal conditions of up to ∼1.5 GPa/800°C took place ∼395–390 Ma (*Tucker et al.*, 2004; *Kylander-Clark et al.*, 2009; *Krogh et al.*, 2011), and possibly earlier in the east, implying exhumation from (U)HP conditions at $\lesssim$1.5 cm a^{-1}.

5. Exhumation was accompanied by widespread extensional deformation including ductile E–W stretching (and in the northwest sinistral shearing), top-W extensional reactivation of the basal thrust between the Baltican basement and overlying allochthons, and juxtaposition of the (U)HP WGR against overlying lower pressure rocks along the top-W, normal-sense NSDZ.

6. Evidence for continued shortening during the timespan of exhumation is scarce, or localized to the northern WGR (*Robinson et al.*, 2012). In the Central WGR, thrusting along the basal Jotun Detachment and in the foreland both apparently ceased prior to (U)HP, at ∼415 Ma and ∼408 Ma, respectively.

7. The intensity of Scandian deformation and partial melting generally decrease eastward across the WGR (*Hacker et al.*, 2010).

8. A similar eastward decrease is apparent in the timing of cooling (through ∼350°C) across the WGR, with ages ranging from ∼400 Ma near the eastern edge of the WGR to as young as ∼360 Ma in the UHP domains (*Root et al.*, 2005; *Walsh et al.*, 2007; *Steenkamp*, 2012).

9. Deposition of Devonian–Carboniferous sediments in extensional basins possibly commenced prior to ∼415 Ma (*Eide et al.*, 2005), and therefore lasted throughout the formation and exhumation of the (U)HP WGR.

Many of the above observations contrast markedly with those from early-orogenic (U)HP terranes, for example the relatively small units in the Western Alps that reached the upper crust only ∼5–10 Myr after (U)HP metamorphism (*Rubatto and Hermann*, 2001; *Berger and Bousquet*, 2008), and similarly rapidly exhumed (U)HP units in the eastern Himalaya (*Parrish et al.*, 2006). Despite its larger volume (∼35,000 km^2 and possibly ∼30 km thick), implying greater buoyancy, the slower exhumation of the WGR suggests that exhumation of these terranes occurred by different mechanisms.

There are other reasons, aside from timing, why exhumation of the WGR cannot easily be reconciled with existing models of syn-convergent exhumation of early-orogenic (U)HP terranes (*Warren et al.*, 2008a; *Beaumont et al.*, 2009). Whereas many early-orogenic examples are 'composite' (U)HP terranes comprising aggregates of units of different provenance and peak (U)HP metamorphic conditions, the broad similarity in the timing and P–T conditions of metamorphism within the WGR, coupled with the apparent gradients in P–T conditions and cooling ages, has led many to conclude that the WGC was exhumed from (U)HP conditions 'intact', perhaps as one relatively undeformed slice of crust (e.g., *Chemenda et al.*, 1995). However, within the UHP domains in particular it is clear that the WGC underwent considerable partial melting and internal deformation (*Terry and Robinson*, 2003, 2004; *Butler et al.*, 2012; *Gordon et al.*, 2013), at least at amphibolite facies and possibly earlier. Moreover, recent mapping in the northern WGR has documented local shear zones representing metamorphic breaks between (U)HP and 'normal pressure' Baltican basement (*Robinson et al.*, 2012). Whether this requires different styles of exhumation for the northern and central WGR is not known, but if so the WGR could not have remained intact during burial and ascent.

Moreover, although exhumation of early-orogenic (U)HP terranes has been widely associated with coeval thrust and normal-sense extensional shearing (at the base and top of the terrane respectively), orogen-scale deformation during exhumation of the WGR was dominated by E–W extension (*Milnes et al.*, 1997; *Andersen*, 1998; *Krabbendam and Dewey*, 1998; *Fossen*, 2010). No basal thrust has been identified beneath the WGR, and if one exists at depth, it does not outcrop in the foreland. Instead, top-SE transport along the Caledonian sole thrust (Jotun Detachment; Fig. 7.2) appears to have ceased by ∼408 Ma, and was followed by top-W shearing around ∼402–394 Ma (*Fossen and Dunlap*, 1998; *Fossen*, 2010), similar to the kinematics of shearing along the NSDZ. Meanwhile, in the foreland basin to the east, the youngest sediments affected by thrusting were deposited in the Late Silurian (423–418 Ma) (*Bockelie and Nystuen*, 1985). Thus, with the exception of the Storli thrust in the northern WGR (*Gee et al.*, 2012; *Robinson et al.*, 2012), exhumation of the WGR appears to have been accommodated solely by orogen-scale extension with no unequivocal evidence for simultaneous or later shortening. The pattern of regional-scale amphibolite facies kinematics (see above) and basin formation has been explained by regional transtension owing to oblique plate divergence, with exhumation of the WGR attributed to extreme vertical thinning of the crust (*Krabbendam and Dewey*, 1998). However, as others have noted, the earliest ages of (U)HP metamorphism within the WGR overlap with the onset of basin formation, suggesting that near-surface crustal extension may have begun during convergence and subduction of the WGR (*Terry et al.*, 2000).

Collectively the data indicate that exhumation of the WGC was accommodated primarily by late- to post-orogenic extension, with some contribution from shortening, yet the underlying mechanics remain unclear. We now describe and present a series of model experiments designed to capture the broad aspects of the Scandinavian Caledonian system outlined above, starting with oceanic subduction and subsequent growth of a thick orogenic wedge formed by accretion of multiple terranes, followed by subduction of a continental margin. Using this basic framework we explore contrasting modes of late- to post-orogenic exhumation of large (U)HP terranes, focusing on the effects of post-orogenic quiescent and divergent plate motions, with an emphasis on understanding the consequent distribution of orogen-scale

shortening and extension.

7.4 Modeling Approach

The models were computed using the nested version of the finite element software SOPALE, which solves thermal-mechanical creeping (Stokes) flows at the upper-mantle scale. An outline of the model design and methods is provided here, with a more detailed overview in the Appendix. The models are computed by solving the equations for incompressible creeping (Stokes) flows (Eqs. 7.1 and 7.2) and energy balance (Eq. 7.3) subject to mechanical and thermal boundary conditions:

$$\frac{\partial \sigma_{ij}}{\partial x_i} - \frac{\partial P}{\partial x_j} + \rho g_j = 0 \quad i,j = 1,2 \tag{7.1}$$

$$\frac{\partial v_i}{\partial x_i} = 0 \quad i = 1,2 \tag{7.2}$$

$$\rho c_p \left(\frac{\partial T}{\partial t} + v_i \frac{\partial T}{\partial x_i} \right) = K \frac{\partial}{\partial x_i} \frac{\partial T}{\partial x_i} + A_R + A_{SH} + v_2 \alpha g T \rho \quad i = 1,2 \tag{7.3}$$

where σ_{ij} is the deviatoric stress tensor, x_i spatial coordinates, P pressure (mean stress), ρ density, g gravitational acceleration, v_i a component of velocity, c_p specific heat, T temperature, t time, K thermal conductivity, A_R (crustal) radiogenic heat production per unit volume, A_{SH} shear heating, and α volumetric thermal expansion. Coupling of the mechanical and thermal solutions is achieved through the advection of radioactive crust, shear heating, thermal activation of viscous flow, and buoyancy forces arising from metamorphic phase changes and thermal expansion. ρ, K, A_R, and α vary among the model materials, and for some materials K and α depend on temperature (Table 7.1).

The model domain is 2700×660 km (10×2 km resolution) and contains a 'nested' sub-domain in the vicinity of the subduction zone (from 1300 to 2300 km) with a resolution of 2×2 km. The initial geometry of the models (Fig. 7.4) is designed to represent a generic Norwegian Caledonian type subduction/accretion system, and

includes a lower plate (procontinent) comprising two microcontinents and a continent with a rifted continental margin, an ocean, and a laterally homogeneous upper plate (retrocontinent). The distal 'outer' microcontinent and the proximal 'inner' microcontinent are termed the OMC and IMC, respectively. Similarly, the outer and inner rift basins are the ORB and IRB, respectively.

For simplicity, we assume subduction and accretion of terranes occurs within a single subduction zone formed at the margin of the retrocontinent. The procontinent microcontinents and margin are separated by regions of thin crust representing rift basins. The continental margins and microcontinents each have relatively weaker upper and stronger lower crusts, and have maximum thicknesses of 32 km and 24 km, respectively. The crustal units, including the rift basins, are capped by a thin, weak sediment cover (4 km). The composite margin with microcontinents and rift basins is a general representation of the 'hyperextended' margin envisaged by *Andersen et al.* (2012).

Deformation of model materials occurs by either frictional-plastic (brittle) or power-law viscous (ductile) flow, with additional parametric strain-softening/strain-weakening mechanisms. Frictional-plastic deformation depends on the dynamical pressure and effective angle of internal friction (ϕ_{eff}; hereafter simply ϕ), through the frictional-plastic Drucker-Prager yield criterion, σ_y:

$$\sigma_y = (J_2')^{1/2} = P\sin\phi_{\text{eff}} + C\cos\phi_{\text{eff}} \tag{7.4}$$

where J_2' is the second invariant of the deviatoric stress, P the dynamical pressure (mean stress), and C the cohesion. The effective angle of internal friction, ϕ_{eff}, is defined to include the effects of pore fluid pressures through the approximate relation:

$$P sin\phi_{\text{eff}} = (P - P_f) sin\phi \tag{7.5}$$

where $\phi = 30°$ is the angle of internal of friction for dry conditions ($P_f = 0$). ϕ_{eff} is an apparent angle of internal friction of the material owing to pore fluid pressure and/or strain-softening (see below).

Ductile deformation is modeled as incompressible power-law flow, for which the

effective viscosity is:

$$\eta_{\text{eff}}^{v} = \frac{f}{W_s} A^{-1/n} \dot{I}_2'^{(1-n)/2n} exp\left(\frac{Q + PV^*}{nRT_K}\right) \tag{7.6}$$

where f is a viscosity scaling factor, W_s a strain-weakening factor, A the pre-exponential factor, converted to the tensor invariant form, $\dot{I}_2'$ the second invariant of the deviatoric strain rate, n the stress exponent, Q activation energy, P pressure, V^* the activation volume for power-law creep, T_K absolute temperature, and R the universal gas constant (Table 7.1).

Crustal materials and the lithospheric mantle soften/weaken in the frictional-plastic and viscous regimes, respectively. Frictional-plastic materials strain-soften through a linear decrease in their effective angle of internal friction, ϕ_{eff}, with accumulated strain: $\phi_{\text{eff}} = \phi_{\text{eff}}(\epsilon)$. $\epsilon = I_2'^{1/2}$, the square root of the second invariant of deviatoric strain, with ϵ (strain) used for simplicity. For most model materials $\phi = 15$–$4°$, where $15°$ includes the effect of hydrostatic pore fluid pressure and $4°$ is the lower limit of ϕ decreased from $15°$ with increasing strain. The 'cover' units and units representing pre-weakened or rifted regions (e.g., the microcontinents) have lower initial values, from $\phi = 6$–$4°$ and $\phi = 8$–$4°$, respectively. Viscous strain-weakening occurs through a linear decrease in effective viscosity by the factor W_s over a specified ϵ range. For all models, crustal materials weaken by $W_s = 10$ over the range $\epsilon = 5$–10.

Viscous flow laws are derived from a small set of reliable laboratory flow laws scaled by a factor f, and strain-weakened by the maximum amount W_s (Table 7.1. For the upper crusts we use scaled wet quartzite (WQ×f, where f varies among crustal units; *Gleason and Tullis*, 1995). For most of the models presented below, the microcontinents use WQ×0.1, on the basis that they represent already strain-weakened fragments of rifted continental margin or previously deformed terranes. The procontinent margin, in contrast, uses WQ×5, on the basis that it represents relatively dry, polymetamorphic continental crust, analogous to Proterozoic granulite facies basement rocks that dominate the WGR. The lower continental and oceanic crusts use a scaled dry Maryland diabase flow law (DMD×0.2 and 0.1 respectively; *Mackwell et al.*, 1998). The mantle materials use a wet olivine flow law (*Karato and Wu*, 1993) scaled to represent either 'wet' sublithospheric mantle or

relatively dehydrated 'dry' lithospheric mantle. The continental and oceanic lithospheric mantle both have a WOL×7.5 flow law, whereas the sublithospheric mantle uses WOL×1.

The model domain has a stress-free upper surface, and no-slip and free-slip sides and base, respectively. Convergence in the models is driven by a velocity boundary condition applied along the side of the procontinent lithosphere, termed V_p. For most model experiments, $V_p = 5$ cm a^{-1}, and decreases to $V_p = 2.5$ cm a^{-1} following collision of the first microcontinent with the retrocontinent. During convergence, the retrocontinent velocity, $V_r = 0$ cm a^{-1}. Later in the models, we systematically vary the procontinent and retrocontinent convergence velocities (V_p and V_r, respectively) in order to assess the consequences of varying boundary conditions on the (U)HP exhumation process.

The thermal boundary conditions include basal heat flux 20.8 mWm^{-2}, a 0°C surface, and insulated side boundaries. Radioactive heat production (A_R) is 1.5 and 0.55 μWm^{-3} for the upper and lower crusts respectively, resulting in an initial steady-state Moho temperature of ∼590°C, and surface heat flow 63 mW m^{-2} on the standard thickness continents. The value of upper crustal heat production is consistent with measurements from granitoid gneisses from Western Norway (*Slagstad*, 2008)

Crustal materials undergo pressure- and temperature-dependent density changes at the eclogite and coesite-eclogite phase transitions. The densities of the continental crust at low, high, and ultra-high pressures are 2800, 2950, and 3000 kg m^{-2}, consistent with the range of measured densities for orthogneisses from the WGR (*Walsh and Hacker*, 2004)

The models include slope-dependent surface erosion above sea-level, where $E_s =$ 1 cm a^{-1} is the erosion rate that acts on a slope of 45°. The effects of higher erosion rates during the timespan of (U)HP exhumation are discussed below.

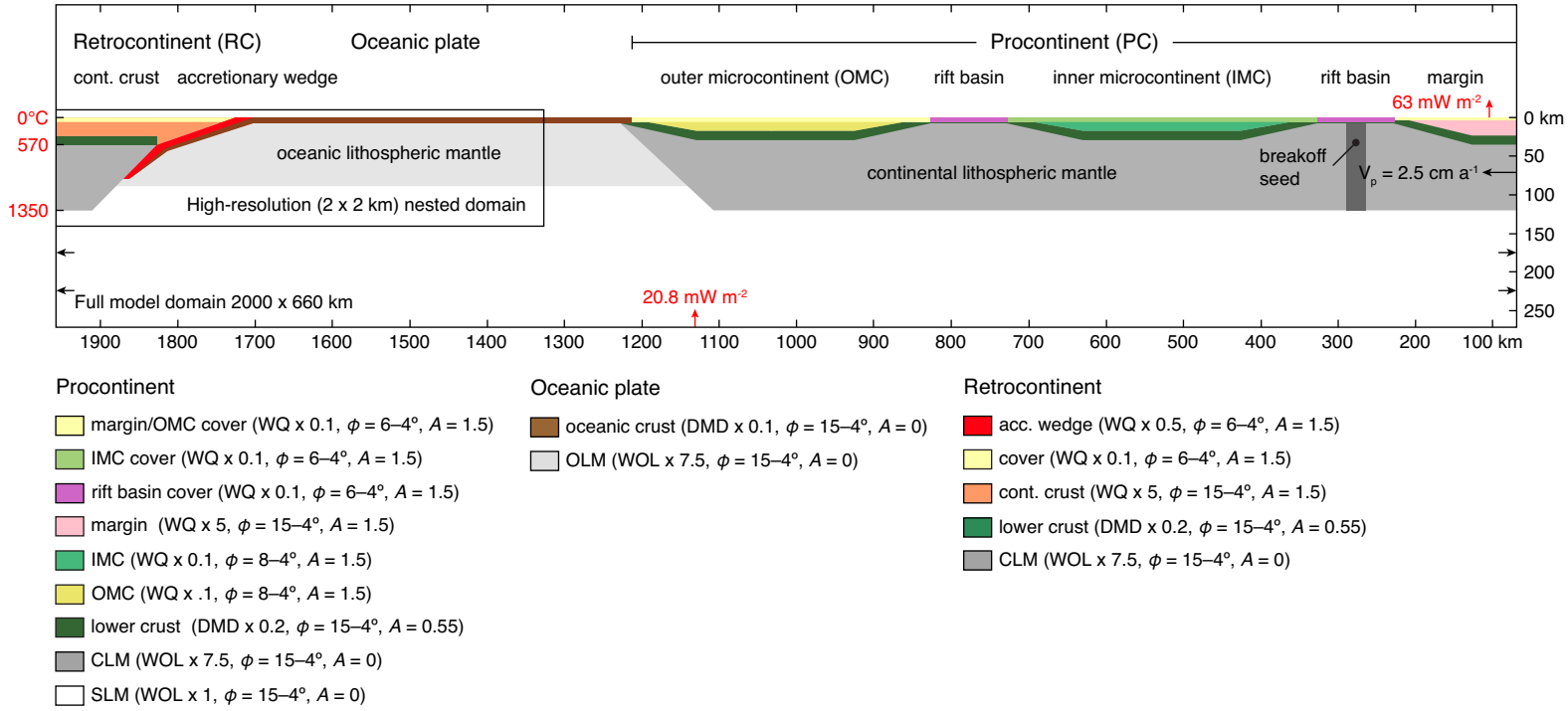

Figure 7.4: Model design. WQ=wet quartzite, DMD=dry Maryland diabase, WOL=wet olivine. ϕ=range of effective angle of internal friction (ϕ_{eff}) owing to strain-softening; A=radiogenic heat production (μWm^{-3}; A_R in text). Inset box shows location of nested domain. Black arrows show velocity boundary conditions. Red arrows show basal and surface heat flux. Horizontal axis reversed to make models appear consistent with westward subduction of Baltica beneath the Laurentia.

Parameter	Units	Cover	PC/RC margin crust	IMC/OMC crust	LC	OC	CLM	OLM	SLM
Mechanical Parameters									
Max. thickness	km	2–6	24	18	12	8	to 120	to 90	600
Reference density[a]	kg m^{-3}	2800	2800	2800	2950	2900	3340	3350	3370
HP density	kg m^{-3}	2850	2850	2850	3300	3400	-	-	-
UHP density	kg m^{-3}	2900	2900	2900	-	-	-	-	-
ϕ_{eff}	deg	6–4	15–4	8–4	15–4	15–4	15–4	15–4	15–4
Flow law	-	WQ	WQ	WQ	DMD	DMD	WOL	WOL	WOL
Flow law reference	-	GT95	GT95	GT95	M98	M98	KW93	KW93	KW93
f	-	0.1	5	0.1	0.2	0.1	7.5	7.5	1
W_s	-	10	10	10	10	10	10	10	1
n	-	4	4	4	4.7	4.7	3	3	3
A[b]	Pa^{-n} s^{-1}	8.57×10^{-28}	8.57×10^{-28}	8.57×10^{-28}	5.78×10^{-27}	5.78×10^{-27}	1.76×10^{-14}	1.76×10^{-14}	1.76×10^{-14}
Q	kJ mol^{-1}	223	223	223	485	485	430	430	430
V^*	m^3 mol^{-1}	0	0	0	0	0	1×10^{-5}	1×10^{-5}	1×10^{-5}
Thermal Parameters									
Heat capacity	m^2 s^{-2} K^{-1}	750	750	750	750	750	1250	1250	1250
Thermal conductivity	W m^{-1} K^{-1}	2.25	2.25	2.25	2.25	2.25	2.25	2.25	52[c]
Thermal diffusivity	m^2 s^{-1}	1×10^{-6}	1×10^{-6}	1×10^{-6}	1×10^{-6}	1×10^{-6}	1×10^{-6}	1×10^{-6}	1.4×10^{-5}
Thermal expansivity	K^{-1}	3×10^{-5}	3×10^{-5}	3×10^{-5}	3×10^{-5}	3×10^{-5}	3.2–3.9×10^{-5}[d]	3.2–3.9×10^{-5}[d]	3.2–3.9×10^{-5}[d]
Heat production (A_R)	μWm^{-3}	1.5	1.5	1.5	0.55	0	0	0	0

[a] Densities calculated at 273 K using listed coefficient of thermal expansion.

[b] Uniaxial pre-exponential factor converted to tensor invariant form.

[c] Thermal conductivity increases linearly over the T range 1620–1630 K

[d] Thermal expansivity increases linearly over the T range 500–2000 K

Table 7.1: Material parameters used in model experiments. 'Cover' has same properties for all units. PC=procontinent, RC=retrocontinent, IMC=inner microcontinent, OMC=outer microcontinent, LC=lower crust, OC=oceanic crust, CLM=continental lithospheric mantle, OLM=oceanic lithospheric mantle, SLM=sublithospheric mantle. Flow law references are *Gleason and Tullis* (1995)(GT95), *Mackwell et al.* (1998)(M98), and *Karato and Wu* (1993)(KW93).

7.5 Model Results

The model results are described in terms of two separate phases. Phase 1 involves oceanic subduction, accretion of both microcontinents, and subduction of the procontinent margin. This phase, termed the reference model (Model R) is identical for all models presented below. Phase 2 is the procontinent margin exhumation phase, for which we present three models that vary in terms of their boundary conditions, ranging from near quiescence, to varying rates of plate divergence. The main parameters explored here represent a subset of the tested parameters, chosen specifically to address some of the unanswered questions concerning the evolution of the WGR as a type example.

7.5.1 Model R (Phase 1): Microcontinent Accretion and Margin Subduction

The models begin with a ∼15 Myr phase of subduction of oceanic lithosphere, driven at $V_p = 5$ cm a^{-1}, during which the retrocontinent remains mainly undeformed. As the leading edge of the outer microcontinent (OMC) contacts the toe of the orogenic wedge, formed by retrocontinent crust, V_p is reduced to 2.5 cm a^{-1}. Subsequent model events are expressed in terms of Myr post-OMC collision (Myr-pc). Following 'collision' (Fig. 7.5a), the leading edge of the OMC, together with some of its cover, is subducted beneath the retrocontinent. A small amount of the OMC reaches (U)HP conditions 8 Myr-pc. The leading edge of the OMC upper crust then decouples from the underlying slab along a basal shear zone that quickly propagates upward, leading to wholesale detachment of the OMC upper crust and formation of a large 'allochthon' at the base of the accretionary wedge, by 10 Myr-pc. Subsequent underthrusting of the outer rift basin (ORB), and then the inner microcontinent (IMC), leads to shortening and subduction of the shallowly accreted OMC allochthon crust to (U)HP conditions from 15–22 Myr-pc (Fig. 7.5b). Continued accumulation of weakened crust in the subduction channel leads to a minor pulse of buoyancy-driven exhumation from 25–30 Myr-pc (Fig. 7.5c). The pulse carries a mixture of deformed (U)HP IMC and OMC crust to the base of the orogenic wedge, where it achieves neutral buoyancy and then stalls. The trailing end of the IMC meanwhile, detaches in a fashion similar to that of the OMC, forming a tapered IMC allochthon. As with

the first allochthon, underthrusting of the inner rift basin (IRB) leads to shortening and subduction of detached IMC allochthon crust, and reburial of OMC crust. By 32 Myr-pc, the model has built a thick (∼24–70 km), ∼300 km-wide orogenic wedge comprising the stacked OMC and IMC allochthons with intervening rift basin crust. The deepest levels of the wedge comprise strongly deformed/mixed (U)HP allochthon crust that has been exhumed to lower crustal depths, whereas toward the foreland the allochthons remain relatively intact.

Collision of the procontinent margin with the orogenic wedge occurs ∼32.5 Myr-pc. Subduction of the relatively strong margin crust beneath the accreted allochthons drives some of the partly exhumed (U)HP allochthon crust up and proward over the subducting margin to shallow crustal depths. With the exception of its cover, which detaches and accretes to the front of the prowedge, the margin crust remains coupled to the slab, reaching (U)HP conditions of ∼3 GPa/650°C by ∼48 Myr-pc. By the end of this stage, the orogenic wedge is ∼50 km thick at its maximum, and ∼300 km wide. The underthrust procontinent margin remains attached the slab and relatively undeformed. The leading ∼50 km of the margin has reached UHP conditions, while the adjacent HP portion is ∼100 km wide.

7.5.2 Phase 2: Exhumation of (U)HP Margin Crust

The result of Phase 1 was used as a starting point for three models that test the effects of contrasting boundary conditions on the style of late- to post-orogenic (U)HP rock exhumation. In Model Q, the procontinent convergence velocity (V_p) was reduced from 2.5 cm a^{-1} in Phase 1 to $V_p = 0.0025$ cm a^{-1}, in order to produce a phase that is effectively quiescent, corresponding to the end of relative plate convergence. Models DV0.25 and DV0.5, in contrast, test the effects of divergent plate motion by applying a velocity to the retrocontinent (V_r) of -0.25 and -0.5 cm a^{-1}, respectively. The consequent plate divergence can likened to the postulated shift from sinistral transpressional to sinistral trantensional plate motions in the late evolution of the Caledonides (*Krabbendam and Dewey*, 1998). In both divergent models $V_p = 0$ cm a^{-1}. Prior to Phase 2, each model was subjected to a short intermediate phase during which breakoff of the subducted portion of the procontinent lithospheric mantle was engineered by instantaneously weakening an embedded 'seed' (Fig. 7.4). Prior experiments showed that slab breakoff is necessary to decouple the

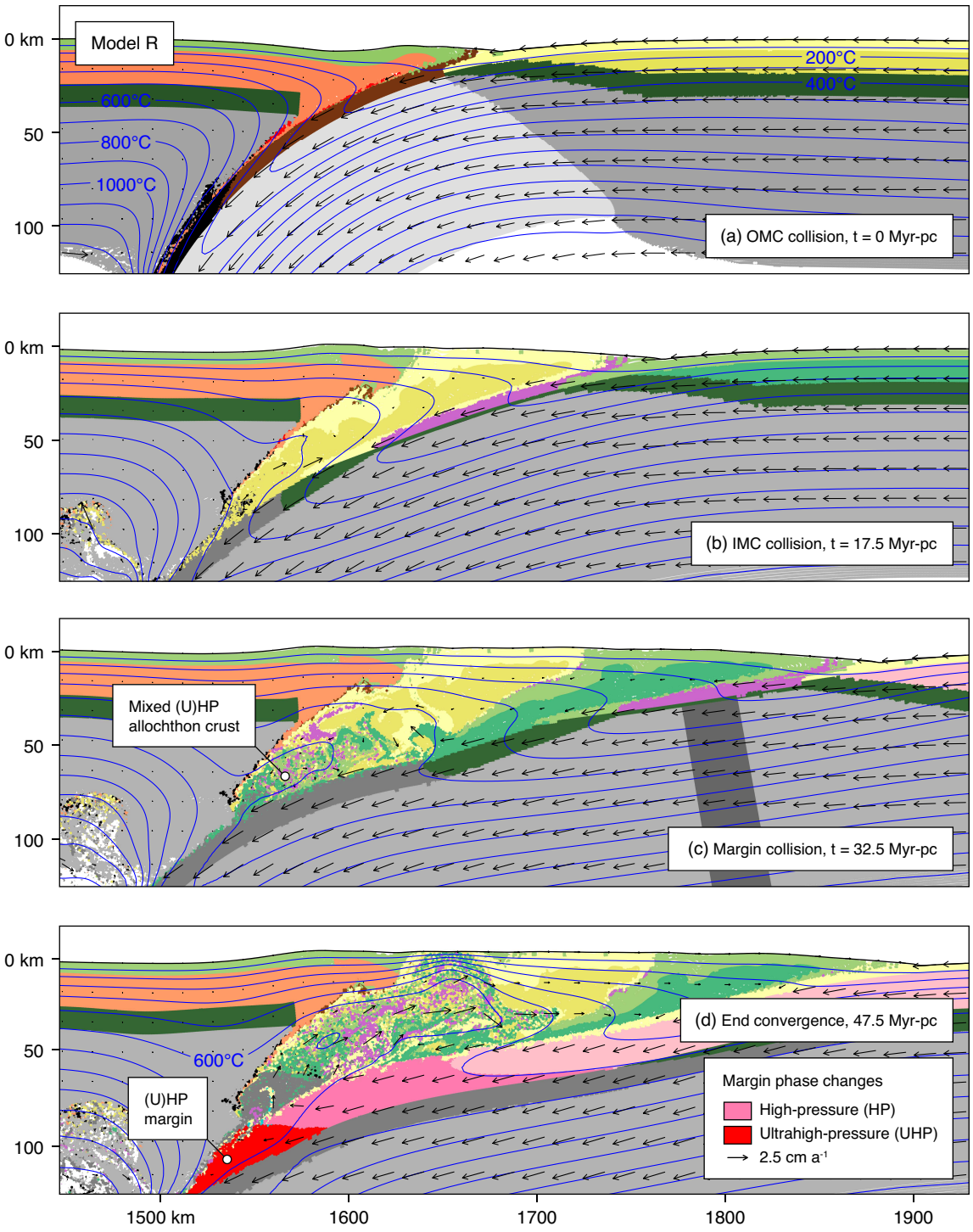

Figure 7.5: Results of Model R. (a–d) Material colours, velocity vectors, and isotherms (blue lines) for model times corresponding to events described in text. (d) Represents the state of the model immediately prior to Phase 2 changes in boundary conditions. The dark grey band within the procontinent lithospheric mantle shows the position of the mechanical zone used to engineer later breakoff of the slab following margin subduction. In (d) the mantle 'seed' has subducted.

continents during subsequent plate divergence. Future work will involve achieving slab breakoff dynamically. For now, the engineered approach allows us to achieve the desired result at the appropriate time in the model evolution. The Phase 2 model results are presented from the point immediately after slab breakoff (47.5 Myr-pc) until 70 Myr-pc. The timespan equates to 23 Myr of quiescence or extension following the end of convergence, and is broadly consistent with the evolution of the WGR where there was 25 Myr between the youngest age of (U)HP metamorphism and the youngest ages of extensional deformation. In the following discussion model times are given in Myr-pb (post-breakoff at 47.5 Myr-pc), as opposed to Myr-pc.

7.5.3 Model Q: Plate Quiescence

Model Q (Figs 7.6 and 7.7) illustrates the case in which convergence effectively ceases following subduction of the procontinent margin to (U)HP conditions. The end of convergence and slab breakoff are immediately followed by the onset of relatively slow buoyant exhumation of (U)HP crust from the subduction channel (Fig. 7.6a). The buoyant ascent of the most deeply buried (U)HP crust leads to some shortening distributed throughout the leading edge of the margin, which is separated from the overlying allochthons and adjacent margin crust by normal- and thrust-sense shear zones, respectively (Fig. 7.7a). At shallower depths, meanwhile, gravitational spreading of the relatively weak orogenic wedge crust leads to continued thrusting of the prowedge over the margin. The exhumed (U)HP margin crust reaches the base of the retrocontinent crust (at $\sim$1 GPa) at 10.5 Myr-pb, by which time a large portion of the orogenic crust has heated to $\gtrsim$700°C; Fig. 7.6b). The rate of gravitational spreading of the allochthons decreases near this time, as erosion at the rear of the orogen (at the back of the plug region) allows the (U)HP crust to exhume from beneath the allochthons along a channel bounded by a retroshear(zone) (Figs 7.6c and 7.7c). At 22.5 Myr-pb, the orogenic wedge built from accreted allochthons remains a full crustal thickness. The top of the margin crust underlying the orogenic plateau remains at middle orogenic crustal depths, at P–T conditions of $\sim$1 GPa/700–800°C. The leading, (U)HP part of the margin, meanwhile, is bent upward and is exposed at the surface along back of the plug, on the retroside of the orogen.

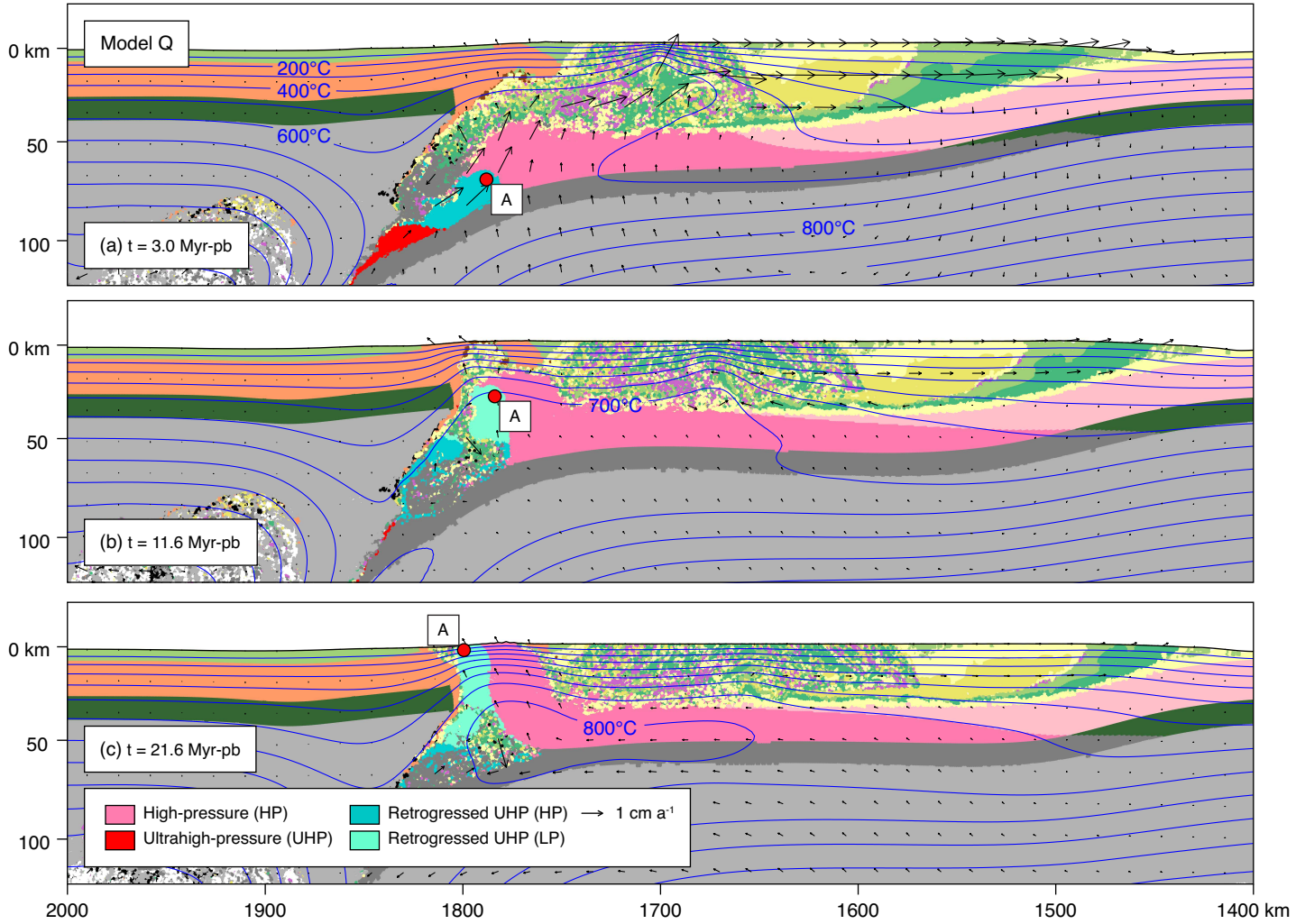

Figure 7.6: Results of Model Q. $V_p = 0.0025$ cm a^{-1}. (a–c) Material colours, velocity vectors, and isotherms (blue lines) for model times corresponding to events described in text. Red circle shows position of P–T–t particle described in Figure 7.12.

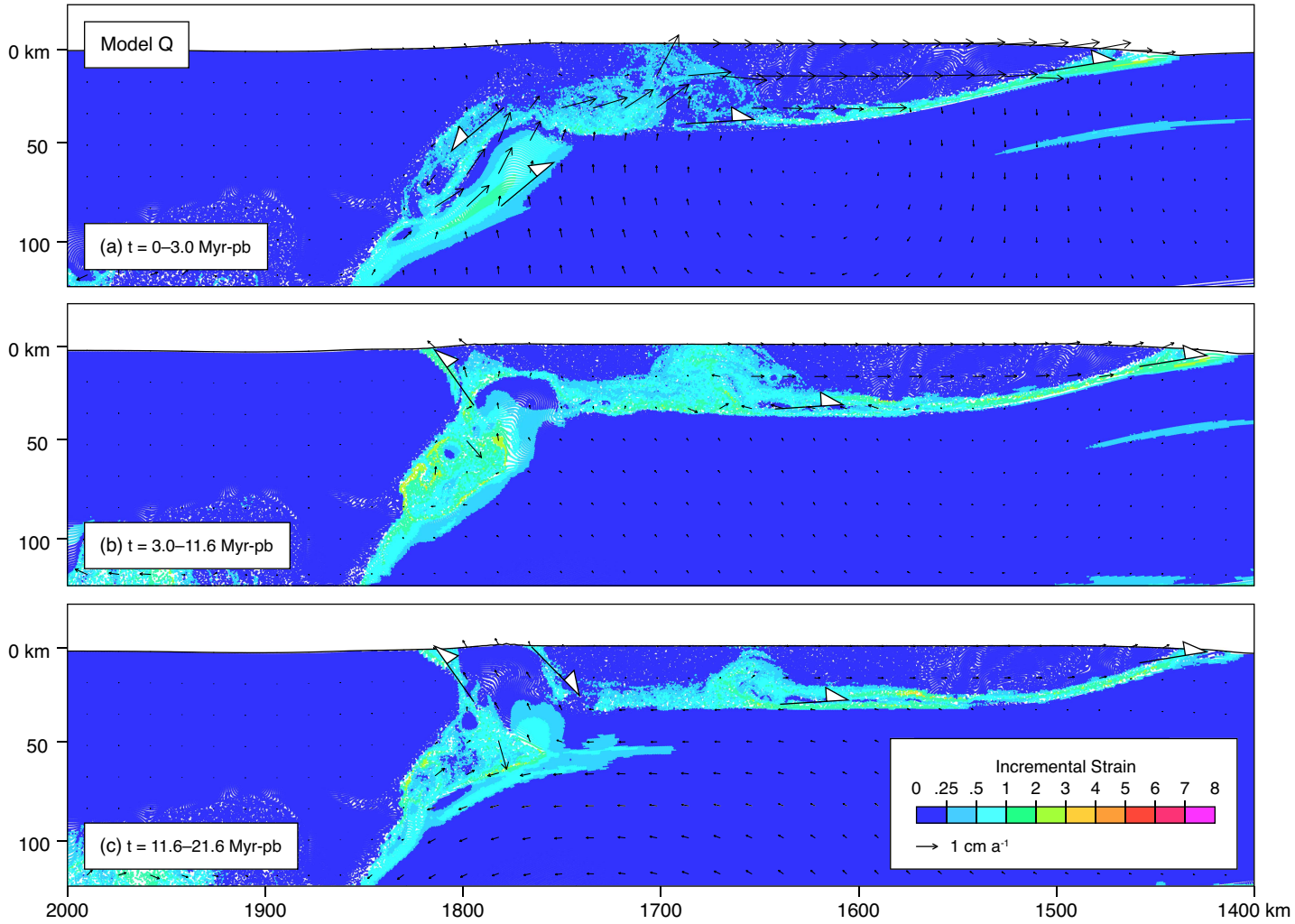

Figure 7.7: Incremental strain plot for Model Q. Colours represent strain (square root of second invariant) accumulated during phases discussed in text. Frames shown correspond to end of interval over which incremental strain was calculated. White-filled arrows show interpreted kinematics of deformation along dominant shear zones.

7.5.4 Model DV0.25: Plate Divergence at 0.25 cm a^{-1}

Model DV0.25 (Figs 7.8 and 7.9) illustrates the case in which cessation of convergence is followed by very slow plate divergence. Similar to Model Q, the orogenic wedge begins gravitational spreading immediately, leading to thrusting over the margin (Figs 7.8a and 7.9a). Exhumation of the (U)HP margin crust appears to be the combined effect of two processes. Similar to Model Q, the leading edge of the margin (U)HP crust undergoes some buoyant exhumation resulting in bulk shortening coupled with coeval normal- and thrust-sense shearing above and below the (U)HP crust, respectively (Figs 7.8a and 7.9a). A small portion of the leading (U)HP edge of the margin remains coupled to the procontinent lithosphere, and later rapidly exhumes through the overlying allochthon crust (Fig. 7.8b). On the larger scale, the leading ∼150 km of the margin ascends in response to the vertical rebound of the procontinent lithosphere, owing to both breakoff of the dense slab, and to extensional removal of the overriding continent. These processes bring the (U)HP margin crust to lower crustal depths by 13 Myr-pb (Fig. 7.8b and 7.9b), earlier than in Model Q. By this time a large portion of the margin has heated to $\gtrsim$700°C. Subsequent extension leads to continued normal-sense shearing along the retrocontinent/allochthon contact as the rear of the orogenic wedge is thinned, whereas the front half of the wedge continues to slowly spread proward, stopping shortly after 12.5 Myr-pb (Fig. 7.9b). Minor deformation also occurs along the rear of the orogen in response to uplift. By 23 Myr-pb, after ∼58 km of divergence (Fig. 7.8c), the allochthonous nappe stack overlying the center of the orogen is somewhat thinner than in Model Q (by ∼5 km), but remains thick. The underlying margin is at similar upper amphibolite facies P–T conditions of ∼1 GPa/700–800°C, although compared with Model Q a much smaller region has reached 800°C, owing to the enhanced crustal thinning. The leading (U)HP edge of the margin has exhumed to a position slightly above the adjacent HP margin crust that underlies the plateau, but has not been exposed along the rear of the orogen as in Model Q.

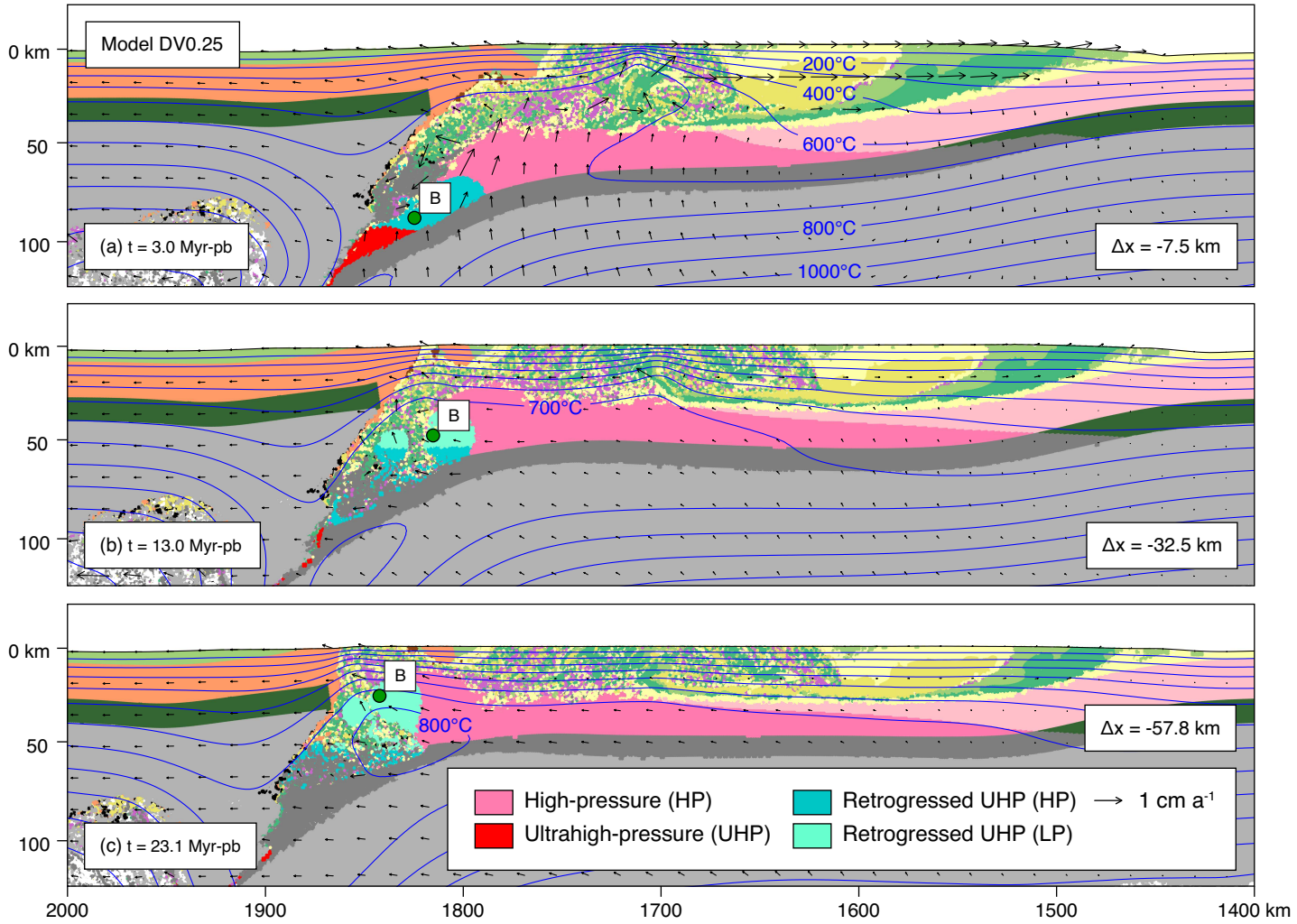

Figure 7.8: Results of Model DV0.25. V_r = -0.25 cm a^{-1}. (a–c) Material colours, velocity vectors, and isotherms (blue lines) for model times corresponding to events described in text. Green circle shows position of P–T–t particle described in Figure 7.12. Δx is amount of plate divergence.

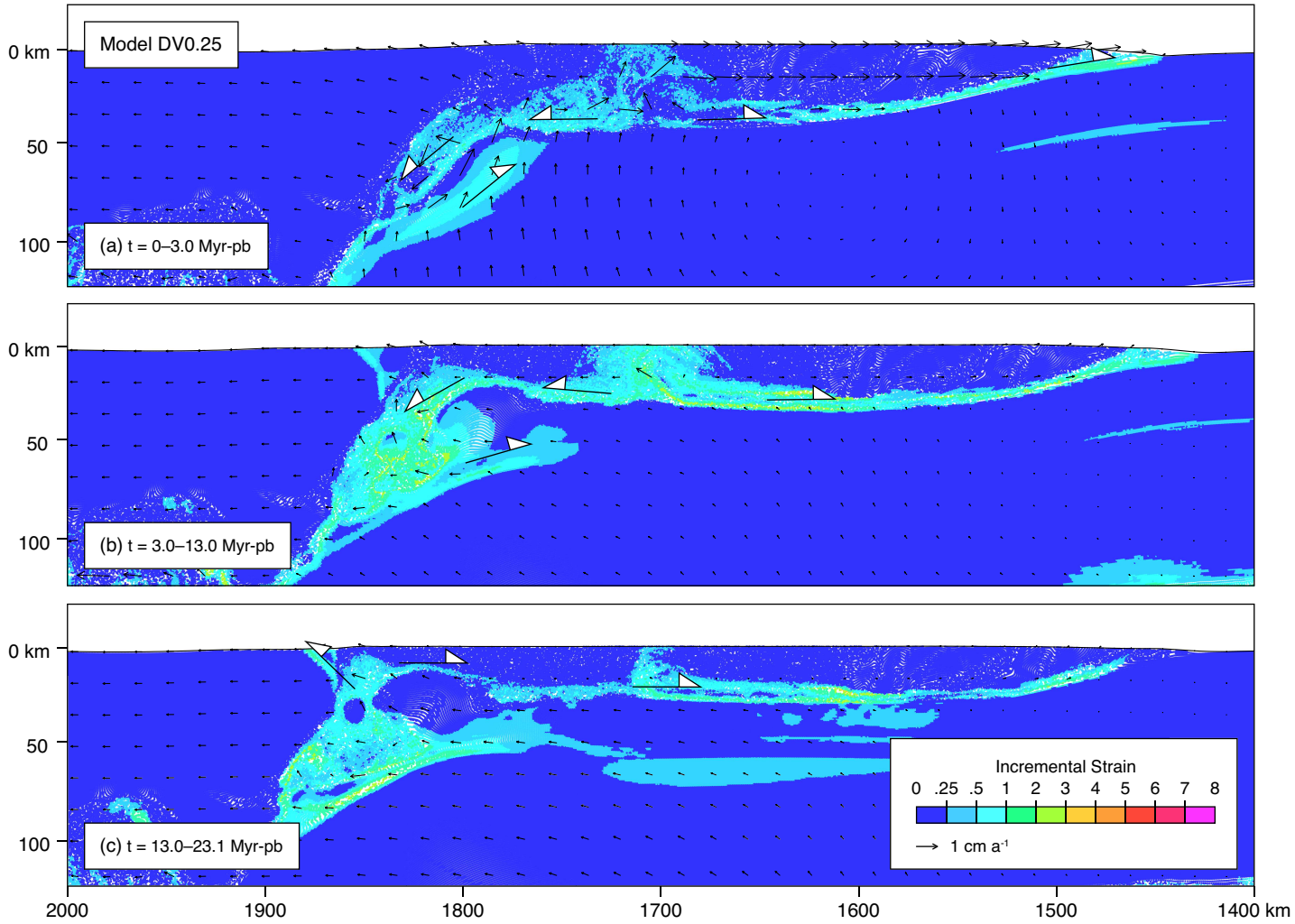

Figure 7.9: Incremental strain plot for Model DV0.25. Colours represent strain (square root of second invariant) accumulated during phases discussed in text. Frames shown correspond to end of interval over which incremental strain was calculated. White-filled arrows show interpreted kinematics of deformation along dominant shear zones.

7.5.5 Model DV0.5: Plate Divergence at 0.5 cm a^{-1}

Model DV0.5 (Figs 7.10 and 7.11) evolves in a manner similar to Model DV0.25, with some subtle but important differences. As in both previous models, the end of convergence leads to immediate gravitational spreading of the orogenic wedge, again resulting in minor proward thrusting over the procontinent (Figs 7.10a and 7.11a). Meanwhile, the (U)HP margin crust begins to detach from the underlying lithosphere and exhume. As in Model DV0.25, exhumation to the lower crust occurs by a combination of crustal buoyancy and regional rebound of the procontinent lithosphere. However, whereas in Model DV0.25 the buoyantly exhuming (U)HP crust outpaces the rest of the slab, i.e., the adjacent margin crust that remains coupled to the lithosphere, in Model DV0.5 the rebounding slab keeps pace with the (U)HP margin crust such that the two appear to remain 'attached' during ascent (Figs 7.10b and 7.11b). Deformation during exhumation is again dominated by top-retroward or normal-sense shearing between the (U)HP margin crust and the overlying allochthons, with the region of top-retroward shearing extending somewhat further proward beneath the allochthons in this model. Only minor shortening occurs within the leading (U)HP part of the margin. Proward spreading of the orogenic wedge ceases earlier in Model DV0.5, by 7.5 Myr-pb. With continued extension the margin crust beneath the orogen thins vertically, and the leading (U)HP edge of the margin detaches from the slab and ascends to a subhorizontal position. By 23 Myr-pb (Figs 7.10c and 7.11c), the orogen has undergone ~115 km of absolute extension. Most of the divergence has been accommodated by vertical rebound of the procontinent lithosphere, coupled with thinning of both the allochthonous nappes and the underlying margin crust. The allochthonous nappe stack is somewhat thinner than in Model DV0.25, but remains close to a normal crustal thickness. The (U)HP margin crust lies in a subhorizontal position at amphibolite facies conditions (temperatures of $\gtrsim$700°C), and appears attached to the adjacent margin crust, despite having undergone greater internal deformation.

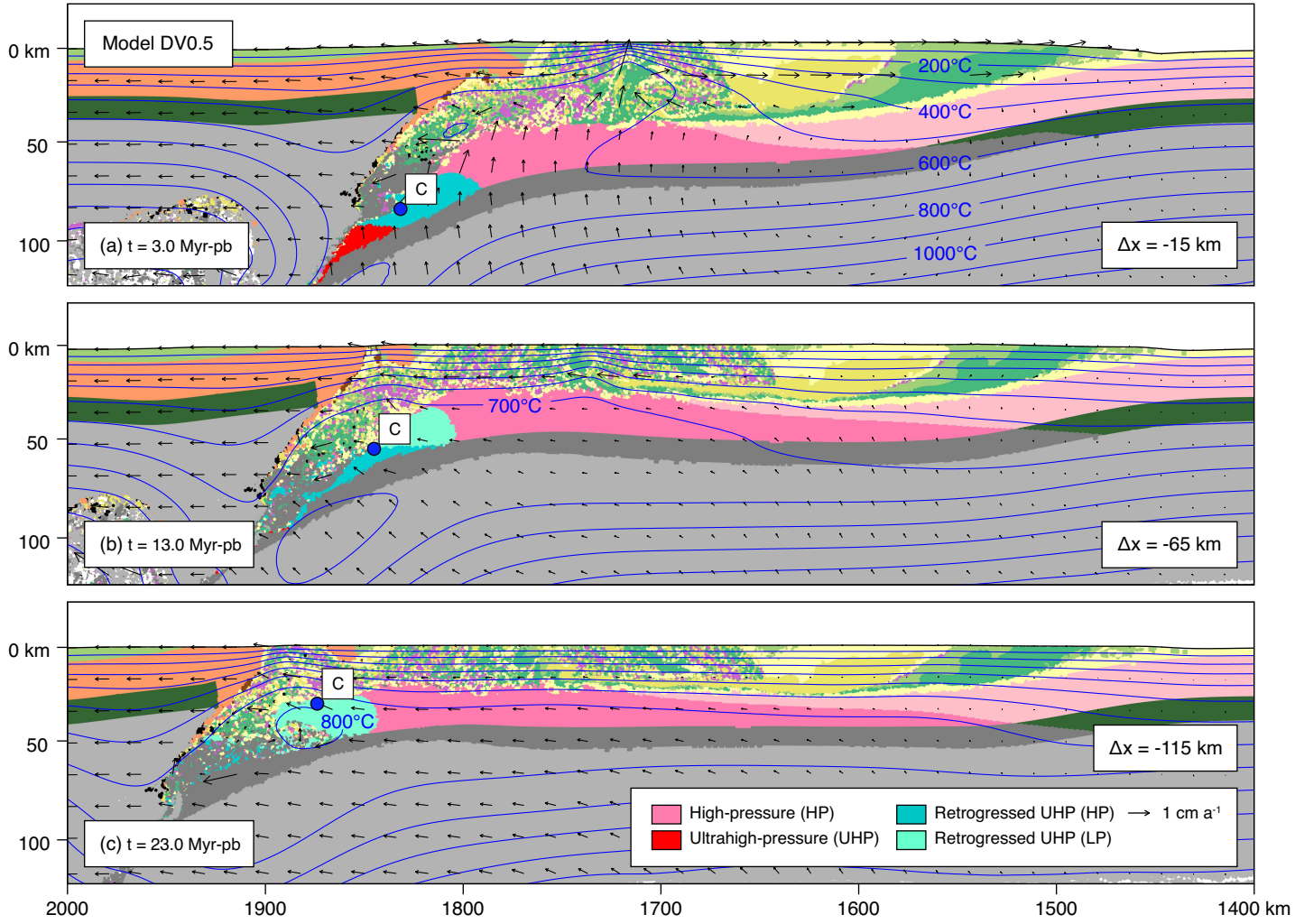

Figure 7.10: Results of Model DV0.5. V_r = -0.5 cm a^{-1}. (a–c) Material colours, velocity vectors, and isotherms (blue lines) for model times corresponding to events described in text. Blue circle shows position of P–T–t particle described in Figure 7.12. Δx is amount of plate divergence.

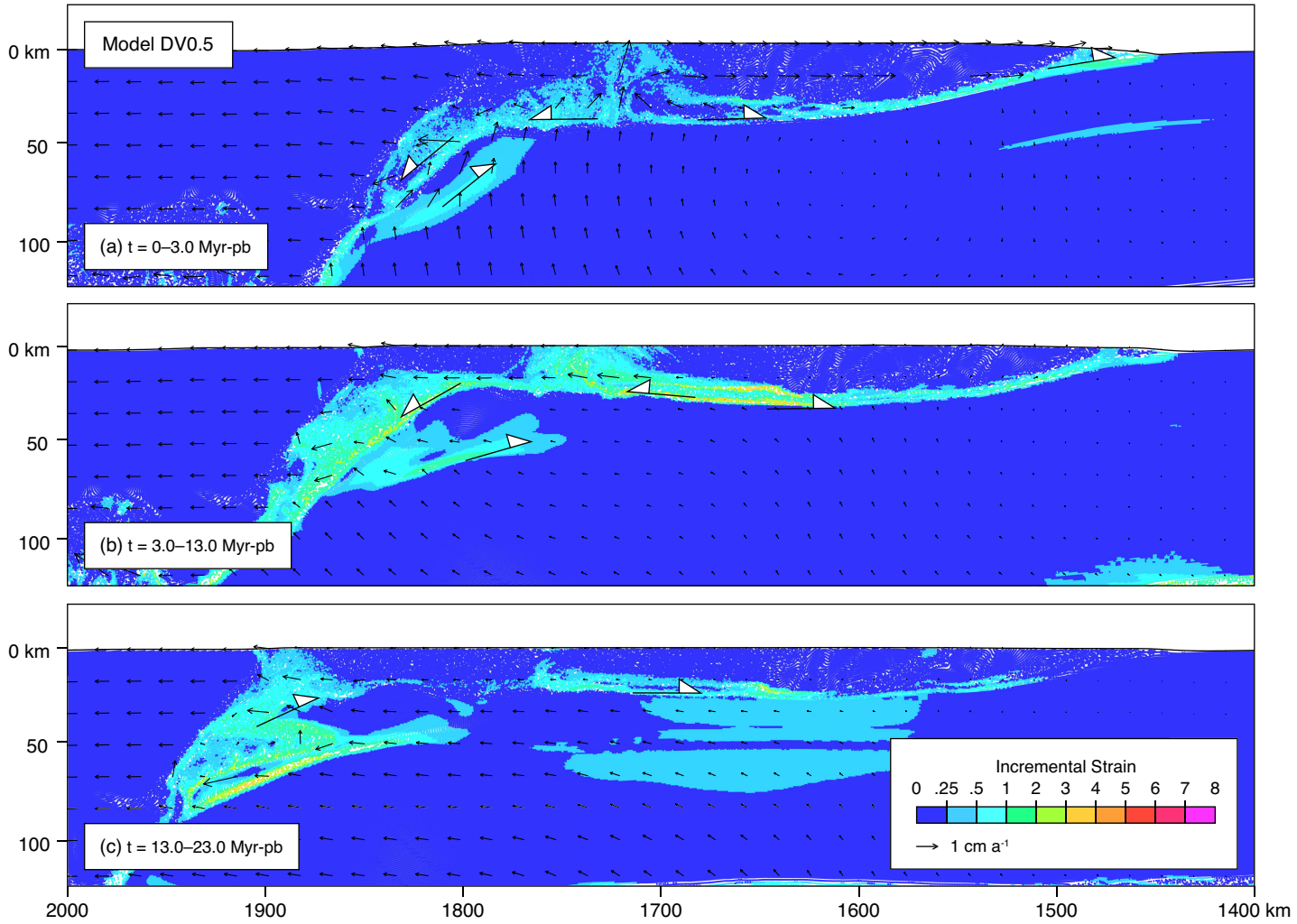

Figure 7.11: Incremental strain plot for Model DV0.5. Colours represent strain (square root of second invariant) accumulated during phases discussed in text. Frames shown correspond to end of interval over which incremental strain was calculated. White-filled arrows show interpreted kinematics of deformation along dominant shear zones.

7.6 Comparison of Model Results with the Western Gneiss Region

7.6.1 Structure and Tectonic Evolution

Although preliminary, the models presented above reproduce several of the key tectonic features of the WGR. The structural and tectonic similarities and differences between the models and the WGR include the following (in broadly chronological order).

1. The model successfully produces a thick and laterally extensive orogenic wedge by the accretion of multiple microcontinents/exotic terranes in response to subduction of procontinent lithosphere (corresponding to Baltica) beneath the retrocontinent (corresponding to Laurentia). (U)HP metamorphism of the microcontinent crust during Phase 1 of the models can be likened to pre-Scandian (U)HP metamorphism locally preserved in allochthons that structurally overlie the Baltican margin. In the models, these allochthons were accreted from the procontinent 'hyperextended' margin.

2. Burial of the procontinent margin to (U)HP conditions beneath the orogenic wedge (see below for discussion of P–T history) can be considered equivalent to burial of the Baltican margin to (U)HP conditions. Minor coeval shallow syn-orogenic extension during this phase, resulting from upward flow of the (U)HP microcontinent crust, may be analogous to the extension that helped form the oldest Devonian basins above the WGR, while subduction continued at depth.

3. In models DV0.25 and DV0.5, exhumation of the (U)HP procontinent margin, corresponding to the WGR, proceeds mainly by top-retroward shearing at amphibolite facies metamorphic conditions along the contact with the overlying allochthons. The style deformation is similar to the top-W shearing documented within the Nordfjord Sogn Detachment Zone, which formed at amphibolite facies conditions similar to those in the models. Vertical thinning of the margin crust, as in Model DV0.5, is also consistent with observations from the WGR.

4. The distribution of deformation within the procontinent margin, from relatively undeformed beneath the plateau (corresponding to the eastern WGR), to more pervasively deformed at the leading (U)HP end of the margin is similar to the westward increase in Scandian deformation within the WGR.

5. The apparent lateral continuity of the procontinent margin crust, despite the deformation noted above, is consistent with the apparent absence of major syn-(U)HP tectonic structures or metamorphic breaks with the WGR.

6. The local top-retroward shearing between the allochthons and the underlying (U)HP margin is similar to 'backsliding' of the orogenic wedge inferred from top-W fabrics within the Jotun Detachment.

7. The limited extent of proward thrusting in the foreland during exhumation of the procontinent margin from (U)HP conditions is consistent the foreland sedimentary record in the southwestern Scandinavian Caledonides.

8. There is no detachment and thrusting of the (U)HP procontinent margin crust onto the procontinent, which is consistent with the lack of evidence for a 'basal' thrust within the WGR.

9. The 'final' width of the orogen, ∼400 km, is similar to the present day width of ∼350–400 km from the western edge of the WGR to the leading edge of the Lower Allochthon in the foreland. The orogen may have been even wider prior to the Mesozoic rifting that affected the Norwegian margin and Greenland.

There are, however, some obvious shortcomings to the models. First, the strong deformation of the (U)HP allochthon crust during Phase 1 results in intense mixing of these units. I am not aware of any equivalent extremely mixed units of this scale within the Norwegian Caledonides. Future modeling will explore alternative mechanisms of microcontinent accretion that may result in less intense internal deformation. Second, the models fail to reproduce shallow frictional-plastic deformation and high-angle normal faulting prior to and during exhumation. In the WGR, upper crustal normal faulting (recorded in extensional basin formation) likely helped to thin the orogenic wedge while subduction continued at depth. During later exhumation, brittle faulting, manifested in listric faults that cut the allochthons (the

LGFZ and NSDZ; Figs 7.2 and 7.3d), was important in exhuming the the WGR to shallow crustal depths. The absence of similar faults in the present models limits potential comparisons to the exhumation of the WGR, in that the models do not yet reproduce the late cooling history. Third, the 2D models are unable to account for orogen-parallel displacements that may have resulted from oblique sinistral plate motions in the Caledonides. Exhumation of the WGR was accompanied or followed by considerable sinistral extension in the northernmost WGR. If this deformation contributed to vertical thinning of the crust (*Krabbendam and Dewey*, 1998), then exhumation of the WGR probably required less orogen-normal extension than indicated by the divergent models. Fourth, the models were designed to produce a single-sided orogen. The Caledonides, in contrast, were a large bivergent orogen with a retrowedge (present-day East Greenland) that underwent hundreds of kilometres of shortening (*Higgins and Leslie*, 2008). Finally, the slab breakoff and subsequent instantaneous changes to the convergence velocity are artificial. Future work will focus on achieving slab breakoff dynamically, as well as testing gradual changes in relative plate motions from convergence, through cessation, to slow divergence.

7.6.2 Distribution and P–T History of Metamorphism

P–T tracking particles (Fig. 7.12a) reveal broad similarities between the models and the evolution of the WGR, but also some critical differences. Peak *P–T* conditions achieved by procontinent margin crust during Phase 1 of the models (same for all models) are ∼3.5 GPa/600°C, i.e., similar to the maximum pressures recorded by WGR eclogites, but substantially cooler. The varying peak pressures shown in Figure 7.12a are the consequence of different particle positions within the margin. The convergence rate chosen for the above models (2.5 cm a^{-1}) results in a delay between the onset of margin collision and (U)HP metamorphism that is at the shorter end of the range permitted by the data. Higher temperatures can be achieved by reducing the convergence rate, which would allow for greater thermal relaxation during crustal thickening and hence higher metamorphic temperatures. Future models will test a broader range of convergence velocities during Phase 1 margin subduction.

The subsequent *P–T* history of the models is quite similar to that of the WGR (Fig. 7.12a). Particles from all three models show decompression to upper amphiboltie/granulite facies conditions of ∼1 GPa/800°C, although Model Q produces

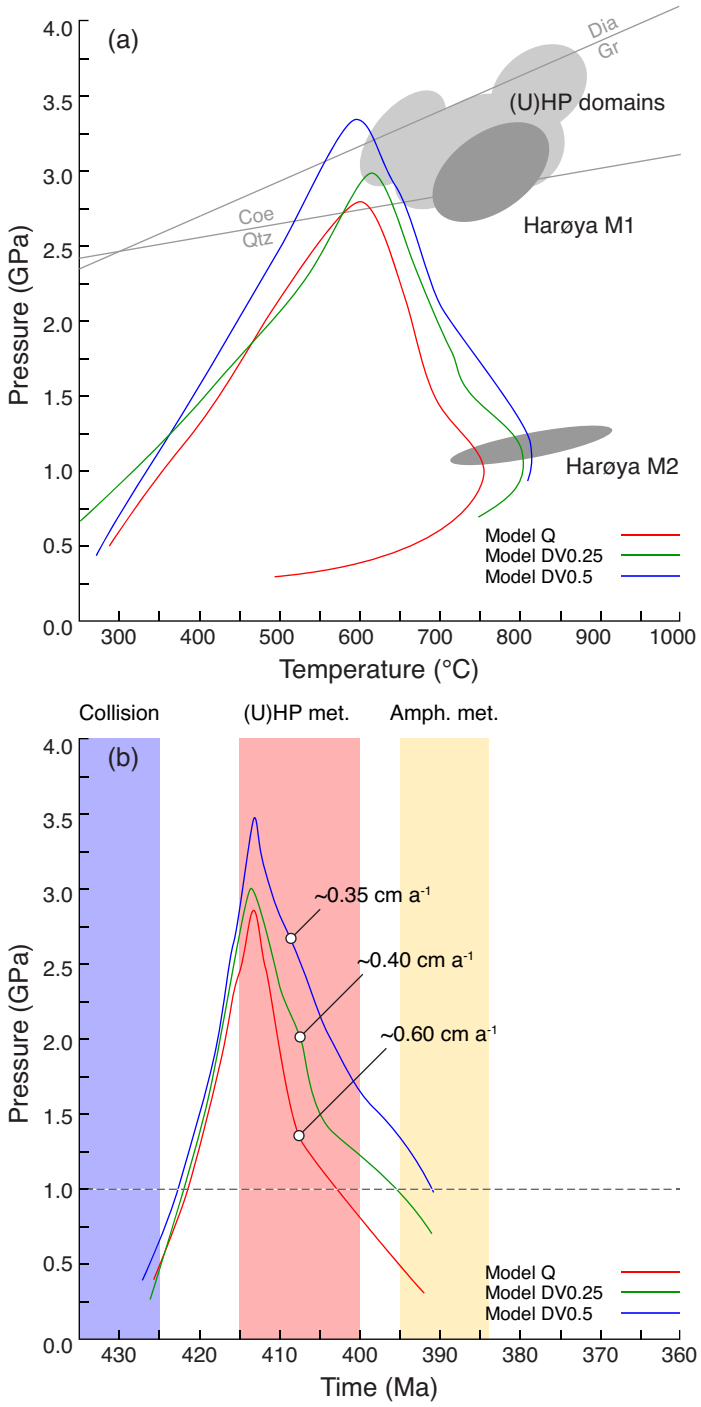

Figure 7.12: Representative model P–T–t paths. (a) Comparison of selected model P–T paths with data from WGR eclogites; see Figure 5.11 for data sources. Grey ellipses represent peak pressure conditions recorded by WGR eclogites. Harøya M1 and M2 ellipses show conditions of (U)HP and subsequent upper amphibolite/granulite facies overprinting in the northwestern WGR (Chapter 5). (b) Comparison of model P–t paths with approximate age constraints for the WGR. Exhumation rates averaged over interval from P_{max} to 1 GPa. (U)HP met.=age range of (U)HP metamorphism (*Krogh et al.*, 2011; *Carswell et al.*, 2003a), Amph. met.=age range of amphibolite facies metamorphism (*Tucker et al.*, 2004; *Krogh et al.*, 2011).

a broader region in which temperatures exceed 800°C. Models DV0.25 and DV0.5 are more similar to the WGR in this sense, where temperatures above 800°C are only documented within the Nordøyane (U)HP domain. However, whereas WGR eclogites underwent near-isothermal decompression and/or minor heating during exhumation, the model particles undergo heating by ∼200°C. Slower convergence, or a longer period of quiescence prior to exhumation would shift heating of the margin to an earlier phase of the models.

The overall timing of metamorphism and subsequent exhumation in the models is also similar to observations from the WGR (Fig. 7.12b). For comparison to absolute geological ages the onset of procontinent margin subduction can be equated to 425 Ma, an acceptable age for the onset of the Scandian phase of the orogeny, although accretion of outboard terranes may have begun earlier (*Gee et al.*, 2012). This places peak metamorphism in the models at ∼413 Ma, consistent with, but toward the upper end of, ages for (U)HP metamorphism from the WGR. Subsequent exhumation rates vary among the models. In Model Q, (U)HP margin crust undergoes an initial phase of rapid exhumation to ∼1.25 GPa, followed by somewhat slower exhumation to 1 GPa by ∼402 Ma (geological time). The corresponding average rate of exhumation from peak pressures to 1 GPa, corresponding to the geochronological constraints from the WGR, is ∼0.6 cm a^{-1}. Models DV0.25 and DV0.5 exhibit similar two-stage histories, with average exhumation rates reaching ∼0.4 and ∼0.35 cm a^{-1}, respectively. All of the models produce average exhumation rates within the range estimated for the WGR. Curiously, the model data show a systematic shift from Model Q to Model DV0.5 toward lower initial exhumation rates. During trans-crustal exhumation in Model Q, maximum surface erosion rates at the rear of the orogen range from ∼1.25–2 mm a^{-1}. The associated trans-crustal exhumation rate (from 1 GPa to the surface) for the Model Q P–T particle shown in Figure 7.12 is ∼0.24 cm a^{-1}. In models DV0.25 and DV0.5, absolute extension removes the slope at the rear of the orogen, leading to less erosion, and consequently the (U)HP margin remains buried beneath the orogenic wedge. Absolute extension may also produce slower overall exhumation because it creates horizontal space for the buoyant (U)HP margin crust to spread laterally, whereas without extension, the crust is confined to the subduction channel, and buoyancy will tend to drive

overlying crust upward to shallower depths.

7.7 Implications for (U)HP Rock Exhumation in the Western Gneiss Region

The models presented here provide new insight into the mechanisms of late- to post-orogenic (U)HP terrane exhumation, and raise several questions for existing models for the evolution of the WGR.

Many conceptual models for exhumation of the WGR (e.g., *Fossen*, 2000; *Hacker et al.*, 2010) invoke orogen-scale (absolute) extension to explain the apparent absence of (top-proward) shortening deformation during the timespan of (U)HP exhumation. In most of these models, subduction is accompanied by relative thrust-sense emplacement of the orogenic wedge (allochthons) over the Baltican margin, and subsequent exhumation is accompanied by reverse, top-retroward motion. However, reducing the convergence rate in all models leads to gravitational spreading, in most cases involving further thrusting toward the foreland. If the Scandian orogenic wedge was indeed thick (and hot), it is likely to have undergone similar gravitational spreading. Gravitational spreading may have begun and ended during slowing of convergence. Alternatively, as shown here, associated thrusting could have continued after convergence ceased. The youngest dated thrust-sense fabrics within the Jotun Detachment formed ∼408 Ma (*Fossen and Dunlap*, 1998), prior to the youngest UHP metamorphism ∼402 Ma. If the Caledonides underwent post-convergent gravitational spreading, then it is possible subduction ended even earlier than 408 Ma. The implication is that the Baltican margin may have 'stalled' at depth for a considerable length of time, prior to being exhumed by later extension. Stalling could also have resulted from a delay in the onset of extension, perhaps if slab breakoff was delayed. Similar to slower convergence, stalling of the margin would provide further incubation time for thermal relaxation, allowing the WGR to reach temperatures $\gtrsim$800°C.

With regard to the absence of Late Scandian shortening within the WGR, the models show that relatively coherent, albeit internally deformed, tracts of (U)HP crust can be exhumed by absolute extension. In contrast, the models with less or no divergence (Model Q) produce greater internal shortening of the margin, as it buoyantly ascends the subduction zone. While models of syn-convergent (U)HP

rock exhumation predict considerable syn-exhumation shortening, typically manifested as thrusting of (U)HP units toward the foreland, internal shortening may also occur during absolute divergence, provided the rate of extension is sufficiently low. Late Scandian shortening has only recently been documented in the WGR (*Robinson et al.*, 2012). Whether it can be explained by this mechanism remains unclear. Nonetheless, the models indicate that some shortening can be produced during overall extension, and that this shortening could be largely overprinted by subsequent amphibolite facies deformation, or simply concentrated in an unexposed part of the terrane (e.g., the present base of the crust; Fig. 7.11b,c).

Finally, although the models presented here are similar, they contain important differences from recent numerical models invoking 'slab eduction' to explain exhumation of the WGR. *Duretz et al.* (2012) presented numerical models in which dynamic slab breakoff leads to buoyant rebound and reverse subduction (eduction) of the subducted continental margin. During the initial stages of exhumation (Fig. 2 in *Duretz et al.*, 2012), the (U)HP margin crust remains attached the slab as it ascends back up the subduction zone, leading to normal-sense shearing at the top of the (U)HP terrane. Subsequent weakening leads to detachment and buoyant ascent of the (U)HP crust, resulting in minor internal shortening. Key to their models is the assumption that subduction is driven solely by the negative buoyancy of slabs; once slab breakoff occurs, subduction ceases. Not only does this assumption ignore any potential force provided by spreading ridges or other external forces, there is evidence from some orogens (e.g., the Alps; *Schmid and Kissling*, 2000; *Schmid et al.*, 2011) that plate convergence may continue for tens of Myr following slab breakoff. The present models differ in that extension is a consequence of absolute motion of the retrocontinent, rather than eduction. Although convergence in the models is prescribed by the velocity boundary conditions, the resulting forces acting on the procontinent during subduction (not shown) are within the range of estimated ridge push forces.

The underlying cause of Late Scandian extension in the Caledonides is unclear (*Krabbendam and Dewey*, 1998). Sinistral extension is recorded throughout the Caledonides, including East Greenland, on the retroside of the orogen. Whether eduction could explain this upper plate extension is not known, although admittedly the

present models also fail to address this problem. Regardless, it is worth noting that the models of *Duretz et al.* (2012) fail to reproduce most of the defining characteristics of the WGR/Caledonides. The models do not produce a large orogenic wedge, and consequently the orogen is far too small (the accretionary/orogenic wedge is ∼100 km wide and ∼ 10 km deep), and the maximum temperatures achieved by the margin crust never exceed ∼400°C during subduction or exhumation. Whether the same style of eduction would occur in models that did reproduce these features is unclear. For example, would the multiple stages of microcontinent accretion and subduction in the present models also produce slab breakoff in their models? And if so, what would drive subsequent convergence? Future work will focus on expanding the above models to include dynamic slab breakoff and force-dependent boundary conditions, in order to further explore the dynamics of Late Scandian extension in the Caledonides.

7.8 A Tectonic Model for Exhumation of the Western Gneiss Region

The geodynamic models presented here can be combined with existing geological data to create a basic model for exhumation of the WGR (Fig. 7.13). In this conceptual 2D model, convergence and absolute extension represent the orogen-normal components of transpression and transtension, respectively. The model integrates data from both the central and northern WGR and therefore assumes that the entire WGR underwent the same exhumation mechanism.

In the interpretation, subduction of the Baltican margin beneath a thick orogenic wedge and the Laurentian mantle lithosphere (Fig. 7.13a), led to (U)HP metamorphism at ∼415 Ma (*Krogh et al.*, 2011). Localized shortening at the top of the subducting slab produced recumbent folding of the allochthon/Baltican margin contact, forming a nappe cored by HP Baltican basement (*Robinson et al.*, 2012), here termed the 'Storli nappe'. Following this, convergence ended or slowed (Fig. 7.13b), leading to the onset of gravitational spreading. Shallow crustal extension of the orogenic wedge led to normal faulting and extensional basin formation. Thrusting, most likely owing to gravitational spreading, continued along parts of the allochthon/margin contact and in the foreland until ∼408 Ma (*Fossen and Dunlap*,

1998). The thrusting of HP over lower-pressure Baltican basement documented by *Robinson et al.* (2012) is interpreted as part of this phase. The Storli nappe was detached and transported toward the foreland over lower-pressure Baltica basement along the Storli thrust (*Robinson et al.*, 2012). Meanwhile, the deepest part of the margin remained at (U)HP conditions, where it underwent further heating during thermal incubation after tectonic convergence ceased. Subsequent extension, resulting from plate divergence and possibly related to slab breakoff, (Fig. 7.13c) led to normal-sense shearing within the orogenic wedge, above the allochthon/margin contact, and to further thinning of the allochthons/orogenic wedge. Exhumation of the (U)HP part of the margin to upper amphibolite facies conditions ($\sim$1 GPa) occurred during this phase, by $\sim$390 Ma (Chapter 6; *Tucker et al.*, 2004; *Krogh et al.*, 2011). Further absolute extension (Fig. 7.13d) produced brittle faulting and cooling of the through muscovite closure by $\sim$360 Ma (*Steenkamp*, 2012). The thickness of the allochthons that covered the WGR at that time is not known, but was probably $\lesssim$15 km, if the geothermal gradient was similar to that produced in the models. Final exposure of the present-day surface of the WGR after $\sim$70 Ma (*Hendriks et al.*, 2007) was probably the cumulative result of gradual erosion and uplift related to Mesozoic rifting.

This interpretation, which is informed by numerical models, differs from previous work in that Late-Scandian thrusting is attributed to gravitational spreading, rather than subduction/convergence, and is coeval with the onset of shallow crustal extension. Gravitational spreading and associated thrusting and extension may have begun either as convergence slowed, or after it ended. Moreover, subsequent absolute extension may not have begun immediately, resulting in stalling and continued (U)HP metamorphism of margin crust. The latter is consistent with local occurrence of (U)HP eclogites as young as $\sim$402 Ma (*Carswell et al.*, 2003a).

7.9 Conclusions

1. The models presented here, although preliminary, successfully reproduce many features of the southwestern Norwegian Caledonies/WGR, including the apparent size of the Scandian orogenic wedge, and the overall style and P–T conditions (with the exception of (U)HP temperatures) of metamorphism and

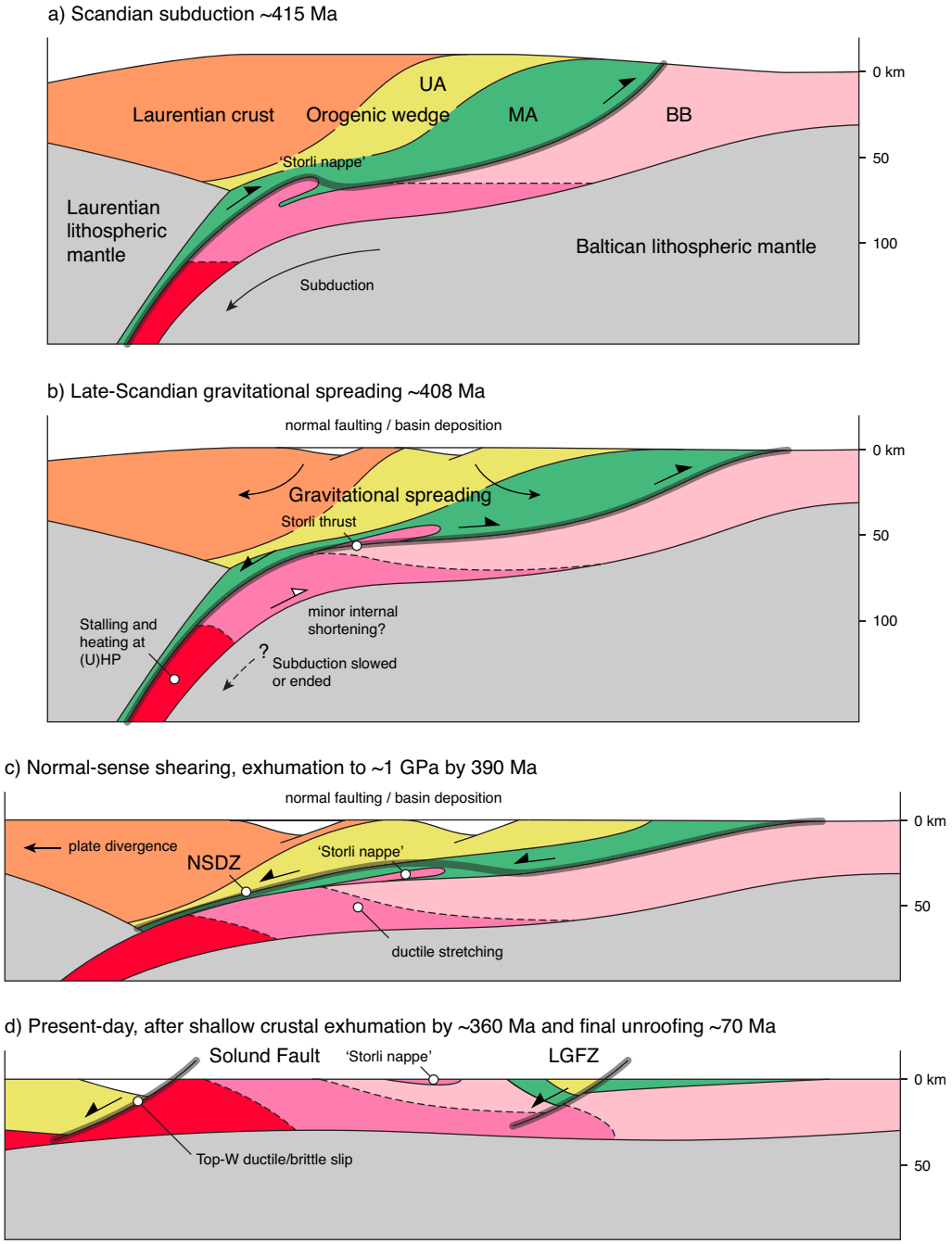

Figure 7.13: Conceptual model for the exhumation of the WGR. The model combines findings of the present study with previous conceptual models for the central WGR (*Milnes et al.*, 1997; *Johnston et al.*, 2007), and data on the Storli thrust from *Robinson et al.* (2012). Ages shown are general guides to the timing of events. See text for details. BB=Baltica Basement, UA=Upper Allochthon, MA=Middle Allochthon, NSDZ=Nordfjord-Sogn Detachment Zone, LGFZ=Lærdal-Gjende Fault Zone. Lower Allochthon excluded for simplicity. Thick transparent lines indicate positions of main structures. The NSDZ is shown as being localized within the Middle Allochthon. It is actually more distributed, affecting the Middle and Lower Allochthons, and underlying Baltica basement (*Johnston et al.*, 2007).

deformation.

2. The observations are most compatible with a model involving slab breakoff followed by plate divergence, in which absolute extension leads to the top-retroward shearing between the (U)HP terrane and overlying allochthons, coupled with vertical thinning of the orogenic wedge.

3. In contrast to models of syn-convergent exhumation, buoyancy-driven flow of the (U)HP terrane plays a subordinate role in exhumation during absolute extension, provided extension is sufficiently rapid. Instead, most of the exhumation is achieved by rebound of the lower plate, resulting from breakoff of the subducting slab and subsequent extension. Some buoyancy-driven flow may lead to minor internal shortening of the (U)HP terrane during this phase, in particular at its leading (most deeply buried) edge, but toward the foreland the terrane remains relatively undeformed. This result is similar to the WGR, where deformation is most intense in the Nordøyane (U)HP domain, which probably represents the most outboard part of the WGR. Future work will explore the extent to which early exhumation relates to buoyant rebound resulting from slab breakoff versus later rebound resulting from absolute extension.

4. This style of exhumation is likely to be preceded or accompanied by gravitational spreading of the hot orogenic wedge, resulting either from the cessation, or slowing, of convergence. Whether or not Late-Scandian thrusting observed in the Norwegian Caledonides was related to convergence or subsequent gravitational spreading is unknown, but if so it is highly likely that thrusting continued after convergence ended. By implication, the apparent gap between the youngest recorded thrusting (∼408 Ma) and the youngest age of (U)HP metamorphism (∼402 Ma) may indicate that the WGR stalled at (U)HP conditions prior to being exhumed.

5. Although the models indicate that absolute extension is a viable mechanism for exhumation of the WGR, the cause of extension remains unknown. Existing models involving slab eduction fail to reproduce the essential geological

features of the WGR. The present models, in contrast, simply assume divergence without appeal to broader plate dynamics. Future work will focus on exploring the potential causes and dynamics of extension in the Caledonides.

Chapter 8

Discussion and Conclusions

8.1 Numerical Modeling of (U)HP Rock Exhumation

The numerical modeling and field/analytical studies presented here were motivated by a single overarching scientific question, *How are (ultra)high-pressure rocks formed and exhumed?* The underlying premise of these studies is that forward numerical geodynamic models based on observational constraints from natural orogens can assist in the understanding of real geological processes. This approach is not unique to this thesis; in fact, several studies using similar numerical approaches have already addressed the problem of (U)HP rock exhumation in general. So what distinguishes the present work from existing studies?

A survey of the existing literature reveals that the criteria for recognizing a geologically viable, or 'working' model (*Beaumont et al.*, 2009), are often ambiguous or vaguely stated. Some consider numerical geodynamic models inherently valid 'simulations' of Earth processes, an approach that tends to lead to increasingly complex models, and in some cases to results that are difficult to interpret or relate to natural systems. An alternative approach, and the one adopted here, is to establish explicit criteria that a forward geodynamic model must reproduce in order to be considered a reasonable representation of the natural system being modeled. Satisfying these criteria provides confidence that the driving forces and mechanisms responsible for (U)HP rock exhumation in the models are probably applicable to nature.

This thesis has addressed the overarching question stated above by offering numerical geodynamic models (supplemented by new field/analytical constraints) that help

to explain a wide variety of observations from two of the most intensively studied orogens/(U)HP terranes on Earth, the Western Alps, and the Greenland/Norwegian Caledonides. To my knowledge, no previous modeling studies have produced results that explain the geodynamics of (U)HP rock exhumation in these specific orogens as comprehensively and with the level of detail achieved by the present models. To some extent the processes underlying (U)HP rock exhumation in these orogens (e.g., buoyancy-driven flow) had been inferred from existing models, but not addressed in a self-consistent manner that integrated these processes with the tectonic features specific to these orogens. The key results of these modeling studies are discussed below, followed by a summary of the key scientific results of the thesis.

8.2 A Tale of Two Orogens

The studies presented here pertain specifically to two orogens, the Alps (in particular the Western Alps) and the Norwegian Caledonides, that contrast markedly in their size, duration of orogeny, details of their tectonometamorphic histories, and styles of (U)HP rock exhumation.

The (Western) Alps (Fig. 3.9) is a relatively small and cold orogen, that apparently underwent early syn-orogenic exhumation involving the buoyant ascent of a composite (U)HP plume along the subduction channel. Exhumation of the (U)HP plume/nappes was accommodated by coeval normal- and thrust-sense shearing at the top and base of the plume respectively, leading to the formation of now well-documented 'local extensional' structures along the Western Alps. Subsequent 'trans-crustal' exhumation was achieved by combined bivergent thrusting, shallow-crustal extension, and erosion, during subsequent underthrusting of the European margin, driven by continued plate convergence. Metamorphic conditions recorded by Western Alps (U)HP rocks are relatively low temperature (mostly $\sim$500–700°C), reflecting burial in a low geothermal gradient subduction zone, the relatively small size of the orogen, the short duration of the orogeny, and the high rate of exhumation.

The Norwegian Caledonides (Fig. 7.13), in contrast, represent the lower plate (procontinent) of a large and hot bivergent orogen closer in size to the Himalayan orogen than the Alps. The Baltican margin may have been subducted to (U)HP

conditions at rates similar to those in the Alps (∼1 cm a^{-1}), but beneath a much larger and hotter orogenic wedge formed by Early Caledonian accretion. Exhumation of the WGR to crustal depths was slower than initial rapid exhumation in the Alps (∼0.5 versus ∼1–3 cm a^{-1}), and was apparently accommodated mostly by top-retroward (normal-sense) shear at the top of the (U)HP terrane coupled with ductile thinning of the orogenic wedge driven by gravitational spreading, and later absolute extension. In contrast to the composite plume in the Western Alps, this mechanism allows for the exhumation of a relatively intact slab of (U)HP margin crust, with internal deformation grading from minor to more significant toward the more deeply subducted part of the margin. Metamorphic conditions from WGR eclogites, with (U)HP temperatures of ∼750–800°C followed by overprinting at ∼1 GPa/800°C, reflect the overall larger/hotter orogen and further incubation heating during the protracted exhumation history.

In both types of models, the subducted (U)HP crust is subject to the same inherent buoyancy force, owing to the low density of the continental crust with respect to the surrounding mantle. The difference between the two modes of exhumation lies mainly in the style of accompanying plate motions. In the Alps, exhumation was driven by the positive buoyancy of the plume, and occurred during plate convergence. In the WGR, the (U)HP crust was probably also buoyant, but did not fully detach from the subducted slab. Instead, the data are most consistent with models in which exhumation of the WGR was accommodated by absolute extension rather than buoyancy-driven channel flow.

8.3 Orogen Size and Exhumation Mechanisms

The contrasting styles of exhumation observed in these two orogens can be interpreted in terms of two main factors: the magnitude and temperature of the orogen during the timespan of (U)HP terrane formation and exhumation, and whether exhumation was accomplished mainly by absolute extension, or alternatively syn-convergent extension resulting from buoyant ascent of (U)HP crust, or underthrusting and 'tectonic expulsion' (see below). The emphasis here is on the primary mechanism of (U)HP exhumation. Absolute extension indicates that the buoyancy

force, although present, was insufficient to drive exhumation. These factors are illustrated in terms of an 'orogen magnitude/temperature versus exhumation mechanism diagram' (MT–EM; Fig. 8.1), based on the 'orogen temperature versus magnitude' diagram of *Beaumont et al.* (2006). Magnitude refers to the areal extent and amount of crustal thickening in an orogen. Temperature refers to the extent to which the geothermal gradient exceeds that expected within 'normal thickness' continental crust. For simplicity, temperature is considered to be the result of crustal thickening and subsequent thermal relaxation, so that magnitude and temperature are correlative (*Beaumont et al.*, 2006), although other factors contribute to the temperature of orogens. The MT axis of the diagram therefore represents a continuum between small cold and large hot orogens (*Beaumont et al.*, 2006). The exhumation mechanisms, i.e., absolute or local syn-orogenic extension, imply opposite plate motions during exhumation. They are therefore considered to be mutually exclusive, and are illustrated as discrete fields. However, it is possible that different stages of exhumation of a single (U)HP terrane may be accomplished by different mechanisms.

The MT–EM diagram can be used to classify (U)HP terranes and/or existing models of (U)HP terrane exhumation (Fig. 8.1a), and to speculate on features that may apply to (U)HP terranes in general (Fig. 8.1b). Many of the conclusions are similar to those of *Kylander-Clark et al.* (2009). The Western Alpine ICMs exemplify (U)HP terranes that underwent exhumation within a relatively small cold orogen resulting from syn-convergent extension (here suggested to have been driven by buoyancy; corner a). The Tso Morari (*Epard and Steck*, 2008; *Beaumont et al.*, 2009) and Kaghan (*Wilke et al.*, 2010) (U)HP terranes, exhumed during the early stages of the Himalayan orogeny, are similar examples. Like the ICMs, these terranes underwent rapid, syn-convergent exhumation ($\sim$1–5 cm a^{-1}) to P–T conditions of $\sim$1–1.5 GPa/600–650°C. The Western Gneiss Region, in contrast, occupies the opposite corner of the MT–EM diagram (b), because its exhumation took place within a large hot orogen, and was accomplished primarily by absolute extension. The higher temperatures achieved by the WGR during subduction and exhumation can be attributed to the slowing of convergence (or stalling), the overall higher geothermal gradient of the orogen, and the fact that because convergence ceased, during exhumation the WGR was not underthrust by cool subducting lithosphere.

Unequivocal examples of terranes representing the other corners of the MT–EM diagram are more difficult to identify. The D'Entrecasteaux Islands (U)HP terrane (PNG terrane in Fig. 8.1; *Little et al.*, 2011; *Ellis et al.*, 2011) may have formed within a small cold orogen (the Papuan Orogen), and was later exhumed by absolute extension (Fig. 8.1a; corner c). However, the high temperatures recorded throughout its history (isothermal decompression at ∼800°C) are probably related to advection of heat during rapid ascent of the terrane from the mantle, rather than the size of the orogen. The PNG terrane therefore provides an example where orogen magnitude and temperature do not correlate, as noted above. Perhaps more suited to the MT–EM diagram are the absolute extension models applied to the Alps presented in Chapter 4. In Model DV0.25 (Chapter 4) absolute extension results in relatively slow exhumation of a partly intact (U)HP terrane (here comprising the microcontinent crust). Similar to the WGR models, stagnation and slow exhumation of the terrane lead to thermal overprinting of the exhumed (U)HP crust. The main difference is that in Alps Model DV0.25, absolute extension is not accompanied by gravitational spreading because the orogenic wedge is too small and cool. In addition, because the orogenic wedge is thin, considerably less extension is required to exhume the (U)HP terrane to shallow crustal depths.

At the opposite end of the diagram (Fig. 8.1a; corner d) lie (U)HP terranes that exhumed within large hot orogens by syn-orogenic extension. The Dabie-Sulu (U)HP terrane is similar in size to the WGR, and some P–T paths point to high temperatures (∼800°C) during exhumation (*Hacker et al.*, 2004). However, existing conceptual models have appealed alternatively to either syn-convergent or absolute extension (*Li et al.*, 2010a; *Guo et al.*, 2012). A more concrete example is provided by Miocene eclogites exposed in the Himalayan orogen (NW Bhutan; *Grujic et al.*, 2011). These HP eclogites probably formed at the base of thickened orogenic crust, which is only possible in large hot orogens, rather than by burial in a subduction channel. Their exhumation to granulite facies conditions ($\lesssim$1 GPa/800°C), is interpreted to have resulted from 'tectonic expulsion' driven by underthrusting of strong Indian continental crust, followed by later, slower exhumation along with the Greater Himalayan Sequence during gravity-driven ductile flow. Whether examples of actual (U)HP terranes, i.e., comprising both HP and UHP crust, at this end of the MT–EM

diagram exist is not clear. If so, they might exhibit many of the structural features found in (U)HP terranes exhumed in small cold orogens by syn-orogenic extension, including upper-boundary normal-sense shear zones, and evidence of thrusting during exhumation. However, in contrast to small cold orogens, the (U)HP terranes exhumed in large hot orogens would likely be subjected to considerable thermal overprinting at crustal depths, and consequently more pervasive ductile overprinting, which would obscure structures related to their initial exhumation from mantle depths.

The size of the exhumed (U)HP terrane (as opposed to the orogen), although not explicitly addressed, can be indirectly related to the MT–EM diagram in several ways. For example, in small cold orogens formation of (U)HP crust is probably restricted to the subduction channel. In large hot orogens, in contrast, crustal thickening may produce broad regions of HP metamorphism. The vast region of HP metamorphism in the WGR may be explained by burial beneath the orogenic wedge, whereas the UHP domains can be interpreted as the leading edge of the Baltican margin that reached greater depths in the subduction channel.

Several other factors may affect the size of (U)HP terranes. In young orogens, syn-collisional subduction of extended continental margin crust may favour the exhumation of small terranes. Larger orogens have, by definition, undergone greater convergence, and may involve the subduction of more inboard, normal thickness continental crust, leading to larger terranes.

The size of the exhumed terrane could also result directly from the exhumation mechanism. The internal deformation of (U)HP plumes exhumed by buoyancy and syn-convergent extension may lead to the appearance of relatively small (U)HP terranes, even if the terranes were exhumed as part of a larger aggregated plume. Several existing analogue and numerical modeling studies show that buoyancy-driven syn-convergent extension can also exhume very large (U)HP terranes (*Chemenda et al.*, 1995; *Gerya et al.*, 2008; *Butler et al.*, 2011), although as noted above an unequivocal example of such a terrane has yet to be found. Absolute extension, in contrast, permits the exhumation of relatively intact (U)HP terranes, which in large hot orogens may include broad regions of HP metamorphism formed by crustal thickening and adjacent UHP regions formed within the subduction channel. These adjacent

HP and UHP regions may be structurally continuous.

It follows that (U)HP terranes exhumed within a single orogen should exhibit very different styles of metamorphism and exhumation depending on the size, thermal state, and subduction dynamics of the orogen at the time of their exhumation (*Kylander-Clark et al.*, 2009). Early-orogenic (U)HP terranes should be small, and undergo relatively little to no thermal overprinting during exhumation, whereas mid- to late-orogenic terranes may be larger, and should experience substantial thermal overprinting within the orogenic crust. Finally, post-orogenic terranes, exhumed by absolute extension, should be large and relatively coherent, and have undergone considerable thermal overprinting related to slowing of convergence, possible stalling at depth, and slow exhumation beneath a large hot orogen. In the Caledonides, pre-Scandian (U)HP metamorphism of the Seve Nappes was followed by granulite facies overprinting, indicating exhumation within an already large hot orogen. In the large hot Himalayan orogen, exhumation of (U)HP crust appears to have been restricted to the syn-collisional Tso Morari and Kaghan (U)HP terranes. Later formation of the NW Bhutan eclogites was related to crustal thickening and not to burial within a subduction channel. Whether the Himalayan orogen will one day expose a large (U)HP terrane exhumed by post-orogenic absolute extension is entirely speculative, but it could be that a vast (U)HP terrane similar in size to the WGR, comprising HP and UHP Indian crust, exists today beneath the orogen (*Searle et al.*, 2001). This is shown on the EM–MT diagram as the speculative 'Greater India' terrane.

Many large hot orogens could in fact be 'floored' by continuous HP and UHP regions like the WGR that simply did not exhume. The ability of the WGR to subduct beneath a large hot orogen yet remain relatively coherent, indicates that it was strong during subduction and exhumation, probably owing to the Proterozoic granulite facies protoliths that dominate the WGR (*Krabbendam et al.*, 2000). That buoyancy alone appears to have failed to exhume the strong WGR crust indicates that deeply buried, strong (U)HP terranes in other orogens may simply be stranded at depth if not exhumed by absolute extension. Stranded terranes may weaken and undergo minor buoyancy-driven exhumation, but only to the base of the orogenic crust, where they achieve neutral buoyancy. Given the that the temperature at the base of thickened orogenic crust ($\sim$80 km) may reach $\sim$900 C$^{\circ}$, these terranes would

likely be extremely weak, resulting in structural assimilation, and would also undergo intense thermal overprinting, perhaps losing all evidence of (U)HP metamorphism. The fact that the largest (U)HP terranes appear to have exhumed more slowly, which seems inconsistent with buoyancy-driven ductile flow, could therefore be the result of preservation bias, where only those terranes that were exhumed by absolute extension, and so remained relatively intact, are recognized.

Certain features of (U)HP terranes are not directly addressed by the MT–EM diagram. For example, as discussed in Chapter 7, the high temperatures recorded at (U)HP conditions within the WGR (∼750–800°C) may be related to slow subduction, rather than the magnitude of the orogen. The fact that some Alpine (U)HP units (e.g., Adula nappe) record similar high temperatures at (U)HP conditions supports this view. Moreover, other mechanisms that may lead to extensive thermal overprinting, such as rollback of the subducting slab and ascent of hot sublithospheric mantle beneath the crust, have not been considered, although my own experiments and recently published studies show this to be another viable mechanism for (U)HP terrane exhumation.

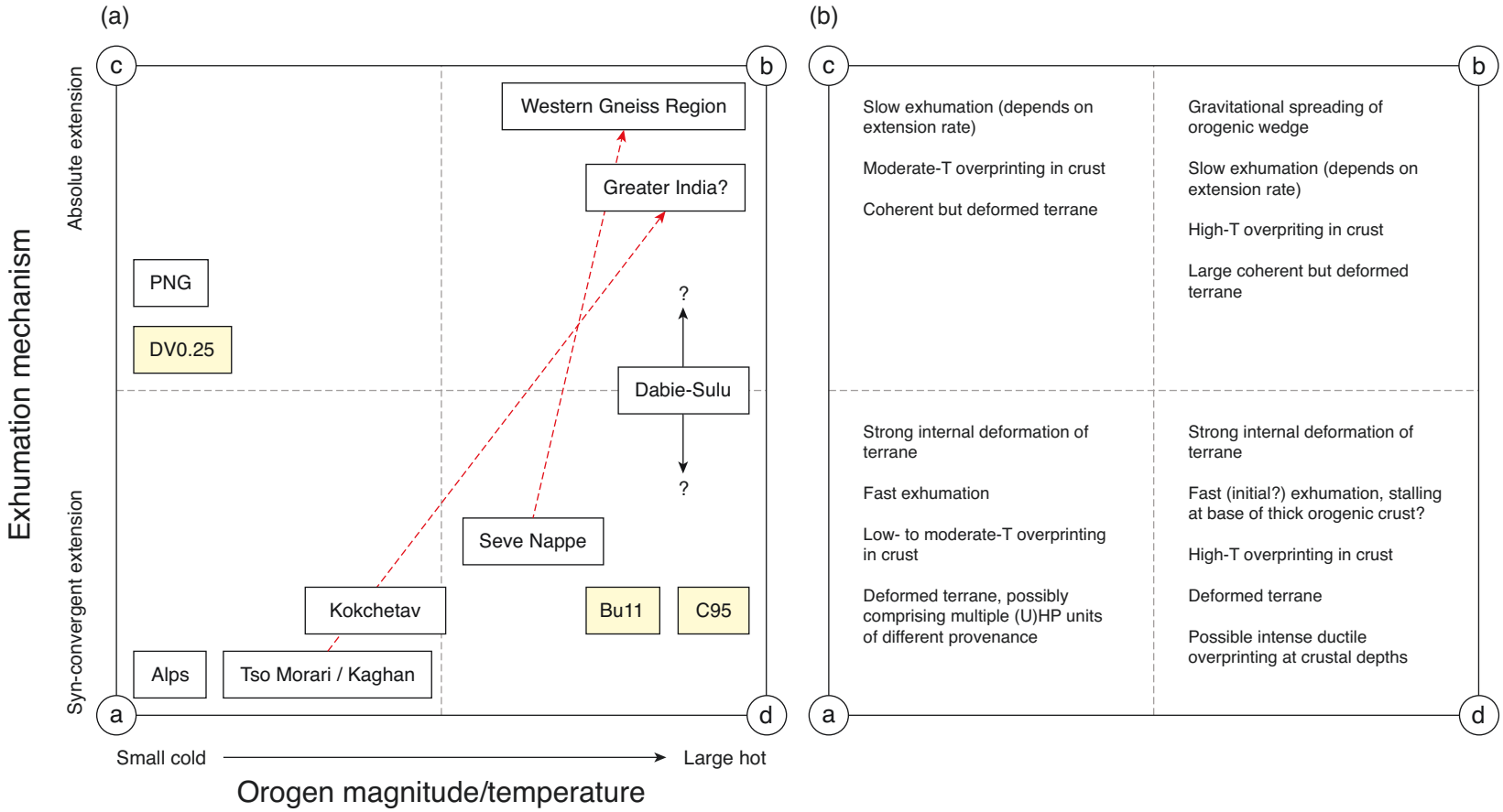

Figure 8.1: Orogen magnitude/temperature and exhumation mechanism (MT–EM) diagram. See text for details. (a) Classification of some natural (U)HP terranes in EM–TM space. Yellow boxes represent modeling studies. DV0.025 is model shown in Chapter 4. Bu11=(*Butler et al.*, 2011), C95=(*Chemenda et al.*, 1995). Red lines indicate progression of (U)HP terranes from a single orogen through time. 'Greater India?' is a speculative (U)HP terrane. (b) Some characteristic features of (U)HP terranes/orogens in MT–EM space. See text for details. Characteristics of terranes in corner c are based on Model DV0.25.

8.4 Comparisons with Previous Studies

The models presented here, although specific to the Alps and Caledonides, support many of the conclusions reached by previous studies concerning the general aspects of (U)HP rock exhumation. The absolute extension models applied to the WGR (Chapter 7) are novel in that, to my knowledge, they are the first models to address this style of exhumation within large hot orogens. In contrast, the syn-convergent exhumation models of the Alps are similar in principle to many existing models, insofar as they involve exhumation by buoyancy-driven channel flow of weak (U)HP crust (*Gerya et al.*, 2008; *Warren et al.*, 2008a; *Yamato et al.*, 2008; *Beaumont et al.*, 2009). The present models support many of the same general conclusions, including that exhumation is driven by buoyancy; that exhumation is primarily accommodated by extension, typically in the form of normal-sense shearing above the (U)HP terrane; that erosion plays a subordinate role in initial rapid exhumation; and, that syn-convergent channel flow exhumation is sensitive primarily to factors including the convergence rate and the buoyancy and strength evolution of the subducted crust. As suggested by other studies (e.g., *Li et al.*, 2010b) (but see *Vrijmoed et al.* (2009b)) tectonic overpressures in the current models are negligible.

The approach adopted here, rooted in the principle of 'Occam's Razor', was to produce a model with the fewest possible assumptions required to explain the observations. In many cases, the present models are simpler than existing models, in that certain petrological processes, such as rheological changes associated with phase transformations or partial melting, are incorporated indirectly through proxy mechanisms such as strain-weakening (Chapter 2). The ability of the models to reproduce the key features of certain orogens despite these simplifications suggests that the importance of specific processes may have been overestimated in some studies (*Gerya et al.*, 2008; *Sizova et al.*, 2012).

As noted in Chapter 1, many other types of models have been proposed to explain (U)HP rock exhumation, ranging from rifting and diapirism to slab eduction. The models presented here do not invalidate these as possible mechanisms for (U)HP rock exhumation, although they arguably offer better explanations for the Alps and Caledonides. Given the growing recognition of diversity among global (U)HP terranes (*Kylander-Clark et al.*, 2012), my view is that case studies that focus in

detail on specific orogens are required to gain deeper insight into which mechanism is responsible for (U)HP exhumation.

Which of the many available models withstand scrutiny in any given case hinges on whether the criteria they were designed to reproduce remain robust, or alternatively are discarded/modified as new or additional data become available. Models based on explicit criteria from specific orogens may therefore be easier to refute, compared with 'generic' models, but can also be refined to address new data. In addition, the models also have predictive capabilities, in that the mechanism of (U)HP rock exhumation in each model can be linked to characteristic patterns of orogen-scale deformation and metamorphism, which could be tested by future field/analytical studies.

8.5 Recommendations for Future Research

Underlying the present models are many assumptions, some justified, and some that clearly must be addressed in future modeling work. First, although the two types of models are distinguished by their underlying relative plate motions, in all of the models the convergence rates are prescribed, and no consideration is given to the dynamic controls on plate motion. Recent modeling by *Duretz et al.* (2012) incorporates dynamic plate motions, but limits the driving force of plate motion to the negative buoyancy of the subducting slab, which is an oversimplification. Future work should investigate the relationship between dynamic plate motions and continental subduction and exhumation. For example, velocity boundary conditions constrained by tectonic forces may be used to understand the dynamic interplay between plate motions and subduction zone processes including crustal accretion/subduction, and slab breakoff.

Second, the 2D nature of the models inherently limits their applicability to natural systems. Although in some cases, including the Alps, (U)HP rock exhumation involved mainly orogen-normal displacements, in the Caledonides exhumation was accompanied by sinistral transtension. Geodynamic modeling in 3D is computationally expensive, and currently requires sacrifices in terms of the timescales and resolution of models, but will certainly provide a more realistic view of the partitioning of deformation during exhumation.

Finally, with regards to field/analytical studies, there is a persistent need for more robust constraints on all aspects of (U)HP terranes, in particular their crustal structure (i.e., crustal-scale cross-sections), and timing of (U)HP metamorphism and exhumation linked to specific P–T constraints. Considerable progress has been made through the application of U–Pb geochronology using microbeam techniques coupled with trace element and inclusion analyses. However, confidently relating the age of zircon and/or other dated accessory phases to specific P–T conditions remains expensive and laborious (*Peters et al.*, 2012). Future experimental and petrological work should focus on better understanding the reactions responsible for zircon formation, and trace element partitioning among zircon and other phases, at (U)HP conditions. Constraining (U)HP metamorphic conditions will similarly benefit from further experimental work focusing on the compositions of major and secondary phases common to eclogites at (U)HP conditions. Improved experimental constraints on the effects of reaction weakening and fluids on the rheology of subducted continental crust will improve field interpretations as well as geodynamic models of (U)HP exhumation.

8.6 Conclusions

The main scientific findings of this thesis can be summarized by Chapter as follows.

1. (U)HP metamorphic crustal rocks can be explained by the burial of crust to mantle depths, resulting from subduction. That (U)HP crustal rocks are now recognized in over 30 orogens worldwide suggests that continental subduction and exhumation were common parts of convergent margin evolution, at least throughout the Phanerozoic. Considerable understanding of these processes has been gained by geodynamic modeling based on observational constraints; however, no one model can explain the formation and exhumation of all (U)HP terranes.

2. The exhumation and crustal emplacement of (U)HP rocks can be understood in terms of the Prowedge-Uplifted Plug-Retrowedge-Conduit (PURC) framework. Using this framework, the orogen-scale style of (U)HP rock exhumation in numerical models can be described in terms of whether the (U)HP crust is

emplaced into the prowedge (P) or retrowedge (R) of an orogen, which depends on the strength of the retrocontinent crust. Retrotransport of exhumed (U)HP rocks may explain the presence of some of the (U)HP rocks in the upper-plate of the Greenland-Norwegian Caledonides, and demonstrates that the presence of (U)HP rocks alone is not a reliable indicator of past subduction polarity.

3. Numerical geodynamic models based on the Western Alps show that exhumation of the (U)HP Internal Crystalline Massifs can be explained by the buoyant ascent of a composite (U)HP plume from within the subduction channel, which leads to coeval thrust- and normal-sense shear at the top and base of the plume. Neither erosion nor absolute extension are required to explain (U)HP rock exhumation in the models, and by extension, in the Western Alps. Interpretation of the models using the PURC framework suggests that the tectonics of the Western Alps can be understood in a simple fashion as the superposition of three contrasting PURC 'flow modes'.

4. Sensitivity tests based on a working model highlight the main controls on (U)HP rock exhumation on in Alpine-type orogens. Many of the differences in the provenance of (U)HP units, peak P–T conditions, and tectonic style along the Alpine orogen can be addressed to some extent by these models. Key controlling factors include the initial strength and geometry of the subducted (U)HP crustal units (e.g., thickness of extended margin) along the Alps, variations in the orogen-normal convergence rate, and contrasts in the strength of the retrocontinent crust. The models also show that, despite being a possible exhumation mechanism in general, plate divergence at reasonable rates produces (U)HP exhumation that is far too slow to match the data from the Alps.

5. Mapping on the island of Harøya, in the Western Gneiss Region of Norway, led to the discovery of a coesite-eclogite – the first documented in northernmost Nordøyane (U)HP domain. Detailed petrology and P–T estimates indicate that the coesite-eclogite reached metamorphic conditions of ∼3 GPa/760°C, followed by decompression and heating to granulite facies conditions of ∼1 GPa/800°C. The data provide robust evidence that the Baltica basement that underlies

Harøya underwent deep continental subduction, and that exhumation was accompanied by widespread partial melting and extensional deformation.

6. U–Pb geochronology and trace element geochemistry of zircon and other accessory phases from eclogites and migmatites from Harøya and neighbouring Finnøya indicate that eclogite facies metamorphism took place ∼410 Ma. Subsequent amphibolite facies extension occurred ∼387 Ma, with later cooling through rutile closure by ∼378 Ma. Partial melting may have occurred during exhumation, ∼400 Ma,. Collectively the data indicate that exhumation of the WGR from (U)HP conditions to the middle orogenic crust occurred at a rate of $\lesssim$1 cm a^{-1}.

7. Numerical modeling indicates that the formation and exhumation of the WGR can be explained by the subduction of the Baltican continental margin beneath a hot and thick orogenic wedge formed by prior accretion, followed by absolute extension. The relatively high temperatures achieved by the WGR at (U)HP conditions (∼800°C) may have resulted from stalling of the WGR at mantle depths as convergence slowed or stopped. Subsequent thermal overprinting at middle crustal depths can be explained by further thermal relaxation of the thick orogenic wedge. The models indicate that the latest thrusting in the Norwegian Caledonides was probably related to gravitational spreading of the orogenic wedge. Exhumation was accomplished mainly by normal-sense shearing and thinning of the orogenic wedge resulting from absolute extension, and erosion.

8. The tectonometamorphic histories of the (U)HP rocks exhumed within the Alps and Caledonides can be contrasted in terms of the magnitude and temperature of the orogen and exhumation mechanism (MT–EM diagram), where the exhumation mechanism refers to whether exhumation-related extension was syn-convergent, or related to absolute extension. The Western Alps ICMs can be considered a near end-member case where the (U)HP ICMs were exhumed in a relatively small cold orogen by syn-convergent extension. The WGR, in contrast, represents a terrane formed beneath a large hot orogen and exhumed mainly by post-convergent absolute extension. Regardless of the

form of extension, (U)HP terranes exhumed in large hot orogens are more likely to undergo extensive thermal overprinting and ductile deformation. Moreover, because they achieve neutral buoyancy at greater depths terranes exhumed in large hot orogens are more likely to stall at depth, leading to lower average exhumation rates.

References

Amato, J. M., C. M. Johnson, L. P. Baumgartner, and B. L. Beard, Rapid exhumation of the Zermatt-Saas ophiolite deduced from high-precision Sm–Nd and Rb–Sr geochronology, *Earth and Planetary Science Letters*, *171*, 425–438, 1999.

Andersen, T., Extensional tectonics in the Caledonides of southern Norway, an overview, *Tectonophysics*, *285*, 333–351, 1998.

Andersen, T., K. Skjerlie, and H. Furnes, The Sunnfjord Melange, evidence of Silurian ophiolite accretion in the west Norwegian Caledonides, *Journal of the Geological Society*, *147*, 59–68, 1990.

Andersen, T., W. Griffin, S. Jackson, T.-L. Knudsen, and N. Pearson, Mid-Proterozoic magmatic arc evolution at the southwest margin of the Baltic Shield, *Lithos*, *73*, 289–318, 2004.

Andersen, T. B., B. Jamtveit, J. F. Dewey, and E. Swensson, Subduction and eduction of continental crust: major mechanisms during continent-continent collision and orogenic extensional collapse, a model based on the south Norwegian Caledonides, *Terra Nova*, *3*, 303–310, 1991.

Andersen, T. B., P. T. Osmundsen, and L. Jolivet, Deep crustal fabrics and a model for the extensional collapse of the southwest Norwegian Caledonides, *Journal of Structural Geology*, *16*, 1191–1203, 1994.

Andersen, T. B., F. Corfu, L. Labrousse, and P.-T. Osmundsen, Evidence for hyperextension along the pre-Caledonian margin of Baltica, *Journal of the Geological Society*, *169*, 601–612, 2012.

Angiboust, S., and P. Agard, Initial water budget: The key to detaching large volumes of eclogitized oceanic crust along the subduction channel?, *Lithos*, *120*, 453–474, 2010.

Artyushkov, E. V., and M. A. Baer, Mechanism of continental crust subsidence in fold belts: The Urals, Appalachians and Scandinavian Caledonides, *Tectonophysics*, *100*, 5–42, 1983.

Augland, L. E., A. Andresen, and F. Corfu, Age, structural setting, and exhumation of the Liverpool Land eclogite terrane, East Greenland Caledonides, *Lithosphere*, *2*, 267–286, 2010.

Austrheim, H., F. Corfu, I. Bryhni, and T. B. Andersen, The Proterozoic Hustad igneous complex: a low strain enclave with a key to the history of the Western Gneiss Region of Norway, *Precambrian Research*, *120*, 149–175, 2003.

Avigad, D., C. Chopin, and R. Le Bayon, Thrusting and extension in the southern Dora-Maira ultra-high-pressure massif (Western Alps): view from below the coesite-bearing unit, *The Journal of Geology*, *111*, 57–70, 2003.

Baldwin, S., L. Webb, and B. Monteleone, Late Miocene coesite-eclogite exhumed in the Woodlark Rift, *Geology*, *36*, 735–738, 2008.

Baldwin, S. L., B. D. Monteleone, L. E. Webb, P. G. Fitzgerald, M. Grove, and E. J. Hill, Pliocene eclogite exhumation at plate tectonic rates in eastern Papua New Guinea, *Nature*, *431*, 263–267, 2004.

Ballèvre, M., and O. Merle, The Combin fault: compressional reactivation of a Late Cretaceous-Early Tertiary detachment fault in the Western Alps, *Schweizerische Mineralogische und Petrographische Mitteilungen*, *73*, 205–227, 1993.

Beaumont, C., S. Ellis, and A. Pfiffner, Dynamics of sediment subduction-accretion at convergent margins: Short-term modes, long-term deformation, and tectonic implications, *Journal of Geophysical Research-Solid Earth*, *104*, 17573–17601, 1999.

Beaumont, C., M. H. Nguyen, R. A. Jamieson, and S. Ellis, Crustal flow modes in large hot orogens, *Geological Society, London, Special Publications*, *268*, 91–145, 2006.

Beaumont, C., R. Jamieson, J. Butler, and C. Warren, Crustal structure: a key constraint on the mechanism of ultra-high-pressure rock exhumation, *Earth and Planetary Science Letters*, *287*, 116–129, 2009.

Behn, M., P. Kelemen, G. Hirth, B. Hacker, and H. Massonne, Diapirs as the source of the sediment signature in arc lavas, *Nature Geoscience*, *4*, 641–646, 2011.

Beltrando, M., R. Compagnoni, and B. Lombardo, (Ultra-) High-pressure metamorphism and orogenesis: an Alpine perspective, *Gondwana Research*, *18*, 147–166, 2010a.

Beltrando, M., G. S. Lister, G. Rosenbaum, S. Richards, and M. A. Forster, Recognizing episodic lithospheric thinning along a convergent plate margin: the example of the Early Oligocene Alps, *Earth-Science Reviews*, *103*, 81–98, 2010b.

Berger, A., and R. Bousquet, Subduction-related metamorphism in the Alps: review of isotopic ages based on petrology and their geodynamic consequences, *Geological Society, London, Special Publications*, *298*, 117–144, 2008.

Bernet, M., M. Brandon, J. Garver, M. L. Balestieri, B. Ventura, and M. Zattin, Exhuming the Alps through time: clues from detrital zircon fission-track thermochronology, *Basin Research*, *21*, 781–798, 2009.

Beucher, R., P. van der Beek, J. Braun, and G. E. Batt, Exhumation and relief development in the Pelvoux and Dora-Maira massifs (Western Alps) assessed by spectral analysis and inversion of thermochronological age transects, *Journal of Geophysical Research*, *117*, F03030, 2012.

Bingen, B., H. Austrheim, and M. Whitehouse, Ilmenite as a source for zirconium during high-grade metamorphism? Textural evidence from the Caledonides of Western Norway and implications for zircon geochronology, *Journal of Petrology*, *42*, 355–375, 2001.

Bingen, B., H. Austrheim, M. J. Whitehouse, and W. J. Davis, Trace element signature and U–Pb geochronology of eclogite-facies zircon, Bergen Arcs, Caledonides of W Norway, *Contributions to Mineralogy and Petrology*, *147*, 671–683, 2004, 10.1007/s00410-004-0585-z.

Bockelie, J., and J. Nystuen, The southeastern part of the Scandinavian Caledonides, *The Caledonide orogen–Scandinavia and related areas*, *1*, 69–88, 1985.

Bose, K., and J. Ganguly, Quartz-coesite transition revisited: reversed experimental determination at 500-1200°C and retrieved thermochemical properties, *American Mineralogist*, *80*, 231–231, 1995.

Bousquet, R., B. Goffé, P. Henry, X. L. Pichon, and C. Chopin, Kinematic, thermal and petrological model of the Central Alps: Lepontine metamorphism in the upper crust and eclogitisation of the lower crust, *Tectonophysics*, *273*, 105–127, 1997.

Bousquet, R., B. Goffé, O. Vidal, R. Oberhänsli, and M. Patriat, The tectono-metamorphic history of the Valaisan domain from the Western to the Central Alps: new constraints on the evolution of the Alps, *Geological Society of America Bulletin*, *114*, 207–225, 2002.

Bowman, D., Exhumation history of Caledonian eclogites in Liverpool Land, East Greenland, and comparisons with eclogites in Norway, Ph.D. thesis, Auburn University, Auburn, Alabama, 2008.

Boyd, F., and J. England, The quartz–coesite transition, *Journal of Geophysical Research*, *65*, 749–756, 1960.

Boyer, H., D. C. Smith, C. Chopin, and B. Lasnier, Raman microprobe (RMP) determinations of natural and synthetic coesite, *Physics and Chemistry of Minerals*, *12*, 45–48, 1985, 10.1007/BF00348746.

Brueckner, H. K., and H. L. van Roermund, Dunk tectonics: a multiple subduction/eduction model for the evolution of the Scandinavian Caledonides, *Tectonics*, *23*, TC2004, 2004.

Brun, J., and C. Faccenna, Exhumation of high-pressure rocks driven by slab rollback, *Earth and Planetary Science Letters*, *272*, 1–7, 2008.

Buchanan, W., Tectonic evolution of a Caledonian-aged continental basement eclogite terrane in Liverpool Land, East Greenland, 2008.

Bucher, S., and R. Bousquet, Metamorphic evolution of the Briançonnais units along the ECORS-CROP profile (Western Alps): new data on metasedimentary rocks, *Swiss Journal of Geosciences*, *100*, 227–242, 2007.

Bucher, S., S. M. Schmid, R. Bousquet, and B. Fügenschuh, Late-stage deformation in a collisional orogen (Western Alps): nappe refolding, back-thrusting or normal faulting?, *Terra Nova*, *15*, 109–117, 2003.

Burlini, L., and D. Bruhn, High-strain zones: laboratory perspectives on strain softening during ductile deformation, *Geological Society, London, Special Publications*, *245*, 1–24, 2005.

Burov, E., L. Jolivet, L. Le Pourhiet, and A. Poliakov, A thermomechanical model of exhumation of high pressure (HP) and ultra-high pressure (UHP) metamorphic rocks in Alpine-type collision belts, *Tectonophysics*, *342*, 113–136, 2001.

Butler, J., C. Beaumont, R. Jamieson, and C. Warren, Controls on late-orogenic exhumation of subducted UHP continental basement, in *2008 Joint Meeting of The Geological Society of America, Soil Science Society of America, American Society of Agronomy, Crop Science Society of America, Gulf Coast Association of Geological Societies with the Gulf Coast Section of SEPM*, 2008.

Butler, J., C. Beaumont, and R. Jamieson, Crustal emplacement of exhuming (ultra)high-pressure rocks: will that be pro- or retro-side?, *Geology*, *39*, 635–638, 2011.

Butler, J., R. Jamieson, H. Steenkamp, and P. Robinson, Discovery of coesite–eclogite from the Nordøyane UHP domain, Western Gneiss Region, Norway: field relations, metamorphic history, and tectonic significance, *Journal of Metamorphic Geology*, 2012.

Canil, D., M. Mihalynuk, and C. Charnell, Sedimentary record for exhumation of ultrahigh pressure (UHP) rocks in the northern Cordillera, British Columbia, Canada, *Geological Society of America Bulletin*, *118*, 1171–1184, 2006.

Carswell, D., R. Tucker, P. O'Brien, and T. Krogh, Coesite micro-inclusions and the U/Pb age of zircons from the Hareidland Eclogite in the Western Gneiss Region of Norway, *Lithos*, *67*, 181–190, 2003a.

Carswell, D. A., H. K. Brueckner, S. J. Cuthbert, K. Mehta, and P. J. O'Brien, The timing of stabilisation and the exhumation rate for ultra-high pressure rocks in the Western Gneiss Region of Norway, *Journal of Metamorphic Geology*, *21*, 601–612, 2003b.

Carswell, D. A., H. L. van Roermund, and D. F. de Vries, Scandian ultrahigh-pressure metamorphism of Proterozoic basement rocks on Fjørtoft and Otrøy, Western Gneiss Region, Norway, *International Geology Review*, *48*, 957–977, 2006.

Castellarin, A., R. Nicolich, R. Fantoni, L. Cantelli, M. Sella, and L. Selli, Structure of the lithosphere beneath the Eastern Alps (southern sector of the TRANSALP transect), *Tectonophysics*, *414*, 259–282, 2006.

Chemenda, A. I., M. Mattauer, J. Malavieille, and A. N. Bokun, A mechanism for syn-collisional rock exhumation and associated normal faulting: results from physical modelling, *Earth and Planetary Science Letters*, *132*, 225–232, 1995.

Cherniak, D., Lead diffusion in titanite and preliminary results on the effects of radiation damage on Pb transport, *Chemical Geology*, *110*, 177–194, 1993.

Cherniak, D., and E. Watson, Pb diffusion in zircon, *Chemical Geology*, *172*, 5–24, 2001.

Chopin, C., Coesite and pure pyrope in high-grade blueschists of the Western Alps: a first record and some consequences, *Contributions to Mineralogy and Petrology*, *86*, 107–118, 1984.

Chopin, C., Ultrahigh-pressure metamorphism: tracing continental crust into the mantle, *Earth and Planetary Science Letters*, *212*, 1–14, 2003.

Chopin, C., and N. Sobolev, Principal mineralogic indicators of UHP in crustal rocks, *Ultrahigh-pressure metamorphism*, pp. 96–133, 1995.

Chopin, C., C. Henry, and A. Michard, Geology and petrology of the coesite-bearing terrain, Dora Maira Massif, Western Alps, *European Journal of Mineralogy*, *3*, 263–291, 1991.

Corfu, F., J. M. Hanchar, P. W. Hoskin, and P. Kinny, Atlas of zircon textures, *Reviews in Mineralogy and Geochemistry*, *53*, 469–500, 2003.

Cuthbert, S., D. Carswell, E. Krogh-Ravna, and A. Wain, Eclogites and eclogites in the Western Gneiss Region, Norwegian Caledonides, *Lithos*, *52*, 165–195, 2000.

Davis, D. W., Optimum linear regression and error estimation applied to U-Pb data, *Canadian Journal of Earth Sciences*, *19*, 2141–2149, 1982.

Davis, D. W., T. E. Krogh, and I. S. Williams, Historical development of zircon geochronology, *Reviews in Mineralogy and Geochemistry*, *53*, 145–181, 2003.

De Voogd, B., L. Serpa, and L. Brown, Crustal extension and magmatic processes: COCORP profiles from Death Valley and the Rio Grande rift, *Geological Society of America Bulletin*, *100*, 1550–1567, 1988.

Dewey, J. F., M. L. Helman, S. D. Knott, E. Turco, and D. H. W. Hutton, Kinematics of the western Mediterranean, *Geological Society, London, Special Publications*, *45*, 265–283, 1989.

Dickin, A. P., *Radiogenic Isotope Geology*, Cambridge University Press, 2005.

Dobrzhinetskaya, L., Z. Liu, P. Cartigny, J. Zhang, D. Tchkhetia, R. Hemley, and H. Green, Synchrotron infrared and Raman spectroscopy of microdiamonds from Erzgebirge, Germany, *Earth and Planetary Science Letters*, *248*, 340–349, 2006.

Dobrzhinetskaya, L. F., E. A. Eide, R. B. Larsen, B. A. Sturt, R. G. Trønnes, D. C. Smith, W. R. Taylor, and T. V. Posukhova, Microdiamond in high-grade metamorphic rocks of the Western Gneiss region, Norway, *Geology*, *23*, 597–600, 1995.

Dodson, M. H., Closure temperature in cooling geochronological and petrological systems, *Contributions to Mineralogy and Petrology*, *40*, 259–274, 1973, 10.1007/BF00373790.

Duretz, T., T. Gerya, B. Kaus, and T. Andersen, Thermomechanical modeling of slab eduction, *Journal of Geophysical Research*, *117*, B08411, 2012.

Eide, E. A., N. E. Haabesland, P. T. Osmundsen, T. B. Andersen, D. Roberts, and M. A. Kendrick, Modern techniques and old red problems–determining the age of continental sedimentary deposits with $^{40}Ar/^{39}Ar$ provenance analysis in west-central Norway, *Norw. J. Geol*, *85*, 133–149, 2005.

Ellis, S., T. Little, L. Wallace, B. Hacker, and S. Buiter, Feedback between rifting and diapirism can exhume ultrahigh-pressure rocks, *Earth and Planetary Science Letters*, *311*, 427–438, 2011.

Engi, M., A. Berger, and G. T. Roselle, Role of the tectonic accretion channel in collisional orogeny, *Geology*, *29*, 1143–1146, 2001.

Engi, M., et al., Metamorphic field gradients in the Central Alps, *Journal of Metamorphic Geology*, *15*, 513–530, 2004.

England, P., and T. Holland, Archimedes and the Tauern eclogites: the role of buoyancy in the preservation of exotic eclogite blocks, *Earth and Planetary Science Letters*, *44*, 287–294, 1979.

Epard, J., and A. Steck, Structural development of the Tso Morari ultra-high pressure nappe of the Ladakh Himalaya, *Tectonophysics*, *451*, 242–264, 2008.

Ernst, W., Tectonic history of subduction zones inferred from retrograde blueschist PT paths, *Geology*, *16*, 1081–1084, 1988.

Ernst, W., and J. Liou, Overview of UHP metamorphism and tectonics in well-studied collisional orogens, *International Geology Review*, *41*, 477–493, 1999.

Faccenda, M., T. V. Gerya, and S. Chakraborty, Styles of post-subduction collisional orogeny: Influence of convergence velocity, crustal rheology and radiogenic heat production, *Lithos*, *103*, 257–287, 2008.

Faure, M., W. Lin, U. Schärer, L. Shu, Y. Sun, and N. Arnaud, Continental subduction and exhumation of UHP rocks. Structural and geochronological insights from the Dabieshan (East China), *Lithos*, *70*, 213–241, 2003.

Federico, L., L. Crispini, M. Scambelluri, and G. Capponi, Ophiolite mélange zone records exhumation in a fossil subduction channel, *Geology*, *35*, 499–502, 2007.

Fisher, C. M., H. P. Longerich, S. E. Jackson, and J. M. Hanchar, Data acquisition and calculation of U–Pb isotopic analyses using laser ablation (single collector) inductively coupled plasma mass spectrometry, *Journal of Analytical Atomic Spectrometry*, *25*, 1905–1920, 2010.

Ford, M., S. Duchêne, D. Gasquet, and O. Vanderhaeghe, Two-phase orogenic convergence in the external and internal SW Alps, *Journal of the Geological Society*, *163*, 815–826, 2006.

Fossen, H., Extensional tectonics in the Caledonides: Synorogenic or postorogenic?, *Tectonics*, *19*, 213–224, 2000.

Fossen, H., Extensional tectonics in the North Atlantic Caledonides: a regional view, *Geological Society, London, Special Publications*, *335*, 767–793, 2010.

Fossen, H., and W. J. Dunlap, Timing and kinematics of Caledonian thrusting and extensional collapse, southern Norway: evidence from $^{40}Ar/^{39}Ar$ thermochronology, *Journal of Structural Geology*, *20*, 765–781, 1998.

Foster, J. J., The construction and development of SHRIMP I: an historical outline, *Precambrian Research*, *183*, 1–8, 2010.

Frezzotti, M., J. Selverstone, Z. Sharp, and R. Compagnoni, Carbonate dissolution during subduction revealed by diamond-bearing rocks from the Alps, *Nature Geoscience*, *4*, 703–706, 2011.

Frost, B. R., K. R. Chamberlain, and J. C. Schumacher, Sphene (titanite): phase relations and role as a geochronometer, *Chemical Geology*, *172*, 131–148, 2001.

Fullsack, P., An arbitrary Lagrangian-Eulerian formulation for creeping flows and its application in tectonic models, *Geophysical Journal International*, *120*, 1–23, 1995.

Furnes, H., Y. Dilek, and R. B. Pedersen, Structure, geochemistry, and tectonic evolution of trench-distal backarc oceanic crust in the western Norwegian Caledonides, Solund-Stavfjord ophiolite (Norway), *Geological Society of America Bulletin*, *124*, 1027–1047, 2012.

Ganguly, J., W. Cheng, and M. Tirone, Thermodynamics of aluminosilicate garnet solid solution: new experimental data, an optimized model, and thermometric applications, *Contributions to Mineralogy and Petrology*, *126*, 137–151, 1996, 10.1007/s004100050240.

Ganne, J., D. Marquer, G. Rosenbaum, J.-M. Bertrand, and S. Fudral, Partitioning of deformation within a subduction channel during exhumation of high-pressure rocks: a case study from the Western Alps, *Journal of Structural Geology*, *28*, 1193–1207, 2006.

Gasco, I., M. Gattiglio, and A. Borghi, Structural evolution of different tectonic units across the Austroalpine–Penninic boundary in the middle Orco Valley (Western Italian Alps), *Journal of Structural Geology*, *31*, 301–314, 2009.

Gasco, I., A. Borghi, and M. Gattiglio, P–T Alpine metamorphic evolution of the Monte Rosa nappe along the Piedmont Zone boundary (Gressoney Valley, NW Italy), *Lithos*, *127*, 336–353, 2011a.

Gasco, I., M. Gattiglio, and A. Borghi, Lithostratigraphic setting and P-T metamorphic evolution for the Dora Maira Massif along the Piedmont Zone boundary (middle Susa Valley, NW Alps), *International Journal of Earth Sciences*, *100*, 1065–1085, 2011b.

Gasco, I., M. Gattiglio, and A. Borghi, Review of metamorphic and kinematic data from Internal Crystalline Massifs (Western Alps): PTt paths and exhumation history, *Journal of Geodynamics*, 2012.

Gee, D., A tectonic model for the central part of the Scandinavian Caledonides, *American Journal of Science*, *275*, 468–515, 1975.

Gee, D. G., Basement-cover relationships in the central Scandinavian Caledonides, *Geologiska Föreningen i Stockholm Förhandlingar*, *102*, 455–474, 1980.

Gee, D. G., M. Janák, J. Majka, P. Robinson, and H. van Roermund, Subduction along and within the Baltoscandian margin during closing of the Iapetus Ocean and Baltica-Laurentia collision, *Lithosphere*, 2012.

Gerya, T., L. Perchuk, and J.-P. Burg, Transient hot channels: perpetrating and regurgitating ultrahigh-pressure, high-temperature crust–mantle associations in collision belts, *Lithos*, *103*, 236–256, 2008.

Gillet, P., J. Ingrin, and C. Chopin, Coesite in subducted continental crust: PT history deduced from an elastic model, *Earth and Planetary Science Letters*, *70*, 426–436, 1984.

Gilotti, J. A., and W. C. McClelland, Characteristics of, and a tectonic model for, ultrahigh-pressure metamorphism in the overriding plate of the Caledonian orogen, *International Geology Review*, *49*, 777–797, 2007.

Gleason, G. C., and J. Tullis, A flow law for dislocation creep of quartz aggregates determined with the molten salt cell, *Tectonophysics*, *247*, 1–23, 1995.

Glodny, J., U. Ring, A. Kühn, P. Gleissner, and G. Franz, Crystallization and very rapid exhumation of the youngest Alpine eclogites (Tauern Window, Eastern Alps) from Rb/Sr mineral assemblage analysis, *Contributions to Mineralogy and Petrology*, *149*, 699–712, 2005.

Gordon, S., D. Whitney, C. Teyssier, A. Kylander-Clark, B. Hacker, and R. Renedo, Timescales and conditions of crustal melting in the Western Gneiss Region UHP Terrane, Norway, *Geological Society of America Abstracts with Programs*, *43*, 495, 2011.

Gordon, S. M., D. L. Whitney, C. Teyssier, and H. Fossen, U-Pb dates and trace-element geochemistry of zircon from migmatite, western gneiss region, norway: Significance for history of partial melting in continental subduction, *Lithos*, 2013.

Green, H., Psychology of a changing paradigm: 40+ years of high-pressure metamorphism, *International Geology Review*, *47*, 439–456, 2005.

Grieve, R., F. Langenhorst, and D. Stöffler, Shock metamorphism of quartz in nature and experiment: II. Significance in geoscience, *Meteoritics & Planetary Science*, *31*, 6–35, 2012.

Groppo, C., M. Beltrando, and R. Compagnoni, The P–T path of the ultra-high pressure Lago Di Cignana and adjoining high-pressure meta-ophiolitic units: insights into the evolution of the subducting Tethyan slab, *Journal of Metamorphic Geology*, *27*, 207–231, 2009.

Grujic, D., C. J. Warren, and J. L. Wooden, Rapid synconvergent exhumation of Miocene-aged lower orogenic crust in the eastern Himalaya, *Lithosphere*, *3*, 346–366, 2011.

Guo, X., J. Encarnacion, X. Xu, A. Deino, Z. Li, and X. Tian, Collision and rotation of the South China block and their role in the formation and exhumation of ultrahigh pressure rocks in the Dabie Shan orogen, *Terra Nova*, *24*, 339–350, 2012.

Hacker, B., *Eclogite formation and the rheology, buoyancy, seismicity, and H_2O content of oceanic crust*, vol. 96, pp. 337–346, AGU, Washington, DC, 1996.

Hacker, B., Pressures and temperatures of ultrahigh-pressure metamorphism: implications for UHP tectonics and H_2O in subducting slabs, *International Geology Review*, *48*, 1053–1066, 2006.

Hacker, B., Ascent of the ultrahigh-pressure Western Gneiss Region, Norway, *Geological Society of America Special Papers*, *419*, 171–184, 2007.

Hacker, B. R., and P. B. Gans, Continental collisions and the creation of ultrahigh-pressure terranes: petrology and thermochronology of nappes in the central Scandinavian Caledonides, *Geological Society of America Bulletin*, *117*, 117–134, 2005.

Hacker, B. R., L. Ratschbacher, and J. Liou, Subduction, collision and exhumation in the ultrahigh-pressure Qinling-Dabie orogen, *Special Publication-Geological Society of London*, *226*, 157–176, 2004.

Hacker, B. R., T. B. Andersen, S. Johnston, A. R. Kylander-Clark, E. M. Peterman, E. O. Walsh, and D. Young, High-temperature deformation during continental-margin subduction & exhumation: the ultrahigh-pressure Western Gneiss Region of Norway, *Tectonophysics*, *480*, 149–171, 2010.

Handy, M. R., S. M. Schmid, R. Bousquet, E. Kissling, and D. Bernoulli, Reconciling plate-tectonic reconstructions of Alpine Tethys with the geological–geophysical record of spreading and subduction in the Alps, *Earth-Science Reviews*, *102*, 121–158, 2010.

Hartz, E., D. Condon, H. Austrheim, and M. Erambert, Rediscovery of the Liverpool Land eclogites (central East Greenland): a post and supra-subduction (U)HP province, *Mitteilungen der Österreichischen Mineralogischen Geselschaft*, *150*, 50, 2005.

Hartz, E., Y. Podladchikov, and M. Dabrowski, Tectonic and reaction overpressure: theoretical models and natural examples, in *Geophysical Research Abstracts*, vol. 9, p. 10430, 2007.

Hartz, E., A. Andresen, K. V. Hodges, and M. W. Martin, Syncontractional extension and exhumation of deep crustal rocks in the east Greenland Caledonides, *Tectonics*, *20*, 58–77, 2001.

Hendriks, B., P. Andriessen, Y. Huigen, C. Leighton, T. Redfield, G. Murrell, K. Gallagher, and S. B. Nielsen, A fission track data compilation for Fennoscandia, *Norsk Geologisk Tidsskrift*, *87*, 143, 2007.

Hermann, J., Experimental constraints on phase relations in subducted continental crust, *Contributions to Mineralogy and Petrology*, *143*, 219–235, 1997, 10.1007/s00410-001-0336-3.

Hermann, J., and C. J. Spandler, Sediment melts at sub-arc depths: an experimental study, *Journal of Petrology*, *49*, 717–740, 2008.

Higgins, A., and A. G. Leslie, Architecture and evolution of the East Greenland Caledonides–an introduction, *Geological Society of America Memoirs*, *202*, 29–53, 2008.

Holland, T. J. B., and R. Powell, An internally consistent thermodynamic data set for phases of petrological interest, *Journal of Metamorphic Geology*, *16*, 309–343, 1998.

Hollocher, K., P. Robinson, E. Walsh, and M. P. Terry, The Neoproterozoic Ottfjället dike swarm of the Middle Allochthon, traced geochemically into the Scandian Hinterland, Western Gneiss Region, Norway, *American Journal of Science*, *307*, 901–953, 2007.

Hoskin, P. W. O., and U. Schaltegger, The composition of zircon and igneous and metamorphic petrogenesis, *Reviews in Mineralogy and Geochemistry*, *53*, 27–62, 2003.

Huang, W., and P. Wyllie, Phase relationships of S-type granite with H2O to 35 kbar: Muscovite granite from Harney Peak, South Dakota, *Journal of Geophysical Research*, *86*, 10515–10529, 1981.

Huismans, R., and C. Beaumont, Symmetric and asymmetric lithospheric extension: Relative effects of frictional-plastic and viscous strain softening, *Journal of Geophysical Research-Solid Earth*, *108*, 2003.

Jaffey, A. H., K. F. Flynn, L. E. Glendenin, W. C. Bentley, and A. M. Essling, Precision measurement of half-lives and specific activities of ^{235}U and ^{238}U, *Physical Review C*, *4*, 1889–1906, 1971.

Jamtveit, B., K. Bucher-Nurminen, and H. Austrheim, Fluid controlled eclogitization of granulites in deep crustal shear zones, Bergen arcs, Western Norway, *Contributions to Mineralogy and Petrology*, *104*, 184–193, 1990.

Janák, M., H. van Roermund, J. Majka, and D. Gee, UHP metamorphism recorded by kyanite-bearing eclogite in the Seve Nappe Complex of northern Jämtland, Swedish Caledonides, *Gondwana Research*, 2012.

Janots, E., M. Engi, D. Rubatto, A. Berger, C. Gregory, and M. Rahn, Metamorphic rates in collisional orogeny from in situ allanite and monazite dating, *Geology*, *37*, 11–14, 2009.

Johnston, S., B. R. Hacker, and M. N. Ducea, Exhumation of ultrahigh-pressure rocks beneath the Hornelen segment of the Nordfjord-Sogn Detachment Zone, western Norway, *Geological Society of America Bulletin*, *119*, 1232–1248, 2007.

Johnston, S. M., E. H. Hartz, H. K. Brueckner, and G. E. Gehrels, U–Pb zircon geochronology and tectonostratigraphy of southern Liverpool Land, East Greenland: implications for deformation in the overriding plates of continental collisions, *Earth and Planetary Science Letters*, *297*, 512–524, 2010.

Jolivet, L., H. Raimbourg, L. Labrousse, D. Avigad, Y. Leroy, H. Austrheim, and T. B. Andersen, Softening triggered by eclogitization, the first step toward exhumation during continental subduction, *Earth and Planetary Science Letters*, *237*, 532–547, 2005.

Kaneko, Y., I. Katayama, H. Yamamoto, K. Misawa, M. Ishikawa, H. Rehman, A. Kausar, and K. Shiraishi, Timing of Himalayan ultrahigh-pressure metamorphism: Sinking rate and subduction angle of the Indian continental crust beneath Asia, *Journal of Metamorphic Geology*, *21*, 589–599, 2003.

Karato, S.-I., and P. Wu, Rheology of the upper mantle: A synthesis, *Science*, *260*, 771–778, 1993.

Košler, J., and P. J. Sylvester, Present trends and the future of zircon in geochronology: laser ablation ICPMS, *Reviews in Mineralogy and Geochemistry*, *53*, 243–275, 2003.

Krabbendam, M., and J. F. Dewey, Exhumation of UHP rocks by transtension in the Western Gneiss Region, Scandinavian Caledonides, *Geological Society, London, Special Publications*, *135*, 159–181, 1998.

Krabbendam, M., A. Wain, and T. Andersen, Pre-Caledonian granulite and gabbro enclaves in the Western Gneiss Region, Norway: indications of incomplete transition at high pressure, *Geological Magazine*, *137*, 235–255, 2000.

Krogh, T., A low-contamination method for hydrothermal decomposition of zircon and extraction of U and Pb for isotopic age determinations, *Geochimica et Cosmochimica Acta*, *37*, 485–494, 1973.

Krogh, T., Improved accuracy of U–Pb zircon ages by the creation of more concordant systems using an air abrasion technique, *Geochimica et Cosmochimica Acta*, *46*, 637–649, 1982.

Krogh, T. E., S. L. Kamo, P. Robinson, M. P. Terry, and K. Kwok, U–Pb zircon geochronology of eclogites from the Scandian Orogen, northern Western Gneiss Region, Norway: 14–20 million years between eclogite crystallization and return to amphibolite-facies conditions, *Canadian Journal of Earth Sciences*, *48*, 441–472, 2011.

Kuhlemann, J., W. Frisch, B. Székely, I. Dunkl, and M. Kázmér, Post-collisional sediment budget history of the Alps: tectonic versus climatic control, *International Journal of Earth Sciences*, *91*, 818–837, 2002.

Kurz, W., R. Handler, and C. Bertoldi, Tracing the exhumation of the Eclogite Zone (Tauern Window, Eastern Alps) by $^{40}Ar/^{39}Ar$ dating of white mica in eclogites, in *Orogenic Processes in the Alpine Collision Zone*, pp. S191–S206, Springer, 2009.

Kylander-Clark, A., B. Hacker, and C. Mattinson, Size and exhumation rate of ultrahigh-pressure terranes linked to orogenic stage, *Earth and Planetary Science Letters*, *321*, 115–120, 2012.

Kylander-Clark, A. R., B. R. Hacker, C. M. Johnson, B. L. Beard, and N. J. Mahlen, Slow subduction of a thick ultrahigh-pressure terrane, *Tectonics*, *28*, TC2003, 2009.

Labrousse, L., L. Jolivet, T. Andersen, P. Agard, R. Hébert, H. Maluski, and U. Scharer, Pressure-temperature-time deformation history of the exhumation of ultra-high pressure rocks in the Western Gneiss Region, Norway, *Special Papers-Geological Society of America*, pp. 155–184, 2004.

Labrousse, L., G. Prouteau, and A.-C. Ganzhorn, Continental exhumation triggered by partial melting at ultrahigh pressure, *Geology*, *39*, 1171–1174, 2011.

Lapen, T., C. Johnson, L. Baumgartner, N. Mahlen, B. Beard, and J. Amato, Burial rates during prograde metamorphism of an ultra-high-pressure terrane: an example from Lago di Cignana, western Alps, Italy, *Earth and Planetary Science Letters*, *215*, 57–72, 2003.

Lapen, T., C. Johnson, L. Baumgartner, G. Piaz, S. Skora, and B. Beard, Coupling of oceanic and continental crust during Eocene eclogite-facies metamorphism: evidence from the Monte Rosa nappe, western Alps, *Contributions to Mineralogy and Petrology*, *153*, 139–157, 2007, 10.1007/s00410-006-0144-x.

Lardeaux, J.-M., S. Schwartz, P. Tricart, A. Paul, S. Guillot, N. Béthoux, and F. Masson, A crustal-scale cross-section of the south-western Alps combining geophysical and geological imagery, *Terra Nova*, *18*, 412–422, 2006.

Larsen, R. B., E. A. Eide, and E. A. J. Burke, Evolution of metamorphic volatiles during exhumation of microdiamond-bearing granulites in the Western Gneiss Region, Norway, *Contributions to Mineralogy and Petrology*, *133*, 106–121, 1998, 10.1007/s004100050441.

Le Bayon, B., and M. Ballèvre, Deformation history of a subducted continental crust (Gran Paradiso, Western Alps): continuing crustal shortening during exhumation, *Journal of Structural Geology*, *28*, 793–815, 2006.

Leake, B. E., A. R. Woolley, C. E. S. Arps, W. D. Birch, G. J. D. Gilbert, M. C., F. C. Hawthorne, A. Kato, K. V. G. Kisch, H. J., K. Linthout, J. Laird, J. A. Mandarino, W. V. Maresch, E. H. Nickel, N. M. S. Rock, J. C. Schumacher, D. C. Smith, N. C. N. Stephenson, L. Ungaretti, E. J. W. Whittaker, and G. Youzhi, Nomenclature of amphiboles: Report of the subcommittee on amphiboles of the International Mineralogical Association, commission on new minerals and mineral names, *American Mineralogist*, *82*, 1019–1037, 1997.

Lenze, A., and B. Stöckhert, Microfabrics of UHP metamorphic granites in the Dora Maira Massif, western Alps–no evidence of deformation at great depth, *Journal of Metamorphic Geology*, *25*, 461–475, 2007.

Lenze, A., B. Stöckhert, and R. Wirth, Grain scale deformation in ultra-high-pressure metamorphic rocks–an indicator of rapid phase transformation, *Earth and Planetary Science Letters*, *229*, 217–230, 2005.

Li, S., T. M. Kusky, G. Zhao, X. Liu, G. Zhang, H. Kopp, and L. Wang, Two-stage Triassic exhumation of HP–UHP terranes in the western Dabie orogen of China: constraints from structural geology, *Tectonophysics*, *490*, 267–293, 2010a.

Li, Z., T. Gerya, and J. Burg, Influence of tectonic overpressure on P–T paths of HP–UHP rocks in continental collision zones: thermomechanical modelling, *Journal of Metamorphic Geology*, *28*, 227–247, 2010b.

Liou, J., T. Tsujimori, R. Zhang, I. Katayama, and S. Maruyama, Global UHP metamorphism and continental subduction/collision: the Himalayan model, *International Geology Review*, *46*, 1–27, 2004.

Liou, J., R. Zhang, F. Liu, Z. Zhang, and W. Ernst, Mineralogy, petrology, U-Pb geochronology, and geologic evolution of the Dabie-Sulu classic ultrahigh-pressure metamorphic terrane, East-Central China, *American Mineralogist*, *97*, 1533–1543, 2012.

Lippitsch, R., E. Kissling, and J. Ansorge, Upper mantle structure beneath the Alpine orogen from high-resolution teleseismic tomography, *Journal of Geophysical Research*, *108*, 2376, 2003.

Little, T., B. Hacker, S. Gordon, S. Baldwin, P. Fitzgerald, S. Ellis, and M. Korchinski, Diapiric exhumation of Earth's youngest (UHP) eclogites in the gneiss domes of the D'Entrecasteaux Islands, Papua New Guinea, *Tectonophysics*, *510*, 39 – 68, 2011.

Mackwell, S., M. Zimmerman, and D. Kohlstedt, High-temperature deformation of dry diabase with application to tectonics on Venus, *Journal of Geophysical Research-Solid Earth*, *103*, 975–984, 1998.

Malusà, M. G., C. Faccenna, E. Garzanti, and R. Polino, Divergence in subduction zones and exhumation of high pressure rocks (Eocene Western Alps), *Earth and Planetary Science Letters*, *310*, 21–32, 2011.

Mancktelow, N., Nonlithostatic pressure during sediment subduction and the development and exhumation of high pressure metamorphic rocks, *Journal of Geophysical Research*, *100*, 571–583, 1995.

Mancktelow, N., Tectonic pressure: theoretical concepts and modelled examples, *Lithos*, *103*, 149–177, 2008.

Massonne, H., A comparison of the evolution of diamondiferous quartz-rich rocks from the Saxonian Erzgebirge and the Kokchetav Massif: are so-called diamondiferous gneisses magmatic rocks?, *Earth and Planetary Science Letters*, *216*, 347–364, 2003.

Massonne, H., Occurrences and PT conditions of high and ultrahigh pressure rocks in the Bohemian Massif, *Geolines*, *23*, 18–26, 2011.

Mattinson, J. M., U–Pb ages of zircons: a basic examination of error propagation, *Chemical Geology: Isotope Geoscience section*, *66*, 151–162, 1987.

Mattinson, J. M., Zircon U–Pb chemical abrasion ("CA–TIMS") method: combined annealing and multi-step partial dissolution analysis for improved precision and accuracy of zircon ages, *Chemical Geology*, *220*, 47–66, 2005.

Meffan-Main, S., R. A. Cliff, A. C. Barnicoat, B. Lombardo, and R. Compagnoni, A Tertiary age for Alpine high-pressure metamorphism in the Gran Paradiso massif, Western Alps: a Rb–Sr microsampling study, *Journal of Metamorphic Geology*, *22*, 267–281, 2004.

Meinhold, G., Rutile and its applications in earth sciences, *Earth-Science Reviews*, *102*, 1–28, 2010.

Milnes, A. G., O. P. Wennberg, Ø. Skår, and A. G. Koestler, Contraction, extension and timing in the South Norwegian Caledonides: the Sognefjord transect, *Geological Society, London, Special Publications*, *121*, 123–148, 1997.

Mitterbauer, U., M. Behm, E. Brückl, R. Lippitsch, A. Guterch, G. R. Keller, E. Koslovskaya, E.-M. Rumpfhuber, and F. Šumanovac, Shape and origin of the East-Alpine slab constrained by the ALPASS teleseismic model, *Tectonophysics*, *510*, 195–206, 2011.

Molnar, P., and D. Gray, Subduction of continental lithosphere: some constraints and uncertainties, *Geology*, *7*, 58–62, 1979.

Morag, N., D. Avigad, Y. Harlavan, M. O. McWilliams, and A. Michard, Rapid exhumation and mountain building in the Western Alps: Petrology and $^{40}Ar/^{39}Ar$ geochronology of detritus from Tertiary basins of southeastern France, *Tectonics*, *27*, TC2004, 2008.

Morimoto, N., J. Fabriés, A. K. Ferguson, G. I. V., M. Ross, F. Seifert, J. Zussman, K. Aoki, and G. Gottardi, A tectonic model for the central part of the Scandinavian Caledonides, *American Mineralogist*, *73*, 1123–1133, 1988.

Mosenfelder, J., and S. Bohlen, Kinetics of the coesite to quartz transformation, *Earth and Planetary Science Letters*, *153*, 133–147, 1997.

Mukherjee, B., H. Sachan, Y. Ogasawara, A. Muko, and N. Yoshioka, Carbonate-bearing UHPM rocks from the Tso-Morari region, Ladakh, India: petrological implications, *International Geology Review*, *45*, 49–69, 2003.

Müller, W., Strengthening the link between geochronology, textures and petrology, *Earth and Planetary Science Letters*, *206*, 237–251, 2003.

Nagel, T. J., Tertiary subduction, collision and exhumation recorded in the Adula nappe, central Alps, *Geological Society, London, Special Publications*, *298*, 365–392, 2008.

Nagel, T.J. and Herwartz, D. and Rexroth, S. and Münker, C. and Froitzheim, N. and Kurz, W., Lu-Hf dating, petrography, and tectonic implications of the youngest Alpine eclogites (Tauern Window, Austria), *Lithos*, 2013.

Nichols, W. P., G.T., and C. Stern, Subduction zone melting of pelagic sediments constrained by melting experiments, *Nature*, *371*, 785–788, 1994.

O'Brien, P., N. Zotov, R. Law, M. Khan, and M. Jan, Coesite in Himalayan eclogite and implications for models of India-Asia collision, *Geology*, *29*, 435–438, 2001.

Ogasawara, Y., K. Fukasawa, and S. Maruyama, Coesite exsolution from supersilicic titanite in UHP marble from the Kokchetav Massif, northern Kazakhstan, *American Mineralogist*, *87*, 454–461, 2002.

Osmundsen, P., and T. Andersen, The middle Devonian basins of western Norway: sedimentary response to large-scale transtensional tectonics?, *Tectonophysics*, *332*, 51–68, 2001.

Page, F. Z., E. Essene, and S. Mukasa, Quartz exsolution in clinopyroxene is not proof of ultrahigh pressures: Evidence from eclogites from the Eastern Blue Ridge, Southern Appalachians, U.S.A., *American Mineralogist*, *90*, 1092–1099, 2005.

Parkinson, C., and I. Katayama, Present-day ultrahigh-pressure conditions of coesite inclusions in zircon and garnet: Evidence from laser Raman microspectroscopy, *Geology*, *27*, 979–982, 1999.

Parkinson, C. D., Coesite inclusions and prograde compositional zonation of garnet in whiteschist of the HP-UHPM Kokchetav massif, Kazakhstan: a record of progressive UHP metamorphism, *Lithos*, *52*, 215–233, 2000.

Parrish, R., S. Gough, M. Searle, and D. Waters, Plate velocity exhumation of ultrahigh-pressure eclogites in the Pakistan Himalaya, *Geology*, *34*, 989–992, 2006.

Parrish, R. R., and T. E. Krogh, Synthesis and purification of ^{205}Pb for U–Pb geochronology, *Chemical Geology: Isotope Geoscience section*, *66*, 103–110, 1987.

Parrish, R. R., and S. R. Noble, Zircon U-Th-Pb Geochronology by Isotope Dilution – Thermal Ionization Mass Spectrometry (ID-TIMS), *Reviews in Mineralogy and Geochemistry*, *53*, 183–213, 2003.

Peacock, S., Thermal and petrologic structure of subduction zones, *Geophysical Monograph Series*, *96*, 119–133, 1996.

Perrillat, J., I. Daniel, J. Lardeaux, and H. Cardon, Kinetics of the coesite–quartz transition: application to the exhumation of ultrahigh-pressure rocks, *Journal of Petrology*, *44*, 773–788, 2003.

Peters, T. J., J. C. Ayers, S. Gao, and X.-M. Liu, The origin and response of zircon in eclogite to metamorphism during the multi-stage evolution of the Huwan Shear Zone, China: insights from Lu-Hf and U-Pb isotopic and trace element geochemistry, *Gondwana Research*, 2012.

Platt, J., Exhumation of high-pressure rocks: a review of concepts and processes, *Terra Nova*, *5*, 119–133, 1993.

Platt, J. P., Dynamics of orogenic wedges and the uplift of high-pressure metamorphic rocks, *Geological Society of America Bulletin*, *97*, 1037–1053, 1986.

Pleuger, J., T. J. Nagel, J. M. Walter, E. Jansen, and N. Froitzheim, On the role and importance of orogen-parallel and -perpendicular extension, transcurrent shearing, and backthrusting in the Monte Rosa nappe and the Southern Steep Belt of the Alps (Penninic zone, Switzerland and Italy), *Geological Society, London, Special Publications*, *298*, 251–280, 2008.

Powell, R., and T. Holland, An internally consistent thermodynamic dataset with uncertainties and correlations: 1. Methods and a worked example, *Journal of Metamorphic Geology*, *3*, 327–342, 2007.

Powell, R., and T. J. B. Holland, On thermobarometry, *Journal of Metamorphic Geology*, *26*, 155–179, 2008.

Radulescu, I. G., D. Rubatto, C. Gregory, and R. Compagnoni, The age of HP metamorphism in the Gran Paradiso Massif, Western Alps: A petrological and geochronological study of "silvery micaschists", *Lithos*, *110*, 95–108, 2009.

Raimbourg, H., L. Jolivet, and Y. Leroy, Consequences of progressive eclogitization on crustal exhumation, a mechanical study, *Geophysical Journal International*, *168*, 379–401, 2007.

Ravna, E., and J. Paquin, Thermobarometric methodologies applicable to eclogites and garnet ultrabasites, *EMU Notes in Mineralogy*, *5*, 229–259, 2003.

Ravna, E. J. K., and M. P. Terry, Geothermobarometry of UHP and HP eclogites and schists – an evaluation of equilibria among garnet–clinopyroxene–kyanite–phengite–coesite/quartz, *Journal of Metamorphic Geology*, *22*, 579–592, 2004.

Ravna, K., The garnet–clinopyroxene Fe^{2+}–mg geothermometer: an updated calibration, *Journal of Metamorphic Geology*, *18*, 211–219, 2000.

Reddy, S., J. Wheeler, R. Butler, R. Cliff, S. Freeman, S. Inger, C. Pickles, and S. Kelley, Kinematic reworking and exhumation within the convergent Alpine Orogen, *Tectonophysics*, *365*, 77–102, 2003.

Reddy, S. M., J. Wheeler, and R. A. Cliff, The geometry and timing of orogenic extension: an example from the Western Italian Alps, *Journal of Metamorphic Geology*, *17*, 573–589, 1999.

Reinecke, T., Very-high-pressure metamorphism and uplift of coesite-bearing metasediments from the Zermatt-Saas zone, Western Alps, *European Journal of Mineralogy*, *3*, 7–17, 1991.

Roberts, D., The Scandinavian Caledonides: event chronology, palaeogeographic settings and likely modern analogues, *Tectonophysics*, *365*, 283–299, 2003.

Roberts, D., and D. G. Gee, An introduction to the structure of the Scandinavian Caledonides, in *The Caledonide Orogen–Scandinavia and related areas*, edited by D. G. Gee and B. A. Sturt, pp. 55–68, Wiley, London, 1985.

Robinson, P., The composition space of terrestrial pyroxenes; internal and external limits, *Reviews in Mineralogy and Geochemistry*, *7*, 419–494, 1981.

Robinson, P., Extension of Trollheimen tectono-stratigraphic sequence in deep synclines near Molde and Brattvåg, Western Gneiss Region, southern Norway, *Norsk Geologisk Tidsskrift*, *75*, 181–198, 1995.

Robinson, P., R. Tucker, M. Terry, S. Kamo, D. Roberts, D. Gee, and J. Butler, A major synmetamorphic Early Devonian thrust and extensional fault system in the Mid-Norway Caledonides: key to exhumation of HP and UHP rocks, in *EGU General Assembly Conference Abstracts*, vol. 14, p. 10250, 2012.

Røhr, T. S., B. Bingen, P. Robinson, and S. M. Reddy, Geochronology of Paleoproterozoic Augen Gneisses in the Western Gneiss Region, Norway: evidence for Sveconorwegian Zircon Neocrystallization and Caledonian Zircon Deformation, *The Journal of Geology*, *121*, 105–128, 2013.

Root, D., and F. Corfu, U–pb geochronology of two discrete Ordovician high-pressure metamorphic events in the Seve Nappe Complex, Scandinavian Caledonides, *Contributions to Mineralogy and Petrology*, pp. 1–20, 2012.

Root, D. B., B. R. Hacker, P. B. Gans, M. N. Ducea, E. A. Eide, and J. L. Mosenfelder, Discrete ultrahigh-pressure domains in the Western Gneiss Region, Norway: implications for formation and exhumation, *Journal of Metamorphic Geology*, *23*, 45–61, 2005.

Rosenbaum, G., and G. S. Lister, The Western Alps from the Jurassic to Oligocene: spatio-temporal constraints and evolutionary reconstructions, *Earth-Science Reviews*, *69*, 281–306, 2005.

Rosenbaum, G., L. Menegon, J. Glodny, P. Vasconcelos, U. Ring, M. Massironi, D. Thiede, and P. Nasipuri, Dating deformation in the Gran Paradiso Massif (NW Italian Alps): implications for the exhumation of high-pressure rocks in a collisional belt, *Lithos*, *144-145*, 130–144, 2012.

Rosenberg, C. L., and A. Berger, On the causes and modes of exhumation and lateral growth of the alps, *Tectonics*, *28*, 2009.

Rosenberg, C. L., and M. R. Handy, Experimental deformation of partially melted granite revisited: implications for the continental crust, *Journal of Metamorphic Geology*, *23*, 19–28, 2005.

Rubatto, D., Zircon trace element geochemistry: partitioning with garnet and the link between U–Pb ages and metamorphism, *Chemical Geology*, *184*, 123 – 138, 2002.

Rubatto, D., and J. Hermann, Exhumation as fast as subduction?, *Geology*, *29*, 3–6, 2001.

Rubatto, D., and J. Hermann, Zircon behaviour in deeply subducted rocks, *Elements*, *3*, 31–35, 2007.

Rubatto, D., J. Hermann, A. Berger, and M. Engi, Protracted fluid-induced melting during Barrovian metamorphism in the Central Alps, *Contributions to Mineralogy and Petrology*, *158*, 703–722, 2009.

Rubatto, D., D. Regis, J. Hermann, K. Boston, M. Engi, M. Beltrando, and S. R. B. McAlpine, Yo-yo subduction recorded by accessory minerals in the Italian Western Alps, *Nature Geoscience*, *4*, 338–342, 2011.

Rutherford, E., and F. Soddy, LXXXIV.-The radioactivity of thorium compounds. II. The cause and nature of radioactivity, *Journal of the Chemical Society, Transactions*, *81*, 837–860, 1902.

Ryan, W., S. Carbotte, J. Coplan, S. O'Hara, A. Melkonian, R. Arko, R. Weissel, V. Ferrini, A. Goodwillie, F. Nitsche, J. Bonczkowski, and R. Zemsky, Global multi-resolution topography synthesis, *Geochemistry Geophysics Geosystems*, *10*, Q03014, 2009.

Sánchez-García, T., C. Quesada, F. Bellido, G.R., and J. G. del Tánago, Two-step magma flooding of the upper crust during rifting: The Early Paleozoic of the Ossa Morena Zone (SW Iberia), *Tectonophysics*, *461*, 72–90, 2008.

Sassi, R., B. Harte, D. Carswell, and H. Yujing, Trace element distribution in Central Dabie eclogites, *Contributions to Mineralogy and Petrology*, *139*, 298–315, 2000.

Sawyer, E., Criteria for the recognition of partial melting, *Physics and Chemistry of the Earth, Part A: Solid Earth and Geodesy*, *24*, 269–279, 1999.

Sawyer, E., *Atlas of Migmatites*, vol. 9 of *Canadian Mineralogist Special Publication*, NRC Research Press, Ottawa, Ontario, 2008, 371 pp.

Schlunegger, F., and S. Willett, Spatial and temporal variations in exhumation of the central Swiss Alps and implications for exhumation mechanisms, *Geological Society, London, Special Publications*, *154*, 157–179, 1999.

Schmid, S., and E. Kissling, The arc of the Western Alps in the light of geophysical data on deep crustal structure, *Tectonics*, *19*, 62–85, 2000.

Schmid, S., O. Pfiffner, N. Froitzheim, G. Schonborn, and E. Kissling, Geophysical-geological transect and tectonic evolution of the Swiss-Italian Alps, *Tectonics*, *15*, 1036–1064, 1996.

Schmid, S. M., B. Fügenschuh, E. Kissling, and R. Schuster, Tectonic map and overall architecture of the Alpine orogen, *Eclogae Geologicae Helvetiae*, *97*, 93–117, 2004, 10.1007/s00015-004-1113-x.

Schmid, S. M., A. Scharf, M. R. Handy, C. Rosenberg, S. Favaro, and A. Bertrand, New tectonic map and cross-sections of the Tauern Window (Eastern Alps, Austria), in *10th Alpine workshop CorseAlp, St. Florent*, 2011.

Schmitt, H., Petrology and structure of the Eiksundal Eclogite Complex, Hareidland, Sunnmøre, Norway, Unpublished Ph.D. Thesis, Harvard University, Cambridge, 1963, 323 pp.

Schwartz, S., P. Tricart, J.-M. Lardeaux, S. Guillot, and O. Vidal, Late tectonic and metamorphic evolution of the Piedmont accretionary wedge (Queyras Schistes lustrés, western Alps): evidences for tilting during Alpine collision, *Geological Society of America Bulletin*, *121*, 502–518, 2009.

Scott, D. J., and M. R. St-Onge, Constraints on Pb closure temperature in titanite based on rocks from the Ungava orogen, Canada: implications for U-Pb geochronology and P–T–t path determinations, *Geology*, *23*, 1123–1126, 1995.

Searle, M., B. R. Hacker, and R. Bilham, The Hindu Kush Seismic Zone as a paradigm for the creation of ultrahigh-pressure diamond-and coesite-bearing continental rocks, *The Journal of Geology*, *109*, 143–153, 2001.

Simon-Labric, T., Y. Rolland, T. Dumont, T. Heymes, C. Authemayou, M. Corsini, and M. Fornari, $^{40}Ar/^{39}Ar$ dating of Penninic Front tectonic displacement (W Alps) during the Lower Oligocene (31–34 Ma), *Terra Nova*, *21*, 127–136, 2009.

Sinclair, H., Flysch to molasse transition in peripheral foreland basins: the role of the passive margin versus slab breakoff, *Geology*, *25*, 1123–1126, 1997.

Sinclair, H. D., and P. A. Allen, Vertical versus horizontal motions in the Alpine orogenic wedge: stratigraphic response in the foreland basin, *Basin Research*, *4*, 215–232, 1992.

Sizova, E., T. Gerya, and M. Brown, Exhumation mechanisms of melt-bearing ultrahigh pressure crustal rocks during collision of spontaneously moving plates, *Journal of Metamorphic Geology*, pp. 927–955, 2012.

Slagstad, T., Radiogenic heat production of Archaean to Permian geological provinces in Norway, *Norwegian Journal of Geology*, *88*, 2008.

Smith, D., Coesite in clinopyroxene in the Caledonides and its implications for geodynamics, *Nature*, *310*, 641–644, 1984.

Smye, A. J., M. J. Bickle, T. J. Holland, R. R. Parrish, and D. J. Condon, Rapid formation and exhumation of the youngest Alpine eclogites: a thermal conundrum to Barrovian metamorphism, *Earth and Planetary Science Letters*, *306*, 193–204, 2011.

Sobolev, S., and A. Babeyko, What drives orogeny in the Andes?, *Geology*, *33*, 617–620, 2005.

Speer, J., Zircon, *Reviews in Mineralogy*, *5*, 67–112, 1982.

Spengler, D., H. K. Brueckner, H. L. van Roermund, M. R. Drury, and P. R. Mason, Long-lived, cold burial of Baltica to 200 km depth, *Earth and Planetary Science Letters*, *281*, 27–35, 2009.

Stacey, J., and J. Kramers, Approximation of terrestrial lead isotope evolution by a two-stage model, *Earth and Planetary Science Letters*, *26*, 207–221, 1975.

Stampfli, G., J. Mosar, D. Marquer, R. Marchant, T. Baudin, and G. Borel, Subduction and obduction processes in the Swiss Alps, *Tectonophysics*, *296*, 159–204, 1998.

Steck, A., Tectonics of the Simplon massif and Lepontine gneiss dome: deformation structures due to collision between the underthrusting European plate and the Adriatic indenter, *Swiss Journal of Geosciences*, *101*, 515–546, 2008, 10.1007/s00015-008-1283-z.

Steenkamp, H. M., A metamorphic history of supracrustal rocks on Harøya and Finnøya, Nordøyane, Western Gneiss Region, Norway, Unpublished M.Sc. Thesis, Dalhousie University, Halifax, NS, 2012, 238 pp.

Steenkamp, H. M., J. P. Butler, R. A. Jamieson, and P. Robinson, Evidence for contrasting P–T histories in supracrustal and basement rocks on Harøya and Finnøya, Western Gneiss Region, Norway, *American Geophysical Union, Fall Meeting 2011*, 2011.

Sue, C., and P. Tricart, Neogene to ongoing normal faulting in the inner western Alps: a major evolution of the late alpine tectonics, *Tectonics*, *22*, 2003.

Taylor, S., S. McLennan, R. Armstrong, and J. Tarney, The composition and evolution of the continental crust: rare earth element evidence from sedimentary rocks [and discussion], *Philosophical Transactions of the Royal Society of London. Series A, Mathematical and Physical Sciences*, *301*, 381–399, 1981.

Terry, M., and P. Robinson, Evolution of amphibolite-facies structural features and boundary conditions for deformation during exhumation of high- and ultrahigh-pressure rocks, Nordøyane, Western Gneiss Region, Norway, *Tectonics*, *22*, 2003.

Terry, M., and P. Robinson, Geometry of eclogite-facies structural features: implications for production and exhumation of UHP and HP rocks, Western Gneiss Region, Norway, *Tectonics*, *23*, 2004.

Terry, M. P., and P. Robinson, Evidence for supersilicic pyroxene in an UHP kyanite eclogite, Western Gneiss Region, Norway, *Lunar and Planetary Institute Contributions*, *1088*, 3842, 2001.

Terry, M. P., P. Robinson, M. A. Hamilton, and M. J. Jercinovic, Monazite geochronology of UHP and HP metamorphism, deformation, and exhumation, Nordøyane, Western Gneiss Region, Norway, *American Mineralogist*, *85*, 1651–1664, 2000.

Tindle, A., and P. Webb, Probe-AMPH spreadsheet program to classify microprobe-derived amphibole analyses, *Computers & Geosciences*, *20*, 1201–1228, 1994.

Torsvik, T. H., Palaeozoic palaeogeography: A North Atlantic viewpoint, *GFF*, *120*, 109–118, 1998.

Tucker, R., A. Røayheim, T. Krogh, and F. Corfu, Uranium-lead zircon and titanite ages from the northern portion of the Western Gneiss Region, south-central Norway, *Earth and Planetary Science Letters*, *81*, 203–211, 1987.

Tucker, R. D., P. Robinson, A. Solli, D. G. Gee, T. Thorsnes, T. E. Krogh, Ø. Nordgulen, and M. E. Bickford, Thrusting and extension in the Scandian hinterland, Norway: new U–Pb ages and tectonostratigraphic evidence, *American Journal of Science*, *304*, 477–532, 2004.

van der Molen, I., and H. van Roermund, The pressure path of solid inclusions in minerals: the retention of coesite inclusions during uplift, *Lithos*, *19*, 317–324, 1986.

van Roermund, H., and M. Drury, Ultra-high pressure (P $>$ 6 GPa) garnet peridotites in Western Norway: exhumation of mantle rocks from $>$ 185 km depth, *Terra Nova*, *10*, 295–301, 1998.

van Roermund, H., M. Drury, A. Barnhoorn, and A. De Ronde, Relict majoritic garnet microstructures from ultra-deep orogenic peridotites in western Norway, *Journal of Petrology*, *42*, 117–130, 2001.

van Roermund, H. L., D. A. Carswell, M. R. Drury, and T. C. Heijboer, Microdiamonds in a megacrystic garnet websterite pod from Bardane on the island of Fjørtoft, western Norway: Evidence for diamond formation in mantle rocks during deep continental subduction, *Geology*, *30*, 959–962, 2002.

Vitorello, I., and H. N. Pollack, On the variation of continental heat-flow with age and the thermal evolution of continents, *Journal of Geophysical Research*, *85*, 983–995, 1980.

Vrijmoed, J., Y. Podladchikov, T. Andersen, and E. Hartz, An alternative model for ultra-high pressure in the Svartberget Fe-Ti garnet-peridotite, Western Gneiss Region, Norway, *European Journal of Mineralogy*, *21*, 1119–1133, 2009a.

Vrijmoed, J. C., H. L. M. van Roermund, and G. R. Davies, Evidence for diamond-grade ultra-high pressure metamorphism and fluid interaction in the Svartberget Fe-Ti garnet peridotite–websterite body, Western Gneiss Region, Norway, *Mineralogy and Petrology*, *88*, 381–405, 2006, 10.1007/s00710-006-0160-6.

Vrijmoed, J. C., D. C. Smith, and H. L. M. van Roermund, Raman confirmation of microdiamond in the Svartberget Fe-Ti type garnet peridotite, Western Gneiss Region, Western Norway, *Terra Nova*, *20*, 295–301, 2008.

Vrijmoed, J. C., Y. Y. Podladchikov, T. B. Andersen, and E. H. Hartz, An alternative model for ultra-high pressure in the Svartberget Fe-Ti garnet-peridotite, Western Gneiss Region, Norway, *European Journal of Mineralogy*, *21*, 1119–1133, 2009b.

Wain, A., New evidence for coesite in eclogite and gneisses: defining an ultrahigh-pressure province in the Western Gneiss region of Norway, *Geology*, *25*, 927–930, 1997.

Wain, A., D. Waters, A. Jephcoat, and H. Olijynk, The high-pressure to ultrahigh-pressure eclogite transition in the Western Gneiss Region, Norway, *European Journal of Mineralogy*, *12*, 667–687, 2000.

Walsh, E. O., and B. R. Hacker, The fate of subducted continental margins: Two-stage exhumation of the high-pressure to ultrahigh-pressure Western Gneiss Region, Norway, *Journal of Metamorphic Geology*, *22*, 671–687, 2004.

Walsh, E. O., B. R. Hacker, P. B. Gans, M. Grove, and G. Gehrels, Protolith ages and exhumation histories of (ultra) high-pressure rocks across the Western Gneiss Region, Norway, *Geological Society of America Bulletin*, *119*, 289–301, 2007.

Warren, C., C. Beaumont, and R. Jamieson, Modelling tectonic styles and ultra-high pressure (UHP) rock exhumation during the transition from oceanic subduction to continental collision, *Earth and Planetary Science Letters*, *267*, 129–145, 2008a.

Warren, C., A. Smye, S. Kelley, and S. Sherlock, Using white mica $^{40}Ar/^{39}Ar$ data as a tracer for fluid flow and permeability under high-P conditions: Tauern Window, Eastern Alps, *Journal of Metamorphic Geology*, *30*, 63–80, 2012a.

Warren, C. J., C. Beaumont, and R. A. Jamieson, Deep subduction and rapid exhumation: role of crustal strength and strain weakening in continental subduction and ultrahigh-pressure rock exhumation, *Tectonics*, *27*, 2008b.

Warren, C. J., D. Grujic, J. M. Cottle, and N. W. Rogers, Constraining cooling histories: rutile and titanite chronology and diffusion modelling in NW Bhutan, *Journal of Metamorphic Geology*, *30*, 2012b.

Warren, C. J., C. Beaumont, and R. A. Jamieson, Formation and exhumation of ultra-high-pressure rocks during continental collision: role of detachment in the subduction channel, *Geochemistry Geophysics Geosystems*, *9*, 2008.

Wetherill, G. W., An interpretation of the Rhodesia and Witwatersrand age patterns, *Geochimica et Cosmochimica Acta*, *9*, 290–292, 1956.

Wheeler, J., S. M. Redddy, and R. A. Cliff, Kinematic linkage between internal zone extension and shortening in more external units in the NW Alps, *Journal of the Geological Society*, *158*, 439–443, 2001.

White, A. P., K. V. Hodges, M. W. Martin, and A. Andresen, Geologic constraints on middle-crustal behavior during broadly synorogenic extension in the central East Greenland Caledonides, *International Journal of Earth Sciences*, *91*, 187–208, 2002.

Whitney, D. L., C. Teyssier, and A. K. Fayon, Isothermal decompression, partial melting and exhumation of deep continental crust, *Geological Society, London, Special Publications*, *227*, 313–326, 2004.

Wilke, F. D., P. J. OBrien, A. Gerdes, M. J. Timmerman, M. Sudo, and M. A. Khan, The multistage exhumation history of the Kaghan Valley UHP series, NW Himalaya, Pakistan from U-Pb and $^{40}Ar/^{39}Ar$ ages, *European Journal of Mineralogy*, *22*, 703–719, 2010.

Willett, S., C. Beaumont, and P. Fullsack, Mechanical model for the tectonics of doubly vergent compressional orogens, *Geology*, *21*, 371–374, 1993.

Worley, B., and R. Powell, High-precision relative thermobarometry: theory and a worked example, *Journal of Metamorphic Geology*, *18*, 91–101, 2000.

Xu, Z., L. Zeng, F. Liu, J. Yang, Z. Zhang, M. McWilliams, and J. Liou, Polyphase subduction and exhumation of the Sulu high-pressure-ultrahigh-pressure metamorphic terrane, *Special Papers-Geological Society of America*, *403*, 93, 2006.

Yamato, P., E. Burov, P. Agard, L. L. Pourhiet, and L. Jolivet, HP-UHP exhumation during slow continental subduction: self-consistent thermodynamically and thermomechanically coupled model with application to the Western Alps, *Earth and Planetary Science Letters*, *271*, 63–74, 2008.

Ye, K., B. Cong, and D. Ye, The possible subduction of continental material to depths greater than 200 km, *Nature*, *407*, 734–736, 2000.

Young, D. J., B. R. Hacker, T. B. Andersen, and F. Corfu, Prograde amphibolite facies to ultrahigh-pressure transition along Nordfjord, western Norway: implications for exhumation tectonics, *Tectonics*, *26*, 2007.

Zhang, J., Occurrences of intergranular coesite in ultrahigh-P rocks from the Sulu region, eastern China: implications for lack of fluid during exhumation, *American Mineralogist*, *81*, 1217–1221, 1996.

Zhang, R., J. Liou, W. Ernst, R. Coleman, N. Sobolev, and V. Shatsky, Metamorphic evolution of diamond-bearing and associated rocks from the Kokchetav Massif, northern Kazakhstan, *Journal of Metamorphic Geology*, *15*, 479–496, 1997.

Zhang, R., J. Liou, and W. Ernst, The Dabie–Sulu continental collision zone: a comprehensive review, *Gondwana Research*, *16*, 1–26, 2009.

Appendix A

Supplementary Material for Chapter 2: End-member Modes of Syn-convergent UHP Rock Exhumation in Simple 2D Orogens: Concepts and Numerical Models

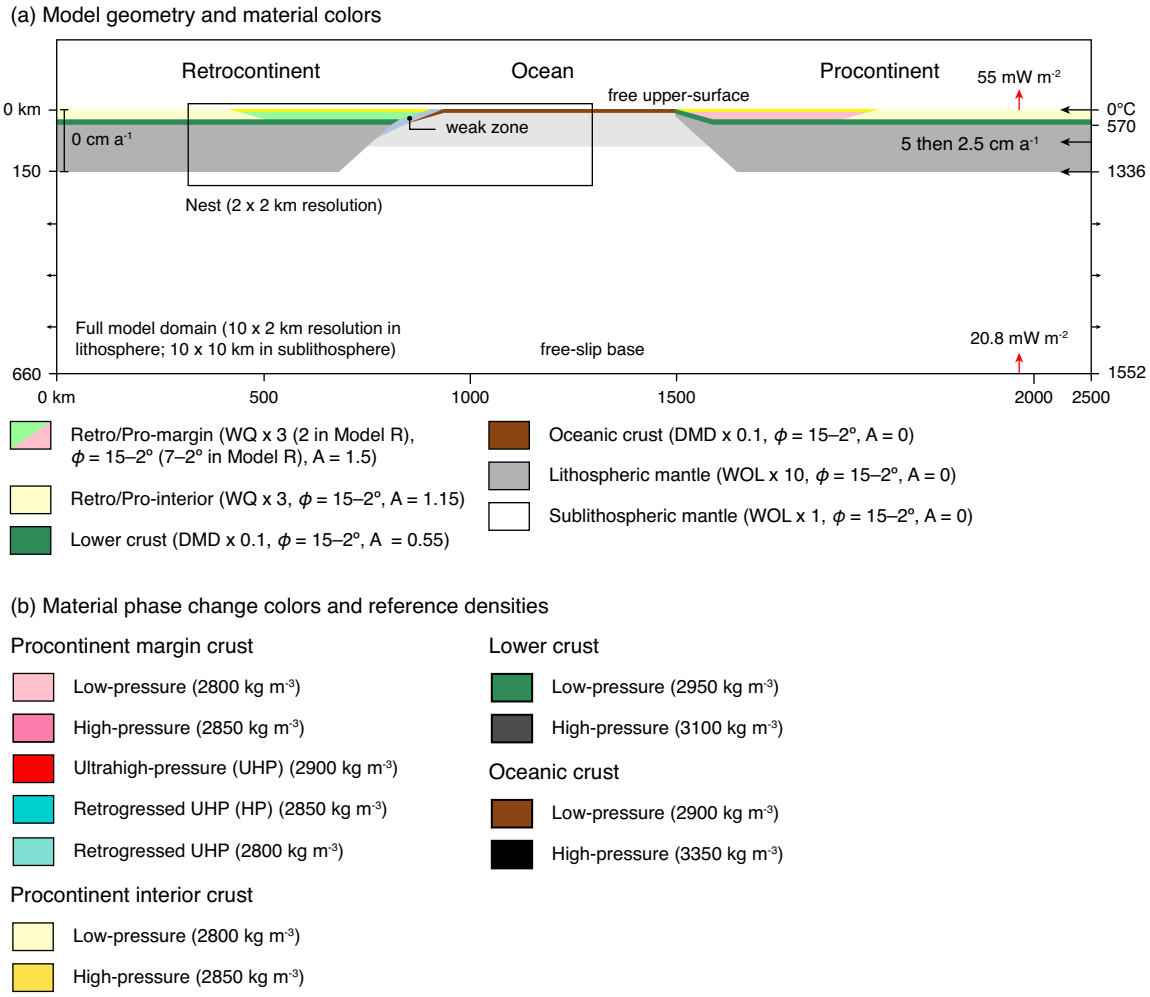

Figure A.1: Detailed model design diagram. (a) Summary description of model geometry, boundary conditions, and selected material properties. Black arrows indicate velocity boundary conditions. Red arrows indicate basal heat flux and calculated surface heat flow within the continental interiors. Calculated Moho, basal lithosphere, and model base temperatures are shown at right. WQ×3, DMD×0.1, WOL×1 and 10 are respectively wet quartzite, dry Maryland diabase and wet olivine flow laws scaled by f; W_s, the viscous strain-weakening factor, is 10 for all crustal materials; ϕ gives range of frictional-plastic strain-softening; A is radioactive heat production (μW m^{-3}), referred to as A_R in text (*Beaumont et al.*, 2009); Retro/Pro-margin values in parentheses refer to properties of retrocontinent margin in Model R. (b) Material phase change colours and corresponding reference densities at reference temperatures given in Table 2.1.

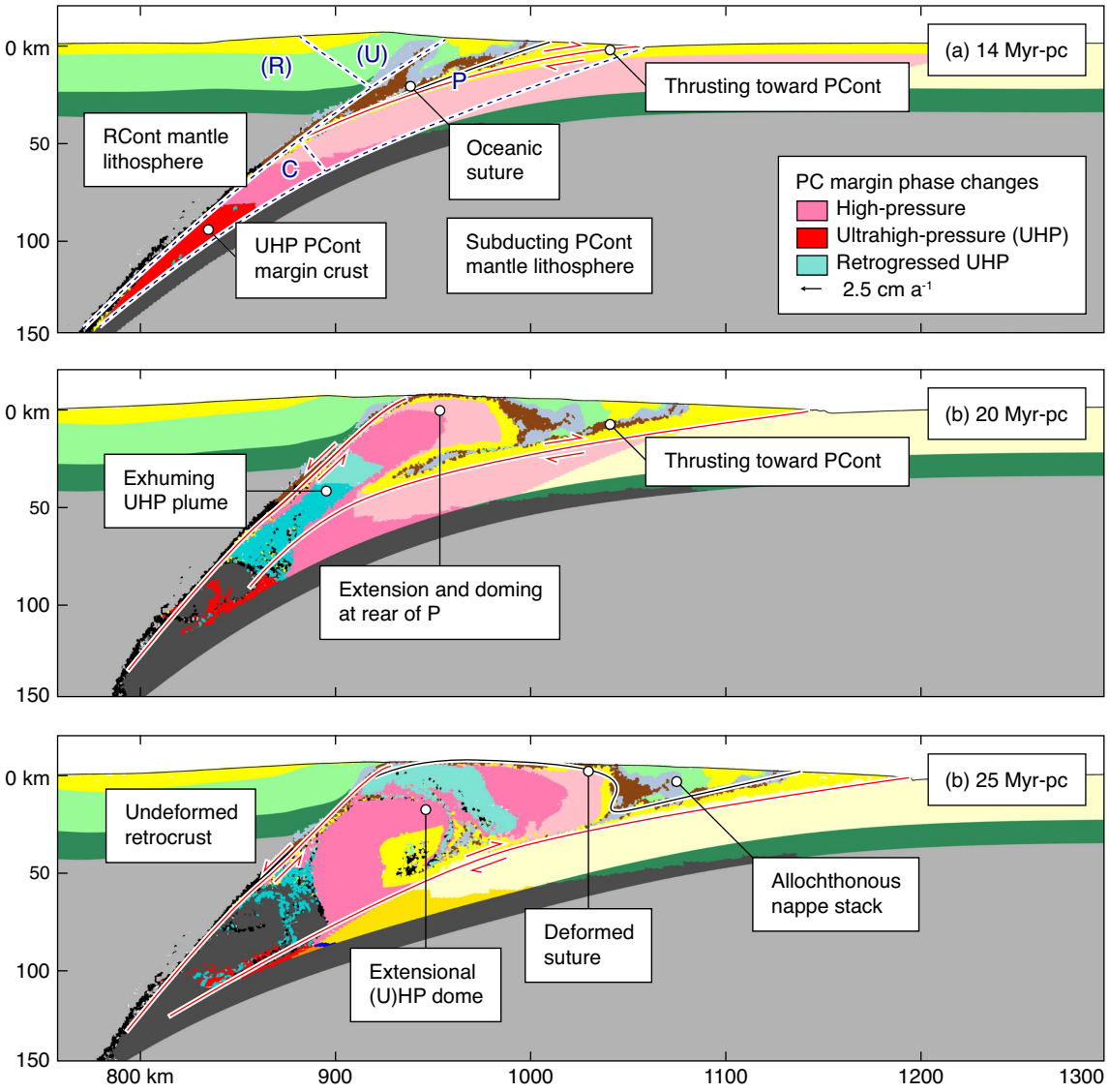

Figure A.2: Annotated Model P results. Blue dashed lines (a) show PURC boundaries. Red lines show shear zones and kinematics. Black lines in (a) and (c) show original and final positions of the oceanic suture zone, respectively. Times (Myr-pc) are time elapsed since collision. PCont=procontinent, RCont=retrocontinent. (a) Subduction of procontinent margin to (U)HP conditions, and shallower accretion of procontinent margin sediment. (b) Buoyant exhumation of (U)HP margin crust from C to P accomplished by coeval normal-sense shearing at the top of the (U)HP plume and thrust-sense shearing at its base. (c) Continued but slower exhumation with the same kinematics as (b) driven by procontinent interior subduction. The end geometry comprises a (U)HP dome at the rear of P and a structurally overlying allochthonous nappe stack toward the foreland. The dislocated part of the suture is attenuated and wrapped around the (U)HP dome, separating it from the overlying nappes, and has undergone considerable transport toward the procontinent.

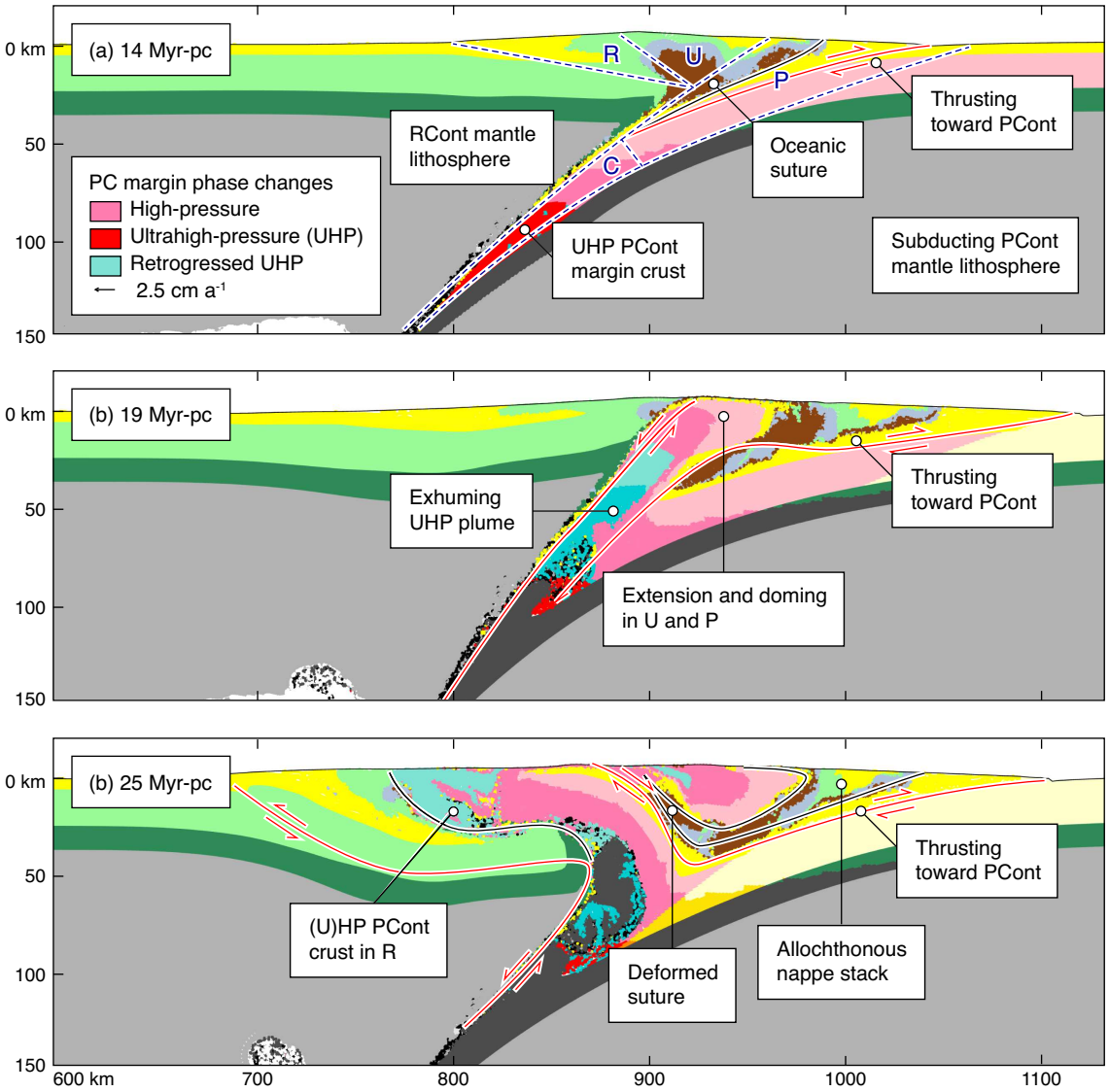

Figure A.3: Annotated Model R results. Features labelled as in Figure A.2. (a) Subduction of procontinent margin material to (U)HP conditions, coupled with accretion of procontinent margin sediment. (b) Buoyant exhumation of (U)HP margin crust begins in the prowedge mode, transporting material from C to P along coeval normal- and thrust-sense shear zones, the former localized at the P/U boundary. (c) Flow of material from P into U leads to retrotransport of the exhumed (U)HP crust within R, accomplished by coeval normal-sense and thrust-sense shearing, similar to models for exhumation in the Greenland Caledonides (*Hartz et al.*, 2001; *White et al.*, 2002). The final geometry consists of a prowedge comprising an allochthonous nappe stack, an uplifted and extended plug, and a retrowedge containing procontinent (U)HP crust overlying normal retrocontinent crust. The dislocated suture is highly attenuated, having been transported both toward P (at the base of the allochthonous nappe stack), and subsequently toward R, where its original tectonostratigraphic position is marked by the contact between the (U)HP procontinent crust and the underlying retrocontinent crust.

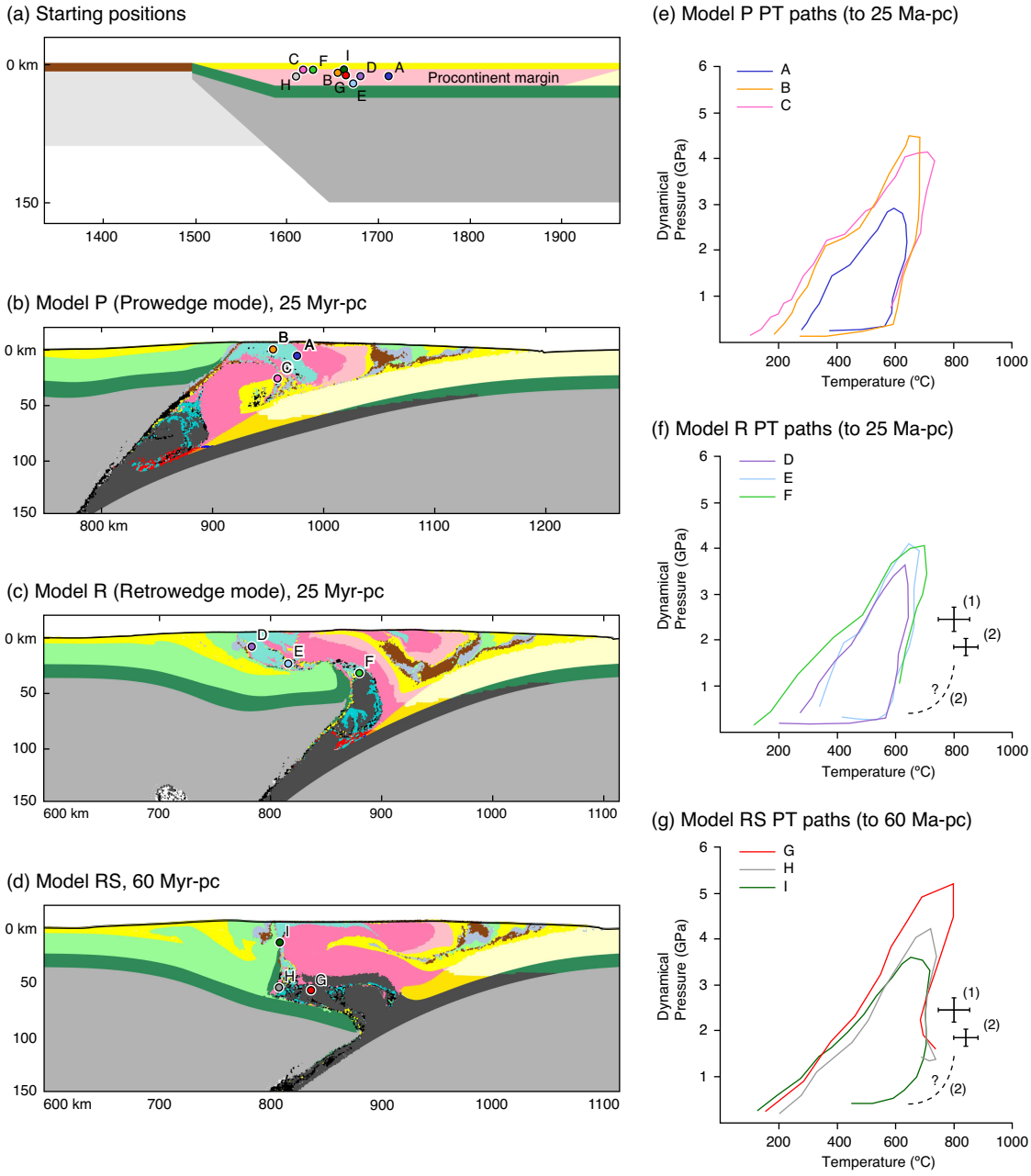

Figure A.4: Representative (P–T) paths. Model RS is like Model R but with a reduced convergence velocity of 1 cm a^{-1}. (a) Starting positions of particles. (b–d) Models P, R, and RS showing final positions of tracked particles at times indicated. (e–g) P–T plots of tracked particles from models P, R, and RS respectively. Black crosses in (f) and (g) show P–T evolution of the Liverpool Land Eclogite Terrane (LLET) from (1) *Hartz et al.* (2005) and (2) (*Buchanan*, 2008). Errors of 0.5 GPa and 50°C were assumed where not provided (e.g., *Hartz et al.*, 2005). Particles from Model RS reach temperatures similar to those estimated for the LLET. The higher temperatures achieved by the LLET may be related to slower convergence, resulting in longer residence at middle/crustal conditions, or higher values of continental margin heat production (e.g., *Warren et al.*, 2008). Model RS is hotter than Model R and may correspond more closely to the Caledonides.

Appendix B

Supplementary Material for Chapter 3: The Alps 1: a Working Geodynamic Model for Burial and Exhumation of (Ultra)high-pressure Rocks in Alpine-Type Orogens

B.1 Modeling Methods

B.1.1 Overview of SOPALE NESTED *Code*

We use two-dimensional thermal-mechanical models computed using the software SOPALE-NESTED (*Fullsack*, 1995; *Beaumont et al.*, 2009) to investigate the dynamics of Alpine-type orogens at the upper-mantle-scale. The models are designed based on data from the Western Alps, but the methodology remains similar to our recent work (*Beaumont et al.*, 2009; *Butler et al.*, 2011) (Described in Chapter 2).

The models are computed by solving the equations for incompressible creeping (Stokes) flows (Eqs. B.1 and B.2) and energy balance (Eq. B.3) subject to mechanical and thermal boundary conditions:

$$\frac{\partial \sigma_{ij}}{\partial x_i} - \frac{\partial P}{\partial x_j} + \rho g_i = 0 \quad i,j = 1,2 \tag{B.1}$$

$$\frac{\partial v_i}{\partial x_i} = 0 \quad i = 1, 2 \tag{B.2}$$

$$\rho c_p \left(\frac{\partial T}{\partial t} + v_i \frac{\partial T}{\partial x_i} \right) = K \frac{\partial}{\partial x_i} \frac{\partial T}{\partial x_i} + A + A_{SH} + v_2 \alpha g T \rho \quad i = 1, 2 \tag{B.3}$$

where σ_{ij} is the deviatoric stress tensor, x_i spatial coordinates, P pressure (mean stress), ρ density, g_i gravitational acceleration, v_i a component of velocity, c_p specific heat, T temperature, t time, K thermal conductivity, A_R (crustal) radiogenic heat production per unit volume, A_{SH} shear heating, and α volumetric thermal expansion. Coupling of the mechanical and thermal solutions is achieved through the advection of radioactive crust, shear heating, thermal activation of viscous flow, and buoyancy forces arising from metamorphic phase changes and thermal expansion.

The models use a sub-grid approach in which a higher-resolution computational domain is 'nested' within a larger, lower-resolution domain. The velocity and thermal solution is first obtained for the full 2000×660 km domain (10×2 km resolution domain). This solution is then interpolated onto the boundaries of the (1×1 km resolution) nested domain encompassing the vicinity of the subduction zone (from 900 to 1560 km, and from 0 to 150 km deep). Coupling of the grids is maintained by using a single cloud of Lagrangian particles, which is passed between the two solutions, with the particles within the nested domain always obeying the higher resolution solution.

B.1.2 Model Design

The models presented here result from a set experiments designed to explore the sensitivity of a 'reference' model (Model R) that reproduces the main tectonic aspects of the Western Alps (Fig. 3.3). The parameter values (Table 3.1) therefore comprise a 'tuned' set, based on numerous sensitivity experiments. Certain aspects of the reference model, namely the viscous strength and magnitude of strain-weakening of the subducted crust, were chosen to maximize the potential for the formation and exhumation of (U)HP crust, based on the results of previous studies (e.g., *Warren et al.*, 2008a). Variations on these parameters in the presented models are discussed below.

The starting geometry of the models (Fig. 3.3a) corresponds to Mesozoic to Cenozoic reconstructions of the Alpine system (*Stampfli et al.*, 1998; *Rosenbaum and Lister*, 2005; *Handy et al.*, 2010) and comprises a retrocontinent (Adria) with a pre-existing orogenic wedge (Austroalpine), an oceanic plate (Piemont-Liguria; ∼500 km wide), and a procontinent (Eurasia) comprising a microcontinent (Brianonnais; ∼175 km wide), a rift basin (Valais 'Ocean'; ∼75 km wide) and a continental (European) margin. The position of the Austroalpine wedge corresponds to the 67 Ma reconstruction of *Handy et al.* (2010) and assumes that some Austroalpine material has already undergone Late Cretaceous (U)HP metamorphism and exhumation (*Rubatto et al.*, 2011).

B.1.3 Material Properties

Model materials deform by either frictional-plastic (brittle) or viscous (ductile) flow that includes additional strain-softening/strain-weakening mechanisms. Brittle deformation is modeled using the frictional-plastic Drucker-Prager yield criterion, σ_y:

$$\sigma_y = (J_2')^{1/2} = P\sin\phi_{\text{eff}} + C\cos\phi_{\text{eff}} \tag{B.4}$$

where J_2' is the second invariant of the deviatoric stress, P the dynamical pressure (mean stress), and C the cohesion. The effective angle of internal friction, ϕ_{eff}, is defined to include the effects of pore fluid pressures through the approximate relation:

$$P sin\phi_{\text{eff}} = (P - P_f) sin\phi \tag{B.5}$$

where $\phi = 30°$ is the angle of internal of friction for dry conditions ($P_f = 0$). ϕ_{eff} is therefore an apparent angle of internal friction of the material owing to pore fluid pressure and/or strain softening (see below). Ductile deformation is modeled as incompressible power-law flow, for which the effective viscosity is:

$$\eta^v_{\text{eff}} = \frac{f}{W_s} A^{-1/n} \dot{I}_2'^{(1-n)/2n} exp\left(\frac{Q + PV^*}{nRT_K}\right) \tag{B.6}$$

where f is a viscosity scaling factor, W_s a strain-weakening factor, A the pre-exponential factor, converted to the tensor invariant form, $\dot{I}_2'$ the second invariant of the deviatoric strain rate, n the stress exponent, Q activation energy, P pressure,

V^* the activation volume for power-law creep, T_K absolute temperature, and R the universal gas constant. For simplicity, we base the model materials on a small set of laboratory-determined flow laws.

Crustal materials and the lithospheric mantle soften/weaken in the frictional-plastic and viscous regimes, respectively. Frictional-plastic materials strain-soften through a linear decrease in their effective angle of internal friction, ϕ_{eff}, with accumulated strain: $\phi_{\text{eff}} = \phi_{\text{eff}}(\epsilon)$. $\epsilon = I_2'^{1/2}$, the square root of the second invariant of deviatoric strain, with ϵ (strain) used for simplicity. Viscous strain-weakening occurs through a linear decrease in effective viscosity by the factor W_s over a specified ϵ range. For the reference model, crustal materials weaken by $W_s = 20$ over the range $\epsilon = 5$–10. Strain-weakening (and softening) as implemented in our models depends on the resolution of the computational grid (1×1 in the nested region). Given that natural shear zones form at finer scales, equivalent natural strain-weakening/softening occurs at smaller offsets across shear zones because the shear zones are narrower than the typical 3 km in these models. It follows that the models weaken/soften more slowly than ones would with higher resolution. By implication, high resolution models will give equivalent results with proportionally larger values of the minimum ϕ_{eff}, and smaller values of W_s. The values used here should therefore be interpreted as minimum and maximum values, respectively.

Each crustal unit comprises an upper/middle crust with ϕ_{eff} (hereafter simply ϕ) = 15–4° (except where noted; Fig. 3.3), and a scaled wet quartzite (WQ) flow law (Gleason and Tullis, 1995), overlying a lower crust with ϕ = 15–4° (where $\phi = 4°$ is fully strain-softened) and a dry Maryland diabase (DMD $\times$ 0.05) flow law, scaled to somewhat weaker than intermediate granulite (*Mackwell et al.*, 1998) (Table 3.1). The accretionary wedge comprises only upper/middle crust (ϕ = 15–4°; WQ $\times$ 2). The procontinent and retrocontinent margins comprise 20 km of upper/middle crust with WQ $\times$ 0.5 and WQ $\times$ 5 upper crust, respectively including a 4 km sediment layer (ϕ = 4–4°; WQ $\times$ 0.25), overlying 12 km of lower crust. These thicknesses are consistent with cross-sections through the Western Alps (*Schmid and Kissling*, 2000). The microcontinent comprises 12 km of upper crust (WQ $\times$ 3), including 4 km of sediment, overlying 10 km of lower crust. The rift basin comprises an upper 4 km of sediment overlying 4 km of lower crust, while the oceanic plate comprises

6 km of oceanic crust (ϕ = 15–4°; DMD × 0.1) overlain by 2 km of sediment. The underlying lithospheric mantle extends to 120 km beneath the continents and to 90 km beneath the oceanic plate, has ϕ = 15–4° and a wet olivine flow law (WOL×10; *Karato and Wu*, 1993) scaled to represent a depleted/dehydrated lithosphere, and overlies sublithospheric mantle (WOL × 1) that extends to 660 km.

The continents have crustal radiogenic heat production (A_R) for the upper and lower continental crust of 2.0 and 1.0 μWm^{-3}, respectively. Coupled with the thermal boundary conditions, the resulting surface heat flow on the continents at full crustal thickness is 73 mWm^{-2}, consistent with the high-end of measurements from non-cratonic Phanerozoic continental lithosphere (*Vitorello and Pollack*, 1980), and surface heat flow measurements (65–75 mWm^{-2}) for the Hercynian crust entering the foreland of the Western Alps (*Artyushkov and Baer*, 1983; *De Voogd et al.*, 1988). The Moho temperature beneath the procontinent margin is ∼590°C, consistent with estimates of 530°C–620°C (*Bousquet et al.*, 1997).

B.1.4 Density, Volume and Mass conservation During Phase Transitions

Crustal materials undergo pressure- and temperature-dependent density changes corresponding to the eclogite and coesite-eclogite phase transitions following *Warren et al.* (2008a) (Table 3.1), and reverse during exhumation. During these phase changes the incompressibility equation is modified to that of mass conservation: $\partial\rho/\partial t = -\partial\rho v_i/\partial x_i$. This accounts for the associated volume change and its effect on the buoyancy and velocity field. This volume change is calculated numerically by applying additional normal, compressive/dilative forces to finite elements at the time they are subjected to phase-related density changes. The value of the excess pressure is $\Delta P = \Delta\rho/\beta_v\rho$, where β_v is the viscous bulk modulus of the material, and $\Delta\rho/\rho$ is the fractional change in density corresponding to the phase change. The excess pressure compresses material locally and only during the model time steps when the phase changes occur, thereby ensuring mass conservation. The compression is applied during one extra nonlinear timestep of the mechanical finite element solution, added after a converged solution has been obtained. The fractional volume change accompanying a phase change is small in these models and its effect on the velocity field is minor because it only applies at the time of the phase change. However,

failure to ensure mass conservation has a long-term effect on the model because the buoyancy forces will be over- or underestimated by the fractional error in the material volume.

B.1.5 Boundary Conditions

The model domain has a stress-free upper surface, and no-slip and free-slip sides and base, respectively. Thermal boundary conditions include a basal heat flux of 20.8 mW m^{-2}, a 0°C surface, and insulated side boundaries (Fig. 3).

Subduction initiates dynamically along a small slice of oceanic crust embedded in the lithosphere at the boundary between the oceanic and retrocontinent. Convergence is imposed by a velocity boundary condition (V_r) prescribed within the retrocontinent lithosphere along the right side of the model, while the procontinent and sublithospheric mantle remain stationary, consistent with the absolute motion of Adria with respect to stationary Europe. Advection of material through the model is modified so that the Eulerian reference frame and computational grid track the Adriatic plate, the result being that despite relative advance of the retrocontinent, the subduction zone remains at a constant distance from the model boundaries. This method allows modeling of the absolute motion of Adria with respect to Europe while avoiding problems from migration of the slab toward the model boundaries. Oceanic subduction is driven by V_r = 1.5 cm a^{-1}, which reduces to 1 cm a^{-1} at collision, defined as when the tip of the microcontinent contacts the accretionary wedge. Elapsed time is expressed as Myr post-collision (Myr-pc). For simplicity, and to be consistent with our generic Alpine-type approach, the convergence rate remains constant during collision. However, we acknowledge that the convergence rate in the Alps varied (*Dewey et al.*, 1989; *Handy et al.*, 2010).

B.1.6 Surface Processes

The models include slope-dependent surface erosion above sea-level (0 km), defined by a maximum erosion rate (E_s) that operates on a slope of 45°, and is scaled down linearly to the local slope of the surface defined by the finite element grid. In all models, E_s = 1.5 cm a^{-1} resulting in typical erosion rates of ∼0.2–1.8 mm a^{-1}.

B.2 Supplemental Figures for Chapter 3

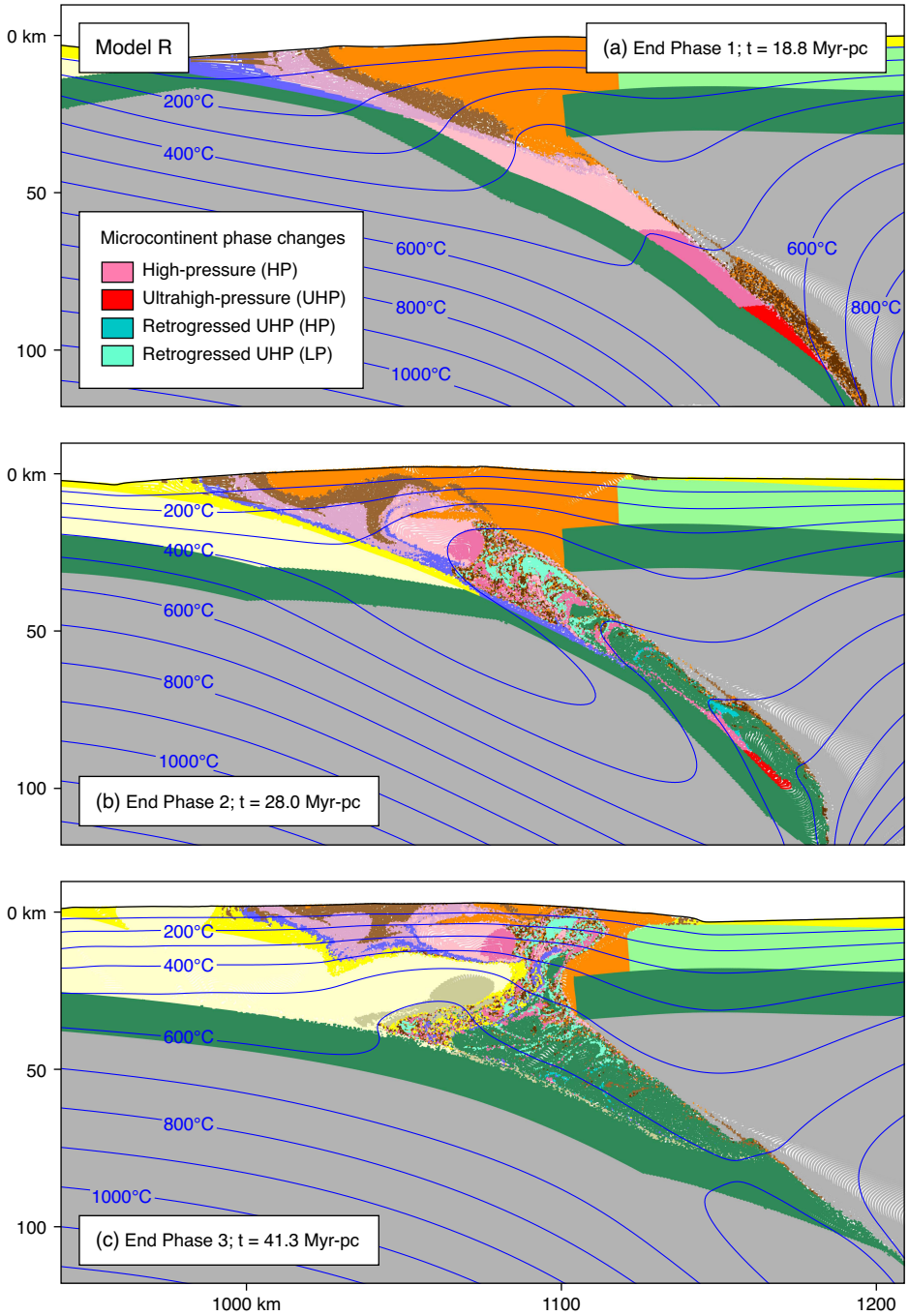

Figure B.1: Results of Model R (microcontinent $f = 3$, $W_s = 20$). Material colours and isotherms (blue lines) for model times corresponding to the end of each phase. The amount of microcontinent crust subducted to UHP conditions is similar to that in Model S, but the plume undergoes greater internal deformation during subsequent exhumation (Fig. B.2).

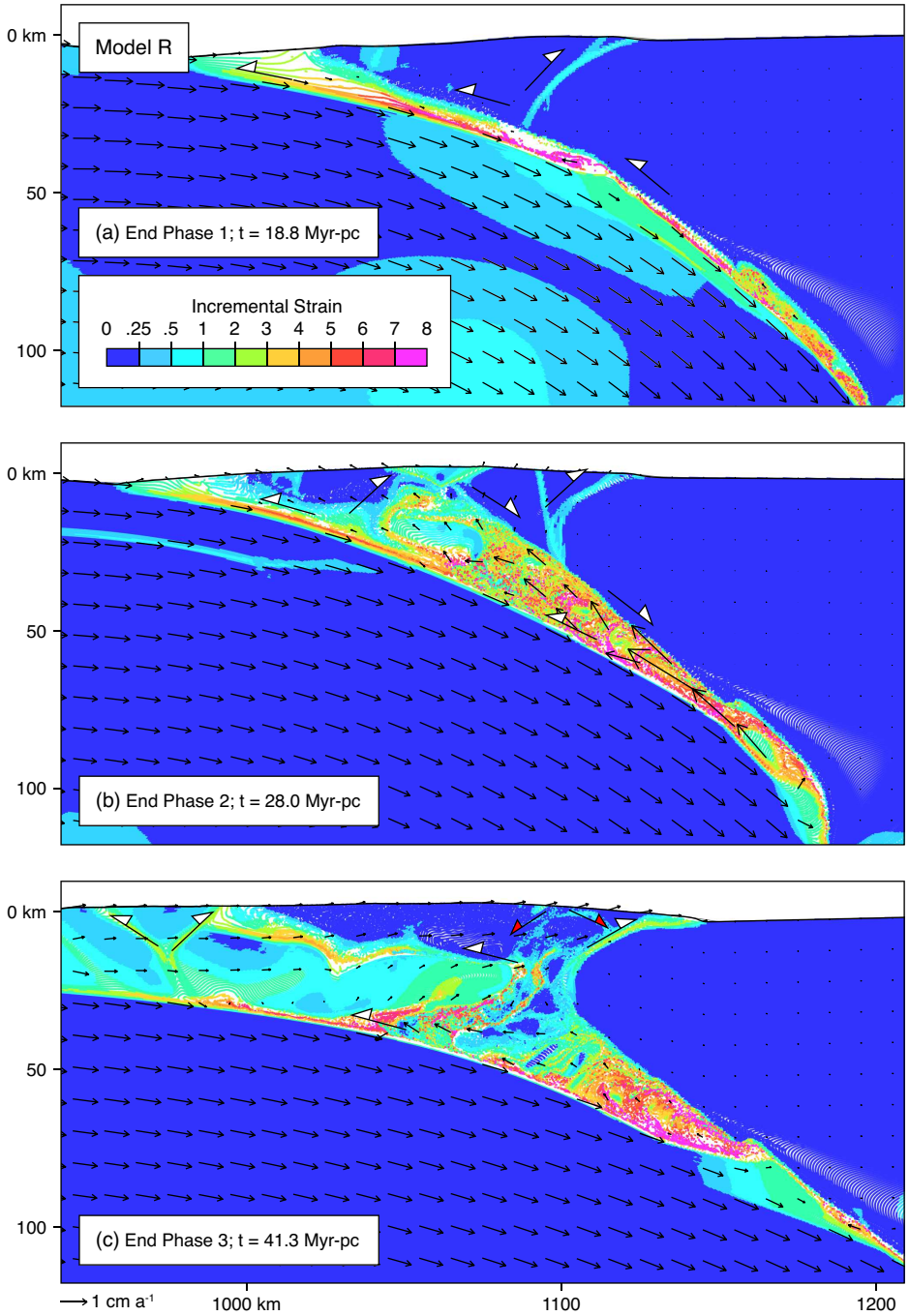

Figure B.2: Incremental strain plots for Model R. Colours show strain (square root of second invariant) accumulated during each phase, overlain by velocity vectors (shown in stationary retrolithosphere reference frame) for the actual time shown in (a–c). White-filled arrows show interpreted kinematics of deformation along dominant shear zones. Red-filled arrows (c) show kinematics of transient normal-sense shear zones flanking the model ICM prior to retrotransport during Phase 3.

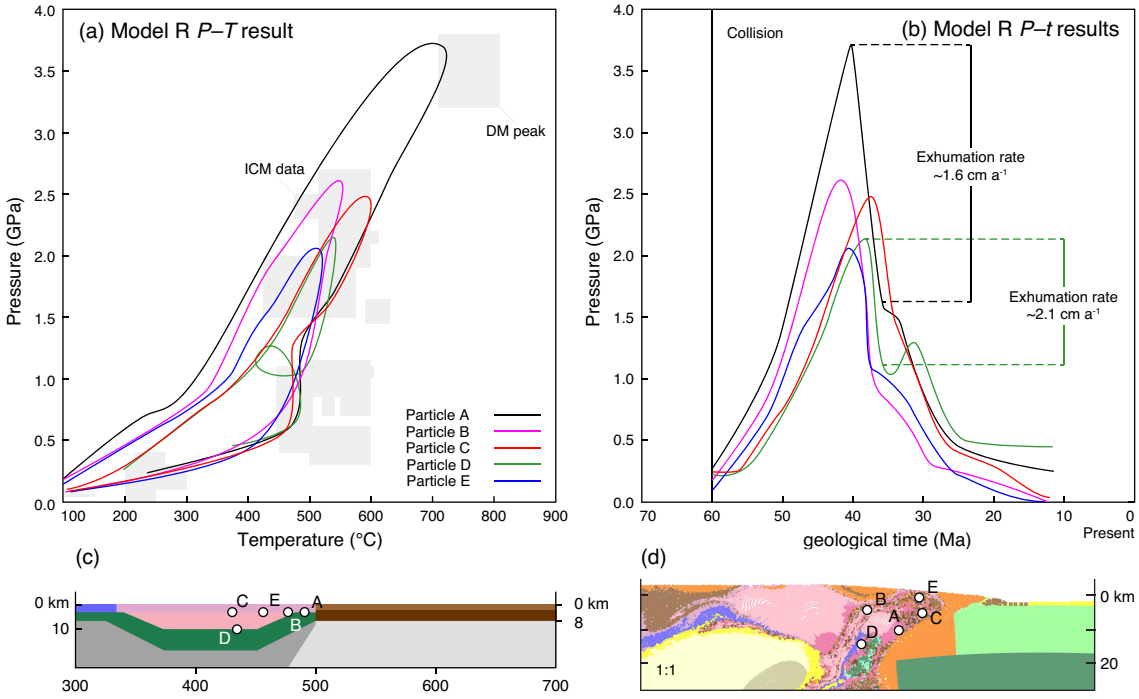

Figure B.3: (a) Selected P–T particle paths from Model R. Lines show model P–T paths, with grey boxes showing positions of published P–T estimates; DM peak=Dora Maira peak conditions (ICM data refers to grey boxes representing peak conditions estimated for the three ICMs). (b) P–t data for Model R particles shown in (a). References for Alps P–T data are shown in Figure 3.8. Exhumation rates for particles in Model R reach up to ∼2 cm a^{-1}.

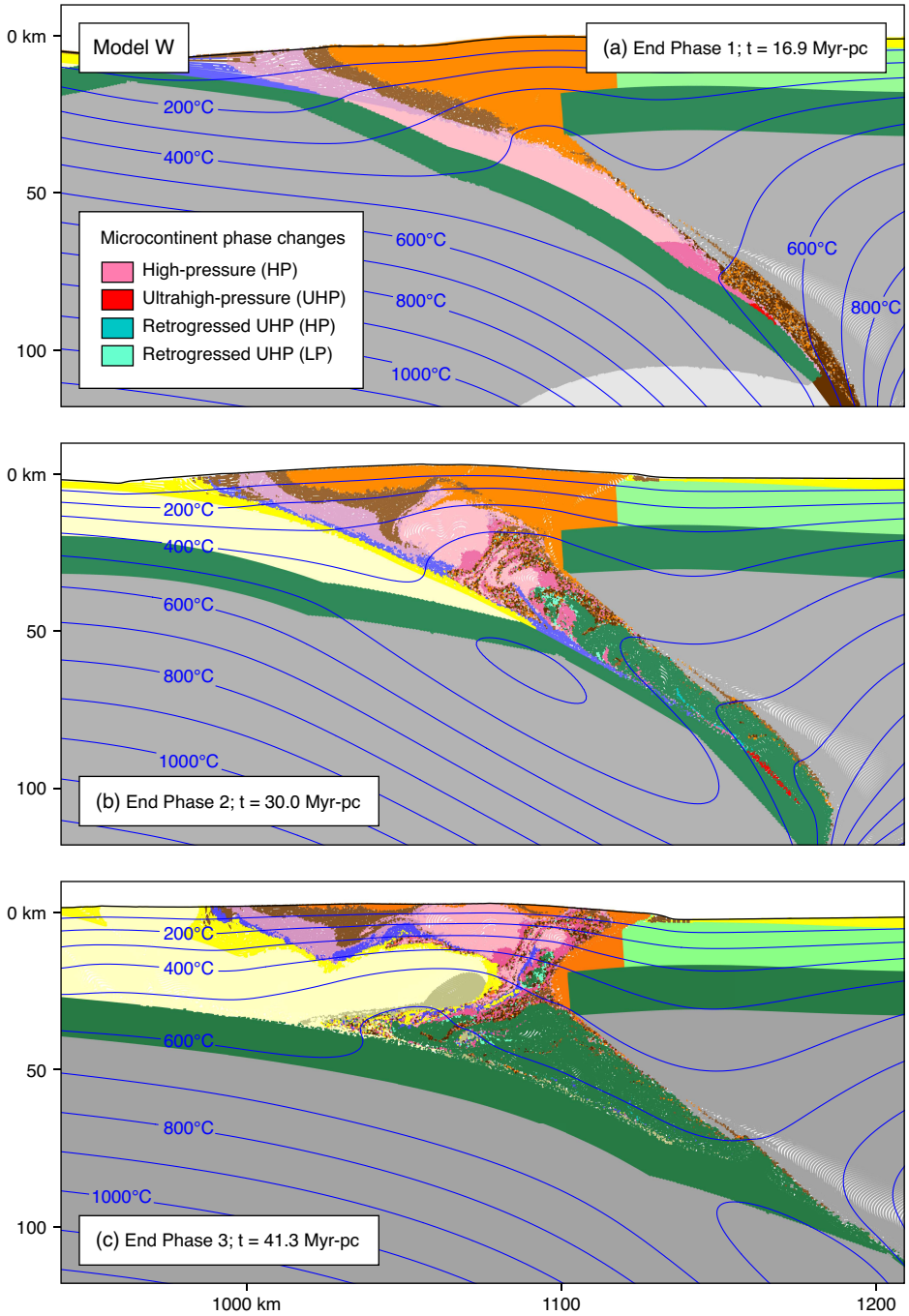

Figure B.4: Results of Model W (microcontinent $f = 1$, $W_s = 10$). Material colours and isotherms (blue lines) for model times corresponding to the end of each phase. Earlier detachment of the microcontinent crust results in a predominantly HP model ICM with substantially less UHP material when compared with Model S, although a small amount of UHP crust is exhumed to the middle crust.

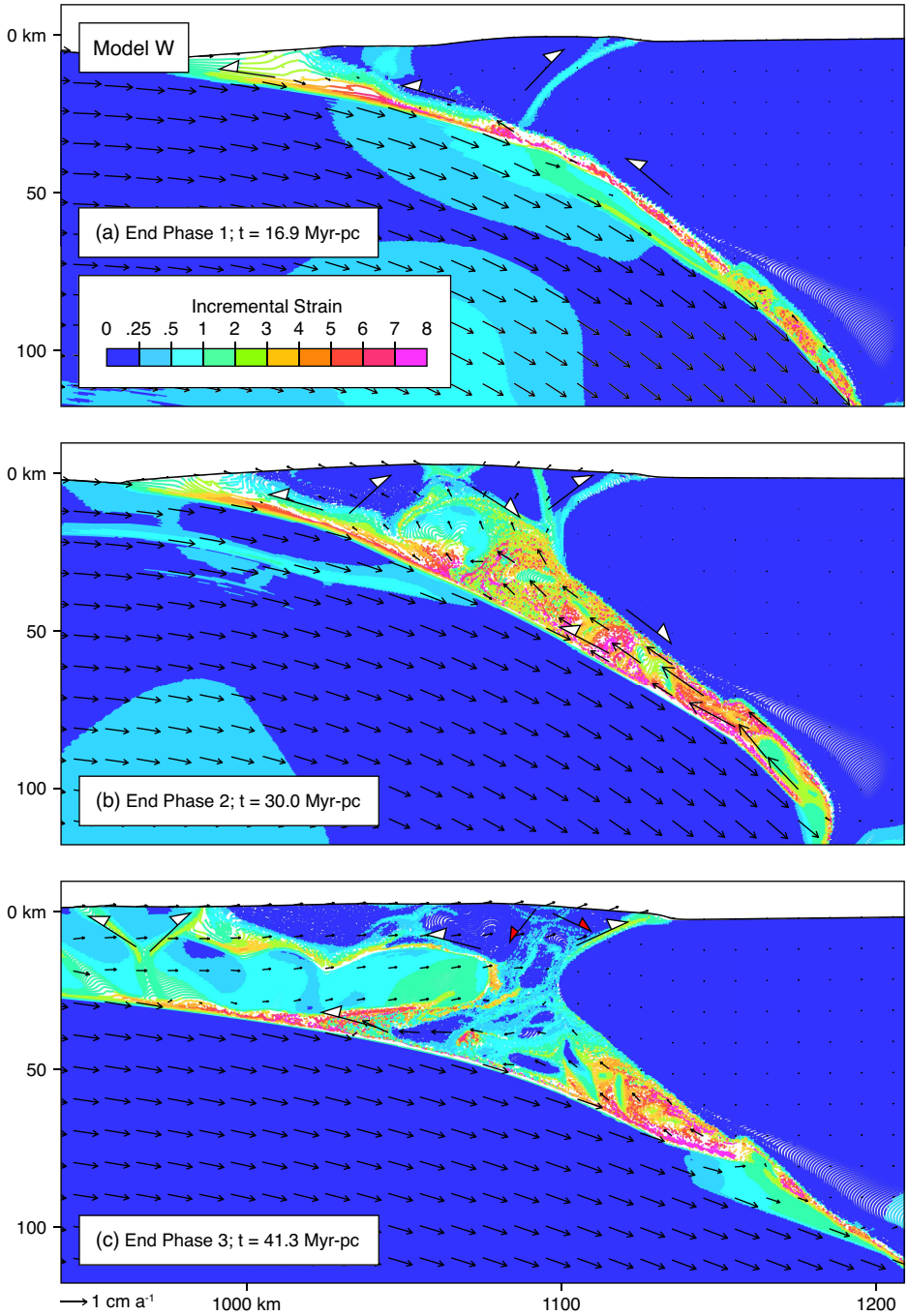

Figure B.5: Incremental strain plots for Model W. Colours show strain (square root of second invariant) accumulated during each phase, overlain by velocity vectors (shown in stationary retrolithosphere reference frame) for the actual time shown in (a–c). White-filled arrows show interpreted kinematics of deformation along dominant shear zones. Red-filled arrows (c) show kinematics of transient normal-sense shear zones flanking the model ICM prior to retrotransport during Phase 3.

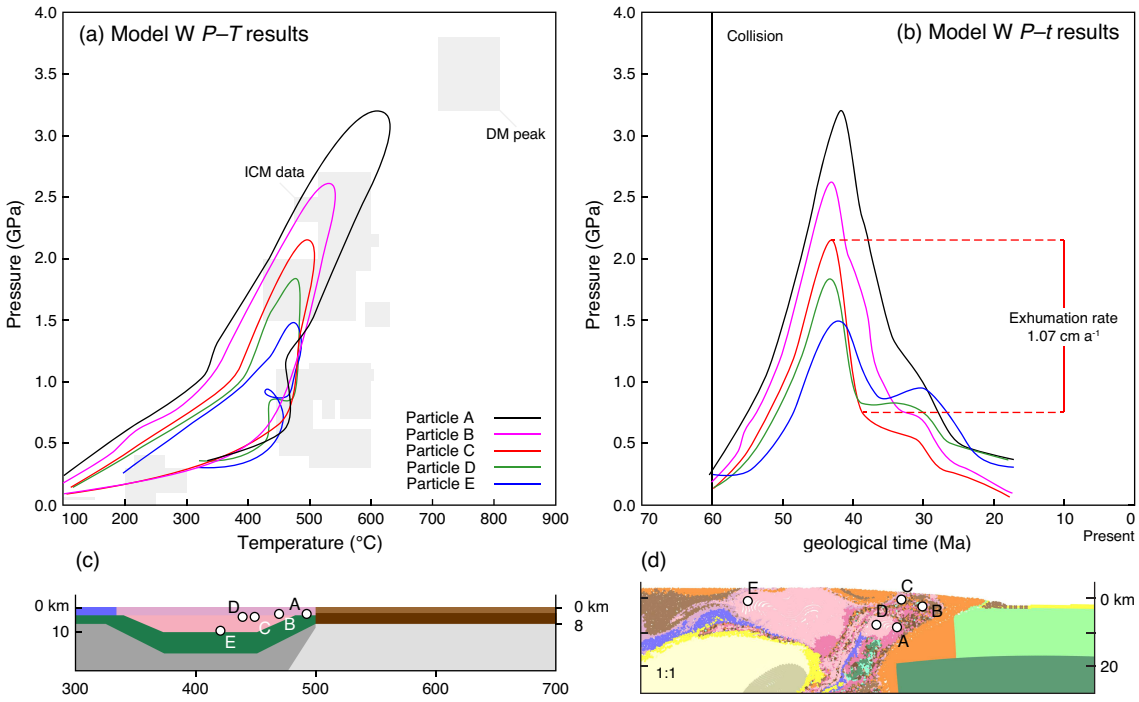

Figure B.6: (a) Selected P–T particle paths from Model W. Lines show model P–T paths, with grey boxes showing positions of published P–T estimates from; DM peak=Dora Maira peak conditions (ICM data refers to grey boxes representing peak conditions estimated for the three ICMs). (b) P–t data for Model W particles shown in (a). References for Alps P–T data are shown in Figure 3.8. Exhumation rates for particles in Model W reach up to ∼1 cm a^{-1}.

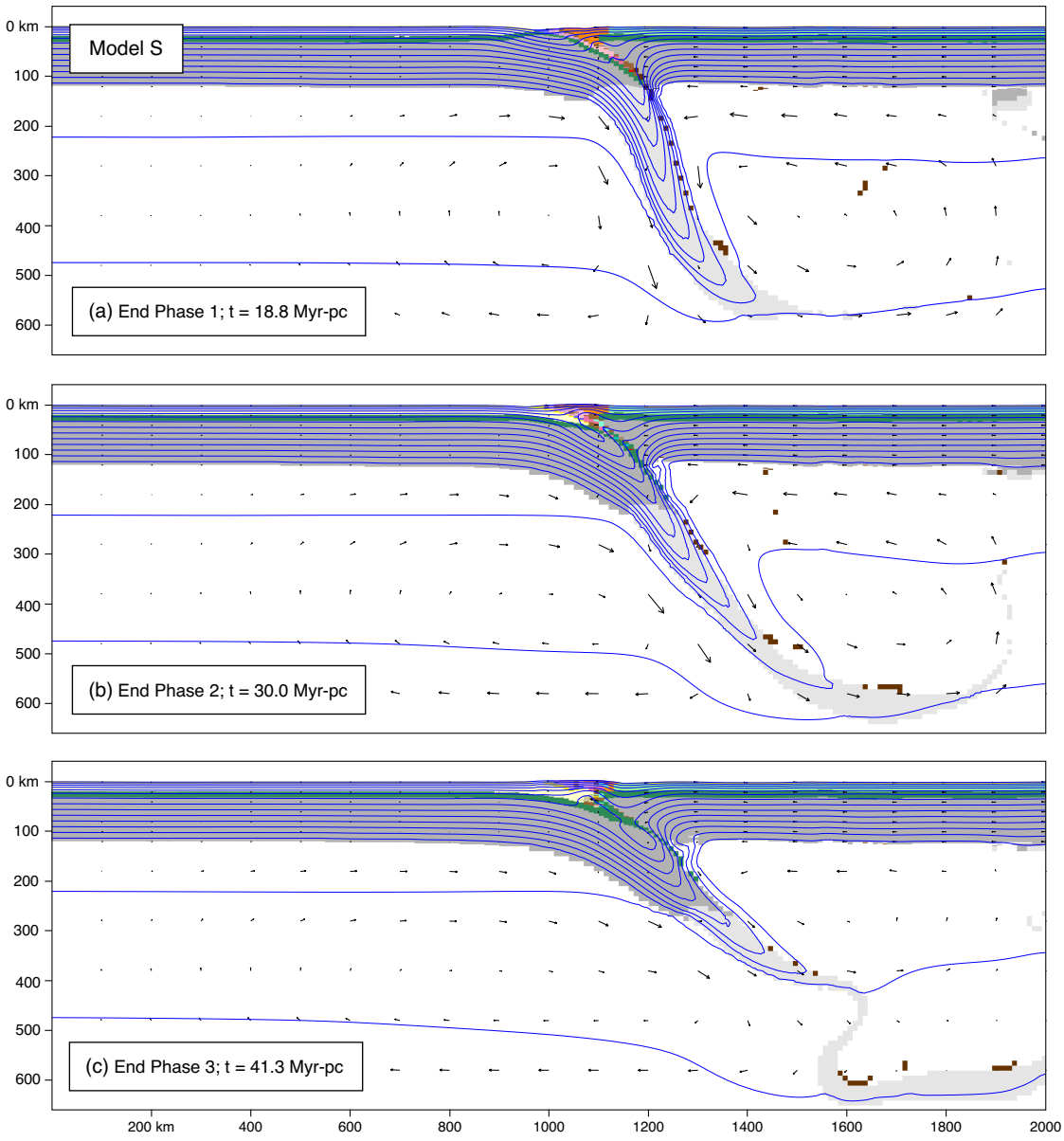

Figure B.7: Model S results showing full model domain. Key frames from Model S showing full 2000 × 660 km model domain. Frames were chosen to illustrate the effect of necking and breakoff of the subducting slab on the model evolution, at times corresponding to the end of the three phases. Velocities are shown in the stationary procontinent reference frame. Necking of the subducted slab commences by the end of Phase 2 (U)HP exhumation at 30 Myr-pc, but final breakoff does not occur until the end of the model run, at ∼41 Myr-pc.

Appendix C

Supplementary Material for Chapter 4: The Alps 2: Variations on the Basic Model with Comments on the Evolution of the Central and Eastern Alps

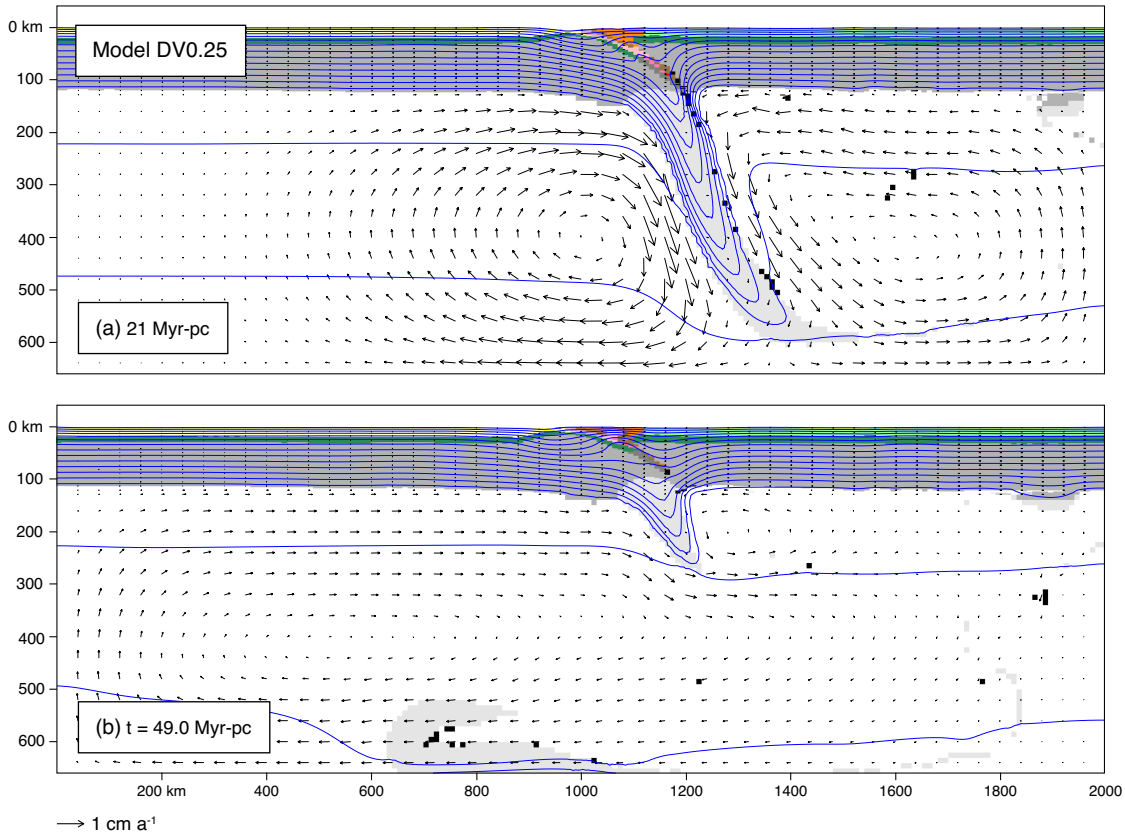

Figure C.1: Model DV0.25 results showing full model domain. Key frames from Model DV0.25 showing full 2000 × 660 km model domain. Frames were chosen to illustrate the effect of necking and breakoff of the subducting slab following the onset of divergent boundary conditions.

Appendix D

Supplementary Material for Chapter 5: Discovery of Coesite-Eclogite from the Nordøyane UHP Domain, Western Gneiss Region, Norway: Field Relations, Metamorphic History, and Tectonic Significance

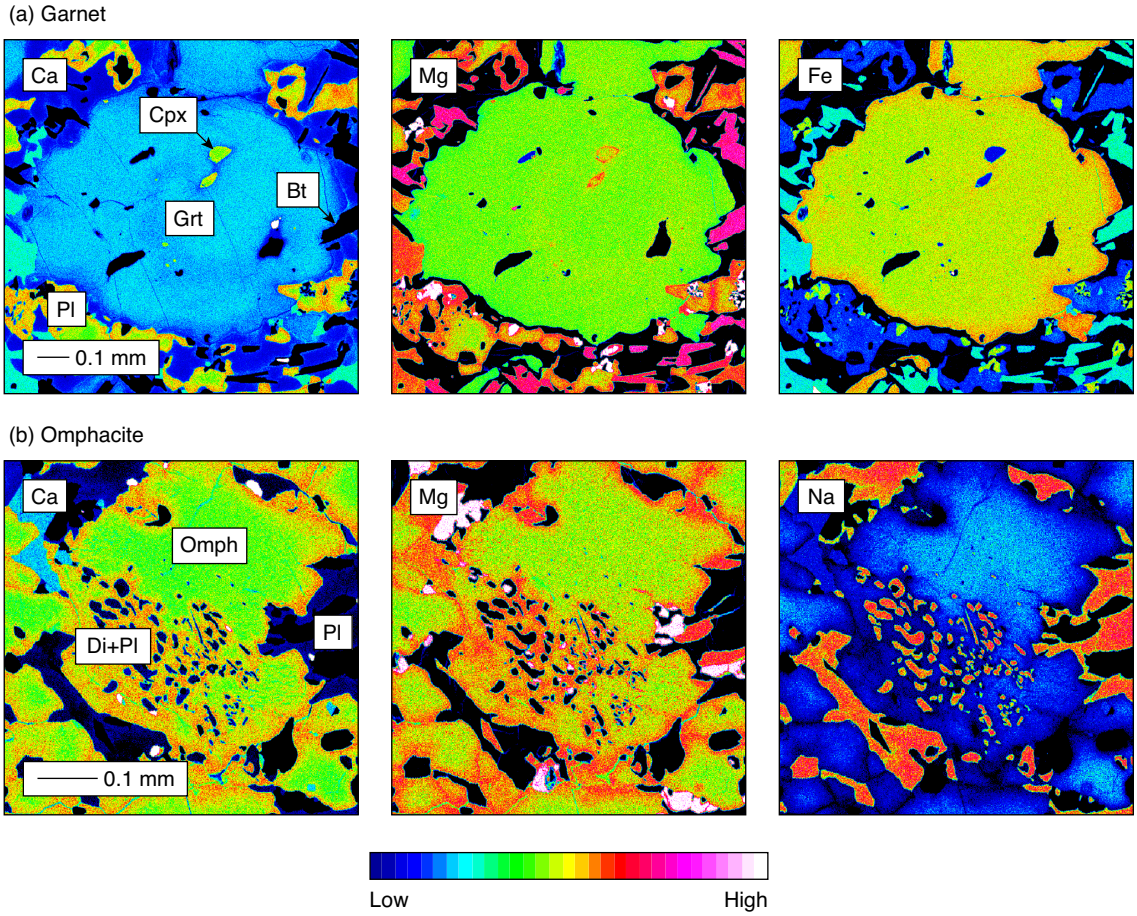

Figure D.1: (a) Representative compositional zoning of Ca, Mg, and Fe in garnet. Colours correspond to increasing X-Ray intensity of the mapped element. The garnets exhibit relatively flat cores with high Ca and Mg, followed by thin rims with increased Fe and Mn (not shown). (b) Representative compositional zoning of Na, Ca, and Mg in matrix clinopyroxene. The clinopyroxenes exhibit zoning from omphacite (Na-rich) cores to diopside rims, and locally to diopside + plagioclase symplectite. Note the abrupt zoning in the adjacent plagioclase.

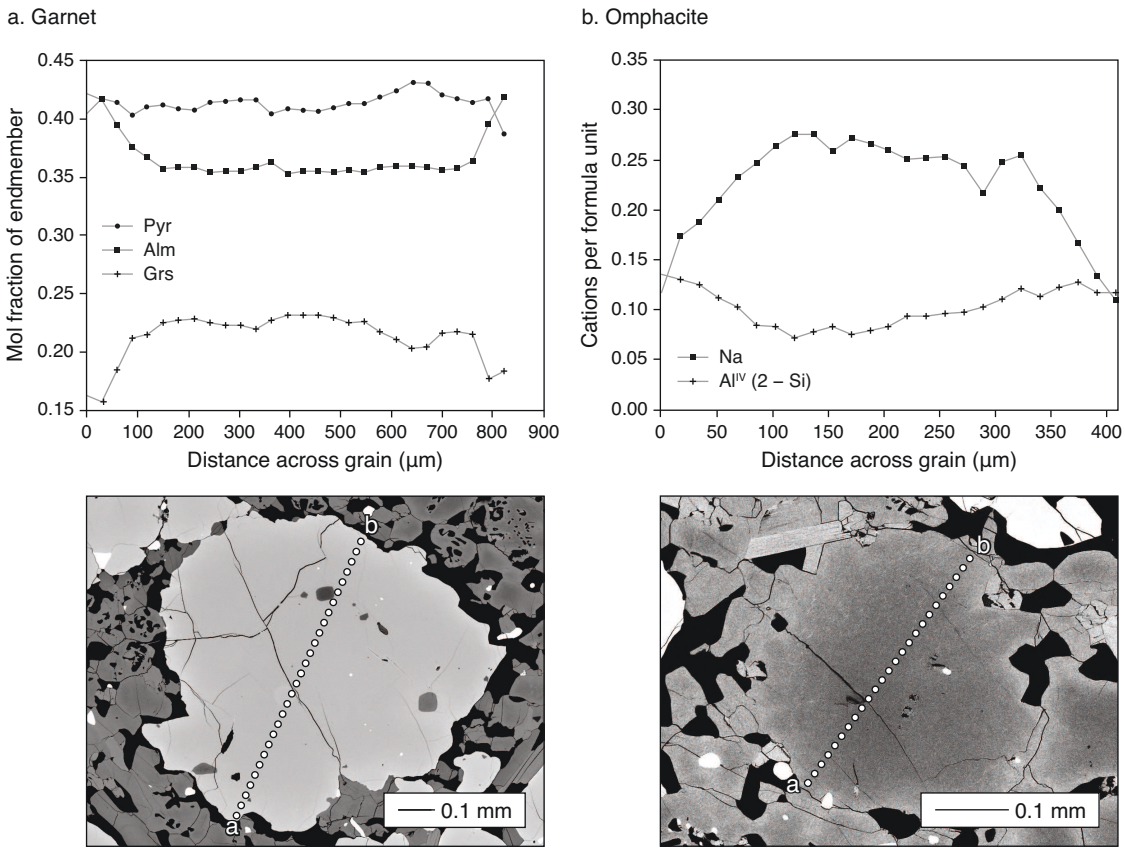

Figure D.2: Zoning profiles for garnet and omphacite. (a) Representative zoning profile of garnet showing Ca-rich cores followed by thin rims in which Fe and Mn (omitted for clarity) increase at the expense of Ca and Mg. (b) Representative zoning profile of matrix clinopyroxene showing decreasing Na from omphacite core to low-Na (diopside) rim, accompanied by a minor increase in Al^{IV}.

Mineral	Grt									
No.	24	129	1044	1077	1093	1111	1140	9	12	102
Setting	c	c	c	c	c	c	c	c	c	c
P–T?						M1				
SiO_2	39.83	39.46	39.12	39.38	39.71	39.67	39.78	39.84	39.88	39.85
TiO_2	0.02	0.02	0.00	0.00	0.00	0.00	0.03	0.04	0.01	0.00
Al_2O_3	22.00	21.75	21.97	22.11	22.02	22.30	22.07	21.95	22.09	22.38
Cr_2O_3	0.03	0.04	0.02	0.03	0.04	0.01	0.00	0.00	0.01	0.00
FeO	17.70	17.56	17.80	17.44	17.23	16.83	17.27	17.90	18.19	17.35
MnO	0.38	0.39	0.37	0.35	0.35	0.28	0.32	0.37	0.44	0.39
MgO	10.61	10.16	10.22	10.67	10.65	10.71	11.09	10.71	10.50	11.09
CaO	9.31	9.45	9.30	9.34	9.64	9.81	8.79	8.68	9.18	8.68
Total	99.88	98.83	98.79	99.32	99.65	99.60	99.34	99.48	100.27	99.75
12 O										
Si	3.00	3.00	2.98	2.98	2.99	2.98	3.00	3.01	2.99	2.99
Ti	0.00	0.00	0.00	0.00	0.00	0.00	0.00	0.00	0.00	0.00
Al	1.95	1.95	1.97	1.97	1.95	1.98	1.96	1.95	1.95	1.98
Cr	0.00	0.00	0.00	0.00	0.00	0.00	0.00	0.00	0.00	0.00
Fe^{2+}	1.11	1.12	1.13	1.10	1.09	1.06	1.09	1.13	1.14	1.09
Mn	0.02	0.03	0.02	0.02	0.02	0.02	0.02	0.02	0.03	0.02
Mg	1.19	1.15	1.16	1.20	1.20	1.20	1.25	1.20	1.17	1.24
Ca	0.75	0.77	0.76	0.76	0.78	0.79	0.71	0.70	0.74	0.70
Total	8.03	8.02	8.03	8.04	8.03	8.03	8.02	8.02	8.03	8.02
End-members										
Prp	38.66	37.59	37.70	38.99	38.80	39.15	40.67	39.38	38.10	40.64
Grs	24.39	25.14	24.67	24.52	25.25	25.78	23.16	22.93	23.95	22.87
Alm	36.17	36.44	36.85	35.76	35.22	34.50	35.52	36.93	37.05	35.68
Spss	0.78	0.82	0.78	0.73	0.73	0.57	0.66	0.77	0.90	0.81
FM	0.483	0.493	0.493	0.478	0.476	0.469	0.466	0.485	0.494	0.468

Table D.1: Representative Electron Microprobe analyses of garnet cores. Analyses normalized to 12 oxygens. All Fe is assumed to be Fe^{2+}. P–T? indicates analyses used in calculation of M1 or M2 P–T conditions. c=core; Prp=pyrope; Grs=grossular; Alm=almandine; Spss=spessartine. FM=$Fe^{2+}/(Fe^{2+} + Mg)$.

Mineral	Grt									
No.	16	142	1034	1053	1125	1152	10	11	15	5
Setting	r	r	r	r	r	r	r	r	r	r
P–T?					M2					
SiO_2	39.44	39.22	39.25	38.98	39.24	39.48	39.42	39.73	39.35	39.37
TiO_2	0.03	0.00	0.04	0.00	0.05	0.07	0.00	0.02	0.00	0.02
Al_2O_3	21.69	21.55	21.82	21.84	21.90	21.87	21.71	21.96	21.68	22.01
Cr_2O_3	0.01	0.03	0.08	0.01	0.05	0.06	0.02	0.00	0.01	0.00
FeO	19.73	20.44	20.68	20.57	20.33	20.46	20.80	20.28	20.91	19.20
MnO	0.48	0.71	0.64	0.54	0.57	0.50	0.61	0.49	0.62	0.49
MgO	9.81	9.32	9.95	10.17	10.95	10.61	10.87	10.90	9.88	10.49
CaO	8.57	7.48	6.27	6.28	6.10	7.00	5.84	6.57	7.38	7.87
Total	99.75	98.75	98.72	98.40	99.19	100.06	99.27	99.97	99.83	99.45
12 O										
Si	3.00	3.01	3.01	3.00	2.99	2.99	3.00	3.00	2.99	2.99
Ti	0.00	0.00	0.00	0.00	0.00	0.00	0.00	0.00	0.00	0.00
Al	1.94	1.95	1.97	1.98	1.96	1.95	1.95	1.95	1.94	1.97
Cr	0.00	0.00	0.01	0.00	0.00	0.00	0.00	0.00	0.00	0.00
Fe^{2+}	1.25	1.31	1.32	1.32	1.29	1.29	1.32	1.28	1.33	1.22
Mn	0.03	0.05	0.04	0.04	0.04	0.03	0.04	0.03	0.04	0.03
Mg	1.11	1.07	1.14	1.16	1.24	1.20	1.23	1.23	1.12	1.19
Ca	0.70	0.62	0.51	0.52	0.50	0.57	0.48	0.53	0.60	0.64
Total	8.03	8.01	8.00	8.01	8.03	8.03	8.02	8.02	8.03	8.03
End-members										
Prp	35.91	35.08	37.66	38.32	40.44	38.71	40.13	39.95	36.22	38.55
Grs	22.56	20.23	17.05	17.01	16.21	18.36	15.50	17.32	19.46	20.81
Alm	40.54	43.17	43.92	43.51	42.15	41.89	43.08	41.70	43.02	39.61
Spss	0.99	1.53	1.37	1.16	1.20	1.04	1.28	1.02	1.29	1.03
FM	0.530	0.550	0.537	0.532	0.510	0.518	0.518	0.510	0.543	0.506

Table D.2: Representative Electron Microprobe analyses of garnet rims. Analyses normalized to 12 oxygens. All Fe is assumed to be Fe^{2+}. *P–T*? indicates analyses used in calculation of M1 or M2 *P–T* conditions. r=rim; Prp=pyrope; Grs=grossular; Alm=almandine; Spss=spessartine. FM=$Fe^{2+}/(Fe^{2+} + Mg)$.

Mineral	Omph in Grt									
No.	40	49	16	38	41	56	50	66	47	46
Setting	i	i	i	i	i	i	i	i	i	i
P–T?										M1
SiO_2	54.01	54.26	54.09	54.21	54.29	54.50	54.61	55.72	55.62	55.73
TiO_2	0.12	0.07	0.09	0.11	0.08	0.10	0.07	0.01	0.02	0.03
Al_2O_3	10.58	10.60	10.27	10.78	10.57	10.58	10.92	10.09	10.55	10.71
Cr_2O_3	0.02	0.01	0.00	0.03	0.03	0.02	0.04	0.05	0.02	0.03
FeO	3.94	4.36	3.99	3.96	3.85	3.73	3.54	3.03	2.81	2.77
MnO	0.04	0.04	0.03	0.05	0.05	0.04	0.03	0.02	0.02	0.04
MgO	10.46	10.34	10.47	10.20	10.45	10.36	10.08	10.39	10.04	10.09
CaO	16.63	16.07	16.47	16.31	16.14	16.35	15.85	15.73	15.00	14.95
Na_2O	4.52	4.84	4.56	4.81	4.68	4.82	5.11	5.50	5.86	5.81
Total	100.32	100.58	99.96	100.46	100.14	100.49	100.26	100.54	99.93	100.16
4 Cat.										
Si	1.93	1.93	1.94	1.93	1.94	1.94	1.94	1.97	1.97	1.97
Ti	0.00	0.00	0.00	0.00	0.00	0.00	0.00	0.00	0.00	0.00
Al^{IV}	0.07	0.07	0.06	0.07	0.06	0.06	0.06	0.03	0.03	0.03
Al^{VI}	0.37	0.37	0.37	0.38	0.38	0.38	0.40	0.39	0.41	0.42
Cr	0.00	0.00	0.00	0.00	0.00	0.00	0.00	0.00	0.00	0.00
Fe^{2+}	0.11	0.10	0.12	0.10	0.11	0.10	0.10	0.07	0.07	0.08
Fe^{3+}	0.01	0.03	0.00	0.01	0.00	0.01	0.01	0.02	0.02	0.01
Mn	0.00	0.00	0.00	0.00	0.00	0.00	0.00	0.00	0.00	0.00
Mg	0.56	0.55	0.56	0.54	0.56	0.55	0.53	0.55	0.53	0.53
Ca	0.64	0.61	0.63	0.62	0.62	0.62	0.60	0.60	0.57	0.57
Na	0.31	0.33	0.32	0.33	0.32	0.33	0.35	0.38	0.40	0.40
Total	4.00	4.00	4.00	4.00	4.00	4.00	4.00	4.00	4.00	4.00
End-members										
Q	67.56	65.45	67.37	65.65	66.54	65.72	63.72	61.71	59.14	59.55
Jd	31.89	32.25	32.28	33.20	33.46	33.54	35.77	36.65	39.19	39.80
Ae	0.55	2.29	0.35	1.15	0.00	0.74	0.51	1.64	1.67	0.65
FM	0.164	0.154	0.176	0.156	0.164	0.154	0.159	0.113	0.117	0.131

Table D.3: Representative Electron Microprobe analyses of omphacite inclusions in garnet. Analyses normalized to 4 cations. Fe^{3+} calculated on basis of ideal stoichiometry following *Robinson* (1981). *P–T*? indicates analyses used in calculation of M1 or M2 *P–T* conditions. i=inclusion; Q=quadrilateral; Jd=jadeite; Ae=aegirine. FM=$Fe^{2+}/(Fe^{2+} + Mg)$.

Mineral	Omph									
No.	60	62	64	65	68	173	174	175	1190	1165
Setting	c	c	c	c	c	c	c	c	c	c
P–T?										
SiO_2	52.78	52.19	52.87	52.74	52.66	52.77	52.69	52.36	54.23	53.55
TiO_2	0.15	0.23	0.09	0.17	0.16	0.16	0.17	0.14	0.05	0.16
Al_2O_3	9.16	8.75	8.38	8.39	8.61	8.27	8.43	8.47	8.70	9.18
Cr_2O_3	0.00	0.07	0.03	0.04	0.03	0.04	0.08	0.05	0.10	0.02
FeO	5.74	5.45	4.98	4.77	5.10	4.94	4.87	5.13	4.86	4.92
MnO	0.03	0.03	0.00	0.01	0.02	0.00	0.03	0.05	0.02	0.02
MgO	11.41	11.03	11.07	11.10	11.06	11.10	10.81	10.96	11.26	11.16
CaO	16.38	17.62	17.34	17.85	17.40	17.63	17.47	17.51	17.00	17.27
Na_2O	4.09	3.55	3.93	3.83	3.94	3.90	4.05	4.00	4.01	3.89
Total	99.74	98.90	98.71	98.90	98.98	98.80	98.62	98.68	100.22	100.17
4 Cat.										
Si	1.90	1.91	1.93	1.92	1.91	1.92	1.92	1.91	1.95	1.92
Ti	0.00	0.01	0.00	0.00	0.00	0.00	0.00	0.00	0.00	0.00
Al^{IV}	0.10	0.09	0.07	0.08	0.09	0.08	0.08	0.09	0.05	0.08
Al^{VI}	0.29	0.28	0.29	0.28	0.28	0.28	0.29	0.27	0.31	0.31
Cr	0.00	0.00	0.00	0.00	0.00	0.00	0.00	0.00	0.00	0.00
Fe^{2+}	0.09	0.12	0.10	0.09	0.09	0.09	0.08	0.07	0.13	0.12
Fe^{3+}	0.08	0.05	0.06	0.06	0.07	0.06	0.07	0.09	0.01	0.02
Mn	0.00	0.00	0.00	0.00	0.00	0.00	0.00	0.00	0.00	0.00
Mg	0.61	0.60	0.60	0.60	0.60	0.60	0.59	0.60	0.60	0.60
Ca	0.63	0.69	0.68	0.70	0.68	0.69	0.68	0.68	0.65	0.66
Na	0.29	0.25	0.28	0.27	0.28	0.28	0.29	0.28	0.28	0.27
Total	4.00	4.00	4.00	4.00	4.00	4.00	4.00	4.00	4.00	4.00
End-members										
Q	69.99	73.68	71.19	71.93	71.05	71.44	70.25	70.39	71.35	71.86
Jd	23.24	22.51	24.05	23.16	23.26	23.20	24.14	22.26	27.53	26.07
Ae	6.77	3.80	4.76	4.90	5.69	5.36	5.61	7.34	1.12	2.07
FM	0.129	0.167	0.143	0.130	0.130	0.130	0.119	0.104	0.178	0.167

Table D.4: Representative Electron Microprobe analyses of matrix omphacite cores. Analyses normalized to 4 cations. Fe^{3+} calculated on basis of ideal stoichiometry following *Robinson* (1981). *P–T*? indicates analyses used in calculation of M1 or M2 *P–T* conditions. i=inclusion; Q=quadrilateral; Jd=jadeite; Ae=aegirine. FM=$Fe^{2+}/(Fe^{2+} + Mg)$.

Mineral	Omph									
No.	61	63	66	67	69	73	78	118	1182	1179
Setting	r	r	r	r	r	r	r	r	r	r
P–T?									M2	
SiO_2	51.45	51.95	53.03	50.95	51.86	51.01	51.53	51.11	51.40	51.97
TiO_2	0.40	0.24	0.12	0.42	0.33	0.30	0.38	0.43	0.22	0.34
Al_2O_3	4.63	2.39	2.48	4.52	3.73	6.08	4.11	4.56	2.44	5.91
Cr_2O_3	0.02	0.08	0.05	0.07	0.09	0.07	0.11	0.00	0.06	0.05
FeO	5.79	5.57	5.72	6.00	5.57	6.21	5.80	5.60	6.80	5.58
MnO	0.01	0.04	0.06	0.05	0.05	0.07	0.06	0.08	0.05	0.07
MgO	13.44	14.72	14.76	13.68	14.28	13.47	14.02	13.89	14.94	13.71
CaO	22.04	22.96	22.55	22.44	22.61	21.14	22.62	22.62	21.89	21.49
Na_2O	1.23	0.80	1.02	1.05	0.99	1.47	1.09	1.04	0.60	1.55
Total	99.01	98.74	99.77	99.18	99.51	99.81	99.72	99.33	98.41	100.67
4 C										
Si	1.90	1.93	1.95	1.88	1.91	1.87	1.89	1.88	1.92	1.88
Ti	0.01	0.01	0.00	0.01	0.01	0.01	0.01	0.01	0.01	0.01
Al^{IV}	0.10	0.07	0.05	0.12	0.09	0.13	0.11	0.12	0.08	0.12
Al^{VI}	0.11	0.03	0.05	0.08	0.07	0.13	0.07	0.08	0.03	0.14
Cr	0.00	0.00	0.00	0.00	0.00	0.00	0.00	0.00	0.00	0.00
Fe^{2+}	0.12	0.09	0.11	0.10	0.10	0.10	0.09	0.09	0.13	0.10
Fe^{3+}	0.06	0.08	0.07	0.08	0.07	0.09	0.09	0.08	0.08	0.07
Mn	0.00	0.00	0.00	0.00	0.00	0.00	0.00	0.00	0.00	0.00
Mg	0.74	0.81	0.81	0.75	0.78	0.73	0.77	0.76	0.83	0.74
Ca	0.87	0.91	0.89	0.89	0.89	0.83	0.89	0.89	0.88	0.83
Na	0.09	0.06	0.07	0.08	0.07	0.10	0.08	0.07	0.04	0.11
Total	4.00	4.00	4.00	4.00	4.00	4.00	4.00	4.00	4.00	4.00
End-members										
Wo	50.26	50.22	49.18	50.97	50.25	49.80	50.96	51.21	47.65	49.87
En	42.64	44.78	44.78	43.24	44.14	44.14	43.95	43.75	45.26	44.27
Fs	7.10	5.01	6.04	5.79	5.61	6.06	5.09	5.04	7.09	5.86
Q	90.78	94.03	92.58	92.07	92.60	88.86	91.87	92.13	95.51	88.48
Jd	6.04	1.70	3.27	3.87	3.66	6.60	3.60	3.87	1.12	7.55
Ae	3.17	4.27	4.15	4.06	3.75	4.55	4.53	4.00	3.38	3.97
FM	0.143	0.101	0.119	0.118	0.113	0.121	0.104	0.103	0.135	0.117

Table D.5: Representative Electron Microprobe analyses of matrix omphacite rims. Analyses normalized to 4 cations. Fe^{3+} calculated on basis of ideal stoichiometry following *Robinson* (1981). *P–T*? indicates analyses used in calculation of M1 or M2 *P–T* conditions. i=inclusion; Wo=wollastonite; En=enstatite; Fs=ferrosilite; Q=quadrilateral; Jd=jadeite; Ae=aegirine. FM=$Fe^{2+}/(Fe^{2+} + Mg)$.

Mineral	Omph		
No.	226	230	228
Setting	'halo'	'halo'	'halo'
P–T?			
SiO_2	52.33	53.14	52.56
TiO_2	0.02	0.00	0.00
Al_2O_3	7.72	8.39	7.74
Cr_2O_3	0.07	0.05	0.08
FeO	4.24	3.81	4.09
MnO	0.04	0.03	0.01
MgO	12.87	12.30	12.75
CaO	20.72	19.69	20.47
Na_2O	2.39	2.94	2.34
Total	100.40	100.35	100.04
4 Cat.			
Si	1.88	1.91	1.90
Ti	0.00	0.00	0.00
Al^{IV}	0.12	0.09	0.10
Al^{VI}	0.21	0.26	0.23
Cr	0.00	0.00	0.00
Fe^{2+}	0.06	0.08	0.09
Fe^{3+}	0.07	0.03	0.03
Mn	0.00	0.00	0.00
Mg	0.69	0.66	0.69
Ca	0.80	0.76	0.79
Na	0.17	0.20	0.16
Total	4.00	4.00	4.00
End-members			
Wo	51.57	50.57	50.45
En	44.56	43.97	43.71
Fs	3.87	5.45	5.84
Q	82.31	78.51	82.71
Jd	13.42	19.11	15.18
Ae	4.28	2.38	2.11
FM	0.080	0.110	0.118

Table D.6: Representative Electron Microprobe analyses of matrix omphacite halos. Analyses normalized to 4 cations. Fe^{3+} calculated on basis of ideal stoichiometry following *Robinson* (1981). *P–T*? indicates analyses used in calculation of M1 or M2 *P–T* conditions. i=inclusion; Wo=wollastonite; En=enstatite; Fs=ferrosilite; Q=quadrilateral; Jd=jadeite; Ae=aegirine. FM=$Fe^{2+}/(Fe^{2+} + Mg)$.

Mineral	Opx									
No.	74	75	76	77	83	84	156	157	159	170
P–T?		M2								
SiO_2	53.28	53.13	53.27	53.47	53.04	52.84	53.66	53.01	52.66	52.95
TiO_2	0.04	0.05	0.06	0.05	0.05	0.10	0.00	0.00	0.02	0.02
Al_2O_3	1.97	1.96	1.52	1.27	2.32	2.23	0.81	1.65	1.75	1.71
Cr_2O_3	0.03	0.05	0.10	0.08	0.01	0.03	0.00	0.03	0.03	0.11
FeO	17.62	17.43	18.11	18.05	17.90	17.44	17.68	17.51	17.16	16.78
MnO	0.17	0.14	0.15	0.15	0.17	0.16	0.21	0.17	0.20	0.15
MgO	26.09	26.25	26.48	26.16	26.37	26.18	26.40	26.02	26.26	26.44
CaO	0.56	0.38	0.38	0.44	0.27	0.28	0.42	0.37	0.28	0.37
Na_2O	0.02	0.00	0.00	0.00	0.01	0.00	0.02	0.02	0.01	0.01
Total	99.77	99.39	100.07	99.66	100.14	99.25	99.20	98.77	98.35	98.54
4 Cat.										
Si	1.94	1.94	1.93	1.95	1.92	1.93	1.96	1.95	1.94	1.94
Ti	0.00	0.00	0.00	0.00	0.00	0.00	0.00	0.00	0.00	0.00
Al^{IV}	0.06	0.06	0.07	0.05	0.08	0.07	0.04	0.05	0.06	0.06
Al^{VI}	0.02	0.02	0.00	0.00	0.02	0.02	0.00	0.02	0.01	0.02
Cr	0.00	0.00	0.00	0.00	0.00	0.00	0.00	0.00	0.00	0.00
Fe^{2+}	0.49	0.49	0.48	0.51	0.48	0.49	0.50	0.50	0.48	0.48
Fe^{3+}	0.04	0.04	0.07	0.04	0.06	0.04	0.04	0.04	0.05	0.04
Mn	0.01	0.00	0.00	0.00	0.01	0.00	0.01	0.01	0.01	0.00
Mg	1.41	1.43	1.43	1.42	1.42	1.42	1.44	1.42	1.44	1.45
Ca	0.02	0.01	0.01	0.02	0.01	0.01	0.02	0.01	0.01	0.01
Na	0.00	0.00	0.00	0.00	0.00	0.00	0.00	0.00	0.00	0.00
Total	4.00	4.00	4.00	4.00	4.00	4.00	4.00	4.00	4.00	4.00
End-members										
Wo	1.13	0.78	0.77	0.89	0.55	0.57	0.84	0.74	0.57	0.75
En	73.27	73.76	74.20	73.03	74.28	73.92	73.68	73.42	74.59	74.64
Fs	25.61	25.46	25.03	26.08	25.17	25.50	25.48	25.84	24.84	24.61

Table D.7: Representative Electron Microprobe analyses of orthopyroxene. Analyses normalized to 4 cations. Fe^{3+} calculated on basis of ideal stoichiometry following *Robinson* (1981). *P–T*? indicates analyses used in calculation of M1 or M2 *P–T* conditions. i=inclusion; Wo=wollastonite; En=enstatite; Fs=ferrosilite. FM=$Fe^{2+}/(Fe^{2+} + Mg)$.

Mineral	Phn				
No.	224	225	227	2-224	2-225
Setting		i	i	i	i
P–T?	M1				
SiO_2	52.23	51.91	51.82	51.39	51.08
TiO_2	0.53	0.50	0.50	0.53	0.50
Al_2O_3	27.53	28.03	28.66	27.93	28.43
Cr_2O_3	0.06	0.05	0.08	0.07	0.05
FeO	0.90	0.90	0.91	0.89	0.90
MnO	0.00	0.01	0.04	0.00	0.00
MgO	3.61	3.50	3.35	3.55	3.44
CaO	0.02	0.00	0.02	0.02	0.00
Na_2O	0.02	0.03	0.02	0.03	0.04
K_2O	9.54	9.42	9.67	9.63	9.51
F	0.01	0.02	0.00	0.01	0.02
Cl	0.05	0.05	0.04	0.05	0.05
Total	94.49	94.41	95.11	94.09	94.02
11 O					
Si	3.46	3.44	3.41	3.42	3.40
Ti	0.03	0.02	0.02	0.03	0.02
Al	2.15	2.19	2.22	2.19	2.23
Cr	0.00	0.00	0.00	0.00	0.00
Fe^{2+}	0.05	0.05	0.05	0.05	0.05
Mn	0.00	0.00	0.00	0.00	0.00
Mg	0.36	0.35	0.33	0.35	0.34
Ca	0.00	0.00	0.00	0.00	0.00
Na	0.00	0.00	0.00	0.00	0.00
K	0.81	0.80	0.81	0.82	0.81
F	0.00	0.00	0.00	0.00	0.00
Cl	0.01	0.01	0.00	0.01	0.01
Total	6.85	6.85	6.86	6.87	6.87

Table D.8: Representative Electron Microprobe analyses of phengite. Analyses normalized to 11 oxygens. *P–T*? indicates analyses used in calculation of M1 or M2 *P–T* conditions. i=inclusion.

Mineral	Bt									
No.	54	54	57	58	85	86	90	91	107	108
P–T?								M2		
SiO_2	37.36	37.06	36.78	36.54	37.03	36.86	36.78	36.94	36.86	36.84
TiO_2	4.87	5.02	4.37	5.28	4.37	4.30	4.27	4.24	5.07	5.11
Al_2O_3	15.14	15.17	14.86	15.33	15.27	15.11	15.17	15.23	15.47	15.07
Cr_2O_3	0.00	0.00	0.07	0.03	0.13	0.09	0.09	0.08	0.07	0.03
FeO	9.62	9.82	10.11	9.93	10.04	9.75	10.16	10.23	10.29	10.18
MnO	0.00	0.00	0.00	0.00	0.00	0.00	0.00	0.00	0.02	0.03
MgO	17.11	17.80	17.27	17.09	17.52	17.68	17.50	17.43	16.96	17.02
CaO	0.00	0.00	0.00	0.02	0.00	0.01	0.05	0.06	0.01	0.00
Na_2O	0.17	0.18	0.06	0.13	0.08	0.05	0.09	0.10	0.11	0.14
K_2O	8.29	8.90	9.58	8.92	9.65	9.22	9.58	9.66	8.95	9.46
F	0.11	0.11	0.11	0.05	0.13	0.11	0.16	0.18	0.07	0.07
Cl	0.07	0.07	0.07	0.05	0.06	0.07	0.08	0.07	0.05	0.06
Total	92.73	94.11	93.29	93.36	94.28	93.25	93.91	94.22	93.92	94.01
11 O										
Si	2.78	2.73	2.75	2.72	2.74	2.75	2.74	2.74	2.73	2.74
Ti	0.27	0.28	0.25	0.30	0.24	0.24	0.24	0.24	0.28	0.29
Al	1.33	1.32	1.31	1.34	1.33	1.33	1.33	1.33	1.35	1.32
Cr	0.00	0.00	0.00	0.00	0.01	0.01	0.01	0.00	0.00	0.00
Fe^{2+}	0.60	0.61	0.63	0.62	0.62	0.61	0.63	0.64	0.64	0.63
Mn	0.00	0.00	0.00	0.00	0.00	0.00	0.00	0.00	0.00	0.00
Mg	1.90	1.96	1.93	1.90	1.93	1.97	1.94	1.93	1.87	1.88
Ca	0.00	0.00	0.00	0.00	0.00	0.00	0.00	0.00	0.00	0.00
Na	0.02	0.03	0.01	0.02	0.01	0.01	0.01	0.01	0.02	0.02
K	0.79	0.84	0.92	0.85	0.91	0.88	0.91	0.91	0.85	0.90
F	0.02	0.02	0.03	0.01	0.03	0.03	0.04	0.04	0.02	0.02
Cl	0.01	0.01	0.01	0.01	0.01	0.01	0.01	0.01	0.01	0.01
Total	7.72	7.79	7.84	7.76	7.84	7.82	7.86	7.87	7.76	7.80
FM	0.240	0.237	0.246	0.246	0.243	0.236	0.245	0.249	0.255	0.251

Table D.9: Representative Electron Microprobe analyses of biotite. Analyses normalized to 11 oxygens. All Fe assumed to be Fe^{2+}. *P–T*? indicates analyses used in calculation of M1 or M2 *P–T* conditions. FM=$Fe^{2+}/(Fe^{2+} + Mg)$.

Mineral	Hbl									
No.	70	71	87	111	113	1224	1225	1229	1292	1293
Setting	m	m	m	m	m	i	i	i	i	i
P–T?	M2									
SiO_2	42.92	43.93	43.70	43.08	43.20	43.82	43.99	43.70	43.63	43.51
TiO_2	2.01	1.82	1.61	1.80	1.88	0.19	0.16	0.18	0.24	0.20
Al_2O_3	12.67	12.32	11.97	12.46	12.43	16.78	16.42	17.22	16.79	16.69
Cr_2O_3	0.04	0.03	0.11	0.05	0.07	0.08	0.13	0.13	0.16	0.07
FeO	9.21	8.98	9.09	9.52	8.87	7.33	7.52	7.47	7.43	7.60
MnO	0.02	0.00	0.03	0.05	0.06	0.00	0.02	0.02	0.04	0.02
MgO	14.60	14.99	15.04	14.69	14.70	14.74	14.50	14.28	14.27	14.06
CaO	11.61	12.05	11.65	11.61	11.69	11.75	11.98	11.90	11.82	12.13
Na_2O	2.23	2.17	2.13	2.24	2.21	2.72	2.74	2.79	2.69	2.81
K_2O	1.14	0.99	0.95	1.14	1.05	0.17	0.16	0.13	0.15	0.16
F	0.07	0.08	0.10	0.01	0.06	0.15	0.14	0.11	0.09	0.07
Cl	0.06	0.06	0.06	0.06	0.06	0.01	0.01	0.01	0.00	0.01
Total	96.59	97.42	96.43	96.70	96.27	97.72	97.76	97.95	97.31	97.33
23 O										
Si	6.28	6.37	6.37	6.29	6.33	6.20	6.25	6.19	6.21	6.23
Ti	0.22	0.20	0.18	0.20	0.21	0.02	0.02	0.02	0.03	0.02
Al^{IV}	1.72	1.63	1.63	1.71	1.67	1.80	1.75	1.81	1.79	1.77
Al^{VI}	0.46	0.47	0.43	0.43	0.48	1.00	1.00	1.06	1.03	1.05
Cr	0.00	0.00	0.01	0.01	0.01	0.01	0.02	0.01	0.02	0.01
Fe^{2+}	0.79	0.86	0.69	0.76	0.81	0.44	0.62	0.59	0.58	0.78
Fe^{3+}	0.33	0.23	0.42	0.40	0.27	0.42	0.27	0.30	0.30	0.13
Mn	0.00	0.00	0.00	0.01	0.01	0.00	0.00	0.00	0.00	0.00
Mg	3.18	3.24	3.27	3.20	3.21	3.11	3.07	3.01	3.03	3.00
Ca	1.82	1.87	1.82	1.81	1.84	1.78	1.82	1.81	1.80	1.86
Na	0.63	0.61	0.60	0.63	0.63	0.74	0.75	0.76	0.74	0.78
K	0.21	0.18	0.18	0.21	0.20	0.03	0.03	0.02	0.03	0.03
F	0.03	0.04	0.05	0.00	0.03	0.07	0.06	0.05	0.04	0.03
Cl	0.01	0.01	0.02	0.02	0.01	0.00	0.00	0.00	0.00	0.00
Total	15.71	15.71	15.66	15.68	15.70	15.62	15.67	15.64	15.61	15.70
FM	0.199	0.210	0.174	0.192	0.201	0.124	0.168	0.164	0.161	0.206

Table D.10: Representative Electron Microprobe analyses of hornblende. Analyses normalized to 23 oxygens with Fe^{3+} estimated following *Leake et al.* (1997) assuming a sum of 13 cations (excluding Ca, Na, and K), using the PROBE-AMPH spreadsheet of *Tindle and Webb* (1994). *P–T*? indicates analyses used in calculation of M1 or M2 *P–T* conditions. FM=$Fe^{2+}/(Fe^{2+} + Mg)$.

Mineral	Pl									
No.	48	49	79	89	112	1234	1235	1248	1274	1280
Setting	c	c	c	c	c	c	c	c	c	c
SiO_2	61.35	60.37	60.65	61.19	62.30	61.40	61.53	62.75	62.25	61.46
Al_2O_3	23.09	23.50	23.70	23.25	22.52	24.42	23.84	23.29	22.83	23.25
FeO	0.13	0.15	0.15	0.14	0.06	0.27	0.14	0.24	0.11	0.25
CaO	4.80	5.40	5.33	4.98	3.95	5.96	5.50	4.65	4.52	5.14
Na_2O	7.60	7.90	8.10	7.90	8.30	7.84	7.96	8.63	8.55	8.33
K_2O	0.42	0.30	0.25	0.20	0.32	0.29	0.34	0.34	0.29	0.26
Total	97.39	97.62	98.19	97.67	97.46	100.17	99.31	99.90	98.55	98.69
8 O										
Si	2.78	2.74	2.74	2.77	2.82	2.72	2.75	2.78	2.79	2.76
Al	1.23	1.26	1.26	1.24	1.20	1.28	1.25	1.22	1.21	1.23
Fe	0.00	0.01	0.01	0.01	0.00	0.01	0.01	0.01	0.00	0.01
Ca	0.23	0.26	0.26	0.24	0.19	0.28	0.26	0.22	0.22	0.25
Na	0.67	0.70	0.71	0.69	0.73	0.67	0.69	0.74	0.74	0.73
K	0.02	0.02	0.01	0.01	0.02	0.02	0.02	0.02	0.02	0.01
Total	4.95	4.98	4.99	4.96	4.96	4.98	4.98	4.99	4.98	4.99
End-members										
An	25.18	26.96	26.29	25.52	20.39	29.07	27.09	22.47	22.23	25.06
Ab	72.17	71.29	72.25	73.24	77.63	69.23	70.92	75.59	76.09	73.44
Or	2.64	1.75	1.47	1.24	1.97	1.70	1.98	1.94	1.68	1.50

Table D.11: Representative Electron Microprobe analyses of plagioclase cores. Analyses normalized to 8 oxygens. An=anorthite; Ab=albite; Or=orthoclase.

Mineral	Pl									
No.	1237	1240	1243	1244	1245	1246	1252	1267	1278	1283
Setting	r	r	r	r	r	r	r	r	r	r
P–T?						M2				
SiO_2	60.34	60.34	61.02	59.89	60.41	59.35	57.94	58.83	59.43	59.28
Al_2O_3	24.80	24.07	24.45	25.14	24.59	25.49	25.36	25.21	24.67	24.74
FeO	0.73	0.43	0.34	0.29	0.32	0.39	0.78	0.23	0.25	0.47
CaO	6.61	5.81	6.15	6.86	6.30	7.38	7.44	7.27	6.78	6.98
Na_2O	7.40	7.18	8.00	7.57	7.62	7.27	6.74	7.15	6.76	7.36
K_2O	0.21	0.26	0.26	0.13	0.17	0.19	0.13	0.15	0.19	0.21
Total	100.09	98.08	100.20	99.87	99.40	100.06	98.39	98.83	98.07	99.04
8 O										
Si	2.69	2.73	2.71	2.67	2.70	2.65	2.63	2.66	2.69	2.67
Al	1.30	1.28	1.28	1.32	1.30	1.34	1.36	1.34	1.32	1.31
Fe	0.03	0.02	0.01	0.01	0.01	0.01	0.03	0.01	0.01	0.02
Ca	0.32	0.28	0.29	0.33	0.30	0.35	0.36	0.35	0.33	0.34
Na	0.64	0.63	0.69	0.65	0.66	0.63	0.59	0.63	0.59	0.64
K	0.01	0.01	0.01	0.01	0.01	0.01	0.01	0.01	0.01	0.01
Total	4.99	4.95	5.00	5.00	4.98	5.00	4.99	4.99	4.95	5.00
End-members										
An	32.66	30.41	29.39	33.13	31.03	35.56	37.62	35.64	35.23	33.96
Ab	66.12	68.00	69.16	66.12	67.95	63.37	61.61	63.50	63.57	64.83
Or	1.22	1.59	1.46	0.75	1.02	1.06	0.78	0.86	1.19	1.21

Table D.12: Representative Electron Microprobe analyses of plagioclase rims. Analyses normalized to 8 oxygens. *P–T*? indicates analyses used in calculation of M1 or M2 *P–T* conditions. An=anorthite; Ab=albite; Or=orthoclase.

UHP domain	Nordfjord	Nordfjord	Nordøyane	Nordøyane
Location	Nordfjord	Drage	Fjørtoft	Harøya
Sample	Y1614B	Drage	1066b	JB10-99
Source	Y07	RT04	T00	This study
Activities				
Grt				
py	0.068	0.138	0.25	0.124
gr	0.053	0.047	0.133	0.049
Cpx				
di	0.42	0.55	0.67	0.5
Ms				
mu	0.45	0.37	0.43	0.47
cel	0.18	0.25	0.22	0.18
Other	coe ky	coe ky	coe ky	coe ky
Mode 3 (Fe-excluded)				
T (°C)	717	653	822	757
s.d.(T)	77	54	61	73
P (GPa)	3.12	3.16	3.48	2.96
s.d.(P)	0.38	0.31	0.29	0.35
correl.	0.573	0.551	0.263	0.456
No. reactions	4	4	4	4
RT04 (Fe-excluded)				
T (°C)	765	732	849	814
P (GPa)	3.21	3.49	3.16	3.25

Table D.13: End-member activities and summary of *P–T* calculations for selected garnet-omphacite-kyanite-phengite-coesite eclogites from the WGR. Mineral analyses from *Young et al.* (2007) (Y07); *Ravna and Terry* (2004) (RT04); and *Terry et al.* (2000) (T00). End-member abbreviations are those used by THERMOCALC: py=pyrope; gr=grossular; di=diopside; mu=muscovite; cel=celadonite. THERMOCALC Mode 3 results used the Fe-excluded approach outlined in the text. RT04 results were calculated following the Fe-excluded approach using the expressions of *Ravna and Terry* (2004). See Fig. 5.1 for sample locations.

Appendix E

Copyright Agreement Forms

May 23, 2013

Copyright Permissions
GSA
PO Box 9140
Boulder, CO 80301-9140
USA

I am preparing my PhD thesis for submission to the Faculty of Graduate Studies at Dalhousie University, Halifax, Nova Scotia, Canada. I am seeking your permission to include a manuscript version of the following paper(s) as a chapter in the thesis:

Crustal emplacement of exhuming (ultra)high-pressure rocks: Will that be pro- or retro-side?

by J. P. Butler, C. Beaumont, and R. A. Jamieson

Geology, 39 (7) , 635–638, 2011

Canadian graduate theses are reproduced by the Library and Archives of Canada (formerly National Library of Canada) through a non-exclusive, world-wide license to reproduce, loan, distribute, or sell theses. I am also seeking your permission for the material described above to be reproduced and distributed by the LAC(NLC). Further details about the LAC(NLC) thesis program are available on the LAC(NLC) website (www.nlc-bnc.ca).

Full publication details and a copy of this permission letter will be included in the thesis.

Yours sincerely,

Jared P. Butler

Permission is granted for:

a) the inclusion of the material described above in your thesis.

b) for the material described above to be included in the copy of your thesis that is sent to the Library and Archives of Canada (formerly National Library of Canada) for reproduction and distribution.

Name: JEANETTE HAMMANN Title: Associate Director, Publications

Signature: _____ Date: _____

Dear Jared Butler,

Thank you for your email request.

Permission is granted for you to use the material requested for your thesis/dissertation subject to the usual acknowledgements and on the understanding that you will reapply for permission if you wish to distribute or publish your thesis/dissertation commercially.

Permission is granted solely for use in conjunction with the thesis, and the article may not be posted online separately.

Any third party material is expressly excluded from this permission. If any material appears within the article with credit to another source, authorisation from that source must be obtained.

Best Wishes,

Verity Butler
Permissions Co-ordinator

Wiley
The Atrium, Southern Gate
Chichester, PO19 8SQ
UK
www.wiley.com
vbutler@wiley.com

WILEY

To view this email as a web page, go here.

Do Not Reply Directly to This Email

To ensure that you continue to receive our emails,
please add rightslink@marketing.copyright.com to your address book.

RightsLink | Copyright Clearance Center

Thank You For Your Order!

Dear Jared Butler,

Thank you for placing your order through Copyright Clearance Center's RightsLink service. Elsevier has partnered with RightsLink to license its content. This notice is a confirmation that your order was successful.

Your order details and publisher terms and conditions are available by clicking the link below:
http://s100.copyright.com/CustomerAdmin/PLF.jsp?ref=fa6e1569-9d19-498b-8845-153ade3a63fe

Order Details
Licensee: Jared P Butler
License Date: Aug 9, 2013
License Number: 3204861346450
Publication: Earth and Planetary Science Letters
Title: The Alps 1: A working geodynamic model for burial and exhumation of (ultra)high-pressure rocks in Alpine-type orogens
Type Of Use: reuse in a thesis/dissertation
Total: 0.00 USD

To access your account, please visit https://myaccount.copyright.com.

Please note: Online payments are charged immediately after order confirmation; invoices are issued daily and are payable immediately upon receipt.

To ensure we are continuously improving our services, please take a moment to complete our customer satisfaction survey.

B.1:v4.2

+1-877-622-5543 / Tel: +1-978-646-2777

This email was sent to: **butlerjp@dal.ca**